
MECHANICS OF THE 21ST CENTURY

MECHANICS OF THE 21ST CENTURY
21st International Congress
of Theoretical and Applied Mechanics

Edited by

WITOLD GUTKOWSKI

TOMASZ A. KOWALEWSKI

Institute of Fundamental Technological Research, Polish Academy of Sciences

Kluwer Academic Publishers
Boston/Dordrecht/London

Contents

Committees	viii
Preface	ix
Acknowledgments	xi
Exhibitors	xii
Congress Statistics	xiii
Opening Ceremony	xv
Closing Ceremony	xxiii
Scientific Program	xxx
Interplay between Air and Water <i>Leen van Wijngaarden</i>	1
Stochastic Dynamics of Engineering Systems <i>Kazimierz Sobczyk</i>	19
Multibody Dynamics: Bridging for Multidisciplinary Applications <i>Jorge A.C. Ambrósio</i>	61
Rapid Formation of Strong Gradients and Diffusion in the Transport of Scalar and Vector Fields <i>Konrad Bajer</i>	89
Wave-Vortex Interactions in the Atmosphere, and Climate Prediction <i>Onno Bokhove</i>	103
Near-critical Point Hydrodynamics and Microgravity <i>Daniel A. Beysens</i>	117
Flaw Tolerant Nanostructures of Biological Materials <i>Huajian Gao, Baohua Ji, Markus J. Buehler, and Haimin Yao</i>	131

Transport and Mixing in the Atmosphere <i>Peter H. Haynes</i>	139
Variational and Multiscale Methods in Turbulence <i>Thomas J. R. Hughes, Victor M. Calo, and Guglielmo Scovazzi</i>	153
Mechanics of Thin Film Structures <i>Henrik M. Jensen</i>	165
Nonlinear Dynamics in Ocean Engineering <i>Edwin J. Kreuzer and Wolfgang M. Sichermann</i>	173
A Bridge between the Micro- and Mesomechanics of Laminates: Fantasy or Reality? <i>Pierre Ladevèze</i>	187
Turbulence and Large-Eddy Simulations <i>Marcel R. Lesieur</i>	203
Nano Mechanical Analysis of IFM Force Profiles on Self-Assembled Monolayers <i>Mingji Wang, Kenneth M. Liechti, Vibha Srinivasan, John M. White, and Peter J. Rosky</i>	217
Collisional Granular Flows with and without Gas Interactions in Microgravity <i>Michel Y. Louge and Haitao Xu</i>	229
Probability Phenomena in Perturbed Dynamical Systems <i>Anatoly Neishtadt</i>	241
Mechanics of Rubberlike Solids <i>Ray W. Ogden</i>	263
Elastic Wave Propagation Development for Structural Health Monitoring <i>Wiesław Ostachowicz</i>	275
On the Damping of a Piezoelectric Truss <i>André Preumont</i>	287
Strength of Nanostructures <i>Rodney S. Ruoff and Nicola M. Pugno</i>	303
Micromechanics of Cells <i>Erich Sackmann, Andreas Reuther, and Doris Heinrich</i>	313
Elastic Interactions of Biological Cells <i>Samuel A. Safran, A. Nicolas and U.S. Schwarz</i>	329

<i>Contents</i>	vii
Electrokinetic Flow Instabilities in Microfluidic Systems <i>Hao Lin, Michael H. Oddy and Juan G. Santiago</i>	343
Molecular Mechanics of Cytoskeletal Components <i>M. Atakhorrami, K.M. Addas, M. Buchanan, G.H. Koenderink F.C. MacKintosh, J.X. Tang, Christoph F. Schmidt</i>	355
Topics in Astrophysical Fluid Dynamics <i>Edward A. Spiegel</i>	365
Miniaturization of Explosive Technology and Microdetonics <i>D. Scott Stewart</i>	379
Foams in Microgravity <i>Denis Weaire and Simon Cox</i>	387
Author Index	395

21ST INTERNATIONAL CONGRESS OF THEORETICAL AND APPLIED
MECHANICS

**President and Chairman of
Local Organizing Committee**

Witold Gutkowski

Co-Chairmen

Michał Kleiber
Włodzimierz Kurnik

Secretary-General

Tomasz A. Kowalewski

Members of Local Organizing Committee

Konrad Bajer (Warszawa)	Wojciech Pietraszkiewicz (Gdańsk)
Romuald Będziński (Wrocław)	Stanisław Radkowski (Warszawa)
Tadeusz Burczyński (Gliwice)	Czesław Rymarz (Warszawa)
Tadeusz Chmielniak (Gliwice)	Kazimierz Sobczyk (Warszawa)
Krzysztof Doliński (Warszawa)	Jarosław Stefaniak (Poznań)
Stanisław Drobniak (Częstochowa)	Jacek Stupnicki (Warszawa)
Józef Giergiel (Kraków)	Andrzej Styczek (Warszawa)
Stanisław Kocańda (Warszawa)	Gwidon Szefer (Kraków)
Józef Kubik (Bydgoszcz)	Eugeniusz Świtoński (Gliwice)
Zenon Mróz (Warszawa)	Andrzej Tylikowski (Warszawa)
Józef Nizioł (Kraków)	Zenon Waszczyszyn (Kraków)
Wojciech Nowacki (Warszawa)	Zbigniew Wesółowski (Kielce)
Janusz Orkisz (Kraków)	Władysław Włosiński (Warszawa)
Andrzej Palczewski (Warszawa)	Czesław Woźniak (Częstochowa)
Piotr Perzyna (Warszawa)	Henryk Zorski (Warszawa)
Henryk Petryk (Warszawa)	Michał Życzkowski (Kraków)

Members of the IUTAM Congress Committee

Hassan Aref (USA) <i>member of XCCC</i>	Yu Ku (USA)
Ted Belytschko (USA) <i>representative of IACM</i>	Gary Leal (USA) representative of ICR
Martin Bendsoe (Denmark) <i>representative of ISSMO</i>	Peter Lugner (Austria) <i>representative of IAVSD</i>
Dimitri Beskos (Greece)	Fernando Lund (Chile)
David Bogy (USA)	Keith Moffatt (UK) <i>Chairman, member of XCCC</i>
Dick van Campen (Netherlands)	Peter Monkewitz (Switzerland)
David Durban (Israel)	Rene Moreau (France) <i>member of XCCC,</i>
Fernand Ellyin (Canada) <i>representative of ICM</i>	<i>representative of HYDROMAG</i>
Juri Engelbrecht (Estonia)	Niels Olhoff (Denmark) <i>member of XCCC</i>
Norman Fleck (UK)	Timothy Pedley (UK) <i>Secretary, member of XCCC</i>
Ben Freund (USA)	Bernhard Schrefler (Italy) <i>member of XCCC</i>
Graham Gladwell (Canada)	Kazimierz Sobczyk (Poland)
Peter Gudmundson (Sweden)	Pierre Suquet (France)
Michael Hayes (Ireland) <i>representative of ISIMM</i>	Ernst Tuck (Australia)
Tsutomu Kambe (Japan)	Manuel Velarde (Italy) <i>representative of CISM</i>
Bhushan Karihaloo (UK) <i>representative of ICF</i>	Eiichi Watanabe (Japan)
Alfred Kluwick (Austria)	Feng-Gan Zhuang (China)
Valery Kozlov (Russia)	
Edwin Kreuzer (Germany)	

Preface

The 21st International Congress of Theoretical and Applied Mechanics (ICTAM04) took place August 15 – 21, 2004, in Warsaw, Poland. It was organized by Polish National Committee of IUTAM, Institute of Fundamental Technological Research of the Polish Academy of Sciences (IPPT PAN) and Warsaw University of Technology. The Congress venue was the main building of Warsaw University of Technology.

The idea of congresses devoted to mechanics, can be traced back to a conference on problems of fluid mechanics in Innsbruck, 1922. It was organized by four individuals, whose names, are and will, remain very well known to next generations of scientists, C. W. Oseen, T. Levi-Civite, T. von Kármán, and L. Prandtl. This conference was so fruitful, that the organizers decided to arrange similar meetings in the future, every four years, and to extend the scope of the future meetings to include solid mechanics. Hence a series of meetings started eighty years ago with the 1st ICTAM held in Delft, Netherlands.

From the meetings of the Congress Committee sprang the idea of a more permanent organization to look out for the world interests in the mechanical sciences. Thus, IUTAM, the International Union of Theoretical and Applied Mechanics, was formed on September 26, 1946. In 1947 IUTAM became a member of ICSU, the International Council of Scientific Unions, itself founded in 1931. The highest authority of IUTAM is the General Assembly, with delegates from the Adhering Organizations, each of which is affiliated with a national learned society in a given country.

Scientific Program

Contemporary mechanics poses both, the fundamental problems from the area of pure science, and its strong links with modern technology. It spreads over such areas of our knowledge as oceanography, physical chemistry, biology, medicine, geophysics and astrophysics. Hence, any conclusions deduced in the framework of mechanics, are likely to have

a value for other fields. We may easily find prove of it in the scientific program of the ICTAM04. It consists of plenary opening and closing lectures, sectional lectures, mini-symposia, and contributed papers presented in lecture and seminar presentation sessions. These were intended to cover all aspects of mechanics.

All contributed papers were peer reviewed. Recommendations had been received from Pre-selection Committees of the National Committees of the nine countries: Canada, France, Germany, Japan, PR China, Poland, Russia, UK and USA. Moreover, recommendations had been received from the Chairs of the Mini-Symposia and of the Pre-nominated Sessions with classifications of the papers submitted within the topics of their Symposia/Sessions. Finally, the International Papers Committee paid careful attention to the above recommendations. Accordingly, of the 2086 eligible submissions 1574 contributions were invited by the IPC for their presentation. The total number of submitted and accepted papers represents a quite substantial enhancement relative to the previous congresses, providing evidence of vitality of the contemporary mechanics.

This volume of Proceedings consists of a book with full texts of invited talks and attached CD-ROM with Extended Summaries of 1225 papers presented during the Congress by authors¹. We have tried to assemble the paper volume with an extensive index of names and papers collected on the CD-ROM. We hope that this volume – pre-ordered at the Congress in record numbers – will be found useful not only as a document of the event but to assess achievements and new paths of research in mechanics of 21st Century.

W. GUTKOWSKI

T.A. KOWALEWSKI

¹From 1273 papers presented during the Congress we exclude multiple presentations and those given by proxy.

Acknowledgments

We would like to express our thanks to our colleagues from the IUTAM Congress Committee, and from the International Papers Committee. Their advice and efforts have helped us to overcome some problems, connected, as usual, with the organization of world-wide meetings.

Special gratitude goes to the Chairs responsible for Mini-Symposiums and Pre-nominated Sessions. Their work in organizing sessions, encouraging papers submission in the area of interest, and later reviewing all papers cannot be overestimated. Smilingly, we are deeply indebted to members of the nine National Committees for their valuable contribution to the reviewing procedure.

The organization and execution of the Congress was performed by the Institute of Fundamental Technological Research of Polish Academy of Sciences and Warsaw University of Technology. The detailed work of organization was due to many persons from both institutions, personnel of PCO Mazurkas Travel as well as numerous external co-workers. Without their extremely valuable help organization of such meeting would be impossible. Thank you all so much!

W. GUTKOWSKI

T.A. KOWALEWSKI

Exhibitors

- Cambridge University Press
- Dantec Dynamics
- EDEN
- Elsevier
- Era Business
- Intelligent Laser Applications
- International Publishing Service
- Institute of Fundamental Technological Research of Polish Academy of Sciences
- Kluwer
- Polish Tourist Organisation
- Springer
- Strategic Test Scandinavia
- Testlab

Congress Statistics

A detailed list of ICTAM04 participants is enclosed on the CD-ROM. Here, for brevity, we give the basic statistics of the Congress.

The total number of pre-registered to ICTAM04 participants was 2928. The Congress organizers received 2245 abstracts of contributed papers before the final deadline of January 16, 2004. Not all abstracts were followed by an extended summary. Hence, the International Papers Committee invited 1574 contributions reviewing 2186 submitted extended summaries. Finally 1235 contributed papers and 38 invited talks were given in Warsaw.

Fluid Mechanics was a subject of 550 presentations, Solid Mechanics was selected as a subject of 611 presentations, and 112 contributions aimed to cover problems involving both areas of mechanics and education in mechanics. The total number of participants, accepted papers and presentations represent a quite substantial enhancement relative to the previous congresses (Table 1), providing evidence of vitality of the contemporary mechanics. Table 2 displays briefly country statistics of the participants and presentations.

Table 1. ICTAM04 compared with four previous congresses

ICTAM	Submitted Papers	Presented papers/ presented from organizers country		Participants/ participants from organizers country	
Grenoble 1988	1262	573	n. a.	951	340
Haifa 1992	1183	420	n. a.	525	85
Kyoto 1996	1642	703	192	936	332
Chicago 2000	1953	1126	445	1430	587
Warsaw 2004	2245 (2186)	1273	144	1515	194

Table 2. ICTAM04 country statistics

	Country	Participants	Presentations	Invited lectures
1	USA	204	185	15
2	Poland	194	144	3
3	France	170	153	5
4	Germany	118	100	3
5	UK	107	98	2
6	Japan	89	72	
7	Russia	79	75	1
8	China	54	41	
9	Netherlands	43	38	3
10	Ukraine	38	36	
11	Israel	37	27	1
12	Denmark	30	21	1
13	Italy	25	19	
14	Belgium	19	15	2
15	Canada	19	13	
16	S. Korea	19	17	
17	Austria	18	15	
18	Sweden	18	11	
19	Taiwan	18	15	
20	Czech Republic	17	14	
21	Spain	14	14	
22	Brazil	13	11	
23	Finland	12	7	
24	India	12	11	
25	Switzerland	12	9	
26	Australia	10	7	
27	Hungary	10	10	
28	Greece	9	9	

	Country	Participants	Presentations	Invited lectures
29	Portugal	9	8	1
30	Estonia	8	8	
31	Iran	8	8	
32	Norway	8	6	
33	Bulgaria	7	5	
34	Ireland	7	4	
35	Latvia	7	5	
36	South Africa	7	4	
37	Romania	5	5	
38	Mexico	5	5	
39	Belarus	4	4	
40	Singapore	4	3	
41	Turkey	4	2	
42	Lithuania	3	3	
43	Serbia	3	2	
44	Slowenia	3	3	
45	Chile	2	1	
46	Kazakhstan	2	2	
47	Libya	2	1	
48	Saudi Arabia	2	1	
49	Algeria	1	1	
50	Armenia	1	1	
51	Croatia	1		
52	New Zealand	1	1	
53	Nigeria	1	1	
54	Qatar	1	1	
55	Slovakia	1	1	
	TOTAL:	1515	1273	38

Opening Ceremony²

Professor W. Gutkowski

Distinguished Guests, Esteemed Colleagues, Ladies and Gentlemen, It is my great honor and pleasure to welcome you to the 21st International Congress of Theoretical and Applied Mechanics.

I welcome you on behalf of the Local Organizing Committee in Poland, here in Warsaw in this historical and beautiful edifice of the Warsaw University of Technology. The edifice, a witness of many scientific, cultural and political events. Just sixty years ago, in August heavy fighting was going on here during the Warsaw Uprising. Today you are in the country of growing economy, and for several months a member of European Community. Mister President, Distinguished Guests and Colleagues, Ladies and Gentlemen! It is my great honor and privilege to announce the opening of the 21st International Congress of Theoretical and Applied Mechanics! We are here, scientists from 55 countries, joined by a common passion, a passion for Mechanics.

Ladies and Gentlemen, let me now introduce our distinguished guests and organizers: Professor Keith Moffatt, President of the International Union of Theoretical and Applied Mechanics and President of the Congress Committee of IUTAM, Professor Werner Schiehlen, Vice-President of IUTAM, Professor Ben Freund, Treasurer of IUTAM, Professor Dick van Campen, Secretary General of IUTAM, Professor Tim Pedley, Secretary General of IUTAM, Professor Michał Kleiber, Minister of Science and Information Technology of Polish Government, Chairman of the State Committee for Scientific Research, Co-chairmen of the Local Organizing Committee, Professor Janusz Lipkowski, Vice-President of Polish Academy of Sciences, Professor Stanisław Mańkowski, President of the Warsaw University of Technology, Professor Włodzimierz Kurnik, Vice-President of the Warsaw University of Technology, Co-Chairman of the Local Organizing Committee, and Professor Tomasz Kowalewski, Secretary-General of the Congress.

Ladies and Gentlemen, to start the Congress I will kindly request Professor Keith Moffatt of the Cambridge University, President of the International Union of Theoretical and Applied Mechanics and President of the IUTAM Congress Committee, to address the Congress.

²The unabridged version of the account of the Opening Ceremony can be found on the accompanying CD-ROM.

Professor K. Moffatt

Distinguished Guests, Dear Colleagues, Ladies and Gentlemen,
I am honoured to stand before you in this magnificent setting of the Warsaw University of Technology, and to say some words of welcome on behalf of IUTAM, the International Union of Theoretical and Applied Mechanics. This is the 21st Congress in our history, so here we celebrate our ‘coming-of-age’. We also celebrate the 80th anniversary of the first Congress of Applied Mechanics (as it was then called), which was held in Delft in 1924. We should pay tribute to the great scientists who had the vision to initiate this series of quadrennial Congresses, particularly J.M. Burgers, Theodore von Karman, Ludwig Prandtl and G.I. Taylor.

I note that this year is the centenary of Prandtl’s seminal paper on boundary-layer theory. An IUTAM Symposium on “One Hundred Years of Boundary Layer Research” has been held just last week in Göttingen, in recognition of the crucial role that this branch of mechanics has played in Aerodynamics and many other fields of application.

IUTAM itself grew from the early Congresses, and was formally established in 1948; Poland was one of the earliest members and has been an Adhering Organisation of IUTAM since 1952. The Congress Committee is appointed by the General Assembly of IUTAM, but otherwise retains the autonomy that it enjoyed from the outset. This means that when things go wrong, IUTAM can blame the Congress Committee; of course, when things go right, IUTAM shares in the credit!

There were 207 participants at that first Congress in Delft; these early pioneers would be gratified to know that there are over 1500 participants at this 21st Congress, as there were also at the 20th Congress in Chicago four years ago. It is a measure of the continuing vigour of our subject that the Congress attracts such strong and widespread participation. Of course we must be careful not to equate quantity with quality; we do however strive to maintain high quality in the papers selected for presentation whether as lectures or as seminar/poster presentations. Here I pay tribute to the hard work of our International Papers Committee, which, advised by National Committees and by Convenors of Mini-Symposia and Pre-nominated Sessions, had to select the papers from more than 2000 that were submitted; their task was extremely demanding, but the quality and range of the programme before us for this Congress will I hope convince you that they have done an excellent job, in spite of the great difficulties.

It is highly appropriate that we hold this Congress in Warsaw, a city of grace and beauty, which has emerged from the dreadful traumas of the last century to face the new century with greatly renewed vigour and

optimism. One cannot visit this land without being deeply conscious of the long years of oppression suffered by the Polish people. It is hard now for us to comprehend the tragedy of the Warsaw uprising, which erupted exactly sixty years ago, and which has been commemorated here this month. The long bleak years of the Cold War gave little solace to the Polish people. Yet throughout these years, there remained for our community a flicker of light in the gloom: I refer to the biennial meetings in fluid mechanics that were organised in Poland throughout the 60s and 70s and well into the 80s by our dear colleague Władek Fiszdon, meetings which enabled scientific contacts between East and West to be established and nurtured across and despite the Iron Curtain, and which helped to keep alive the universal and apolitical spirit of our subject. Władek Fiszdon became a member of the General Assembly of IUTAM in 1971; he is now a life-member in recognition of his devoted services. His health unfortunately does not allow him to be with us today, but I am sure you would wish me to convey to him the very good wishes of the whole IUTAM community.

IUTAM is an organisation founded on principles of friendly collaboration between scientists irrespective of race, creed or gender. It is a privilege to come to its Congresses, and to renew acquaintance with so many old friends and colleagues. It is also a particular privilege for me to welcome to this Congress younger scientists who may be attending an IUTAM Congress for the first time. I remember vividly my own such experience: With the encouragement of my late mentor George Batchelor, I attended the 10th Congress in Stresa, Italy, in 1960. It was an exhilarating experience, which opened my eyes to the great scope and challenges of our vast field of endeavour. If this is your first IUTAM Congress, I hope that you will find it a similarly exhilarating experience, and that you will look forward to succeeding Congresses with ever-keener anticipation. G.I. Taylor once told me that he liked to save his best paper in each four-year period for presentation at ICTAM; we should do well to follow his good example!

The time for thanks will come at the end of the Congress on Friday, but I'd like now to say at least a preliminary thank you to the local team who have worked so hard on all the preparations: the Congress President Witold Gutkowski, the Secretary-General of the Congress Tomasz Kowalewski, and the whole Local Organising Committee. They have done a superb job, and I sense that this is going to be a correspondingly superb Congress.

Thank you, Witold and Tomasz!

Now without further ado, I have much pleasure in confirming the Opening of ICTAM04.

Welcome to Warsaw, and we wish you a fruitful Congress; or, as it is said here:

Witamy w Warszawie i życzymy udanego Kongresu!

Professor W. Gutkowski

Thank you very much, Keith, for your kind words about Polish contribution to international mechanics. Let me also express our great appreciation for you, IUTAM Bureau and Executive Committee of the Congress Committee for the support and valuable advice during four years of preparation for the Congress. Let me ask now Professor Michał Kleiber, Minister of Science and Information Technology of Polish government, Chairman of the State Committee for Scientific Research and Co-chairman of the Local Organizing Committee to address the Congress.

Professor M. Kleiber

Mr. President of IUTAM, Very Distinguished Guests of the Congress, Colleagues and Friends,

On behalf of the government of the Republic of Poland I have the honour and great pleasure to welcome you to the 21st International Congress of Theoretical and Applied Mechanics here in Warsaw.

I hope you will forgive me if I start on a rather personal note but I want to emphasize how special for me is this opportunity of addressing you, dear colleagues, in my current double capacity as a co-chairman of the Congress and as a representative of the Polish public administration. Frankly, I have to admit that because of my other duties I have not done much in terms of the Congress organization, and it is my colleagues at the Institute of Fundamental Technological Research of Polish Academy of Science and the Warsaw University of Technology who at the end of the week will deserve to be congratulated for their exceptional engagement and, I am sure, organizational perfection.

The Congress is something very special in every respect – it attempts to summarize what we have accomplished in the last 4 years, it facilitates everyone's research planning for the future, it stimulates interactions with other fields of science and technology, it strengthens our professional and personal links, it gives us a marvellous feeling of being a group of people coming from so many, sometimes very distant, places all over the world, but a group of people who share similar interests, similar vision of rationality in all human endeavors, similar perception of ways to better understand and improve the world around us.

I am one of those who consider the fields of mechanics as a true research success story of last decades – contrary perhaps to some people

from outside of our profession, I have no doubts that the progress we have achieved together definitely places mechanics on one of the very top locations in the hierarchy of modern research disciplines – with tremendous impact on both our perception of the physical world and the means to implement new technologies so much improving the quality of our life.

We are very glad to host you, distinguished delegates, in Poland, in the city of Warsaw. You will find here, I am sure, traditional hospitality and openness of the people, great public interest in the Congress debates and interesting encounters with the country and its capital so much rooted in the complex history of Europe – country which has only recently managed to definitely overcome its politically so much unfortunate and undeserved past, country which, as a new member of the European Union, looks forward with unmatched optimism and aspirations to contributing to the progress in science and its positive implications for all of us.

I wish all the participants vivid, instructive presentations and discussions and, at the same time, enjoyable stay in Warsaw.

Professor W. Gutkowski

Thank you, Professor Kleiber. I would like to express my gratitude for your initiative to organize the Congress in cooperation with the Institute of Fundamental Technological Research and the Warsaw University of Technology, in this beautiful edifice. This has been a great idea. Special thanks also for strong financial support of the Congress by the Ministry of Science and Information Technology.

May I ask Professor Janusz Lipkowski, Vice President of the Polish Academy of Sciences, representing the President of the Polish Academy of Sciences, to the podium.

Professor J. Lipkowski

Mr. President, Excellences, Distinguished Guests and Participants of the Congress,

The Polish Academy of Sciences consists of three parts. First, it is a corporation of elected members, the most distinguished scientists of our country who represent the Polish science. The Academy also organizes the scientific life in the country through its scientific committees. There are more than 100 committees in all scientific disciplines and scientists from all institutions in Poland, universities, institutes, societies etc. serve as members of the committees. One of these, Polish National Committee of the International Union of Theoretical and Applied Mechanics, is coorganizing the present Congress. Last but not least, the Academy has scientific institutes performing high level research studies.

About 9% of all scientific ‘population’ in Poland are employed in the institutes while their output measured by the number of scientific publications amounts to more than one quarter of all scientific output in the country. We are proud of our institutes; please feel invited to visit any of them during your stay in Poland, you will be more than welcome. I am pleased to mention that one of the institutes, the Institute of Fundamental Technological Research, is also a coorganizer of the Congress. By the way, it is the mother institution of our Minister of Scientific Research and Information Technology who served as its director before joining the government of Poland.

Ladies and Gentlemen,

I made this brief introduction to our Academy of Sciences in the belief that you would become interested in developing scientific cooperation with our Academicians and institutions. We do count on international joint research which is an obvious choice in the XXIst century.

I wish you a very fruitful conference, and a pleasant and enjoyable stay in Poland!

Professor W. Gutkowski

Thank you very much, Professor Lipkowski. The Polish Academy of Sciences gave us very strong support when we were proposing the organization of the Congress here in Warsaw. Almost all members of the Local Organizing Committee are members of the Committee of Mechanics of the Academy. Let me now request Professor Stanisław Mańkowski, President of the Warsaw University of Technology, to address the Congress.

Professor St. Mańkowski

Professor, Minister, Ladies and Gentleman, Distinguished Guests, The Warsaw University of Technology, with its tradition of teaching in the field of technical and exact sciences reaching the year 1826, the symbol of which is the Main Building, erected over a 100 years ago and where the Large Hall is an expression of beauty, but also of application of the theoretical and applied mechanics, would like to extend a warm welcome to the participants of this, already the 21st, congress. The Warsaw University of Technology which teaches approximately 32 000 students is the largest technical university in this part of Europe. Teaching and research are inseparable. Therefore I believe that the 21st International Congress of Theoretical and Applied Mechanics is organised in the right place.

I wish the authors of the presented scientific contributions many practical applications, accurate theoretical descriptions and many quota-

tions. I would like to express my gratitude to the International Committee for this decision, and the Polish National Committee, the Institute of the Fundamental Technological Research of the Polish Academy of Sciences and the Team of the Warsaw University of Technology led by Vice-President Prof. Włodzimierz Kurnik – for the passion and effort put into the organisation of the congress.

Professor W. Gutkowski

Thank you very much. It is my great pleasure to say that Professor Mańkowski, together with Professor Włodzimierz Kurnik, Vice-President of the University, have undertaken an enormous organizing task to host us in this historical building.

Ladies and Gentlemen, I believe you will like the city of Warsaw, and other places in Poland. There are so many interesting historical and cultural places to visit. Palaces, beautiful gardens, museums, concert halls and theaters. Unfortunately, within a couple of days you will be able to see just a few of them. So, we are bringing to you here a small fragment of our cultural heritage – the music of Chopin. For a quarter of an hour, Mr. Marcin Rudziński, a student of the Fryderyk Chopin Academy of Music, will present us some of the nicest pieces of this famous composer.

...

Ladies and Gentlemen, Dear Colleagues,
Mechanics is flourishing! No doubt! Increasing number of submissions from ICTAM to ICTAM is showing theoretical and applied importance of mechanics and its multidisciplinary relations with other sciences. In Kyoto there were 1642 submitted papers, in Chicago 1953, and in Warsaw 2186! Thank you for coming, and for contributing with your papers to the development of Mechanics in the 21st century.

We can say that all submitted papers present the latest, up-to-date results of our research. Really latest! Suffice it to say that on January 5, four days before the submission deadline, only 600 papers reached our server. I needn't say that no smile could be seen on our faces. Then during the last four days, the number of incoming papers started to grow exponentially with time. Finally, at midnight on the 9th of January the number of submitted paper reached 21 hundred! The authors were then really anxious to send their latest results. Let me mention an e-mail message we received in the late afternoon on Friday. The author of the message was kindly asking if the deadline at midnight should be considered at Greenwich time or at local time!

The authors constitute the core and the essence of the Congress. However, its realization strongly depends on sponsoring. Let me then ac-

knowledge numerous supporting institutions and sponsors who helped us to start the organization of ICTAM04.

First of all, I would like to express our thanks to the Polish Universities and Institutes supporting the Congress, and contributing, at the same time, to the exhibition “Mechanics in Poland”.

...

Speaking about Polish Mechanics, I would like to turn your attention to a booklet by Professor Zbigniew Olesiak, which you will find in your congress bag. The book shows the 19th century roots of our mechanics embedded in our difficult history of that time³.

Let me next express gratitude to numerous scientific journals for publishing our announcements. This certainly increased the number of people interested in the congress.

Let me express appreciation for our friends, organizers of the Chicago ICTAM, for their support, very much needed at the beginning of the Congress preparations. It would be impossible to mention all our sponsors by name. To all of them presented on these two banners, I am sending, on behalf of the Local Organizing Committee our deepest thanks.

Ladies and Gentlemen. Before we start our work I will ask Professor Tomasz Kowalewski, Secretary-General of the Congress to give you some latest information.

Professor T. Kowalewski

I am very touched to see here, in Warsaw, so many *old friends* and all those numerous new ones, with whom I had pleasure to exchange thousands of emails during the last four years. Thank you very much for coming ...

– began his talk Secretary-General of the Congress. After passing on the latest technical information concerning organizational matters, Prof. Kowalewski expressed his gratitude to numerous young volunteers who were of great help in the last stages of the congress preparation.

Professor W. Gutkowski

Thank you, Tomasz.

In a few minutes Professor Leen van Wijngaarden will present an Opening Lecture. Presiding the session are Professor Hassan Aref from the USA and Michał Kleiber from Poland. I cordially wish you successful presentations and discussions of your papers.

Enjoy your stay in Warsaw!

Thank you for your attention.

³The text of the book can be found on the accompanying CD-ROM.

Closing Ceremony¹

Closing Address by Professor Keith Moffatt, President of IUTAM

Dear Colleagues, Ladies and Gentlemen,

We have now come to the Closing Ceremony of this Congress. We shall announce the Bureau Prizes in the course of this ceremony. But my first duty is to call on Professor Tim Pedley, Secretary of the Congress Committee, to present his report on ICTAM04.

Congress Report by Professor Tim Pedley, Secretary General of the Congress Committee

Well, Ladies and Gentlemen, another ICTAM has come to an end. It has been a wonderful Congress and the biggest yet — even slightly bigger than the Millennium Congress in Chicago four years ago. There were 1445 active participants, including students, up from 1430, from 57 different countries (up from 54). That last number is a welcome increase in view of IUTAM's aim of spreading interest and understanding in mechanics more and more widely in the world.

...

This has been a resoundingly successful Congress, both scientifically and organisationally. On behalf of the IUTAM Congress Committee, and of yourselves, I would like to express our profound thanks to the President of the Congress, Professor Witold Gutkowski, and to the Secretary-General, Professor Tomasz Kowalewski, for their immense contribution to ensuring that success. Possibly most impressive, on the organisational front, was the provision of fully synchronised computer facilities in all the lecture rooms, with the uploading of all computerised presentations in advance.

...

On behalf of the Congress Committee, I would also like to thank the members of the International Papers Committee (IPC) for their dedicated hard work in evaluating and selecting the papers to be presented at the Congress. These were Professors Peter Monkewitz, Howard Stone, Bernhard Schrefler, Kazimierz Sobczyk and Viggo Tvergaard. A lot of

¹The unabridged version of the account of the Closing Ceremony can be found on the accompanying CD-ROM.

reading was required in February and March of this year, and culminated in an intense four day meeting in Warsaw at the end of March. The IPC were guided by the recommendations of the chairs of the mini-symposia and the pre-nominated sessions, and by the national committees of nine major countries: Canada, China, France, Germany, Japan, Poland, Russia, UK and USA. All those involved in the paper assessment process deserve our warm thanks.

...

Professor Keith Moffatt

Now, Ladies and Gentlemen, I have great pleasure in announcing that the Congress Committee agreed yesterday on the location of the next IUTAM Congress, which will be held in August 2008. As you will know, we have now held 21 Congresses, all in the Northern hemisphere. The next Congress will, for the first time, be in the Southern hemisphere. The Australasian bid to hold the Congress in Adelaide, South Australia, has been successful. The Congress President will be Professor Ernie Tuck, and I have pleasure in now inviting him to say a few words.

Professor Tuck expressed his gratitude for electing Adelaide for the next congress, inviting all participants to Australia in 2008.

Acknowledgments by Professor Witold Gutkowski, President of ICTAM04 and Chairman of the Local Organizing Committee

Mister President, Ladies and Gentlemen, Dear Colleagues,
The organization of an ICTAM consists, among other things, in cooperation of many bodies: Congress Committee, International Papers Committee, Chairs of Sessions, and National Committees of IUTAM. I would like to express our gratitude to all those, for their very effective cooperation, which facilitated our complex work of the Local Organizing Committee. Sincere thanks!

As you already know, there are three institutions standing behind the organization of ICTAM, here in Warsaw.

The idea of organizing an ICTAM in Poland has its long history. It originated in the Committee of Mechanics of the Polish Academy of Sciences and at the same time the Polish National Committee of IUTAM. Without the intellectual encouragement of the whole Polish mechanics community, the organization of the congress in our country wouldn't be possible. This is then right time and right place to express my sincere appreciation to all members of the Committee of Mechanics,

for emboldening us in the organization of ICTAM04. Thanks to you we could disseminate information about the Congress to a very broad international scientific community. Sincere thanks!

The Institute of Fundamental Technological Research, known as IPPT, has also been, for years, strongly supporting the organization of an ICTAM in Poland. When the Congress Committee of IUTAM invited us to organize the congress, the institute became the center of preparatory works. All scientists and administration were highly supportive. IPPT hosted meetings of IUTAM Bureau and XCCC, as well as the International Papers Committee. I wish to express my sincere thanks to the directors of the institute, Professors Kleiber and Nowacki, for their help and for their patience, when watching the disorder inevitable in such situations and paying sharply growing telephone bills.

Thank you, Professor Kleiber, thank you, Professor Nowacki, thank you, all friends from IPPT.

The idea of organizing the Congress in Warsaw found many supporters at the largest university in Poland, the Warsaw University of Technology. The university has offered its beautiful edifice we are now in as a site of the congress. The organization of ICTAM here was strongly encouraged by Professor Stanisław Mańkowski, President of the university and the host of the Welcome Reception. Thanks to the team led by Professor Włodzimierz Kurnik, Vice President of the University and Co-chairman of the Local Organizing Committee, together with Professor Stanisław Radkowski, we had this beautiful building prepared for our gathering. (...) Professors Mańkowski, Kurnik and all friends from the university — many thanks!

Such a great event as our congress couldn't be organized without the help of a professional bureau organizing large conferences. We asked Mazurkas Travel to: take care of your money, make hotel reservation, serve lunches and coffees, prepare poster stands, transportation, organization of excursions and many other things for good comfort of participants. Let me then express my thanks to Mazurkas Travel and its director Mrs. Barbara Zygmunt.

The dissemination of information started with the first announcement and then continued with the second. The nice booklet of the second announcement is the work by Professor Krzysztof Doliński, member of the Local Organizing Committee.

...

It is impossible, to mention by names all young volunteers, mostly PhD students. It has been a real pleasure to see all those strongly motivated young girls and boys working hard and trying to do their

best. They were led by two extremely active and efficient members of the Congress Bureau — Mrs. Izabella Ślęczkowska and Dr. Kamil Kulesza.

Professor K. Doliński, Mrs. Ślęczkowska, Dr. Kulesza and all young volunteers, your contribution to the successful Congress cannot be over-estimated. Thank you!

Last but not least, I am acknowledging the heart, soul, brain and calculator of the Congress organization — Professor Tomasz Kowalewski, Secretary General of ICTAM 2004!

You have been meeting him from the beginning, at the congress page, that is since September 2000. Tomasz has loaded for you all update information. For the first time in the history of IUTAM Congresses, participants could see the program and read an abstract and extended summary of an arbitrary paper, still being home, before reaching the congress site. This was Tomasz's idea and his realization. The perfect preparation of the meeting of the International Paper Committee helped much to take right decisions on accepting papers for presentations. Again, this was Tomasz's idea and realization with the help of several PhD students. Suffice it to say that each of 2000 papers could be found within seconds by title, author's name or country.

And with all that, thousands, thousands of e-mails sent and replied to. It is impossible to enumerate all the works he has done, but I should add at least two others. He kept our finances under strict control and he infected the minds of all young people who worked with him with his enthusiasm for organization of ICTAM 2004.

...

There are not enough words to express my deepest thanks to you and I hope all participants will join me in conveying you our sincere thanks for your great contribution to the success of the Congress. Thank you, Tomasz. In order to commemorate your great contribution to organization of the Congress, let me hand you this 19th century statuette of a Bacchanate, a woman, as we know enjoying good wines. The statuette is inscribed in Polish: *To Professor Tomasz Kowalewski for his outstanding contribution to organization of ICTAM04. Organizing Committee.*

IUTAM Bureau Prizes — Professor Keith Moffatt (certificates), Professor Witold Gutkowski (statuettes)

The members of the Bureau have this week been attending many lectures and seminar/poster presentations given by young researchers. The word 'young' is of course a relative term: I regard everyone younger than myself as young! But to be eligible for a Bureau prize, you must be really



young, and that means under 35 years of age. The Bureau met today over lunch to agree on the winners, and I have to say first that the competition was a stiff one — we may well say of Olympic standard; and three 'gold medallists' have emerged from this competition. The prizes consist of a certificate, a cheque for \$500, and, as a special gesture from the local organisers, a beautiful owl, symbol of wisdom, cast in bronze.

The three prizes are awarded as follows:

- Ingo Kaiser, of the Institute of Robotics and Mechatronics, Wessling, Germany, for his lecture on “The running behaviour of an elastic wheelset”; Ingo gave a beautiful demonstration of the effect of elastic deformation on the stability wheels running on a track; you should be warned of this if you plan to return home by rail after the Congress!
- Taisuke Sugii, of the University of Tokyo, Japan, for his seminar/poster presentation entitled “Molecular dynamics study of permeation process of small molecules through a lipid bilayer”; biomechanics is a field of tremendous potential and rapidly growing importance; this paper provides an excellent example of the application of mechanical principles at the biomolecular level.

- Pantxica Otheguy, of LadHyX, Ecole Polytechnique, Palaiseau, France, for her lecture on “Instability of corotating vertical vortices in a stratified fluid: why strongly stratified turbulence is not similar to 2D turbulence”; Pantxica gave a beautiful interpretation of the ‘zig-zag instability’ to which such vortices are subject, illustrated by a video of an experiment showing the nonlinear outcome of this instability.

We congratulate these three young scientists on the excellence of their presentations.

Ladies and Gentlemen,

This week the General Assembly of IUTAM met twice, and as part of its business elected its new Bureau to serve our Union for the next four years from 1st November 2004. The President will be Professor Ben Freund from Brown University, Providence, Rhode Island, USA, who has served IUTAM so successfully as Treasurer for the past eight years. Professor Dick van Campen will continue as Secretary-General for a further four-year term. Dick has been extremely successful in implementing recommendations of a previous Appraisal Committee, both as regards setting up Working Parties in nine different priority areas, and in developing an excellent website for IUTAM, at which information about all our activities can be easily accessed. We are most grateful to him for his willingness to continue to carry this heavy responsibility.

Professor Juri Engelbrecht, from Estonia, who has served on the Bureau for eight years, has accepted the important position of Treasurer. I myself continue, according to IUTAM rules, as Vice President for the next four years. Four other members of the Bureau have been elected by the General Assembly. These are: Professors Tsutomu Kambe (Japan), Alfred Kluwick (Austria), Niels Olhoff (Denmark) and Zhemin Zheng (China).

I wish to thank the retiring members of the Bureau, Carlo Cercignani, Roddam Narasimha, Jean Salençon and Werner Schiehlen (retiring Vice-President) who have served with great conscientiousness and wisdom.

We have also elected four new members-at-large of the General Assembly, in recognition of their distinction in mechanics and their service to our Union: these are Professors Andy Acrivos (USA), Sol Bodner (Israel), Werner Schiehlen (Germany) and Franz Ziegler (Austria). So you see that we have done our best to ensure that IUTAM will continue to be well governed!

Now I just have to add some words of thanks myself: first to my old friend and colleague, Tim Pedley, who will continue as Secretary of the Congress Committee for a further four years. This is a task of great

responsibility, which Tim has carried out with flair and efficiency. I ask you to join me in thanking him.

Second, I wish to thank Witold Gutkowski, who has been such a gracious host to us here in Warsaw. The smooth running of the Congress owes much to his efforts over the last four years.

Finally, I wish to echo Professor Gutkowski's remarks concerning Tomasz Kowalewski, Secretary-General of the Congress. Tomasz has been indefatigable in his control of every detail of this immense organisation, in which he has shown amazing skill, patience, good humour and efficiency, and we all owe both Tomasz and Witold a resounding vote of thanks.

And even more finally, I wish to thank all of you, Invited Sectional Lecturers, Convenors of Mini-Symposia, Chairmen of Pre-nominated Sessions, contributors of lectures and seminar/poster presentations, and all of you who by your presence have made this Congress such a brilliant success.

I wish you all a safe journey home, and will look forward to seeing you again down under in Adelaide in August 2008, if not before!

Keith Moffatt

Scientific Program

On the following pages the contents of the scientific program of the Congress are listed. The program consists of plenary opening and closing lectures, eighteen sectional lectures, six minisymposia, and sixty pre-nominated sessions devoted to all aspects of mechanics.

- OL Opening Lecture
- CL Closing Lecture
- SL Sectional Lectures

Mini Symposia

- MS1 Smart materials and structures
- MS2 Tissue, cellular and molecular biomechanics
- MS3 Mechanics of thin films and nanostructures
- MS4 Microfluids
- MS5 Microgravity flow phenomena
- MS6 Atmosphere and ocean dynamics

Pre-Nominated Sessions on Fluid Mechanics

- FM1 Biological fluid dynamics
- FM2 Boundary layers
- FM3 Combustion and flames
- FM4 Complex and smart fluids
- FM5 Compressible flow
- FM6 Computational fluid dynamics
- FM7 Convective phenomena
- FM8 Drops and bubbles
- FM9 Environmental fluid dynamics
- FM10 Experimental methods in fluid mechanics
- FM11 Flow control
- FM12 Flow in porous media
- FM13 Flow instability and transition
- FM14 Flow in thin films
- FM15 Fluid mechanics of materials processing
- FM16 Fluid mechanics of suspensions
- FM17 Granular flows
- FM18 Low-Reynolds-number flow
- FM19 Magnetohydrodynamics
- FM20 Multiphase flows
- FM21 Solidification and crystal growth
- FM22 Stirring and mixing
- FM23 Topological fluid mechanics
- FM24 Turbulence
- FM25 Vortex dynamics
- FM26 Waves

Pre-Nominated Sessions on Solid Mechanics

SM1	Computational solid mechanics
SM2	Contact and friction mechanics
SM3	Control of structures
SM4	Damage mechanics
SM5	Dynamic plasticity of structures
SM6	Elasticity
SM7	Experimental methods in solid mechanics
SM8	Fatigue
SM9	Fracture and crack mechanics
SM10	Functionally graded materials
SM11	Impact and wave propagation
SM12	Material instabilities
SM13	Mechanics of composites
SM14	Mechanics of phase transformations (jointly with IACM)
SM15	Mechanics of porous materials
SM16	Mechatronics
SM17	Multibody dynamics
SM18	Plasticity and viscoplasticity
SM19	Plates and shells
SM20	Rock mechanics and geomechanics
SM21	Solid mechanics in manufacturing
SM22	Stability of structures
SM23	Stochastic micromechanics
SM24	Structural optimization
SM25	Structural vibrations
SM26	Vehicle dynamics
SM27	Viscoelasticity and creep

Topics Involving Both Fluid Mechanics and Solid Mechanics

FSM1	Acoustics
FSM2	Chaos in fluid and solid mechanics
FSM3	Continuum mechanics
FSM4	Fluid-structure interaction
FSM5	Mechanics of foams and cellular materials
FSM6	Multiscale phenomena in mechanics
FSM7	Education in mechanics

The description of the session consists of the session ID, the descriptive name of the session (e.g. ‘Smart materials and structures’) and the list of responsible co-chairs in parentheses. The list of the contributions follows. It is sorted by the unique lecture ID.

The Mini Symposia (MS1...MS6), apart from the Lecture Presentations and Seminar Presentations contain Introductory Lectures. The latter are distinguished by the boldface letters of the author names.

 OL – Opening Lecture

 10498 Leen van Wijngaarden (*Netherlands*): Interplay between Air and Water

CL – Closing Lecture

 10697 Kazimierz Sobczyk (*Poland*): Stochastic Dynamics of Engineering Systems

SL – Sectional Lectures

- 10042 Konrad Bajer (*Poland*): Rapid Formation of Strong Gradients and Diffusion in the Transport of Scalar and Vector Fields
- 10143 Raymond W. Ogden (*UK*): Mechanics of Rubberlike Solids
- 10158 Edward Spiegel (*USA*): Problems in Astrophysical Fluid Dynamics
- 10495 Harry L. Swinney (*USA*): Scaling in Quasi-2D Turbulence Experiments in a Rotating Flow
- 10508 Pierre J. Ladev ze (*France*): A Bridge Between the Micro- and Mesomechanics of Laminates: Fantasy or Reality?
- 10512 Roland Keunings (*Belgium*): Non-Newtonian Fluid Mechanics Using Molecular Theory
- 10529 D.A. Saville (*USA*): Electrokinetics & Electrohydrodynamics in Microfluids
- 10544 Edwin Kreuzer (*Germany*): Nonlinear Dynamics in Ocean Engineering
- 10551 Anatoly Neishtadt (*Russia*): Probability Phenomena in Perturbed Dynamical Systems
- 10731 Marcel Lesieur (*France*): Turbulence and Large-Eddy Simulations
- 10772 Huajian Gao (*Germany*): Nanoscale Mechanics of Biological Materials
- 10880 Daniel A. Beysens (*France*): Near-Critical Point Hydrodynamics and Microgravity
- 10930 Andre Preumont (*Belgium*): Some Issues in Active Vibration Control of Smart Structures
- 11040 Jorge Ambr sio (*Portugal*): Multibody Dynamics: Bridging for Multidisciplinary Applications
- 11327 Erich Sackmann (*Germany*): Microviscoelasticity of Cells: Cells as Viscoplastic Bodies
- 12160 John F. Brady (*USA*): Suspensions: From Micromechanics to Macroscopic Behavior
- 12781 Peter B. Rhines (*USA*): Ocean Circulation and its Influence on Climate
- 13003 Thomas J.R. Hughes (*USA*): Variational and Multiscale Methods in Turbulence
-

MS1 – Smart materials and structures (J. Holnicki-Szulc, Poland & N. Sottos, USA)

- 10680 **Wiesław M. Ostachowicz** (*Poland*): Elastic Wave Propagation Development for Structural Health Monitoring
- 10722 **Richard D. James** (*USA*): A Way to Search for Smart Materials with Unprecedented Physical Properties
- 13010 **Scott R. White** (*USA*): Autonomic Healing of Polymers and Composites
- 10136 Mieczysław S. Kuczma (*Poland*): Composite Plates with Active Fibres
- 10784 Hans Irschik (*Austria*): Transient Eigenstrains Without Incremental Displacements in a Hyperelastic Body
- 10821 Hisaaki Tobushi (*Japan*): Shape Fixity and Shape Recovery of Shape Memory Polymer and their Applications
- 10985 Ji-Hwan Kim (*S. Korea*): Vibration Control of Stiffened Plates with Integrated Piezoelectrics
- 11685 Nancy R. Sottos (*USA*): Stress Effects on Ferroelectric Thin Film Patterning, Properties and Performance
- 11731 Kaushik Bhattacharya (*USA*): A Novel Approach to the Application of Ferroelectric Thin Films to Micro-actuation

- 11752 Sven Lentzen (*Germany*): A Geometrically Non-Linear Finite Shell Element with Piezoelectric Layers
- 11857 Cun-Fa Gao (*Japan*): Thermal-Induced Fracture of Electroded Piezoelectric Composites
- 12011 Rivka Gilat (*Israel*): Thermal Buckling of Active Composite Plates with Shape Memory Alloy Fibers
- 12016 Daining Fang (*China*): Study of Non-Linear Magnetomechanical Constitutive Relations of Ferromagnetic Materials
- 12018 Fumihiko Ashida (*Japan*): Optimum Control of Thermoelastic Deformation in a Smart Composite Disk
- 12027 Catherine L. Brinson (*USA*): SMA Hybrid Composites: Self-healing, Self-Stiffening and Shape Control Simulations
- 12147 Sadagopan Narayanan (*India*): Active Control of FGM Plates Using Distributed Piezoelectric Sensors and Actuators
- 12637 Michal Landa (*Czech Republic*): Ultrasonic Characterization of Phase Transformation in NiTi Wire During Thermomechanical Loading
- 12786 Mitsunori Denda (*USA*): Upper and Lower Bounds of Electric Induction Intensity Factors for Multiple Piezoelectric Cracks by the BEM
- 13007 Andrew Smyth (*USA*): Direct Identification of the State Equation in Complex Non-linear Systems
- 13011 Alan Jones (*USA*): Self-Healing Polymer Composites for Extended Fatigue Life
- 13015 Piotr Pawłowski (*Poland*): The Concept of Multifoldig and Its Experimental Validation

MS2 – Tissue, cellular and molecular biomechanics (D. Barthés-Biesel, France & A. Hoger, USA)

- 10709 **Christoph F. Schmidt** (*Netherlands*): Molecular Mechanics of Cytoskeletal Components
- 10933 **Susan S. Margulies** (*USA*): Tissue Mechanics
- 12811 **Samuel A. Safran** (*Israel*): Elastic Interactions of Biological Cells
- 10627 Erik van der Giessen (*Netherlands*): Micromechanics of Cytoskeletal Actin Networks
- 10670 Tobias Olsson (*Sweden*): Residual Stress Fields in Soft Tissues
- 10689 Katarzyna A. Rejniak (*USA*): From Individual Cells To Complex Tissues – an Immersed Boundary Approach
- 10838 Kazimierz Piechór (*Poland*): Travelling Waves in a Model of Skin Pattern Formation
- 10988 Norman A. Fleck (*UK*): Mechanics of Deep Penetration of Soft Solids
- 11102 Andrejs Cebers (*Latvia*): Mechanics of Elastic and Viscous Magnetic Filaments
- 11148 Samuel Sideman (*Israel*): Intracellular Control Mechanisms of Cardiac Contraction & Energetics
- 11581 Yoel Forterre (*France*): Mechanics of Venus' flytrap Closure
- 11808 Jarosław Piekarski (*Poland*): Approximations of Stiffness Tensor of Bone – Determining and Accuracy
- 11866 Thomas R. Powers (*USA*): Theory of Polymorphism in Bacterial Flagella
- 11961 Dominique Barthés-Biesel (*France*): Hydrodynamic Interaction Between Two Bioartificial Capsules in Shear Flow
- 12031 Christoph Hartmann (*Germany*): Stress and Strain in a Yeast Cell under High Hydrostatic Pressure
- 12059 Alexander V. Kondrachuk (*Ukraine*): Models of Hair Cell Bundle Functioning
- 12064 Edoardo Mazza (*Switzerland*): Measuring the Mechanical Properties of Soft Biological Tissues
- 12100 Stanisław Jemioło (*Poland*): Anisotropic Hyperelastic and Pseudo-Hyperelastic Materials and Applications to Soft Tissue Modelling
- 12192 Taisuke Sugii (*Japan*): Molecular Dynamics Study of Permeation Process of Small Molecules Through A Lipid Bilayer

- 12315 Tomasz Lekszycki (*Poland*): Modeling of Periodic Load Effects in Bone Tissue Adaptation
 12453 Ken-ichi Tsubota (*Japan*): A Particle Method Computer Simulation of Blood Flow
 13049 Luigi Gambarotta (*Italy*): Wrinkling and Buckling of Isotropic Biological Tissues

MS3 – Mechanics of thin films and nanostructures (H.M. Jensen, Denmark & Z. Suo, USA)

- 11070 **Henrik M. Jensen** (*Denmark*): Mechanics of Thin Film Structures
 11594 **Rodney S. Ruoff** (*USA*): Mechanics of Nanostructures
 12132 **Kenneth M. Liechti** (*USA*): A Hybrid Molecular/Continuum Analysis of IFM Experiments on a Self-assembled Monolayer
 10105 Min Zhou (*USA*): Thermomechanical Continuum Representation of Atomistic Deformation at Arbitrary Time and Size Scales
 10699 Rui Huang (*USA*): Ratcheting-induced Wrinkling of an Elastic Film on a Metal Layer Under Cyclic Temperatures
 11122 Akihiro Nakatani (*Japan*): Atomistic Study of Size Effect in Torsion Tests of Nanowire
 11279 Wei Yang (*China*): Microstructural and Atomistic Simulation for Deformation of Nano-grained Metals
 11444 Kinga Nalepka (*Poland*): Energy-Based Approach to Limit States in Nanostructures. Calculation of the Critical Values of Energy from First Principles
 11474 Pradeep Sharma (*USA*): Size-dependent Elastic State of Embedded Nano-inclusions & Quantum Dots
 11599 Mikhail N. Perelmutter (*Russia*): Fracture Criterion for Bridged Crack: from Macro to Nanoscale
 12181 Fenghuan Sha (*China*): Investigation of Wave Propagation in Multiwall
 12251 Małgorzata Chwał (*Poland*): Homogenisation Models of Carbon Nanocomposites Mechanical Properties
 12314 Xi-Qiao Feng (*China*): Micro- and Nano- mechanics of Carbon Nanotubes Composites
 12384 Jurg Dual (*Switzerland*): Characterization of MEMS Materials
 12386 Daniel S. Balint (*UK*): An Analytical Model of Oxide Rumpling as the Mechanism Leading to Failure in Thermal Barrier Coatings
 12432 Raymond Parnes (*Israel*): Instabilities of Composite Materials Reinforced by Nano-Fibres: a Re-examination of Elastic Buckling
 12486 Xuejun J. Zheng (*China*): Interfacial Adhesion of PZT Ferroelectric Thin Films Determined by Nano-Indentation Method
 12627 Simon P.A. Bill (*UK*): A Cellular Automaton for Modelling Evolution of Heteroepitaxial Systems
 12705 Taher Saif (*USA*): Mechanical Behaviour of Nano Grained Metals
 12778 Kyung-Suk Kim (*USA*): Nano-scale Planar Field Projection of Atomistic Decohesion of Crystalline Solids

MS4 – Microfluids (R.J. Adrian, USA & J. Santiago, USA)

- 12960 **Patrick Tabeling** (*France*): Slip, Patterns, and other small Things in Microfluidic Systems
 12961 **J. Santiago** (*USA*): Electrokinetic Flow Instabilities in Microfluidic Systems
 12976 **D. Scott Stewart** (*USA*): Miniaturization of Explosive Technology and Microdetonics
 10723 Carlo Cercignani (*Italy*): Plane Poiseuille Flow in a Rarefied Gas with General Boundary Conditions
 10971 Anna Kucaba-Piętal (*Poland*): Water Flows in Copper and Quartz Nanochannels
 11437 Nicolas G. Hadjiconstantinou (*USA*): A Second-Order Slip Model for Early-Transition-Regime Flows
 11604 Kenneth S. Breuer (*USA*): Direct Measurement and Simulation of Apparent Slip Velocities in Sub-Micron-Scale Flows

- 11607 Eiichiro Yamaguchi (*USA*): Theoretical and Experimental Study of Microchannel Blockage Phenomena
- 11777 Todd M. Squires (*USA*): Induced-Charge Electro-Osmosis: Theory and Microfluidic Applications
- 12047 Laure Menetrier (*France*): Using Microfluidics to Investigate Reaction-diffusion Phenomena in Simple Flows
- 12130 Guillaume Degré (*France*): Magnetic Particles Aggregation in the Presence of a Hydrodynamic Shear
- 12536 Marie Caroline Jullien (*France*): Chaotic Mixing and Resonances in a Microfluidic System
- 12673 Pierre Joseph (*France*): An Accurate Velocity Profile Measurement System for Microfluidics: A Direct Measurement of the Slip Length
- 12966 Piotr Garstecki (*USA*): Tunable Microfluidic Bubble Generator

MS5 – Microgravity flow phenomena (J.I.D. Alexander, USA & P. Neitzel, USA)

- 10598 **Denis Weaire** (*Ireland*): Foams, Films and Surfaces in Microgravity
- 10714 **Michel Y. Louge** (*USA*): Collisional Granular Flows with and without Gas Interactions in Microgravity
- 11133 **George M. Homsy** (*USA*): Microgravity and Microscale Fluid Mechanics
- 10958 Dmytro V. Yevdokymov (*Ukraine*): Hydrodynamic Effect of Slow Phase Transitions in Microgravity
- 10980 M.C. Charrier Mojtabi (*France*): Heat Transfer Due to High Frequency Vibration: a New Approach for Achieving Thermally Optimum Geometry Under Microgravity Conditions
- 11757 Vladislav V. Pukhnachov (*Russia*): Mathematical Models of Microconvection for Isothermally Incompressible and Weakly Compressible Liquids
- 11843 Michael K. Ermakov (*Russia*): Onset of Oscillations in High-Prandtl Thermocapillary Liquid Bridges: Linear-stability Analysis vs. Experiment
- 12402 Tatyana P. Lyubimova (*Russia*): Spherical Two-phase Interface in a Near-critical Fluid. Gradient Approach
- 12447 Iwan Alexander (*USA*): Capillary Pressure of a Liquid Between Uniform Spheres Arranged in a Square-packed Layer
- 12651 G. Paul Neitzel (*USA*): Recent Advances in Permanent Noncoalescence and Nonwetting

MS6 – Atmosphere and ocean dynamics (M.E. McIntyre, UK & J. Sommeria, France)

- 10716 **Onno Bokhove** (*Netherlands*): Wave Vortex Interactions in the Atmosphere and Oceans; with Applications to Climate
- 10803 **Olivier Talagrand** (*France*): Assimilation of Observations into Numerical Models
- 10987 **Peter Haynes** (*UK*): Transport and Mixing in the Atmosphere
- 10261 Peter J. Thomas (*UK*): Modelling Oceanographic Coastal Currents in Small-scale and Large-scale Laboratory Experiments
- 10513 Pierre Carlotti (*France*): Near-surface Turbulence in a Neutral Planetary Boundary Layer: Comparison of LES with the CASES'99 Experiment Observations
- 10634 Gordon Swaters (*Canada*): Meridional Flow of Source Driven Grounded Abyssal Flow in a Wind Driven Basin with Topography
- 10977 Michael E. McIntyre (*UK*): Remote Recoil and Wave Capture: Wave-vortex Interactions in Atmosphere-Ocean Models
- 11152 Boris Galperin (*USA*): Anisotropic Large-Scale Turbulence on Giant Planets and in the Ocean
- 11336 Jean Noel Reinaud (*UK*): Strong Vortex Interactions in Quasi-Geostrophic Flows
- 11499 Ross Griffiths (*Australia*): Turbulent Horizontal Convection and the Global Thermohaline Circulation of the Oceans

- 11547 Joel Sommeria (*France*): Instability of Gravity Driven Coastal Current in a Turntable Experiment
- 11585 Marius Ungarish (*Israel*): Intrusive Gravity Currents in a Stratified Ambient – Novel Theoretical Results and Insights
- 11732 Shinya Shimokawa (*Japan*): Irreversible Transition to a State with Higher Entropy Production in Oceanic General Circulation
- 11829 Jan-Bert Flór (*France*): Interactions of Planar Waves with a Baroclinic Vortex
- 11942 Semion Sukoriansky (*Israel*): A New Spectral Closure Model of Turbulent Flows with Stable Stratification and Its Application to Atmospheric SBLS
- 12035 Dieter Etling (*Germany*): Roll Vortices in the Atmospheric Boundary Layer
- 12104 Jacques Vanneste (*UK*): Spontaneous Generation of Inertia-Gravity Waves by Balanced Motion
- 12140 Jun-Ichi Yano (*France*): The Energy Cycle of the Tropical Madden-Julian Oscillations seen through Wavelets
- 12157 Oliver Buhler (*USA*): Wave Capture and Wave-vortex Duality
- 12169 Keke Zhang (*UK*): A New Theory For Convection In Rapidly Rotating Spherical Systems
- 12194 Takeshi Miyazaki (*Japan*): Vortex-based Models of Quasigeostrophic Turbulence
- 12210 Jonas Nycander (*Sweden*): Generation of Internal Waves in the Deep Ocean by Barotropic Tides
- 12294 Pantxika Otheguy (*France*): Instability of Corotating Vertical Vortices in a Stratified Fluid: Why Strongly Stratified Turbulence is not Similar to 2D Turbulence
- 12408 Yuliya Kanarska (*Ukraine*): Laboratory and Numerical Modelling of Exchange Flows
- 12463 Alastair D. Jenkins (*Norway*): Wave-Mean Flow Interaction in Coupled Atmosphere-Ice-Ocean Systems
- 12494 Peter L. Read (*UK*): Multiple Jet Formation in a Convectively Driven Flow on a Beta-plane
- 12601 Pascale Bouruet-Aubertot (*France*): Intermittency in Stratified Turbulence Produced by Breaking Internal Gravity Waves
- 12722 Fabrice Veron (*USA*): Measurements of the Influence of Ocean Surface Kinematics on Air-sea Heat Fluxes
- 12776 Francisco J. Beron-Vera (*USA*): Linear Waves and Baroclinic Instability in an Inhomogeneous-Density Layered Primitive-Equation Ocean Model
- 13017 Silvia Ferrarese (*Italy*): Simulation of Sea Surface Temperature Trends Under Severe Wind Forcing With a Full Atmosphere-Ocean Coupled Model

FM1 – Biological fluid dynamics (M. Gharib, USA & F. van de Vosse, Netherlands)

- 10132 Takeshi Sugimoto (*Japan*): Mechanics of the Bounding Flight Revisited
- 10741 Thomas Podgorski (*France*): Deformation of Vesicles Flowing Through a Capillary
- 11013 Charles N. Baroud (*France*): How to Breathe in a Liquid-Filled Lung: Symmetry of Airway Reopening
- 11187 Tony W.H. Sheu (*Taiwan*): Computational Exploration of Liver Acinus Microstructure
- 11441 Tomonobu Goto (*Japan*): Bacterium Swimming Motion Close to a Wall
- 11851 Maheshwaran K. Kolandavel (*UK*): A CFD Study of the Effects of Physiological Vessel Wall Motion on Oxygen Transport in Coronary Arteries
- 11900 Peter Vennemann (*Netherlands*): In Vivo PIV Measurement in the Embryonic Chicken Heart
- 11908 David M. Lewis (*UK*): A Model of Plankton Dynamics Coupled with a LES of the Surface Mixed Layer
- 11943 Adrian S. Carabineanu (*Romania*): Self-Propulsion of an Oscillatory Wing
- 12063 Oleksiy S. Galaktionov (*Netherlands*): Bioirrigation in Marine Sediments: Ecological Conclusions from Numerical Modelling

- 12124 Cyrus K. Aidun (*USA*): Direct Numerical Simulation of Red Blood Cell Flow and Aggregation
- 12295 Andrew L. Hazel (*UK*): Three-Dimensional Airway Reopening – Finite-Reynolds-Number Effects
- 12400 Philippe Marmottant (*Netherlands*): Cell Permeabilisation and Transport Focused Around Oscillating Microbubbles
- 12409 Maciej K. Ginalski (*Poland*): Computational Model of Selected Transport Processes in an Infant Incubator
- 12423 Manouk Abkarian (*USA*): Red Blood Cell Dynamics, Deformation and Rheology via Microfluidic Experiments
- 12522 Masanori Nakamura (*Japan*): Flow in an Integrated Model of Heart and Aorta
- 12655 Sang-Joon Lee (*S. Korea*): In Vivo Visualization of the Water Refilling Process in Xylem Vessels Using Synchrotron X-Ray Micro-Imaging
- 12784 Mory Gharib (*USA*): On the Issue of Optimal Trans-Mitral Flow

FM2 – Boundary layers (P.W. Duck, UK & A. Kluwick, Austria)

- 10103 James P. Denier (*Australia*): The Development (and Suppression) of Very Short-Scale Instabilities in Buoyant Boundary Layers
- 10275 Yury S. Kachanov (*Russia*): 3D Distributed Boundary-Layer Receptivity to Non-Stationary Free-Stream Vortices in Presence of Surface Roughness
- 10948 Matthias H. Buschmann (*Germany*): Extending the Generalized Logarithmic Law to the Wall
- 11017 Ihor Nesteruk (*Ukraine*): Sub- and Supersonic Shapes without Separation and Cavitation
- 11083 Bernhard Scheichl (*Austria*): Non-Unique Quasi-Equilibrium Turbulent Boundary Layers
- 11084 Stefan Braun (*Austria*): Near Critical Unsteady Three-Dimensional Triple Deck Flows
- 11210 Frank T. Smith (*UK*): Long Layers Exhibiting Local Jumps, in Industrial and Biomedical Applications
- 11339 Victor V. Kozlov (*Russia*): Secondary Instability of Stationary Vortex Packets in a Swept Wing Boundary Layer
- 11397 Anatoly I. Ruban (*UK*): Discontinuous Solutions of the Boundary-Layer Equations
- 11780 Vladimir B. Zametaev (*Russia*): New Numerical Method for Complex Interacting Flows
- 11887 Peter W. Carpenter (*UK*): Why do Dolphins Have Cutaneous Ridges?
- 11984 Patrick D. Weidman (*USA*): Two-Fluid Jets and Wakes
- 12030 Herbert Steinrueck (*Austria*): The Trailing Edge Problem for Mixed Convection Flow Past a Horizontal Plate
- 12062 Tomas Vit (*Czech Republic*): Experimental and Theoretical Study of Heated Coanda Jet
- 12241 Matthew R. Turner (*UK*): A Combined Numerical and Asymptotic Approach to Boundary Layer Receptivity Problems
- 12320 Owen R. Tutty (*UK*): Flow Along a Long Thin Cylinder
- 12631 Narayanan Vinod (*India*): Aspects of the Laminar-Turbulent Transition in Axisymmetric Boundary Layers

FM3 – Combustion and flames (N. Peters, Germany & P. Wolański, Poland)

- 10367 Ay Su (*Taiwan*): Enhancement of the Impinging Diffusion Flame by Splash Plate
- 10747 Oluwole Daniel Makinde (*South Africa*): Exothermic Explosions in a Slab: a Case Study of Series Summation Technique
- 10918 David Lo Jacono (*Switzerland*): A Nearly 1-D Non-Premixed Flame Near Extinction. Cell Formation and the Effect of the Direction of Bulk Flow
- 11031 Aidarkhan Kaltayev (*Kazakhstan*): Simulation of Flame Propagation in a Tube with Obstacles

- 11888 Tim Broeckhoven (*Belgium*): Large Eddy Simulation of Piloted and Bluff – Body Diffusion Flame
- 11914 Artur Tyliczszak (*Poland*): Influence of the Subgrid Models on Combustion Modelling
- 12199 Yeshayahou Levy (*Israel*): Chemical Aspects of the Flameless Oxidation Applied for GasTurbine Combustor
- 12348 Pedro J. Coelho (*Portugal*): Experimental and Numerical Investigation of a Flameless Oxidation Combustor
- 12745 Piotr Wolański (*Poland*): Detonations of Hexane Vapor/Droplets-Air Mixtures
- 12843 Arkadiusz Kobiera (*Poland*): Simulation of Ram Accelerator with PETN Layer
- 12911 Zbigniew A. Walenta (*Poland*): Simple Model of a Detonating Gas for use with the Direct Monte-Carlo Simulation Technique

FM4 – Complex and smart fluids (B. Khusid, USA & A. Yarin, Israel)

- 10140 Konstantin G. Kornev (*USA*): Capillary Microfluidics for Viscoelastic Fluids
- 10753 Boris Khusid (*USA*): Field-Induced Dielectrophoresis and Phase Separation in Suspension
- 10932 Alexander L. Yarin (*Israel*): Electrospinning of Nanofibers from Polymer Solutions
- 11165 Ping Sheng (*China*): The Giant Electrorheological Effect in Suspensions of Nanoparticles
- 11184 Sławomir Błoński (*Poland*): Electrospinning of Liquid Jets
- 11209 Kevin D. Dorfman (*France*): Modeling DNA Separations in Self-Assembled Magnetic Arrays: Comparison of Theory and Experiment
- 11603 Ilker Bayer (*USA*): Contact Angle Dynamics of Droplets Impacting on Flat Substrates
- 11648 Semyon P. Levitsky (*Israel*): Dissipation Features at Nonlinear Pulsations of Bubbles in Viscoelastic Fluids
- 11954 Aleksey N. Rozhkov (*Russia*): Break up of Polymer Solution Drop Impacting a Small Target
- 11982 Markus Zahn (*USA*): Ferrohydrodynamic Hele-Shaw Cell Flows and Instabilities with Simultaneous DC Axial and In-Plane Rotating Magnetic Fields
- 12254 Daniel A. Weiss (*Germany*): Spray Impact on Solid Walls of Non-Newtonian Fluids, Including Yield Stress and Thixotropic Behavior
- 12319 Eyal Zussman (*Israel*): Nanowires Assembly Using Microfluidic: an Experimental Investigation
- 12437 Antonio Castellanos (*Spain*): Particle Manipulation in Microfluidics: the Role of Dielectrophoresis, Electrohydrodynamics and AC Electrokinetics
- 12894 Paul C. Duineveld (*Netherlands*): Non-Newtonian Effects of Ink-Jet Printed Droplets
- 12910 Agnieszka Słowicka (*Poland*): Conditions for Creating Thin Liquid Layers at the Contact Surface of Two Other Liquids

FM5 – Compressible flow (H.G. Hornung, USA)

- 10531 Mikhail S. Ivanov (*Russia*): Hysteresis-Related Phenomena in Shock Wave Reflection
- 10789 Alfred Kluwick (*Austria*): Nonclassical Dynamics of Laminar Dense Gas Boundary Layers
- 10945 Helmut E. Sobieczky (*Germany*): Analytical Models for Shocks in Compressible Flow
- 10984 Holger Babinsky (*UK*): LDA Investigation of a Transonic Bump Flow
- 11049 Kazuyoshi Takayama (*Japan*): Unsteady Drag Force Measurements of Shock Loaded Bodies Suspended in a Vertical Shock Tube
- 11072 Beric W. Skews (*South Africa*): Shock Wave Reflection in a Non-Circular Inlet
- 11560 Susumu Hasegawa (*Japan*): Numerical Optimization of 2D Scramjet Inlets
- 11730 John K. Hunter (*USA*): The Mach Reflection of Weak Shocks
- 11864 Susumu Kobayashi (*Japan*): Effect of Surface Roughness on Mach Reflection
- 12066 Vladimir V. Serebryakov (*Ukraine*): On the Theory for Subsonic, Transonic and Supersonic Flows in Water with Supercavitation
- 12219 Vaclav Dvorak (*Czech Republic*): Interaction of Supersonic Flows in an Ejector

- 12997 Ryszard Szwaba (*Poland*): Shock Wave-Boundary Layer Interaction Control by Streamwise Vortices
- 13016 Joel Delville (*France*): Correlation of Nearfield Pressure with Mixing Layer Velocity in a Supersonic Jet

FM6 – Computational fluid dynamics (L. Kleiser, Switzerland & W. Schroeder, Germany)

- 10163 Randolph C.K. Leung (*China*): Non-Reflecting Boundary Condition for Direct Aeroacoustic Computation
- 10857 Jaime Klapp (*Mexico*): Treesph Simulations of Choked Flow Systems Using Smoothed Particle Hydrodynamics
- 10921 Piotr Boroński (*France*): Poloidal-Toroidal Decomposition in Cylindrical von Karman Flow
- 11348 Manuel Garcia-Villalba (*Germany*): On Inflow Boundary Conditions for Large Eddy Simulation of Turbulent Swirling Jets
- 11456 Rubens Campregher (*Brazil*): Numerical Simulation of the Flow over a Backward-Facing Step in a Beowulf-Class Cluster
- 11485 Alexey N. Kudryavtsev (*Russia*): Development and Practical Application of WENO Schemes for Compressible Fluid Flow Computations
- 11569 Jae-Woo Lee (*S. Korea*): Numerical Analysis and Design Optimization of Lateral Jet Controlled Missile
- 11578 Tadeusz Chmielniak (*Poland*): Numerical Prediction of Energy Dissipation in Condensing
- 11602 Erik R. Dick (*Belgium*): A Pressure-Correction Method for All Mach Numbers
- 11702 Jan Vimmr (*Czech Republic*): Numerical Computation of Compressible Viscous Flow Through a Male Rotor-Housing Gap of Screw Compressors
- 11763 Piotr G. Kowalczyk (*Poland*): Fast Numerical Method for the Boltzmann Equation on Nonuniform Grids
- 11937 Lorena A. Barba (*UK*): Computation of Viscous Vortices with Fully Meshless Method
- 12076 Sławomir Kubacki (*Poland*): Dirichlet/Dirichlet and Neumann/Neumann Parallel Non-Overlapping Domain Decomposition Method
- 12337 Milan Schuster (*Czech Republic*): CFD Methods in Industrial Applications Vehicle External Aerodynamics and Aerodynamic Interaction of Moving Vehicles
- 12510 Guillaume Dufour (*France*): Numerical Error Evaluation for Tip Clearance Flow Calculations in Centrifugal Compressor
- 12565 Andrzej Styczek (*Poland*): Simulation of a Viscous Flow Past a Three Dimensional Obstacle Using Vortex Particles
- 12583 Petros Koumoutsakos (*Switzerland*): Multiscale Simulations Using Particles
- 12618 Jerzy Majewski (*Poland*): Investigation of WENO Scheme for 3D Unstructured Grids
- 13030 Fedderik van der Bos (*Netherlands*): Commutator – Errors in Large-Eddy Simulation of Turbulent Flow
- 13051 Patrick Bontoux (*France*): Three-Dimensional Rayleigh-Benard Instability in a Supercritical Fluid by Direct Numerical Simulation

FM7 – Convective phenomena (G. de Vahl Davis, Australia & K. Zhang, UK)

- 10306 Alexander V. Getling (*Russia*): Cellular Compressible Magnetoconvection: a Mechanism for Magnetic-Field Amplification and Structuring
- 10438 Martin P. King (*Italy*): Scaling Laws for Thermal Convections
- 10538 Aleksandra Aleksandrovna Bozhko (*Russia*): On Features of Magnetic Convection in Ferrofluid
- 10914 Katarzyna Borońska (*France*): Multiplicity of Patterns in Cylindrical Convection
- 11053 Igor Rogachevskii (*Israel*): Large-Scale Semi-Organized Structures in Geophysical Turbulent Convection

- 11160 Tomasz Michalek (*Poland*): Natural Convection for Anomalous Density Variation of Water — Numerical Benchmark
- 11251 C.M. Rindt (*Netherlands*): 3D Flow Transition Behind a Heated Cylinder
- 11440 Jonathan M. Aurnou (*USA*): Experimental Studies of Planetary Core Convection and Dynamo Processes
- 11673 Antonio Cenedese (*Italy*): Penetrative Convection in Stratified Fluids: Velocity Measurements by Image Analysis
- 11905 Heiko Meironke (*Germany*): Experimental and Numerical Studies of Convection Flow in a Cylindrical-Conical Fermenting Tank
- 11972 Vanda Bouché (*Italy*): Sea Convective Motions Driven by Random Buoyancy Inputs
- 12126 Michael Le Bars (*UK*): Thermochemical Convection in Two Superimposed Miscible Viscous Fluids
- 12168 Xinhao Liao (*China*): Nonlinear Convective Patterns in Spherical Rayleigh-Benard Systems
- 12173 Elzbieta Fornalik (*Poland*): Visualization of the Flow Structure and Temperature Field in the Region of Mixed Convection
- 12220 Anne Sergent (*France*): Large Eddy Simulation of Rayleigh-Benard Convection in an Infinite Fluid Layer
- 12267 Aleksander Alekseevich Kozlov (*Russia*): The Influence of Translational Vibration of Circular Polarization on Fluid Convection Stability and Flow Patterns
- 12344 Dmitry V. Lyubimov (*Russia*): Thermal Buoyancy Convection in Systems with Deformable Interfaces
- 12730 Alexander A. Smirnovskii (*Russia*): Convective Phenomena in Rotating Annuli Heated on Periphery
- 12850 Avshalom Manela (*Israel*): On the Rayleigh-Benard Problem in the Continuum Limit
- 13005 Vasilii A. Novosiadlii (*Russia*): The Influence of Vibration on the Onset of Marangoni Convection in Horizontal Fluid Layer
- 13022 Hiroyuki Ozoe (*Japan*): Air Convection in a Cubic Enclosure with Laterally Shifted Electric Coil without a Gravity Field.

FM8 – Drops and bubbles (J. Eggers, UK & A. Prosperetti, USA)

- 10580 Yuriy A. Semenov (*Ukraine*): Method for Solving Nonlinear Problems on Unsteady Free-Boundary Flows
- 11026 Miguel F. Moctezuma Sanchez (*Mexico*): Bubble Wall Interaction and Bubble Pairs Motion Using Potential Flow Theory
- 11250 Olga M. Lavrenteva (*Israel*): Locomotion of a Viscous Drop, Induced by the Internal Secretion: Boundary Effects
- 11289 Gary L. Leal (*USA*): Theoretical Studies of Flow-Induced Coalescence
- 11299 Teruo Kumagai (*Japan*): Occurrence of Micro-Bubbles During the Coalescence of Two Bubbles
- 11317 Nicolas Bremond (*Netherlands*): Atomization of an Undulating Liquid Sheet
- 11330 Eric Lauga (*USA*): Evaporation-Driven Assembly of Colloidal Particles
- 11411 Eligiusz Wajnryb (*Poland*): High-frequency Linear Viscosity of Emulsions Composed of Two Viscoelastic Fluids
- 11462 Christian Wagner (*Germany*): Molecule Configurations in a Droplet Detachment Process of a Semdilute Xanthan Solutions
- 11614 Christophe Josserand (*France*): Spreading and Retraction of Impacting Drops
- 11669 Slavka S. Tcholakova (*Bulgaria*): Main Factors Controlling the Emulsification Process under Turbulent Conditions. Experiment and Data Interpretation
- 11670 Teresa Parra (*Spain*): Water Mist Behavior as Flame Supressant
- 11723 Stefan Zaleski (*France*): Numerical Simulation of Liquid-Gas Interfaces with Applications to Atomization
- 11855 Ernest O. Tuck (*Australia*): Viscous Extensional Flow and Drop Break-Off Under Gravity

- 11911 Jacques J. Magnaudet (*France*): Evolution of a Pair of Spherical Bubbles Rising Side by Side at Moderate Reynolds Number
- 11979 Patrick Le Quéré (*France*): On the Numerical Simulation of Two Phase Liquid-Vapor Phenomena
- 11999 Manish Arora (*Netherlands*): Cavitation Inception on Micro-particles: a Self Propelled Particle Accelerator
- 12106 Peter D.M. Spelt (*UK*): Level-Set Simulations of Shear Flow with Inertia Pas a Droplet Adhering to a Wall with Moving Contact Lines
- 12163 Marianne Francois (*USA*): Modelling Surface Tension Using a Ghost Fluid Technique within a Volume of Fluid Formulation
- 12190 Andrei S. Topolnikov (*Russia*): Dynamics of Bubble Supercompression in Organic Liquids
- 12311 Ryszard Pohorecki (*Poland*): Hydrodynamics of Gas Bubbling through Organic Liquids
- 12329 Michael A. Rother (*USA*): Surfactant Effects on Buoyancy-Driven Coalescence of Spherical Drops
- 12388 Laurent Duchemin (*UK*): Static Shapes of Levitating Viscous Drops
- 12429 Wendy W. Zhang (*USA*): A Long-Wavelength Model of Viscous Entrainment
- 12547 Ulderico P. Bulgarelli (*Italy*): Entrainment of Air Bubbles During Strong Vorticity-Free-Surface Interaction
- 12548 Marco A. Fontelos (*Spain*): Spreading of Charged Microdroplets
- 12596 C. Wang (*Singapore*): Multiple Bubbles Dynamics Using Level Set Indirect Boundary Element Method
- 12741 Andrew J. Griggs (*USA*): Low-Reynolds-Number Motion of a Drop Between Two Parallel Plane Walls
- 12873 Andrzej Zachara (*Poland*): Thermodynamic Parameters of Vapour Bubble Growth by Image Analysis
- 13025 Salima Rafai (*France*): Singular Droplets

FM9 – Environmental fluid dynamics (H.E. Huppert, UK & R. Narasimha, India)

- 10366 Owen M. Phillips (*USA*): The Growth and Structure of Double-Diffusive Cells Adjacent to a Side-Wall in a Salt-Stratified Environment
- 10467 Zbynek Janour (*Czech Republic*): Flow and Dispersion in the Atmospheric Boundary Layer Investigation by Physical Modelling
- 10576 Krzysztof Dekajło (*Poland*): Experiments on Up-slope to Down-slope Transition in an Inclined Box Filled with Water
- 10733 Mohammad J. Kazemzadeh-Parsi (*Iran*): Analysis of Double-Free Surface Flow through Gates Using Element-Free Galerkin Method
- 11164 Hitoshi Miyamoto (*Japan*): Free Surface Behavior in Turbulent Open-Channel Flows
- 11182 Gregory F. Lane-Serff (*UK*): Integral and Laboratory Modelling of Sedimentation from Turbulent Buoyant Jets
- 11294 Falin Chen (*Taiwan*): Modified Shallow Water Equations for Inviscid Gravity Currents
- 11346 Ramon Fernandez-Feria (*Spain*): Dam-Break Flow for Arbitrary Slope of the Bottom
- 11433 Oksana E. Poloukhina (*Russia*): Extended Nonlinear Theory for Topographic Rossby Waves
- 11703 Andrew A. Osipov (*Russia*): The Propagation of Viscous Gravity Currents over a Rigid Conic Surface
- 12072 James G.A. Croll (*UK*): An Alternative Model for “Pingo” Formation in Permafrost Regions
- 12099 Tarmo Soomere (*Estonia*): Fast Ferry Traffic as a New Forcing Factor of Environmental Processes in Non-Tidal Sea Areas
- 12266 Jarosław Ciechanowski (*Poland*): Dynamics of Separation Zone behind the 2D Hill in Oscillating Incident Wind.
- 12270 Arne Moe (*Norway*): Effects of Curvature in Avalanche Deflecting Dams

- 12396 Jim N. McElwaine (*UK*): Lobe and Cleft Formation at the Head of a Gravity Current
 12410 Sabine Decamp (*France*): Experimental and Numerical Simulation of Dense Water Overflows on a Continental Slope
 12592 Szymon P. Malinowski (*Poland*): High Resolution Modelling of Atmospheric Flow over Southern Poland
 12626 Alfred J. Wüest (*Switzerland*): Formation and Rapid Expansion of Double Diffusive Layering in Lake Nyos
 12738 John E. Holeman (*USA*): Joint Urban 2003 Surface Energy Budget Measurements and Analysis
 12980 A.S. Vasudeva Murthy (*India*): Nocturnal Temperature Inversions Under Calm Clear Conditions: an Analytical Study

FM10 – Experimental methods in fluid mechanics (A. Leder, Germany & J. Westerweel, Netherlands)

- 10445 Grazia Lamanna (*Germany*): On the Evaporation of a Monodisperse Droplet Stream at High-Pressure
 11088 Jerry Westerweel (*Netherlands*): HPIV using Polarization Multiplexing Holography in Bacteriorhodopsin (bR)
 11455 Valery Chernoray (*Sweden*): Time-resolved Wall Shear Stress Measurements using MEMS
 11909 Raymond P.H.M. Bergmann (*Netherlands*): Void Collapse and Jet Formation: The Impact of a Disk on a Water Surface.
 11916 Andrzej S. Witkowski (*Poland*): Comprehensive Experimental and Computational Investigations of the Unsteady Flow in an Axial Flow Low Speed Compressor Stage
 12070 Tov Elperin (*Israel*): Experimental Detection of the New Phenomenon of Turbulent Thermal Diffusion
 12213 Nikita A. Fomin (*Belarus*): 3D Vortices Structure Monitoring in Turbulent Flows by Digital Speckle Photography
 12719 Anna Matvienko (*Canada*): Thermal-Wave Resonator Cavity: Modelling and Applications for Water Mixtures
 12855 Piotr M. Korczyk (*Poland*): Particle Image Velocimetry (PIV) for Cloud Droplets – Laboratory Investigations
 13048 Albert Baars (*Germany*): Optical Diagnosis Systems for Measuring Thermofluid-dynamical Phenomena in Liquid Biosystems Under Ultra High Pressure

FM11 – Flow control (J.B. Freund, USA & M. Gad-el-Hak, USA)

- 10128 Mohamed Gad-el-Hak (*USA*): Liquids: The Holy Grail of Microfluidics Modeling
 10872 Ramesh K. Agarwal (*USA*): Active Control of Shock/Boundary Layer Interaction in Transonic Flow Over Airfoils
 11043 Rong F. Huang (*Taiwan*): Manipulating a Vee-Shaped Bluff Body Wake Using a Fluidic Oscillator
 11394 Sedat F. Tardu (*France*): Response on the Near Wall Turbulence to Localized Unsteady Blowing Periodical and Dissymmetric in Time
 11636 Haecheon Choi (*S. Korea*): Passive Control of Turbulent Flow behind a Model Vehicle for Drag Reduction Using Wake Disrupter
 11918 Andrzej Szumowski (*Poland*): Control of Internal Supersonic Flow Separation
 12013 Junwoo Lim (*USA*): A Singular Value Analysis of Boundary Layer Control
 12068 Tom Weier (*Germany*): Separation Control by Stationary and Time Periodic Lorentz Forces
 12156 Victor F. Kopiev (*Russia*): On the Possibility and Prospects of Turbulent Flow Noise Control
 12244 Hervé Illy (*France*): Control of Flow Oscillations over a Cavity by Means of a Spanwise Cylinder

- 12258 Zdenek Travnicek (*Czech Republic*): Synthetic Jet Actuation at the Resonance Frequency
- 12305 Alan Guegan (*France*): Optimal Energy Growth and Optimal Control of the Swept Attachment – Line Boundary Layer
- 12387 Tim Colonius (*USA*): Feedback Control of Vortex Shedding in a Separated Diffuser
- 12491 Seichiro Izawa (*Japan*): Reduction of Aerodynamic Noise Induced by Flow over a Cavity
- 12602 Philippe Konieczny (*France*): Control of Turbulent Streaks by Active Wall Movement
- 12624 Mark Pastoor (*Germany*): Model-Based Control of Shear Flows Using Low-Dimensional Galerkin- and Vortex Models
- 12736 Marek Morzyński (*Poland*): Numerical Analysis of the Wake Control behind a Circular Cylinder with Oscillatory Rotation

FM12 – Flow in porous media (Abder Kader Mojtabi, France & V. Nikolaevskiy, Russia)

- 10199 Vasily Govorukhin (*Russia*): Numerical Investigation of Convective Regimes in a Planar Filtrational Convection Problem
- 10234 Michel Quintard (*France*): Dissolution in Porous Media: Upscaling, Instabilities and Heterogeneity Effects
- 10548 Guzel T. Bulgakova (*Russia*): Instability and Dynamic Chaos of Non-equilibrium Filtration of Gaseous Liquid
- 11109 Victor N. Nikolaevskiy (*Russia*): Plastic Mass Flow of Sand Under Action of Pore Pressure Gradient
- 11115 Dmitry Nikolaevich Mikhaylov (*Russia*): P-Waves Behavior at Transition from Liquid to Gas-Saturated Porous Media
- 11248 Włodzimierz Bielski (*Poland*): Nonstationary Flow of Stokesian Fluid through Elastic Skeleton with Hierarchical Structure
- 11343 Franck Plouraboue (*France*): Confined Air-liquid Drainage: Local Analysis and Invasion Percolation Model
- 11487 Thomas Loimer (*Austria*): A Joule-Thomson Process of a Wetting Fluid Near Saturation
- 11994 Piotr Szymczak (*Poland*): Microscopic Simulations of the Dissolution of Rock Fractures
- 12376 Marie-Christine Néel (*France*): Fractional Model for Solute Spreading in Randomly Heterogeneous Porous Media
- 12528 Liana Kovaleva (*Russia*): Oscillatory Modes of Adsorption in the Flow of Multicomponent Systems
- 12611 Mieczysław Cieszko (*Poland*): Extended Description of Pore Space Structure and Fluid Flow through Anisotropic Porous Materials
- 12617 Robert P. Behringer (*USA*): Onset of Convection for a Miscible Fluid in a Porous Medium

FM13 – Flow instability and transition (P. Huerre, France & P.A. Monkewitz, Switzerland)

- 10185 Aomar Ait Aider (*France*): Instabilities in a Taylor-Dean Open Flow
- 10188 François Lusseyran (*France*): Shear Layer Instability and Frequency Modes Inside an Open Cavity
- 10313 Bruno Eckhardt (*Germany*): Travelling Waves and Transition to Turbulence in Pipe Flow
- 10487 Joseph T.C. Liu (*USA*): Nonlinear Mechanics of Wavy Instability of Steady Longitudinal Vortices and Drag Rise in Boundary Layer Flow
- 10489 J.M. Floryan (*Canada*): Stability of Flow in a Rough Channel
- 10525 Stéphane Leblanc (*France*): Stability of Lagrangian Ideal Flows
- 10640 Laurette Tuckerman (*France*): Instability Thresholds of Flow Between Exactly Counter-Rotating Disks

- 10916 Peter W. Duck (*UK*): Transient Growth in Developing Plane and Hagen Poiseuille Flow
- 11186 Denis Martinand (*UK*): Three-dimensional Global Modes in Spatially Varying Rayleigh-Benard-Poiseuille Convection
- 11396 Laurent Lacaze (*France*): Elliptical Instability in a Rotating Spheroid
- 11461 Jacob Cohen (*Israel*): The Instability of a Localized Vortex Disturbance in Uniform Shear Flow
- 11647 Maher Lagha (*France*): Subcritical Transition to Turbulence in Plane Couette Flow
- 11995 Eckart Meiburg (*USA*): Three-Dimensional Vortex Breakdown in Swirling Jets and Wakes
- 12150 Jonathan J. Healey (*UK*): A New Convective Instability with Growth Normal to a Boundary Layer
- 12233 Guillemette G. Caulliez (*France*): By-pass Laminar-Turbulent Transition of the Wind-Driven Free Surface Flow
- 12280 Denis S. Goldobin (*Russia*): Influence of Swirl Vibrations on Flow in Long Cylinder
- 12291 Masato Nagata (*Japan*): Nonlinear Stability of Rotating Channel Flow
- 12372 Uwe Ehrenstein (*France*): On Instability Mechanisms in a Separating Boundary-layer Flow
- 12381 Leandro Franco de Souza (*Brazil*): Gortler Vortex Secondary Stability: Varicose Mode
- 12425 François Gallaire (*France*): Spiral Vortex Breakdown as a Global Mode
- 12431 Dwight Barkley (*UK*): Computational Study of Turbulent-Laminar Bands in Couette Flow
- 12483 Arnaud Antkowiak (*France*): A Generic Mechanism for By-Pass Transition in Vortices
- 12508 Thierry Feraille (*France*): Global Stability of the Flow Induced by Wall Injection
- 12509 Christophe Millet (*France*): Acoustic Field Generated by Instability Waves in the Transonic Regime
- 12542 Ilmars Grants (*Latvia*): Nonlinear Transition of a Flow Driven by a Rotating Magnetic Field
- 12711 Jean-Marc Chomaz (*France*): Fully Nonlinear Global Modes and Transition to Turbulence in Open Flows
- 12766 Cherif Nouar (*France*): Stability of Plane Poiseuille Flow and Energy Growth in the Case of a Bingham Fluid
- 13019 Jens Norkaer Sørensen (*Denmark*): Instability of the Far Wake Behind a Wind Turbine

FM14 – Flow in thin films (N. Aksel, Germany & V. Shkadov, Russia)

- 10220 Serafim Kalliadasis (*UK*): Dynamics of a Reactive Falling Film at Large Peclet Numbers
- 10543 Alexander Oron (*Israel*): Long-Wave Marangoni Instability in Binary-Liquid Films with Soret Effect
- 10557 Vasilis Bontozoglou (*Greece*): Solitary Waves on Liquid Film Flowing Along a Periodic Wall
- 10642 Nuri Aksel (*Germany*): Effect of Bottom Undulations on the Stability of Film Flow Down Inclined Planes
- 10928 Andreas Wierschem (*Germany*): Hydraulic Jumps and Resonance in Gravity-Driven Flows of Liquid in Inclined Wavy Channels: Transition and Hysteresis
- 11089 Jens G. Eggers (*UK*): Hydrodynamic Theory of De-Wetting
- 11413 Norbert Alleborn (*Germany*): Linear Response of a Viscous Liquid Sheet
- 11477 Le Han Tan (*Australia*): Experimental and Numerical Study of Marangoni-Natural Convection
- 11509 Dirkjan B. van Dam (*Netherlands*): Layer Thickness Distribution of Thin-Film Ink-Jet Printed Structures.
- 11739 Takao Yoshinaga (*Japan*): Amplification of Nonlinear Disturbances on a Falling Liquid Sheet

- 12155 Gregory P. Chini (*USA*): Thin Film Flows Near Isolated Humps and Interior Corners
 12293 Tatiana Gambaryan-Roisman (*Germany*): Gravity- and Shear- Driven Thin Films Flow on Heated Hicrostructured Walls
 12656 Jaroslav Tihon (*Czech Republic*): Hydrodynamics of the Solitary Waves Travelling Down a Liquid Film
 12858 John Tsamopoulos (*Greece*): Transient Displacement of Viscoelastic Liquids by Air

FM15 – Fluid mechanics of materials processing (F. Dupret, Belgium & R. Moreau, France)

- 10363 Jeffrey J. Derby (*USA*): Analysis of Flow-Induced, Step-Bunching Instabilities During the Growth of Crystal from Liquid Solutions
 10860 René J. Moreau (*France*): Relevance of Alfvén Waves in Process Metallurgy under a High Magnetic Field
 11386 Mohammed El Ganaoui (*France*): Effect of Thermal Boundary Modulation in a Restricted Fluid Domain of a 3D Vertical Bridgman Apparatus
 11893 Viatcheslav V. Kolmychkov (*Russia*): 3D Computer Simulation of Time-Depended Solutal Convection
 11903 Geoffrey M. Evans (*Australia*): Liquid and Gas Jets Impinging on a Moving Wetted Surface
 11929 Vadim I. Polezhaev (*Russia*): Convective Instabilities in Czochralski Model
 12349 Andreas Cramer (*Germany*): New Possibilities for Velocity Measurements and Model Experiments in Liquid Metal Processing
 12591 François Dupret (*Belgium*): Dynamic Simulation of the Entire Crystal Growth Process: Multi-Scale Analysis of Melt Flow Transients
 12636 Othman Bouizi (*France*): Sensitive Regions and Optimal Perturbations in the Floating Zone Using the Adjoint System

FM16 – Fluid mechanics of suspension (R. Bonnecaze, USA & E. Guazzelli, France)

- 10248 François Feuillebois (*France*): Effective Viscosity of an Inhomogeneous Dilute Suspension Flowing Along a Wall
 10361 Andreas Acrivos (*USA*): Velocity Fluctuations in Non-Brownian Suspensions Undergoing Simple Shear Flows
 10603 Vishwajeet Mehandia (*India*): The Collective Dynamics of Self-Propelled Particles
 10993 Krzysztof Sadlej (*Poland*): Microstructure of a Dilute Sedimenting Suspension
 11236 B.U. Felderhof (*Germany*): Sedimentation of Dilute Suspensions
 11409 Maria L. Ekiel-Jezewska (*Poland*): Relaxation Time for Sedimenting Spheres of a Suspension with Periodic Boundary Conditions
 11418 Anthony Ladd (*USA*): Numerical Simulations of Particle Suspensions in a Rotating Flow
 11431 Gerhard Naegele (*Germany*): A Mode-Mode Coupling Scheme of Colloidal Electrolyte Friction
 11473 Helen J. Wilson (*UK*): The Effect of Different Particle Contacts on Suspension Rheology
 11480 Evgeny S. Asmolov (*Russia*): Evolution of Suspension Sedimenting in a Container Bounded by Horizontal Walls
 11588 Elisabeth Guazzelli (*France*): Spreading Fronts and Fluctuations in Sedimentation: Part I Experiments
 11725 Alan L. Graham (*USA*): Constant Force and Constant Velocity Momentum Tracers in Concentrated Suspensions
 11749 Cyril Cassar (*France*): Flow of a Concentrated Suspension Down a Rough Plane
 11850 Jeffrey F. Morris (*USA*): Inertial Migration of Rigid Spherical Particles in Poiseuille Flow
 11884 Gabriel Seiden (*Israel*): Segregation of Suspended Particles in a Rotating Fluid-Filled Horizontal Cylinder – Experiment and Theory

- 11991 Roger T. Bonnecaze (*USA*): Migration of Buoyant Mono- and Bi- Disperse Suspensions in Low Reynolds Number Pressure-Driven Pipe Flow
- 12005 David Saintillan (*USA*): Dynamic Simulations of the Instability of Sedimenting Fibers
- 12056 Howard Stone (*USA*): Mobility of Membrane-Trapped Particles: Protrusion into the Surrounding Fluid
- 12345 E. John Hinch (*UK*): Spreading Fronts and Fluctuations in Sedimentation: Part II Computer Simulations
- 12452 Ileana C. Carpen (*USA*): Single Particle Motion in Colloidal Dispersions
- 12574 Michel Cloitre (*France*): Slip and Flow in Pastes

FM17 – Granular flows (R. Behringer, USA & I. Goldhirsch, Israel)

- 10253 Detlef Lohse (*Netherlands*): Impact
- 10371 Joe D. Goddard (*USA*): Maximum-Entropy Estimates and Virtual Thermomechanics for Granular Assemblies
- 10524 Herbert E. Huppert (*UK*): Granular Column Collapse
- 10959 J. Rajchenbach (*France*): Gravity Flow of a Densely-Packed Granular Material
- 11169 Irena Sielamowicz (*Poland*): Particle Image Velocimetry Analysis of Granular Material Flows
- 11751 Maxime Nicolas (*France*): Pore Pressure Relaxation During Granular Compaction
- 11775 Pierre Jop (*France*): Granular Flows on a Heap
- 11876 Osamu Sano (*Japan*): Collapse, Growth and Merging of Cavity Regions in a Granular Material Due to Viscous Flow
- 11883 Akiko Ugawa (*Japan*): Undulations and Ripples of a Thin Granular Layer Due to Vertical Vibration
- 12073 Christine Hrenya (*USA*): Species Segregation Driven by a Granular Temperature Gradient
- 12308 Isaac Goldhirsch (*Israel*): Kinetics of Weakly Frictional Granular Gases
- 12338 John R. de Bruyn (*Canada*): Morphology and Scaling of Impact Craters in Granular Media
- 12399 Lou Kondic (*USA*): Extended Granular Temperature
- 12445 J.C. Tsai (*USA*): Evolution of Internal Structure of Sheared Dense Granular Flows: Crystallization and History-Dependent Final States
- 12790 Radosław L. Michałowski (*USA*): Arching in Granular Media
- 12883 Renaud L. Delannay (*France*): Transverse Motion, Segregation and Rotations in 2D Granular Flows
- 13029 Sylvain Courrech du Pont (*UK*): Velocity Profiles During Granular Avalanches

FM18 – Low-Reynolds-number flow (R.H. Davis, USA & C. Pozrikidis, USA)

- 10297 Ryszard Staroszczyk (*UK*): Radially Symmetric Polar Ice Sheet Flow with Evolving Anisotropic Fabric
- 10565 Robert B. Jones (*UK*): Hydrodynamic Interaction of a Spherical Particle in Poiseuille Flow Between Planar Walls
- 10766 Mark G. Blyth (*UK*): Two-Layer Stagnation Point Flows
- 10983 Lisa A. Mondy (*USA*): Free Surface Deformation in Suspensions Near a Rotating Rod
- 11300 Bogdan Cichocki (*Poland*): Particles Located on a Planar Free-Surface-Hydrodynamic Interactions in Quasi-Two-Dimensional System
- 11460 Alexander Prokunin (*Russia*): Microcavitation and Detachment of a Stokes Particle in Near-Wall Slow Motion
- 11915 Emin Fuad Kent (*Turkey*): Flow Visualization Experiments of Cellular Stokes Flows Induced by Rotation of a Cylinder Variously Positioned Inside Channels
- 11922 Izabella Pieńkowska (*Poland*): Many-Sphere Hydrodynamic Interactions: Weak Convective Inertia Effects
- 12164 Michał Branicki (*UK*): Viscous Eddy Structures in an Oscillating Cylinder with Sharp Corners

- 12859 George K. Karapetsas (*Greece*): Transient Squeeze Flow of Viscoplastic Liquids
 12981 Devanayagam Palaniappan (*Qatar*): Slow Rotation of a Double Sphere in a Viscous Fluid

FM19 – Magnetohydrodynamics (P.A. Davidson, UK & A. Thess, Germany)

- 10025 Antoine Sellier (*France*): Migration and Interaction of two Conducting Particles Freely Immersed in a Liquid Metal
 10235 Vladimir Shtern (*USA*): Bifurcation of Conical Magnetic Field
 10931 Ulrich Müller (*Germany*): Complementary Experiments at the Karlsruhe Dynamo Test Facility
 11120 Jurij B. Kolesnikov (*Germany*): Liquid Metal Flow Under Inhomogeneous Magnetic Field
 11124 Peter A. Davidson (*UK*): Small-Scale Motion in the Core of the Earth
 11429 Hubert Baty (*France*): Magnetohydrodynamic Instabilities of Astrophysical Jets
 11458 Yuji Hattori (*Japan*): Magnetohydrodynamic Motion of Toroidal Magnetic Eddies
 11621 Jacques Léorat (*France*): Fluid Dynamos and Precession Driving
 11637 Jungwoo Kim (*S. Korea*): Large Eddy Simulation of Magnetic Damping of Jet
 11681 Daniel P. Lathrop (*USA*): Observations of the Magnetorotational Instability in Spherical Couette Flow
 11809 Steinar Borve (*Norway*): Simulating the Orszag-Tang vortex using RSPH
 11906 Uwe Krieger (*Germany*): Homogenisation of Electrically Heated Glass Melts by Lorentz Forces
 12090 Andre D. Thess (*Germany*): A Model for Liquid Metal Current Limiters
 12107 Krzysztof A. Mizerski (*Poland*): The Magnetohydrodynamic Couette Flow in a Plane and Spherical Geometries with Singular Hartmann Boundary Layers
 12120 Avalos-Zuñiga (*France*): Mean Electromotive Force for a Ring of Helical Vortices
 12125 Andreas Tilgner (*Germany*): Numerical Simulations of Dynamo Experiments
 12290 Vaclav Kocourek (*Germany*): Stability of Liquid Metal Drops Affected by High-Frequency Magnetic Fields
 12330 Nathanaël Schaeffer (*France*): Quasi-Geostrophic Dynamos
 12363 Serge Barral (*Poland*): Model of Gas Flow Inside a Plasma Thruster
 12587 Jörg Stiller (*Germany*): Numerical Study of the Flow in a Finite Cylinder Driven by a Rotating Magnetic Field
 12605 Hartmut Brauer (*Germany*): Interface Reconstruction in Cylindrical Two-Compartment-Systems Using Magnetic Field Tomography
 12613 Frank Stefani (*Germany*): Contactless Inductive Flow Tomography: Theory and Experiment
 12979 Jonathan A. Mestel (*UK*): Dynamo Action in Steady Helical Pipe Flow

FM20 – Multiphase flows (S. Balachandar, USA & J. Magnaudet, France)

- 10416 Konstantin Volkov (*UK*): Large-Eddy Simulation of Particle Dispersion in the Duct with Fluid Injection
 10690 Maria Josefina Ferreira (*Portugal*): Sings of Flooding Instability in Inclined Liquid Films at High Pressure and Mass Transfer in High Density Gas Slugs
 10843 Daniel Joseph (*USA*): Viscous and Viscoelastic Potential Flow
 11189 Urbano J. Sánchez Domínguez (*Spain*): Separation and Sorting of Heavy Particles Suspended in a Fluid by Settling in a Periodic Vorticity Field
 11655 Elena Trostinetsky (*Israel*): Gas-Liquid Interfacial Distribution in Inclined Downward Pipe Flow
 11745 Stanisław Anweiler (*Poland*): Videogrametry in Fluidized Bed Reactors
 12092 Thomas Seon (*France*): Gravity Induced Mixing of Miscible Fluids in Vertical and Inclined Tubes
 12139 Frederic Risso (*France*): Oscillatory Motion of Freely-Moving Light Bodies: from Cylinders to Disks

- 12342 Touvia Miloh I. (*Israel*): Non-Uniform Flow Hydrodynamics of Deformable Shapes
 12383 Veronique Roig (*France*): Mean Motion Induced in a Liquid by Rising Bubbles
 12397 Jacobus J. Derksen (*USA*): Plane Couette Flow of Dense Liquid-Particle Suspensions
 12886 Daniel Zajac (*Poland*): Image Processing Method in Estimation of Bubble Column's Work
 13012 Cristian Marchioli (*Italy*): Statistics and Preferential Distribution of Micro-Particles in Turbulent Boundary Layer: Implications for Resuspension Mechanisms

FM21 – Solidification and crystal growth (M. Glicksman, USA & M.G. Worster, UK)

- 11058 Chuan F. Chen (*USA*): Experimental Observations of Hydrate Formation in a Convection Tank
 11208 Chih-Ang Chung (*Taiwan*): Morphological Stability of Directional Solidification under Temperature Modulations
 11270 Peter Guba (*UK*): Nonlinear Oscillatory Convection in Mushy Layers
 11320 Pascale Aussillous (*UK*): Magnetic Resonance Imaging of Structure and Convection in Solidifying Mushy Layers
 11328 Andrew Thompson (*USA*): Solidification and Compositional Convection of a Ternary Alloy
 11331 Michael A. Gonik (*Russia*): AHP Setup for Low Lamellar Melt Flow Study in Crystal Growth
 11362 Liliana Braescu (*Romania*): Optimization of the Growth Conditions of a Nd:YVO₄ Cylindrical Bar
 11364 Jerzy Banaszek (*Poland*): Front Tracking Technique on a Fixed Grid in Modelling of Binary Mixture Solidification with Natural Convection
 11926 George G. Tsykin (*Russia*): Salt Precipitation in Geothermal Reservoirs
 12276 Jacqueline Ashmore (*UK*): Boundary-Layer Analysis of Chimney Structures in Mushy Layers
 12278 Irina Fayzrakhmanova (*Russia*): Travelling Magnetic Field Influence on Crystal Growth by Bridgman Method
 12312 Gustav Amberg (*Sweden*): A Semi-Sharp Phase Field Method for Quantitative Phase Change Simulations
 12365 Sven Eckert (*Germany*): Directional Solidification of Pb-Sn Alloys Affected by a Rotating Magnetic Field
 12543 Marc Georgelin (*France*): Cell Shapes in Directional Solidification: a Global Study
 12743 Leszek Czechowski (*Poland*): Convection Driven by Tidal Heating: Numerical Model and Parameterized Theory
 12768 Daniel M. Anderson (*USA*): Ternary Alloy Convection in Mushy Layers
 13008 Chang Kyun Choi (*S. Korea*): Convective Instabilities During Solidification of a Mushy Layer

FM22 – Stirring and mixing (H. Aref, USA & E. Villermaux, France)

- 10130 Frank C.G.A. Nicolleau (*UK*): Development of the Fractal Dimension of Material Elements in Homogeneous Isotropic Turbulence Using Kinematic Simulation
 10497 Stephen M. Cox (*Australia*): Chaotic Advection in a Mixer with Changing Geometry
 10532 Patrice Meunier (*France*): Enhanced Mixing by Vortices
 10896 Jörg Schumacher (*Germany*): Geometric Features of High-Schmidt Number Scalar Mixing
 11190 Alain Pocheau (*France*): Front Propagation in Laminar Cellular Flows: an Experimental Study
 11293 Stephen Wiggins (*UK*): On the Design of 3D Micromixers Having the Bernoulli Property
 12048 Alain Pumir (*France*): Intermittent Distribution of Heavy Inertial Particles in Turbulent Flows

- 12110 Alexandre Gourjii (*Ukraine*): Chaotic Stirring of Passive Fluid by a Vortex Pair in Circular Domain
- 12158 Mark A. Stremler (*USA*): Chaotic Advection and Mixing in Pulsed Source-Sink Systems
- 12209 Shenyang Shy (*Taiwan*): On Dissipative Structures of Stirring-Grids Turbulence
- 12257 Tatyana S. Krasnopolskaya (*Ukraine*): Evaluation of Transport Properties by Exchange Matrix Method
- 12326 Emmanuel Villermaux (*France*): Mixing Is an Aggregation Process
- 12415 Jerzy Baldyga (*Poland*): Stirring and Mixing Effects in Agglomerative Precipitation
- 12439 Dmitri L. Vainchtein (*USA*): Resonances and Mixing in Stokes Flows
- 12442 Philip Boyland (*USA*): Mixing in Multiconnected Planar Domains
- 12545 Richard J. Keane (*UK*): Eulerian Measures for Lagrangian Stirring in a Thermally Driven Flow
- 12610 Marek Jaszczur (*Poland*): An Analysis of Mixing Process in a Static Mixer
- 12633 Dennis van der Woude (*Netherlands*): Stirring by Blinking Rotlets in a Bounded Stokes Flow
- 12731 Alain Bergeon (*France*): Weak Inertia and Mixing Between Rough Surfaces
- 12761 Frederic Bottausci (*USA*): Active Shear Superpositon Micromixer

FM23 – Topological fluid mechanics (P.L. Boyland, USA & K. Ohkitani, Japan)

- 10247 Morten Brons (*Denmark*): Streamline Topology of the Nearwake of a Circular Cylinder at Low Reynolds Numbers
- 10938 Koji Ohkitani (*Japan*): Eulerian-Lagrangian Analysis of Navier-Stokes Turbulence
- 11060 Matthew D. Finn (*UK*): Topological Chaos in Simple Mixers
- 11166 Tsutomu Kambe (*Japan*): Gauge Principle for Ideal Fluids and Variational Principle
- 11660 Yoshi Kimura (*Japan*): Particle Transport by a Vortex Soliton
- 11677 Robert W. Ghrist (*USA*): Generic Hydrodynamic Instability
- 12484 Mitsuaki Funakoshi (*Japan*): Relation Between Mixing Efficiency and Geometrical Property of Stable Manifolds
- 12868 Dmytro I. Cherniy (*Ukraine*): Topological Aspects of the Tornado Problem

FM24 – Turbulence (Olivier Metais, France & R.D. Moser, USA)

- 10149 Julian Andrzej Domaradzki (*USA*): Large Eddy Simulations of Decaying Rotating Turbulence
- 10455 Maxim S. Loginov (*Germany*): Large-Eddy Simulation of Shock-Wave / Turbulent-Boundary-Layer Interaction
- 10506 Sebastien Poncet (*France*): Experimental Study of Rotor-Stator Flows with Centripetal Fluxes
- 10564 Marta Waclawczyk (*Poland*): PDF Computation of Turbulent Flows with a New Near-Wall Model
- 10937 Naoya Takahashi (*Japan*): Interaction Between a Columnar Vortex and External Turbulence
- 11116 Rainer Friedrich (*Germany*): Turbulence Scalings in Supersonic Channel Flow
- 11151 Enrico Pasero (*Italy*): On the Scale Similarity in Large Eddy Simulation
- 11161 Tomasz Lipniacki (*Poland*): Two Scale Approach to Anisotropic Turbulence in Hel II
- 11256 Stefan Hickel (*Germany*): Optimization of an Implicit Subgrid-Scale Model for LES
- 11303 Agnes Maurel (*France*): Study of the Turbulent Energy Spectrum Build Up in an Experimental Vortex Burst
- 11454 Bernd R. Noack (*Germany*): Empirical Galerkin Models for Incompressible Flow — Pressure-Term and 'Subgrid' Turbulence Representations
- 11488 Yu-L. Liu (*China*): Orthonormal Wavelet Analysis of CGT in Fully Developed Asymmetric Turbulent Channel Flow
- 11802 Xiangyu Hu (*Germany*): The Cellular Structure and Its Tracks of a H₂/O₂/Ar Detonation Waves

- 11814 Frederic Moisy (*France*): Energy Spectrum in Rotating Turbulence
 12004 Akira Rinoshika (*Japan*): Three-Dimensional Turbulent Structures of Different Scales
 12151 Tomomasa Tatsumi (*Japan*): Inertial Similarity of Velocity Distributions in Homogeneous Isotropic Turbulence
 12430 Robert M. Kerr (*UK*): A New Mixed Nonlinear LES Models for Boundary Layers
 12564 Thomas Indinger (*Germany*): 3D-Measurements in an Adverse-Pressure-Gradient Turbulent Boundary Layer over Smooth and Ribbed Surfaces
 12652 Song Fu (*China*): POD Analysis of Coherent Structures in Turbulent Flows
 12675 Vladimir I. Borodulin (*Russia*): Resonant Interactions of 3D Instability Waves in an Airfoil Boundary Layer for Harmonic and Broadband Perturbations
 12740 Pierre Comte (*France*): Compressibility Effects and Sound Propagation in Turbulent Channel Flow
 12965 Hassan M. Nagib (*USA*): Impact of Pressure-Gradient Conditions on High Reynolds Number Turbulent Boundary Layers

FM25 – Vortex dynamics (G.J.F.van Heijst, Netherlands & E. Krause, Germany)

- 10683 Miguel A. Herrada (*Spain*): New Means of Vortex Breakdown Control
 11391 Paul Billant (*France*): Instabilities of a Vortex Pair in a Stratified and Rotating Fluid
 11467 Eugene Benilov (*Ireland*): Stability of Oceanic Vortices: a Solution to the Problem
 11615 Yasuhide Fukumoto (*Japan*): Curvature Instability of a Vortex Ring
 11676 Fernando L. Ponta (*USA*): Numerical Experiments on Vortex Shedding From an Oscillating Cylinder
 11683 Denis Blackmore (*USA*): Bifurcation of Motions of Three Vortices and Applications
 11741 Hung-Cheng Chen (*Taiwan*): Strong Cyclonic Vortices over Topography on a Beta-Plane
 11964 Gert Jan F. van Heijst (*Netherlands*): Spontaneous Sign Reversals in Self-Organized States of Forced Two-Dimensional Turbulence on a Bounded Square Domain
 12032 Felix B. Kaplanski (*Estonia*): A Model for the Formation of 'Optimal' Vortex Rings with Taking into Account Viscosity
 12041 Katsuya Ishii (*Japan*): Numerical Simulation of Vortical Flows Using a Highly Accurate Finite Difference Scheme
 12051 Michael D. Patterson (*UK*): The Development of an Axisymmetric Gravity Current
 12080 Ewa Tuliszk-Sznitko (*Poland*): Numerical Investigation of the Laminar-Turbulent Transition of the Flow in a Rotor-Stator Cavity
 12108 Ramiro Godoy-Diana (*France*): Viscous Vertical Length Scale Selection in Stratified Fluids
 12161 S. Balachandar (*USA*): On Local Vortex Identification
 12196 Vyacheslav V. Meleshko (*Ukraine*): The Modelling of The Dynamics of Hairpin Vortex Packets in Wall Turbulence
 12275 Marcin Kurowski (*Poland*): Coherent Structure of Point Vortices Influenced by Uniform Straining Flow
 12690 Wolfgang Schröder (*Germany*): Strong Shock-Vortex Interaction a Numerical Study
 12748 Oscar U. Velasco Fuentes (*Mexico*): Isolated Vortices over Seamounts: Laboratory Experiments and Numerical Simulations
 12821 Klaus W. Hoyer (*Switzerland*): Three Dimensional Velocity Field of Vortices Impinging on a Wall Obtained by Scanning Particle Tracking Velocimetry
 12836 Pawel Regucki (*Poland*): Study of the Vortex Rings Interaction by 3d Vorticity Particle-In-Cell Method

FM26 – Waves (W.K. Melville, USA & V.I. Shrira, UK)

- 10245 Lev Shemer (*Israel*): Unidirectional Steep Waves in Wave Tanks
 10746 Tetsu Hara (*USA*): Wave Breaking and Equilibrium Surface Wave Spectra
 10762 T.R. Akylas (*USA*): Propagation and Interactions of Nonlinear Internal Gravity Wave Beams

- 10861 Vladimir E. Zakharov (*USA*): Weak-Turbulent Theory of Wind-Driven Sea
- 11126 Hu Huang (*China*): Shallow-Water Theory for Wave-Current-Bottom Interactions
- 11134 Gennady El (*UK*): Unsteady Undular Bore Transition in Fully Nonlinear Dispersive Wave Dynamics
- 11144 Anatoli Ivanovich Dobrolyubov (*Belarus*): The Theory of Travelling Deformation Waves and Its Applications in Biomechanics, Engineering, and Geophysics
- 11179 William R. Phillips (*USA*): The Spacing of Langmuir Circulation in Strong Wavy Shear
- 11199 Thomas Peacock (*USA*): Experiments on Rotating and Reflecting Internal Wave Beams
- 11230 Paul A. Hwang (*USA*): Spatio-Temporal Measurements of Capillary-Gravity Waves
- 11290 Gérard Iooss (*France*): Standing Gravity Waves in Deep Water
- 11345 Emilian I. Ráráu (*UK*): Nonlinear Three-Dimensional Free Surface Flows in Finite and Infinite Depth
- 11417 Dorian Fructus (*Norway*): Dynamics of Crescent Wave Patterns in a Channel
- 11468 Colm Howlin (*Ireland*): Evolution of Packets of Surface Gravity Waves over Smooth Topography
- 11548 Walter Craig (*Canada*): Three Dimensional Gravity Water Waves
- 11591 Vasyl P. Lukomsky (*Ukraine*): Sharpening and Breaking of Subharmonic Gravity Waves on Deep Water
- 11680 Xin Zhang (*USA*): Short Wind Waves and Surface Wind Drift
- 11746 Takeshi Kataoka (*Japan*): Transverse Instability of Surface Solitary Waves
- 11803 Jan Erik Weber (*Norway*): A Lagrangian Approach to Wave-Induced Oceanic Mass Transport
- 12087 Victor I. Shrira (*UK*): Effect of Horizontal Component of the Coriolis Force on Propagation of Near-Inertial Waves in the Ocean
- 12089 Frédéric Dias (*France*): Generalized Internal Solitary Waves and Fronts
- 12268 Igor A. Brovchenko (*Ukraine*): Intermittent Mixing by Multiscale Breaking of Wind Waves: Implications for Oil Dispersion
- 12424 Chantal Staquet (*France*): Focusing of an Inertia-Gravity Wave Packet with a Baroclinic Shear Flow
- 12715 Jean-Marc Vanden-Broeck (*UK*): Steep Capillary Waves in Electrified Fluid Sheets
- 12813 Georgy I. Burde (*Israel*): Bi- Directional Water Waves and Integrable High Order KDV Equations

SM1 – Computational solid mechanics (T. Belytschko, USA & P. Wriggers, Germany)

- 10270 Chung-Yue Wang (*Taiwan*): Elastic-Plastic Large Deformation Analysis of 2D Frame Structure
- 10274 Terumi Touhei (*Japan*): Multiscale Analysis of Scattered Elastic Waves Based on the Lippmann-Schwinger Equation
- 10423 Hans H. Müller-Slany (*Germany*): Model Updating a Multicriteria Optimization Process in Mechanics
- 10559 Yuan Lin (*China*): Experiment and Quasicontinuum Simulation of Nanoindentation of Single Crystal Copper
- 10665 Vasilios G. Mokos (*Greece*): A BEM Solution to Transverse Shear Loading of Beams
- 10728 Anatoli Stulov (*Estonia*): Mechanical Features of Piano Hammer Felt
- 10829 Larry D. Libersky (*USA*): A Dual Particle Computational Method for Continua
- 11154 Jarosław Knap (*USA*): Mesh Optimization for the Quasicontinuum Method: A Generalization of VALE
- 11193 Jiann-Tsair Chang (*Taiwan*): Derivation of the Higher-Order Stiffness Matrix of a Space Frame Element for Geometric Nonlinear Analysis of Structures
- 11202 Pavlo A. Steblyanko (*Ukraine*): The Method of Solving of Non-Stationary Coupled Problems of the Theory Thermal-Plasticity for the Rotation Shells

- 11211 Julia Mergheim (*Germany*): A New Approach for the FE Modelling of Cohesive Cracks
- 11291 Stanisław A. Lukaszewicz (*Canada*): Effective Solution for Finite Element Problems with Nonlinear Constraints
- 11298 Etienne L.G. Pecquet (*Belgium*): Lingopti Project: Semi-Continuous Casting Process of Copper-Nickel Alloys
- 11334 George Mejak (*Slovenia*): Two Scale Finite Element Method
- 11389 Grzegorz W. Zboiński (*Poland*): Problems of Application of Hierarchical Modelling, Displacement FEM and a Posteriori Residual Error Estimation to Static and Dynamic Adaptive Analysis of Complex Structures
- 11482 Florian Kovacs (*Hungary*): Statics And Kinematics of Symmetric Swelling Viruses
- 11580 Jixin Yang (*China*): A Numerical Approach for Large-Scale Computation CEM
- 11720 Zhenhan Yao (*China*): Some Investigations on FM Bem in Solid Mechanics
- 11769 Anthony Nouy (*France*): Radial-Type Approximation Technique for a Space-Time Multiscale Computational Strategy
- 11797 Julien Réthoré (*France*): An Energy Conserving Scheme for Time Dependent Problems Using the Extended Finite Element Method
- 11817 Seyoung Im (*S. Korea*): Development of a Novel 'Crack' Finite Element for Propagation Simulation
- 12054 Alexandre V. Vakhrouchev (*Russia*): Modelling of Static and Dynamic Processes of Nanoparticles Interaction
- 12101 Andras Lengyel (*Hungary*): Singularities of the Four-Sided Antiprism Ring
- 12115 Ercan Guerses (*Germany*): Analysis of Evolving Deformation Microstructures in Instable Inelastic Solids Based on Energy Relaxation Methods
- 12131 Rene L.J.M. Ubachs (*Netherlands*): Microstructural Behaviour of Solder Joints
- 12167 Sergey N. Medyanik (*USA*): Molecular Mechanics Simulations of Carbon Nanostructures Using Multi-Scale Boundary Conditions
- 12177 Hirohisa Noguchi (*Japan*): Multiscale Buckling Analyses of Corrugated Fiberboard
- 12237 Pierre Feissel (*France*): Modified Error in Constitutive Relation and Its Application to Dynamic Tests with Corrupted Boundary Conditions
- 12310 Juha A. Mäkipelto (*Finland*): Geometry Based Rational Enrichment Functions for Triangular Plane Elasticity Element
- 12340 Marek S. Karaś (*Poland*): Solving of Indirect Problems Using Trefftz Method
- 12351 Alexey V. Borisov (*Russia*): Tensor Invariants and Mechanisms of Transition to Chaos in Nonholonomic Dynamical Systems
- 12359 Mathieu Cloirec (*France*): Analysis of a Structural Detail Using a Two-Scale Approach
- 12441 Robert B. Haber (*USA*): Adaptive Discontinuous Galerkin Method for Elastodynamics on Unstructured Spacetime Grids
- 12455 Marino Arroyo (*USA*): Continuum Mechanics and Carbon Nanotubes
- 12458 Katerina D. Papoulia (*USA*): Toward Convergence in Initially Rigid Cohesive Fracture Models
- 12534 Stefan Loehnert (*Germany*): Computational Homogenisation of Microheterogeneous Materials Including Decohesion at Finite Strains
- 12562 Antoni John (*Poland*): The Load Cases in Numerical Model of Pelvic Bone with Artificial Acetabulum
- 12579 Andrzej Siemaszko (*Poland*): Shakedown Safety Criterion in Reliability Analysis
- 12584 Eiris F.I. Boerner (*Germany*): A New Finite Element Formulation Based on the Theory of a Cosserat Point
- 12607 Ilson P. Pasqualino (*Brazil*): Arc-Length Method for Explicit Dynamic Relaxation
- 12723 Ekaterina Viatkina (*Netherlands*): Modelling of Non-Uniform Deformation of Metals with Dislocation Cell Structure
- 12727 Frederic Grondin (*France*): The Numerical Homogenization of the Concrete Behavior
- 12737 A. Amine Benzerga (*USA*): Discrete Dislocation Calculations of the Stored Energy of Cold Work

- 12844 Huu Nam Tran (*Czech Republic*): Deformation Analysis of Inflated Cylindrical Membrane of Composite Material with Rubber Matrix Reinforced by Cords
 12845 Dimitri E. Beskos (*Greece*): Dynamic Analysis of Gradient Elastic Solids by BEM
 12901 Kian-Meng Lim (*Singapore*): Variable-Order Singular Boundary Element for Calculation of Three-Dimensional Stress Intensity Factors
 12924 Ellen Kuhl (*Germany*): Application of the Material Force Method to Structural Optimization

SM2 – Contact and friction mechanics (A. Klarbring, Sweden & G. Szefer, Poland)

- 10211 Mykhaylo G. Pantelyat (*Ukraine*): Thermocontact Interaction of Bodies of Revolution During Induction Heating
 10342 Victor M. Musalimov (*Russia*): Dynamic Characteristics and Monitoring of Rubbing Surfaces Quality
 10459 Herman N.V. Parland (*Finland*): Contact Mechanical Analysis of Elastic Multibody Structures
 10686 L.E. Anderson (*Sweden*): Existence and Uniqueness of Steady State Solutions in Thermoelastic Contact With Frictional Heating
 10718 Hamid Reza Irannejad (*Iran*): FE Analysis of Bond for Smooth FRP Rods Embedded in Concrete
 10999 Sergey A. Chizhik (*Belarus*): Modelling of Contact of Structured Materials Based on Data from Scanning Probe Microscopy
 11008 Graham J. Weir (*new zealand*): A Universal Property of Geometrical Hardening
 11074 Istvan Paczelt (*Hungary*): Contact Optimization Problems Associated with the Wear Process
 11135 Feodor M. Borodich (*UK*): Molecular Adhesive Contact for Indenters of Non-Ideal Shapes
 11196 Irina G. Goryacheva (*Russia*): Adhesive Component of the Rolling Friction Force
 11215 Leon M. Keer (*USA*): Fundamental Relations for Frictional and Adhesive Nanoindentation Tests
 11365 Denis Elaguine (*Sweden*): Hertz Contact at Finite Friction and Arbitrary Profiles
 11452 Józef Joachim Telega (*Poland*): Frictional Contact with Wear Diffusion
 11481 Jan Awrejcewicz (*Poland*): On the Contact Thermoelastic Problem with Frictional Heating, Wear and Auto-Vibrations
 11611 Ganna Shyshkanova (*Ukraine*): Three-Dimensional Problem of the Contact by Doubly Connected Domain Taking into Account Roughness and Friction
 11613 Alfred Zmitrowicz (*Poland*): Evolutions of Friction Anisotropy and Heterogeneity
 11697 Victor A. Shevchuk (*Ukraine*): Inverse Problems of Thermoelasticity for Frictionally Interacting Layers
 11778 Alexey A. Kireenkov (*Russia*): Multidimensional Model of Combined Dry Friction
 11933 Yuriy Letser (*Ukraine*): Numerical Modeling of Contact Fracture of Elasto-Plastic Cracked Bodies
 11987 Demirkan Coker (*USA*): Crack-Like and Pulse-Like Modes of Frictional Sliding along an Interface Under Dynamic Shear Loading
 12082 Leila Abdou (*France*): Experimental and Numerical Study of the Brick-Mortar Interface
 12086 Markus Lindner (*Germany*): Experimental and Analytical Investigation of Rubber Friction
 12382 Marius Cocou (*France*): A Dynamic Unilateral Contact Problem for a Cracked Body
 12412 Larissa Gorbatiikh (*USA*): A Simple Model to Account for the Locking Effect Between Two Rough Surfaces under Cyclic Loading
 12553 Stanisław Stupkiewicz (*Poland*): Boundary Layers Induced by Contact of Rough Bodies
 12559 Alexandr A. Olshevsky (*Russia*): The Accounting of Surface Roughness in Contact of Arbitrary Shaped Bodies Using FEM

- 12563 Thibaut Putelat (*UK*): Frictional Sliding of a Multislip System
 12646 Antonio Pinto da Costa (*Portugal*): Second-Order Cone Complementarity Formulation for Quasi-Static Incremental Frictional Contact Problem in Three-Dimensional Space
 12773 Yves Gonthier (*Canada*): A Novel Contact Model Based on Volumetric Information

SM3 – Control of structures (F. Chernousko, Russia & S. Pellegrino, UK)

- 10098 Anupam S. Ahlawat (*India*): Coupled Optimal Design of Building with TMD
 10457 Bartłomiej Błachowski (*Poland*): Optimal Vibration Control of Guyed Masts
 10458 Paweł Hołobut (*Poland*): Time-Optimal Control of Hydraulic Manipulators
 10879 Kazuo Tanizawa (*Japan*): Surface Accuracy of Inflatable Reflector Covered with Stretched Cable
 11036 Daniela G. Marinova (*Bulgaria*): H-inf Control for Smart Multistory Building Structures
 11163 Firdaus E. Udawadia (*USA*): Exact Tracking Control for Nonlinear Structural and Mechanical Systems
 11219 Nikolai N. Bolotnik (*Russia*): Pre-Acting Impact Isolation Systems
 11243 Felix L. Chernousko (*Russia*): Control of Multibody Systems Moving along a Plane
 11265 Agnessa S. Kovaleva (*Russia*): Control of Random Dynamics of a Rigid Rocking Block
 11287 Jong-Dar Yau (*Taiwan*): Suppression of Train-Induced Vibrations of Continuous Truss Bridge by Hybrid TMDs
 12756 Walerian Szyszkowski (*Canada*): Optimization of Active Control of Structural Vibration by the Beam Analogy
 13004 Andre Fenili (*Brazil*): Control of a Nonlinear Slewing Flexible Beam

SM4 – Damage mechanics (M. Chrzanowski, Poland & P. Steinmann, Germany)

- 10011 Noël Challamel (*France*): Stability and Creep Damage of Quasi-Brittle Materials
 10456 Akrum Abdul-Latif (*France*): Modeling of the Damage Evolution at the Granular Scale in Polycrystals under Complex Cyclic Loadings
 10865 Robert Svendsen (*Germany*): Continuum Thermodynamic and Variational Modeling and Simulation of Ductile Failure at Large Deformation with Application to Engineering Structures
 10960 Kari J. Santaoja (*Finland*): Material Models for Hookean Materials with Voids or Cracks
 10961 Chi L. Chow (*USA*): Localized Necking Criterion Based on Acoustic Tensor for Materials with Anisotropic Damage
 10974 René Billardon (*France*): An Elasto-Viscoplastic Model Coupled to Damage and Grain Growth to Take Account of Material Variability
 11228 Andrzej Litewka (*Portugal*): Damage and Failure of Brittle Solids
 11406 Sabine Ricci (*Germany*): Numerical Analysis of Nonlocal Anisotropic Continuum Damage
 11414 Ekkehard Ramm (*Germany*): Discrete Models and Their Application in Damagemechanics
 11415 Ron H.J. Peerlings (*Netherlands*): A Nonlocal Plasticity – Damage Formulation Based on the Micromechanics of Defect Growth
 11665 Marcin Chrzanowski (*Poland*): Propagation of Cracks in Terms of Continuum Damage Mechanics
 11779 Larisa V. Stepanova (*Russia*): An Asymptotic Analysis of Mode I Crack in Creeping Damaged Solids
 11796 Jacek J. Skrzypek (*Poland*): Damage Acquired Anisotropy in Elastic-Plastic Materials
 11885 Jean-Louis Chaboche (*France*): A CDM Approach of Ductile Damage with Plastic Volume Changes

- 11886 Issam Doghri (*Belgium*): Micromechanical Modelling of the Deformation and Damage of Inelastic Brittle Three-Phase Composites: Application to Fiber-Reinforced Concrete
- 12021 François Hild (*France*): Damage Field Identification using Full-Field Displacement Measurements
- 12036 Jian-Ying Wu (*China*): A New Energy-Based Elastoplastic Damage Model for Concrete
- 12088 Henning Schuette (*Germany*): Lifetime Prediction with a Damage Model Based on Mixed-Mode Microcrack Propagation
- 12116 Serdar Goektepe (*Germany*): A Micromechanically Based Network Model for Rubbery Polymers Incorporating Mullins-Type Stress Softening
- 12277 Gilles Lubineau (*France*): Computational Micro-Meso Modeling for Laminates Under Thermomechanical Fatigue and an Oxidizing Atmosphere
- 12298 Ilaria Monetto (*Italy*): A Non-Associative Anisotropic Damage Model for Brittle Materials
- 12333 Andrzej Stachurski (*Poland*): Robust Identification of an Augmented Gurson Model for Elasto-Plastic Porous Media
- 12335 Artur W. Ganczarski (*Poland*): Low Cycle Fatigue Based on Unilateral Damage Evolution
- 12341 Thierry J. Massart (*Belgium*): Coupled Meso-Macro Simulation of Masonry Cracking
- 12749 George Chatzigeorgiou (*Greece*): Coupling Between Progressive Damage and Permeability of Concrete
- 12913 Vincent P. Godard (*France*): Anisotropic Damage Model for Concrete Including Unilateral Effects

SM5 – Dynamic plasticity of structures (N. Jones, UK & T. Wierzbicki, USA)

- 11022 Vikram S. Deshpande (*UK*): Blast Resistance of Clamped Sandwich Beams
- 11051 Tongxi Yu (*China*): Collision Between Two Deformable Structures
- 11107 D. Karagiozova (*Bulgaria*): Counterintuitive Response of Long Circular Tubes to Axial Impact
- 12043 Rami Masri (*Israel*): Self Similar Dynamic Expansion of a Spherical Cavity in Elastoplastic Media
- 12949 Piotr Perzyna (*Poland*): Numerical Investigation of Dynamic Shear Bands in Inelastic Solids as a Problem of Mesomechanics
- 12982 Narinder K. Gupta (*India*): On Non-Axisymmetric Collapse of Thin Tubes

SM6 – Elasticity (R. Kienzler, Germany & L. Wheeler, USA)

- 10442 Katarzyna Kowalczyk-Gajewska (*Poland*): On Invariants of the Elasticity Tensor for Orthotropic Materials
- 10972 Tsolo P. Ivanov (*Bulgaria*): Motion and Stability of an Elastic Heavy Top
- 11220 David M. Haughton (*UK*): Stability of Compressible Elastic Blocks
- 11523 Reuven Segev (*Israel*): Generalized Stress Concentration Factors
- 11526 Lenser A. Aghalovyan (*Armenia*): On Asymptotic Method of Static and Dynamic Boundary Problems Solution
- 11901 Charles Ruimy (*France*): Axisymmetric Force Solution for a Semi-Infinite Cubic Solid
- 11960 Tungyang Chen (*Taiwan*): An Exactly Solvable Microgeometry in Torsion
- 11998 Xiaojing Zheng (*China*): A New Nonlinear Constitutive Relation for Magnetostrictive Materials
- 12039 Gaza H. Maluleke (*South Africa*): Nonlinear Radial Oscillations of Anisotropic Thin-Walled Cylindrical Tubes
- 12122 Marcelo Epstein (*Canada*): Nonlocal Eshelby Entities: a One-Dimensional Example
- 12189 Iwona M. Jasiuk (*USA*): Analysis of Trabecular Bone as a Hierarchical Material
- 12289 Valery P. Matveyenko (*Russia*): Investigation of Couple-Stress Effects in Elastic Bodies Under Deformation

- 12324 Serge N. Gavrilov (*Russia*): New Analytical Approach for Investigation of Non-Stationary Dynamics of Media with Moving Inhomogeneities
- 12354 Gearoid P. Mac Sithigh (*USA*): Agmon's Condition for Incompressible Elasticity: a Variational Formulation
- 12434 Elena F. Grekova (*Russia*): Modelling of Complex Elastic Crystals by Means of Micromorphic Gyrocontinua
- 12575 Vyacheslav V. Lyakh (*Ukraine*): Truncated Elastic Wedge under Torsional Load
- 12685 Valeriy A. Buryachenko (*USA*): Homogenization of Triply Periodic Elastic Media with Random Imperfections
- 12987 Roberta Sburlati (*Italy*): On the Impact Law in Elastic Plate-Like Bodies

SM7 – Experimental methods in solid mechanics (I. Emri, Slovenia & J.L. Freire, Brazil)

- 10492 Keyu Li (*USA*): An Optical Strain Rosette/Ring – Core Method Applied on Laser Weld
- 10691 Masashi Sato (*Japan*): Estimation of Principal Axes of Inertia
- 11556 Michael N. Osipov (*Russia*): The Whole Field Non-Destructive Optical Slicing Method in Three-Dimensional Photoelasticity
- 11617 Sylwester Samborski (*Poland*): Porous Ceramics – Experimental Research and Modelling
- 11764 Yilong Bai (*China*): Critical Sensitivity in Rock Experiments
- 12272 Vsevolod V. Shchennikov (*Russia*): Phase Transitions and Mechanical Properties of Ternary Chalcogenides
- 12551 Saed Mousavi (*Sweden*): SHPB Technique for Identification of Complex Modulus Under Condition of Non-Uniform Stress
- 12666 Michał A. Miskiewicz (*Poland*): In-Situ Observation of Fatigue Crack Growth in Carbon Steel
- 12799 Tadeusz Uhl (*Poland*): New Solutions in Experimental Modal Analysis of Mechanical Structures

SM8 – Fatigue (J. Dominguez, Spain & K. Reifsnider, USA)

- 10698 Jaime Dominguez (*Spain*): Influence of Contact Conditions on Fretting Fatigue Under Spherical Contact
- 11371 Krystyna Majorkowska-Knap (*Poland*): Fatigue Investigations into a Composite Glider Structure
- 11686 Yi Sun (*China*): A Microscopic Mechanics Model
- 11737 Byeongchoon Goo (*S. Korea*): Fatigue Life Prediction Considering Residual Stress Relaxation
- 11920 Pavlo Maruschak (*Ukraine*): Effects of Frequency Temperature and Loading Waveform on Fatigue Crack Growth Rate in Steel 15Kh13MF
- 11927 Steffen Brinckmann (*Netherlands*): Stress Concentrations Caused by Dislocations at the Free Surface
- 12034 Ki-Seok Kim (*S. Korea*): Probabilistic Analysis of Fatigue Crack Growth using Moment Method
- 12217 René C. Alderliesten (*Netherlands*): Energy Release Rate Approach for Delamination in a Fatigue Crack Configuration in Glare
- 12228 Marion Risbet (*France*): Modelling Fatigue Crack Growth with Time-Derivative Equations
- 12391 Youshi Hong (*China*): Characteristics of Very-High-Cycle Fatigue for a High Carbon Low Alloy Steel
- 12914 Dorota I. Kocańda (*Poland*): Modelling of Short Fatigue Crack Growth in a Metal in HCF Range
-

SM9 – Fracture and crack mechanics (D. Gross, Germany & A. Needleman, USA)

- 10250 Michael P. Wnuk (*USA*): A Fractal Cohesive Crack Model
- 10334 Daniel Kujawski (*USA*): Influence of Stress State on Crack-Tip Driving Force
- 10338 Mokhtar Adda-Bedia (*France*): Branching Instability of Brittle Fracture
- 10419 Vidya Sagar Remalli (*India*): Size Effect in Tensile Fracture of Concrete – A Study Based on Lattice Model Applied to CT-Specimen
- 10429 Octavian Pop (*France*): Numerical and Experimental Study of the Plastic Zone in the Vicinity of the Crack Tip by the Optical Caustics Method
- 10579 Vera E. Petrova (*Russia*): Thermoelastic Problems for a Bimaterial with Defects/Singularities
- 10646 Parissa Hosseini-Tehrani (*Iran*): Dynamic Crack Analysis Under Thermal Shock
- 10676 Huijian Li (*China*): Experimental Investigation on Concrete Shear Crack Extension
- 10824 Igor Guz (*UK*): Effect of Inter- and Intralaminar Damage on the Compressive Fracture of Hyperelastic Materials
- 10864 Liviu Marsavina (*Romania*): Experimental and Numerical Crack Growth in a Special Geometry
- 10897 Nikita F. Morozov (*Russia*): Elastodynamics Problems in Domains with Edges
- 10910 Alan Needleman (*USA*): 3D Microstructural Effects on Plane Strain Ductile Crack Growth
- 11045 Andreas Ricoeur (*Germany*): Weight Functions for Cracks in Piezoelectrics
- 11195 Oleksandr V. Menshykov (*Ukraine*): Elastodynamic Contact Problem for Two Penny-Shaped Cracks
- 11321 José Domínguez (*Spain*): Numerical Approach for Dynamic Fracture in Piezoelectric Solids
- 11425 Yasuhide Shindo (*Japan*): Finite Element Analysis of Fracture and Polarization Switching Behavior in Modified Small Punch Testing of Piezoelectric Ceramics
- 11484 Axel Müller (*Germany*): On Crack Assessment at Bimaterial Interfaces
- 11568 Hai-Tao Wang (*China*): A Quasi-Spherical Coordinate System and Its Application to the Determination of Vertex-Type Singularities
- 11626 Asher A. Rubinstein (*USA*): Failure Model of Protective Coatings
- 11856 Alla V. Balueva (*USA*): Modeling of Environment Assisted Delamination I. Quasi-static Case
- 11910 Ewa M. Turska (*Poland*): The Influence of Remote Stresses on the Near Crack Tip Stress Field
- 11934 Yu Shouwen (*China*): The Elasto-Plastic Thin Film/Substrate Via Buckle-Driven Delamination and Crack Growth
- 11980 Andrzej Kaczyński (*Poland*): On 3-D Thermoelastic Problems of Interfacial Cracks in a Periodic Stratified Space
- 12044 Karsten Kolk (*Germany*): Automatic 3D Crack Growth Simulation Based on Boundary Elements
- 12171 Irene Arias (*USA*): Massively Parallel Simulations of Dynamic Fracture and Fragmentation of Brittle Solids
- 12174 Ping Wang (*China*): the Shield Effect of Phase Transformation Stress Field at Crack Tip
- 12249 Volodymyr V. Loboda (*Ukraine*): Contact Zone Approach to the Analysis of Interface Cracks in Thermomechanically Loaded Piezoelectric Bimaterials
- 12378 Krishnaswamy Ravi-Chandar (*USA*): Interaction of Propagating Cracks and Shear Waves
- 12393 Jean-Baptiste M. Leblond (*France*): Disorder of the Front of a Tensile Tunnel-Crack Propagating in Some Inhomogeneous Medium
- 12492 Yichun Zhou (*China*): Creep Deformation in Thermal Barrier Coatings Due to the Effect of Thermal Growth Oxidation and Temperature Gradient
- 12798 Abdulhamid Al-Abduljabbar (*Saudi Arabia*): Numerical Analysis of Strain Hardening and Pressure Sensitivity Effects on J-Integral

SM10 – Functionally graded materials (R. Batra, USA & G.H. Paulino, USA)

- 10045 Andrzej Tylikowski (*Poland*): Dynamic Stability of Functionally Graded Plate Under In-Plane Compression
- 10135 Lizhi Sun (*USA*): Micromechanics-Based Elastic Model for Functionally Graded Materials with Particle Interactions
- 10364 Jiann-Quo Tarn (*Taiwan*): A State Space Formalism for Piezothermoelasticity of Functionally Graded Materials
- 10501 Weichen Shi (*China*): Conservation Laws of Functionally Graded Materials in Elastodynamics
- 10836 Chuanzeng Zhang (*Germany*): Transient Dynamic Crack Analysis in FGMs Under Impact Loading
- 11177 Dharendra V. Kubair (*India*): Asymptotic Analysis of a Stationary Crack in a Ductile Functionally Graded Material
- 11551 Linzhi Wu (*China*): The Plane Crack Problem in a Functionally Graded Orthotropic Strip
- 11572 Bing-Zheng Gai (*China*): Frictional Slip Between a Gradient Non-Homogeneous Layer and a Half-Space in Anti-Plane Elastic Wave Field
- 11592 Juri Engelbrecht (*Estonia*): Wave Propagation in Functionally Graded Materials
- 11671 Eduard Rohan (*Czech Republic*): Adaptive Modelling of Microscopic Heterogeneous Medium Undergoing Large Deformation
- 12093 Joël A. Pouget (*France*): Actuator and Sensor Modelling for Laminated Piezoelectric Plates
- 12273 Arthur H. England (*UK*): Complex-Variable Methods Applied to Functionally-Graded Elastic Plate Problems
- 12461 Takemasa Seto (*Japan*): Study of Two-Dimensional Elasticity on FGM
- 12465 Yoshihiro Ootao (*Japan*): Three-Dimensional Transient Thermoelastic Analysis of Orthotropic Functionally Graded Rectangular Plate
- 12594 R.C. Batra (*USA*): Adiabatic Shear Bands in Functionally Graded Materials
- 12665 Emilio C.N. Silva (*Brazil*): Topology Optimization Applied to the Design of Functionally Graded Material (FGM) Structures
- 12968 Sathyanaraya Hanagud (*USA*): First Principles-Based Equations of State for Functionally Graded Materials
- 12978 Minoru Taya (*USA*): Design of FGM Bimorph Piezo-Actuators
- 13018 Lavinia S.A. Borges (*Brazil*): Thermoelastic Analysis of Functionally Graded Materials Submitted to Shocks

SM11 – Impact and wave propagation (A. Norris, USA & K. Wilmański, Germany)

- 10072 Bettina Albers (*Germany*): Surface Waves on an Impermeable Boundary of a Poroelastic Medium
- 10114 Alexander M. Samsonov (*Russia*): Bulk Solitons do not Decay in Elastic Wave Guides
- 10344 Toshiaki Hata (*Japan*): Stress-Focusing Effect in a Spherical Zirconia Inclusion with Dynamically Transforming Strains
- 10422 Toshiro Maeda (*Japan*): Simultaneous Simulation of Dispersion Curves and H/V Spectra
- 10426 Nikolai N. Myagkov (*Russia*): Nonlinear Waves in Shock-Loaded Solids
- 10612 Krzysztof Wilmański (*Germany*): Critical Time for Acoustic Waves in Weakly Nonlinear Poroelastic Materials
- 10891 Semra Ahmetolan (*Turkey*): Rayleigh-Like Surface Waves on a Nonlinear Layered Elastic Half Space
- 11085 Istvan A. Veres (*Switzerland*): Non-Destructive Testing of Wood by Wave Propagation
- 11099 Ji Wang (*China*): A Two-Dimensional Analysis of Surface Acoustic Waves in Finite Anisotropic Solids with Electrodes
- 11242 Karima R. Khusnutdinova (*UK*): Nonlinear Wave Processes in a Bi-Layer

- 11271 Gabriel E. Chao (*Netherlands*): Shock-Induced Surface Waves in Porous Reservoirs
 11360 Janusz Klepaczko (*France*): Trapping of Plastic Waves by Adiabatic Deformation
 11377 Kateryna V. Terletska (*Ukraine*): Modeling of Solitary Impulses in a Composite Material Using Wavelet Analysis
 11401 Igor Selezov (*Ukraine*): Some Degenerated and Extended Wave Models of Elasto- and Hydrodynamics with Finite Velocity Disturbance Propagation
 11596 Angelo Morro (*Italy*): Uniqueness Results for the Reflection-Transmission Problem
 11620 Andres Braunbrueck (*Estonia*): Wave Interaction Resonances in Inhomogeneous Elastic Materials
 11682 Martin Ostoja-Starzewski (*Canada*): Acceleration Wavefronts in Random Media
 11812 Philippe S. Boulanger (*Belgium*): Inhomogeneous Circularly Polarized Waves in Orthorhombic Crystals
 11813 Andrus Salupere (*Estonia*): Hidden and Driven Solitons in Microstructured Media
 11853 Witold Kosiński (*Poland*): Thermo-Mechanical Wave Propagation in Materials with Internal State Variables
 11989 Sergey K. Kanaun (*Mexico*): Self-Consistent Methods in the Problem of Elastic Wave Propagation Through Matrix Composite Materials
 12203 Anton G. Pegushin (*Russia*): Waves of Deformation Propagation in Nonlinear Viscoelastically Elastic Porous Material
 12313 Bernhard Pichler (*Austria*): Elastoplasticity of Gravel Protecting Rockfall-Endangered Steel Pipelines
 12418 Toshihiko Sugiura (*Japan*): Flaw Identification by Angle Beam Electromagnetic Acoustic Transducers
 12481 Anton M. Krivtsov (*Russia*): Impact Fracture of Rock Materials Due to Percussive Drilling Action
 12514 Anil C. Wijeyewickrema (*Japan*): Dispersion and Stability Analysis of Waves in Pre-Stressed Imperfectly Bonded Layered Composites
 12568 Olari Ilison (*Estonia*): On the Propagation of Solitary Waves in Microstructured Solids
 12763 Chokri Zammali (*France*): Level-Sets and Mixed Approaches for Dynamic Contact Problems
 12772 Mahmoud I. Hussein (*USA*): Analysis and Design of Dispersive Materials and Structures

SM12 – Material instabilities (D. Bigoni, Italy & H. Petryk, Poland)

- 10265 Ahmed Benallal (*France*): Material Instabilities in Thermo-Mechanical Processes
 10314 Peter B. Beda (*Hungary*): Dynamical Systems Theory in Material Instabilities
 10867 Eugene I. Ryzhak (*Russia*): An Idea and Theory of Hypothetical Device for Investigating the Localization Phenomena
 10996 Henryk Petryk (*Poland*): Incremental Energy Minimization in Material Instability Problems
 11254 Davide Bigoni (*Italy*): Dynamics of Perturbations and Shear Band Instabilities
 11277 Paul Steinmann (*Germany*): On Convexity Conditions in Spatial and Material Settings of Hyperelasticity
 11432 Yoshihiro Tomita (*Japan*): Computational Characterization of Micro- to Macroscopic Mechanical Behavior of Carbon Black-Filled Rubber
 11705 Jose Merodio (*Spain*): Material Instabilities of Fiber-Reinforced Nonlinearly Elastic Solids
 12025 Walter J. Drugan (*USA*): Ultrastiff Elastic Composites via Negative Stiffness Inclusions, and Material Stability Implications
 12223 Pavel V. Tkachev (*Russia*): Stability of Ideal Infinite Crystal Under Finite Uniform Deformation
 12419 Igor Dobovsek (*Slovenia*): Explosive Instabilities in a Class of Hyperelastic Materials with Higher-Order Gradients

- 12682 Joao A. Martins (*Portugal*): On the Concept of “Dynamic (In)Stability of Quasi-Static Paths”
- 12751 Yves M. Leroy (*France*): Strain Localization at the Brittle-Ductile Transition of the Earth’s Continental Crust.

SM13 – Mechanics of composites (S. Adali, South Africa & N.A. Fleck, UK)

- 10189 Mohammad Reza Khoshnavan (*Iran*): Numerical Evaluation of Mixed Mode Delamination in a U.D. Glass/Epoxy Composite in 2D and 3D States
- 10244 Ryszard Pyrz (*Denmark*): Interfacial Properties of Nanowire-Polymer Composites
- 10347 Józef Ignaczak (*Poland*): Plane Harmonic Waves in a Microperiodic Layered Thermoelastic Solid Revisited
- 10412 Tong-Earn Tay (*Singapore*): Damage Progression by the Element-Failure Method (EFM) and Strain Invariant Failure Theory (SIFT)
- 10483 Hossein M Shodja (*Iran*): Effective Properties of Solids Containing Randomly Distributed Multi-Phase Spherical Particles
- 10555 Lidiya Nazarenko (*Ukraine*): Porous Anisotropic Composites under Microfractures
- 10667 Petri J. Kere (*Finland*): Reissner-Mindlin-Von Karman Type Plate Modle for Post-buckling Analysis of Laminated Composite Structures
- 10745 Kanmi Aderogba (*Nigeria*): Three-Dimensional Transmission in Plane Layered Elastic Composites
- 11014 Y. Jack Weitsman (*USA*): Aspects of the Mechanical Response of Randomly Reinforced, Chopped Fiber Strand, Polymeric Composites
- 11080 Javier LLorca (*Spain*): Computational Modeling of Deformation and Damage in Particle-Reinforced Composites
- 11162 Martin G. Andrews (*USA*): Elastic Interaction of Multiple Delaminations in Laminated Structures
- 11176 Federico J. Sabina (*Mexico*): Overall Properties of Periodic Biocomposites
- 11180 Christophe Bouvet (*France*): Damage Tolerance of Composite Structures with Thermal Shield
- 11387 Mike J. Clifford (*UK*): Can it Be Made? Predicting the Formability of Textile Composite Components
- 11426 Fumio Narita (*Japan*): Electroelstic Fields Concentrations and Polarization Switching by Circular Electrodes in Piezoelectric Disk Composites
- 11457 Aleksander Muc (*Poland*): Fuzzy Set Approach to Modelling Composite Mechanical Properties
- 11507 Amna Rekik (*France*): Evaluation of Linearization Procedures Sustaining Nonlinear Homogenisation Theories
- 11610 Tomo Takeda (*Japan*): Three-Dimensional Thermoelastic Analysis of Plain Weave Glass/Epoxy Composities with Cracks at Cryogenic Temperatures
- 11747 Andras Szekrenyes (*Hungary*): Advanced Beam Model for Fiber-Bridging in Unidirectional Composite Double-Cantilever Beam Specimens
- 11782 John R. Willis (*UK*): Interfacial Jump Conditions in Strain-Gradient Plasticity and Relations of Hall-Petch Type
- 11794 Brian Nyvang Legarth (*Denmark*): A Study of Particle Debonding with Anisotropy
- 11805 Emmanuelle Chabert (*France*): Nonlinear Affine Extension of the Three-Phase Sphere Model
- 11895 Barbara Gambin (*Poland*): H-Convergence and Multilayering in Piezocomposites
- 12148 Jorn S. Hansen (*Canada*): A Homogenization Based Laminated Beam Theory
- 12214 Ulrik Borg (*Denmark*): Compressive Strength of Fiber Composite with Porosity
- 12242 Zhong Ling (*China*): Thermal Residual Stress in Al₂O₃/SiCnano Ceramic Composites Measured by Nanoindenter
- 12321 Heinz E. Pettermann (*Austria*): Composites with Planar Random Fiber Arrangements
- 12489 Jan Schjødt-Thomsen (*Denmark*): Inclusion Dispersion: Effects on Stress and Effective Properties

- 12496 Shiguo Long (*China*): Thermal Fatigue of MMC Induced by Laser Heating
- 12531 Lingadahally S. Ramachandra (*India*): Thermo-Mechanical Stability and Vibration Analysis of Composite Shells
- 12560 Aleksander Muc (*Poland*): New Trends in Optimal Design of Composite Materials
- 12576 Robert Boehm (*Germany*): An Anisotropic Damage Model for the Prediction of the Degradation Behaviour of Novel Textile Reinforced Composites
- 12588 Vladyslav Danishevskyy (*Ukraine*): Asymptotic Study of Imperfect Interfacial Bonding in Periodic Composite Materials
- 12667 Antoni A. Gałka (*Poland*): T-Inclusion Regions for the Effective Transport Coefficients of Two-Phase Media
- 12680 Akke S.J. Suiker (*Netherlands*): Crack Tunneling in Laminates
- 12732 Ryszard Wojnar (*Poland*): Macroscopic Relations for Nonlinear Thermodiffusion in Heterogeneous Elastic Medium
- 12818 Arwen Smits (*Belgium*): Study of the Usability of Various Cruciform Geometries for Biaxial Testing of Fiber Reinforced Composites
- 12970 Marek Lefik (*Poland*): Incremental Effective Constitutive Law for Composite Material in the Form of Artificial Neural Network
- 13009 Ali Daneshmehr (*Iran*): Analysis of Thick Laminated Panel With Piezoelectric Sensors Based on Three-Dimensional Theory of Elasticity

SM14 – Mechanics of phase transformations (F.D. Fischer, Austria & A. Molinari, France)

- 10046 Wojciech K. Nowacki (*Poland*): Temperature and Strain Rate Effects on TRIP Sheet Steel. Measurement of Temperature by Infrared Thermograph
- 10088 Thomas Antretter (*Austria*): A Numerical Approach to Martensitic Phase Transformations
- 10434 Tatsuo Inoue (*Japan*): Macro-, Meso- and Micro-Scopic Metallo-Thermo-Mechanics
- 10648 Sergio R. Turteltaub (*Netherlands*): Multiscale Modeling of Steels assisted by Transformation-Induced Plasticity
- 10721 Isaac V. Chenchiah (*Germany*): The Nature of Stress and Strain Fields in Shape Memory Polycrystals
- 11308 Elżbieta Alicja Pieczyska (*Poland*): Shape Memory Alloy Under Strain and Stress Controlled Conditions – Thermomechanical Aspects of Martensite and Reverse Transformations
- 11325 Valery I. Levitas (*USA*): High Pressure Mechanochemistry: Conceptual Multiscale Theory and Interpretation of Experiments
- 11393 Arkadi Berezovski (*Estonia*): Stress-Induced Martensitic Phase Transition Front Propagation
- 11395 Shangping Chen (*Netherlands*): Modeling Martensite Transformation in the Elasto-Plastic Material at Finite Strain
- 11625 Sabine M. Schlögl (*Germany*): Modeling of the Microstructural Evolution in Cr-Mo Steels During Tempering and Hydrogen Exposure
- 11837 Alexander B. Freidin (*Russia*): Equilibrium and Stability of Two-Phase Deformations within the Framework of Phase Transition Zones
- 11852 Cristian Faciu (*Romania*): On Modeling the Longitudinal Impact of Two Shape Memory Bars
- 12077 Thorsten Bartel (*Germany*): A Micromechanical Model for Single-Crystal Shape-Memory-Alloys
- 12121 Claus Oberste-Brandenburg (*Germany*): Simulation of Discontinuity Movement by Boundary Elements
- 12225 Christian LExcellent (*France*): Determination of Phase Transformation Yield Surface of Anisotropic Shape Memory Alloys
- 12421 Fabrice Barbe (*France*): Numerical Determination of Diffusional Transformation Induced Plasticity from Computations of Random Microstructures

- 12747 Salem Meftah (*France*): Numerical Analyses of the Interaction Classical Plasticity – TRIP
- 12881 Qingping Sun (*China*): Nucleation and Motion of Phase Boundary in Shape Memory Alloy Microtubes

SM15 – Mechanics of porous materials (W. Ehlers, Germany & J.M. Huyghe, Netherlands)

- 10198 Tim Ricken (*Germany*): Biodegradation in Porous Landfill Bodies
- 10790 Michio Kurashige (*Japan*): Mandel and Cryer Problems For Fluid-Saturated Foams With Negative Poisson's Ratio
- 10792 Wolfgang Ehlers (*Germany*): Localization and Stability of Unsaturated Soil
- 11119 Martin Schanz (*Germany*): Convolution Quadrature Based Boundary Element Method for Quasi-Static Poroelasticity
- 11194 Bernd Markert (*Germany*): Theory and Numerics of Multicomponent Mixture Models for Soft Biological Tissues
- 11463 Jörg Hohe (*Germany*): Probabilistic Homogenization of Hyperelastic Solid Foams
- 11941 Luc Dormieux (*France*): Coupling Between Permeability and Damage: a Micromechanical Approach
- 12114 Stefano Dal Pont (*France*): Thermo-Hydro-Chemical-Mechanical Analysis of Concrete at High Temperatures
- 12358 Jacek Tejchman (*Poland*): FE-Investigations on Shear Localizations in Granular Bodies within Hypoplasticity
- 12518 Ragnar Larsson (*Sweden*): Modelling of Composites Processing Using a Two-Phase Porous Media Theory
- 12566 Michał Pakuła (*Poland*): Wave Propagation in High Porosity Bones – a Cellular Model
- 12567 Mariusz Kaczmarek (*Poland*): Soft Porous Media Model of Magnetic Fluid
- 12577 Józef Kubik (*Poland*): Mechanics of Saturated High Porosity / Soft Materials
- 12614 Daniela M. Bauer (*France*): A Three Layer Porous Media Model of Cutaneous Circulation with Application to Mechanical Skin Irritation
- 12713 Joël Sarout (*France*): Identification of Some Chemoporoelastic Parameters of a Reactive Shale from Experimental Data
- 12771 Michael W. Crochet (*USA*): Mesoscale Predictions for the Thermomechanics of Granular Energetic Composites
- 12903 Alan C.F. Cocks (*UK*): The Structure of Constitutive Laws for Powder Metallurgical Components
- 12917 Csaba I. Sinka (*UK*): Experimental Characterisation and Numerical Modelling of Density Distribution in Tablets
- 13006 Jacek Banaszak (*Poland*): Stresses and Fractures in Capillary – Porous Materials Under Drying

SM16 – Mechatronics (W.O. Schiehlen, Germany & M. Tomizuka, USA)

- 10510 Ya-Pu Zhao (*China*): Stability Analyses of Electrostatic Torsional RF MEMS Switch
- 10553 Dominique de Blaise (*France*): Improvement of Positioning Accuracy of Delta Parallel Robot
- 10809 Friedrich G. Pfeiffer (*Germany*): Dynamics and Control of a Hydraulically Driven Boring Plant
- 10900 Dalius Mazeika (*Lithuania*): Investigation of Powerful and High Precision Piezoelectric Actuator for Two-Dimensional Positioning
- 11282 Wim Symens (*Belgium*): Gain-Scheduling Control of Machine Tools with Varying Structural Flexibilities
- 12417 Horst Schulte (*Germany*): A Systematic Load Identification Procedure for Parallel Robot Manipulators

- 12546 Alfredas Busilas (*Lithuania*): Development of Positioning of Mechanisms with Piezo-electric Engines
 12712 Li-Sheng Wang (*Taiwan*): Hierarchical Tracking Control of Wheeled Mobile Robot
 12758 Matthias Weber (*Germany*): Rapid Prototyping of Model Based Control Algorithms for Diesel-Engines with Turbocharger

SM17 – Multibody dynamics (M. Geradin, Italy & F. Pfeiffer, Germany)

- 10026 Wojciech Blajer (*Poland*): A Geometrical Framework for Modeling and Simulation of Nonholonomic Mechanical Systems
 10533 Gakhip Ualiyev (*Kazakhstan*): Research of Movement of the Mechanism Sufficient with Elastic Part
 10624 Katica Stevanović Hedrih (*Serbia*): Homoclinic Orbits Layering in the Coupled Rotor Nonlinear Dynamics and Chaotic Clock Models
 10647 Pavel Polach (*Czech Republic*): Design of the Rear Carriage Stabilizer of a Low-Floor Articulated Trolleybus
 10779 Yuriy N. Kononov (*Ukraine*): Stabilization by Rotating Rigid Bodies for Unstable Rotation of a Rigid Body with Cavities Containing a Fluid
 10893 Oleg N. Dmitrochenko (*Russia*): Simulation of Constrained Rigid and Elastic Bodies Without Constraint Equations
 11020 Harry J. Dankowicz (*USA*): Analysis of Grazing Bifurcations in Impact Microactuators
 11223 Nils Guse (*Germany*): Low Energy Control of Periodic Motions in Manufacturing
 11352 Amalia Pielorz (*Poland*): Selected Problems of Discrete-Continuous Mechanical Systems with Local Nonlinearities
 11361 Gilles Saussine (*France*): Modeling Ballast Behavior Using a Three-Dimensional Polyhedral Discrete Element Method
 11375 Arun K. Banerjee (*USA*): Efficient Generalized Speeds in a Recursive Formulation of Flexible Multibody Dynamics
 11640 Dmitry Yu. Pogorelov (*Russia*): On Approximate Jacobian Matrices in Simulation of Stiff Multibody Systems
 11674 Jean Lerbet (*France*): Intrinsic Formulation of Dynamics of Curvilinear Systems
 11688 Dmitry G. Agapov (*Russia*): Simulation of Track Ballast
 11700 Kazuo Tanizawa (*Japan*): Configuration Control and Dynamic Analysis of Redundant Link-Type Manipulators
 12029 Johannes Gerstmayr (*Austria*): The Absolute Coordinate Formulation with Reduced Strain and Stiffening
 12071 Juan Valverde (*Spain*): Stability Analysis of a Tethered System
 12133 Beate Muth (*Germany*): Simulation of Contacting Spatial Polyhedral Particles
 12134 Robert Seifried (*Germany*): Plastic Deformation by Impacts in Multibody Systems
 12208 Olivier Bruls (*Belgium*): A Systematic Model Reduction Method for the Control of Flexible Multibody Systems
 12464 Kohichi Miura (*Japan*): Expression on the Deflection of a Flexible Thin Rod and Its Measurement
 12537 Naoki Sugano (*Japan*): Dynamic Analysis and Vibration Control of The Planar Beams Moving Along the Axial Direction
 12539 Guy Bessonnet (*France*): Generating Optimal Motions of Constrained Multibody Systems
 12569 Sine Leergaard Pedersen (*Denmark*): Contact Problems in Roller Chain Drive Systems.
 12582 Katsuhisa Fujita (*Japan*): Motion and Vibration Control of the Lift Mechanism of a Ladder Truck
-

SM18 – Plasticity and viscoplasticity (E. Van der Giessen, Netherlands & P. Perzyna, Poland)

- 10064 Ryszard B. Pęcherski (*Poland*): Metal Forming Processes Conditioned by Cyclic Loading. A New Challenge for the Theory of Plasticity
- 10383 Milan V. Micunovic (*Serbia*): Quasi Rate-Independent Viscoplastic FCC-Polycrystals
- 10393 George Z. Voyiadjis (*USA*): Physically Based Thermomechanical Modeling of Metals over a Wide Range of Strain Rates and Temperatures
- 10652 Norimasa Chiba (*Japan*): Plastic Properties Identification With Plural Sharp Indenters
- 10734 Alexis Rusinek (*France*): Advanced Thermo-Visco-Plastic Constitutive Relations for Direct Applications in Numerical Analyses
- 10797 Giulio Maier (*Italy*): Calibration of Anisotropic Elastic-Plastic Models for Thin Layers and Foils in Microtechnologies: Two Novel Techniques
- 10955 John D. Clayton (*USA*): Simulation of Dynamic Polycrystalline Thermoelastoviscoplasticity and Fracture
- 11005 Ricardo A. Lebensohn (*USA*): Assessing Different Self-Consistent Approximations by Comparison with Full-Field Simulations in Viscoplastic Polycrystals
- 11110 André Dragon (*France*): Three-Dimensional Modelling of Thermo-Elasto / Viscoplastic Solids Containing Adiabatic Shear Bands
- 11185 Wiera Oliferuk (*Poland*): Energy Storage Rate in Non-Homogeneous Deformation
- 11295 Kazuwo Imai (*Japan*): Dynamic Behavior of Many-Dislocation Systems in Silicon
- 11309 Alain L. Molinari (*France*): The Eshelby Problem for Elastic-Viscoplastic Materials
- 11344 J.A.W. van Dommelen (*Netherlands*): Multiscale Modeling of the Structure-Property Relationship for Semicrystalline Materials
- 11350 Mamoru Mizuno (*Japan*): Modeling of Viscoplastic Constitutive Equation for Polymers by Taking into Account Strain Recovery
- 11410 Peter Gudmundson (*Sweden*): Thickness Dependent Yield Strength of Thin Films
- 11498 Stephane André Berbenni (*USA*): Yield Surfaces Using an Extension of the Regularized Schmid Law to Polycrystalline Materials
- 11790 Christian F. Niordson (*Denmark*): Size-Effects in Void Growth
- 11820 Amit Acharya (*USA*): On the Accounting of Dislocation Internal Stress in Continuum Plasticity
- 11930 Nicolaie Dan Cristescu (*USA*): Steady-Flow of a Non-Homogeneous Bingham Material Over a Wedge
- 11953 Anguel I. Baltov (*Bulgaria*): Modelling of Elastic-Plastic or Viscoplastic Materials Sensitive to the Type of Processes – Different Approaches
- 11963 Marc G. Geers (*Netherlands*): Strain Gradient Crystal plasticity Incorporating Grain Boundary Effects
- 11975 Wiktor L. Gambin (*Poland*): Metal Forming and Texture Development Modelling
- 12058 Dieter Weichert (*Germany*): Limit and Shakedown Analysis with Decohesive Effects
- 12339 Fahmi Zaïri (*France*): A Constitutive Law for Glassy Polymers and Blends
- 12469 Cedric Doudard (*France*): Development and Identification of a Probabilistic Two-Scale Model for High Cycle Fatigue Prediction
- 12549 Thomas Böhlke (*Germany*): Modeling the Crystallographic Texture Evolution Based on the Maximum Entropy Method
- 12634 Absamad El Adb (*France*): An Elastoplastic Model for Prediction of Permanent Deformations of Unbound Granular Pavement Layers
- 12697 Maxime Sauzay (*France*): Intragranular Kinematic Hardening Modelling and Validation
- 13038 Oliver Pierard (*Belgium*): Mean Field Homogenization of Elasto-(Visco) Plastic Composites: Formulation for Time-Dependent and Independent Behaviors
-

SM19 – Plates and shells (H. Mang, Austria & E. Ramm, Germany)

- 10071 Gennadiy Lvov (*Ukraine*): The Stress Analysis of the Multilayered Plates and Shells with Defects of the Structure
- 10233 Parthasarathi Mandal (*UK*): Some New Thoughts on the Buckling of Thin Cylindrical Shells
- 10287 Wojciech Pietraszkiewicz (*Poland*): Continuity Conditions in Elastic Shells with Phase Transformation
- 10770 Kenzo Sato (*Japan*): Analytical Solution of Bending of a Clamped Elliptical Plate Under Lateral Load and In-Plane Force
- 11021 Herbert A. Mang (*Austria*): Sensitivity Analysis Concerning the Initial Postbuckling Behavior of Elastic Structures
- 11238 Jan Sladek (*Slovakia*): Meshless LBIE Formulations for Viscoelastic Thin Plates
- 11815 Maryna A. Varyanychko (*Ukraine*): Effect of a 'Static' Resonance in Elastic Thin-Walled Cylinders
- 11890 Izabela Lubowiecka (*Poland*): Energy-Conserving Scheme for Nonlinear Dynamics of Shells – Numerical Examples
- 12224 Takeshi Sakiyama (*Japan*): Mindlin Cylindrical Panels with Twist and Double Curvature
- 12328 Zdzisław Nowak (*Poland*): Application of the Return Mapping Algorithm to Perzyna Viscoplasticity for Plane Stress
- 12346 Eelco L. Jansen (*Netherlands*): A Perturbation Method for Nonlinear Vibrations of Structures
- 12350 Lidija V. Kurpa (*Ukraine*): Nonlinear Vibrations of Shallow Shells and Thin Plates of Arbitrary Shape

SM20 – Rock mechanics and geomechanics (Z. Mróz, Poland & I. Vardoulakis, Greece)

- 10231 Zdzisław A. Więckowski (*Poland*): The Material Point Method in Soil Mechanics Problems
- 10374 Leopold Kruszka (*Poland*): Dynamic Behaviours of Soils and Rocks in a Wide Pressure Range
- 10866 Niels P. Kruyt (*Netherlands*): Micromechanical Study of Macroscopic Friction and Dissipation in Idealised Granular Materials: The Effect of Interparticle Friction
- 11584 Marcin Maździarz (*Poland*): Influence of Contact Phenomena on Structure-Subsoil Interaction: Finite Elements Method Analysis
- 11667 Nathalie Boukpeti (*Belgium*): Modeling of Static Liquefaction and Evolving Failure Modes
- 11845 Joseph F. Labuz (*USA*): Development of Shear Banding in Sandstone
- 12364 Bojan Guzina (*USA*): On the Use of Second-Order Topological Information for Sub-surface Imaging by Elastic Waves
- 12462 Yuji Kishino (*Japan*): Incremental Nonlinearity in Constitutive Relation for Granular Media
- 12779 Martin J. Schmidt (*USA*): A High-Pressure High Strain Rate Elastic-Viscoplastic Model for Cementitious Materials
- 12848 Jan Maciejewski (*Poland*): The Influence of Teeth on the Earth-Working Processes

SM21 – Solid mechanics in manufacturing (B. Heimann, Germany & T. Inoue, Japan)

This session has been cancelled

SM22 – Stability of structures (Z. Gaspar, Hungary & S. Kyriakides, USA)

- 10378 J. Blachut (*UK*): Shallow Spherical Caps Under External Pressure
- 10692 Nobutada Ohno (*Japan*): Elastoplastic Microscopic Bifurcation and Post-Bifurcation Behavior of Periodic Cellular Solids
- 10915 Zsolt Gaspar (*Hungary*): Statical Models to Illustrate Special Instabilities

- 11097 Sergio Pellegrino (*UK*): Wrinkles in Square Membranes
- 11172 Ioannis G. Raftoyiannis (*Greece*): Nonlinear Dynamic Stability of Multi-Suspended Roof Systems
- 11174 Alain Combescure (*France*): Coupling of Axisymmetric and 3D Shell Models for Non Linear Elastoplastic Buckling Prediction of Mainly Axisymmetric Shells
- 11600 Theodoro A. Netto (*Brazil*): Dynamic Arrest of Propagating Buckles in Offshore Pipelines
- 11653 Suresh Shrivastava (*Canada*): Bifurcation Buckling of Sandwich Plates and Shells in Plastic Range
- 11816 Hans Troger (*Austria*): On the Stability of the Sky-Hook
- 11939 Alexander P. Seyranian (*Russia*): Stability of Parametrically Excited Structures: New Results
- 11962 Philippe Le Grogneq (*France*): A Unified Treatment for the Elastoplastic Bifurcation of Structural Elements
- 12084 Hans Obrecht (*Germany*): Buckling and Imperfection – Sensitivity of Axially Compressed Cylindrical Shells with Compliant Cores
- 12297 Esben Byskov (*Denmark*): Stability of Shear-Flexible Frames
- 12420 Djenane C. Pamplona (*Brazil*): Instabilities of Initially Stressed Hyperelastic Cylindrical Membrane and Shell Under Internal Pressure
- 12558 Dinar R. Camotim (*Portugal*): Generalised Beam Theory Formulation to Analyse the Post-Buckling Behaviour of Orthotropic Laminated Plate Thin-Walled Members
- 12669 Simon D. Guest (*UK*): The Stiffness of Prestressed Frameworks: A Unifying Approach
- 12688 Giles W. Hunt (*UK*): Twist Buckling and the Foldable Cylinder: An Exercise in Origami
- 12931 Szymon Imielowski (*Poland*): On Stability of Systems Subject to Generalized Follower Force
- 12934 Jarosław Weronko (*Poland*): Dynamic Instability of a High-Speed Flexible Shaft with a Massive Disc and Follower Load.
- 12967 Ciprian D. Coman (*UK*): Secondary Bifurcations and Localisation of Buckle Patterns
-
- SM23 – Stochastic micromechanics (Y. Brechet, France & Y. Shibutani, Japan)
- 10242 Andrejs Krasnikovs (*Latvia*): Creep Rupture and Fiber Breaks Accumulation in Unidirectional Composite
- 12380 Jan Zeman (*Czech Republic*): Homogenization of Plain Weave Composites with Imperfect Microstructure
- 12571 Yoji Shibutani (*Japan*): Collective Prismatic Dislocation Loops Mechanism
-
- SM24 – Structural optimization (K.K. Choi, USA & J. Herskovits, Brazil)
- 10048 Yoon-Young Kim (*S. Korea*): Shape Sensitivity Analysis for Fixed-Grid Analysis Based on Oblique Boundary Curve Approximation
- 10052 Tomasz Lewiński (*Poland*): Perturbation of the Compliance Functional Due to the Appearance of a Small Cavity in an Elastic Body
- 10433 Niels Olhoff (*Denmark*): Topology Optimization of Vibrating Structures with Hydrodynamic Surface Pressure Loading
- 10594 José N. Herskovits (*Brazil*): A Technique for Nonsmooth Optimization Based on the Interior Point Feasible Directions Algorithm
- 10621 Timo J. Saksala (*Finland*): Nash Equilibrium in Bicriteria Structural Optimization
- 10669 Pauli Pedersen (*Denmark*): On Shape Optimization for Eigenvalue Problems
- 11015 Valeri Markine (*Netherlands*): Shape Optimisation of Railway Wheel Profile
- 11137 Tadeusz S. Burczyński (*Poland*): Shape Optimization of Thermomechanical Structures in the Presence of Convection and Radiation Using Parallel Evolutionary Computation
- 11316 Jeong Sam Han (*Germany*): Efficient Optimization of Transient Dynamic Problems for a Micro Accelerometer Using Model Order Reduction

- 11349 Krzysztof Dems (*Poland*): Damage Identification in Structures by Means of Thermographic Methods
- 11486 Antoni Źochowski (*Poland*): Topological Optimization for Contact Problems
- 11532 Yuanxian Gu (*China*): Coupled Sensitivity and Design Optimization for Thermo-Structural Systems
- 11623 George I.N. Rozvany (*Hungary*): New Classes of Analytically Derived Optimal Topologies and Their Numerical Confirmation
- 11634 Paweł Smaś (*Poland*): Optimal Structures for Buckling Forces and Buckling Displacements
- 11744 Søren Halkjaer (*Denmark*): Optimization of Beam Properties with Respect to Maximum Band-Gap
- 11760 Sławomir Czarnecki (*Poland*): Optimal Layout of Two Materials within the Core Layer of a Sandwich Plate. Relaxed Formulation and Its Computational Algorithm
- 11826 Su-Young Chang (*S. Korea*): Material Cloud Method for Topology Optimization
- 11858 Doo-Ho Lee (*S. Korea*): Optimal Design of Unconstrained Damping Layer on Beams
- 11936 Niels L. Pedersen (*Denmark*): On Separation of Eigenfrequencies in Two-Material Structures
- 12074 Gregor Kotucha (*Germany*): Density Gradient Based Regularization of Topology Optimization Problems
- 12075 Michał Źyczkowski (*Poland*): New Results of Structural Optimization for Post-Buckling Behaviour
- 12079 Thomas Buhl (*Denmark*): Compliant Mechanism Design for Adaptive Trailing Edge Flaps
- 12098 Erik Lund (*Denmark*): Structural Optimization of Composite Shell Structures Using a Discrete Constitutive Parameterization
- 12185 Gil Ho Yoon (*S. Korea*): Why Parameterizing Element Connectivity for Topology Optimization?
- 12200 Sami Holopainen (*Finland*): Topology Optimization of the Geometrically Nonlinear Structures Made of Rubber-Like Material
- 12222 Jakob S. Jensen (*Denmark*): Optimal Design of Lossy Bandgap Structures
- 12287 Lijuan Li (*China*): Non-Gap Design Method and Test for Post-Tensioned Prestressed R.C. Structure
- 12302 Atsushi Kawamoto (*Denmark*): Design of Articulated Mechanisms with a Degree of Freedom Constraint Using Global Optimization
- 12413 Michał Nowak (*Poland*): Simulation of Trabecular Bone Adaptation – Creating the Optimal Structure
- 12573 Sandor Kaliszky (*Hungary*): Optimal Design of Elasto-Plastic Structures Subjected to Normal Loads and Earthquake
- 12628 Andrzej Garstecki (*Poland*): Optimal Force Action and Reaction in Structural Design and Identification
- 12679 Piotr Kowalczyk (*Poland*): DSA for Elastic-Plastic Finite Rotation Shells under Dynamic Loads
- 12789 Florin Bobaru (*USA*): Optimization of Functionally Graded Materials with Temperature Dependent Properties. A Meshfree Solution
- 12870 Vassili Toropov (*UK*): Optimum Blank Design for Deep Drawing Using Interaction of High and Low Fidelity Simulation
- 12916 Henrik T. Møller (*Denmark*): Computational Tricks for Efficient Design Sensitivity Analysis
- 13013 Gengdong D. Cheng (*China*): The Concurrent Design of Materials and Structures for Cellular Materials on Efficiency of Heat Dissipation

SM25 – Structural vibrations (I. Blekhman, Russia & K. Popp, Germany)

- 10166 Jianbing Chen (*China*): Extreme Value Distribution and Dynamic Reliability of Stochastic Structures
- 10408 Alexander Vakakis (*Greece*): Experimental Study of Nonlinear Energy Pumping

- 10470 Marian Wiercigroch (*UK*): Nonlinear Vibrations of Jeffcott Rotor with Preloaded Snubber Ring
- 10656 Victor Z. Gristchak (*Ukraine*): Non-Linear Stochastic Vibration Problems for the Plates with Time-Dependent Parameters
- 10750 Debasish Roy (*India*): A Multi-Step Transversal Linearization Method in Nonlinear Dynamics
- 10863 Stephen H. Crandall (*USA*): Equivalent Stochastic Linearization as an Alternative to Solving the Fokker-Planck Equation
- 11055 Iliya I. Blekhman (*Russia*): Nonlinear Effects, Observed in the Process of the Liquid Flowing Out of the Vibrating Vessels: Theory, Experiment and Applications
- 11066 Akihiko Higashi (*Japan*): Propagation Analysis of Flexural Waves by Wavelet Transform
- 11079 Oleg Gendelman (*Israel*): Bifurcations of Damped Nonlinear Normal Modes: Linear Oscillator with Strongly Nonlinear Attachment
- 11082 Gamal Mohamed Ashawesh (*Libya*): Effect of Root Flexibility on the Aeroelastic Analysis of a Composite Wing Box
- 11246 Herve Riou (*France*): Reanalysis of an SEA High – Frequency Vibration Calculation Based on the VTCR
- 11261 Utz von Wagner (*Germany*): Active Control of Disk Brake Squeal
- 11273 Marcin Luczak (*Poland*): Experimental and Theoretical Modal Analysis of Three Support Rotor Test Rig Using LMS CADA-X and ABAQUS
- 11338 Jacob P. Meijaard (*UK*): Stability of a Rotor with Periodically Varying Angular Velocity
- 11384 Tibor Tarnai (*Hungary*): Paradoxical Behaviour of Vibrating Systems Challenging Rayleigh's Theorem
- 11494 Carlos E.N. Mazzilli (*Brazil*): Imperfection Sensitivity of Circular Arch's Non-Linear Modes
- 11536 Alexei A. Mailybaev (*Russia*): Optimal Shapes of Parametrically Excited Beams
- 11679 Alexander J. Fidlin (*Germany*): Non Trivial Effect of Strong High-Frequency Excitation on a Nonlinear Controlled System
- 11699 Igor Zeidis (*Germany*): An Approach to Worm-Like Motion
- 11712 Alla D. Firsova (*Russia*): Dynamics of a Rotor Rolling Along a Circular Surface
- 11716 Yuri Leonidovich Menshikov (*Ukraine*): The New Statement of Problem of Unbalance Identification
- 11719 Ekaterina V. Shishkina (*Russia*): Vibrorheology: Main Results, New Problems
- 11759 Vladimir Zeman (*Czech Republic*): Nonlinear Vibrations of Gear Drives
- 11783 Rob H.B. Fey (*Netherlands*): Passive Vibration Control of a Piecewise Linear Beam System
- 11834 Ye Ping Xiong (*UK*): A power Flow Mode Theory Based on Inherent Characteristics of Damping Distributions in Systems and Its Applications
- 11867 T.H. Young (*Taiwan*): Stability of a Spinning Disk Under a Stationary Oscillating Unit
- 11904 Seyed Saleh Hosseini Yazdi (*Iran*): High Revolving Speed Spindles Definition Due to Transient Vibration Conditions
- 12026 Fadi Dohnal (*Austria*): Suppressing Self-Excited Vibrations in a Coupled Pendulum System
- 12322 Ingo Kaiser (*Germany*): The Running Behaviour of an Elastic Wheelset
- 12404 Andrew N Norris (*USA*): Thermoelastic Relaxation in Thin Plates with Applications to MEMS and NEMS Oscillators
- 12498 Jacek Cieřlik (*Poland*): Estimation of the Vibration Energy Characteristics for Joints of Constructional Elements
- 12511 Marek S. Kozien (*Poland*): Sound Radiation by the White Noise Excited Viscoelastic Shallow Shells
- 12535 Thomas Marc Richard (*Belgium*): Self-Excited Stick-Slip Oscillations of Drag Bits

- 12593 Yoshikazu Sugiura (*Japan*): Vibration Characteristics of the Main Tower, the Byaon Temple
- 12632 Viktorija E. Volkova (*Ukraine*): Application of Extended Phase Space to Investigation of Forced Biharmonic Oscillations
- 12659 Robert Jankowski (*Poland*): Non-Linear Modelling of Earthquake Induced Pounding of Buildings
- 12694 Jon J. Thomsen (*Denmark*): Discontinuous Transformations and Averaging for Vibro-Impact Analysis
- 12759 Pedro M. Ribeiro (*Portugal*): Experimental Analysis of Modal Interactions in the Non-Linear Vibrations of a Plate
- 12770 Arkadiusz Mężyk (*Poland*): Optimum Selection of Design Features of Electromechanical Drive Systems Incorporating a Control Unit
- 12785 Christian Seidel (*Germany*): Mode Switching of Rain-Wind Induced Vibrations
- 12814 Pankaj Wahi (*India*): Regenerative Tool Chatter Near a Codimension-2 Hopf Point
- 12977 Stanisław Radkowski (*Poland*): Characteristics of Vibroacoustic Signals in Diagnosing Early Stages of Defects
- 12984 Tadeusz Majewski (*Poland*): Entering the Excitation into a Mechanical System with Dynamic Eliminators of Vibration
- 12989 Gayane Manucharyan (*Ukraine*): Frictional Auto-Oscillations under the Action of Almost Periodic and Periodic Excitations

SM26 – Vehicle dynamics (S. Iwnicki, UK & R. Sharp, UK)

- 10701 Robin S. Sharp (*UK*): Optimal Path Following Road Vehicle Steering Control
- 10909 Simon Iwnicki (*UK*): Simulation and Testing of a Wheelset with Induction Motor Driven Independent Wheels
- 11589 Vladislav Yazykov (*Russia*): Railway Vehicle Simulation Using Non-Elliptical Wheel-Rail Contact Model
- 11672 Georg Rill (*Germany*): A Modelling Technique for Fast Computer Simulations of Configurable Vehicle Systems
- 11795 Per-Anders Jönsson (*Sweden*): Experimental and Theoretical Analysis of Freight Wagon Link Suspension
- 11832 Zbigniew Lozia (*Poland*): Mathematical Models and Simulation of Stick-Slip Processes in a Car Steering System

SM27 – Viscoelasticity and creep (F. Cocks, UK & N. Ohno, Japan)

- 10018 Boris P. Maslov (*Ukraine*): Nonlinear Overall Viscoelastic Properties of the Random Multicomponent Media
- 10906 Renata S. Engel (*USA*): Sintering Simulation of Stainless Steel Powder Compacts
- 11201 Alan R.S. Ponter (*UK*): Characterisation of the Cyclic Behaviour of Elastic-Plastic-Creeping Bodies
- 11368 Holm Altenbach (*Germany*): A Creep Continuum Damage Theory for Beams, Plates and Shells
- 11506 Jinghong Fan (*USA*): Multiscale Modeling Schemes Spanning a Large Range of Scales
- 11827 Ji-Hyun Cho (*S. Korea*): Constitutive Modeling of Rubber Components Under Small Vibration Superimposed on Large Static Deformation Considering Strain-Dependent Properties
- 11957 Zbigniew L. Kowalewski (*Poland*): An Influence of Cold Work on Creep of Engineering Materials
- 11981 Roman Lackner (*Austria*): Multi-Scale Model for Low-Temperature Creep of Asphalt
- 12450 Fusahito Yoshida (*Japan*): A Model of Cyclic Viscoplasticity with Special Reference to Yield-Point Phenomena
-

 FSM1 – Acoustics (T. Geers, USA & N. Peake, UK)

- 10294 Nobumasa Sugimoto (*Japan*): Dissipative Effects on Propagation of the Acoustic Solitary Waves
- 10907 Jonathan B. Freund (*USA*): An Empirical 'lower bound' on Free-Shear-Flow Noise
- 11249 Jeremy Astley (*UK*): Special Short Wave Finite Elements for Flow Acoustics
- 11337 Sergey V. Sorokin (*Denmark*): Wave Propagation in and Sound Emission from a Sandwich Plate Under Heavy Fluid Loading
- 11373 David S. Burnett (*Italy*): 3-D Structural Acoustics Modeling with HP-Adaptive Finite Elements
- 11508 Dmitry V. Churochkin (*Russia*): The Low-Temperature Acoustical and Thermal Properties of Materials Due to the Dynamics of Linear Topological Defects
- 11561 Takao Suzuki (*USA*): Shock Leakage Through a Vortex-Laden Mixing Layer Causing Jet Screech
- 11896 Natasha V. Movchan (*UK*): Transmission of Elastic Waves and Localised Modes in Composite Structures
- 11973 Murthy N. Guddati (*USA*): Arbitrarily Wide-Angle Wave Equations and their Applications to Unbounded Domain Modeling and Subsurface Imaging
- 12149 Tatiana Andreeva (*USA*): Ultrasonic Travel-Time Technique for Diagnostic of Grid-Generated Turbulence
- 12180 Jeff D. Eldredge (*USA*): The Acoustics of Two-Dimensional Leapfrogging Vortex Interactions
- 12477 Edward J. Kerschen (*USA*): A Theoretical Model for Resonances in Flow Past a Cavity
- 12497 Paul W. Hammerton (*UK*): Structure of Sonic Booms in a Medium with Multiple Relaxation Modes
- 12516 Alexander Alexeev (*Germany*): Gas Oscillations in a Closed Tube at Resonance
- 12527 Iain D.J. Dupere (*UK*): The Effect of Viscosity on the Propagation of Acoustic Waves Through Fine Cylindrical Meshes
- 12533 Lars V. Hansen (*Denmark*): Modelling of Hydrophone Based on a DFB Fiber Laser
- 12555 Józef Lewandowski (*Poland*): Numerical Analysis of the Texture and Acousto-Elastic Properties of Prestressed Polycrystalline Aggregate
- 12586 Rossano Stefanelli (*Switzerland*): Measurements and Calculations Related to Curve Squealing in the Railway System
- 12643 Fernando Lund (*Chile*): Acoustic Wave Propagation Through a Random Array of Dislocations
- 12691 George Biros (*USA*): Distributed Parameter Control of a 2D Acoustic Helmholtz Problem on a Halfspace
- 12717 Loukas F. Kallivokas (*USA*): Frequency- and Directionality- Continuation Schemes for Scatterer Shape Detection in Acoustics

 FSM2 – Chaos in fluid and solid mechanics (I. Mezic, USA & G. Rega, Italy)

- 10252 Gabor Stepan (*Hungary*): Nonlinear Dynamics of High-Speed Milling
- 10499 John S. Hogan (*UK*): The Effect of Smoothing on Bifurcation and Chaos Computations in Non-Smooth Mechanics
- 11183 Remco I. Leine (*Switzerland*): A Set-Valued Force Law For Spatial Coulomb-Contensou Friction
- 11241 Ugo Galvanetto (*UK*): Chaotic Attractors with Long Regular Sequences
- 11302 Ekaterina E. Pavlovskaja (*UK*): Reduction of Multidimensional Flow to Low Dimensional Map for Piecewise Smooth System Experiencing Chaos
- 11363 P. Piiroinen (*UK*): Numerical Detection and Continuation of Sliding Bifurcations in a Dry-Friction Oscillator
- 11416 Elżbieta Tyrkiel (*Poland*): On Generating Chaotic Dynamics in Nonlinear Vibrating Systems
- 11535 Ken Kiyono (*Japan*): Low-Dimensional Chaotic Dynamics in Dripping Faucets

- 12014 Kohei Yamasue (*Japan*): Influence of Remaining Chaos on Convergence of Solutions in Time Delayed Feedback Controlled Duffing System
- 12129 Giuseppe Rega (*Italy*): A Dynamical Systems Analysis of the Overturning of Rigid Blocks
- 12468 Igor Mezic (*USA*): On the Nonlinear Dynamics of Multicomponent Dynamical Systems
- 12482 Theodoros Karakasidis (*Greece*): Short-Time Dynamical Behavior of Fluids at the Atomic Scale
- 12674 Li-Qun Chen (*China*): Nonlinear Dynamics of Axially Moving Viscoelastic Strings Based on Translating Eigenfunctions
- 12927 Zbigniew Peradzyński (*Poland*): Nonlinear Oscillators with Time Delays
- 12972 Radosław Iwankiewicz (*South Africa*): Non-Linear Oscillator Under Random Renewal-Driven Trains of Impulses

FSM3 – Continuum mechanics (K.R. Rajagopal, USA & G. Saccomandi, Italy)

- 11096 James Casey (*USA*): Pseudo-Rigid Bodies Viewed as Globally Constrained Continua
- 11140 Lev Steinberg (*USA*): Constitutive Equations of Mesoelastic Deformation
- 11227 Luis A. Dorfmann (*Austria*): Nonlinear Response of Magnetoelastic Solids
- 11247 Bohuslav Striz (*Czech Republic*): Application of Continuum Mechanics in the Textile Fabrics
- 11347 Gerard A. Maugin (*France*): Generalized Continuum Mechanics: Three Paths
- 11638 Victor M. Tigoiu (*Romania*): Viscoelastic Fluid Flows in a Falling Cylinder Viscometer and the Evaluation of Shear Viscosity
- 11642 Stanisław Tokarzewski (*Poland*): Fundamental Inequalities for the Bounds on the Effective Transport Coefficients of Two-Phase Media
- 11704 Glenn B. Sinclair (*USA*): On the Source of Singularities in Mechanics
- 11818 Michael A. Hayes (*Ireland*): Extended Polar Decompositions for Finite Plane Strain
- 11840 Włodzimierz Domański (*Poland*): Nonlinear Waves in Elastic Solids
- 11950 Michel Destrade (*France*): Explicit Secular Equations for Surface and Interface Waves in Anisotropic Solids
- 12392 Andreas Menzel (*Germany*): Views on Material Forces in Multiplicative Elastoplasticity
- 12406 Jan J. Sławianowski (*Poland*): Affine Symmetry in Mechanics of Discrete and Continuous Systems

FSM4 – Fluid-structure interaction (J. Grue, Norway & M.P. Paidoussis, Canada)

- 10520 Elena G. Gavrilova (*Bulgaria*): Coupled Frequencies of a Fluid-Structure Interaction Cylindrical System
- 10826 Matej Vesenjak (*Slovenia*): Fluid Structure Interaction in Multiphase Mixing Vessel
- 10911 Tatiana Khabakhpasheva (*Russia*): Piston Impact Onto the Boundary of Two-Layer Fluid
- 11078 Michael P. Paidoussis (*Canada*): Nonlinear Dynamics of Pinned-Pinned Cylinders in Axial Flow
- 11668 Ming-Jyh Chern (*Taiwan*): Interaction of Oscillating Flow with a Pair of Side-By-Side Square Cylinders
- 11736 Anthony D. Lucey (*Australia*): The Hydroelastic Destabilisation of Finite Compliant Panels
- 11758 Hiroshi Kagemoto (*Japan*): Water-Surface Dynamics Among a Periodic Array of Floating Bodies Subject to Regular Incident Waves
- 11801 Charlotte Py (*France*): The Mixing Layer Instability of Wind Over a Flexible Crop Canopy
- 11833 Jing Tang Xing (*UK*): An Updated Arbitrary-Lagrangian-Eulerian Description in Continuum Mechanics and Its Application to Nonlinear Fluid-Structure Interaction Dynamics

- 11912 Wolfgang M. Sichertmann (*Germany*): Slender Body Theory Approach to Nonlinear Ship Motions
 11986 Andrzej Herczyński (*USA*): Inverse Magnus Force in Free Molecular Flow
 12521 Yu Zhou (*China*): Effect of an Oscillating Cylinder on a Neighbouring Cylinder Wake
 12557 John R. Chaplin (*UK*): Disturbed-Laminar Flow Over an Oscillating Cylinder
 12956 John Grue (*Norway*): PIV Experiments on Vortex Induced Vibrating Cylinders at High Reynolds Numbers
 13050 Ahcene Bouabdallah (*Algeria*): Influence of the Circular Cylinder Cross-Section Variation on the Near Wake Behaviour

FSM5 – Mechanics of foams and cellular materials (S. Hilgenfeldt, Netherlands & D.L. Weaire, Ireland)

- 10597 Sascha Hilgenfeldt (*Netherlands*): Bubble Shapes in Foams: The Importance of Being Isotropic
 11095 Benjamin Dollet (*France*): Mechanics of Bidimensional Liquid Foams
 11240 Martin E. Glicksman (*USA*): Average N-hedra as Descriptors of 3D Network Cells
 11292 H.X. Zhu (*UK*): Modelling the Round-off and the Tensile/Compressive Failure Behaviour of Plant and Vegetable Tissues
 11605 Stelios Kyriakides (*USA*): On the Crushing Response of Open Cell Foams
 11663 Alfonso H.W. Ngan (*China*): A Statistical Mechanics Theory of Random Honeycomb and Open-Cell Foam Structures
 12052 Isabelle Cantat (*France*): Dissipation in 2D Foam Flow
 12212 Arnaud Saint-Jalmes (*France*): Surfactant and Protein Foams: Differences in Drainage and Rheology
 12373 Adrian D. Staicu (*Netherlands*): Determining Stress During Finger Propagation in 2D Foams
 12395 Jing Tian (*UK*): Thermal Flow through Brazed Woven Screens
 12435 James E. Coons (*USA*): Drainage of Emulsion and Foam Films in Scheludko-Exerowa Cells
 12578 Vincent Labiausse (*France*): Shear-Induced Normal Stress Differences in Aqueous Foams
 12851 Stephen J. Neethling (*UK*): The Dispersion of Particles within Foams
 12986 Pacelli L. Zitha (*Netherlands*): Investigation of Foam Development in Porous Media Using X-Ray Computed Tomography
 13033 Fabian Lipperman (*Israel*): Nucleation of Cracks in Two-Dimensional Periodic Cellular Material

FSM6 – Multiscale phenomena in mechanics (A. Carpinteri, Italy & C. Miehe, Germany)

- 10399 Justyna Czerwińska (*Germany*): Simulations of Micro- and Nano- Channel Flows by a Dissipative Particle Dynamics Method
 11224 Alberto Carpinteri (*Italy*): Multi-Scaling Approach in the Mechanics of Disordered Materials
 11237 Wiesław Larecki (*Poland*): Grad-Type Expansion About Nonequilibrium States for the Relaxion-Time Approximation of the Boltzmann-Peierls Equation
 11340 Heike Emmerich (*Germany*): Two-Scale Simulations of Epitaxial Surfaces
 11471 Pilar Ariza (*Spain*): A Geometrical Theory of Discrete Dislocations in Lattices, with Applications to Dislocation Dynamics and Crystal Plasticity
 11476 Krishna Garikipati (*USA*): Stress-Defect Interactions at Molecular / Continuum Scales
 11806 Bhushan L. Karihaloo (*UK*): Deterministic Size Effect in the Strength of Cracked Quasi-Brittle Structures
 11830 Varvara Kouznetsova (*Netherlands*): Multi-Scale Second-Order Computational Homogenization of Heterogeneous Materials
 11862 Yutaka Shimomura (*Japan*): Jumping of a Spinning Spheroid
 12040 Luca Placidi (*Germany*): Characteristics of Orientation and Grain-Size Distributions

- 12078 Antoine Gloria (*France*): Numerical Homogenization of a Locally Hyperelastic Constitutive Law
- 12112 Joachim Dettmar (*Germany*): Multiscale Analyses of Granular Media at Finite Strains Based on Micro-Macro Transitions with Different Boundary Constraints
- 12113 Christian Miehe (*Germany*): Exploitation of Incremental Energy Minimization Principles in Computational Multiscale Analyses of Inelastic Solids
- 12118 Martin Becker (*Germany*): Non-Convex Homogenization of Inelastic Composites with Interaction of Material and Structural Instabilities on Different Scales
- 12334 Luciano Colombo (*Italy*): Physical Modeling of Fracture Mechanics in Complex Materials
- 12336 Frederic Legoll (*France*): Analysis of a Variational Method Coupling Discrete and Continuum Mechanics

FSM7 – Education in mechanics (R. Engel, USA & B. Karihaloo, UK)

- 10003 Hassan Aref (*USA*): Toys and Games in Mechanics Education
- 10016 Keith Moffatt (*UK*): African Institute for Mathematical Sciences: a Capacity Building Initiative in which IUTAM Has an Active Involvement
- 10226 Carl T. Herakovich (*USA*): On Mechanics/Engineering Science Education
- 11724 Aleksandr Kositsyn (*Ukraine*): Mechanics – a New Internet Tutor
- 11765 Yilong Bai (*China*): Teaching Mechanics as an Engineering Science in China
- 11869 Vasily Yaremchuk (*Russia*): Education and Tutorial on Fluid Mechanics on the Basis of Computer Laboratory
- 12259 Vitauts Tamuzs (*Latvia*): Education in Mechanics in Latvia Higher Schools
- 12488 Yasuaki Nohguchi (*Japan*): Simulator, Nohguchi Bottle, of Soil Liquefaction for Education
- 12603 Anders Boström (*Sweden*): Mechanics Education in Sweden
- 12642 Donovan L. Evans (*USA*): Rigid Body Dynamics: Student Misconceptions and Their Diagnosis
- 12752 Kamal B. Rojiani (*USA*): Web-Based Instructional Units for Teaching Mechanics
-



Professor Leen van Wijngaarden delivers the ICTAM04 Opening Lecture

INTERPLAY BETWEEN AIR AND WATER

Leen van Wijngaarden
J.M.Burgers Centre for Fluid Dynamics
University of Twente, Enschede, The Netherlands.
l.vanwijngaarden@tn.utwente.nl

Abstract In the Prologue I recall, among others, the period of the Cold War in which, thanks to Polish colleagues, scientific contacts between East and West were maintained. After that, several aspects of the flow of mixtures of air and water will be discussed and illustrated by examples. Finally I will give some comments on the differences and similarities between fundamental and applied science and scientists.

Keywords: Multiphase flow, bubbly flows

1. Prologue

It is a great honour to be invited to deliver the Opening Lecture at ICTAM 2004, especially now that it is here in Warsaw, a city of great significance for Mechanics. It reminds me of the Cold War when East was East and West was West. They could nevertheless meet here in Poland, where Władek Fiszdon organized once in two years a “Symposium on Advanced Problems and Methods in Fluid Mechanics”. Participation was on invitation and those invited travelled to Warsaw and stayed there one night. The next day they were transported by bus to some place found by magician Władek where there was food and accommodation, modest but sufficient. One could meet in this way with famous Russian scientists as Barenblatt, Zel’dovich, Ladyshenskaya and others. The fluid dynamics community is greatly indebted to Władek Fiszdon for organizing these Symposia. Unfortunately, his health condition does not allow him to be here today. From this place I would like to thank him for all he did for Fluid Mechanics in this way.

The first time that I was invited to participate in such an event was in 1969 in Kazimierz (not named after my friend and colleague Kazimierz Sobczyk who will present the Closing Lecture next Friday). George Bat-

chelor was a key figure in these Symposia. He had great authority (he was a Foreign Member of the Polish Academy of Sciences), Władek Fiszdon asked his advice whom to invite and he was always very relaxed and willing to lecture on everything that he was working on. I remember very well that he gave a lecture on the sedimentation problem on which he was working at the time and what was to become the subject of his celebrated paper “Sedimentation in a dilute dispersion of spheres” [1]. This concerns the velocity with which a cloud of heavy particles sedimentates in a fluid. The, until that time unsolved, difficulty in this and similar problems is that the velocity which a small particle induces in its vicinity falls off very slowly, as the reciprocal distance from its center. The calculation of the average sedimentation speed results, because of this in not uniformly convergent integrals, with which J.M. Burgers struggled already in the 1930’s. George found a way, a renormalization, to overcome this difficulty. His renormalization technique has found wide application in other areas. His presentation in Kazimierz induced me to think about the analogous problem where a cloud of bubbles rises under buoyancy.

2. Air and Water

The flow around a bubble is, to a good approximation, a potential flow. The velocity which one bubble induces in another falls off as (distance from centre to centre)⁻³. In contrast with the falling particle inertia effects are here dominant, the Reynolds number is large. This (distance)⁻³ behaviour is faster than that with the falling particle but not fast enough to overcome difficulties with not uniformly convergent integrals. When a bubble is accelerated, the surrounding liquid exerts a reaction force on the bubble, which is proportional to the acceleration. The multiplying factor has dimension of mass and is called virtual or added mass, because in calculations it can be treated as a virtual mass of the bubble which is itself of course almost massless. It appears that this mass depends on the presence of nearby bubbles in a manner which gives rise to convergence problems. Consider N bubbles in a configuration C_N with probability density $P(C_N)$. When there is always one bubble in the point \mathbf{r}_0 , such a configuration is indicated with $C_{N-1}|\mathbf{r}_0$ and the corresponding probability density with $P(C_N|\mathbf{r}_0)$. In the course of the calculation one needs to know the average velocity in the centre of a bubble in the presence of all the others, and with respect to the volume velocity \mathbf{U}_0 of the suspension,

$$\langle \mathbf{u} \rangle - \mathbf{U}_0 = 1/N! \int \{ \mathbf{u}(\mathbf{r}_0, C_N) - \mathbf{U}_0 \} P(C_N|\mathbf{r}_0) dC_N. \quad (1)$$

For low concentration by volume one considers, just as in the case of dilute gases, the interaction between two particles only or, in this case, bubbles. Then Eq. (1) becomes

$$\langle \mathbf{u} \rangle - \mathbf{U}_0 = \int \{ \mathbf{u}(\mathbf{r}_0 + \mathbf{r}, \mathbf{r}_0) - \mathbf{U}_0 \} P(\mathbf{r}_0 + \mathbf{r} | \mathbf{r}_0) d^3 \mathbf{r}. \quad (2)$$

The quantity in curly brackets in Eq. (2) behaves at large distance r as r^{-3} and therefore the integral does not converge. The essence of Batchelor's renormalisation technique starts in this case with noting that if in Eq. (1) we take just $P(C_N)$, that means when we consider the average velocity in a point whether in fluid or in gas, then the result is zero,

$$0 = 1/N! \int \{ \mathbf{u}(\mathbf{r}_0, C_N) - \mathbf{U}_0 \} P(C_N) dC_N. \quad (3)$$

When reduced to the interaction of two bubbles also this integral does not converge. The only difference with the right-hand side of Eq. (1) is that there is in the latter always a bubble in \mathbf{r}_0 and in Eq. (3) – sometimes. However we know the exact result Eq. (3). Now we subtract Eq. (3) from Eq. (1). Since in the absence of long-range order in the suspension we have at a large distance from \mathbf{r}_0

$$P(C_N | \mathbf{r}_0) = P(C_N),$$

the *difference* of the two integrals converges when the configuration is reduced to two bubbles and this overcomes the problem because we are left with the calculation of the integral

$$\int \{ \mathbf{u}(\mathbf{r}_0, \mathbf{r}_0 + \mathbf{r}) - \mathbf{U}_0 \} \{ P(\mathbf{r}_0 + \mathbf{r} | \mathbf{r}_0) - P(\mathbf{r}_0 + \mathbf{r}) \} d^3 \mathbf{r},$$

which is now convergent. Although this problem could be solved, [2], the general problem to understand the dynamics of air-water mixtures is today far from being solved.

Particle – liquid flow can either show random configurations or fixed configurations. With air and water many more topologies are possible. I mentioned as a first example the bubbly suspension, a common device in the chemical industry where it serves as a reactor column.

Some more examples are:

- Niagara Falls (American and Canadian).

Air is first entrained by river water falling down and mixes with this during its fall. The air leaves eventually together with only a little bit of water, forming with it a spray, or mistflow. There are in fact



Figure 1. The Niagara Falls, in the foreground the horseshoe-shaped Fall on the Canadian side, and the American Fall in the background.

two falls, one on the Canadian side, with the shape of a horseshoe, and one on the American side. Although the picture is not very good, you can clearly see that with the Canadian fall water droplets are in the upward flow entrained with the air *above* the original level from where they originated. They derive some energy from the air. This does not happen at the American fall. The reason seems to me that there is, in the restricted space available for the downflow of the Canadian one, a pressure built up pushing a strong upward air flow entraining droplets.

- Breaking wave with trapped air.

In the case of a breaking wave air is trapped in the overturning wave. This entrained air plays an important role in the dynamics of the wave, and of its impact on walls. A striking effect of the trapped air is a tremendous change in the compressibility of the mixture. Even an air concentration of a few percent dramatically alters the sound velocity which is directly related to the compressibility. This can be made clear as follows.

Denoting the velocity of sound of the mixture with c_m , we have from thermodynamics

$$(c_m)^2 = (dp/d\rho)_s, \quad (4)$$



Figure 2. A breaking wave at Coogee Beach, Sydney, Australia. Photograph taken by D.H. Peregrine, University of Bristol, and reproduced here with his permission.

where p , ρ and s denote pressure, density and entropy respectively. The density is made up from that of air, with volume fraction α , and that of water, with volume fraction $1 - \alpha$. Referring to air and water with subscripts a and w respectively, we have therefore

$$\rho = \alpha \rho_a + (1 - \alpha) \rho_w. \quad (5)$$

We neglect a possible velocity difference between air and water. Then the mass of air in a unit mass of the mixture is constant, whence

$$\rho_a \alpha / \{ \rho_a \alpha + \rho_w (1 - \alpha) \} = \text{constant}. \quad (6)$$

We assume further that the pressure in water and air is the same (later we shall see when this ceases to be realistic). Then it follows from Eq. (4)–Eq. (6) that for α not too close to zero or to unity

$$(c_m)^2 = \gamma p / \rho_w (1 - \alpha) \alpha, \quad (7)$$

γ being the ratio of specific heats of the air. In Fig. 3 graphs of the complete expression are shown for various ambient pressures. Even with a volume concentration α of air of one percent, the velocity of sound is in an air-water mixture only 100 m/s, far below the sound speed in either air or water. (Air was, of course, also involved in the generation of the wave. That is an old problem in hydrodynamics.

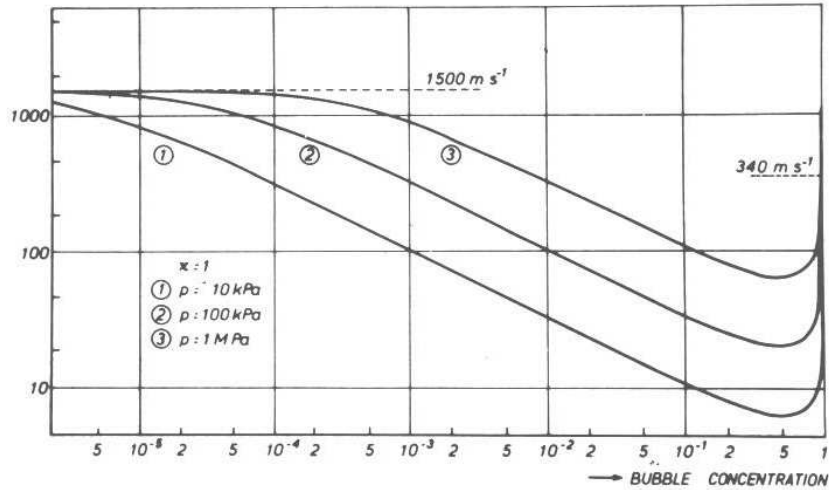


Figure 3. The sound velocity, c , in a mixture of air and water. The air concentration by volume α is indicated along the horizontal axis, the sound velocity along the vertical axis.

In the last 50, or so, years much has been clarified but it is not completely solved.)

The air trapped in water has also a profound effect on the radiation of sound when the flow is turbulent. The late Sir James Lighthill has shown in one of his finest contributions to fluid mechanics, [3], that turbulence produces, inefficiently, quadrupole sound. The presence of air gives a new, by far dominating, monopole contribution, which leads as shown by Crighton and Ffowcs Williams [4], for not too low void fraction, to a sound emission larger by a factor $(c_w/c_m)^4$ which can be for air and water of the order 10^6 or an intensity increase of 60 dB. Think about this when you hear these waves speak!

- Cavitation.

Another two-phase situation is encountered in cavitation, for example at a hydrofoil, see Fig. 4. Due to the low pressure in the flow along the hydrofoil, a propeller blade, microscopic nuclei become unstable and grow to macroscopic size. In a region of higher pressure these bubbles, filled with air and vapour, collapse again and may cause at the final stage of the collapse considerable damage to the blade.

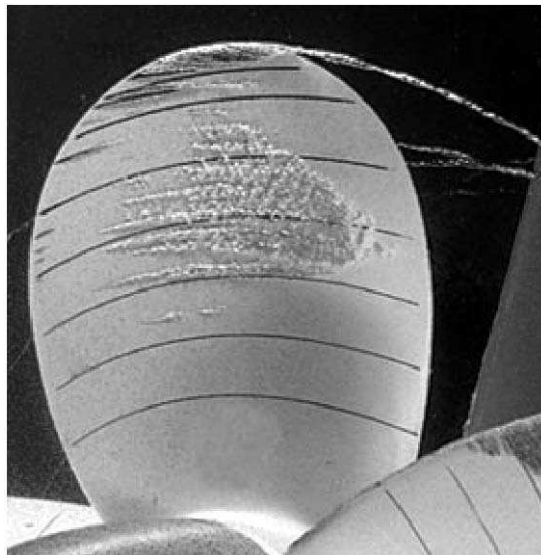


Figure 4. Cavitation on a ship's model propeller turning in a water tunnel. There is cavitation on the blade but also in the tip vortex. Courtesy of the Maritime Research Institute of the Netherlands (MARIN) at Wageningen.

In all these cases there is interaction between the gaseous phase and the liquid phase and the title of my lecture refers to this. In a further part of the lecture I shall in a symbolic way imagine the air which is above as the domain of fundamental research and the water, down below, as applied science, which will give opportunity to share some thoughts about science and engineering with you.

In the spray above the Niagara waterfall we have a lot of air and some water, in the case of a bubbly suspension we have a lot of water and some air. At both ends there are unsolved problems forming a challenge for fluid mechanics.

3. Bubbly Flow

Compared with the Niagara fall, the rising suspension looks quiet and peaceful. But lo and behold what happens when we increase, with bubbles of about 1mm radius, the void fraction to about 25%. A violent transition to slug flow occurs. (During the presentation a video of the transition to slug flow was shown). Both phenomena, the homogeneous rise at low concentration and the transition to slug flow are ill understood.

Let us start with the former. The interest in bubbles has always been great. Bubbles smaller than about 0.8 mm radius rise in a straight line. For example bubbles rising in champagne or beer. The application in champagne is due to Dom Pérignon who was a contemporary of Sir Isaac Newton. Their simultaneous occupations are described by Michel Onfray [5] as “*while the first (Pérignon) prepares beverages with rising bubbles, the second (Newton) derives formulas based on falling fruits*“ (my translation from the French text). This quotation from the chapter “*Une petite théorie des bulles*” of Onfray’s book illustrates on a day like this very appropriately the unity of mechanics.

Bubbles with a radius above 0.8 mm do not rise linearly in water but perform spiralling or zigzag motion, in contrast to falling particles which fall in a straight line. This was already known to Leonardo da Vinci, who made a sketch of what he saw, Fig. 5, and is therefore called nowadays Leonardo’s Paradox, see e.g. Ohl, Tijink and Prosperetti [6].

Recently, see e.g. de Vries et al. [7], it has been observed that these spiralling bubbles have a wake trailing behind them consisting of two vorticity bearing threads, see Fig. 6. The relevant bifurcation has been also described numerically, Maugin & Magnaudet [8], but the underlying physical mechanism is not yet understood.

The flow around a bubble rising in clean water is well described by potential flow supplemented with thin boundary layers. These, of the



Figure 5. Sketch by Leonardo da Vinci of a spiralling bubble (Courtesy of Musée du Louvre, Paris). The “Paradox”, for further details see [6], is in the fact that a falling particle has a straight trajectory but a rising bubble – a spiralling path.

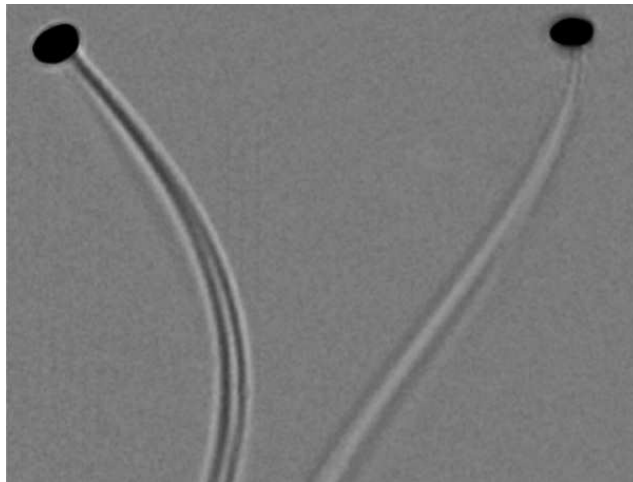


Figure 6. Two mutually perpendicular projections of a bubble spiralling in hyper-clean water. The effective bubble radius is about 1 mm. Clearly seen is the double-threaded wake behind the rising bubble. Courtesy of Christian Veldhuis.

same thickness as with rigid bodies, have now only to overcome the difference in shear stress between the outer flow and the zero stress at the interface. Just as in the study of dilute gases, it is natural to start with looking at binary interactions. Numerical work and analytical work with this model unfortunately predict clustering of bubbles and not the homogeneously rising bubbles as observed in experiments. This can be made plausible as follows: Imagine two bubbles with their line of centres making, at time $t = 0$, an angle of more than 36 degrees with the vertical direction which is parallel to gravity. The hydrodynamic forces are such that after a time of order a/V , where a is the bubble radius and V the terminal velocity, the line of centres is horizontal. This is therefore a statistically highly probable situation. But in this configuration there is only an attractive force between the bubbles. They bounce for a while but even when this is a purely elastic collision, the motion gets exhausted by viscous friction, which explains the clustering in the numerical simulation.

How in reality the lack of repulsive forces, the basic reason for the clustering, is overcome is another unsolved problem of two-phase flow. I have made recently [9] the suggestion that the above mentioned two-threaded wakes could play a role here.

To continue with unsolved problems in two-phase flow I recall the transition to slug flow. Also this awaits an explanation. There is an analogous phenomenon in fluid beds. There the homogeneous bed becomes unstable, big gas bubbles are formed, as a result of the instability of concentration waves. It has been thought for some time that transition to slug flow is similarly due to instability of such waves. Evidence, Lammers & Biesheuvel [10] shows this not to be the case. The instability of concentration waves (or void fraction waves) occurs but before slugs appear, there is an intermediate flow regime characterized by a pointed transverse velocity and concentration distribution.

You might have the impression by now that in two-phase flow there are mainly riddles and unsolved problems. This is certainly not the case. I will illustrate this with two examples. The first is about expansion waves in a two-phase flow. We have seen that the bubbly suspension has a low velocity of sound. So, we can play at low velocities the whole organ of compressible gases. For example the theory and experiments of waves of finite amplitude. There is, however, an important difference. If pressure changes become very rapid, the relation Eq. (7) for the speed of sound is no longer valid. My compatriot Marcel Minnaert measured in the 1930's the frequency of volume oscillations of small air bubbles in water in an ingenious way, described in [11]. He determined the frequency of the audible popping sound of the bubbles formed in his

apparatus by means of tuning forks. He also derived a formula for this frequency, f , say,

$$f = 1/(2\pi a)\{3\gamma(p - p_v)/\rho_l\}^{1/2}. \quad (8)$$

This is for a bubble with radius of 1mm about 3kHz. When now in a bubbly suspension pressure changes are not far from this Minnaert frequency, the bubbles do no longer passively follow the pressure changes but pressure differences between the two phases develop due to the inertia of the liquid. As a result the medium becomes dispersive which expresses itself in various ways. One of these is that the velocity of propagation of a wave of finite amplitude depends not only on the amplitude, as is the case for “normal” compressible fluids, but also of the frequency, or wavelength. With weak nonlinearity and weak dispersion the famous Korteweg-de Vries equation is valid for the pressure in the wave. Some time ago we did [12] the following experiment:

At the entrance of a semi-infinite bubbly flow, a time-dependent pressure was established in the form of a rectangular triangle, a shock wave followed by a rarefaction. For this special initial profile the KdV equation can be solved exactly with help of the so-called inverse scattering theory. The evolution in the mixture of this initial profile is into a train of solitons according to this theory. The nice thing about this is that the associated mathematical equation, a Schrödinger equation, has for this particular profile an exact solution in the form of an Airy function and that the number of evolving solitons is equal to the zeros of this Airy function in a certain interval. In the experiment that we did, the shape of the evolving waves was not quite that of solitons (they were still evolving) but the number agreed exactly with the predictions, see Fig. 7.

Another example is directly connected to Minnaert’s early finding. Much later it was discovered that also the sound of rain on a water surface is due to bubbles but in a special way.

The falling drop forms a crater in the water which is filled with air. As the crater closes again the air escapes but sometimes a small air bubble is trapped. This produces noise while oscillating in its Minnaert frequency. Experiments, see Oğuz & Prosperetti [13], with drops of various speeds and sizes show that a bubble is trapped only in a narrow portion of the speed/size plane (see Fig. 8). In nature the speed of the raindrop depends on its size and hence the intersection of this line with the above mentioned area gives the size of the raindrops producing bubbles and accompanying sound. This explains the rather narrow frequency spectrum of rain noise.

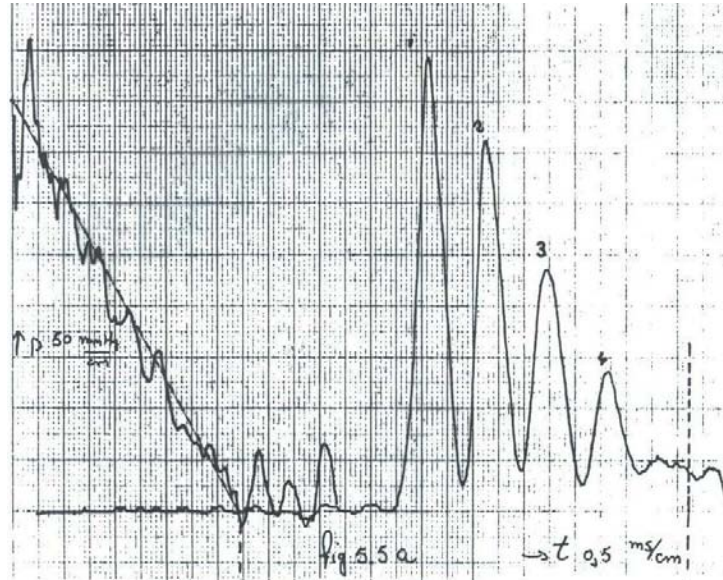


Figure 7. From an initial pressure profile shaped in terms of time as a rectangular triangle by a shock wave followed by an expansion wave, (left-hand side of picture) develops, after the wave has travelled a long distance in the bubbly flow, a series of solitons (right-hand side of picture).

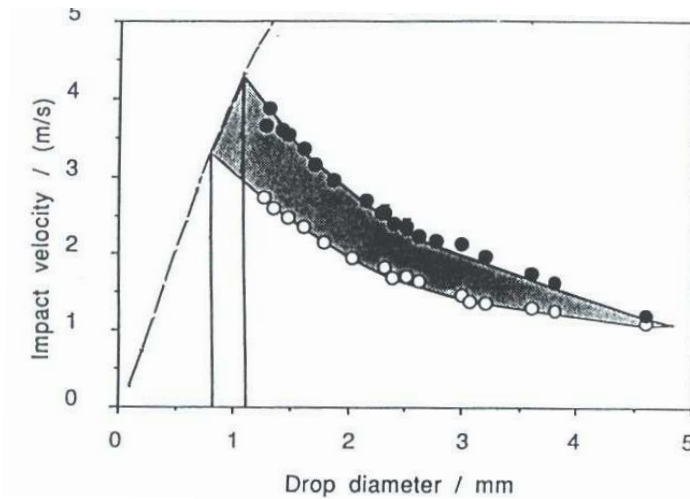


Figure 8. The shaded area bounds that portion out of the diameter/impact plane of falling drops, that marks the occurrence of a trapped air bubble. The broken line represents the relation between diameter and impact velocity of raindrops. Hence the intersection of this line with the shaded area gives the range of raindrops which produce air bubbles and thereby sound. The picture is from [13] and reproduced here with permission of *Ann. Rev. Fluid Mech.*

4. Fundamental and Applied, The Scientist and the Engineer

I will now use the freedom of the lecturer on an occasion as this one to compare in a symbolic sense the interplay just described with the interplay between fundamental and applied science. Fundamental science high up in the air, the applications down below where the water is. Sometimes the interplay is not obvious. Famous are the words spoken by the German mathematician David Hilbert when he was asked to comment on the relation between pure and applied science. He said “*Meine Herren, sie haben gar nichts mit einander zu tun*” (they have nothing to do with each other). This points at a lack of appreciation. In my case I have been lucky to see a lot of both in my professional life. Both have their peculiarities of which I shall give two examples. First the “ \sim ” and the “ $=$ ”. What do I mean by this? Suppose you are designing a device which includes flow of water, of kinematic viscosity $\nu = 10^{-6} \text{ m}^2/\text{s}$, with a velocity $U=0.10 \text{ m/s}$ in a pipe with diameter $D=1 \text{ cm}$. You want to know for the operation of your device, what entry length l is needed for the flow to become fully developed. You turn for advice to a theoretical physicist. He takes his copy of Landau & Lifshitz, Fluid Mechanics [14], from the shelf in his office and finds on page 150

$$l/D \sim \text{Re}. \quad (9)$$

This means that the dimensionless entrance length l is a multiple of order unity times the Reynolds number UD/ν . Landau & Lifshitz point out that the thickness δ of the laminar boundary layer along the pipe wall grows, with x running along the pipe axis, as

$$\delta \sim (\nu x/U)^{1/2},$$

where again \sim means that the boundary layer thickness is a multiple of order unity times the shown quantity. Putting now the thickness equal to the diameter gives Eq. (9) for the entrance length l . In this particular case Re is 1000. You feel uneasy over it and you ask the physicist, do I really need thousand diameters, which is 10 m? The physicist does not listen anymore. Your problem is now an engineering problem and he does not care. So, you turn to an engineer, for example R.S. Brodkey, who tells you in his book Brodkey 1967 [15] on page 129 that exact calculation gives

$$l/D = 0.06 \text{ Re}. \quad (10)$$

This is, to your great relief, only 60 diameters or 60 cm.

As another example I mention granular materials. This is nowadays a popular subject in physics. It has been, however, widely studied in

civil engineering and in mechanical engineering since long ago. In the second part of the last century A.W. Jenike (1914-2003) has dominated research in the field of bulk solids. The research in this field has had results. During the last ICTAM of the last century, Chicago 2000, in one invited lecture, Roux & Radjaï [16], we read “ The quasi-static behaviour of granular materials is already a mature field in which a number of elasto-plastic models reproduce very accurately the available experimental tests. *They allow us to design civil engineering structures with confidence*”. The authors of these lines come from civil engineering. At the same ICTAM there was another invited lecturer, Goldhirsch [17], a physicist, from whose lecture I quote: “Granular matter is often described as “unpredictable”, “irreproducible” or “erratic”. These and other adjectives used to characterize granular matter *are a clear sign that much is still lacking in our understanding of these “materials”* (my italics). In my opinion the physicists could have in this case more appreciation for the work done and results obtained by engineers.

5. Epilogue

The great experience in ICTAM is that both fundamental and applied scientists can listen to each other and talk to each other during and outside the many sessions. And in spite of differences of approach, illustrated in the previous Section with some examples, there are many aspects in their work that they share. Whereas consultant firms apply high per-hour rates for every service that they deliver, we all are referees and editors for journals, sit in committees, do work for funding organisations, you name it, without payment or at most a modest compensation for subsistence costs. Why do we do that? There are immaterial rewards in the form of prizes and other signs of recognition. But above all it is out of a sense of duty to the scientific community. The British writer and philosopher Iris Murdoch [18] points out that our sense of duty stems from the fact that we are not perfect beings, “A totally good being would not experience the call of duty, might be said to lack or not need the concept since all acts and decisions would emerge from virtuous insight and its orderly process”. But just this sense of duty saves us, according to an Editorial in *Science* [19], from becoming victims of human frailty. I quote from this article entitled “The Roots of Scientific Integrity”: “The system of rewards and punishments tends to make honest, vigorous, conscientious hardworking scholars out of people who have human tendencies of slothfulness and no more rectitude than the law requires”.

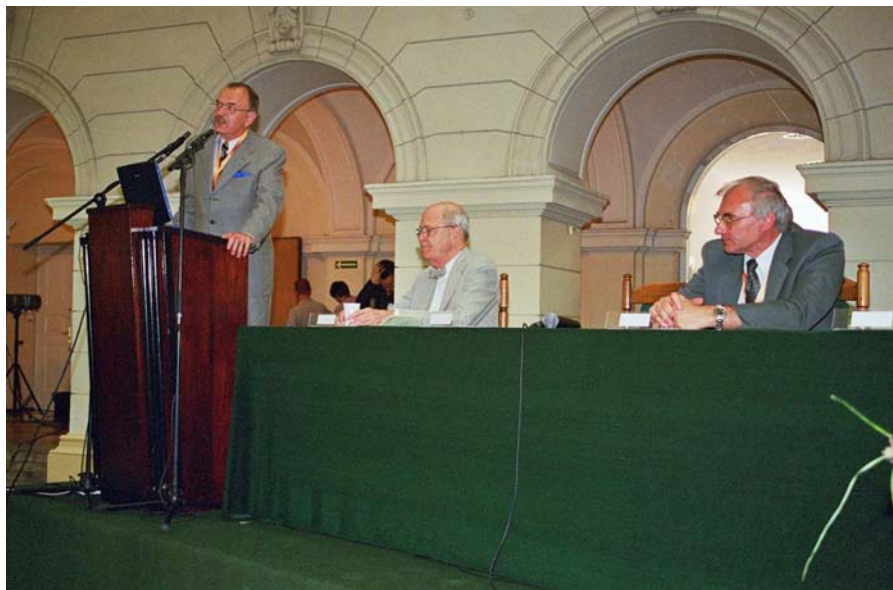
With this quotation Mr Chairman, intended to make us all feel good, I come to the end of my presentation. I wish you all an enjoyable and rewarding ICTAM 2004 and I thank you for your attention.

I thank my colleagues of the Physics of Fluids Group of the University of Twente for their helpful comments, Michel Versluis for teaching me Power Point and Raymond Bergmann, Peter Eshuis, and Christian Veldhuis for their expert help in preparing the Power Point version of this lecture.

References

- [1] G.K. Batchelor, Sedimentation in a dilute dispersion of spheres, *J.Fluid Mech.*, Vol.52, pp.245-268, 1972.
- [2] L. van Wijngaarden, Hydrodynamic interaction between gas bubbles and liquid, *J.Fluid Mech.*, Vol.77, pp.27-44, 1976.
- [3] M.J. Lighthill, On sound generated aerodynamically 1. General theory, *Proc.R.Soc.London*, Vol.A211, pp.564-587, 1952.
- [4] D.G. Crighton and J.E. Ffowcs Williams, Sound generation by turbulent two-phase flow, *J. Fluid. Mech.*, Vol.36, pp.585-603, 1969.
- [5] M. Onfray, Gourmande La Raison, Grasset et Fasquelle, 1995.
- [6] C.D. Ohl, A. Tijink, A. Prosperetti, The added mass of an expanding bubble, *J.Fluid Mech.*, Vol.482, pp.271-291, 2003.
- [7] A.W.G. de Vries, A. Biesheuvel, L. van Wijngaarden, Notes on the path and wake of a gas bubble rising in pure water, *Intn'l J.Multiphase Flow*, Vol.28, pp.1823-1834, 2002.
- [8] G. Mougin, J. Magnaudet, Path instability of a rising bubble, *Phys.Rev. Lett.*, Vol.88, 014502- 1-014502-3, 2002.
- [9] L.van Wijngaarden, Bubble velocities induced by trailing vortices behind neighbours, Submitted to *J.Fluid Mech.*, 2004.
- [10] J.H Lammers, A. Biesheuvel,, Concentration waves and the instability of bubbly flows, *J.Fluid Mech.*, Vol.328, pp.67-93, 1996.
- [11] M. Minnaert, On musical air bubbles and the sound of running water, *Phil. Mag.*, Vol.16, pp.235-245, 1933.
- [12] L.van Wijngaarden, Evolving Solitons in Bubbly Flows, *Acta Applicanda Mathematicae*, Vol.39, pp.507-516, 1995.
- [13] A. Prosperetti, H.N. Oğuz, The impact of drops on liquid surfaces and the underwater noise of rain, *Annu. Rev. Fluid Mech.* Vol.25, pp.486-537, 1993.
- [14] L.D. Landau, E.M. Lifshitz, *Fluid Mechanics*, Pergamon, 1959.
- [15] R.S. Brodkey, *The Phenomena of Fluid Motion*, Addison-Wesley, 1967.
- [16] S. Roux, R. Radjaï, Statistical Approach to the mechanical behaviour of granular media, In *Mechanics for a New Millenium* [Eds.] H. Aref, and J.W. Phillpps, pp.181-197, Kluwer Academic Publishers, 2001.

- [17] I. Goldhirsch, Kinetic and continuum descriptions of granular flows, *Mechanics for a New Millenium*, Eds. H. Aref and J.W. Phillips, pp.345-359, Kluwer Academic Publishers, 2001.
- [18] I. Murdoch, *Metaphysics as a guide to morals*, Penguin Books, 1993.
- [19] Editorial Essay "The roots of scientific integrity", *Science*, Vol.139, pp.3161, 1963.



Professor Sobczyk delivers the ICTAM04 Closing Lecture

STOCHASTIC DYNAMICS OF ENGINEERING SYSTEMS

Origins, challenges and results

Kazimierz Sobczyk
Institute of Fundamental Technological Research
Polish Academy of Sciences
Świętokrzyska 21, 00-049 Warszawa
ksobcz@ippt.gov.pl

Abstract This lecture presents a concise exposition of the basic features of contemporary stochastic dynamics of physical/engineering systems with emphasis on its methodological principles, applicatory power and recent challenges.

Keywords: Stochastic systems, random vibration, stochastic degradation models, random loads, reliability assessment, failure models, information dynamics, noise-induced phenomena

1. Introduction

Historical Origins: Hundred Years from the Beginnings – W. Gibbs (1903), A. Einstein, M. Smoluchowski (1905/06), P. Langevin (1908)

Stochastic dynamics is today a greatly advanced field of science investigating real dynamical systems with use of stochastic process theory. It develops the models and methods for investigation of various dynamical systems subjected to parametric and external random excitations.

The genesis of stochastic dynamics is connected with problems in physics. Although the first probabilistic/statistical concepts were introduced to physics already in the 19-th century (kinetic theories of gases; the Maxwell distribution of velocities of the molecules of a gas, Boltzmann H -theorem), the first years of the 20-th century brought systematic formulations of statistical mechanics/dynamics, including the stochastic description of the phenomenon of the Brownian motion.

One should mention first the Gibbsian construction of statistical mechanics (described by Gibbs [1] in 1903) where the problem of time evolution of a large number of material particles (described by Hamiltonian differential equations) is treated probabilistically. Because of difficulties in the exact determination of the dynamical variables and the fact that the systems considered in statistical physics include a very large number of particles, a statistical description of the motion of the system was introduced. The basic role is played by the so-called phase probability density $f(\mathbf{x}, t)$, where \mathbf{x} denotes a point in the phase space (of generalized coordinates and velocities): $\mathbf{x} = (x_1, x_2, \dots, x_{6N})$, and N denotes the number of particles. Since the motion of the system is governed by the deterministic Hamiltonian equations, the principle of conservation of probability leads to the well-known Liouville equation for $f(\mathbf{x}, t)$

$$\frac{\partial f}{\partial t} + \sum_{k=1}^{6N} \frac{\partial}{\partial x_k} \{ \dot{x}_k f(\mathbf{x}, t) \} = 0, \quad f(\mathbf{x}, t_0) = f_0(\mathbf{x}_0), \quad (1)$$

where $f_0(\mathbf{x}_0)$ denotes the probability density of the initial state of the system. The initial value problem described by Eq. (1) can be regarded as the *first connection between probability and differential equations*.

Another phenomenon belonging to physics, which influenced tremendously the development of probabilistic thinking in natural sciences, is the Brownian motion – an extremely irregular movement of a small particle suspended in a fluid. This phenomenon discovered experimentally by R. Brown in 1827 is one of the most interesting examples of random physical processes. During many years after the Brown's discovery, various experiments were performed attempting to measure the properties of the Brownian particles (e.g. experiments of F. Exner and R.A. Zsigmondy). Although some qualitative hypotheses were formulated, as well as some results of quantitative nature were provided (e.g. dependence of the particle displacement on its size or the temperature of the medium), none of these findings was able to shed brighter light on the true nature of the phenomenon of Brownian motion. As S.G. Brush [2] writes in his historical work: “three quarters of a century of experimentation produced almost no useful results, simply because no theorist had told the experimentalists what quantity should be measured!”.

The first fruitful and breakthrough results came from mathematical model of the Brownian motion by Einstein [3,4] and Smoluchowski [5,6] – (1905/06). These great physicists, proposed - independently and via different approaches – the theoretical description and explanation of the Brownian motion. Einstein's reasoning was inspired by the ideas of the

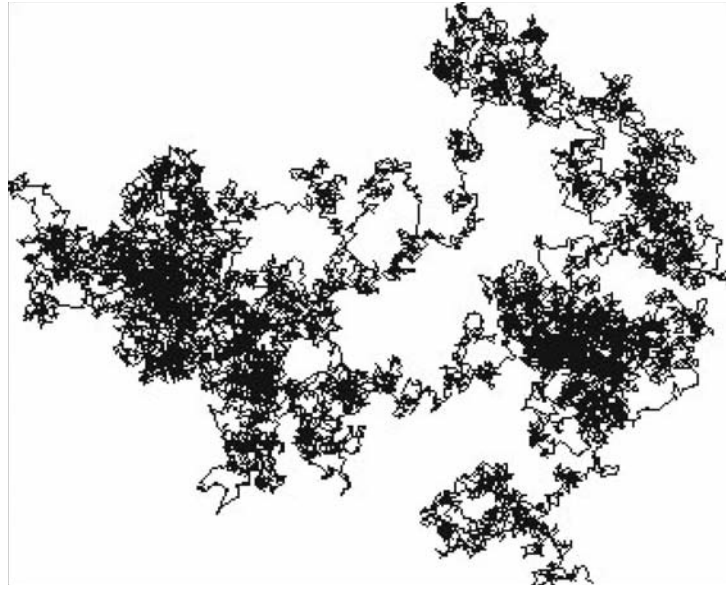


Figure 1. Illustration of the trajectory of the Brownian particle on a plane. (cf. www.math.yale.edu)

diffusion theory, whereas Smoluchowski's arguments were based on combinatorics and the mean-free-path approximation of the kinetic theory.

It is worth noting that Einstein and Smoluchowski pointed clearly that the basic measurable characteristic of the phenomenon of Brownian motion should be – not, as their predecessors believed, the velocity of particles but – the mean square of their displacements per second. Einstein and Smoluchowski obtained for the mean square displacement $\langle x^2 \rangle$ in time interval t the same formula (with a slight discrepancy in the numerical factor – due to various approximations used; in his later papers Smoluchowski accepted the Einstein's numerical factor). This formula is as follows:

$$\langle x^2 \rangle = t \frac{kT}{N} \frac{1}{3\pi\eta r}, \quad (2)$$

where k is the Boltzmann constant, N is the Avogadro number (a number of point molecules in unit volume), T is the absolute temperature, r is the radius of the spherical particle and η is the viscosity coefficient of the medium.

Equation (2) shows that the mean square of the displacement of the Brownian particle grows linearly in time – the result which (as we know today) has had very profound implications in the mathematical theory

of Brownian motion and stochastic dynamics in general (e.g. the Wiener process/model of Brownian motion). The exact experimental confirmation of the Einstein and Smoluchowski theory was provided by Perrin [7] (using the Brownian motion experiments Perrin determined also the Avogadro number N). In this context, the value of experimental work of T. Svedberg should also be underlined.

Although the scientists mentioned above worked in different places, there was among them quite a strong, natural interaction by correspondence. For example, as Pais [8] writes (pp.101) “Six letters between Einstein and Smoluchowski have survived. All show cordiality and great natural respect”; cf. also Średniawa [9].

Nearly in the same time (exactly, in 1908) Langevin [10] formulated a “phenomenological” description of the erratic motion of a “heavy Brownian particle” of mass m immersed in a liquid, using the Newtonian equation for the particle. The interaction of the surrounding fluid with the Brownian particle gives rise to two distinct forces: a dissipative force (due to dynamic friction in the course of a motion of a particle in viscous fluid), and a fluctuation force (arising from the molecular collisions). So, Langevin wrote down a differential equation of the motion of the particle

$$m \frac{dv}{dt} = f(t), \quad f(t) = F_r(t) + F_{irr}(t), \quad (3)$$

where v is the component of velocity of particle along the x axis and $f(t)$ – the total force caused by a surrounding medium consists of two parts: $F_r(t) = -\beta v(t)$ being a regular component, and $F_{irr}(t)$ representing irregular or random force acting on the particle by collisions. Denoting:

$$\beta/m = \alpha, \quad F_{irr}(t)/m = \xi(t)$$

one obtains

$$\frac{dv}{dt} + \alpha v = \xi(t). \quad (4)$$

If one assumes that the particle is spherical with radius r and the liquid has a viscosity parameter η then the constant $\alpha = 6\pi r\eta/m$. Symbol $\xi(t)$ represents the unknown force due to the molecular impacts; this force is random in nature and can only be described probabilistically (the Langevin force). Langevin assumed that its mean value (over the ensemble) should be zero and the correlation of each two fluctuating forces at different times should be negligibly small when time difference $t_2 - t_1$ is meaningful. The above hypotheses concerning the features of molecular collisions are usually formalized in physics as follows:

$$\langle \xi(t) \rangle = 0, \quad \langle \xi(t_1)\xi(t_2) \rangle = D\delta(t_2 - t_1), \quad D > 0, \quad (5)$$

where $\delta(t_2 - t_1)$ is the Dirac function, D is a constant and $\langle \cdot \rangle$ denotes averaging over the ensemble of collision process. Therefore, $\xi(t)$ in Eq. (4) is a very peculiar process; today, in stochastic theory it is called a “white noise”. Such a process does not exist in the conventional sense. For this reason, during a long time period it was not clear what should be the appropriate rigorous interpretation of the Eq. (4).

Equation (4) is commonly known as the *Langevin equation*. It can be regarded historically as the *first stochastic differential equation*. Although the original Langevin equation is linear (and in a scalar form), nowadays (especially in physics) more general, nonlinear equations (also – in vectorial form) with white noise additional excitation are often termed the Langevin equations; various forms of this equation serve as models of real systems in contemporary stochastic dynamics.

It is worth noting, that the value for the mean square of the Brownian particle displacement $\langle x^2 \rangle$ obtained from the Langevin equation (4) agrees exactly with the Einstein-Smoluchowski formula (2) – cf. Lindsay [11].

Origins of Stochastic Dynamics of Real Engineering Systems

Uncertainty and random fluctuations are a very common feature of a variety of real dynamical engineering systems. Most of engineering systems (control systems, mechanical, structural, etc.) are subjected to complicated external and internal (time-varying) influences. These complex excitations and the associated responses can, most rationally, be described in terms of stochastic processes. Among the examples are: structural response due to earthquake, wind load, sea waves etc., random vibration of road vehicles (response to random road roughness), response/and reliability of aerospace structures to random turbulent field, response (and stability) of suspension bridges. In the case of such systems as above, the ultimate objective of stochastic dynamics is to provide a new tools for the *reliability estimation*. In other situations, the qualitative characterization and effects of random excitation are of interest (e.g. stochastic bifurcations, stochastic resonance, effect of random noise on deterministic chaos).

Stochastic dynamics of engineering systems emerged nearly exactly fifty years ago. First – in the context of automatic control theory (cf. Booton [12], Kazakov [13]) and, a little later, in the analysis of dynamics of aerospace, mechanical and structural systems. The primary reasons for stochastic analysis was the need to assure a satisfactory performance of engineering systems in the presence of real random noises/excitations.

For a proper assessment of reliability of a wide class of systems the stochastic analysis of their response turned out to be necessary.

In the context of engineering systems of mechanical nature, *the pioneering work* belongs to the following great scientists (alphabetically): Ariaratnam [14] (1960), Bolotin [15] (1959), Caughey [16] (1959), Crandall [17] (1958), Kozin [18] (1961), Lin [19] (1963), Lyon [20] (1956), Shinozuka [21] (1964). The books by Bolotin [22], Crandall and Mark [23], Lin [24], Robson [25] give an excellent exposition of the early efforts and results.

Today, stochastic dynamics of physical/engineering systems has a very extensive literature dealing both with mathematical bases as well as with specific applications. This literature includes also a number of books-monographs. The books of Bolotin [26], Lin and Cai [27], Roberts and Spanos [28], Sobczyk [29], and Soong and Grigoriu [30] provide an adequate presentation of the existing results.

General Unifying Scheme of Stochastic Dynamics

A general methodical scheme of stochastic dynamics of mechanical systems can be illustrated as it is shown in the Fig. 2.

The random excitation acting on the system is described by a random/stochastic process (in general vectorial) $X(t, \gamma)$, where time t belongs to a prescribed time interval $[t_0, \infty]$ or $[t_0, T]$, whereas γ symbolizes randomness, $\gamma \in \Gamma$ where Γ is a space of elementary events. More exactly, we have the basic probability space (Γ, F, P) where F is a family of subsets of Γ (σ -algebra) on elements of which the probability P is defined; $0 \leq P(A) \leq 1$, $A \in F$. A random variable $X(\gamma)$ is a measurable function which maps Γ into R^n . A stochastic process $X(t, \gamma)$ is a function which for each t gives a random variable. This function

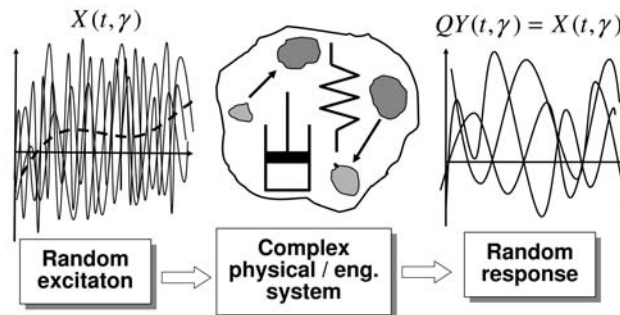


Figure 2. General scheme of stochastic dynamics.

is characterized partially by its mean $\langle X(t, \gamma) \rangle = m_X(t)$, by its correlation function $K_X(t_1, t_2) = \langle X(t_1, \gamma)X(t_2, \gamma) \rangle$ and by other – more complicated – averages. A complete characterization of $X(t, \gamma)$ is given by probability distributions for various subsets of t -values. Having the probability distribution of $X(t, \gamma)$ we can calculate the probability of various events associated with $X(t, \gamma)$, e.g. the probability that values of $X(t, \gamma)$ belong to a given set D . A stochastic process can be, for example, stationary or non-stationary, Gaussian or non-Gaussian, Markovian etc. For a systematic presentation, a reader is referred to the books on stochastic processes (e.g. see the references in Sobczyk [29]).

In stochastic dynamics problems the excitation process $X(t, \gamma)$ is assumed to be given; most often it must be inferred from the empirical data on real processes. A dynamical system transforms $X(t, \gamma)$ into another process $Y(t, \gamma)$; this response process is unknown and should be characterized via the mathematical/stochastic analysis.

Major Challenges

The following problems constitute the major tasks of stochastic dynamics of engineering systems.

- System modeling and characterization of real random excitations.

This is a problem of formulation of the governing equations adequately to the specific system under consideration and selection of the appropriate stochastic processes characterizing external and/or parametric excitations. Although the system modeling follows, to a great extent, the basic principles of model building in deterministic theory, here in stochastic dynamics there are some specific factors which should be taken into account. For example, in modeling of the system dynamics (under random excitations) with simultaneous degradation taking place in it, the coupled response-degradation model has to be consistent with the nature of randomness; also, the initial and boundary conditions (which are posed for random functions) should be defined according to stochastic nature of the problem. The characterization of random loads acting on specific engineering systems is an involved problem itself (we will discuss it in the next section).

- Characterization of the response; effective solution methods.

This is a problem of solving the adequate systems of stochastic differential equations (mostly nonlinear) with specified real random excitations. This means that we are looking for a stochastic process, which satisfies (in the appropriate sense) a given system

of equations along with the effective method of quantifying the probabilistic characteristics of this process (moments, probability distribution, etc.). The most notable methods will be discussed in Sec. 5.

- Failures of stochastic dynamical systems; reliability assessment.

The ultimate purpose of stochastic analysis of engineering systems is characterization of safety or reliability of systems of practical importance. Having obtained the probabilistic characteristics of the response (e.g. displacement, stress, etc.) from the dynamic analysis, we can use them to assess the conditions of a system performance for various failure mechanisms. In most cases the reliability of systems in question can be defined and quantified in terms of some random variables associated with the response process. However, for a wide class of problems (where the Markov process theory can be used) the reliability can be assessed more directly via differential equations for the reliability function (derivable from the governing stochastic differential equations). Section 6 expounds this problem.

- Qualitative phenomena / effects.

In addition to the problems indicated above and primarily important for engineering practice, there exists a class of interesting questions which are qualitative in nature and are associated with the basic dynamical features of a system in the presence of random noise. Is a random excitation acting on / in a system just an annoying factor - which makes our life more difficult or - maybe - it can generate some new and interesting physical phenomena? It turns out that random perturbations, when combined with nonlinearity, can induce multifarious specific “noise-induced” phenomena and effects; they have a potential to change some internal features of system dynamics (stability, bifurcations, resonances, etc.). The last part of this lecture will shed some light on these problems.

2. General Mathematical Model of Stochastic Dynamics

Stochastic Differential Systems. Basic Interpretations

A general model for a wide class of physical and engineering systems subjected to time-varying random disturbances can be represented in

the vectorial form as follows:

$$d\mathbf{Y}/dt = \mathbf{F}(\mathbf{Y}, t) + \mathbf{G}(\mathbf{Y}, t)\mathbf{X}(t, \gamma), \quad \mathbf{Y}(t_0) = \mathbf{Y}_0, \quad t \in [t_0, T], \quad (6)$$

where $\mathbf{Y}(t, \gamma) = [Y_1(t, \gamma), \dots, Y_n(t, \gamma)]$ is an unknown vectorial response process, $\mathbf{X}(t, \gamma) = [X_1(t, \gamma), \dots, X_m(t, \gamma)]$ is m -dimensional stochastic process (characterizing random excitations acting on the system);

$$\mathbf{F}(\mathbf{y}, t) = [F_1(\mathbf{y}, t), \dots, F_n(\mathbf{y}, t)]$$

is a given vector-valued function of indicated variables describing the regular (deterministic) component of the motion,

$$\mathbf{G}(\mathbf{y}, t) = [G_{ij}(\mathbf{y}, t)]_{i=1, \dots, n}^{j=1, \dots, m}$$

is a given matrix-valued function characterizing the state-dependent intensity of the random excitation $\mathbf{X}(t, \gamma)$, \mathbf{Y}_0 is an initial state of the system (deterministic or random).

If \mathbf{G} in Eq. (6) does not depend on \mathbf{Y} , the model Eq. (6) describes dynamics with an external random excitation. It is seen that the classical Langevin equation (4) is a special case of Eq. (6) when

$$\mathbf{F} = -\alpha v, \quad \mathbf{G}\mathbf{X} = X/m = \xi.$$

It is clear that functions $\mathbf{F}(\mathbf{y}, t)$ and $\mathbf{G}(\mathbf{y}, t)$ – taking on specific mathematical forms in modeling real systems – should belong to the class of functions which satisfy the appropriate conditions assuring the existence and uniqueness of a solution of Eq. (6).

If the stochastic process $\mathbf{X}(t, \gamma)$ is sufficiently regular (e.g. continuous and differentiable) then system Eq. (6) can be called a regular stochastic differential system. The majority of problems for such systems can be analyzed by use of the methods which are analogous to those in deterministic theory of ordinary differential equations; in spite of this fact, such stochastic equations give rise to serious solution problems (cf. Sobczyk [29]).

If the stochastic process $\mathbf{X}(t, \gamma)$ is very irregular (e.g. white noise, Brownian motion process, jump process) then the system Eq. (6) requires more sophisticated probabilistic analysis. Let us assume that $\mathbf{X}(t, \gamma) = \xi(t, \gamma)$ where $\xi(t, \gamma)$ is a vectorial white noise i.e.

$$\xi(t, \gamma) = [\xi_1(t, \gamma), \dots, \xi_m(t, \gamma)].$$

In this case the stochastic system Eq. (6) is commonly represented in the form of the Langevin-type equation

$$d\mathbf{Y}/dt = \mathbf{F}(\mathbf{Y}, t) + \mathbf{G}(\mathbf{Y}, t)\xi(t, \gamma), \quad \mathbf{Y}(t_0) = \mathbf{Y}_0, \quad t \in [t_0, T]. \quad (7)$$

As we have already mentioned, Eq. (7) – as it stands – should be regarded as a “pre-equation” which needs an appropriate interpretation. The generally accepted interpretation is associated with the equation

$$d\mathbf{Y}/dt = \mathbf{F}(\mathbf{Y}, t) + \mathbf{G}(\mathbf{Y}, t)d\mathbf{W}(t, \gamma), \quad \mathbf{Y}(t_0) = \mathbf{Y}_0, \quad t \in [t_0, T], \quad (8)$$

or, equivalently, with the following stochastic integral equation:

$$\mathbf{Y}(t) = \mathbf{Y}_0 + \int_{t_0}^t \mathbf{F}(\mathbf{Y}(s), s)ds + \int_{t_0}^t \mathbf{G}(\mathbf{Y}(s), s)d\mathbf{W}(s), \quad (9)$$

where $\mathbf{W}(t, \gamma) = [W_1(t, \gamma), \dots, W_m(t, \gamma)]$ is the m -dimensional Wiener (or Brownian motion) process. Because of the peculiar properties of the Wiener process (e.g. trajectories of $\mathbf{W}(t, \gamma)$ are continuous but nowhere differentiable and have unbounded variation on each finite interval), the second integral in Eq. (9) has to be defined in a special way. Two basic definitions are associated with the names of Itô and Stratonovich (cf. Arnold [31], Sobczyk [29]). Depending on the choice of the definition of the integral with respect to $d\mathbf{W}(t)$, we obtain two different interpretations of Langevin-type Eq. (7) via Eq. (8); those are the Itô and Stratonovich interpretations. When $\mathbf{G}(\mathbf{y}, t)$ occurring in Eq. (7) depends explicitly on \mathbf{y} , the Itô and Stratonovich interpretations lead to different solution processes $\mathbf{Y}(t)$. There exists, however, simple relationship between the Itô solution and Stratonovich solution. Namely, the Stratonovich solution coincides with the Itô solution of Eq. (8) if the components of the drift term $\mathbf{F}(\mathbf{y}, t)$ in Eq. (8) are replaced by the following ones

$$F_i(\mathbf{Y}, t) = F_i^*(\mathbf{Y}, t) + \frac{1}{2} \sum_{j=1}^n \sum_{k=1}^m G_{jk}(\mathbf{Y}, t) \frac{\partial G_{ik}(\mathbf{Y}, t)}{\partial Y_j}, \quad (10)$$

where $F_i^*(\mathbf{Y}, t)$, $i = 1, \dots, n$ are the drift components in the Stratonovich equation. The diffusion term is the same in both interpretations. In what follows we will adopt the Itô interpretation of the nonlinear Langevin “pre-equation” (7).

Main Theorem; Relation to F-P-K Equation

Let us concentrate our attention on the Itô stochastic differential model Eq. (8). Suppose the following conditions are satisfied:

- (a) the vector-valued function $\mathbf{F}(\mathbf{y}, t)$ and the $(n \times m)$ -matrix valued function $\mathbf{G}(\mathbf{y}, t)$ are defined and continuous for $t \in [t_0, T]$, $\mathbf{y} \in R^n$,

- (b) the functions $F(\mathbf{y}, t)$ and $\mathbf{G}(\mathbf{y}, t)$ satisfy the Lipschitz condition (with respect to \mathbf{y}),
- (c) the functions $\mathbf{F}(\mathbf{y}, t)$ and $\mathbf{G}(\mathbf{y}, t)$ grow (with respect to \mathbf{y}) at most linearly,
- (d) the random variable $\mathbf{Y}(t_0) = \mathbf{Y}_0$ is independent of $\mathbf{W}(t) - \mathbf{W}(t_0)$ for each $t > t_0$.

Then Eq. (8) has on $t \in [t_0, T]$ a unique solution satisfying the initial condition, almost all realizations of the solution process $\mathbf{Y}(t)$ are continuous, and the solution $\mathbf{Y}(t)$ is a Markov diffusion process on $[t_0, T]$ with the following drift vector $\mathbf{A}(\mathbf{y}, t)$ and diffusion matrix $\mathbf{B}(\mathbf{y}, t)$:

$$\mathbf{A}(\mathbf{y}, t) = \mathbf{F}(\mathbf{y}, t), \quad \mathbf{B}(\mathbf{y}, t) = \mathbf{G}(\mathbf{y}, t)\mathbf{G}^T(\mathbf{y}, t). \quad (11)$$

This means that the transition probability density $p(\mathbf{y}, t | \mathbf{y}_0, t_0)$ of process $\mathbf{Y}(t)$ satisfies the following Fokker-Planck-Kolmogorov (F-P-K) equation

$$\frac{\partial p}{\partial t} + \sum_{i=1}^n \frac{\partial}{\partial y_i} [F_i(\mathbf{y}, t)p(\mathbf{y}, t)] - \frac{1}{2} \sum_{i,j=1}^n \frac{\partial}{\partial y_i \partial y_j} [b_{ij}(\mathbf{y}, t)p(\mathbf{y}, t)] = 0, \quad (12)$$

with the appropriate initial and boundary conditions. In Eq. (12)

$$b_{ij}(\mathbf{y}, t) = \{\mathbf{G}(\mathbf{y}, t)\mathbf{G}^T(\mathbf{y}, t)\}_{ij} = \sum_{r=1}^n G_{ir}(\mathbf{y}, t)G_{jr}(\mathbf{y}, t). \quad (13)$$

The theorem stated above shows that a wide class of diffusion Markov processes can be constructed – via the stochastic Eq. (8) – on the basis of increments of the Wiener process. It also indicates that a wide class of real dynamical systems modeled by the Langevin-type equation (7) can be characterized by solving the partial differential Eq. (12). The methods for obtaining solutions of the F-P-K equation (12) have been a subject of a great research effort (cf. Soize [32], Langtangen [33], Spencer and Bergman [34]). Although the progress is significant, the effective characterization of the transition probability density for systems of higher dimension (e.g. $n > 5$) still constitutes a serious problem. The situation is simpler if one is interested in stationary solutions of stochastic systems (8), i.e. when $t \rightarrow \infty$, and the F-P-K equation becomes “time-independent”.

3. Engineering Stochastic Vibratory Systems: Response and Degradation Models

Basic Model

A general model for dynamics of mechanical/structural systems with random excitation (both – external and/or parametric) can be formulated in the following form

$$\mathbf{M}\ddot{\mathbf{Y}}(t) + \mathbf{C}\dot{\mathbf{Y}}(t) + \mathbf{R}[\mathbf{Y}(t), \dot{\mathbf{Y}}(t), \mathbf{X}_1(t, \gamma)] = \mathbf{X}_2(t, \gamma), \quad (14)$$

where \mathbf{M} and \mathbf{C} represent the constant mass and damping matrices, respectively, $\mathbf{Y}(t)$ is an unknown response vector process, \mathbf{R} characterizes the nonlinear restoring force, and $\mathbf{X}_1(t, \gamma)$, $\mathbf{X}_2(t, \gamma)$ are the random processes characterizing parametric and external excitations, respectively. When the original system is of a continuous type (e.g. beam, plate, shell), the Eq. (14) is a spatially discretized version (e.g. via Galerkin of finite-element methods) of the original equations and it describes the system response (as a function of time) in fixed spatial points. The stochastic system of Eq. (14), which can be easily represented in the form of a system of the first order equations, characterizes (when appropriately specified) adequately a variety of real systems of engineering practice, e.g. complicated multibody vibrating vehicle systems (cf. Schiehlen [35]), structural/ mechanical vibrating components in bridges, offshore structures as well as aerospace systems (cf. examples in Roberts and Spanos [28], Lin and Cai [27]).

In modeling of real physical / engineering problems, the stochastic processes $\mathbf{X}_1(t, \gamma)$ and $\mathbf{X}_2(t, \gamma)$ describing the parametric and external exci-

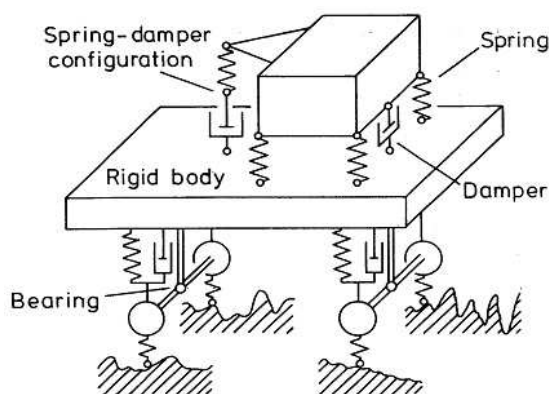


Figure 3. Exemplary multibody vehicle system with random excitation (cf. W. Schiehlen [35]).

tations may have quite diverse probabilistic properties. From the point of view of analytical treatment and computational efficiency it is most convenient if these random processes can be assumed to be random white noises (i.e. uncorrelated for different instants of time); as we know from Sec. 2, in such a case one can make use of the advantages of the theory of Itô stochastic equations (and Markov process theory). It turns out, however, that these theories can also be used for a wide class of random excitations with finite correlation time; especially for excitations which can be represented as a response of dynamical systems to a white noise excitation $\xi(t, \gamma)$. An arbitrary Gaussian and stationary random process with rational spectral density can be obtained as an output of a linear system (filter) with white noise as the input.

Therefore, in order to represent the model Eq. (14), with random excitations $\mathbf{X}_1(t, \gamma)$, $\mathbf{X}_2(t, \gamma)$ being real (or, “colored”) random processes, we extend the state space of the system by defining the extended state vector $[\mathbf{Y}_1, \mathbf{Y}_2, \mathbf{X}_1, \mathbf{X}_2]$, where $\mathbf{Y}_1 = \mathbf{Y}$, $\mathbf{Y}_2 = \dot{\mathbf{Y}}$. The vibratory system governed by Eq. (14) can in this way be represented as the following system of first-order Itô stochastic equations:

$$\begin{aligned} d\mathbf{Y}_1(t) &= \mathbf{Y}_2(t)dt, \\ d\mathbf{Y}_2(t) &= -\mathbf{M}^{-1}[\mathbf{C}\mathbf{Y}_2 + \mathbf{R}(\mathbf{Y}_1, \mathbf{Y}_2, \mathbf{X}_1(t)) - \mathbf{X}_2]dt, \\ d\mathbf{X}_1(t) &= -\mathbf{A}_1\mathbf{X}_1(t)dt + \phi_1(t)d\mathbf{W}_1(t, \gamma), \\ d\mathbf{X}_2(t) &= -\mathbf{A}_2\mathbf{X}_2(t)dt + \phi_2(t)d\mathbf{W}_2(t, \gamma), \end{aligned} \quad (15)$$

where $\mathbf{X}_1(t, \gamma)$ and $\mathbf{X}_2(t, \gamma)$ are the outputs of the filter driven by white noises $\xi_1(t, \gamma)$ and $\xi_2(t, \gamma)$, respectively; \mathbf{A}_1 and \mathbf{A}_2 are the filters operators (matrices) associated with real excitations $\mathbf{X}_1(t, \gamma)$ and $\mathbf{X}_2(t, \gamma)$, whereas $\phi_1(t, \gamma)$ and $\phi_2(t, \gamma)$ are the time-dependent intensities of white noises $\xi_1(t, \gamma)$ and $\xi_2(t, \gamma)$, respectively; $\mathbf{W}_1(t, \gamma)$ and $\mathbf{W}_2(t, \gamma)$ are the Wiener (or Brownian motions) processes in the Itô representation of “pre-equations” of Langevin – type with white noises $\xi_1(t, \gamma)$ and $\xi_2(t, \gamma)$, respectively.

Therefore, adding the additional filter equations (for real excitations $\mathbf{X}_1(t, \gamma)$ and $\mathbf{X}_2(t, \gamma)$), to the original system Eq. (14) enables us to use the Markov process theory, including the analytical and numerical methods developed for Itô stochastic equations (cf. Sobczyk [29]). Of course, the filter can also be governed by higher order differential equations. Another possibility of treating system Eq. (14) with real random noises gives the Khasminskii averaging method (cf. Lin and Cai [27], Sobczyk [29], Soong and Grigoriu [30]).

Stochastic Dynamics of Degrading Systems

In fact, stochastic governing equations for many mechanical / structural systems should be represented in a more general form which accounts for inelastic behaviour and simultaneous degrading processes taking place in the system. Above all, these are elastic-plastic vibratory systems (under severe random loadings) in which the restoring force has a hereditary nature (cf. Casciati [36], Irshik and Zigler [37], Wen [38]).

Therefore, instead of model (14) we construct the coupled system of equations for the response problem in which the restoring force, in general, depends on the time history of the response. The model is as follows:

$$\mathbf{M}\ddot{\mathbf{Y}}(t) + \mathbf{C}\dot{\mathbf{Y}}(t) + \mathbf{R}[\mathbf{Y}(t), \dot{\mathbf{Y}}(t), \mathbf{Z}(t), \mathbf{X}_1(t, \gamma)] = \mathbf{X}_2(t, \gamma), \quad (16)$$

where $\mathbf{Z}(t)$ characterizes various specific processes responsible for degradation phenomena. Process $\mathbf{Z}(t)$ is governed by its own equation (coupled with $\mathbf{Y}(t)$). In general, it has a form

$$\dot{\mathbf{Z}}(t) = \mathbf{H}[\mathbf{Z}(t), \mathbf{Y}(t), \dot{\mathbf{Y}}(t)], \quad \mathbf{Z}(t_0) = \mathbf{Z}_0, \quad (17)$$

where function $\mathbf{H}[\mathbf{z}, \mathbf{y}, \dot{\mathbf{y}}]$ should be constructed for specific situations. Its mathematical form is inferred from the elaboration of empirical data, or it is derived from the analysis of the physics of the process.

It seems that a need for the coupled models dynamics Eqs. (16,17) arose for the first time in the analysis of structural response to earthquake. Indeed, structures under strong earthquake excitation become inelastic with restoring forces being nonlinear and depending on the time history of the response. In this situation process $\mathbf{Z}(t)$ describes a hysteretic loop and is most often represented by model (17) in which $\mathbf{Z}(t) = Z(t)$ is a scalar process, and function \mathbf{H} depends only on (z, \dot{y}) and has the form (the Bouc-Wen [39] model)

$$\mathbf{H}[z, \dot{y}] = \alpha \dot{y} - \beta |\dot{y}| |z| |z|^{n-1} - \delta \dot{y} |z|^n, \quad (18)$$

where α, β, δ, n characterize the amplitude and shape of the hysteretic loop. In the situation considered, a degradation $D(t)$ taking place in the system has been defined in terms of the total hysteretic energy dissipation characterizing the cumulative effect of severe response and expressed by the state variables (z, \dot{y}) . Therefore, the coupled response-degradation problem for randomly excited dynamic hysteretic systems is governed by Eqs. (16,17). These equations have been the subject of detailed analysis for many specific situations under various hypotheses concerning random external excitation (the restoring force R does not depend on $\mathbf{X}_1(t, \gamma)$; cf Wen [39]).

There is a class of practically important problems governed generally by the coupled Eqs. (16,17) in which $\mathbf{Z}(t)$ characterizes directly the degradation of the system. A general model can be formulated in the following form

$$\mathbf{M}\ddot{\mathbf{Y}}(t) + \mathbf{C}\dot{\mathbf{Y}}(t) + \mathbf{R}[\mathbf{Y}(t), \dot{\mathbf{Y}}(t), \mathbf{D}(t)] = \mathbf{X}(t, \gamma), \quad (19)$$

$$\mathbf{Q}[\mathbf{D}(t), \dot{\mathbf{D}}(t), \mathbf{Y}(t), \dot{\mathbf{Y}}(t)] = 0, \quad (20)$$

where $\mathbf{Q}[\cdot]$ symbolizes a relationship between degradation and response processes. In Eq. (20) dependence on the response can be regarded in some relaxed sense, i.e. degradation rate may depend not on the actual values of $\mathbf{Y}(t)$ but – on some functionals of $\mathbf{Y}(t)$.

In the fatigue degradation problem (more exactly – in the analysis of response of vibrating system with the stiffness degradation due to fatigue accumulation), it is natural to quantify the degradation $\mathbf{D}(t) = D(t)$ by a “normalized” crack size and adopt as an evolution Eq. (20) one of the “kinetic” equations for fatigue crack growth. These equations, however, contain the stress intensity factor range, so the degradation rate $\dot{\mathbf{D}}(t)$ depends on the quantity related to $\mathbf{Y}_{\max} - \mathbf{Y}_{\min}$. In this situation, Eq. (20) has the form

$$\dot{\mathbf{D}}(t) = \mathbf{H}[\mathbf{D}(t), \mathbf{Y}_{\max} - \mathbf{Y}_{\min}]. \quad (21)$$

Another version of an equation for $\mathbf{D}(t)$ in the coupled response–degradation problem is obtained if the functional relationship (20) does not include $\dot{\mathbf{D}}(t)$, and the degradation $\mathbf{D}(t)$ depends on some functionals defined on the response process $[\mathbf{Y}(t), \dot{\mathbf{Y}}(t)]$, i.e. (20) takes the form (\mathcal{F} denotes here the appropriate functional)

$$\mathbf{D}(t) = \mathcal{F}\left\{\mathbf{Y}(t), \dot{\mathbf{Y}}(t)\right\}. \quad (22)$$

Important examples include randomly vibrating systems in which a degradation process depends on the time length which the response $\mathbf{Y}(t)$ spends above some critical level \mathbf{y}^* (or, $\mathbf{D}(t)$ depends on the number of crossings of the level \mathbf{y}^* by the trajectories of the process $\mathbf{Y}(t)$ within a given interval $[0, T]$). This is the case of an elastic-plastic oscillatory system with $\mathbf{D}(t)$ interpreted as an accumulated plastic deformation generated by the “excursion” of the response process $\mathbf{Y}(t)$ into plastic domain (in this situation $\mathbf{y}^* = y^*$ may be regarded as the yield limit of the material component in question, cf. Grossmayer [40]). This is also a situation of randomly vibrating plate with fatigue – induced stiffness degradation; in this case $\mathbf{D}(t)$ is interpreted as accumulated fatigue damage due to exceeding the fatigue limit by the response process.

The analysis of the stochastic response-degradation problem for elastic-plastic vibratory systems and for the system with fatigue-induced degradation can also be analyzed by the more explicit cumulative model for degradation $\mathbf{D}(t)$. We mean the situation in which relationship (20) is represented as follows (in scalar form):

$$D(t) = D_0 + \sum_{i=1}^{N(t)} \Delta_i(Y, \gamma), \quad (23)$$

where $\Delta_i = \Delta_i(Y, \gamma)$ are random variables characterizing the elementary degradations taking place in the system; the magnitude of Δ_i depends on the characteristics of the process $Y(t)$ above a fixed (critical) level y^* . Process $N(t)$ is a stochastic counting process characterizing the number of degrading events in the interval $[t_0, t]$. In the case of elastic-plastic oscillator (cf. Grossmayer [40]) $\Delta_i(Y, \gamma)$ are the yielding increments taking place in a single yielding duration τ_Y which is related to the time interval which the response process spends above the yield level during a single excursion or during a single clump of excursions. In the case of fatigue Δ_i , $i = 1, 2, \dots, N(t)$ can be regarded as the magnitudes of elementary (e.g. within one cycle) crack increments (cf. Sobczyk and Trębicki [41,42] as well as Sobczyk and Spencer [43]).

4. Characterization of Real Random Dynamic Loads

General Remarks

It is clear that a key factor affecting the system behaviour is the excitation (load) to which a system is exposed. So, the appropriate (adequate to the physical / mechanical situation) modelling of real random loads is a crucial task within the whole methodical effort of applied stochastic dynamics. This is a problem of statistical inference from the empirical data (and from the basic physical mechanisms of the excitation in question) about the most informative features of a random excitation under consideration.

Depending on the type of engineering structure and its operational task, we meet various kinds of random load processes. For example: *gust wind loads* (acting on tall slender, tower-shaped structures such as TV masts, chimneys, some bridges, etc. as well as on various aerospace structures) induced by atmospheric turbulence; *sea wave loads* (acting on offshore platforms, ships, storage tanks etc.) dominated by gravity forces; *earthquake excitations* (acting on all structural systems) caused by tectonic phenomena and complex interaction of seismic waves; *ground-*

induced excitations (acting on road vehicles) generated by a roughness of real road surfaces; *traffic loads* (acting on long-span bridges) caused by moving vehicles. The character and intensity of the load fluctuations in the examples given above depend on the shape of a structure and its orientation with respect to the load direction. Of course, in the case of turbulent wind its probabilistic characteristics depend additionally on meteorological conditions, the geographical position, the height over the Earth's surface, etc. So, the statistical inference on the real random excitations acting on engineering systems has to make use of various hypotheses and simplifications. Let us consider here two important types of random excitation: the sea wave excitation acting on the steel offshore platform and the earthquake excitation.

Characterization of Sea Wave Excitation

This type of excitation is generated by wind and sea waves. Waves, in turn, occur as a result of complicated interaction between wind and water. This leads to a loading process that is often described by a series of continuously varying sea states. The nature of offshore loading and the complex interactions likely in the seawater environment make establishment of standard load characteristics (e.g. spectra) for offshore structures much more difficult than for aircraft structures.

Although sea motion (or sea states) can be partially characterized by some parameters (e.g., the wave height h_s , the mean wave period T_s , the wave direction θ), an underlying quantity in stochastic theory is the sea elevation $\eta(x, y, t)$, which is regarded as a random function of position and time. Probabilistic properties of $\eta(x, y, t)$ are derived partially from the measurements and partially from hydrodynamic wave theory. In almost all studies in ocean engineering, it is assumed that the sea wave process is a stationary stochastic process. Under such a hypothesis, the process $\eta(x, y, t)$, for fixed (x, y) , is characterized by the spectral density $g_\eta(\omega)$.

Various forms of the spectral density of sea surface elevation $\eta(t)$, for fixed (x, y) , have been proposed in the literature. The most popular form used in practice is the Pierson-Moskowitz spectrum

$$g_\eta(\omega) = A a_g^2 \omega^{-5} \exp[-B(a_g/\omega v_0)^4], \quad \omega > 0, \quad (24)$$

where A and B are dimensionless constants taken to be $A = 8.1 \times 10^{-3}$, $B = 0.74$; v_0 is the mean wind velocity at a height of 19.5 m above the still sea surface; and a_g is the acceleration of gravity. Using a linearized wave theory, one obtains a relationship between the fluid particle velocity $u(x, y, z, t)$ and the surface elevation $\eta(x, y, t)$. This relationship allows

to determine the statistics of particle velocity; e.g. the spectral density of the horizontal component of u and acceleration \dot{u} (cf. Madsen [44] et al.)

If the characteristic dimension of a structure is small compared with the wave length, then the load consists of two basic components: a drag force proportional to the square of the normal component of the incident particle velocity and an inertia or mass force associated with the normal component of the particle acceleration. These forces are combined in the *Morison formula* for the force per unit length of a fixed cylinder:

$$\mathbf{P} = k_d \mathbf{u} |\mathbf{u}| + k_m \dot{\mathbf{u}} \equiv \mathbf{X}(t, \gamma), \quad (25)$$

where \mathbf{u} is the incident particle velocity normal to the cylinder, and k_d and k_m are given in terms of the drag and mass coefficients. The total Morison force on a fixed vertical cylinder is obtained by an integration of Eq. (25) with respect to z over the interval $[-d, 0]$.

It should be noticed that even when the sea surface elevation is Gaussian, the non-linearity of the Morison formula yields a force $\mathbf{P}(t)$ which, in general, is a non-Gaussian process. The departure from the Gaussian distribution (at a given cross-section) depends on the coefficients k_d and k_m . The non-Gaussian character of the forces acting on offshore structures causes additional problems with their proper characterization. The spectral density, in this situation, provides only a partial characterization of the process. Higher order statistics should be estimated from the data. The local extremes of a random wave force $\mathbf{P}(t)$ were investigated by Grigoriu [45]. The application to the response analysis of tension-leg platform can be found e.g. in Spanos and Agarwal [46].

Description of Earthquake Excitation

An earthquake action, i.e. a complicated ground motion caused by tectonic phenomena, is a result of complex interaction of seismic waves propagating from the source through inhomogeneous layered media. Multiple scattering of waves at randomly distributed inhomogeneities makes the surface displacement fields highly unpredictable (cf. Sobczyk [47]).

Various stochastic models for a strong ground motion have been proposed. Modelling started from uncorrelated impulses (Housner G.W.) and white-noise representations (Bycroft G.N.) and has been developed to account for non-uniform spectra (Kanai K., Tajimi H.) as well as for the temporal non-stationarity of a random seismic action (Bolotin V.V., Amin M., Ang A.H.S.). These investigations lead to a commonly accepted model for (horizontal) ground acceleration having the form of

a non-stationary modulated stochastic process

$$\ddot{X}(t, \gamma) = A(t)X_1(t, \gamma), \quad (26)$$

where $A(t)$ is a deterministic envelope function imposed on stationary process $X_1(t, \gamma)$.

More general model has the form

$$\ddot{X}(t, \gamma) = \sum_k A_k(t)X_k(t, \gamma)I(t), \quad (27)$$

where $X_k(t, \gamma)$ are stationary random processes, $A_k(t)$ – deterministic functions (envelopes) and $I(t)$ is the Heaviside function.

One of the methods of obtaining a tractable model for the reliability predictions consists in treating the system transmitting the motion from the source to the ground surface, as a suitable filter characterized by a frequency transfer function. This transfer function characterizes approximately the averaged effects of wave propagation through the earth strata. The required frequency transfer function is approximated on the basis of the analytical theory of wave propagation and system identification techniques. A specific common formula for the spectral density of the ground displacement was identified in: Kanai [48], Ruiz and Penzien [49].

Recently, Suzuki and Minai [50] elaborated the model:

$$\ddot{X}(t, \gamma) = a_1(t)V(t, \gamma) + a_2(t)\zeta_2(t, \gamma), \quad (28)$$

where $V(t, \gamma)$ is the output of a time-dependent linear filter driven by Gaussian white noise $\zeta_1(t, \gamma)$; $\zeta_2(t, \gamma)$ is another white noise independent of $\zeta_1(t, \gamma)$.

There is also possible another way of characterizing the earthquake excitation acting on the structures. It consists in representation of the earthquake process as a series of random impulses. The original idea is attributed to Housner (1947), but the model which we have in mind has the general form

$$X(t, \gamma) = \sum_{k=1}^{N(t)} Z_k(\gamma)s(t, \tau_k), \quad (29)$$

where function $s(t, \tau_k)$ describes the shape of a pulse at random time instant τ_k , $Z_k(\gamma)$ is a random amplitude of the k -th pulse and $N(t)$ is a stochastic counting process characterizing the number of impulses in the interval $[t_0, t]$. Lin [24] indicated the conditions under which there may be valid reasons for modelling an earthquake excitation by uncorrelated or correlated random impulses. The response analysis of

many specific systems subjected to excitation in the form (29) has been performed by many authors (cf. book of Iwankiewicz [51] and references therein).

The processes of the form (29) can also be used for modelling vehicular traffic flow and the corresponding loading of highway bridges.

5. Characterization of Response: Effective Solution Methods

Existing Approaches

The most notable approaches used in engineering stochastic dynamics are as follows.

- Perturbation method.

If the nonlinearity in the system is weak, a small parameter $\varepsilon \ll 1$ is introduced into the governing equations, and the solution process $\mathbf{Y}(t)$ is looked for in the form of a series expansion with respect to this small parameter. Introducing this expansion into the equations of dynamics and equating terms of the same order in ε , we obtain a recurrent sequence of linear differential equations for the successive terms $\mathbf{Y}_0, \mathbf{Y}_1, \mathbf{Y}_2, \dots$ of the expansion. These equations, especially when the excitation is Gaussian, can serve to obtain two first statistical moments of the solution.

- Statistical linearization.

A nonlinear stochastic system is replaced by “equivalent” linear equations whose coefficients are determined from the condition of minimum of the difference between nonlinear and the “equivalent” linear part of the system equations (e.g. mean-square criterion); to evaluate the coefficients of the “equivalent” linear equations one has to assume a specific form of the probability distribution of the unknown solution. Most often the Gaussian approximation is used (for systems with Gaussian external excitation and very weak nonlinearity). The procedure has been used mostly to compute the second order statistical moments of the stationary response; cf. Spanos [52], Socha and Soong [53].

- Equivalent nonlinear systems.

A given nonlinear system (with random excitation) which is too complicated for effective quantitative analysis is replaced “equivalently” by another nonlinear system which is simpler to handle mathematically and computationally; e.g. by a nonlinear system

for which a stationary solution exists and its probability density is available (cf. Caughey [54], Cai and Lin [55]).

- Equations for moments and closure hypotheses.

From a given nonlinear stochastic system the equations for the statistical moments of the response are derived, which are differential for a nonstationary solution process and algebraic for a stationary solution. Because of nonlinearity of the original equations, these moment equations constitute an infinite hierarchy of equations, so the appropriate closure assumptions have been proposed and used to obtain a finite system of equations (these are various hypothetical relationships between higher- and lower-order moments); cf. Crandall [56], Wu and Lin [57], Sobczyk and Trębicki [58]. Once the equations were “closed” they can be solved and, therefore, give the approximate moments of the response.

- Stochastic averaging method.

This method is associated with the question: can the system with real random excitations be treated by the use of the Itô stochastic differential equations (without extension of the state space of an unknown process)? A positive answer to this question is due to Stratonovich and Khasminskii. Stratonovich [59] noticed that for a wide class of excitation processes $\mathbf{X}(t)$ acting on nonlinear systems, the stochastic effects become truly important for the time intervals of order $1/\varepsilon$ or $1/\varepsilon^2$. He also enunciated heuristically a theorem assuring that on time intervals of length of order $1/\varepsilon^2$, process $\mathbf{Y}^\varepsilon(t)$ approaches a Markov diffusion process. A rigorous mathematical formulation and proof of this theorem was provided by Khasminskii [60] along with explicit formulae for the drift vector and diffusion matrix of a limiting diffusion process. This theorem constitutes a ground for the efficient method known in stochastic dynamics as the stochastic averaging method; its numerous applications to practical problems can be found in the books cited above.

- Numerical schemes for stochastic differential systems.

In the last decades various numerical schemes for approximation of the solutions of stochastic differential and integral equations have been elaborated. Although they can be viewed as being an extension of the corresponding schemes of deterministic numerical analysis (e.g. stochastic Euler scheme, stochastic Runge-Kutta scheme, etc.), in the stochastic case one meets specific and complex problems. In contrast to the deterministic situation, in the

case of stochastic Itô equation different schemes can converge to different solutions for the same noise sample and initial conditions. In addition we can consider various types of approximation; the most common are: (i) mean-square approximation, (ii) pathwise (or, sample function) approximation, (iii) approximation of moments $\langle [f(Y_t)] \rangle$. Additional difficulties occur in multidimensional case; in this case the solution process can not be, in general, expressed as a continuous functional of the Wiener process alone; the detailed presentation can be found in the book by Kloeden and Platen [61], cf. also Chapter 5 of the book by Sobczyk [29].

- Numerical methods for the Fokker-Planck-Kolmogorov equation.

Since a wide class of physical engineering stochastic systems can be analysed via the diffusion Markov processes (generated by the Itô stochastic differential equations), the numerical solutions of the appropriate F-P-K equations are of a great interest. The F-P-K equation(12) associated with the basic stochastic model Eq. (8) is a partial differential equation of parabolic type and, as such, is – in principle – accessible to the existing numerical methods. However, one should keep in mind that the F-P-K equation for the transition probability density $p(\mathbf{y}, t | \mathbf{y}_0, t_0)$ is for practical problems an equation in multi-dimensional space with variable coefficients and with specific conditions associated with the probabilistic nature of unknown function (initial, boundary conditions and global normalization condition for the probability density). So, the applicability of the numerical methods (including FEM) is still limited to systems of lower dimensions, that is to the cases when unknown probability density depends on at most four spatial variables. Extension to higher dimensions, as concluded by the authors of paper by Spencer and Bergman [34] “... while posing no logical problems ... is beyond the capability of the current computer hardware”. An interested reader is referred to the book by Soize [32], and the paper of Spencer and Bergman [34].

An approach to approximate solving the Fokker-Planck-Kolmogorov equation which has attracted some interest has its roots in R. Feynman’s work on a space-time approach to quantum mechanics and is known as the path integration method; it consists in using the Chapman-Smoluchowski equation for discretized time variable (cf. Wehner and Wolfer [62], Naess and Johsen [63]). But, like in the previous techniques, its application to higher-dimensional systems seems to be difficult.

Each of the above approaches to quantitative characterization of the solution (or response) of stochastic systems has its own methodical draw-

backs and restrictions. As far as numerical methods are concerned, the computational efficiency (especially, for real multi-dimensional systems) is still not satisfactory. Undoubtedly, elaboration of the efficient computational methods for multidimensional stochastic systems constitutes today one of the greatest challenges within the stochastic dynamics research.

In what follows we will report briefly on the approach elaborated recently for evaluation of the probability distribution of the solution of stochastic equations and based on the moment equations and the informational entropy of the system.

Maximum Entropy Method for Stochastic Systems

The maximum entropy principle (MEP), originating in statistical physics, states that of all the probability distributions that satisfy the appropriate moment constraints (given information) one should choose the distribution having the largest informational Shannon entropy. Since the entropy characterizes a global uncertainty of a random quantity in question, the principle of maximum entropy means that maximum entropy distribution is maximally noncommittal with regard to missing information. The above idea has been widely used in statistics and in variety of other applications. In its classical formulation MEP deals with random variable with unknown probability density, the partial information about which is given by a finite number of moments. It has been tempting to try to adopt this principle to determining the unknown probability distribution of the solution of a stochastic system. The first attempt toward such a goal has been made by Sobczyk and Trębicki [64] where the general scheme of the method and some illustrative examples have been presented. In the papers by Sobczyk and Trębicki [65,66], Trębicki and Sobczyk [67], the idea has been extended to more complicated situations.

Let the system of interest be governed by the following stochastic Itô equation for the vector process $\mathbf{Y}(t) = [Y_1(t), \dots, Y_n(t)]$:

$$d\mathbf{Y}(t) = \mathbf{F}[\mathbf{Y}(t)]dt + \mathbf{G}[\mathbf{Y}(t)]d\mathbf{W}(t, \gamma), \quad (30)$$

where $\mathbf{W}(t, \gamma) = [W_1(t, \gamma), \dots, W_m(t, \gamma)]$ is the m -dimensional Wiener process. Under known conditions specified in Sec.2 the solution of Eq.(30) is a diffusion Markov process with the drift vector $\mathbf{A}(\mathbf{y})$ and diffusion matrix $\mathbf{B}(\mathbf{y})$ defined in Sec.2 (see Eq.(11)).

The equations for moments are derived easily by use of the Itô formula (or, Itô differentiation rule) to the function $h_{\mathbf{k}} = Y_1^{k_1}, \dots, Y_n^{k_n}$ of the solution and taking the average. The symbol \mathbf{k} denotes here the multi-index, i.e. $\mathbf{k} = (k_1, \dots, k_n)$; we will denote: $|\mathbf{k}| = k_1 + \dots + k_n$ and

$|\mathbf{k}| = 1, 2, \dots, K$. The moments of process $\mathbf{Y}(t)$ at time t are defined as usual by

$$m_k = \langle Y_1^{k_1} \dots Y_n^{k_n} \rangle_f = \langle h_k(\mathbf{Y}(t)) \rangle_f, \quad (31)$$

where $\langle \rangle_f$ denotes the mean value of the quantity indicated, i.e., $\langle \rangle_f$ is the integral of the product function $h_k(y) = y_1^{k_1} \dots y_n^{k_n}$ with respect to the true probability density $f(\mathbf{y}; t) = f(y_1, \dots, y_n; t)$ of the solution process. The general form of the moment equations is

$$\frac{dm_k(t)}{dt} = \sum_i \left\langle F_i \frac{\partial h_k}{\partial Y_i} \right\rangle_f + \frac{1}{2} \sum_l \sum_{i,j} \left\langle G_{il} G_{jl} \frac{\partial^2 h_k}{\partial Y_i \partial Y_j} \right\rangle_f. \quad (32)$$

The initial conditions $m_k(t_0)$ are specified from the given probability density $f(\mathbf{y}; t_0)$ of the initial condition $\mathbf{Y}_0(\gamma)$.

According to the spirit of the maximum entropy principle, the approximate probability density $p(\mathbf{y}; t)$ of the stochastic process $\mathbf{Y}(t)$ governed by the general system Eq. (30) is determined as a result of maximization of the information entropy functional

$$H[p] = - \int p(\mathbf{y}; t) \ln p(\mathbf{y}; t) d\mathbf{y} \quad (33)$$

under constraints Eq. (32) and the normalization condition

$$\int p(\mathbf{y}; t) d\mathbf{y} = 1. \quad (34)$$

The integration in Eqs. (33,34) is extended over the range of the possible values $\mathbf{Y}(t)$ for each t .

Let us notice that constraints Eqs. (32,34) in the maximum entropy scheme can be represented as

$$dm_k(t)/dt = \langle Q_k(\mathbf{y}) \rangle_p, \quad \int p(\mathbf{y}; t) - 1 = 0, \quad (35)$$

where

$$Q_k(\mathbf{y}) = \sum_i F_i \frac{\partial h_k(\mathbf{y})}{\partial y_i} + \frac{1}{2} \sum_l \sum_{i,j} G_{il} G_{jl} \frac{\partial^2 h_k(\mathbf{y})}{\partial y_i \partial y_j}. \quad (36)$$

It has been shown (cf. Trębicki and Sobczyk [67]) that the probability density which maximizes the entropy functional Eq. (33) under constraints Eq. (35) has the form

$$p(\mathbf{y}; t) = C(t) \exp \left\{ - \sum_{|\mathbf{k}|=1}^K \lambda_k(t) Q_k(\mathbf{y}) \right\}, \quad (37)$$

where $|\mathbf{k}| = k_1 + \dots + k_n = 1, 2, \dots, K < n$, $k_i = 0, 1, \dots, n$ and $C(t)$ is the normalizing factor equal to $e^{-\lambda_0(t)-1}$. Functions $\lambda_k(t)$ being the unknown Lagrange multipliers are determined by substituting density Eq. (37) into constraints Eq. (35). This means that all moments m_r , for $r > |\mathbf{k}|$ occurring in the set of moment Eq. (35), which is not closed, are calculated with the use of probability density Eq. (37); this is just the maximum entropy closure.

In the stationary case when the probability density of the solution process $\mathbf{Y}(t)$ does not depend on t , multipliers are constant, i.e., $\lambda_k(t) = \lambda_k$ and the moment equations are algebraic (cf. Sobczyk and Trębicki [65]). Hence, instead of Eq. (37) we have

$$p(\mathbf{y}) = C \exp \left\{ - \sum_{|\mathbf{k}|=1}^K \lambda_k Q_k(\mathbf{y}) \right\}. \quad (38)$$

In such a way the problem of determining a probability distribution of the solution of a general stochastic system is reduced to the solution of a system of deterministic equations (differential or algebraic) for the Lagrange multipliers; the approximate probability density itself is represented in analytical form. A reader interested in details of the method is referred to the papers cited at the beginning of this subsection.

Empirical Characterization of Random Response, Optimal Experiment Design, Remarks

Although the theoretical analysis dominates the research in stochastic dynamics, in many situations the empirical information acquired from measurements on randomly vibrating structures is necessary. In addition, the nature of the state (response) variables often does not allow much flexibility as to which states can be measured. The problem consists in estimation of the probabilistic characteristics of random fields (e.g. displacements, stresses of randomly vibrating beams, plates, shells) on the basis of a statistical sample obtained in a finite number of points. It is clear that the informational content of the data depends on the number of measurement points and their locations. The experiments should be designed optimally. In distributed parameter systems an important optimal experiment design variable is the spatial location of the measurement sensors.

In the paper by Papadimitriou, Haralampidis and Sobczyk [68] a general method was given for optimising the number and positions of sensors on randomly vibrating structures for the purpose of the response prediction at the unmeasured locations. The dynamics of the structure is governed by a linear partial differential equation subjected to space-time

random excitation with given mean and correlation function. The response characteristics, when obtained from the random vibration analysis, are used in the kriging method to obtain the response predictions (and the corresponding mean-square errors) at unmeasured locations. The optimal sensor locations are chosen to minimize the total averaged (over all prediction points) mean-square error of the response prediction in unmeasured points. The dependence of the optimal sensor locations on the type of response variable (displacement, strain), the characteristics of the random excitation and number of sensors have been determined and illustrated via numerical calculations. The interested reader will find the details of the analysis in the paper cited above, along with the appropriate references.

Information Dynamics, Remarks

Analysis of many problems of stochastic dynamics leads naturally to the concepts and tools of the information theory. This is not only due to the fact that the basic notions of mathematical information theory are based on the probability theory, but also because the apparatus of information theory is applicable to any probabilistic system of inference (in which we seek information).

When the language and tools of information theory (e.g. Shannon entropy, mutual information between random events and processes, information flow) are used in system dynamics, we come to the notion of information dynamics. The premises, challenges and results of this emerging field are presented in Sobczyk [69].

Effects of Spatial Randomness, Remarks

In the present lecture I have restricted my attention to dynamical systems in which randomness is time-dependent. The systems material parameters remain deterministic and constant. It is clear however that in reality, an engineering system can never fulfill strictly such ideal requirements; manufacturing processes of structural/mechanical components introduce some imperfections and inhomogeneity into the material structure. Therefore, in many situations there is a need for taking into account the spatial randomness of the system properties (e.g. random bending stiffness of beams, plates, etc., or span length in an N-span beam). This randomness, when characterized by random variables, is usually called a random disorder (cf. Lin and Cai [27] – Sec. 9).

In many situations one should assume that the material property randomly varies in space; this leads to the governing partial differential equations with spatial randomness in coefficients, and subsequently – to

random eigenvalue problems (cf. early papers by Shinozuka and Astill [70], Sobczyk [71]) and stochastic finite elements (Shinozuka and Deodatis [72], Ghanem and Spanos [73]). In a sense, the analysis of wave propagation in stochastic media belongs to this category (cf. the book by Sobczyk [47] and references therein) and it constitutes today a fairly advanced field.

6. Failures of Stochastic Dynamical Systems – Reliability Assessment

General Formulation

Next important step in stochastic analysis of dynamical engineering systems – strongly connected with the response characterization – is the evaluation of the *system performance* and its *reliability*.

The character of systems being a subject of stochastic dynamics (complexity of interaction between the system constituents and external excitation, material property degradation due to dynamics, etc.) requires much more sophisticated formulations and methods than the traditional safety assessment. Not only the probability concepts have to play a key role in the analysis but also (and above all) the fact that system performance changes in time. So, today there is a common agreement between the researchers that failures (of various modes) of dynamical systems should be defined as outcrossings or exits of the appropriate stochastic processes (or, random fields) out of an acceptable (safety) domain.

Let us assume that the system states in each time instant are characterized by a random response process $\mathbf{Y}(t, \gamma)$, i.e. for each $t \in [t_0, \infty]$ – by a random vector \mathbf{Y} belonging to the state space of the system. In order to describe the system performance and its reliability it is convenient to define quality states of the system and the quality space. A quality is characterized by a vector $\hat{\mathbf{Y}}$. For each state \mathbf{y}_t in the state space there exists a corresponding quality state $\hat{\mathbf{y}}_t$ in the quality space.

A set of system states and consequently, a set of corresponding quality parameters admissible from the point of view of quality (or reliability) requirements defines in the quality space a set D_r which can be interpreted as a safety or reliability domain. A boundary of D_r corresponds to the limit (or critical) states.

Reliability function $R(t)$ of a system under consideration is defined as the probability of its admissible performance during the time interval $[0, t]$, i.e.

$$R(t) = P\{\hat{\mathbf{Y}}(\tau) \in D_r; \quad \tau \in [0, t]\}. \quad (39)$$

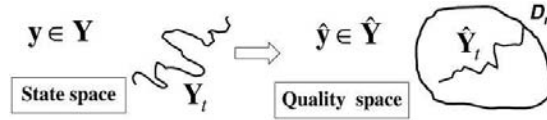


Figure 4. Illustration of the system reliability problem.

The complement of $R(t)$ to unity defines the *probability of failure*,

$$P_f(t) = 1 - R(t) \quad (40)$$

i.e. the probability that at least one outcrossing of set D_r by process $\hat{\mathbf{Y}}(t)$, in the direction normal to the boundary of D_r , will occur within the time interval $[0, t]$.

The time of satisfactory system performance T_{D_r} (i.e. the time duration within which $\hat{\mathbf{Y}}_t \in D_r$, is called a *life-time*; it is a random variable. Reliability is related to T_{D_r} by the formula

$$R(t) = P\{T_{D_r} > t\}. \quad (41)$$

Analysis of the reliability problems depends crucially on the specific failure mechanisms. Engineering systems (e.g. machines, structures, etc.) subjected to random dynamic load may fail due to various failure modes that can occur during the designed lifetime. They depend on the material properties, system characteristics and excitations. The basic failure modes are:

- (1) the motion of a system becomes *unstable*,
- (2) the system response (or, the appropriate function of it) at a critical location exceeds, *for the first time*, the prescribed safety boundary,
- (3) the *accumulated damage* (due to $\mathbf{Y}(t)$ – fluctuations) *exceeds the fixed critical limit* (e.g. fatigue failures).

It is clear that evaluation of the reliability function $R(t)$ is a basic problem in the reliability assessment of stochastic dynamical systems. Solving such a problem in practical situations (i.e. obtaining exact values of the probability Eq. (39)) meets serious difficulties. So, various approximations and bounds on reliability and failure probability have been proposed (e.g. cf. Bolotin [74], Lin and Cai [27] – Chapter 8). In general, the boundary of safety domain D_r can be random. Therefore, the problem consists in evaluation of the probability of passing of the process $\hat{\mathbf{Y}}(t)$ outside the safety domain D_r with random boundary; this introduces additional difficulties.

Stochastic Stability/Instability

As far as stability or instability is concerned, it has always been of a great concern in the analysis of dynamical systems. In the stochastic case, when the system response is generally an n -dimensional stochastic vector process \mathbf{Y} – measured from a referenced solution (regarded as the trivial solution) – stability is defined in terms of boundedness and convergence (for $t \rightarrow \infty$) of the norm $\|\mathbf{Y}(t)\|$. But, these properties can be characterized in different probabilistic meanings. So, various stochastic stability notions have been introduced and a variety of stochastic stability criteria obtained. Nowadays the existing literature concerning stability of stochastic dynamical systems is very extensive; it is concerned both with a beautiful mathematical analysis and with specific applications. The essential advances are concerned with elaboration of the stochastic Lapunov function method and with the analysis of the asymptotic behaviour (when $t \rightarrow \infty$) of stochastic systems, including stability, by using the Lapunov exponents; cf. for example: Khasminskii [75], Arnold and Wihstutz [76], Ariaratnam and Xie [77], Wedig [78], Bucher and Lin [79], Tylikowski [80,81].

It is worth noticing that the system stability/instability can be characterized via the basic formula (39). Indeed, the system stability can be defined in terms of probability that the response process \mathbf{Y} does not leave a spherical domain, say D_{st} of radius $\varepsilon > 0$ centered at the equilibrium point \mathbf{y}_0 , where D_{st} is a set of points \mathbf{y} such that $\|\mathbf{y} - \mathbf{y}_0\| < \varepsilon$.

First-excursion Failures: Stochastic Diffusion Markov Systems

As we have already stated in Section 7, the transition probability density $p(\mathbf{y}, t; \mathbf{y}^0, t_0)$ of the solution process of Itô stochastic dynamical system (let us assume here that its drift and diffusion coefficients do not depend explicitly on time) satisfies the Fokker-Planck-Kolmogorov Eq. (12) with respect to \mathbf{y} and t . It turns out that $p(\mathbf{y}, t; \mathbf{y}^0, t_0)$ satisfies also – with respect to the “backward” variables \mathbf{y}^0, t_0 – the backward Kolmogorov equation. Using this equation it can be shown that the reliability function $R(t|\mathbf{y}^0, t_0)$ satisfies the equation

$$\frac{\partial}{\partial t_0} R + \sum_{i=1}^n m_i(\mathbf{y}_0) \frac{\partial R}{\partial y_i^0} + \frac{1}{2} \sum_{i,j=1}^n b_{ij}(\mathbf{y}_0) \frac{\partial^2 R}{\partial y_i^0 \partial y_j^0} = 0. \quad (42)$$

This equation is supplemented by the appropriate initial and boundary conditions.

Equation (42) along with the imposed conditions constitutes a general mathematical basis for characterization of the reliability of a wide class of stochastic dynamical systems. As one could expect, however, closed form solutions are known only for simple cases (cf. the book by Lin and Cai [27]).

To make the reliability problem more tractable, instead of evaluation of the (conditional) reliability function we restrict ourselves to the calculation of statistical moments of the probability distribution of the (first) passage time T_D of the response process $\mathbf{Y}(t)$ across the boundary of the safety domain D_r . For example, the mean value of the first passage time satisfies the equation (known as the Pontryagin equation)

$$\frac{1}{2}b(y_0)\frac{d^2\langle dT \rangle}{dy_0^2} + m(y_0)\frac{d\langle T \rangle}{dy_0} = -1. \quad (43)$$

The boundary conditions for this equation at the ends of the safety interval considered, say $[\alpha, \beta]$ are: $\langle T \rangle = 0$ for $y_0 = \alpha$, $y_0 = \beta$, since the first passage time is zero when $Y(t)$ starts on the boundary of the safety set.

The moments of the first passage time have been evaluated for various practical situations. In general, the Galerkin finite element method can be used (cf. Spencer [82]). However, numerical difficulties are usually encountered when we are dealing with higher-dimensional random response processes.

Cumulative Failures: Fatigue in Randomly Vibrating Systems

An important deterioration or failure mechanism in structural and mechanical components subjected to time-dependent (deterministic or stochastic) loading is fatigue. According to fracture mechanics, the fatigue is due to nucleation and growth of cracks. In engineering, a measurable characteristic of fatigue is usually the size of a dominant crack, and ultimate failure occurs when this crack reaches the critical size. To capture the basic features of random fatigue crack growth, various stochastic models have been proposed in the literature (cf. Sobczyk and Spencer [43] and references therein). A model which takes into account the empirical information and randomness inherent in the fatigue crack growth consists in randomization of the empirical crack growth equation (e.g. Paris-Erdogan equation) by introducing to the equation an appropriate stochastic process $X(t, \gamma)$. The resulting equation has the general form

$$\frac{dA(t)}{dt} = F[A(t), \Delta S, \text{constants}]X(t, \gamma), \quad (44)$$

where $A(t)$ is the crack size at time t , ΔS characterizes the stress range, and F is the empirical (nonlinear) function of the indicated variables. Assuming that $X(t, \gamma) = m_x + \sqrt{2D}\xi(t, \gamma)$ and using the empirical Paris equation, the following probability density of fatigue life-time T_F was derived in Sobczyk [83]

$$f_{T_F}(t) = \frac{\alpha}{\sqrt{2\pi}t^{3/2}} \exp\left[-\frac{1}{2} \frac{(\alpha - \beta t)^2}{t}\right], \quad (45)$$

which is the inverse Gaussian distribution (α, β are constant parameters including Paris constants, A_0, m_x, D and ΔS). Such distribution has been earlier hypothesized as a possible lifetime model.

The inverse Gaussian distribution for a fatigue life-time has also been derived by Ditlevsen [84] by an alternate approach based on an incremental version of Paris-Erdogan equation. Other approaches to the characterization of the fatigue life-time can be found in some recent publications (cf. Doliński and Colombi [85]).

7. Qualitative Phenomena: Noise – Induced Effects. Examples

Introductory Remarks

In the previous four sections I focused my attention on the quantitative aspects of stochastic dynamics, which are of interest in applied (engineering) problems. One could therefore get an impression that stochastic dynamics is primarily concerned with numerical effects of random noises and it does not deal with the phenomena which might be generated in the system solely by random excitations and which have a power to change the system dynamics qualitatively. Such a view would not be correct. The questions which naturally come to mind are, for example:

- (i) Does a random excitation (acting on the system) have any influence on the most essential, internal features of a system dynamics?
- (ii) Is a random noise just an annoying factor we have to live with or is there any interesting physics induced that is not present when the random fluctuations are absent?

All macroscopic systems of interest in physics, biology, engineering, chemistry, etc. are subjected to irregular perturbations, internal and external, which – when combined with nonlinearity – can display a rich variety of specific “noise-induced” phenomena and effects. For example, stochastic instability, bifurcations, the also called – noise-induced transitions of the equilibrium states of the system, etc. It has to be kept in

mind that in the presence of random (internal/external) excitations the state of the system is no longer characterized by a simple number (or vector) but by a probability distribution.

In order to shed some light on the phenomena and effects which random excitations may generate in the dynamical system we will discuss a few “simple” examples.

Stabilization and Destabilization by Random Noise

Since some time it has been observed by engineers (first, in radioelectronic systems) that noise can affect a system in two opposite ways. It can destabilize a system as well as stabilize it (cf. the survey article of Roberts and Spanos [86] and the paper by Bucher and Lin [79]). As it is well known, a linear oscillatory system (cf. Arnold [87] et al.)

$$\ddot{Y}(t) + 2\beta\dot{Y}(t) + Y(t) = 0 \quad (46)$$

is stable for $\beta > 0$. Let us perturb the constant stiffness term by a random noise $\xi(t)$, where $\xi(t)$ is a stationary random process with a given spectral density $g(\omega)$ and with intensity $\sigma > 0$. So, we have the damped linear oscillator with random restoring force

$$\ddot{Y}(t) + 2\beta\dot{Y}(t) + [1 + \sigma\xi(t)]Y(t) = 0. \quad (47)$$

The Lapunov exponent $\lambda = \lambda(\beta, \sigma)$, a counterpart of the real parts of the eigenvalues, is the indicator of stability ($\lambda < 0$) or instability ($\lambda > 0$). For *small noise* ($\sigma \rightarrow 0$) and underdamped case ($\beta^2 < 1$):

$$\lambda = -\beta + \frac{\pi g(2\sqrt{1-\beta^2})}{4(1-\beta^2)}\sigma^2 + O(\sigma^3). \quad (48)$$

For overdamped case ($\beta^2 > 1$):

$$\lambda = -\beta + \sqrt{\beta^2 - 1} - 4[(\beta^2 - 1)]^{-1} \int_0^\infty e^{-2\tau\sqrt{\beta^2-1}} K(\tau) d\tau. \quad (49)$$

Therefore, in the underdamped case, a small noise *destabilizes* the motion since a positive term is added to $\lambda = -\beta$. However, in the overdamped case, a small noise stabilizes the motion since a positive term is subtracted from the value $\lambda = -\beta + (\beta^2 - 1)^{1/2}$. For a more general analysis of the stabilization by noise cf. Arnold [88] and the references therein, and the book by Khasminskii [75].

Noise-Induced Bifurcations

Stochastic bifurcation analysis deals with the qualitative changes in parameterised families of stochastic systems

$$\dot{\mathbf{Y}}(t) = \mathbf{F}[\mathbf{Y}(t), \mathbf{X}(t), \lambda], \quad (50)$$

where λ is a parameter.

It seems that the bifurcation problems for stochastic equations were first studied by physicists (cf. Horsthemke and Lefever [89] and references therein). In these studies the qualitative change of stationary solutions of the Fokker-Planck-Kolmogorov equation is used as an indicator of bifurcation. More explicitly, the extremes of the stationary density $p_{st}(y; \lambda)$ are regarded as indicators of qualitative changes in the system dynamics; these changes are called the phase transitions. The number and positions of the extrema of p_{st} in the stochastic case and the extrema of the potential (of the system considered) in the deterministic case are the characteristic features of the steady-state behaviour of the system.

Let us write down the deterministic system corresponding to Eq. (50) in the form (for $n = 1$)

$$\dot{Y}(t) = F_\lambda(Y(t)). \quad (51)$$

It is convenient to represent this equation as

$$\dot{Y}(t) = -\frac{d}{dY}V_\lambda(Y), \quad V_\lambda(Y) = -\int_0^Y F_\lambda(z)dz, \quad (52)$$

where $V_\lambda(y)$ is called the *potential* of Eq. (50). The stable steady states of the system Eq. (51) correspond to the minima of $V_\lambda(y)$ and the unstable steady states to the maxima.

The maxima of $p_{st}(y)$ are the states in whose neighbourhood the system spends relatively much time, and they are most likely to be observed in an experiment; the minima of $p_{st}(y)$ correspond to the valleys of a potential (stable steady states). The minima of $p_{st}(y)$ are the states that the system leaves rather quickly (the unstable steady states). Depending on the value of the bifurcation parameter λ , density $p_{st}(y)$ may exhibit one-peak to two-peak or crater-like density.

The analysis of the extrema of stationary probability density in multi-dimensional cases is, of course, much more involved. The analysis of a nonlinear Duffing-Van der Pol oscillators along this line was presented by Wiesenfeld and Knobloch [90].

Let us take the deterministic Duffing-Van der Pol oscillator

$$\ddot{Y} = \alpha Y(t) + \beta \dot{Y}(t) - Y^3(t) - Y^2(t)\dot{Y}(t), \quad \alpha, \beta \in R^1. \quad (53)$$

For this system in a deterministic case, trajectories do not explode in finite time, and there exists a (parameter-dependent) attracting compact set. When β is fixed and is less than zero, whereas α varies, the pitchfork bifurcation occurs for $\alpha = 0$. When $\alpha < 0$ is fixed and β varies, the Hopf bifurcation can be observed at $\beta = 0$ (cf. the bifurcation diagrams in Schenk-Hoppé [91]). Let the noisy version of Eq. (53) have the form

$$\ddot{Y}(t) = [\alpha + \sigma\xi(t)]Y(t) + \beta\dot{Y}(t) - Y^3(t) - Y^2(t)\dot{Y}(t). \quad (54)$$

The analysis of a stationary F-P-K equation corresponding to Eq. (54) shows that for β sufficiently negative, the Dirac delta shape of probability density is the only possible. Increasing β , we observe the birth of a bell-shaped density and when β increases further (crossing $\beta = 0$) this density undergoes a “P-bifurcation” (at $\beta = \beta_p$) and it becomes crater-like.

The above effects of noise on “P-bifurcation” are inferred from the stationary probability density $p_{st}(y)$ which characterizes a system for long times and therefore it does not carry information on the transient states. However, recently a serious effort has also been made to understand the bifurcations of stochastic systems on the dynamic level. Extensive simulations of stochastic dynamic systems, their random attractors and invariant measures provided interesting results. For example, it has been found (cf. Arnold et al. [92]) that random noise splits deterministic multiple eigenvalues. For $\beta^2 < -4\alpha$ (where α is fixed and negative) and $\sigma = 0$, the deterministic linear system has two complex-conjugate eigenvalues $0.5\beta \pm i\omega_d$ what amounts to just one Lapunov exponent $\lambda_1(\beta) = \beta/2$ with multiplicity 2; for $\sigma \neq 0$, however, a linearized system has two different simple Lapunov exponents.

Chaotic Dynamics Subjected to Random Noise

An important inner property of deterministic nonlinear systems is *chaos*. It causes unpredictability of the long-term behaviour of the system. As one may expect, there has to exist the influence of external random noise on various characteristics of a chaotic dynamics. The effects of noise on chaos, and – more generally – the interplay between chaos and externally introduced randomness has been a topic of research in nonlinear dynamics and statistical physics (cf. Grasman and Roerdink [93], Kapitaniak [94], Ying Cheng Lai [95] et al.).

Among various reported results are the following:

- in the common route to chaos (the period-doubling bifurcations) the random noise tends to smooth out the transition and induces chaos in the parameter regime where there is no chaos otherwise,

- some authors found (cf. Grasman and Roedrik [93]) that noise may regularize chaotic dynamics causing a decrease of the Lapunov exponent λ (“noise-induced order”),
- for multidimensional systems (in chaotic regime) represented in the form of a system of first-order differential equations, different Lapunov exponents λ_i , ($i = 1, 2, \dots, n$) may react differently to the changes of the noise intensity. To obtain a measure of the averaged effect of noise, some authors compute a “global” exponent defined as

$$\lambda_g = m + \sum_{i=1}^m \frac{\lambda_i}{|\lambda_{m+1}|}, \quad (55)$$

where $\lambda_1 \geq \lambda_2 \geq \dots$ and m is the largest integer such that

$$\lambda_1 + \dots + \lambda_m > 0.$$

For the Van der Pol oscillator (represented by a system of three differential equations of the first order) λ_g decreases as the noise intensity σ increases. Although the maximum exponent λ_1 slightly increases with σ , the system is “regularized” by noise in a global sense.

Stochastic Resonance. Remarks

Another phenomenon which makes stochastic dynamics fascinating is *stochastic resonance*. It occurs as a result of interplay of nonlinearity, periodicity and randomness. Intuition suggests that when noise is added to a signal prior to or during transmission through a system/communication channel, the received signal will be more corrupted (deteriorated) than if the uncorrupted signal had been transmitted. The amount of corruption is usually characterized by the so-called *signal – to noise ratio* (SNR) of the output. For linear systems, the output SNR decreases monotonically with increasing noise intensity. The peculiarity of stochastic resonance lies in the fact that (for a large class of nonlinear systems) there occurs an increase in the SNR up to a maximum, with added random noise. This phenomenon has attracted much attention in the recent years. Besides numerous theoretical studies also numerical simulations and experimental work are today in the progress (cf. Benzi et al. [96], McNamara and Wiesenfeld [97], and references therein).

Korteweg de Vries Solitons in Randomly Varying Medium. Remarks

Phenomenon which occurs in spatially extended material media (fluids, solids) and results due to the interplay between nonlinearity and dispersion of the medium is known as solitary waves or solitons. One of the best known equations describing solitons is the Korteweg de Vries equation

$$\frac{\partial u}{\partial s} + u \frac{\partial u}{\partial \xi} + \frac{\partial^3 u}{\partial \xi^3} = 0, \quad (56)$$

where $u = u(s, \xi)$ characterizes the medium disturbance as a function of time and one-dimensional spatial coordinate. A characteristic feature of this equation is the existence of the so-called stationary waves (solitons) which do not change their form during propagation (usually, nonlinearity distorts the wave profile). For example, waves in shallow water, ion-acoustic waves in plasma are governed by the above equation. If, however, the medium is perturbed by a random inhomogeneity (e.g. random roughness of the bottom of the water channel, random impurity of plasma density), the *KdV* solitary waves are attenuated and the amount of attenuation depends on the magnitude of randomness of the medium (cf. Sobczyk [99] and references therein).

8. Closing

Stochastic dynamics is still at the stage of its development. Nowadays, the methodology presented in this lecture extends its models and methods to new fields of human endeavours. For example, a great intellectual effort is concentrated today on stochastic dynamics of economic (and financial) systems as well as on the atmospheric processes (weather and climate forecasting). Are there any other, fundamental, expectations concerning probabilistic / stochastic methods in science (and ... in everyday life)?

David Munford, the past president of the International Mathematical Union, in his article "The dawning of the age of stochasticity", published in the distinguished volume [100] writes: "My overall conclusion is that I believe stochastic methods will transform pure and applied mathematics in the beginning of the third millennium. Probability and statistics will come to be viewed as the natural tools to use in mathematical and scientific modelling".

Acknowledgments

I wish to express my sincere thanks to the Congress Committee of IUTAM for selecting stochastic dynamics for a very prestigious, plenary presentation at the XXI-st IUTAM Congress. I was very pleased and honoured to deliver this exceptional lecture.

Also I owe a great debt of gratitude to many colleagues of my Institute who have contributed, by their friendly advices, to the clarity of my lecture. In particular, I wish to express my appreciation to dr. Jerzy Trębicki for his painstaking work on the visualization of my presentation, as well as – for bringing the typescript to its final form.

References

- [1] J.W. Gibbs, *Elementary Principles in Statistical Mechanics*, Yale University Press, 1903.
- [2] S.G. Brush, A history of random processes. I. Brownian motion from Brown to Perrin, *Arch. Hist. Exact Sci.*, Vol.5, 1-36, 1968.
- [3] A. Einstein, Über die von der molekulärtheoretischen Theorie der Wärme geforderte Bewegung von den in ruhenden Flüssigkeiten suspendierten Teilchen, *Ann. der Phys.*, Vol.17, 549-560, 1905.
- [4] A. Einstein, Zur Theorie der Brownschen Bewegung, *Ann. der Phys.*, Vol.19, 371-381, 1906.
- [5] M. Smoluchowski, Zarys kinetycznej teorii ruchów Browna i roztworów mętnych (in Polish) (Outline of the kinetic theory of Brownian motion and dull solutions), *Rozpr. Wydz. Mat. - Przyr. Akademii Umiejętności w Krakowie*, XLVI, Ser. A, 257-281, 1906.
- [6] M. Smoluchowski, Zur kinetischen Theorie der Brownschen Molekularbewegung und der Suspensionen, *Ann. der Phys.*, Vol.21, 756-780, 1906.
- [7] J. Perrin, *Brownian Movement and Molecular Reality* (F. Soddy – transl.), Taylor and Francis, London, 1910.
- [8] A. Pais, *The Science and the Life of Albert Einstein*, Oxford Univ. Press, Oxford, N. York, 1982.
- [9] B. Średniawa, Marian Smoluchowski's collaboration with experimentalists in the investigations of Brownian motion and density fluctuations, *Rep. of the Inst. of Physics* (Dept. of Theor. Physics) of the Jagiellonian University – Cracow, March 1991.
- [10] P. Langevin, On theory of Brownian motion (in French), *Comptes Rendus Acad. Sci.*, Paris, Vol.146, 530, 1908.
- [11] R.B. Lindsay, *Introduction to Physical Statistics*, Dover Publ., Inc., N. York, 1968.
- [12] R.C. Booton, Nonlinear control systems with random inputs, *Trans. IRE*, CT-1, 1954.
- [13] I.E. Kazakov, Approximate method for statistical analysis of nonlinear systems (in Russian), *Rep. of Zhukowski Institute*, N° 394, 1954.

- [14] S.T. Ariaratnam, Random vibrations of nonlinear suspensions, *J. Mech. Eng. Sci.*, Vol.2, 195-201, 1960.
- [15] V.V. Bolotin, Statistical theory of seismic resistance of structures (in Russian), *Izv. Acad. Nauk SSSR, Mekhanika I Mashinostroyeniye*, N° 4, 123-129, 1959.
- [16] T.K. Caughey, Response of nonlinear string to random loading, *J. Appl. Mech.*, Vol.26, 341-348, 1959.
- [17] S. H. Crandall (Ed.), Random Vibration, Vol.I, *Technology Press*, Cambridge, Mass, 1958.
- [18] F. Kozin, On the probability densities of the output of some random systems, *J. Appl. Mech.*, Vol.28, 161-164, 1961.
- [19] Y. K. Lin, Nonstationary response of continuous structures to random loading, *J. Acoust. Soc. Amer.*, Vol.35, 222-227, 1963.
- [20] R. H. Lyon, Response of strings to random noise fields, *J. Acoust. Soc. Amer.*, Vol.28, 391-398, 1956.
- [21] M. Shinozuka, Probability of structural failure under random loading, *J. Eng. Mech. Div.*, Amer. Soc. Civil Engrs., Vol.90, (EM 5), 147-170, 1964.
- [22] V.V. Bolotin, Statistical Methods in Structural Mechanics (in Russian: Moscow 1961; English transl., Holden-Day, San Francisco, 1965).
- [23] S.H. Crandall, W. D. Mark, Random Vibration of Mechanical Systems, *Academic Press*, N. York, 1963.
- [24] Y.K. Lin, Probabilistic Theory of Structural Dynamics, *Mc Graw Hill*, N. York, 1967.
- [25] J.D. Robson, An Introduction to Random Vibrations, *Elsevier*, Amsterdam, 1964.
- [26] V.V. Bolotin, Random Vibrations of Elastic Systems (in Russian), *Izd. Nauka*, Moscow, 1979; English language translation: *Martinus Nijhoff Publ.*, Hague, 1984.
- [27] Y.K. Lin, G. Q. Cai, Probabilistic Structural Dynamics: Advanced Theory and Applications, *Mc Graw Hill*, N. York, 1995.
- [28] J.B. Roberts, P.T.D. Spanos, Random Vibration and Statistical Linearization, Chichester, *Wiley*, 1990
- [29] K. Sobczyk, Stochastic Differential Equations with Applications to Physics and Engineering, *Kluwer Acad. Publ.*, Dordrecht, 1991.
- [30] T.T. Soong, M. Grigoriu, Random Vibration of Mechanical and Structural Systems, *Prentice Hall, Englewood Cliffs*, New Jersey, 1993.
- [31] L. Arnold, Stochastic Differential Equations: Theory and Applications, *Wiley*, N. York, 1974.
- [32] C. Soize, The Fokker-Planck equation for stochastic dynamic systems and its explicit steady state solutions, *World Scientific*, Singapore, 1994.
- [33] H. P. Langtangen, A general numerical solution method for Fokker-Planck equations with application to structural reliability, *Probab. Eng. Mech.*, Vol.6, 1, 33-48, 1991.
- [34] B.D. Spencer, L. A. Bergman, On the numerical solutions of Fokker-Planck equation for nonlinear stochastic systems, *Nonlinear Dynamics*, Vol.4, 357-372, 1993.

- [35] W. Schiehlen, Probabilistic analysis of vehicle vibrations, *Probab. Eng. Mech.*, Vol.1, 2, 99-104, 1986.
- [36] F. Casciati, Stochastic dynamics of hysteretic systems, *Structural Safety*, Vol.6, 2-4, 1987.
- [37] H. Irschik, F. Ziegler, Nonstationary random vibrations of yielding frames, *Nucl. Eng. Design*, Vol.90, 357-364, 1985.
- [38] Y.K. Wen, Methods of random vibration for inelastic structures, *Appl. Mech. Rev.*, Vol.42, 2, 39-52, 1989.
- [39] Y.K. Wen, Stochastic response and damage analysis of inelastic structures, *Probab. Eng. Mech.*, Vol.1, 49-57, 1986.
- [40] R.I. Grossmayer, Elastic-plastic oscillators under random excitations, *J. Sound and Vibrations*, Vol.65, 3, 353-379, 1979.
- [41] K. Sobczyk, J. Trębicki, Modelling of random fatigue by cumulative jump processes, *Eng. Fracture Mechanics*, Vol.34, 477-493, 1989.
- [42] K. Sobczyk, J. Trębicki, Stochastic dynamics with stiffness degradation, *Probab. Eng. Mech.*, 15, 91-99, 2000.
- [43] K. Sobczyk, B. D. Spencer, Random Fatigue: From Data to Theory, *Academic Press*, Boston, 1992.
- [44] H. O. Madsen, S. Krenk, N. C. Lind, Methods of Structural Safety, *Prentice-Hall*, N. Jersey, 1986.
- [45] M. Grigoriu, Extremes of wave forces, *J. Eng. Mech.*, ASCE, Vol.110, EM12, 1731-1742, 1984.
- [46] P.T.D. Spanos, V.K. Agarwal, Response of a simple tension-leg platform model to wave forces, *J. Energy Res. Techn.*, Vol.103, 243-249, 1981.
- [47] K. Sobczyk, Stochastic Wave Propagation, *Elsevier*, Amsterdam, 1985.
- [48] K. Kanai, Some empirical formulas for the seismic characteristics of the ground, *Bull. Earthquake Res. Institute*, Univ. Tokyo, Vol.35, 309-325, 1957.
- [49] P. Ruiz, J. Penzien, Stochastic seismic response of structures, *J. Eng. Mech. Div.*, ASCE, 441-456, April 1971.
- [50] Y. Suzuki, R. Minai, Application of stochastic differential equations to seismic reliability analysis of hysteretic structures, *Probabilistic Eng. Mech.*, Vol.3, 1, 1988.
- [51] R. Iwankiewicz, Dynamical Mechanical Systems under Random Impulses, *World Scientific, Ser. on Advances in Math. and Appl. Sci. (36)*, World Scientific, Singapore, 1995.
- [52] P.T.D. Spanos, Statistical linearization in structural dynamics, *Appl. Mech. Rev.*, Vol.34, 1, 1-8, 1981.
- [53] L. Socha, T.T. Soong, Linearization in analysis of nonlinear stochastic systems, *Appl. Mech. Rev.*, Vol.44, 10, 399-422, 1991.
- [54] T.K. Caughey, On the response of non-linear oscillators to stochastic excitation, *Probab. Eng. Mech.*, Vol.1, 2-4, 1986.
- [55] G.Q. Cai, Y. K. Lin, A new approximate solution technique for randomly excited nonlinear oscillators, *Intern. J. of Nonlinear Mech.*, Vol.23, 409-420, 1988.

- [56] S.H. Crandall, Non-Gaussian Closure for random vibration of nonlinear oscillators, *Int. J. Nonlinear Mech.*, Vol.15, 303-313, 1980.
- [57] W.F. Wu, Y.K. Lin, Cumulant-neglect closure for nonlinear oscillators under parametric and external excitations, *Int. J. Nonlinear Mech.*, Vol.19, 349-362, 1984.
- [58] K. Sobczyk, J. Trębicki, Maximum entropy closure for nonlinear stochastic systems, in: *Vibration of Nonlinear, Random, and Time-Varying Systems, Proc. of 1995 Design Eng. Conf.*, DE-Vol.84-1, ASME, 1995.
- [59] R.L. Stratonovich, *Topics in the Theory of Random Noise, Gordon and Breach*, N. York, 1963 (translation from Russian).
- [60] R.Z. Khasminskii, A limit theorem for the solution of differential equations with random right-hand side (in Russian), *Teorija Veroyatn. Prim.*, Vol.11, 3, 1966.
- [61] P.E. Kloeden, E. Platen, *The Numerical Solutions of Stochastic Differential Equations, Springer*, Berlin, 1992.
- [62] M.F. Wehner, W. G. Wolfer, Numerical evaluation of path integral solutions to F-P-K equations, *Phys. Rev.* Vol.A27, 2663-70, 1983.
- [63] A. Naess, J. M. Johsen, Response statistics of nonlinear, compliant offshore structures by the path integral solution method, *Probab. Eng. Mech.*, Vol.8, 91-106, 1993.
- [64] K. Sobczyk, J. Trębicki, Maximum entropy principle in stochastic dynamics, *Probab. Eng. Mech.*, Vol.5, 3, 102-110, 1990.
- [65] K. Sobczyk, J. Trębicki, Maximum entropy principle and nonlinear stochastic oscillators, *Physica A*, Vol.193, 448-468, 1993.
- [66] K. Sobczyk, J. Trębicki, Approximate probability distributions for stochastic systems: maximum entropy method, *Comput. Methods Appl. Mech. Eng.*, Vol.168, 91-111, 1999.
- [67] J. Trębicki, K. Sobczyk, Maximum entropy principle and nonstationary distributions of stochastic systems, *Probab. Eng. Mech.*, Vol.11 (3), 169-178, 1996.
- [68] C. Papadimitriou, Y. Haralampidis, K. Sobczyk, Optimal experiment design in stochastic structural dynamics, *Probab. Eng. Mech.*, 2004.
- [69] K. Sobczyk, Information dynamics: Premises, challenges and results, *Mech. Systems and Signal Processing*, Vol.15(3), 475-498, 2001.
- [70] M. Shinozuka, C. J. Astill, Random eigenvalue problems in structural analysis, *AIAA Journal*, Vol.10, 4, 456-462, 1972.
- [71] K. Sobczyk, Free vibrations of elastic plate with random properties – the eigenvalue problem, *J. Sound and Vibration*, Vol.21, 4, 1972.
- [72] M. Shinozuka, G. Deodatis, Response variability of stochastic finite element systems, *ASCE Jour. Eng. Mech.*, Vol.114, 39, 499-519, 1988.
- [73] R.G. Ghanem, P. D. Spanos, *Stochastic Finite Elements: A Spectral Approach, Springer*, Berlin, 1991.
- [74] V.V. Bolotin, *Prediction of Service Life of Machines and Structures* (in Russian: *Mashinostroienje, Moskov*, 1984; English edition: *ASME Press*, N. York, 1989).

- [75] R.Z. Khasminskii, Stability of Differential Equations with Random Perturbation of Parameters (in Russian) *Nauka, Moskov*, 1969; English transl. Stochastic Stability of Differential Equations, *Sijthoff and Noordhoff*, Alphen, 1980.
- [76] L. Arnold, V. Wihstutz, Lapunov exponents: a survey, in: L. Arnold, V. Wihstutz (Eds.): Lapunov exponents, *Lecture Notes in Math. 1186*, Springer, 1-26, Berlin, 1986.
- [77] S.T. Ariaratnam, W.C. Xie, Lapunov exponents and stochastic stability of coupled linear systems under real noise excitation, *ASME J. Appl. Mech.*, Vol.59, 3, 664-673, 1992.
- [78] W. Wedig, Stability of nonlinear stochastic systems, in: C. Dafermos, G. Ladas, G. Papanicolau (Eds.) *Lecture Notes in Pure and Appl. Math.*, Dekker, N. York, 1988.
- [79] C.G. Bucher, Y. K. Lin, Effect of spanwise correlation of turbulence field on the stability of long-span bridges, *J. of Fluids and Structures*, Vol.2, 437-451, 1988.
- [80] A. Tylikowski, Dynamic stability of nonlinear antisymmetrically laminated cross-ply rectangular plates, *J. Appl. Mech., ASME*, Vol.56, 375-381, 1989.
- [81] A. Tylikowski, Stabilization of parametric vibrations of a nonlinear continuous system, *Meccanica*, Vol.38, 6, 659-668, 2003.
- [82] B.F. Spencer, Reliability of randomly excited hysteretic structures, *Lecture Notes in Engineering* (C. A. Brebbia, S. H. Orszag, eds.) Springer, N. York, 1986.
- [83] K. Sobczyk, Modelling of fatigue crack growth, *Eng. Fracture Mech.*, Vol.24, 609-623, 1986.
- [84] O. Ditlevsen, Random fatigue crack growth – a first passage problem, *Eng. Fracture Mechanics*, Vol.23,2, 467-477, 1986.
- [85] K. Doliński, P. Colombi, Fatigue life time under stochastic loading with random overloading pulse trains, *Comp. Meth. Appl. Mech. Eng.*, 168, 1999.
- [86] J. B. Roberts, P. D. Spanos, Stochastic averaging: An approximate method of solving random vibration problems, *Int. J. Nonlinear Mechanics*, Vol.21, 111-134, 1986.
- [87] L. Arnold, G. Papanicolau, V. Wihstutz, Asymptotic analysis of the Lapunov exponent and rotation number of the random oscillator and applications, *SIAM J. Appl. Math.*, Vol.46, 3, 427-450, 1986.
- [88] L. Arnold, Stabilization by noise, *ZAMM*, Vol.70, 7, 235-246, 1990.
- [89] W. Horsthemke, R. Lefever, Noise-Induced Transitions, Springer, Berlin, 1984.
- [90] K.A. Wiesenfeld, E. Knobloch, Effect of noise on the dynamics of a nonlinear oscillator, *Phys. Rev.* Vol.A26, 5, 2946-2953, 1982.
- [91] K.R. Schenk-Hoppé, Bifurcation scenarios of the noisy Duffing-Van der Pol oscillator, *Nonlinear Dynamics*, Vol.11, 255-274, 1996.
- [92] L. Arnold, N. Sri Namachchivaya, K. R. Schenk-Hoppé, Toward an understanding of stochastic Hopf bifurcation: A case study, *Int. J. Bifurc. and Chaos*, Vol.6, 11, 1947-1975.
- [93] J. Grasman, J. B.T.M. Roerdink, Stochastic and chaotic relaxation oscillations, *J. Statist. Physics*, Vol.54, 3/4, 949-970, 1989.

- [94] T. Kapitaniak, *Chaos in Systems with Noise*, *World Scientific*, Singapore, 1988.
- [95] Y-Cheng Lai, Z. Liu, L. Billings, I.B. Schwartz, Noise-induced unstable variability and transition to chaos in random dynamical systems, *Phys. Rev.*, Vol.E 67, 026210, 2003.
- [96] R. Benzi, A. Sutera, A. Vulpiani, The mechanism of stochastic resonance, *Journ. of Physics A*, Vol.141, L453-L457, 1981.
- [97] B. McNamara. K. Wiesenfeld, Theory of stochastic resonance, *Phys. Rev.* Vol.A39, 4854-4869, 1989.
- [98] L. Schimansky-Geier et al., Noise induced order: Stochastic resonance, *Int. J. Bifurc. and Chaos*, Vol.8, 5, 869-879, 1998.
- [99] K. Sobczyk, Korteweg-de Vries solitons in a randomly varying medium, *Intern. Journ. Nonlin. Mech.*, Vol.27, 1, 1-8, 1992.
- [100] D. Mumford, The Dawning of the Age of Stochasticity, in: V. Arnold, M. Atiyah, P. Lax, B. Mazur (Eds.) *Mathematics: Frontiers and Perspectives*, *Amer. Math. Soc.*, 2000.

MULTIBODY DYNAMICS: BRIDGING FOR MULTIDISCIPLINARY APPLICATIONS

Jorge A.C. Ambrósio

IDMEC Instituto Superior Técnico, Av. Rovisco Pais 1, 1049-001 Lisboa, Portugal

Abstract Simple or complex systems characterized by large relative motions between their components find in the multibody dynamics formalisms the most general and efficient computational tools for their analysis. Initially restricted to the treatment of rigid bodies, the multibody methods are now widely used to describe the system components deformations, regardless of their linear or nonlinear nature. The ease of including in the multibody models different descriptions of the contact problems, control paradigms or equations of equilibrium of other disciplines is demonstrated here to show the suitability of these approaches to be used in multidisciplinary applications

Keywords: Flexible multibody dynamics, contact, biomechanics, vehicle dynamics, railway dynamics, crashworthiness.

1. Introduction

The design requirements of advanced mechanical and structural systems and the real-time simulation of complex systems exploit the ease of use of the powerful computational resources available today to create virtual prototyping environments. These advanced simulation facilities play a fundamental role in the study of systems that undergo large rigid body motion while their components experience material or geometric nonlinear deformations, such as vehicles, deployable structures, space satellites, machines operating at high speeds or robot manipulators. Some examples of engineering and biological systems for which the large overall motion is of fundamental importance are exemplified in Fig. 1. If on the one hand the nonlinear finite element method is the most powerful and versatile procedure to describe the flexibility of the system components, on the other hand the multibody dynamic formulations are the basis for the most efficient computational techniques that

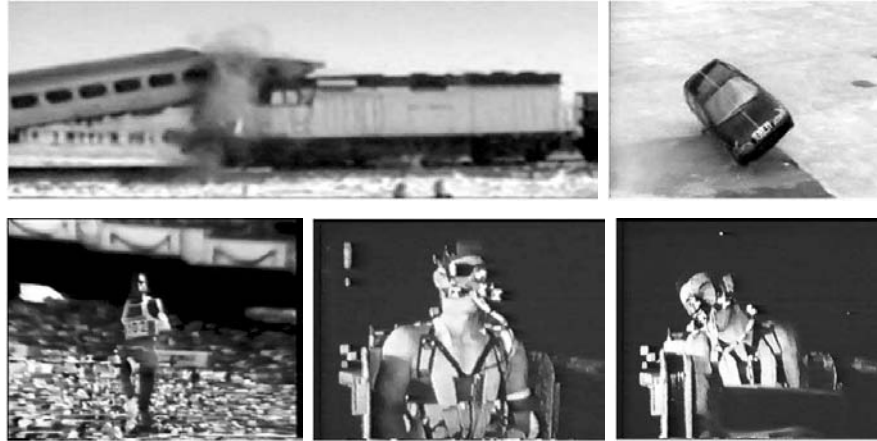


Figure 1. Natural biological and artificial engineering systems for which multibody dynamics provides irreplaceable modeling methodologies.

deal with large overall motion. Therefore, it is no surprise that many of the most recent formulations on flexible multibody dynamics and on finite element methods with large rotations share some common features.

In multibody dynamics methods, the body-fixed coordinate frames are generally adopted to position each one of the system components and to allow for the specification of the kinematic constraints that represent the restrictions on the relative motion between the bodies. Several formalisms are published suggesting the use of different sets of coordinates, such as Cartesian [1], natural [2] and relative coordinates [3]. Depending on the type of applications, each of these types of coordinates has advantages and disadvantages. Due to the ease of the computational implementation, their physical meaning and the widespread knowledge of their features, all the formalisms presented in this work are based on the use of Cartesian coordinates.

The methodological structure of the equations of motion of the multibody system obtained allows the incorporation of the equilibrium equations of a large number of disciplines and their solution in a combined form. The description of the structural deformations exhibited by the system components by using linear [5] or non-linear finite elements [6] in the framework of multibody dynamics is an example of the integration of the equations of equilibrium of different specialties. Of particular importance for the applications pursued with the methodologies proposed is the treatment of contact and impact, which is introduced in the multibody systems equations by using either unilateral constraints

[7] or a continuous contact force model [8]. The availability of the state variables in the multibody formulation allows for the use of different control paradigms in the framework of vehicle dynamics, biomechanics or robotics and their integration with the multibody equations [9]. The coupling between the fluid and structural dynamics equations allows for the development of applications, where the fluid-structure interaction is analyzed, especially for cases with large absolute or relative rotations in the system components, are of importance [10, 11].

The research carried at IDMEC provides the examples offered in this work. Application cases involving the modeling of realistic mechanisms, passive safety of road and rail vehicles, impact and human locomotion biomechanics, automotive and railway dynamics are used to demonstrate the developments reviewed here.

2. Rigid Multibody Dynamics

A multibody system is defined as a collection of rigid and/or flexible bodies constrained by kinematic joints and eventually acted upon by a set of internal and/or external forces. The position and orientation of each body i in the space is described by a position vector \mathbf{r}_i and a set of rotational coordinates \mathbf{p}_i , which are organized in a vector as [1]:

$$\mathbf{q}_i = [\mathbf{r}^T, \mathbf{p}^T]_i^T. \quad (1)$$

According to this definition, a multibody system with nb bodies is described by a set of coordinates in the form:

$$\mathbf{q} = [\mathbf{q}_1^T, \mathbf{q}_2^T, \dots, \mathbf{q}_{nb}^T]^T. \quad (2)$$

The dependencies among system coordinates, which result from the existence of mechanical joints interconnecting several bodies, are defined through the introduction of kinematic relationships written as [1]:

$$\Phi(\mathbf{q}, t) = \mathbf{0}, \quad (3)$$

where t is the time variable, which is used only for the driving constraints. The second time-derivative of Eq.(3) with respect to time yields:

$$\ddot{\Phi}(\mathbf{q}, \dot{\mathbf{q}}, \ddot{\mathbf{q}}, t) = \mathbf{0} \equiv \mathbf{D}\ddot{\mathbf{q}} = \boldsymbol{\gamma}, \quad (4)$$

where \mathbf{D} is the Jacobian matrix of the constraints, $\ddot{\mathbf{q}}$ is the acceleration vector and $\boldsymbol{\gamma}$ is the vector that depends on the velocities and time.

The system kinematic constraints are added to the equations of motion using the Lagrange multipliers technique [1]. Denoting by $\boldsymbol{\lambda}$ the

vector of the unknown Lagrange multipliers, the equations of motion for a mechanical system are written as

$$\begin{bmatrix} \mathbf{M} & \mathbf{D}^T \\ \mathbf{D} & \mathbf{0} \end{bmatrix} \begin{Bmatrix} \ddot{\mathbf{q}} \\ \boldsymbol{\lambda} \end{Bmatrix} = \begin{Bmatrix} \mathbf{f} \\ \boldsymbol{\gamma} \end{Bmatrix} \quad (5)$$

where \mathbf{M} is the global mass matrix, containing the mass and moments of inertia of all bodies, and \mathbf{f} is the force vector, containing all forces and moments applied to the system bodies plus the gyroscopic forces.

The Lagrange multipliers, associated with the kinematic constraints, are physically related with the reaction forces generated between the bodies interconnected by kinematic joints, given by [1]

$$\mathbf{f}^{(c)} = -\Phi_{\mathbf{q}}^T \boldsymbol{\lambda}, \quad (6)$$

The usual procedures to handle the integration of sets of differential-algebraic equations must still be applied in this case in order to eliminate the constraint drift or to maintain it under control [1, 2].

Forward Dynamics

The computational strategy used to solve the forward dynamics of the system, represented by Eq. (5), is outlined in Fig. 2. The solution procedure starts by the determination of the initial positions and velocities of the system components. Next, the system inertia, the Jacobian matrices, the forces and the right-hand-side of the kinematic acceleration constraint equations vectors, are calculated and assembled in the equations of motion. Equation (5) is then solved to find the system accelerations, and in the process the Lagrange multipliers. By integrating the current velocities and the system accelerations, at time t , the new positions and velocities for time $t + \Delta t$ are calculated by using a variable

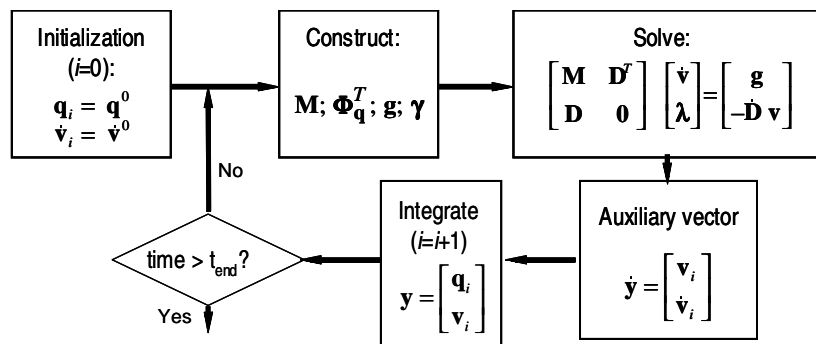


Figure 2. Solution of the forward dynamic analysis of a multibody system.

order, variable time-step integration procedure [1, 2, 4]. The forward dynamics simulation proceeds until the previously set final time is reached.

The procedure outlined in Fig. 2 is used in general purpose multibody dynamics codes, such as DAP-3D [1]. Throughout this work it is demonstrated that all engineering applications foreseen here are implemented, either by developing specific kinematic constraints or by implementing force models in Eq. (5).

Application Example of a Roller Coaster. When a body travels along a guide, not only its path has to be followed, but also its spatial orientation has to be prescribed, according to spatial characteristics of the curve. The formulation adopted to implement these kinematic constraints, using the moving Frenet frame associated with the track centerline based on the work by Pombo and Ambrósio [12], is outlined next.

Prescribed Motion Constraint. The objective here is to define the constraint equations that enforce that a point of a rigid body follows the reference path [12]. Consider a point R , located on a rigid body i , that has to follow the specified path depicted in Fig. 3. The path is defined by a parametric curve $\mathbf{g}(L)$, which is controlled by a global parameter L that represents the length travelled along the curve until the current location of point R . The kinematic constraint is

$$\Phi^{(pmc,3)} = \mathbf{0} \equiv \mathbf{r}_i^R - \mathbf{g}(L) = \mathbf{0}, \quad (7)$$

where $\mathbf{r}_i^R = \mathbf{r}_i + \mathbf{A}_i \mathbf{s}_i^R$ represents the coordinates of point R with respect to the global coordinate system (x, y, z) , \mathbf{r}_i is the vector that defines the location of the body-fixed coordinate system $(\xi, \eta, \zeta)_i$, \mathbf{A}_i is the transformation matrix from the body i fixed coordinates to the global reference frame, and \mathbf{s}_i^R represents the coordinates of point R with re-

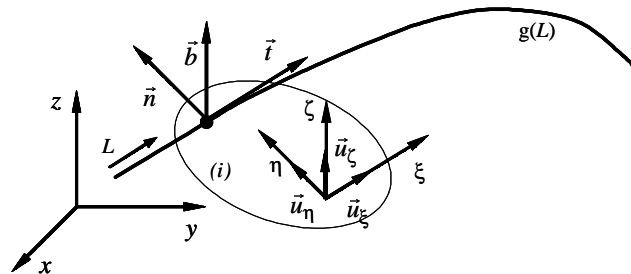


Figure 3. Local frame alignment constraint.

spect to the body-fixed reference frame. For notational purposes $(\cdot)'$ means that (\cdot) is expressed in body-fixed coordinates.

The second part of the constraint ensures that the spatial orientation of body i remains unchanged with respect to the moving frame of the reference path represented in Fig. 3. Consider that $(\mathbf{u}_\xi, \mathbf{u}_\eta, \mathbf{u}_\zeta)_i$ represent the unit vectors associated with the axis of the body-fixed coordinate system $(\xi, \eta, \zeta)_i$. Let the Frenet frame of the general parametric curve $\mathbf{g}(L)$ be defined by the principal unit vectors $(\mathbf{t}, \mathbf{n}, \mathbf{b})_L$. At the initial time of analysis, the relative orientation between the body vectors $(\mathbf{u}_\xi, \mathbf{u}_\eta, \mathbf{u}_\zeta)_i$ and the local frame $(\mathbf{t}, \mathbf{n}, \mathbf{b})_L$ leads to

$$\Phi^{(fac,3)} = \mathbf{0} \equiv \begin{Bmatrix} \mathbf{n}^T \cdot \mathbf{u}_\xi \\ \mathbf{b}^T \cdot \mathbf{u}_\xi \\ \mathbf{n}^T \cdot \mathbf{u}_\zeta \end{Bmatrix} - \begin{Bmatrix} a \\ b \\ c \end{Bmatrix} = \mathbf{0}. \quad (8)$$

This kinematic constraint ensures that the alignment remains constant throughout the analysis. The transformation matrix from the body i fixed coordinates to the global coordinate system is:

$$\mathbf{A}_i = [\mathbf{u}_\xi \quad \mathbf{u}_\eta \quad \mathbf{u}_\zeta]_i \quad (9)$$

defining the following unit vectors as:

$$\mathbf{u}_1 = \{1 \quad 0 \quad 0\}^T; \quad \mathbf{u}_2 = \{0 \quad 1 \quad 0\}^T; \quad \mathbf{u}_3 = \{0 \quad 0 \quad 1\}^T. \quad (10)$$

Equation (8) is now rewritten in a more usable form as:

$$\Phi^{(fac,3)} = \mathbf{0} \equiv \begin{Bmatrix} \mathbf{n}^T \mathbf{A}_i \mathbf{u}_1 \\ \mathbf{b}^T \mathbf{A}_i \mathbf{u}_1 \\ \mathbf{n}^T \mathbf{A}_i \mathbf{u}_3 \end{Bmatrix} - \begin{Bmatrix} a \\ b \\ c \end{Bmatrix} = \mathbf{0}, \quad (11)$$

which constitutes the second part of the path following constraint.

Roller-Coaster Dynamics. Let the roller-coaster rail be defined with the spatial geometry described in Fig. 4. The path-following constraint is used to enforce the vehicles to follow the rail for the prescribed geometry.

The roller coaster vehicle consists of a train with three cars that are interconnected by linking bars, represented in Fig. 5. The multibody model of the vehicle is assembled using eleven rigid bodies, corresponding to 3 car bodies, 6 wheelsets and 2 connection bars.

The complete vehicle model only has 1 d.o.f., which is the longitudinal motion of the cars. The motion of the vehicle is guided by the dynamics described by Eq. (5). A view of the motion of the roller coaster is displayed in Fig. 6 and the details of the analysis are found in reference [13].

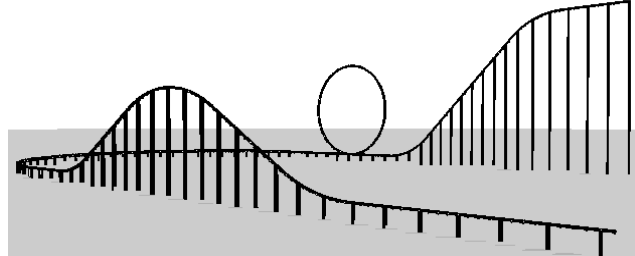


Figure 4. View of the roller coaster as used in the simulation.

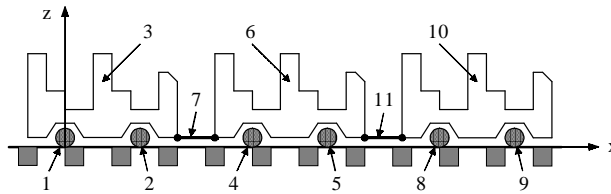


Figure 5. Multibody model of the roller coaster vehicle.

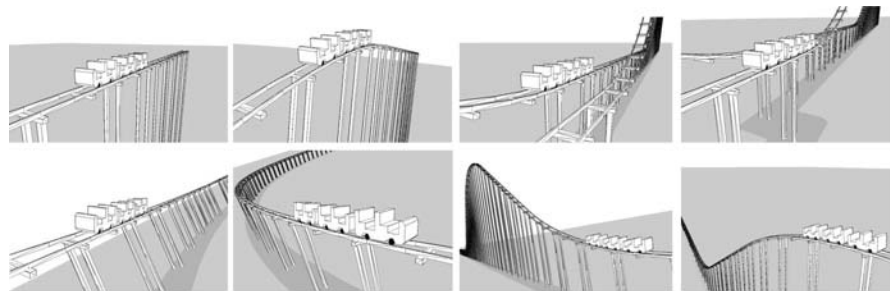


Figure 6. Snap shots of the roller coaster motion as observed from the second car.

Note that the study of these vehicles only requires the use of the path-following constraint. The contact forces are not explicitly used but they can be calculated from the Lagrange multipliers associated to the path constraint.

Inverse Dynamics

In many applications all external forces are known and the motion of the system is also known. Therefore, the only unknowns are the internal forces. Let the first row of Eq. (5) be re-written as

$$\mathbf{M}\ddot{\mathbf{q}} + \mathbf{D}^T \boldsymbol{\lambda} = \mathbf{g} \quad (12)$$

which is

$$\mathbf{D}^T \boldsymbol{\lambda} = \mathbf{g} - \mathbf{M}\ddot{\mathbf{q}}. \quad (13)$$

Equation (13) emphasizes that the only unknowns of the system are the Lagrange multipliers. The reaction forces at the joints are given by:

$$\mathbf{g}^{(c)} = -\mathbf{D}^T \boldsymbol{\lambda}. \quad (14)$$

The solution of the equations of motion in inverse dynamics can be used to solve for the internal forces of the human body, i.e., muscle and anatomical joint reaction forces, that develop for known motions.

Application to Biomechanics: Gait Analysis

For biomechanical applications in gait a three-dimensional model, presented in Fig. 7, is used [14]. It has a kinematic structure made of thirty-three rigid bodies, interconnected by revolute and universal joints, in such a way that sixteen anatomical segments are represented.

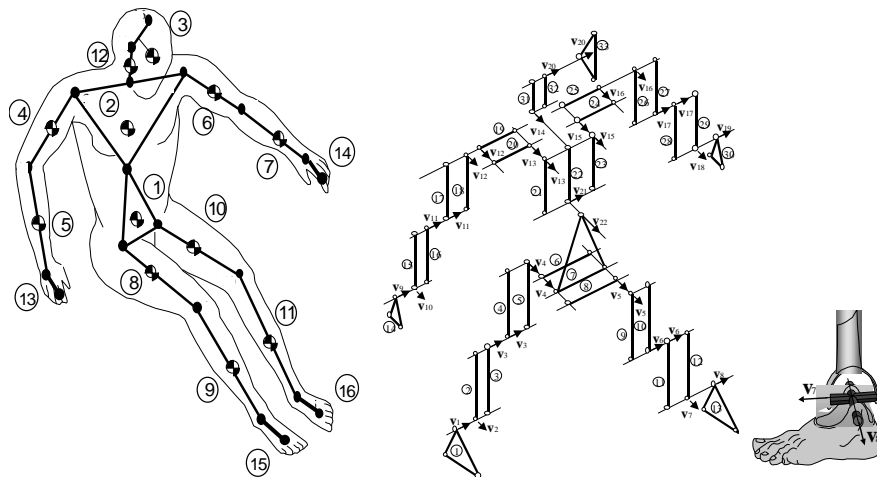


Figure 7. The biomechanical model, its kinematic structure and a detail of the ankle joint.

Joint Moments-of-Force: A Determinate Problem. To drive the biomechanical model in the inverse dynamic analysis, joint actuators such as the one represented in Fig. 8 for the knee joint, are specified. The actuators are the kinematic constraints in which the angle between two adjacent segments is a known function of time. These additional equations are added to the system kinematic equation so that the number of

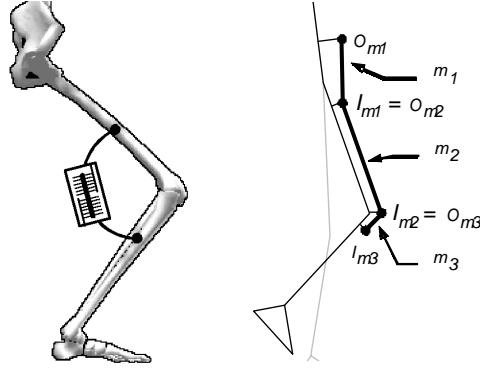


Figure 8. Joint actuator associated with the knee joint and muscle actuator.

non-redundant constraint equations becomes equal to the number of coordinates. Equation (13) is solved to obtain the Lagrange multipliers associated with the joint actuators, representing the net moments-of-force of the muscles that cross those joints. The inverse dynamics problem, as stated here, is totally determined.

Muscle Forces: A Redundant Problem. The solution of the inverse dynamics problem with muscle actuators introduces indeterminacy in the biomechanical system, since it involves more unknowns than equations of motion. By using optimization techniques to find the muscle forces that minimize a prescribed objective function, a solution for the problem is obtained. The optimization problem is stated as:

$$\begin{aligned} & \text{minimize } F_0(u_i) \\ & \text{subject to } \begin{cases} f_j(u_i) = 0, & j = 1, \dots, n_{ec}, \\ f_j(u_i) \geq 0, & j = (n_{ec} + 1), \dots, n_{tc}, \\ u_i^{\text{lower}} \leq u_i \leq u_i^{\text{upper}} & i = 1, \dots, n_{sv} \end{cases} \quad (15) \end{aligned}$$

where u_i are the state variables bounded respectively by u_{lower} and u_{upper} , $F_0(u_i)$ is the objective or cost function to minimize and $f_i(u_i)$ are constraint equations that restrain the state variables.

The minimization of the cost functions simulate the physiological criteria adopted by the central nervous system when deciding which muscles to recruit and what level of activation to obtain the adequate motion. Several cost functions have been proposed for the study of the redundant problem in biomechanics [15]. The minimization of the sum of the cube of the muscle stresses [16] is often used in applications involving human

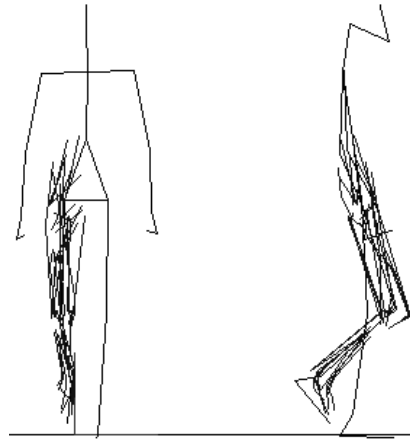


Figure 9. Lower extremity muscle apparatus.

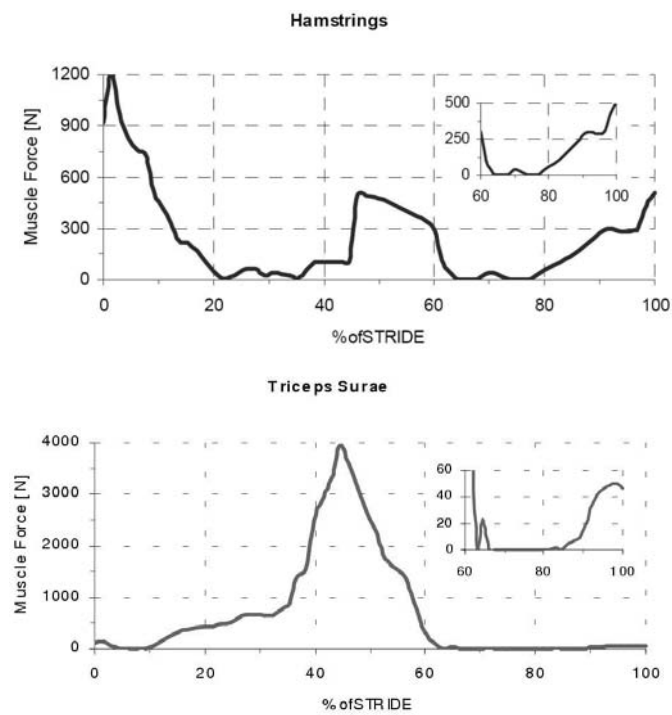


Figure 10. Muscle forces for the hamstrings and triceps surae.

locomotion

$$F_0 = \sum_{m=1}^{n_{ma}} \left(\bar{\sigma} \frac{F_l^m F_i^m}{F_0^{m2}} a^m \right)^3 \quad (16)$$

where n_{ma} are the number of muscle actuators and $\bar{\sigma}$ is the specific muscle strength with a constant value of 31.39 N/cm² [17]. The human locomotion apparatus, represented in Fig. 9, is modeled having the muscles with the physiological data described in Yamaguchi [17]. The state variables associated with muscle actuators represent muscle activations that can only assume values between 0 and 1.

To illustrate the type of results obtained for the muscle forces in a case of normal cadence gait of a 50%ile male, the muscle forces for the hamstrings and triceps surae are presented in Fig. 10.

3. Contact and Impact

Let a triangular patch, where point k of the body shown in Fig. 11 will impact, be defined by points i , j and l . The normal to the outside surface of the contact patch is defined as $\vec{n} = \vec{r}_{ij} \times \vec{r}_{jl}$. The position of the point k with respect to point i of the surface is

$$\mathbf{r}_{ik} = \mathbf{r}_k - \mathbf{r}_i \quad (17)$$

which is decomposed in a tangential and a normal component, given by

$$\mathbf{r}_{ik}^t = \mathbf{r}_{ik} - (\mathbf{r}_{ik}^T \mathbf{n}) \mathbf{n}; \quad \mathbf{r}_{ik}^n = (\mathbf{r}_{ik}^T \mathbf{n}) \mathbf{n}. \quad (18)$$

The necessary conditions for contact are that node k penetrates the ‘front’ surface of the patch, but not through its ‘back’ surface, with which a thickness e is associated. These conditions are written as

$$0 \geq \mathbf{r}_{ik}^T \mathbf{n} \geq e. \quad (19)$$

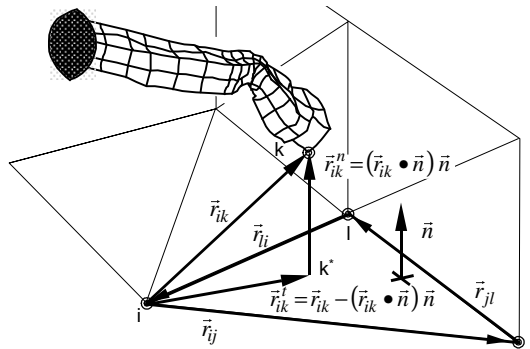


Figure 11. Contact detection between a finite element node and a surface.

The remaining necessary conditions for contact result from the need for the node to be inside of the triangular patch. These three extra conditions are

$$\left(\tilde{\mathbf{r}}_{ik}^t \mathbf{r}_{ij}\right)^T \mathbf{n} \geq 0; \quad \left(\tilde{\mathbf{r}}_{ik}^t \mathbf{r}_{jl}\right)^T \mathbf{n} \geq 0 \text{ and } \left(\tilde{\mathbf{r}}_{ik}^t \mathbf{r}_{ki}\right)^T \mathbf{n} \geq 0. \quad (20)$$

Equations (19) and (20) are necessary conditions for contact. However, depending on the contact force model actually used, they may not be sufficient to ensure effective contact.

Unilateral Constraints

If contact between a node and a surface is detected, a kinematic constraint is imposed. For flexible bodies let us assume a fully plastic nodal contact, i.e., the normal components of the node k velocity and acceleration, with respect to the surface, are null during contact

$$\dot{\mathbf{q}}_k = \dot{\mathbf{q}}_k^{(-)} - \left(\dot{\mathbf{q}}_k^{(-)T} \mathbf{n}\right) \mathbf{n}; \quad \ddot{\mathbf{q}}_k = \ddot{\mathbf{q}}_k^{(-)} - \left(\ddot{\mathbf{q}}_k^{(-)T} \mathbf{n}\right) \mathbf{n} \quad (21)$$

where $\dot{\mathbf{q}}_k^{(-)}$ and $\ddot{\mathbf{q}}_k^{(-)}$ represent the nodal velocity and acceleration immediately before impact respectively. The kinematic constraint implied by Eqs. (21) is removed when the normal reaction force between the node and the surface becomes opposite to the surface normal, i.e.,

$$\mathbf{f}_k^n = -\mathbf{f}_k^T \mathbf{n} > 0. \quad (22)$$

It should be noted that the contact force is related to the Lagrange multiplier associated by the kinematic constraint defined by Eqs. (22). Therefore, the change of sign of the force is in fact the change of sign of the multiplier.

This contact model is not suitable to be used directly with rigid body contact. The sudden change of the rigid body velocity and acceleration would imply that the velocity and acceleration equations resulting from the kinematic constraints would not be fulfilled. Other forms of this contact model can be found in the work by Pfeiffer and Glocker [7].

Continuous Contact Force Model

An alternative description of contact considers this to be a continuous event where the contact force is a function of the penetration between the surfaces. This leads to the continuous force contact model, proposed by Lankarani and Nikravesh [8], and briefly described here. Let the contact force between two bodies be written as

$$\mathbf{f}_{s,i} = \left(K\delta^n + D\dot{\delta}\right) \mathbf{u} \quad (23)$$

where δ is the pseudo-penetration, $\dot{\delta}$ is the pseudo-velocity of penetration, K is the equivalent stiffness, D is a damping coefficient and \mathbf{u} is a unit vector normal to the impacting surfaces. Using the hysteresis dissipation model and the equivalent stiffness, calculated for instance for Hertzian elastic contact [18], the nonlinear contact force is

$$\mathbf{f}_{s,i} = K\delta^n \left[1 + \frac{3(1-e^2)}{4} \frac{\dot{\delta}}{\dot{\delta}^{(-)}} \right] \mathbf{u} \quad (24)$$

where $\dot{\delta}^{(-)}$ is the initial contact velocity and e is the restitution coefficient. Note that K is a function of the geometry and material properties of the impacting surfaces.

Application to Railway Dynamics – The Wheel-Rail Contact Problem

One of the interesting applications of multibody dynamics with contact mechanics is the description of the wheel-rail contact in railway dynamics, represented in Fig. 12. The stability of the running vehicle depends ultimately on the rail-wheel contact and on the vehicle primary suspension. Therefore, methodologies that provide accurate models to represent the phenomena are of particular importance.

In a general case of a railway vehicle one or two points of each wheel are in contact with the rail, as shown in Fig. 12. The diametric section that contains the wheel flange contact point makes an angle s_{Rw}^f with the diametric section that contains the wheel tread contact point. The possibility of detecting contact in different diametric sections allows predicting derailment and it is, therefore, of utmost importance.

Let the generalized geometry of the rail and wheel be described by generalized surfaces resulting from sweeping the rail profile along the rail

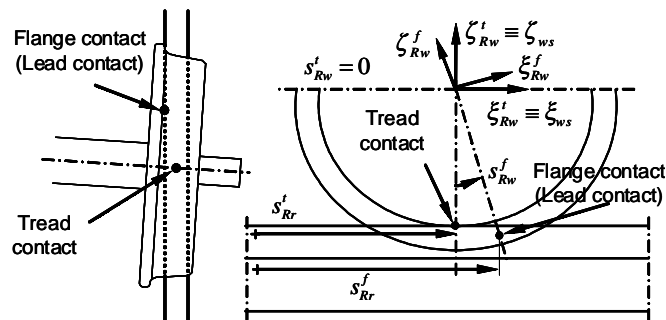


Figure 12. Two points of contact in the rail and wheel surfaces: lead contact.

centerlines and the wheel profiles around the base circle of the wheel. In order to ensure that the search for the contact points is between convex surfaces, the wheel profile is divided in tread and flange profiles. The contact between the rail and one of the wheel surfaces is described generically in Fig. 13, where the mating surfaces are represented as free surfaces.

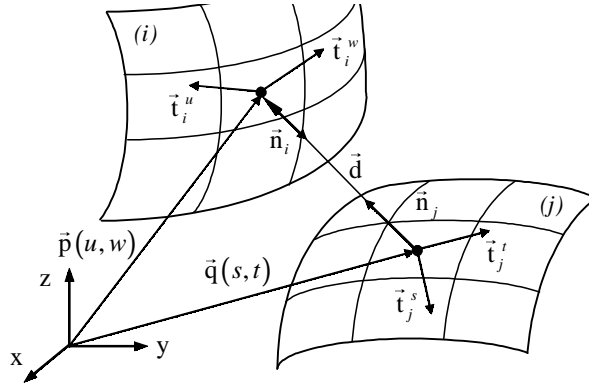


Figure 13. Candidates to contact points between two parametric surfaces.

The geometric conditions for contact between the convex surfaces are defined by vector products defined between the surfaces. The first condition is that the surfaces normals \mathbf{n}_i and \mathbf{n}_j at the candidates to contact points have to be parallel. This condition means that \mathbf{n}_j has null projections over the tangent vectors \mathbf{t}_i^u and \mathbf{t}_i^w :

$$\mathbf{n}_j \times \mathbf{n}_i = \mathbf{0} \Leftrightarrow \begin{cases} \mathbf{n}_j^T \mathbf{t}_i^u = 0, \\ \mathbf{n}_j^T \mathbf{t}_i^w = 0. \end{cases} \quad (25)$$

The second condition is that the vector \mathbf{d} , which represents the distance between the candidates to contact points, has to be parallel to the normal vector \mathbf{n}_i . This condition is mathematically written as:

$$\mathbf{d} \times \mathbf{n}_i = \mathbf{0} \Leftrightarrow \begin{cases} \mathbf{d}^T \mathbf{t}_i^u = 0, \\ \mathbf{d}^T \mathbf{t}_i^w = 0. \end{cases} \quad (26)$$

The geometric conditions (25) and (26) provide four nonlinear equations with four unknowns, the four parameters u , w , s and t that define the two surfaces. This system of equations provides solutions for the location of the candidates to contact points that have to be sorted out.

The coordinates of the candidates to contact points are determined by solving an optimal problem and the distance between such points is calculated in the process. The points are in contact if

$$\mathbf{d}^T \mathbf{n}_j \leq 0. \tag{27}$$

When contact is detected, the normal force is calculated using Eq. (24) and the tangential forces are evaluated using the Kalker theory, the Polach formulation or the Heuristic nonlinear creep model. It has been found that the Polach formulation provides the best approach for the tangent forces, and it is used hereafter [13].

The wheel-rail contact model outlined here is used to model the ML95 trainset, shown in Fig. 14, which is used by the Lisbon subway company (ML) for passengers' traffic.

The multibody model of the trailer vehicle of the train, developed in the work by Pombo [13], is composed of the car shell suspended by a set of springs, dampers and other rigid connecting elements on the bogies. This assembly of connective elements constitutes the secondary suspension, sketched in Fig. 15, which is the main one responsible for the passenger's comfort.

The connections between the bogies chassis and the wheelsets, also achieved by another set of springs, dampers and rigid connecting ele-

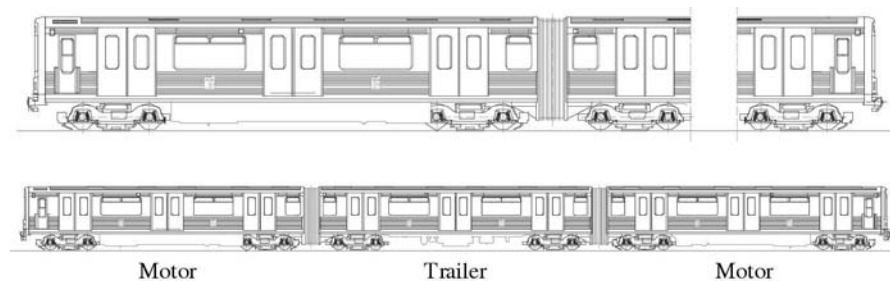


Figure 14. Schematic representation of the ML95 trainset.

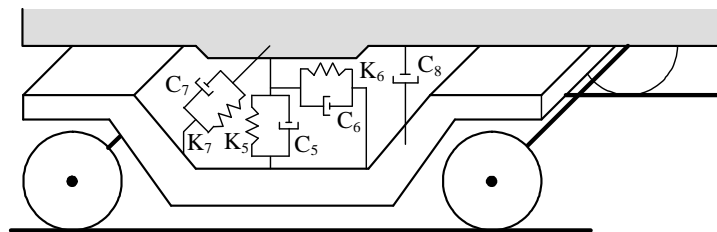


Figure 15. Secondary suspension model of the ML95 trailer vehicle.

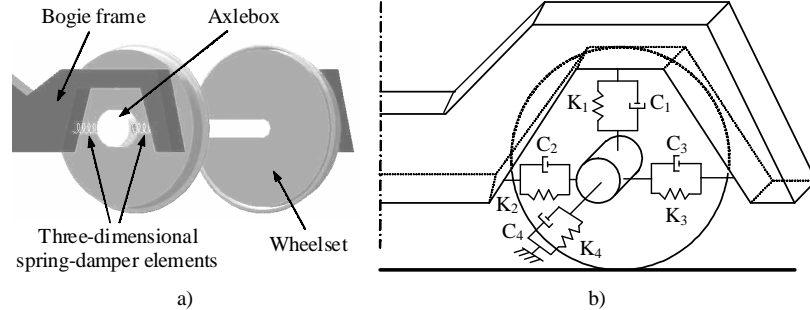


Figure 16. Primary suspension model of the ML95 trailer bogie: a) Three-dimensional spring-damper elements; b) Suspension model with springs and dampers.

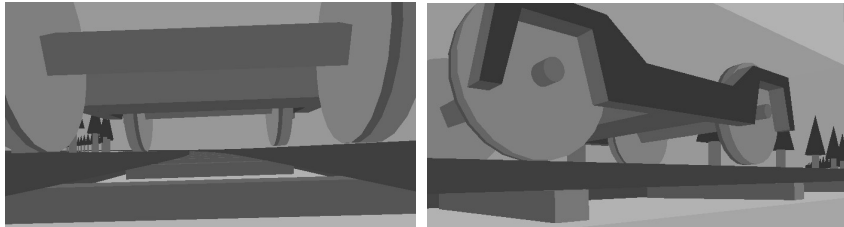


Figure 17. Lift of the right wheel of the leading wheelset for vehicle forward velocities of 10 and 20 m/s, using the Kalker linear theory.

ments, constitute the primary suspension represented in Fig. 16. The primary suspension is the main suspension responsible for the vehicle running stability.

The simulation results of the vehicle, running in a circular track with a radius of 200 m with velocities of 10 and 20 m/s, show that the prediction of flange contact is of fundamental importance. Fig. 17 shows that contact forces obtained with the Kalker linear theory originate the lift of the outer wheel of the front wheelset at the entrance of the curve. Despite this wheel lift, derailment does not occur and the analysis proceeds up to end. Nevertheless, such results are not realistic since the existence of flange contact involves high creepages, which makes the Kalker linear theory inappropriate to compute the creep forces. Therefore only the Heuristic and the Polach creep force models must be considered.

Another aspect to note is that flange contact is detected with all creep force models. Even when running at the speed of 10 m/s, where the centrifugal forces effect is balanced by the track cant, flange contact occurs. Lateral flange forces develop on the wheels of both wheelsets of the front bogie as presented in Fig. 18 for a vehicle forward velocity of 10 m/s and

using the Polach creep force model. During curve negotiation, the outer wheel of the leading wheelset and the inner wheel of the rear wheelset have permanent flange contact.

Referring to Fig. 19, for the velocity of 10 m/s, the flange contact occurs on the outer and in the inner wheels of the vehicle. For the velocity of 20 m/s, only the outer wheels have flange contact. This is explained by the fact that, when running at 20 m/s, the vehicle negotiates the curve with a velocity higher than the balanced speed.

4. Flexible Multibody Dynamics with Plastic Hinges

Many applications of multibody dynamics require the description of the flexibility of its components. For structural crashworthiness it is

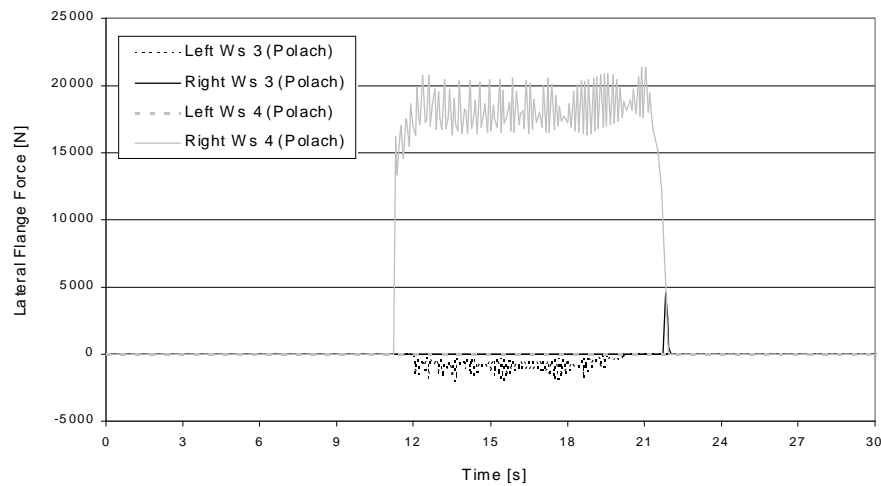


Figure 18. Lateral flange forces on the wheels of both wheelsets of the front bogie for a vehicle forward velocity of 10 m/s, using the Polach creep force model.

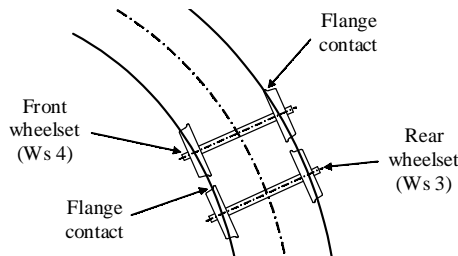


Figure 19. Contact configuration during curve negotiation.

often unfeasible to use large nonlinear finite element models. The use of multibody dynamics with plastic hinges is an alternative formulation that allows building insightful models for crashworthiness.

Formulation of Plastic Hinges

In many impact situations, the individual structural members are overloaded giving rise to plastic deformations in highly localized regions, called plastic hinges. These deformations, presented in Fig. 20 for structural bending, develop at points where maximum bending moments occur, load application points, joints or locally weak areas [19]. Multi-body models obtained with this method are relatively simple, which makes the procedure adequate for the early phases of vehicle design. The methodology described herein is known in industry as conceptual modeling [20].

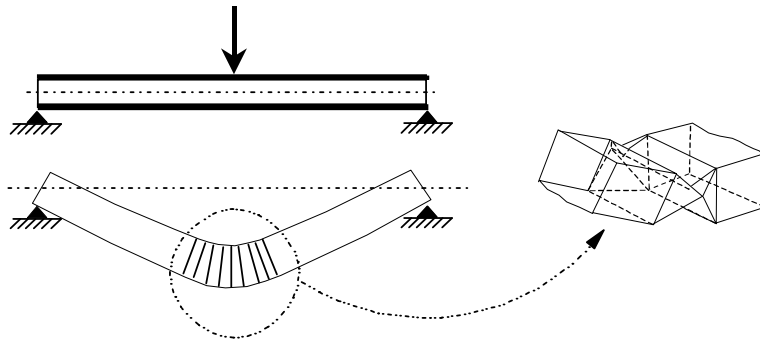


Figure 20. Localized deformations on a beam and a plastic hinge.

The plastic hinge concept has been developed by using generalized spring elements to represent constitutive characteristics of localized plastic deformation of beams and kinematic joints to control the deformation kinematics [21], as illustrated in Fig. 21. The characteristics of the spring-damper that describes the properties of the plastic hinge are obtained by experimental component testing, finite element nonlinear analysis or simplified analytical methods.

The plastic hinge constitutive equation can be modified to account for the strain rate sensitivity of some materials. A dynamic correction factor is used to account for the strain rate sensitivity given by [21].

$$P_d/P_s = 1 + 0.07V_0^{0.82}, \quad (28)$$

where P_d and P_s are the dynamic and static forces, respectively, and V_0 is the relative velocity between the adjacent bodies. The force or moment

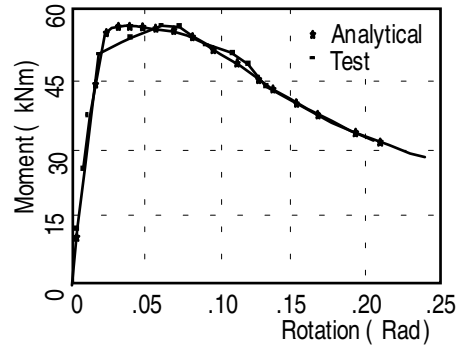


Figure 21. Plastic hinge bending moment and its constitutive relationship.

to apply due to the plastic hinge is multiplied by the ratio calculated in Eq. (28) before it is used in the force vector of the multibody equations of motion.

Application of the Plastic Hinge Approach to Crashworthiness of Surface Vehicles

The multibody of an off-road vehicle with three occupants, shown in Fig. 22, is used to demonstrate the plastic hinge approach to complex crash events. The model includes all moving components of the vehicle, suspension systems and wheels, and a tire model [16]. The biomechanical models for the occupants are similar to those described in Fig. 7.

The three occupants, with a 50%tile, integrated in the vehicle are seated. Two occupants in the front of the vehicle have shoulder and lap

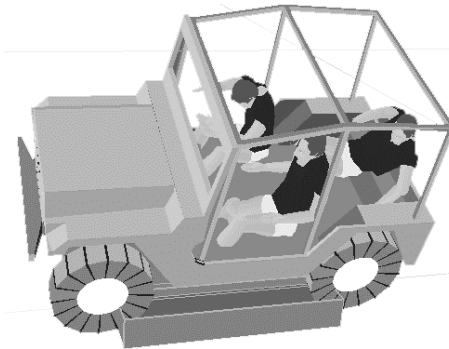


Figure 22. Initial position of the vehicle and occupants for the rollover.

seat belts while the occupant seated in the back of the vehicle has no seatbelt.

The rollover situation for the simulation is such that the initial conditions correspond to experimental conditions where the vehicle moves on a cart with a lateral velocity of 13.41 m/s until the impact with a water-filled decelerator system occurs. The vehicle is then ejected with a roll angle of 23 degrees.

The results of the simulation are pictured in Fig. 23 by several frames of the animation. The vehicle first impacts the ground with its left tires. At this point the rear occupant is ejected. The rollover motion of the vehicle proceeds with an increasing angular velocity, mainly due to the ground – tire contact friction forces. The occupants in the front of the vehicle are held in place by the seat belts. Upon continuing its roll motion, the vehicle impacts the ground with its rollbar cage, while the ejection of the rear occupant is complete. Bouncing from the inverted position, the vehicle completes another half turn and impacts the ground with the tires again. The HICs for all occupants largely exceed 1000, which indicates a very high probability of fatal injuries for the occupants under the conditions simulated.

An experimental test of the vehicle was carried out at the Transportation Research Center of Ohio [22], being an overview of the footage obtained shown in Fig. 24. The outcome of the experimental test, which is rather similar to the outcome of the simulation, is further used to validate the vehicle model [21].

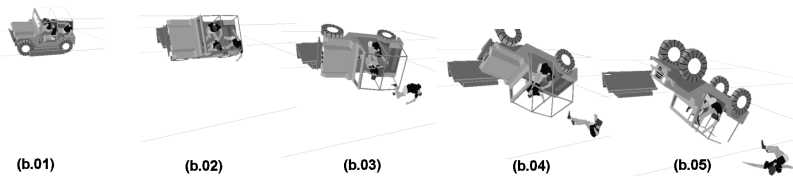


Figure 23. Views of the outcome of the rollover simulation of a vehicle with three occupants.



Figure 24. View of the experimental test for the truck rollover.

5. Flexible Multibody Dynamics with Finite Elements

General Equations of Motion of a Single Body

Let the principle of the virtual works be used to express the equilibrium of the flexible body in the current configuration $t+\Delta t$ and let an updated Lagrangean formulation be used to obtain the equations of motion of the flexible body [23]. Let the finite element method be used to represent the equations of motion of the flexible body. Referring to Fig. 25, the assembly of all finite elements used in the discretization of a single flexible body results in its equations of motion written as [6]

$$\begin{bmatrix} \mathbf{M}_{rr} & \mathbf{M}_{rf} & \mathbf{M}_{rf} \\ \mathbf{M}_{\phi r} & \mathbf{M}_{\phi\phi} & \mathbf{M}_{\phi f} \\ \mathbf{M}_{fr} & \mathbf{M}_{f\phi} & \mathbf{M}_{ff} \end{bmatrix} \begin{bmatrix} \ddot{\mathbf{r}} \\ \dot{\boldsymbol{\omega}}' \\ \ddot{\mathbf{u}}' \end{bmatrix} = \begin{bmatrix} \mathbf{g}_r \\ \mathbf{g}'_{\phi} \\ \mathbf{g}'_f \end{bmatrix} - \begin{bmatrix} \mathbf{s}_r \\ \mathbf{s}'_{\phi} \\ \mathbf{s}'_f \end{bmatrix} - \begin{bmatrix} \mathbf{0} \\ \mathbf{0} \\ \mathbf{f} \end{bmatrix} - \begin{bmatrix} \mathbf{0} & \mathbf{0} & \mathbf{0} \\ \mathbf{0} & \mathbf{0} & \mathbf{0} \\ \mathbf{0} & \mathbf{0} & \mathbf{K}_L + \mathbf{K}_{NL} \end{bmatrix} \begin{bmatrix} \mathbf{0} \\ \mathbf{0} \\ \mathbf{u}' \end{bmatrix} \quad (29)$$

where $\ddot{\mathbf{r}}$ and $\dot{\boldsymbol{\omega}}'$ are respectively the translational and angular accelerations of the body-fixed reference frame and $\ddot{\mathbf{u}}'$ denotes the nodal accelerations measured in body fixed coordinates. The local coordinate frame $\xi\eta\zeta$ attached to the flexible body, is used to represent the gross motion of the body and its deformation.

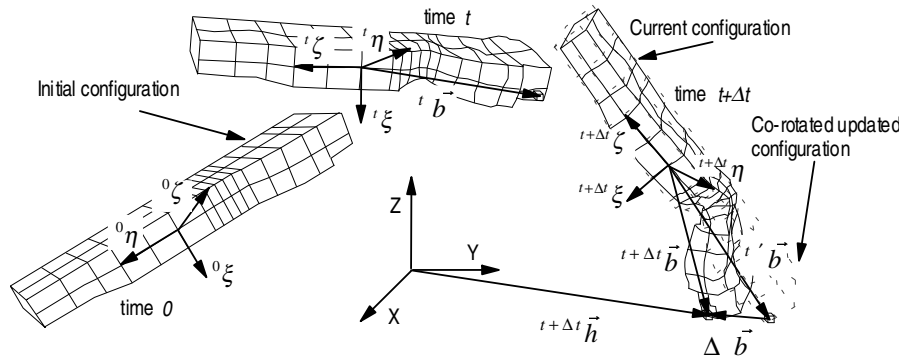


Figure 25. General motion of a flexible body.

Linear Deformations of Flexible Bodies

In many situations it is enough to consider that the components of the multibody system experience only linear elastic deformations. Furthermore, assume that the mode superposition technique can be used. Then, the flexible part of the body is described by a sum of selected modes of vibration as

$$\mathbf{u}' = \mathbf{X}\mathbf{w} \quad (30)$$

where the vector \mathbf{w} represents the contributions of the vibration modes towards the nodal displacements and \mathbf{X} is the modal matrix. Due to the reference conditions, the modes of vibration used here are constrained modes. Due to the assumption of linear elastic deformations the modal matrix is invariant. The reduced equations of motion for a linear flexible body are [5]

$$\begin{bmatrix} \mathbf{M}_r & \mathbf{M}_{rf}\mathbf{X} \\ \mathbf{X}^T\mathbf{M}_{fr} & \mathbf{I} \end{bmatrix} \begin{Bmatrix} \ddot{\mathbf{q}}_r \\ \ddot{\mathbf{w}} \end{Bmatrix} = \begin{Bmatrix} \mathbf{g}_r \\ \mathbf{X}^T\mathbf{g}_f \end{Bmatrix} - \begin{Bmatrix} \mathbf{s}_r \\ \mathbf{X}^T\mathbf{s}_f \end{Bmatrix} - \begin{Bmatrix} \mathbf{0} \\ \mathbf{\Lambda}\mathbf{w} \end{Bmatrix} \quad (31)$$

where $\mathbf{\Lambda}$ is a diagonal matrix with the squares of the natural frequencies associated with the modes of vibration selected. For a more detailed discussion on the selection of the modes used the interested reader is referred to [5].

The methodology is demonstrated through the application to the simulation of the unfolding of a satellite antenna, the Synthetic Aperture Radar (SAR) antenna that is a part of the European research satellite

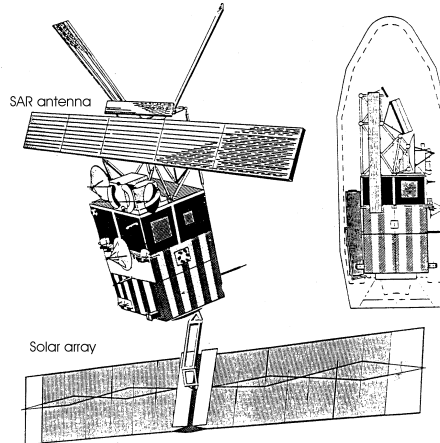


Figure 26. The European satellite with the folded and unfolded configurations of the antenna.

ERS-1, represented in Fig. 26. During the transportation the antenna is folded, in order to occupy as little space as possible. After unfolding, the mechanical components take the configuration shown in Fig. 26(a).

The SAR antenna consists in two identical subsystems, each with three coupled four-bar links that unfold two panels on each side. The central panel is attached to the main body of the satellite. Each unfolding system has two degrees of freedom, driven individually by actuators located in joints A and B. In the first phase of the unfolding process the panel 3 is rolled out, around an axis normal to the main body, by a rotational spring-damper-actuator in joint A, while the panel 2 is held down by blocking the joints D and E. The second phase begins with the joint A blocked, next the panels 2 and 3 are swung out to the final position by a rotational spring-damped-actuator.

The model used for one half of the folding antenna, schematically depicted Fig. 27, is composed of 12 bodies, 16 spherical joints and 3 revolute joints. The central panel is attached to the satellite, defined as body 1, which has much higher mass and inertia. The data for this antenna is reported in the work of Anantharamann [24].

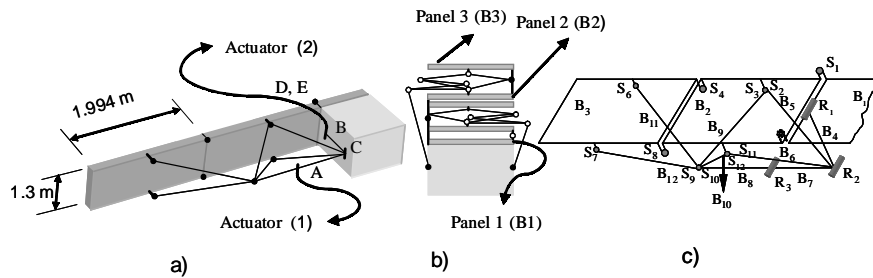


Figure 27. The SAR antenna: a) half unfolded state b) folded antenna; c) multibody model.

In the first phase of the unfolding antenna, the rotational spring-damped-actuator is applied in the revolute joint R_3 . For the second phase, the revolute joint R_3 is blocked and the system is moved to the next equilibrium position by a spring-actuator-damped positioned in joint R_1 . The unfolding processes for rigid and flexible models are shown in Fig. 28, only for its first phase.

The different behavior between the rigid and the flexible models is noticeable in Fig. 28. Though not shown here, the rotational actuator moment responsible for the start of the unfolding is not correctly predicted by the rigid multibody model. Being a very light and flexible structure, the discrepancies, if not identified during the design stage, would lead to the failure of the unfolding process.

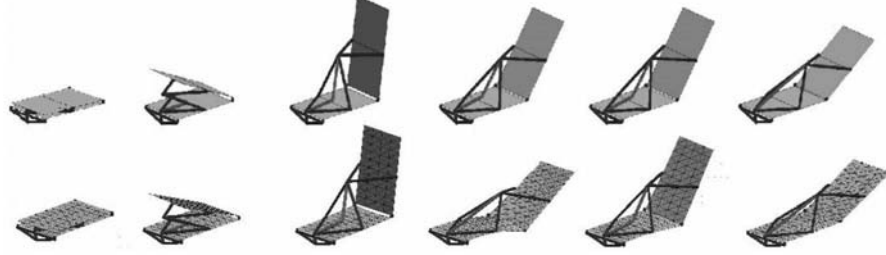


Figure 28. First phase of the unfolding of the SAR antenna (rigid and flexible models).

Nonlinear Deformations in Multibody Systems

For flexible multibody systems experiencing nonlinear geometric and material deformations, the equations of motion for a flexible body are given by Eq. (29). However, due to the time variance of all its coefficients, Eq. (29) is not efficient for computational implementation. Instead, by considering a lumped mass formulation for the mass matrix and referring the nodal accelerations to the inertial frame, the equations of motion for a single flexible body take the form of [6]

$$\begin{bmatrix} m\mathbf{I} + \bar{\mathbf{A}}\mathbf{M}^*\bar{\mathbf{A}}^T & -\bar{\mathbf{A}}\mathbf{M}^*\mathbf{S} & \mathbf{0} \\ -(\bar{\mathbf{A}}\mathbf{M}^*\mathbf{S})^T & \mathbf{J}' + \mathbf{S}^T\mathbf{M}^*\mathbf{S} & \mathbf{0} \\ \mathbf{0} & \mathbf{0} & \mathbf{M}_{ff} \end{bmatrix} \begin{bmatrix} \ddot{\mathbf{r}} \\ \dot{\boldsymbol{\omega}}' \\ \ddot{\mathbf{q}}'_f \end{bmatrix} = \begin{bmatrix} \mathbf{f}_r + \bar{\mathbf{A}}\mathbf{C}'_\delta \\ \mathbf{n}' - \tilde{\boldsymbol{\omega}}'\mathbf{J}'\boldsymbol{\omega}' - \mathbf{S}^T\mathbf{C}'_\delta - \bar{\mathbf{I}}^T\mathbf{C}'_\theta \\ \mathbf{g}'_{ff} - \mathbf{f} - (\mathbf{K}_L + \mathbf{K}_{NL})\mathbf{u}' \end{bmatrix} \quad (32)$$

where the absolute nodal displacements are written as

$$\ddot{\mathbf{q}}'_{kf} \equiv \begin{bmatrix} \ddot{\mathbf{d}}' \\ \ddot{\boldsymbol{\alpha}}' \end{bmatrix}_k = \ddot{\mathbf{u}}'_k + \begin{bmatrix} \mathbf{A}^T & -(\tilde{\mathbf{x}}_k + \dot{\boldsymbol{\delta}}_k)' \\ \mathbf{0} & \mathbf{I} \end{bmatrix} \begin{bmatrix} \ddot{\mathbf{r}} \\ \dot{\boldsymbol{\omega}}' \end{bmatrix} + \begin{bmatrix} \tilde{\boldsymbol{\omega}}'\tilde{\boldsymbol{\omega}}'(\mathbf{x}_k + \boldsymbol{\delta}_k)' + 2\tilde{\boldsymbol{\omega}}'\dot{\boldsymbol{\delta}}'_k \\ \tilde{\boldsymbol{\omega}}'\dot{\boldsymbol{\theta}}'_k \end{bmatrix} \quad (33)$$

with \mathbf{x}_k being the position of node k in the reference configuration. In Eq. (32) \mathbf{M}^* is a diagonal mass matrix containing the mass of the n boundary nodes,

$$\bar{\mathbf{A}}^T = [\mathbf{A} \dots \mathbf{A}]^T, \quad \mathbf{S} = \left[(\tilde{\mathbf{x}}'_1 + \tilde{\boldsymbol{\delta}}'_1)^T \dots (\tilde{\mathbf{x}}'_n + \tilde{\boldsymbol{\delta}}'_n)^T \right]^T$$

and $\bar{\mathbf{I}} = [\mathbf{I} \dots \mathbf{I}]^T$ where \mathbf{A} is the transformation matrix from the body fixed to global coordinate coordinates and \mathbf{x}_k denotes the position of node k . Vectors \mathbf{C}'_δ and \mathbf{C}'_θ represent respectively the reaction force and moment of the flexible part of the body over the rigid part, given by

$$\begin{aligned} \mathbf{C}'_\delta &= \mathbf{g}'_\delta - \mathbf{F}_\delta - (\mathbf{K}_L + \mathbf{K}_{NL})_{\delta\delta} \delta' - (\mathbf{K}_L + \mathbf{K}_{NL})_{\delta\theta} \theta', \\ \mathbf{C}'_\theta &= \mathbf{g}'_\theta - \mathbf{F}_\theta - (\mathbf{K}_L + \mathbf{K}_{NL})_{\theta\delta} \delta' - (\mathbf{K}_L + \mathbf{K}_{NL})_{\theta\theta} \theta'. \end{aligned} \tag{34}$$

The coupling between the rigid body motion and the system deformations is fully preserved. For a more detailed description of the formulation, and the notation, the interested reader is referred to reference [6].

As an application example of the nonlinear formulation for flexible multibody systems, a sports vehicle with a front crash-box is analyzed for various impact scenarios, represented in Fig. 29, where the angle of

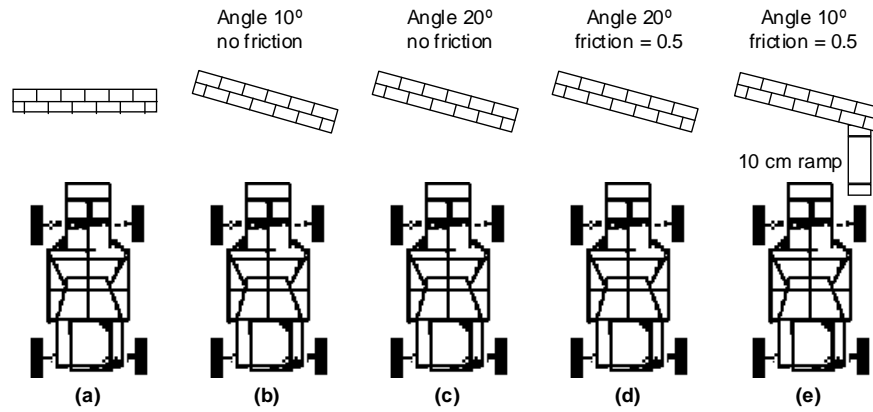


Figure 29. Different impact scenarios for the sports vehicle.

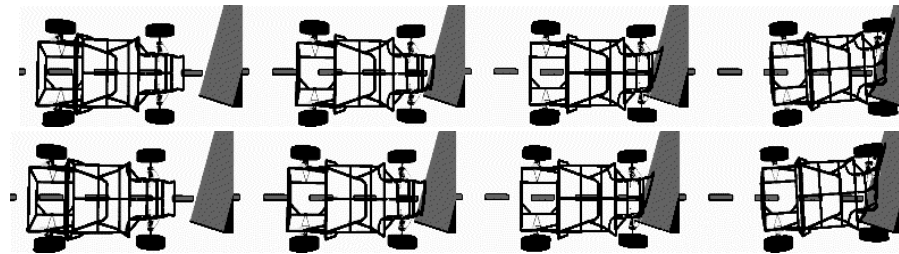


Figure 30. Motion of the vehicle for a 20° oblique impact without contact friction and for impact with an oblique surface for a vehicle traveling over a ramp.

impact and the topology of the road are different. The simulations are carried until the vehicle reaches a full stop.

The vehicle motion, for the oblique impact scenario presented in Fig. 29, is characterized by a slight rotation of the vehicle during impact. This rotation is more visible in the case of frictionless impact. At the simulated impact speed the influence of the car suspension elements on the deformation mechanism is minimal.

6. Conclusions

The multibody dynamics formalisms provide an extremely efficient framework to incorporate different disciplines. The behavior of a good number of phenomena in different problems can be represented by kinematic constraints (e.g., contact, muscle action, guidance) or by contact forces (e.g, impact phenomena, control, general interactions). However, different disciplines use different preferred numerical methods to solve their equilibrium equations which lead to difficulties in the co-simulation of different systems. The use of multibody formalisms in biomechanics presents a strong increase due to the suitability to model contacts, muscles, anatomical joints, data processing, etc. The treatment of structural components with large rotations or of rotating bodies with structural deformations finds in the flexible multibody dynamics efficient methods to deal with the problem. A continued effort to close the gap between the flexible multibody dynamics and the nonlinear finite element method is required. The need for more robust and efficient numerical methods to handle the specific forms of the MBS equations and the discontinuities associated to intermittent and ‘fast’ behaviors are still required.

Acknowledgements

The contents of this work result from a team effort and collaborations with many co-workers among which the contribution by Miguel Silva, João Gonçalves, João Pombo, Manuel Seabra Pereira, João Abrantes, Augusta Neto and Rogério Leal are gratefully acknowledged.

References

- [1] P. Nikravesh, *Computer-Aided Analysis of Mechanical Systems*, Prentice-Hall, Englewood Cliffs, New Jersey 1988.
- [2] J. Garcia de Jalon, E. Bayo, *Kinematic and Dynamic Simulation of Mechanical Systems – The Real-Time Challenge*, Springer-Verlag, Berlin 1994.
- [3] P. Nikravesh and G. Gim, Systematic construction of the equations of motion for multibody systems containing closed kinematic loops, *Journal of Mechanical Design*, Vol. 115, No.1, pp.143–149, 1993.

- [4] C.W. Gear, Numerical solution of differential-algebraic equations, *IEEE Transactions on Circuit Theory*, Vol. CT-18, pp.89–95, 1981.
- [5] J. Gonçalves and J. Ambrósio, Complex flexible multibody systems with application to vehicle dynamics, *Multibody System Dynamics*, Vol. 6, No.2, pp.163–182, 2001.
- [6] J. Ambrósio and P. Nikravesh, Elastic-plastic deformation in multibody dynamics, *Nonlinear Dynamics*, Vol. 3, pp.85–104, 1992.
- [7] F. Pfeiffer and C. Glocker, *Multibody Dynamics with Unilateral Contacts*, John Wiley and Sons, New York 1996.
- [8] H. Lankarani and P. Nikravesh, Continuous contact force models for impact analysis in multibody systems, *Nonlinear Dynamics*, Vol. 5, pp.193–207, 1994.
- [9] M. Valasek, Z. Šika, Evaluation of dynamic capabilities of machines and robots, *Multibody System Dynamics*, Vol. 5, pp.183–202, 2001.
- [10] H. Møller and E. Lund, Shape Sensitivity Analysis of Strongly Coupled Fluid-Structure Interaction Problems, [in:] *Proc. 8th AIAA/USAF/NASA/ISSMO Symposium on Multidisciplinary Analysis and Optimization*, Long Beach, CA. AIAA Paper No.2000–4823, 2000.
- [11] H. Møller, E. Lund, J. Ambrósio and J. Gonçalves, Simulation of fluid loaded flexible multiple bodies, *Multibody Systems Dynamics*, Vol. 13, No.1, 2005.
- [12] J. Pombo and J. Ambrósio, General spatial curve joint for rail guided vehicles: kinematics and dynamics, *Multibody Systems Dynamics*, Vol. 9, pp.237–264, 2003.
- [13] J. Pombo and J. Ambrósio, *A multibody methodology for railway dynamics applications*, Technical Report IDMEC/CPM-04/002, IDMEC, Instituto Superior Técnico, Lisboa, Portugal, 2004.
- [14] M. Silva and J. Ambrósio, Kinematic data consistency in the inverse dynamic analysis of biomechanical systems, *Multibody System Dynamics*, Vol. 8, pp.219–239, 2002.
- [15] D. Tsirakos, V. Baltzopoulos and R. Bartlett, Inverse Optimization: Functional and Physiological Considerations Related to the Force-Sharing Problem, *Critical Reviews in Biomedical Engineering*, Vol. 25, Nos.4&5, pp.371–407, 1997.
- [16] M. Silva and J. Ambrósio, *Human Motion Analysis Using Multibody Dynamics and Optimization Tools*, Technical Report IDMEC/CPM-04/001, IDMEC, Instituto Superior Técnico, Lisboa, Portugal, 2004.
- [17] G.T. Yamaguchi, *Dynamic Modeling of Musculoskeletal Motion*, Kluwer Academic Publishers, Boston 2001.
- [18] H. Hertz *Gesammelte Werke*, Leipzig, Germany 1895.
- [19] N.W. Murray, The static approach to plastic collapse and energy dissipation in some thin-walled steel structures, [in:] *Structural Crashworthiness*, N. Jones and T. Wierzbicki [eds.], pp.44–65, Butterworths, London 1983.
- [20] C.M. Kindervater, Aircraft and helicopter crashworthiness: design and simulation, [in:] *Crashworthiness Of Transportation Systems: Structural Impact And Occupant Protection*, J.A.C. Ambrósio, M.S. Pereira and F.P Silva [eds.], NATO ASI Series E. Vol. 332, pp.525–577, Kluwer Academic Publishers, Dordrecht 1997.

- [21] P.E. Nikravesh, I.S. Chung, and R.L. Benedict, Plastic hinge approach to vehicle simulation using a plastic hinge technique, *J. Comp. Struct.* Vol. 16, pp.385–400, 1983.
- [22] *30 mph Rollover Test of an AM General Model M151-A2 1/4 Ton Jeep*, The Transportation Research Center of Ohio, Test Report, 1985.
- [23] K.-J. Bathe and S. Bolourchi, Large displacement analysis of three-dimensional beam structures, *Int. J. Num. Methods in Engng.*, Vol. 14, pp.961–986, 1979.
- [24] M. Anantharaman and M. Hiller, Numerical simulation of mechanical systems using methods for differential-algebraic equations, *Int. J. Num. Meth. Eng.*, Vol. 32, pp.1531–1542, 1991.

RAPID FORMATION OF STRONG GRADIENTS AND DIFFUSION IN THE TRANSPORT OF SCALAR AND VECTOR FIELDS

Konrad Bajer
Institute of Geophysics
Warsaw University
kbajer@fuw.edu.pl

Abstract An important issue in the theory of transport by moving fluids is the role of dissipation when the medium is *nearly ideal*. The central problem of this nature is understanding of the viscous dissipation at very large Reynolds numbers. We will discuss a few problems in the same category but *linear* and therefore more promising although, as it turns out, surprisingly rich and far from being solved. Their common denominator is the interplay between diffusion and advection. In a typical flow the latter tends to decrease the characteristic length scales of the spatial variations of the transported quantity, thus increasing the rate of diffusion. Depending on a particular configuration, either this rapid diffusion prevails and efficiently annihilates all gradients, or a kind of balance is reached and a quasi-steady dissipative structure emerges.

Keywords: Accelerated diffusion, shear dispersion, current sheets, passive scalar, vortex dynamics, Poiseuille flow.

Introduction

Dissipative processes are, in general, strongly affected by the motion of the medium. In a stationary fluid, a passive quantity like temperature or concentration of a contaminant would change its distribution only through molecular processes that, in a wide range of physical problems, may be well modelled as ‘simple’ Fickian diffusion. When the fluid is in motion, the diffusive process in the Lagrangian frame of every material element may result in great complexity of the Eulerian distribution of the transported quantity. In particular, the interplay of advection and diffusion typically increases the rate at which the latter smoothes out the spatial variations of that quantity’s distribution. The archetypal

formula describing this interplay is the advection-diffusion equation for an intensive quantity, say temperature,

$$\frac{\partial T}{\partial t} + \mathbf{u} \cdot \nabla T = \kappa \nabla^2 T. \quad (1)$$

The dynamics of various physical processes, other than advection-diffusion of a passive scalar, often reduces to the Eq. (1) or to another linear equation of similar type that exhibits the same salient feature of enhanced rate of diffusion associated with non-uniform fluid motion. In simple geometries the evolution of magnetic fields in electrically conducting liquids and plasmas can sometimes be reduced exactly to an advection-diffusion problem with important implications in all branches of magnetohydrodynamics whether cosmic, solar, geophysical or that applied in the theory of nuclear fusion devices and in metallurgy. The evolution of weak background vorticity in presence of a strong coherent structure – an important mechanism in two-dimensional turbulence – is described by a linearised vorticity equation that, in spite of some extra complications, is a linear equation (scalar when the flow is two-dimensional) containing both advection and diffusion ingredients. The same equation also describes the evolution of small perturbations induced in a strong vortex by a weak external irrotational flow.

We shall illustrate the phenomenon, called *accelerated diffusion*, with simple solutions of the Eq. (1) for two basic steady flows $\mathbf{u}(\mathbf{x})$.

1. Accelerated Diffusion

Let us consider an initial value problem for the advection-diffusion equation (1) in an unbounded two-dimensional domain. The problem is linear, so every initial distribution of the scalar, $T(\mathbf{x}, t = 0)$, can be decomposed into independently evolving Fourier modes. For simplicity we take the initial distribution to be harmonic in the x direction (see Fig. 1b),

$$T(\mathbf{x}, t = 0) = T_0 e^{ik_0 x}, \quad (2)$$

i.e. the initial wave vector is $\mathbf{k}_0 = (k_0, 0)$.

We shall consider two steady flows $\mathbf{u}(\mathbf{x})$ (see Fig. 1a) - a stagnation point flow (irrotational linear strain),

$$\mathbf{u}(\mathbf{x}) = (-\alpha x, \alpha y, 0), \quad (3)$$

and a linear shear flow

$$\mathbf{u}(\mathbf{x}) = (\alpha y, 0, 0). \quad (4)$$

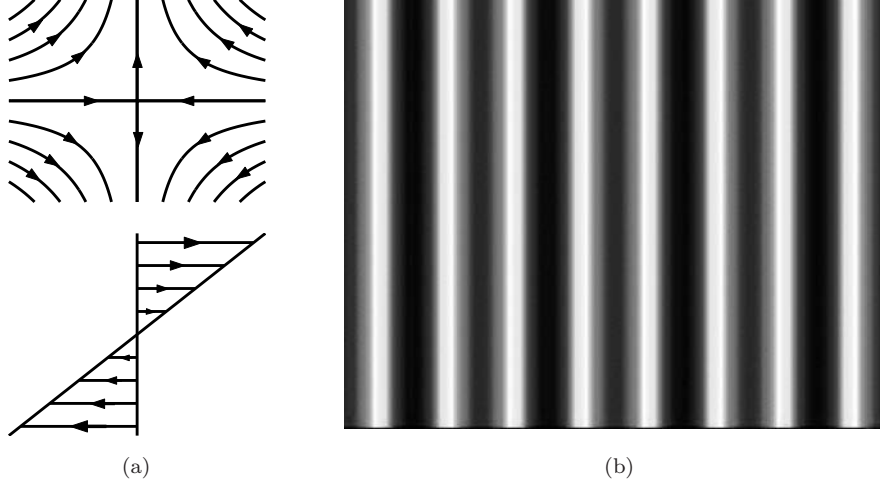


Figure 1. (a) Two types of the flow considered — a stagnation point flow (irrotational linear strain, top) and linear shear (bottom); (b) Initial distribution of the scalar field subject to advection and diffusion.

Both flows impose a characteristic *advection time scale* determined by the value of strain/shear coefficient α ,

$$t_A = \alpha^{-1}. \quad (5)$$

The initial scalar distribution has a characteristic length scale, k_0^{-1} , and the associate diffusion time scale

$$t_D = (\kappa k_0^2)^{-1}. \quad (6)$$

The ratio of the two time scales is called *Schmidt number* when the transported scalar field T is the mass concentration of some material admixture (an extensive quantity) and *Péclet number* in the case of temperature (an intensive quantity),

$$\text{Pe} = \frac{t_D}{t_A} = \frac{\alpha}{k_0^2 \kappa}. \quad (7)$$

In both cases the solution has the general form of a single Fourier mode but with time-dependent wave vector and amplitude,

$$T(\mathbf{x}, t) = T_0 F(t) e^{i\mathbf{k}(t) \cdot \mathbf{x}}. \quad (8)$$

For the stagnation point flow (3) we obtain

$$\frac{\partial T}{\partial t} - \alpha x \frac{\partial T}{\partial x} = \kappa \nabla^2 T \quad (9)$$

and the solution is

$$\mathbf{k}(t) = k_0 (e^{\alpha t}, 0), \quad (10a)$$

$$F(t) = e^{-\frac{1}{2}\text{Pe}^{-1}e^{2\alpha t}} = \exp(-\exp(2\alpha t - \ln \text{Pe} - \ln 2)). \quad (10b)$$

The wavelength in the x -direction decreases exponentially. That in the y -direction would, in general, increase exponentially but with the initial condition (2) it started being already infinite (cf. Fig. 2a). The decay of the amplitude $F(t)$ is *super-exponential*, i.e. extremely fast. The initial variations of the scalar field distribution are therefore eliminated by a very rapid process of *strain diffusion* on the time scale

$$t_{\text{strain}} = (\ln \text{Pe}) t_A \quad (11)$$

which is much shorter than that of ordinary diffusion, in fact only slightly longer than the advection time scale, even when the Péclet number is very large.

For the linear shear (4) we have

$$\frac{\partial T}{\partial t} + \alpha y \frac{\partial T}{\partial x} = \kappa \nabla^2 T \quad (12)$$

and the corresponding solution is

$$\mathbf{k}(t) = k_0 (1, -\alpha t), \quad (13a)$$

$$F(t) = \exp \left[-\frac{t}{t_D} - \frac{1}{3} \left(\frac{t}{t_D \text{Pe}^{-2/3}} \right)^3 \right]. \quad (13b)$$

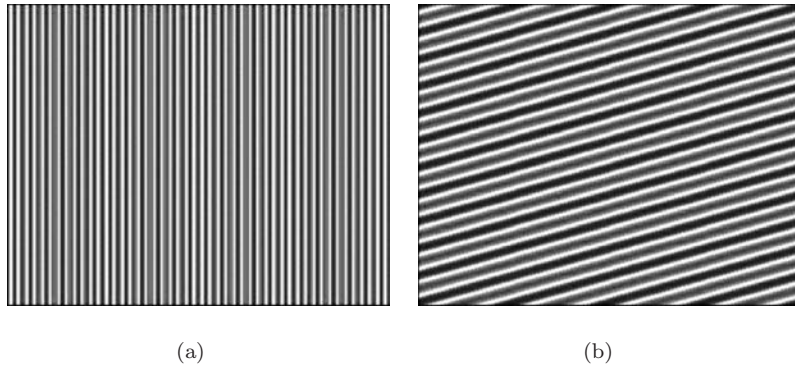


Figure 2. The distribution of the scalar subject to advection and diffusion in a stagnation point flow (a) and in a linear shear flow (b) (cf. Fig. 1a). The initial distribution is shown in Fig. 1b.

Here the wavenumber in the x -direction remains unchanged while that in the y -direction increases *linearly* in time. This linear growth, considerably slower than the exponential one in the straining flow, accounts for slower decay of the amplitude $F(t)$. For times shorter than t_A we have

$$F(t) \sim e^{-t/t_D}, \quad t \ll t_A = P_e^{-1}t_D. \quad (14)$$

Therefore, initially, for a short time, the dissipative process is simple diffusion. Later we have

$$F(t) \sim e^{-\frac{1}{3}(t/t_S)^3}, \quad t \gg t_A, \quad (15)$$

which means that the process considerably accelerates. Firstly, the exponent changes from t^1 to t^3 . Secondly, the time scale of the decay becomes

$$t_S = P_e^{-2/3}t_D = P_e^{1/3}t_A. \quad (16)$$

This intermediate *shear diffusion* time scale, considerably shorter than that of the ordinary diffusive process, but longer than t_A , was identified early in the context of scalar diffusion (Rhines & Young 1983) and in the context of magnetic field transport (Moffatt & Kamkar 1983).

The two special *linear* flows chosen here, i.e. a stagnation point flow and linear shear, may seem to be too simple and lacking all the complications encountered in real transport problems. However, there are at least two reasons to single them out. Firstly, they are often good local approximations of the large-scale, time-dependent flows when the initial spatial scale of the transported scalar is small compared with that of the flow itself *and* the *local* time-scale, say t_S , is short compared with that of the flow variations. Secondly, these flow configurations, possibly with a modified geometry, are often found in different physical problems of special interest. We will discuss the transport in a stagnation point flow in the context of flux- and current-sheet formation, common in magnetohydrodynamics, where a flow of this kind is essential. Further, we will consider shear that is always associated with a strong, concentrated vortex, both in its core and outside and affects any passive scalar or weak vorticity that may be present.

2. Current Sheets and Flux Sheets

The evolution of the magnetic field $\mathbf{B}(\mathbf{x}, t)$ penetrating an electrically conducting fluid moving with velocity $\mathbf{u}(\mathbf{x}, t)$ is governed by the induction equation,

$$\frac{\partial \mathbf{B}}{\partial t} = \nabla \times (\mathbf{u} \times \mathbf{B}) + \eta \nabla^2 \mathbf{B}, \quad (17)$$

where the magnetic diffusivity of the fluid, η , is inversely proportional to its electrical conductivity. This approximation of the Maxwell's equation is used within the framework of magnetohydrodynamics (MHD) to describe processes much slower than electromagnetic waves. This is a kind of advection-diffusion equation for a vector quantity $\mathbf{B}(\mathbf{x}, t)$. In general it describes a much richer variety of phenomena than its scalar counterpart, the kinematic dynamo problem possibly being the most spectacular one (Childress & Gilbert 1995), but in some special symmetric configurations the two are actually equivalent¹. We will now consider two simple steady solutions of the induction equation (17), both with $\mathbf{u}(\mathbf{x}, t)$ corresponding to the stagnation point flow (3), that illustrate an important MHD phenomenon, namely the formation of large, localised gradients of the magnetic field (Bajer 2004). Strong electric currents, $\mathbf{j}(\mathbf{x}, t) = \nabla \times \mathbf{B}$, are associated with such gradients implying intense Ohmic heating. The structures of this type, called *current sheets*, play an important role in various MHD processes like, for example, the heating of the solar corona.

The first solution describes the magnetic field lying in the same plane as the flow, $\mathbf{B}(\mathbf{x}) = (B_x(x, y), B_y(x, y), 0)$, in which case (17) reduces to the advection-diffusion equation (1) for the only component of the *vector potential*,

$$\frac{\partial A}{\partial t} - \alpha x \frac{\partial A}{\partial x} = \eta \nabla^2 A, \quad \mathbf{B} = \nabla \times \mathbf{A}, \quad \mathbf{A} = (0, 0, A(x, y, t)). \quad (18)$$

As we could see in the previous section, individual Fourier modes 'travel' across the Fourier space towards smaller scales (larger k). However, an imposed boundary condition may act as a 'source' of one or more Fourier modes and a steady state may be established. In particular, forcing the $k = 0$ mode,

$$\mathbf{A}(\mathbf{x}, t) = A(x)\hat{\mathbf{e}}_z, \quad A(x) \xrightarrow{x \rightarrow \pm\infty} \pm A_0, \quad (19)$$

we obtain

$$A(x) = A_0 \operatorname{erf}\left(\sqrt{\frac{\alpha}{2\eta}}x\right), \quad B(x) = -A'(x) = -A_0\sqrt{\frac{2\alpha}{\pi\eta}}e^{-\frac{\alpha}{2\eta}x^2}. \quad (20)$$

This solution represents a *flux sheet*, i.e., a layer of strong magnetic field with Gaussian profile, similar in nature to a Burgers vortex layer in which stretching is in balance with diffusion. This is also a *double current*

¹With linear stretching in the direction of the field \mathbf{B} the Eq.(17) reduces to a scalar advection-diffusion equation with an extra 'source term' (Bajer & Moffatt 1997).

sheet with two adjacent layers of strong current in opposite directions. The Ohmic heating D_m is strong, in fact for a given flux $D_m \xrightarrow{\eta \rightarrow 0} \infty$, but the magnetic energy E_m stored in such sheets also grows without bounds as $\eta \rightarrow 0$, so they cannot be easily created in flows with finite energy supply (Bajer 2004). They are, therefore, more relevant to the solar dynamo than to the coronal heating problem.

When the field $\mathbf{B} = B(x)\hat{\mathbf{e}}_y$ is *perpendicular* to the stagnation point flow $\mathbf{u} = (-\alpha x, 0, \alpha y)$, we also obtain an advection-diffusion equation but this time for a single component of the field, $B(x)$, rather than its vector potential. Imposing $B(x) \rightarrow \pm B_0$ for $x \rightarrow \pm\infty$ we now obtain a steady solution describing a *current sheet*,

$$B(x) = B_0 \operatorname{erf}\left(\sqrt{\frac{\alpha}{2\eta}}x\right), \quad j(x) = B'(x) = B_0\sqrt{\frac{2\alpha}{\pi\eta}} e^{-\frac{\alpha}{2\eta}x^2}. \quad (21)$$

Ohmic dissipation in such current sheets is small, $D_m \xrightarrow{\eta \rightarrow 0} 0$, so the direct heating effect of an individual sheet is weak.

However, in a highly conducting medium the magnetic energy stored in such current sheets is small, $E_m \rightarrow 0$ as $\eta \rightarrow 0$, so they can be easily created even in weak flows. The cumulative direct heating effect may be augmented when many such sheets are created (Parker 1963a). This is likely to be the case when a weakly perturbed integrable field relaxes towards a new equilibrium and current sheets appear on the whole range of spatial scales with their distribution, at least in some regions, becoming *dense* in the limit of infinite electric conductivity of the medium (Bajer 2004).

Besides their energetics in a steady or quasi-steady state, the details of the dynamic formation process of strong field gradients are also important. The collapse of an X-type neutral point is probably the generic mechanism (Parker 1957, 1963a; Moffatt 1990; Linardatos 1993). In spite of the relatively low heat release, the associated magnetic reconnection process locally lifts the topological constraints of ideal MHD thus enabling further relaxation towards yet lower energy states. The role of topological constraints and their violation is a challenging open problem from the physical and from the mathematical point of view, both in linked and in open-ended, braided flux systems (Moffatt 1985; Moffatt & Ricca 1992).

In this section we have discussed some fundamental, ubiquitous MHD processes involving stagnation point flows. Now we will consider a category of archetypal transport processes ruled by the shear flows.

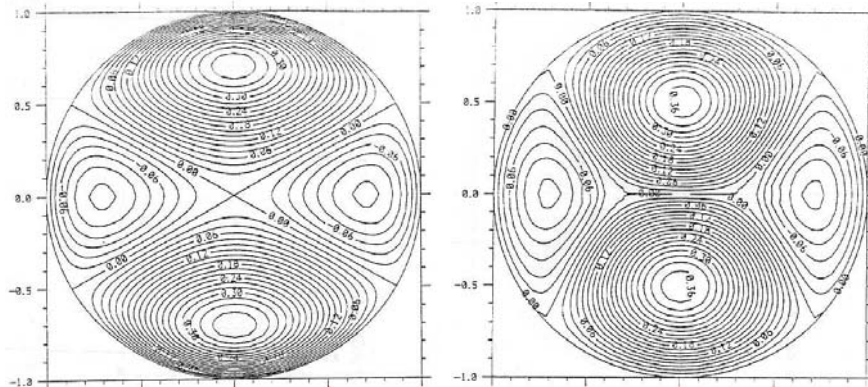


Figure 3. The formation of a current sheet as a result of the collapse of an X-type neutral point. The cylindrical cavity, surrounded by perfectly conducting solid is filled with viscous, perfectly conducting fluid penetrated by non-equilibrium magnetic field initially containing an X-type neutral point (left panel). Under the evolution governed by the full, nonlinear MHD equations, the neutral point collapses and the system relaxes towards an ideal magnetostatic equilibrium containing a tangential discontinuity of the field across which the field direction reverses. In a perfectly conducting fluid this corresponds to a singular, delta-like current while in a fluid of finite conductivity the singular layer would be replaced by a quasi-steady current sheet of finite length and with finite current.

3. Passive Scalar Outside and Inside a Vortex

The dynamics of many flows is best understood in terms of the evolution of coherent vortices and their interactions. For some time this is known to be the case with two-dimensional turbulence (McWilliams 1984) where vortices are sizeable compared with the length scale of the forcing (driven flow) or with the size of the domain (decaying flow). In three-dimensional turbulence the vortices are prominent at small scales (Bajer & Moffatt 2002), their diameters seem to be of the order of the Kolmogorov scale (Moffatt, Kida & Ohkitani 1994). It is therefore of interest to understand the advection-diffusion processes in the presence of concentrated vortices. Locally, the flow near a vortex is simple shear. An initial blob of passive scalar which is small compared with the streamline curvature experiences shearing by a flow similar to (4) (Flohr & Vassilicos 1997) and the initial-value problem for its evolution can be decomposed into Fourier modes evolving according to (8).

However, if the initial spatial variations of the scalar are much *larger* than the size of the vortex, then, on the scale of the vortex, the initial scalar isolines are, to a good approximation, straight. They are then *wrapped* around the vortex in the manner shown in Fig. 4. Should the

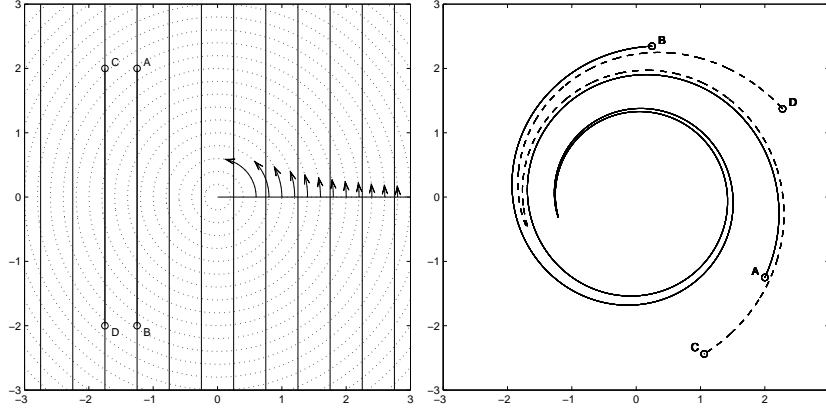


Figure 4. The evolution of two stretches of different material lines, AB and CD, in the flow due to a point vortex located at the centre. Dashed lines in the left panel mark the streamlines of the flow. Each of the two intervals, originally rectilinear, is wound into a double spiral (right panel). As time progresses, the spirals are increasingly tight and the separation of the two material lines decreases like t^{-1} .

scalar be non-diffusive, this spiral wind-up would continue forever. In Fig. 4 we see that the distance between given isolines decreases with time. It is proportional to t^{-1} , just like for a single Fourier mode in *linear* shear (cf. eqn. 13). Such decrease in the radial length scale boosts diffusion which eventually prevails. The details of this process inside and outside the vortex are somewhat different, but the essential ingredient, i.e. shear, is present in both regions. Looking at the outer region we can approximate the flow by that of a point vortex and obtain both a steady solution (when one mode is forced by a distant boundary condition) or an unsteady, similarity solution in an unbounded domain (Bajer 1998).

The steady solution describes the balance inside a cylindrical cavity of radius R filled with inviscid liquid of finite thermal diffusivity. The motion is irrotational but for a line vortex of circulation Γ on the axis. Uniform temperature gradient, $T = T_0 y = T_0 r \sin \theta$, is imposed on the solid surface of the cylinder. This surprisingly simple solution of Eq. (1) with $\mathbf{u} = \Gamma/(2\pi r)\hat{\mathbf{e}}_\theta$,

$$T = T_0 \text{Re} \left[f(r, t) e^{i\theta} \right], \quad (22a)$$

$$f(r, t) = f(r) = -i \left(\frac{r}{R} \right)^{\sqrt{1+iPe}}, \quad Pe = \frac{\Gamma}{\kappa}, \quad (22b)$$

describes, in particular, a thermal boundary layer on the cylinder surface with isotherms wound into a double logarithmic spiral and, also, the

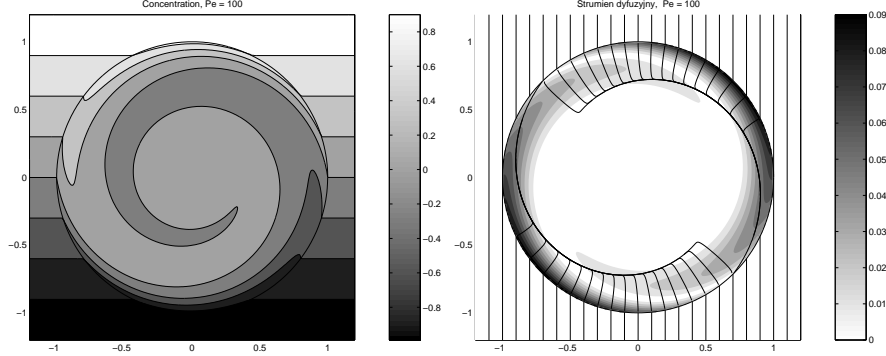


Figure 5. Point vortex in the initially uniform temperature gradient. Boundary condition fixes one mode which makes a steady state possible. The left panel shows isotherms being wound into double logarithmic spirals in a thermal boundary layer on the surface of the cylinder (lighter colours correspond to warmer fluid). The right panel shows the heat flux expelled from the central region (solid lines - integral curves of the heat flux; grey scale - magnitude of the heat flux).

expulsion of the heat flux from the central region (Fig. 5). A straightforward MHD analogue of this solution describes the magnetic flux expulsion, an important phenomenon discovered some forty years ago (Parker 1966; Weiss 1966). Corresponding similarity solutions, $f(r, t) = f(r^2/t)$, for a point-vortex flow (Bajer 1998) and for the Lamb vortex (Pearson & Abernathy 1984; Moore 1985) describe spiral structures *propagating outwards* in an unbounded domain. Spiral structures appear in different contexts in the theory of turbulence and vortex dynamics (Gilbert 1988; Moffatt 1993; Kimura & Herring 2001; Pullin & Lundgren 2001). A gigantic magnetic structure of this kind encompassing the entire solar system is called *Parker's heliospheric spiral* (Parker 1963b).

The wind-up and accelerated diffusion are direct consequences of shear in a vortical flow. This is present both outside a vortex and in its core. However, the radial profiles of the shear in the two regions are different. The shear, defined as the angular velocity gradient, is proportional to r^{-3} in the outer region and to r near the centre of the vortex. The details of the gradient annihilation will thus be different. In particular, the shear *vanishes* at $r = 0$. Interestingly, there is another exact solution of (1) with parabolic core vorticity profile, i.e. $\mathbf{u} = (\alpha_0 r + \alpha_1 r^3)\hat{\mathbf{e}}_\theta$ (where $\alpha_0, \alpha_1 \neq 0$ are arbitrary constants) of the same general form (22a) with (Lighthill 1966; Brunet & Haynes 1995; Bajer, Bassom & Gilbert 2001)

$$f(r, t) = g(t)e^{-i\alpha_0 t - ih(t)r^2}, \quad (23a)$$

$$g(t) = (\cosh \mu t)^{-2}, \quad h(t) = \alpha_1 \mu^{-1} \tanh \mu t, \quad \mu = (1 + i)\sqrt{2\alpha_1/Pe}. \quad (23b)$$

This solution describes the three phases of annihilation of the gradient of a passive scalar inside a vortex: spiral wind-up, accelerated (shear) diffusion moving in from the region of stronger shear towards the centre and the survival of longer-living remnant around the origin where the shear vanishes. The latter is an ‘eigenmode’ decaying without change of shape on a time scale $t_I = t_D Pe^{-1/2}$, intermediate between t_S and t_D (cf. Eq. (16)) (Bajer, Bassom & Gilbert 2001).

4. Vortex-Background Interaction

The interplay between advection and diffusion resulting in the formation of strong gradients and in accelerated diffusion is also a feature of transport of physical quantities that cannot be regarded as passive. Vorticity in a two-dimensional flow is, for example, an ‘active’ scalar field governed by the vorticity equation. How important is its coupling to the transporting velocity field depends on particular circumstances. When vorticity field can be naturally separated into a strong coherent part, Ω and weak background ω (Kevlahan & Farge 1997; Farge, Holschneider & Colona 1990; Beta et al. 2003), the vorticity equation for the background can be linearised and becomes, in some sense, an extension of the advection diffusion equation for ω in the flow \mathbf{U} associated with Ω ,

$$\frac{\partial \omega}{\partial t} + \mathbf{U} \cdot \nabla \omega = \partial(\psi, \Omega) + F + \nu \nabla^2 \omega, \quad \nabla^2 \psi = -\omega. \quad (24)$$

Compared with the Eq. (1) there is the source term, F , that corresponds to a possible external forcing of the flow. There is also an extra term, $\partial(\psi, \Omega)$, corresponding to the *displacement* of the coherent vorticity Ω by the flow $\mathbf{u} = \nabla \psi \times \hat{\mathbf{e}}_z$ associated with the weak background vorticity ω . This is an Eulerian effect which needs to be separated from the ‘genuine’ evolution of the background.

If we choose for Ω the Lamb vortex (diffusing Gaussian vorticity distribution) which is *moving* with prescribed velocity $(\dot{X}(t), \dot{Y}(t))$ and for the initial ω – a distribution with locally uniform gradient, we find that there is only one choice of $(X(t), Y(t))$ consistent with the far-field boundary conditions. We then obtain both the evolution of the background *and* the motion of the strong vortex.

An important conclusion is that a single, strong coherent vortex immersed in a non-uniform weak background vorticity is set in motion by the flow associated with a perturbation of the background that the strong vortex creates (Bajer, Bassom & Gilbert 2004). The vortex also homogenises the background around itself, thus making a ‘hole’ in the

background vorticity gradient. Therefore, the viscous solution of the linearised vorticity equation confirms Batchelor's general prediction about uniformisation of vorticity in flows with closed streamlines (Batchelor 1956).

Acknowledgement

Much of the material presented in this review relates to the collaborative work with Andrew Bassom and Andrew Gilbert that I enjoyed over several years. I am indebted to Keith Moffatt for drawing my attention to a range of focal physical problems and for sharing his insights.

The support from the Centre of Excellence in Small Scale Atmospheric Research, CESSAR (EU grant no EVK2-CT-2002-80010), is gratefully acknowledged.

References

- K. Bajer, Flux expulsion by a point vortex, *Eur. J. Mech. B/Fluids* **17**(4):653–664, 1998.
- K. Bajer, Abundant singularities, *Fluid Dyn. Res.* Submitted, 2004.
- K. Bajer, A.P. Bassom, and A.D. Gilbert, Accelerated diffusion in the centre of a vortex, *J. Fluid Mech.* **437**:395–411, 2001.
- K. Bajer, A.P. Bassom, and A.D. Gilbert, Vortex motion in a weak background shear flow. *J. Fluid Mech.* **509**:281–304, 2004.
- K. Bajer, H.K. Moffatt, On the effect of a central vortex on a stretched magnetic flux tube, *J. Fluid Mech.* **339**:121–142, 1997.
- K. Bajer, and H.K. Moffatt, Tubes, Sheets and Singularities in Fluid Dynamics, Kluwer, 2002.
- G.K. Batchelor, On steady laminar flow with closed streamlines at large Reynolds number, *J. Fluid Mech.* **1**:177–190, 1956.
- C. Beta, K. Schneider, M.Farge, and H. Bockhorn, Numerical study of mixing of passive and reactive scalars in two-dimensional turbulent flows using orthogonal wavelet filtering, *Chem. Eng. Sci.* **58** (8):1463–1477, 2003.
- G. Brunet, and P.H. Haynes, The non-linear evolution of disturbances to a parabolic jet, *J. Atmos. Sci.* **52**:464–477, 1995.
- S. Childress and A.D. Gilbert, *Stretch, Twist, Fold: The Fast Dynamo*, Springer, 1995.
- M. Farge, M. Holschneider, J.F. Colona, Wavelet analysis of coherent structures in two-dimensional turbulent flows, [In:] *Topological Fluid Mechanics* (ed. H.K. Moffatt & A. Tsinober), Cambridge University Press, 1990.
- P. Flohr, J.C. Vassilicos, Accelerated scalar dissipation in a vortex, *J. Fluid Mech.* **348**:295–317, 1997.
- A.D. Gilbert, Spiral structures and spectra in two-dimensional turbulence, *J. Fluid Mech.* **193**:475–497, 1988.
- N.K.R. Kevlahan, M. Farge, Vorticity filaments in two-dimensional turbulence: creation, stability and effect, *J. Fluid Mech.* **346**:49–76, 1997.

- Y. Kimura and J.R. Herring, Gradient enhancement and filament ejection for a non-uniform elliptic vortex in two-dimensional turbulence, *J. Fluid Mech.* **439**:43–56, 2001.
- M.J. Lighthill, Initial development of diffusion in a Poiseuille flow, *J. Inst. Maths. Applics.* **2**:87–108, 1966.
- D. Linardatos, Determination of 2-dimensional magnetostatic equilibria and analogous Euler flows, *J. Fluid Mech.*, **246**:569–591, 1993.
- J.C. McWilliams, The emergence of isolated coherent vortices in turbulent flow, *J. Fluid Mech.* **146**:21–434, 1984.
- H.K. Moffatt, Magnetostatic equilibria and analogous Euler flows with arbitrary complex topology, *J. Fluid Mech.* **159**:359–378, 1985.
- H.K. Moffatt, Structure and stability of solutions of the Euler equations: a Lagrangian approach, *Phil. Trans. Roy. Soc. A* **333**:321–342, 1990.
- H.K. Moffatt, Spiral structures in turbulent flows, [in:] *New Approaches and Concepts in Turbulence (Monte Verità)*, Birkhauser 1993.
- H.K. Moffatt and H. Kamkar, On the time-scale associated with flux expulsion, [in:] *Stellar and Planetary Magnetism*, pp.91–97. Gordon & Breach, 1983.
- H.K. Moffatt, S. Kida, and K. Ohkitani, Stretched vortices – the sinews of turbulence: high Reynolds number asymptotics, *J. Fluid Mech.* **259**:241–264, 1994.
- H.K. Moffatt and R. Ricca, Helicity and the Călugăreanu invariant, *J. Proc. Roy. Soc. A*, **439**:411–429, 1992.
- D.W. Moore, The interaction of a diffusing vortex and an aligned shear flow, *Proc. R. Soc. Lond. A* **399**:367–375, 1985.
- E.N. Parker, Sweet’s mechanism for merging magnetic fields in conducting fluids, *J. Geophys. Res.* **62**:509–520, 1957.
- E.N. Parker, Dynamics of the interplanetary gas and magnetic fields, *Astrophys. J.* **128**:664–676, 1958.
- E.N. Parker, The solar-flare phenomenon and the theory of reconnection and annihilation of magnetic fields. *Astrophys. J. Suppl.* **8**:177–211, 1963a.
- E.N. Parker, *Interplanetary Dynamical Processes*, Wiley-Interscience, New York 1963b.
- R.L. Parker, Reconnection of lines of force in rotating spheres and cylinders, *Proc. Roy. Soc. A*, **291**:60–72, 1966.
- C.F. Pearson and F.H. Abernathy, Evolution of the flow field associated with a stream-wise diffusing vortex, *J. Fluid Mech.* **146**:271–283, 1984.
- D.I. Pullin and T.S. Lundgren, Axial motion and scalar transport in stretched spiral vortices, *Phys. Fluids*, **13**(9):2553–2563, 2001.
- P.B. Rhines, W.R. Young, How rapidly is a passive scalar mixed within closed streamlines? *J. Fluid Mech.* **133**:133–145, 1983.
- N.O. Weiss, The expulsion of magnetic flux by eddies, *Proc. Roy. Soc. Lond. A* **293**:310–328, 1966.

WAVE-VORTEX INTERACTIONS IN THE ATMOSPHERE, AND CLIMATE PREDICTION

Onno Bokhove

Numerical Analysis and Computational Mechanics, Department of Applied Mathematics IMPACT, University of Twente, P.O. Box 217, Enschede, The Netherlands

`o.bokhove@math.utwente.nl`

Abstract Can we construct an accurate atmospheric climate model with a balanced model representing its fluid mechanics, and with dissipative as well as non-dissipative parameterization schemes for the gravity-wave activity? To address this question, we focus our attention on a $1\frac{1}{2}$ -layer atmospheric model with an isentropic troposphere and isothermal stratosphere. We investigate parcel dynamics in a hybrid Eulerian-Lagrangian formulation, potential vorticity conservation, static stability, linear modes and the concept of balanced flow; and briefly discuss wave-vortex interactions and recent advances in numerical solution techniques.

Keywords: hybrid Eulerian-Lagrangian fluid parcel dynamics, linear modes, balanced models, gravity waves, weather and climate prediction

Introduction

Numerical weather and climate prediction is complicated because only the flow scales larger than at least $\sim 10 \times 10 \times 1 \text{ km}^3$ can be resolved to date. When we use the (inviscid) primitive Navier-Stokes equations on these scales, the commonly used (semi-Lagrangian) numerical schemes implicitly filter all acoustic waves and some of the gravity-wave (GW) motion. The rapid small-scale three-dimensional turbulence is then certainly not resolved. Consequently, also the feedback of the unresolved wave and (quasi-two-dimensional) turbulent motions on the large-scale dynamics requires parameterization.

A lot of attention has been paid to simplified or balanced versions of the primitive equations, in which preservation of the conservation laws (of the inviscid dynamics) such as mass, energy and potential vorticity (PV) has been advocated to enhance the stability of these so-called ba-

lanced models. The large-scale flow is generally close to hydrostatic and geostrophic balance; the former due to the anisotropy of horizontal and vertical scales and the latter due to the rapid rotation of the Earth, both in these balanced models (by default) and the numerical integration schemes used. Consequently, one has a choice to use either the primitive equations or balanced models.

Birner et al. (2002) observed that vertical temperature profiles are nearly constant in the stratosphere with a distinct kink at the tropopause between the troposphere and stratosphere. To analyze several properties of atmospheric flows, we therefore derive a conceptual model of the atmosphere with an isentropic troposphere and isothermal stratosphere, where the entropy or potential temperature θ and temperature T are constant, respectively. Subsequently, we illustrate the concept of balance by deriving a balanced model describing only the vortical motion from this so-called “ θ - T -model”.

A novel derivation of this θ - T -model from the three-dimensional Euler equations, using a combination of asymptotic methods and physical simplifications, is given in the framework of a hybrid Eulerian-Lagrangian description of a fluid parcel (Section 1). This hybrid formulation of the Euler equations (Dixon and Reich, 2004) describes the Hamiltonian dynamics of each parcel as a dynamical system with six degrees of freedom with the internal and potential energy as function of space and time. The formulation is passive when this function is given. In contrast, an integral equation for the density using the Jacobian between Eulerian and Lagrangian space links the dynamics of all fluid parcels into a dynamically consistent continuum.

In the linearized θ - T -model, three time derivatives (or four in the parcel framework) in the model give rise to a pair of fast GW modes and one slow geostrophic mode, whose eigen-periods are separated in time on the f -plane. However, the dynamics are nonlinear and there may be a conversion of energy and momentum between these slow and fast modes. In Section 2 (i.e., Fig. 4), this is illustrated in simulations of the nonlinear dynamics initialized by a linear mode at finite amplitude, in which a simple hydraulic, dissipative wave-breaking parameterization is used.

In the nonlinear dynamics, the slow modes survive approximately on a slow manifold of lower dimension. Balanced models of vortical dynamics describe the slow motion on a slow manifold (Section 3), on which the dimension of phase space is reduced by two thirds (or half in the parcel framework) due to the removal of the pair of (fast) GW modes. Within the Eulerian-Lagrangian framework of parcel dynamics, we illustrate the derivation of (Hamiltonian) balanced models using two velo-

city constraints which arise in asymptotic expansions in a relevant small parameter (such as the Rossby or Froude number). These constraints define the reduction of the phase space to the slow or slaving manifold. We compare balanced and unbalanced trajectories in simplified simulations in Fig. 1(b). The generation of gravity waves by instabilities of a balanced flow, or the absorption of gravity waves by the nearly balanced mean flow through wave-vortex interactions indicate, however, that the slow manifold is not an exact manifold (Bühler and McIntyre, 2003; Vanneste and Yavneh, 2004).

In balanced models, these unbalanced GW effects can only be included by explicitly parameterizing the gravity waves. Likewise, in numerical weather and climate prediction small-scale, unresolved gravity waves require parameterization. We finish by briefly discussing idealized wave-vortex interactions and some recently developed numerical schemes for geophysical flows (Sections 4 and 5), and their relevance to General Circulation Models (GCMs).

1. Eulerian-Lagrangian Dynamics of Fluid Parcels

Three-dimensional compressible Euler equations

Consider Newton's equations of motion for a fluid parcel with position $\mathbf{x} = (x, y, z)^T$ and velocity $\mathbf{u} = (u, v, w)^T$ [$(\cdot)^T$ denotes the transpose] in a rotating reference frame with rotation vector $\boldsymbol{\Omega}$

$$\frac{d\mathbf{x}}{dt} = \mathbf{u} = \frac{\partial H_{3D}}{\partial \mathbf{u}}, \quad \frac{d\theta}{dt} = 0 \quad \text{and} \quad (1)$$

$$\frac{d\mathbf{u}}{dt} = -\theta \nabla \Pi - \nabla \phi - 2\boldsymbol{\Omega} \times \mathbf{u} = -\frac{\partial H_{3D}}{\partial \mathbf{x}} - 2\boldsymbol{\Omega} \times \frac{\partial H_{3D}}{\partial \mathbf{u}} \quad (2)$$

with the parcel energy (extending Frank and Reich, 2003)

$$H_{3D}(\mathbf{x}, \mathbf{u}, \theta, t) = |\mathbf{u}|^2/2 + \theta \Pi(\mathbf{x}, t) + \phi(\mathbf{x}), \quad (3)$$

three-dimensional gradient ∇ ; external potential ϕ , *e.g.*, $\phi = gz$; potential temperature $\theta = T(p/p_r)^{-\kappa}$; temperature $T(\mathbf{x}, t)$; pressure $p(\mathbf{x}, t)$ and reference pressure p_r ; and Exner function $\Pi = c_p(p/p_r)^\kappa$ for an ideal gas $p = \rho RT$ with density $\rho(\mathbf{x}, t)$, gas constant R , specific heat at constant pressure c_p , and $\kappa = R/c_p$. Note that $\theta \nabla \Pi = (1/\rho) \nabla p$, so that (2) attains its usual form (Dixon and Reich, 2004). We can write (1)–(3) as a non-canonical Hamiltonian system $dq/dt = J \partial H_{3D} / \partial q$ with state vector $q = (x, y, z, u, v, w, \theta)^T$ and a skew-symmetric tensor J . The state vector q is a function of time and fluid labels $\mathbf{a} = (a, b, c)^T =$

$(a_1, a_2, a_3)^T$, so $q = q(\mathbf{a}, t)$. If the parcel energy is a function of q and t , then (1)–(3) is non-autonomous.

The continuum character of the fluid, albeit hidden in the representation (1)–(3), appears through the density

$$\begin{aligned} \rho(\mathbf{x}, t) &= \int_D \rho(\mathbf{x}', t) \delta(\mathbf{x} - \mathbf{x}') dx' dy' dz' \\ &= \int_{D_0} \rho_0(\mathbf{a}) \delta(\mathbf{x} - \mathbf{x}'(\mathbf{a}, t)) da db dc \end{aligned} \quad (4)$$

with $\mathbf{x}' = \mathbf{x}'(\mathbf{a}, t)$ in a domain D or D_0 , since the Jacobian between label and position space is proportional to the inverse density

$$\rho_0(\mathbf{a})/\rho(\mathbf{x}, t) = \det |\partial \mathbf{x} / \partial \mathbf{a}|. \quad (5)$$

Hence, an element of mass dm relates to the density as follows:

$$dm = \rho(\mathbf{x}, t) dx dy dz = \rho_0(\mathbf{a}) da db dc. \quad (6)$$

A common choice is $\rho(\mathbf{x}, 0) = \rho_0(\mathbf{a})$ and $\mathbf{x}(\mathbf{a}, 0) = \mathbf{a}$. The system (1)–(4) is closed and represents the fluid as a continuum. From (1), (4) and (5), we can derive the continuity equation

$$d\rho(\mathbf{x}, t)/dt = \partial_t \rho(\mathbf{x}, t) + \mathbf{u} \cdot \nabla \rho(\mathbf{x}, t) = -\rho(\mathbf{x}, t) \nabla \cdot \mathbf{u}(\mathbf{x}, t). \quad (7)$$

Similarity to 2D vorticity dynamics. We note that this hybrid description is akin to the (more familiar) situation in inviscid, incompressible, two-dimensional vorticity dynamics, where the passive or kinematic advection of each fluid parcel is described by a given stream function $\psi(x, y, t)$ as Hamiltonian with horizontal coordinates $\mathbf{x}_h = (x, y)^T$ and time t . Thus, $dx/dt = u = -\partial\psi/\partial y$ and $dy/dt = v = \partial\psi/\partial x$. In contrast, a dynamically consistent formulation appears when the vorticity $\omega = \nabla_h^2 \psi$ is conserved on each fluid parcel and linked to the continuum of parcels using

$$\omega(x, y, t) = \int_{D_0} \omega_0(a, b) \delta(\mathbf{x}_h - \mathbf{x}'_h(a, b, t)) da db$$

with domain D_0 , delta function $\delta(\cdot)$, parcel position $\mathbf{x}'_h(a, b, t)$, and $\omega_0(a, b)$ denoting the initial distribution of vorticity on parcels identified by labels a and b . Given ω on each parcel, we calculate ψ . Hence, the dynamical description is closed, since incompressibility yields $dx dy = da db$. With $\mathbf{v} = (u, v)^T$ and gradient ∇_h in the horizontal direction, we find $d\omega/dt = \partial\omega/\partial t + \mathbf{v} \cdot \nabla_h \omega = 0$.

Static stability. To illustrate the formulation of the hybrid parcel dynamics, parcel oscillations in a static atmosphere with given parcel energy $H_{3D} = |\mathbf{u}|^2/2 + \theta\Pi(z) + gz$ are shown in Fig. 1(a). We choose $\Pi = \Pi(z)$ with potential temperature $\theta = \theta_g(z)$ in its thermodynamics to satisfy hydrostatic balance $\theta_g(z)\partial\Pi/\partial z = -g$. Hence, we find $d^2z'/dt^2 = -N^2z'$ for small amplitude oscillations with $z' = z - z_r$ and a reference level z_r . Oscillations are then stable with Brunt–Väisälä frequency N , when $N^2 = [g(d\theta_g/dz)/\theta_g]_{z=z_r} > 0$, neutral when $N^2 = 0$, and unstable when $N^2 < 0$. Note that θ is conserved on each parcel of air and generally different from $\theta_g(z)$.

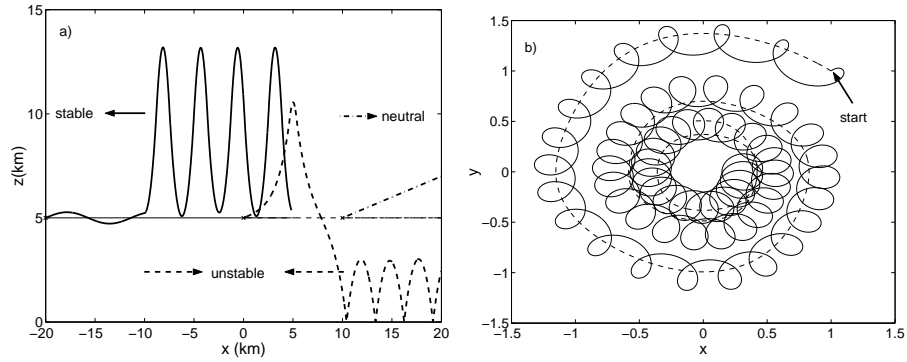


Figure 1. (a) Three trajectories are shown of parcel oscillations in the atmosphere for a given parcel energy. The stratification of the atmosphere is statically stable ($d\theta/dz = \text{cst.} > 0$) for $x < -10$ km, unstable ($d\theta/dz = \text{cst.} < 0$) for $-10 \text{ km} < x < 10$ km, and neutral (constant θ) for $x > 10$ km and $z < 10$ km, and isothermal and stable for $z > 10$ km. The stable oscillations have a period of 10.84 min. When the atmosphere is hydrostatic, these oscillations disappear as the thin lines at $z_r = 5$ km illustrate. (b) 41.7 days of (dimensionless) geostrophically balanced and unbalanced Hamiltonian motion of a particle in a simple, given Montgomery potential $M_2(x, y)$ starting at $(x, y) = (1, 1)$. The predictability horizon lies around 14 days whereafter the balanced (dashed lines) and unbalanced (solid lines) trajectories depart from one another significantly.

Hydrostatic primitive equations

The atmosphere is shallow for larger scales, and the aspect ratio δ between vertical and horizontal length and velocity scales (D, W and L, U) arises as a small parameter $\delta = W/U \ll 1$. At leading order in δ , we find from the scaled version of system (1)–(4) the dynamics and

hydrostatic balance

$$\frac{d\mathbf{x}_h}{dt} = \mathbf{v} = \frac{\partial H_p}{\partial \mathbf{v}}, \quad (8)$$

$$\frac{d\mathbf{v}}{dt} = -\theta \nabla_h \Pi - f \hat{\mathbf{z}} \times \mathbf{v} = -\frac{\partial H_p}{\partial \mathbf{x}_h} - f \hat{\mathbf{z}} \times \frac{\partial H_p}{\partial \mathbf{v}}, \quad (9)$$

$$\frac{d\theta}{dt} = 0 \quad \text{and} \quad 0 = -\theta \partial \Pi / \partial z - g \quad (10)$$

with $f = 2\Omega_3$, $\hat{\mathbf{z}}$ the unit vector in the vertical direction, and the hydrostatic parcel energy

$$H_p(x, y, z, u, v, \theta, t) = (u^2 + v^2)/2 + M(x, y, z, t) \quad (11)$$

with Montgomery potential $M = \theta \Pi(x, y, z, t) + g z$. The vertical velocity dz/dt follows by insisting hydrostatic balance persists in time. We use these interim results next in the derivation of the conceptual $1\frac{1}{2}$ - and 2-layer models.

A $1\frac{1}{2}$ - and 2-layer atmosphere

Birner et al. (2002) measured the vertical temperature profiles which suggest a conceptual model with an isentropic troposphere and an isentropic or isothermal stratosphere. We therefore simplify the stratification of the atmosphere into an isentropic tropospheric layer and an isentropic or isothermal stratospheric layer, see Fig. 2(a). In this figure, we define the variables and constants used subsequently and denote their dependence, if any, on x, y and t .

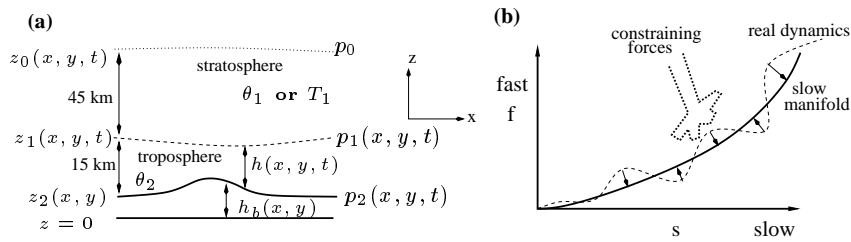


Figure 2. (a) Sketch of a simplified atmosphere with an isentropic troposphere and isentropic or isothermal stratosphere. p_0 is a passive and constant pressure, and p_1 and p_2 are active pressures. (b) The slow manifold sketched has a third (or half) of the dimension of the entire Eulerian (or Lagrangian) phase space, with fast and slow variables f and s . Constraining forces, “the hand”, place the full dynamics on the manifold. When s and f are small, the dynamics is linear and separated in time such that $f \rightarrow 0$, as it is sketched.

Integrating hydrostatic balance $\theta \partial \Pi / \partial z + g = 0$ in the tropospheric layer from $z = z_2 = h_b$ to z with $z_2 < z < z_1$, we obtain the Montgomery potential

$$M_2(p_2) = \theta \Pi + g z = c_p \theta (p/p_r)^\kappa + g z = c_p \theta_2 (p_2/p_r)^\kappa + g h_b. \quad (12)$$

In an isentropic stratospheric layer one finds likewise, by integrating from z_1 to z with $z_1 < z < z_0$ and using (12) at $z = z_1$ with $p(x, y, z_1, t) = p_1$, that

$$\begin{aligned} M_1(p_1, p_2) &= \theta \Pi + g z = g(z_0 - Z_0) = c_p \theta (p/p_r)^\kappa + g z \\ &= c_p (\theta_1 - \theta_2) (p_1/p_r)^\kappa + c_p \theta_2 (p_2/p_r)^\kappa + g(h_b - Z_0), \end{aligned} \quad (13)$$

while in an isothermal stratospheric layer, one obtains similarly

$$\begin{aligned} M_1(p_1, p_2) &= \theta \Pi + g z = g(z_0 - Z_0) = c_p \theta (p/p_r)^\kappa + g z \\ &= RT_1 \ln(p_1/p_0) + c_p \theta_2 ((p_2/p_r)^\kappa - (p_1/p_r)^\kappa) + g(h_b - Z_0). \end{aligned} \quad (14)$$

Note that, without any loss of generality, we have added a constant reference level Z_0 to which we can fix the top of the stratospheric layer z_0 at a later stage. Any initial z -independence in each layer remains intact, so only two parcels in a vertical column of fluid suffice for closure. Hence, the two-layer tropospheric-stratospheric model is the hydrostatic model (8)–(9) applied in each layer

$$\frac{d\mathbf{x}_\alpha}{dt} = \mathbf{v}_\alpha = \frac{\partial H_\alpha}{\partial \mathbf{x}_\alpha}, \quad (15)$$

$$\frac{d\mathbf{v}_\alpha}{dt} = -f \hat{\mathbf{z}} \times \mathbf{v}_\alpha - \nabla_h M_\alpha = -f \hat{\mathbf{z}} \times \frac{\partial H_\alpha}{\partial \mathbf{v}_\alpha} - \frac{\partial H_\alpha}{\partial \mathbf{x}_\alpha} \quad (16)$$

with $\alpha = 1, 2$; $\mathbf{x} = (x, y)_\alpha^T$ and parcel energy

$$H_\alpha(x_\alpha, y_\alpha, u_\alpha, v_\alpha, t) = (u_\alpha^2 + v_\alpha^2)/2 + M_\alpha(x_\alpha, y_\alpha, t). \quad (17)$$

Closure of these two-layer equations is reached via the layer pseudo-density

$$\sigma_\alpha(x, y, t) = \int_{D_{H_0}} \sigma_0(a, b) \delta(\mathbf{x} - \mathbf{x}'_\alpha(a, b, t)) da db \quad (18)$$

relating the horizontal label and position spaces with (using $\partial p / \partial z = -\rho g$)

$$dm = \rho dx dy dz = -dx dy dp / g = da db dc \quad (19)$$

$$\Delta m_2 = \sigma_2 dx dy = [(p_2 - p_1) / g] dx dy = \sigma_{2_0}(a, b) da db \quad (20)$$

$$\Delta m_1 = \sigma_1 dx dy = [(p_1 - p_0) / g] dx dy = \sigma_{1_0}(a, b) da db \quad (21)$$

$$\sigma_{\alpha_0} / \sigma_\alpha = \partial_x a \partial_y b - \partial_y a \partial_x b. \quad (22)$$

We emphasize that in each layer the Eulerian velocity is independent of depth, so $\mathbf{v}_\alpha = \mathbf{v}_\alpha(x, y, t)$. Hence $\partial_z \mathbf{v}_\alpha$ remains zero once it was initially so.

Again, we can derive continuity equations $\partial_t \sigma_\alpha + \nabla_h \cdot (\sigma_\alpha \mathbf{v}_\alpha) = 0$ and a materially conserved PV: $dQ_\alpha/dt = 0$ with

$$Q_\alpha = (f + \hat{\mathbf{z}} \cdot \nabla \times \mathbf{v}_\alpha) / \sigma_\alpha.$$

$1\frac{1}{2}$ -layer models. When the stratospheric layer is much deeper than the tropospheric layer, *e.g.*, 45 km versus 15 km, we approximate the top z_0 to Z_0 and neglect the motion in the stratospheric layer. Thus, from (13) or (14) one finds $M_1(p_1, p_2) = 0$. The stratospheric pressure p_1 remains active, but the dynamics [(15) and (16) for $\alpha = 2$] is evolved in the tropospheric layer. The bottom pressure p_2 used to define M_2 [(12)] in the tropospheric momentum equations (16) is then determined from $\sigma_2 = (p_2 - p_1)/g$ and $M_1(p_1, p_2) = 0$.

Static stability. Static stability means that a fluid parcel perturbed in the vertical oscillates around a certain height with the Brunt-Väisälä frequency N rather than taking off. The eigen-values a of the $1\frac{1}{2}$ -layer equations [(15) and (16) for $\alpha = 2$ with $\sigma_2 = (p_2 - p_1)/g$ and $M_1(p_1, p_2) = 0$] are

$$a^2 \propto \begin{cases} c_p \kappa (\theta_1 - \theta_2) (p_1/p_r)^{\kappa-1} (p_2 - p_1)/p_r & (\theta_2 - \theta_1\text{-model}) \\ (p_2 - p_1) (p_r R T_1 / p_1 - c_p \theta_2 \kappa (p_1/p_r)^{\kappa-1}) & (\theta_2 - T_1\text{-model}). \end{cases} \quad (23)$$

These eigen-values are real when the atmosphere is statically stable or $d\theta/dz > 0$: this occurs when $\theta_1 > \theta_2$ in the $\theta_2 - \theta_1$ -model, and when $T_1 > \theta_2 (p_1/p_r)^\kappa$ in the $\theta_2 - T_1$ model. While the $\theta_2 - \theta_1$ model remains statically neutral or stable if it is initially so, the stability of the $\theta_2 - T_1$ model thus depends on $p_1(x, y, t)$.

2. Linear Modes

Linearized around a “rest depth” H with $\sigma = \sigma_2 = H(x, y) + \eta$, the $1\frac{1}{2}$ -layer models [(15) and (16) for $\alpha = 2$] become

$$\partial_t \mathbf{v} = -f \hat{\mathbf{z}} \times \mathbf{v} - g' \nabla_h \eta \quad \text{and} \quad \partial_t \eta + \nabla_h \cdot (H \mathbf{v}) = 0 \quad (24)$$

with velocity $\mathbf{v} = \mathbf{v}'_2$ and effective gravity g' . This linearized system is akin to the classical, linearized shallow water equations with (for $h_b = 0$)

$$g' \propto \begin{cases} \frac{(\theta_1 - \theta_2) P_1^{\kappa-1}}{(\theta_1 - \theta_2) P_1^{\kappa-1} + \theta_2 P_2^{\kappa-1}} & (\theta_2 - \theta_1\text{-model}) \\ \frac{p_r R T_1 / P_1 - c_p \kappa \theta_2 (P_1/p_r)^{\kappa-1}}{R T_1 / P_1 + c_p \kappa \theta_2 (P_2^{\kappa-1} - P_1^{\kappa-1})} & (\theta_2 - T_1\text{-model}) \end{cases} \quad (25)$$

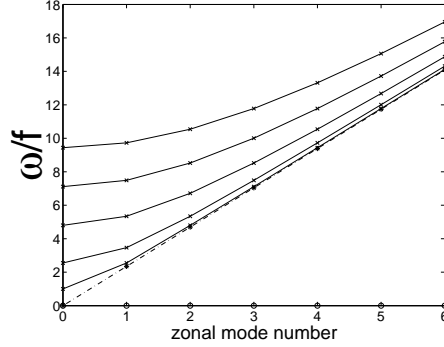


Figure 3. Dispersion relation of linear modes in a periodic channel for the θ_2 - θ_1 -model.

and the rest state $H = (P_2 - P_1)/g$, which is consistent with (23). In a periodic channel with constant H , the linear modes using $\eta \propto e^{i(kx + \omega t)}$ ($i^2 = -1$) consist of: a vortical or geostrophic mode with frequency $\omega = 0$, Poincaré GW modes with $\omega^2 = f^2 + g' H (k^2 + l^2)$, and counterclockwise propagating boundary-trapped Kelvin modes with $\omega^2 = g' H k^2$ (for constant $f > 0$). We observe in the dispersion diagram in Fig. 3 that there is a time-scale separation between the vortical and GW modes, except perhaps for the lowest-order Kelvin modes and the geostrophic solution.

As usual, a linear mode analysis is limited in scope. First, the dynamics is nonlinear, so there is no clear notion of a time scale separation anymore. Nonlinear “slow” dynamics can have high-frequency overtones triggering resonances or interactions with “fast” dynamics. Second, approaching the equator, the effective Coriolis parameter $f \rightarrow 0$, giving rise to equatorial Kelvin waves and mixed Rossby-gravity waves or mixed slow-fast linear modes. Consequently, linear Kelvin or gravity mode solutions of larger amplitude used as initial condition, can develop vortex motion and, vice versa, linear geostrophic or Rossby modes can develop GW motion from instabilities. Mixed fast-slow motion emerges in simulations, see Fig. 4, of the nonlinear evolution of a linear Kelvin mode solution in a zonally periodic channel used as initial condition. In particular PV is constant (in time and/or space) for a Kelvin or Poincaré mode,

$$Q_2 = Q = (f + \hat{\mathbf{z}} \cdot \nabla \times \mathbf{v})/\sigma = f/H \quad \text{and} \quad \partial_t Q + (\mathbf{v} \cdot \nabla_h)Q = 0, \quad (26)$$

before the occurrence and parameterization of wave breaking. These constant PV regions are then distinguished, ideally, from regions where

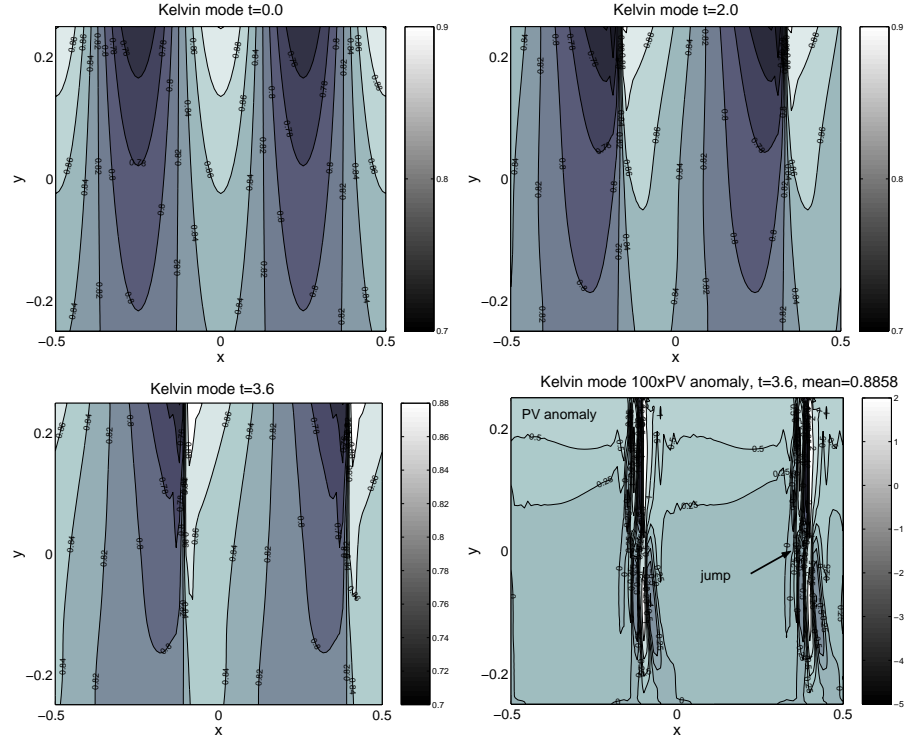


Figure 4. Top: contour plots of σ in simulations of the 1.5-layer θ_2 - θ_1 -model with shock-capturing numerics which, however, do not conserve absolute vorticity σQ . Bottom: simulations displaying σ (left) and $100\times$ PV anomaly ($Q - f/H$) (right) at the final time. Non-dimensional quantities are displayed, for example in a domain of 4000×2000 km with $z_1 \approx 15$ km and $Z_0 \approx 60$ km.

a wave breaking parameterization generates non-constant PV anomalies $Q - f/H$ (*cf.*, Peregrine and Bokhove, 1998).

3. Balanced Dynamics

The concept of balanced large-scale flow arises from the observation that at mid-latitudes the atmosphere and oceans are in approximate geostrophic balance, and near the equator the Earth's rotation remains influential. Locally — due to topography, strong (tropical) convection, dissipative and non-dissipative (GW) instabilities — balance often fails. The notion of balance may be formalized in various ways: small Rossby and Froude numbers are identified from measurements, observations or simulations, and then used in scaling arguments. Subsequently, a perturbative or iterative approach is applied to approximate the full or parent

model. The resulting dynamics evolves on a slow or slaving manifold of reduced dimensionality, see the sketch in Fig. 2(b).

The preservation of certain conservation laws, or the variational or Hamiltonian structure, may be imposed heuristically in these balanced approximations. Whether the conservative or non-conservative approach to balanced dynamics is better, remains undecided and depends on the, perhaps subjective, value placed on (point-wise) accuracy, and long-term stability.

Geostrophic balance denotes the alignment of the wind vectors along the pressure or Montgomery potential isobars. To derive this leading order balance, we rewrite the $1\frac{1}{2}$ -layer equations [(16) for $\alpha = 2$] and drop the layer subscripts

$$\frac{du_i}{dt} = \frac{f}{R} \epsilon_{ij} u_j - \frac{1}{R} \partial_{x_i} M = \frac{f}{R} \epsilon_{ij} \frac{\partial H}{\partial u_i} - \frac{1}{R} \frac{\partial H}{\partial x_i} \quad (27)$$

with the permutation symbol ϵ_{ij} , $\mathbf{v} = (u_1, u_2)^T$ and $i, j = 1, 2$. The Rossby number $R = U/(fL) \ll 1$ is placed in (27) at the relevant locations, as the ratio of the GW time scale $1/f$ and the vortical time scale L/U with typical length and velocity scales L and U . At leading order in R , we find geostrophic balance from (27) as a constraint on the velocity with M/f being a stream function in the balance relations $u = -\partial_y M/f$ and $v = \partial_x M/f$. In general, (higher-order) velocity constraints obtain the form

$$\phi_i = u_i - u_i^C[\sigma(\mathbf{x})] \stackrel{e.g.}{=} u_i + \frac{1}{f} \epsilon_{ij} \partial_{x_j} M, \quad (28)$$

in which $u^C[\sigma]$ operates (non-locally) on σ and, hence, through σ on the parcel coordinates x and y . Next, we use these constraints to derive balanced models.

Conservative balanced models: slaved Hamiltonian approach

We illustrate the derivation of Hamiltonian balanced models in the hybrid parcel framework. The variables (x_i, u_i) are transformed to (x_i, ϕ_i) using (28), and a constrained variational derivative is introduced

$$\left. \frac{\partial H}{\partial x_i} \right|^C = \frac{\partial H}{\partial x_i} + \frac{\partial H}{\partial u_j} \frac{\partial u_j^C}{\partial x_i}, \quad (29)$$

where $(\cdot)|^C$ denotes that $\phi_i = 0$ in derivatives of x and y . The evolution on the slow manifold of reduced dimensionality becomes, using (15)

and (16),

$$\frac{dx_i}{dt} = \frac{\partial H}{\partial u_i} = u_i \quad \text{and} \quad 0 = \frac{d\phi_i}{dt} = -\frac{\partial H^C}{\partial x_i} + \epsilon_{ij}\sigma Q^C u_j \quad (30)$$

with $\sigma Q^C = f + \partial v^C/\partial x - \partial u^C/\partial y$. The slaved Hamiltonian dynamics on the slow manifold is concisely written as

$$\frac{dx_i}{dt} = (L^{-1})_{ij} \frac{\partial H^C}{\partial x_j} \quad \text{or} \quad \frac{dF^C}{dt} = \frac{\partial F^C}{\partial x_i} (L^{-1})_{ij} \frac{\partial H^C}{\partial x_j} \quad (31)$$

[*cf.* Dirac (1958)] with skew-symmetric matrix $L_{ij} = \epsilon_{ij}\sigma Q^C$ and arbitrary function $F^C = F^C(x, y)$ and $H^C = H(x, y, u^C, v^C)$. Simplified numerical integrations are explained in Fig. 1(b). It is unclear whether the parcel balanced dynamics (31) presented is a didactic simplification, or equivalent to the results for the Eulerian balanced equations in Vanneste and Bokhove (2002).

4. Wave-Vortex Interactions and Numerical Schemes

The parameterization of unresolved gravity waves is a critical component in numerical GCMs. Gravity waves can influence the large-scale dynamics in various ways: (i) breaking gravity waves dissipate energy to small scales and deposit momentum to drive the mean, large-scale flow (McFarlane, 1987); (ii) instabilities of balanced vortical flows locally excite gravity waves, which can transport energy and momentum away (Vanneste and Yavneh, 2004); and (iii) non-dissipative wave-vortex interactions, such as remote recoil, can lead to a cumulative forcing of the mean vortical flow (Bühler and McIntyre, 2003). The crucial question is how to parameterize these unresolved GW-effects, studied hitherto in isolation, in numerical models for large-scale flows on advective time scales, given the resolved large-scale flow.

New numerical schemes have emerged with a focus on improved meshes without pole problem, conservation properties and advection-dominated time integration. Based on gas dynamics and novel finite-element discretizations (Bokhove, 2005; Fig. 4), an impulse formulation of the θ - T -model with 3 prognostic equations can be used, which are shock-capturing but with explicit time stepping limited by the largest GW speed. In atmospheric dynamics, the velocity formulation with 3 prognostic equations is often preferred (Ringler and Randall, 2002). The GW speed is then still the limiting factor. Hamiltonian Particle Mesh methods (HPM) involve (15)–(18) with 4 prognostic equations and 1 integral equation (Frank and Reich, 2003). By smoothing the pseudo-density,

time step restrictions can be lifted. To emphasize the vortical dynamics, a mass-divergence-vorticity formulation is used by Thuburn (1997) and Ringler and Randall (2002) resulting in 3 prognostic and 2 elliptic equations. The advective time step is then used after some numerical stabilization. The approaches by Ringler and Randall conserve mass, energy, potential enstrophy and vorticity. Mass or PV conserving balanced models consist of a prognostic equation and 2–4 elliptic equations of the first and second order. These elliptic inversions are time consuming and require special (multi-grid) techniques.

5. Conclusions

The HPM and related semi-Lagrangian numerical schemes, as well as the ones using vorticity-divergence variables (Frank and Reich, 2003; Thuburn, 1997; and Ringler and Randall, 2002) seem to be most advantageous as they use the larger advective time step, at the expense of introducing an artificial numerical GW-vortex parameterization. It may be a good strategy to test GW-vortex parameterizations in both the balanced models and high-resolution (in space and time) primitive equations. Otherwise, it is unclear to what extent the (artificial) numerical GW parameterizations in the numerical schemes jeopardize the physical ones. Clearly, the potential interplay between physical and (hidden) numerical parameterizations of gravity waves is a research question with important implications for GCMs. Finally, a thorough answer to the initial question whether a balanced model can provide accurate climate predictions needs to be postponed, although Olaguer's (2002) results seem to be encouraging.

Acknowledgments

The criticism of J. Frank and B.J. Geurts has been much appreciated. The θ - T -model originates from an unpublished work with W.T.M. Verkley.

References

- T. Birner, A. Dörnbrack and U. Schumann. How sharp is the tropopause at midlatitudes? *Geophys. Res. Lett.* **29**: 10.1029, 2002.
- O. Bokhove. Flooding and drying in finite-element discretizations of shallow-water equations. Part 1: One dimension. *J. Sci. Comput.* **22**, To be published, 2005.
- O. Bokhove and W.T.M. Verkley. Constrained isentropic models of tropospheric dynamics. Submitted to *Quart. J. Roy. Meteor. Soc.*, 2004.
- O. Bühler and M.E. McIntyre. Remote recoil: a new wave-mean interaction effect. *J. Fluid Mech.* **492**, 207–230, 2003.

- P.A.M. Dirac. Generalized Hamiltonian dynamics. *Proc. Roy. Soc. Lond. A* **246**, 326–332, 1958.
- M. Dixon and S. Reich. Symplectic time-stepping for particle methods. *GAMM*, to appear, 2004.
- J. Frank and S. Reich. Conservation properties of smoothed particle hydrodynamics applied to shallow water equations. *BIT* **43**, 40–54, 2003.
- N.A. McFarlane. The effect of orographically excited gravity wave drag on the general circulation of the lower stratosphere and troposphere. *J. Atmos. Sci.* **44**, 1775–1800, 1987.
- E.P. Olaguer. An efficient 3-D model for global circulation, transport and chemistry. *IMA Vol. Math. Appl.* **130**, 205–276, 2002.
- D.H. Peregrine and O. Bokhove. Vorticity and surf zone currents. *Proceedings of the 26th International Conference on Coastal Engineering 1998, ASCE, Copenhagen.* 745–758, 1998.
- T.D. Ringler and D.A. Randall. A potential enstrophy and energy conserving numerical scheme for solution of the shallow-water equations on a geodesic grid. *Mon. Wea. Rev.* **130**, 1397–1410, 2002.
- J. Thuburn. A PV-based shallow-water model on a hexagonal-icosahedral grid. *Mon. Wea. Rev.* **125**, 2328–2347, 1997.
- J. Vanneste and O. Bokhove. Dirac-bracket approach to nearly-geostrophic Hamiltonian balanced models. *Physica D* **164**, 152–167, 2002.
- J. Vanneste and I. Yavneh. Exponentially small inertia-gravity waves and the breakdown of quasi-geostrophic balance. *J. Atmos. Sci.* **61**, 211–223, 2004.

NEAR-CRITICAL POINT HYDRO-DYNAMICS AND MICROGRAVITY

Daniel A. Beysens

CEA, Service des Basses Températures, Grenoble 

ESPCI, PMMH, 10, rue Vauquelin, 75015, Paris Cedex 05, France

dbeysens@cea.fr

Abstract Near their critical point, fluids exhibit anomalous behavior of thermodynamic parameters (divergence of specific heat, compressibility and expansion coefficients) and transport coefficients (heat conductivity, thermal diffusivity). Weightlessness ("microgravity") environment permits to go very close to the critical point, thus allowing key tests of the Renormalization Group theory to be made. It also results in a very particular hydrodynamics of dense and hyper-compressible gases, where weightlessness experiments play a key role. For instance, a very fast thermalization effect ("Piston effect") is evidenced, where a thermal boundary layer expands and adiabatically heats the whole fluid, leading in some cases to an (apparent) violation of the laws of thermodynamics. Another one is concerned with the use of critical slowing down and microgravity to investigate the dynamics of phase separation with no gravity-induced sedimentation. The key role of the coalescence of domains makes valid only two simple growth laws; they can be successfully applied to a quite different situation, the evolution laws in the well-known biological problem of sorting of the embryonic cells. Other situations are concerned with the effect of vibrations. The investigation of the above thermal and phase transition problems suggest that a periodic excitation can act as a kind of artificial gravity, which induces thermal convection, speeds up phase transition and localizes the liquid and vapor phases perpendicular to it. Some of these phenomena still persist at higher temperature and pressure. Fluids in such supercritical conditions are very appealing to the industry as non-polluting solvents or hosts of chemical reactions with high yield.

Keywords: Critical point, supercritical fluids, phase transition, thermalization, cell sorting, Piston effect, microgravity, vibrations, cell sorting

1. Introduction

It is widely believed that a fluid can exist only as a gas or a liquid. However, there is another state, the "supercritical state", that fluids can exhibit (Fig. 1a). Since Baron Charles Cagniard de La Tour discovered in 1821 that the liquid and gas phases of a carbon dioxide sample became undistinguishable after crossing a "critical" temperature of 31°C and a "critical" pressure of 72 bar, the intriguing properties of this very particular state has motivated a great number of studies.

The critical point co-ordinates vary according to the particular fluid under study. For instance, the critical point of carbon dioxide (CO_2) is observed at 31°C and 72 bar, that of water (H_2O) at 375°C and 225 bar and that of hydrogen (H_2) at 33 K and 13 bar. Above the critical temperature and pressure, supercritical fluids exhibit a number of specific properties (large density, low viscosity, large diffusivity) which make them intermediate between liquids and gases [1]. In addition, their isothermal compressibility and thermal expansion can become very large, especially when they approach the critical point. The highly variable properties of near-critical fluids make them very attractive for studying many phenomena that hold for all fluids because of the critical universality. Supercritical fluids are increasingly used by the food and waste management industry [3] for their solubilization properties (e.g. supercritical CO_2), as host of "cold" combustion (e.g. supercritical water), in energetics (supercritical thermal or nuclear plants), and in astronautics (e.g. storage of cryogenic fluids).

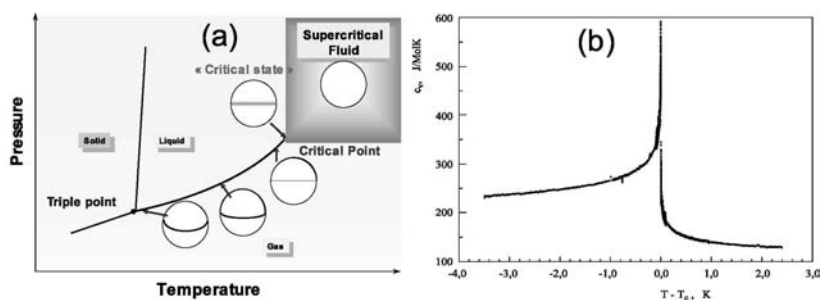


Figure 1. (a): Phase diagram of a pure substance. The supercritical "state" corresponds to a compressed gas that exhibits the density of a liquid. (b): Critical anomaly of the specific heat at constant volume (C_v) measured under zero-gravity in SF_6 (Spacelab D2, 1993). (From [2]).

Near-critical Fluids and Microgravity

Fluids in their near-critical or supercritical state are strongly affected by gravity. As they are highly compressible, gravity compresses them under their own weight. The density varies in the sample, thus preventing a close approach to the critical point to be made, cf. [4].

They exhibit anomalies in the transport of heat so that convection and buoyancy phenomena, often turbulent, appear for even minute temperature gradients. We show in the following that space experiments have enabled new phenomena to be discovered thanks to a close approach to the critical point and the removal of convection and buoyancy.

The effects of gravity can be removed in space thanks to spacecrafts and satellites. On earth, microgravity conditions can be obtained during a short time period in a free fall tower (a few s) and in parabolic flights of planes (20 s) and sounding rockets (2–12 min.). Some other means can be used with liquid mixtures. Liquid mixtures near their consolute critical point exhibit a number of common features with pure fluids, when concentration is replaced by density as an order parameter of the transition. Some aspects can be then studied with binary liquid mixtures that have been made density-matched by partial deuteration [5].

The compensation of gravity forces in simple fluids is more difficult. The large diamagnetism susceptibility of H_2 was used to compensate gravity by a magnetic force, proportional to its density. By using a superconducting coil it became possible to study, without gravity effects, the process of solidification and gas-liquid phase transition over a wide range, from the triple point (13.8 K) to above the critical point (33 K) [6]. A vibration device has also been implemented using a special sapphire sample.

2. Universality and Scaling Laws

An important aspect of the critical region is that most of the anomalies of the thermodynamic and transport properties can be set in the form of scaled, universal (power law) functions with respect to the critical point (CP) coordinates. Then, any results obtained with one single fluid can be immediately generalized to a whole class of systems, the "class of fluids", to which belong also liquid mixtures, including polymer melts and solutions, microemulsions, molten salts, monotectic liquid metals, etc. [1]. This scaling is of fundamental nature and stems from the universal behavior that the free energy must asymptotically obey to fulfill the conditions of a 2nd order phase transition – the CP. In a sense, scaling is generic to CP phenomena. By permitting the measurements to be extremely close to the critical point, zero-g experiments

have made possible the precise measurements of important, weak power-law divergence, such as that of the specific heat at constant volume C_v (Fig. 1-b). From space experiments, the temperature divergence of the specific heat has been determined with a very high precision. With the reduced temperature $\tau = (T - T_c)/T_c$ (T is temperature, T_c is the absolute critical temperature), the specific heat diverges as $C_v \sim \tau^{-\alpha}$ near the critical point. The "critical" exponent α is universal. Its precise determination was a key test of the 'Renormalization Group' theory, which has been developed in order to try to improve the classical macroscopic description of fluid behavior close to the critical point [7]. The value deduced from the space experiments, $\alpha = 0.1105 \pm 0.027$ [2], indeed appears to be very close to the result of the Renormalization Group theory, $\alpha = 0.110 \pm 0.005$.

3. Phase Transition Kinetics and Morphology

Let us describe a typical phase separation experiment (Fig. 2a) and what has been learned from the space experiments [9]–[10]. The supercritical fluid is thermally quenched from a region of the phase diagram where it is homogeneous (at temperature T_i) to a region where it is thermodynamically stable as two phases (at temperature T_f). Droplets nucleate and their development is limited by coalescence events. When the volume fraction of the new phase that has nucleated is low (Fig. 2b), the droplets collide by Brownian motion and coalesce. The average radius of the drops R or the average distance L_m between them evolves as

$$R\phi^{-1/3} \sim L_m = 2\pi(k_B T/6\pi\eta)t^{1/3}, \quad (1)$$

where t is time, η is the shear viscosity, T is absolute temperature and k_B is the Boltzmann constant. It is worth noting that this law is practically independent of the distance $(T - T_c)$ from the critical point.

To a given ϕ corresponds a typical interaction length ($\approx R/3$) between domains. When $\phi > 0.3$, it is found [10] that the flow generated by a coalescence event is able to move a neighboring drop and thus induces another coalescence. Such a process therefore creates a chain reaction of coalescence. In the viscous limit, the pattern looks to be interconnected. Growth is limited by the balance between the capillary pressure gradient σ/R (σ is the gas-liquid surface tension) and the friction due to the shear viscosity, so that (late times)

$$L_m = b(\sigma/\eta)t. \quad (2)$$

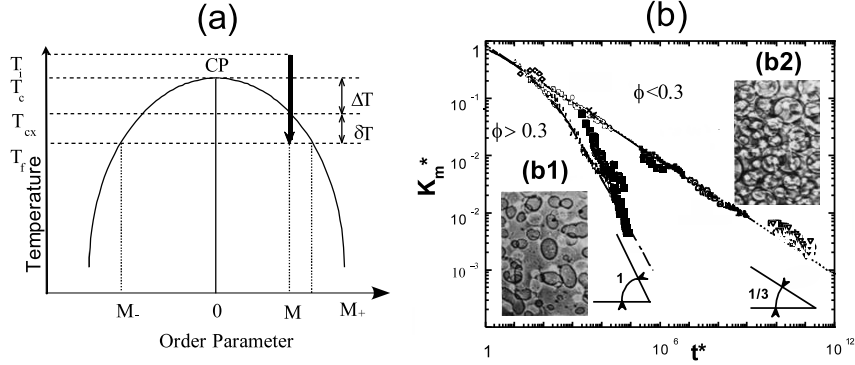


Figure 2. (a): Schematic phase diagram for simple fluids and liquid mixtures in the plane $T - M$. CP: critical point. T : temperature. M : order parameter; $M = (\rho/\rho_c) - 1$ for simple fluids and $M = c - c_c$ for liquid mixtures. $\rho(\rho_c)$ is density (critical density). $c (c_c)$ is concentration (critical concentration). The coexistence curve is described by $M = B\tau^\beta$ with B being a system-dependent amplitude and $\beta = 0.325$ an universal exponent. (b): Growth laws when gravity effects are absent. Fluids (SF_6 , CO_2): all data points except open squares. Liquid mixtures (partially deuterated Cyclohexane and Methanol): letters and open squares. The evolution of the average distance between the domains (L_m) is expressed in the scaled units $K_m^* = 2\pi\xi/L_m$ and $t^* = t/t_\xi$ (see text). Lines are theoretical predictions. The lower curve ($\phi > 0.3$) corresponds to a "fast" growth law and an interconnected morphology (pattern in insert b1) and the reduced upper curve ($\phi < 0.3$) refers to a "slow" growth and a disconnected morphology (pattern in insert b2). (From Ref. [9]).

Here $b \approx 0.03$ is a universal constant. All experiments can be rescaled by the natural lengthscale and timescale: the correlation length ξ of density fluctuations (ξ diverges as $\tau^{-\nu}$), and the associated diffusion time t_ξ (t_ξ diverges as $\tau^{-3\nu}$).

Application to Biological Tissues

The development of domains by coalescence events, as reported above, is very general. The universality of behavior, which is observed in fluids and liquid mixtures, can be extended to other areas of science. In particular, it can be applied to developmental biology where tissues can be considered as very viscous liquids (viscosity $\eta \approx 10^6$ Po), with a surface tension arising from the balance of adhesion sites between the tissue cells (effective interfacial tension $\sigma \approx 10$ dyn.cm $^{-1}$). When analyzing both the kinetics and morphology of cell sorting in embryonic chicken tissues, [11](Fig. 3), the development of the pattern can be interpreted as

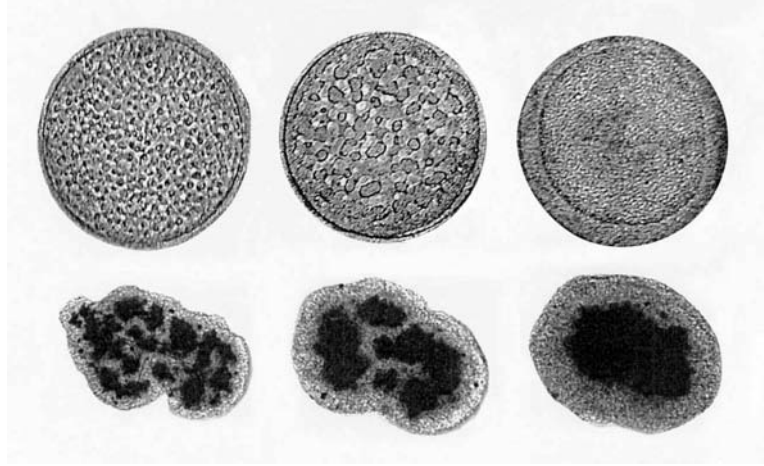


Figure 3. Upper sequence: gas and liquid phase ordering in SF_6 under reduced gravity, after a thermal quench to $T_c - 0.7$ mK. Cell diameter: 12 mm. Gas and liquid eventually order with the liquid phase wetting the container wall and surrounding the gas phase, corresponding to $\sigma_{wl} < \sigma_{wg}$. Here σ_{wl} and σ_{wg} are the wall-liquid and wall-gas interfacial tensions, respectively. The three pictures from the left correspond to states at 120 s, 275 s and 3960 s after quench, respectively. Lower sequence: sorting out of chicken embryonic pigmented epithelial cells (dark) from chicken embryonic neural retinal cells (light). Aggregate size: $200 \mu\text{m}$. At the end of sorting, neural retinal cells preferentially wet the external tissue culture medium surrounding the aggregates. Here $\sigma_{tn} (=1.6 \text{ dyn/cm}) < \sigma_{tp} (=12.6 \text{ dyn/cm})$, where σ_{tn} and σ_{tp} are the tissue culture medium-neural retina and the tissue culture medium-pigmented epithelium interfacial tensions, respectively. The three pictures from the left correspond to 17 h, 42 h and 73 h after initiation of sorting, respectively. (From [11]).

a result of the coalescence of domains that rearrange like droplets. The domains continuously coalesce and form a network, showing the same linear evolution as the fast growth in liquids. The pseudo-period between domains can indeed be fitted to a linear growth law $L_m = bt$. The value of parameter b turns out to be comparable to that extracted from Eq. (2), although surface tension and viscosity values differ by factors as large as 10^8 .

4. Thermalization

The "Piston" Effect

The thermal diffusivity of fluids vanishes near the critical point and a simple calculation [12] shows that it would need more than one month to reach thermal equilibration in a sample of 1 cm^3 at $T - T_c = 1 \text{ mK}$.

At the beginning of the microgravity experiments, it thus seemed hopeless to the scientists to try to homogenize in temperature and density a sample of fluid close to the critical point in a reasonable experiment time. However, in 1986, a preliminary experiment by Straub in a sounding rocket [8] indicated that thermalization might be much faster than expected. In a workshop in 1989 on thermal equilibration near the critical point, Onuki pointed out the importance of "adiabatic heating". We proposed a hydrodynamic mechanism of thermalization that was based on hydrodynamics where, at the sample wall the hot diffuse boundary layer expands and compresses adiabatically the whole fluid. Thermalization proceeds at the velocity of sound. As a result, a spatially uniform heating of the bulk fluid should be observed. There should be a real flow at the boarder between the bulk fluid and the expanding diffuse layer, later observed under microgravity as real "jet" flows. Onuki and Ferrell and the Gammon team proposed a similar process, an "adiabatic heating". In the Physical Review A issue of December, 1990 [12]-[14] Onuki and Ferrell, the Gammon team and our group exposed their views on the subject and all concluded a fast thermalization by this effect. Other reports (Meyer in [15]) came out nearly at the same time. We coined in [12] this adiabatic heating phenomenon the "Piston Effect" (PE), a name which has been accepted by the scientific community.

Can Heat Flow Backwards?

This effect is at the origin of a very particular behavior [17] when the vapor is in equilibrium with liquid below the critical point (Fig. 4b). While heating the cell, the temperature of the vapor becomes greater than that of the wall. That heat flow could seemingly flow from cold to hot contradicts the laws of thermodynamics. However, as we are here in presence of a thermo-mechanical conversion where the hot boundary layer compresses more the gas than the liquid, the violation is only apparent.

These results concerning the PE have been adapted and modified to the earth's environment, where gravity couples to the PE-induced flows and the geometry of the phases. Paradoxical phenomena, such as the cooling of the bulk fluid after a heat pulse, have also been obtained [18]. Also, the accelerations of the shuttle have been used (rotation and maneuvering the shuttle) to investigate the effect of density destratification, a study performed with Air Liquide Company to validate the codes that are now used in the pressurization of the reservoirs of the Ariane 5 rocket.

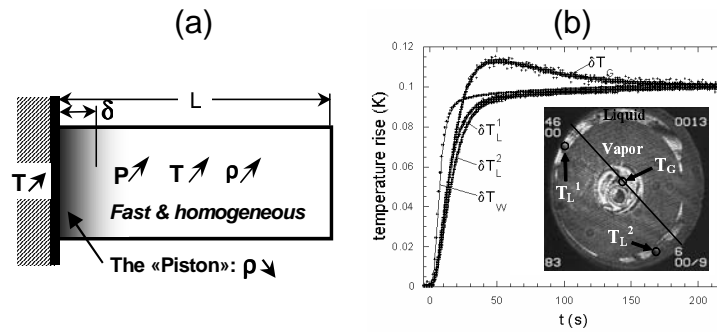


Figure 4. (a): The Piston Effect mechanism [12]-[16]: a thin hot boundary layer expands and compresses the bulk fluid. The corresponding temperature profile shows a thin zone of strong gradients near the heated boundary (thermal boundary layer δ) and a homogeneous rise in the rest of the fluid, that settles at the speed of sound. (b): overheating of nearly 20% obtained in the gas phase of a SF_6 sample at 10 K below the critical point (ALICE in MIR, 1999). A temperature rise of $T_w = 0.1K$ is imposed at the cell wall. The temperature evolution of the gas (δT_G), that of the liquid (δT_L , at two locations) are shown. In the insert is reported the sample with the thermistors. The fact that heat can flow from “cold” to “hot” apparently violates thermodynamics. It is a spectacular demonstration of the reality of the “piston” in the “Piston Effect”. (From Ref.[17]).

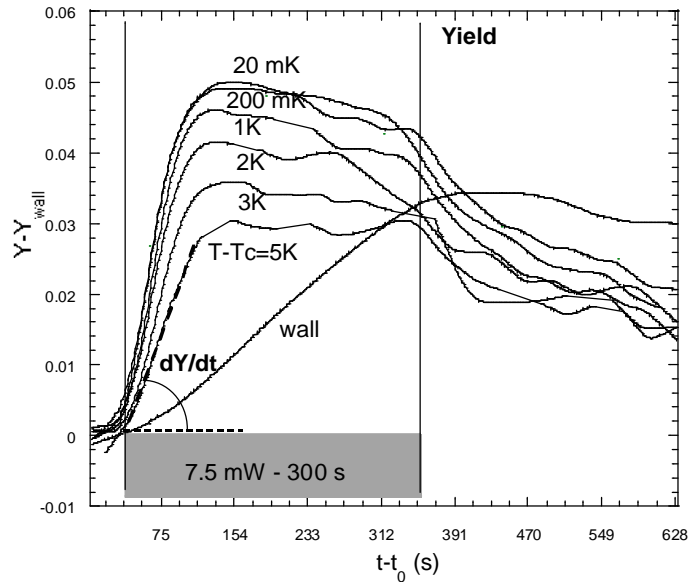


Figure 5. Yield $Y = \text{transmitted power} / \text{incident power}$ vs time (s) at various $T - T_c$. Fluid is H_2 ($T_c = 33 K$). At time t_0 , power (7.5 mW) is sent for 300 s at one end of the cell. The transmitted power is measured at the other end. The conduction Y_{wall} by the wall of the sample cell (curve “wall”) has been subtracted.

Since temperature outside the thermal boundary layers is homogeneous, the bulk fluid acts as a thermal short circuit. A question arises whether it is possible to use this Piston effect as a kind of heat pipe to carry heat on long distances. Experiments and simulation have been performed with H₂ [19] in a magnetic gravity compensation set-up [6]. The results (Fig.5) show that the heat transfer is very fast, in contrast to the usual conduction process. In particular, the yield Y (see Fig. 5 caption) shows a finite slope at initial time, in contrast with conduction in the cell walls where the slope is zero. The maximum yield increases when T approaches T_c . Its value corresponds to the heat transfer in the steady conduction state (at infinite time).

5. High Frequency Vibrations

At high frequency excitation - i.e. frequencies larger than the inverse typical hydrodynamics times - the time average of the Bernoulli pressure, which is proportional to the fluid square velocity, is non-zero. The pressure gradient that appears in a non-homogeneous fluid can thus induce flows perpendicular to the vibration direction. However, at low frequency, vibration acts by its instantaneous acceleration and can induce flows parallel to the vibration (as usually gravity does). In the following, a will denote the vibration amplitude, f the frequency and $\omega = 2\pi f$ the angular frequency.

Vibrational Thermal Effects

When a fluid is submitted to a vibrational acceleration in a thermal gradient in the Rayleigh-Bénard configuration, convection is able to start at conditions corresponding to a vibrational Rayleigh number [20]

$$R_{av} = \frac{[a\omega(\partial\rho/\partial T)_p\Delta T e]^2}{2\eta D} \quad (3)$$

larger than a few thousands. Here ΔT is the temperature difference between two fluid layers separated by the distance e and D is the thermal diffusivity coefficient. As the fluid temperature becomes closer to the critical temperature, R_{av} diverges as $(T - T_c)^{-1.9}$. The fluid then becomes extremely sensitive to vibration as the critical point is approached.

Measurements of flow velocities performed in the MIR station in CO₂ and in SF₆ confirm this expectation [22]-[23] (Fig. 6). A heat flux was sent into the fluid from a point-like source (thermistor). Depending on the oscillation velocity, two regimes of heat propagation are observed: (i) at low frequency, heat is convected during one oscillation period to form plumes parallel to vibration (Fig. 6b); (ii) at high frequency, heat

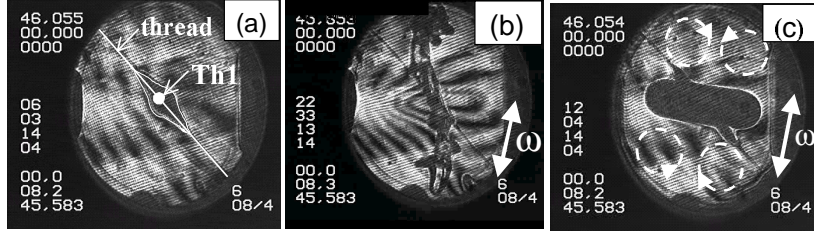


Figure 6. Interferometer image of the hot boundary layer around a heating thermistor *Th1*, supported by a thread. Fluid: SF_6 at $T_c + 0.5$ K. (a) no vibration (hot region underlined in white); (b) under low frequency; (c) under high frequency vibration. Here convection rolls form. (ALICE in MIR, 1999, from [27]).

is convected by convection rolls perpendicularly to the direction of oscillation (Fig. 6c). A numerical simulation and analysis of the convection has been performed by Jounet in [21], emphasizing the role of vortices.

Vibrational Phase Ordering

A plane liquid-vapor layer vertically vibrating parallel to gravity displays two different regimes [24]. Far from the critical point, a square wave-pattern deformation arises (the usual Faraday instability). At a temperature T_0 close to the critical temperature ($T_c - T_0 \approx 20$ mK for CO_2), a transition to a new pattern comprised of lines occurs. This transition is due to the increase of dissipation near the critical point. This is a rather unique example of a strong coupling between two different critical point phenomena: the critical point of interface instability and the thermal critical point of the liquid-vapor phase transition.

When acceleration is perpendicular to gravity, a Kelvin-Helmholtz-like instability is observed [25], with the interface modulated as a "frozen" roll wave pattern (Fig. 7a). The mechanism of the instability results from the relative motion of the two fluids induced by vibration. A perturbation becomes unstable if the cell velocity ($a\omega$) is larger than the threshold velocity [26]

$$(a\omega)_0 = \frac{(\rho_L + \rho_G)^3}{\rho_L \rho_G \Delta\rho} \sqrt{\frac{\sigma g}{\Delta\rho}}. \quad (4)$$

Here ρ_L (ρ_V) is the liquid (vapor) density and $\Delta\rho = \rho_L - \rho_G$ is the liquid-vapor density difference. This destabilization is due to the increasing effect of the Bernoulli - type pressure arising from the velocity difference between gas and liquid.

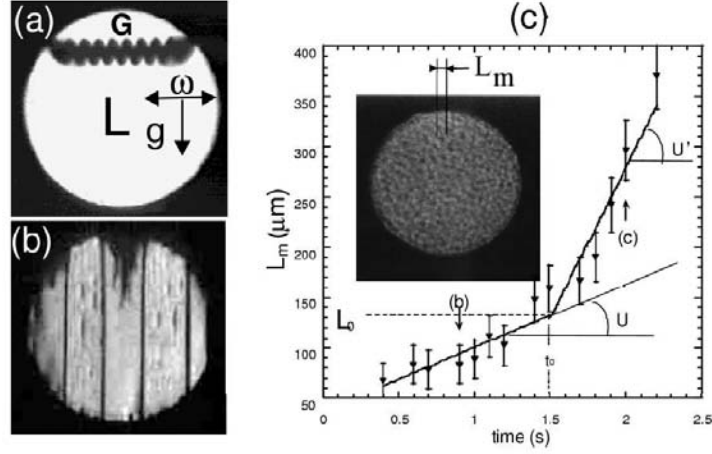


Figure 7. (a-b): CO_2 gas-liquid phases show up under 1-g as gas phase (G) above the liquid phase (L) separated by a flat meniscus. When submitted to vibration, the phases can order in a different way: (a) under 1-g, the interface exhibits "frozen waves"; (b) under zero-g, gas-liquid phases order in layers. Cell diameter: 10 mm (sounding rocket Maxus 5, April, 2003). (c): Typical phase separation in H_2 at $T_c - 1.06 \text{ mK}$ with $a = 0.3 \text{ mm}$ and $f = 20 \text{ s}^{-1}$. From [28].

Three samples of different gas volume fractions and various $T - T_c$ were vibrated at several amplitudes and frequencies ranging from 0.1 mm to 5 mm and 0.1 Hz to 60 Hz, respectively [27]. Although the initial state of the sample was either an emulsion of vapor drops, or a single drop, the final state remains the same: vapor and gas phases are forming alternate layers perpendicular to the direction of acceleration. An instability, similar to Kelvin-Helmoltz' with inviscid, zero surface tension, develops as liquid fingers from the cell walls. The fingers coalesce with the droplets in the bulk and/or with the fingers that have grown from the opposite side. Here the viscous boundary layer $\lambda = (2\eta/\rho\omega)^{1/2}$ is the natural lengthscale of the phenomenon.

Phase Transition under Vibration

A study of phase separation was performed in H_2 under magnetic compensation of gravity (Fig. 7c), for volume fraction $\phi > 0.3$ [28]. The domains are interconnected. When L_m is lower than the viscous boundary layer λ , liquid and gas domains have the same velocity and their growth is unaffected. From Eq. (2), the growth velocity $U = dL_m/dt = b\sigma/\eta$. When $L_m > \lambda$, the domains exhibit different velocities whose difference is proportional to the gas-liquid difference. The corresponding shear flow

between the domains speeds up the growth (see Fig. 7c where the crossover is denoted L_0) as $U'/U = 1 + \Delta U/U$, with $\Delta U/U \sim (\Delta\rho)(a/\lambda)$.

These observations suggest that a periodic excitation can act as a kind of artificial gravity, which speeds up phase transition and localizes the liquid and vapor phases perpendicular to it.

6. Conclusion

Supercritical fluids are of both the fundamental interest (universality of phase transition, supercritical hydrodynamics) and industrial interest (supercritical solubilization, nucleation of nanomaterials, oxidation, thermalization, storage). The field of Critical Point Phenomena has achieved some major breakthroughs during the last 15 years thanks to microgravity research; in particular, a new thermalization process has been discovered, the "Piston Effect", that reveals novel hydrodynamics in such near-critical fluids. The study has strongly modified our vision of critical point phenomena and even of hydrodynamics: the very unusual hydrodynamics of these supercritical fluids, compressible, dense, and weakly viscous, makes their behavior quite particular when compared to gas or liquids. Future experiments will certainly lead to the discovery of new and unexpected phenomena that will be of interest for both the fundamental and applied science.

Acknowledgments

This review has been made possible thanks to the friendly help and contribution of Y. Garrabos, B. Zappoli, J. Hegseth, P. Evesque and V. Nikolayev. The financial support of CNES is gratefully acknowledged.

References

- [1] See e.g. H.E. Stanley, *Introduction to phase transitions and critical phenomena*, Clarendon Press, Oxford, New York, 1971; D. Beysens, J. Straub, D. Turner, [in:] *"Fluid Sciences and Materials Science in Space"*, H.U. Walter [Ed.], pp.221–256, Springer, Berlin, 1987.
- [2] A. Haupt, J. Straub, *Phys. Rev. E* 59, pp.1795–1802, 1999.
- [3] F. Cansell, P. Beslin, B. Berdeu, *Environmental Progress* 17, pp.258–263, 1998; S. Yesodharan, *Current Science* 82, pp.1112–1122, 2002.
- [4] M.R. Moldover, J.V. Sengers, R.W. Gammon, R.J. Hocken, *Rev. Mod. Phys.* 51, pp.79–99, 1979.
- [5] D. Beysens, *Acta Astron.* 12 525-530, 1985; C. Houessou, P. Guenoun, R. Gastaud, F. Perrot, D. Beysens, *Phys. Rev. A* 32, pp.1818–1833, 1985.
- [6] R. Wunenburger, D. Chatain, Y. Garrabos, D. Beysens, *Phys. Rev.E* 62, pp.469–476, 2000; see <http://www.spaceflight.esa.int>.

- [7] K.G. Wilson, J. Kogut, Phys. Reports C 12, 75, 1974.
- [8] K. Nitsche, J. Straub, Naturwissenschaften 73, 370, 1986; J. Straub, L. Eicher, A. Haupt, Phys. Rev. E 51, pp.5556–5563, 1995.
- [9] D. Beysens, Y. Garrabos, Physica A 281, 361-380, 2000 and refs. therein.
- [10] V. Nikolayev, D. Beysens, P. Guenoun, Phys. Rev. Lett. 76, pp.3144–3147, 1996; V. Nikolayev, D. Beysens, Physics of Fluids 9, pp.3227-3234, 1997.
- [11] D.A. Beysens, G. Forgacs, J.A. Glazier, P.N.A.S. 97, pp.9467-71, 2000; *ibid.*, *Networks of droplets induced by coalescence: application to cell sorting*, in: Dynamical Networks in Physics and Biology, D. Beysens and G. Forgacs [Eds.], pp.161–169, Springer & EDP Sciences, Berlin & Les Ulis, 1998.
- [12] B. Zappoli, D. Bailly, Y. Garrabos, B. Le Neindre, P. Guenoun, D. Beysens, Phys. Rev. A 41, pp.2264–2267, 1990.
- [13] A. Onuki, H. Hao, R.A. Ferrell, Phys. Rev.A 41, pp.2255-2259, 1990; A. Onuki, R.A. Ferrell, Physica A 164, pp.245–264, 1990.
- [14] H. Boukari, J.N. Shaumeyer, M.E. Briggs, R.W. Gammon, Phys. Rev. A 41, pp.2260–2263, 1990.
- [15] R.P. Behringer, A. Onuki, H. Meyer, J. Low Temp. Phys. 81, pp.71–102, 1990.
- [16] See e.g. Y. Garrabos, M. Bonetti, D. Beysens, F. Perrot, T. Fröhlich, P. Carlés, B. Zappoli, Phys. Rev. E. 57, pp.5665-5681, 1998.
- [17] R. Wunenburger, Y. Garrabos, C. Chabot, D. Beysens and J. Hegseth, Phys. Rev. Lett. 84, pp.4100–4103, 2000; M. Sincell, Science 288, pp.789–791, 2000.
- [18] T. Fröhlich, D. Beysens, Y. Garrabos, V. Nikolayev, A heat flux can cool a near-critical fluid, preprint, 2004.
- [19] D. Beysens, D. Chatain, V. Nikolayev, Y. Garrabos, 4th International Conference on Launcher Technology *Space Launcher Liquid Propulsion*, 3-6 December 2002 – Liege, Belgium.
- [20] G.Z. Gershuni, D.V. Lyubimov, *Thermal Vibrational Convection*, John Wiley & Sons, New-York, 1998.
- [21] A. Jounet, Phys. Rev. E, 65, pp.37301–37304, 2002
- [22] S.V. Avdeev, A.I. Ivanov, A.V. Kalmykov, A.A. Gorbunov, S.A. Nikitin, V.I. Polezhaev, G.F. Putin, A.V. Zuzgin A.V., V.V. Sazonov, D. Beysens, Y. Garrabos, T. Fröhlich, B. Zappoli, *Experiments in the far and near critical fluid aboard the MIR station with the use of the 'Alice-1' instrument*, in Proceedings of the Joint Xth European and Vith Russian Symposium on Physical Science in Microgravity, St. Petersburg, Russia, 15-21 June 1997, Vol.1, pp.333–340, V.S. Avduyevsky and V.I. Polezhaev [Eds.], Institute for Problems in Mechanics, RAS, Moscow.
- [23] Y. Garrabos, D. Beysens, C. Chabot, R. Wunenburger, V. Polezhaev, V. Emelianov, A. Ivanov, A. Kalmykov, *Thermo-Convectional Phenomena Induced by Vibrations in Supercritical SF6 Under Low Gravity*, preprint, 2004.
- [24] S. Fauve, K. Kumar, C. Laroche, D. Beysens, Y. Garrabos, Phys. Rev. Lett. 68, pp.3160–3163, 1992.
- [25] R. Wunenburger, P. Evesque, C. Chabot, Y. Garrabos, S. Fauve, D. Beysens, Phys. Rev. E 59, pp.5440–5445, 1999.

- [26] D.V. Lyubimov, A. Cherepanov, *Izvestiya Akademii Nauk SSSR, Mekhanika Zhidkosti i Gaza* 6, 8-13, translated in *Fluid Dynamics* 86, pp.849–854, 1987.
- [27] D. Beysens, C. Chabot, Y. Garrabos, *Microgravity Sci. Technol.* 11, pp.113–118, 1998.
- [28] D. Beysens, D. Chatain, P. Evesque, Y. Garrabos, *Phase separation under vibrations in near-critical hydrogen free of gravity effects*, submitted, 2004.

FLAW TOLERANT NANOSTRUCTURES OF BIOLOGICAL MATERIALS

Huajian Gao*, Baohua Ji, Markus J. Buehler, and Haimin Yao
*Max Planck Institute for Metals Research,
Heisenbergstrasse 3, 70569 Stuttgart, Germany*

Abstract Bone-like biological materials have achieved superior mechanical properties through hierarchical composite structures of mineral and protein. Gecko and many insects have evolved hierarchical surface structures to achieve superior adhesion capabilities. We show that the nanometer scale plays a key role in allowing these biological systems to achieve such properties, and suggest that the principle of flaw tolerance may have had an overarching influence on the evolution of the bulk nanostructure of bone-like materials and the surface nanostructure of gecko-like animal species. We demonstrate that the nanoscale sizes allow the mineral nanoparticles in bone to achieve optimum fracture strength and the spatula nanoprotusions in Gecko to achieve optimum adhesion strength. Strength optimization is achieved by restricting the relevant dimension to nanometer scale so that crack-like flaws do not propagate to break the desired structural link. Continuum and atomistic modeling have been conducted to verify this concept.

1. Introduction

New challenges in materials science in the 21st century will include the development of multi-functional and hierarchical materials systems. Nanotechnology promises to enable mankind to design materials using a bottom-up approach, that is, to construct multi-functional and hierarchical material systems by tailor-designing structures from atomic scale and up. However, to this date, there is almost no theoretical basis on how to design a hierarchical material system to achieve a particular set of functions. One strategy is to look among solutions in nature for hints on advanced materials design.

*hjgao@mf.mpg.de

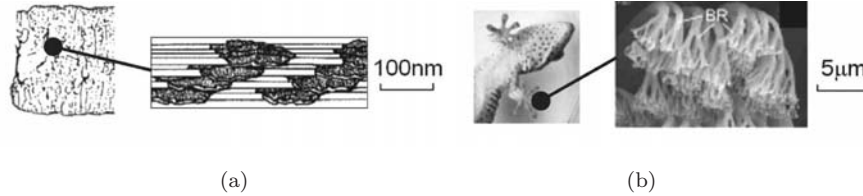


Figure 1. Nanostructure of bones (a) and the toe of geckos (b) that consists of a terminal nanostructure called spatula of about 200–500 nm in diameter.

Biological materials, such as bone [1] exhibit many levels of hierarchical structures from macroscopic to microscopic length scales. The smallest building blocks in such materials are generally on the nanometer length scale. For instance, the nanostructure of bone (Fig. 1a) consists of mineral crystal platelets with thickness around a few nanometers embedded in a collagen matrix [1,2].

Interesting nanostructures of biological systems for superior mechanical properties are not just limited to the nanocomposite structure of bone. Gecko and many insects have evolved elaborate hierarchical surface structures in their foot hair to achieve extraordinary adhesion capabilities. These animals possess ability to adhere to vertical surfaces and ceilings. A gecko is found to have hundreds of thousands of keratinous hairs or setae on its foot; each seta is $30 \sim 130\mu\text{m}$ long and contains hundreds of protruding nanoscale structures called spatula (Fig. 1b). We attempt to address the following questions. Why is nanoscale is so important to biological systems? What are the basic mechanisms and principles behind biological nanostructures?

2. The Protein-mineral Bulk Nanostructure of Bone-like Biocomposites

Experimental observations (e.g. [1,3] and further references in [4]) have shown that, at the most elementary structure level, biological materials exhibit a generic structure consisting of staggered mineral platelets embedded in a soft matrix (Fig. 2a). Under an applied tensile stress, the path of load transfer in the mineral-protein biocomposites can be represented by a tension-shear chain model [4] where the mineral platelets carry tensile load and the protein transfers load between mineral crystals via shear (Fig. 2b). In this tension-shear chain model, the mineral-protein composite is simplified to a one-dimensional chain consisting of tensile springs (mineral) interlinked by shear springs (protein). The integrity of the composite chain structure is hinged upon the strength of mineral platelets since breaking of the platelets would destroy the cri-

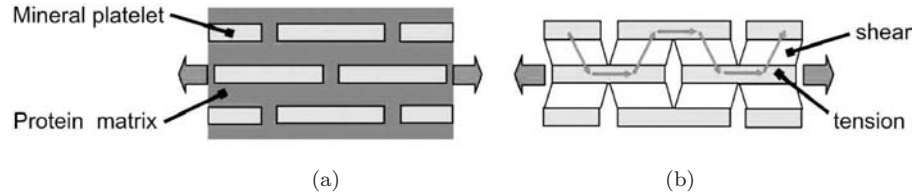


Figure 2. A simple tension-shear chain model of biocomposites. (a) Schematic of staggered mineral crystals embedded in a soft (protein) matrix. (b) Tension-shear chain model showing the path of load transfer in the mineral-protein composites.

tical structural links in the composite, leading to disintegration of the protein-mineral network. The strength of mineral platelets plays a crucial role in the fracture energy of the composite. In order to achieve high fracture energy, the mineral platelets must be able to sustain large tensile stress without fracture.

How to optimize the strength of the mineral platelets? The Griffith theory of fracture [5] and common engineering experiences have shown that the strength of brittle solids is determined by pre-existing flaws. It was pointed out that the nanometer scale is the key to optimizing mineral strength [4]. At the simplest level, this can be understood from the following consideration. A perfect, defect-free mineral particle should be able to sustain mechanical stress near the theoretical strength σ_{th} of the material. However, we assume that the particle contains crack-like flaws. For example, protein molecules trapped within the mineral crystals during the biomineralization process are mechanically equivalent to embedded microcracks. Considering all potentially existing cracks in a thin strip, the largest crack, and hence the most dangerous one, will be a crack about half the strip width. The key idea of flaw tolerance [4,6] is that cracks confined in a small structure do not propagate until the material around the crack uniformly reaches the theoretical strength. This can also be demonstrated with the crack configuration shown in Fig. 3. In this configuration, the strength of the material can be calculated from the Griffith theory as $\sigma_f = \sqrt{4\gamma E^*/h}$ for a mineral platelet width h and fracture surface energy γ , where $E^* = E/(1 - \nu^2)$, E being the Young's modulus and ν the Poisson ratio. According to this expression, the strength of the material approaches infinity when h goes to zero. This is physically impossible since the largest stress a material can sustain is limited by an upper bound (theoretical strength) σ_{th} . This suggests that there exists a transition between crack propagation governed by the Griffith criterion and uniform rupture of atomic bonds

at theoretical strength at a critical length scale [4]

$$h_{cr} = \frac{4\gamma E^*}{\sigma_{th}^2}. \quad (1)$$

Taking a rough estimate $\gamma = 1 \text{ J/m}^2$, $E_m = 100 \text{ GPa}$, and $\sigma_{th} = E_m/30$, we found h_{cr} to be around 30 nm for a half-cracked platelet [4]. The nanometer scale not only allows the strength of mineral particles to be optimized near theoretical strength but also renders these particles insensitive to crack-like defects (flaw tolerance).

This concept has so far also been studied by atomistic simulations (details see [6]). Figure 3(a) plots the critical failure stress normalized by the theoretical strength, indicating a smooth transition between crack propagation governed by the Griffith condition for thick layers ($\sqrt{h_{cr}/h} < 1$) to uniform rupture at theoretical strength for thin layers ($\sqrt{h_{cr}/h} > 1$). This result is fully consistent with the continuum mechanics analysis [4]. Figure 3(b) plots the distribution of normal stress ahead of the crack. As the strip width is decreased, stress concentration at crack tip disappears and the stress distribution becomes uniform near the crack tip, and thus the solid has become insensitive to flaws.

Further analysis of the protein-mineral bulk nanostructure of bone on stiffness (discussion of the interplay of the soft protein matrix and the stiff mineral platelet material, and the impact of the aspect ratio of mineral platelet) and fracture energy (including a discussion on sacrificial Ca^{++} bonds) can be found in [6]. The interested reader is referred to references [4,6-9] for further details of our group on this topic.

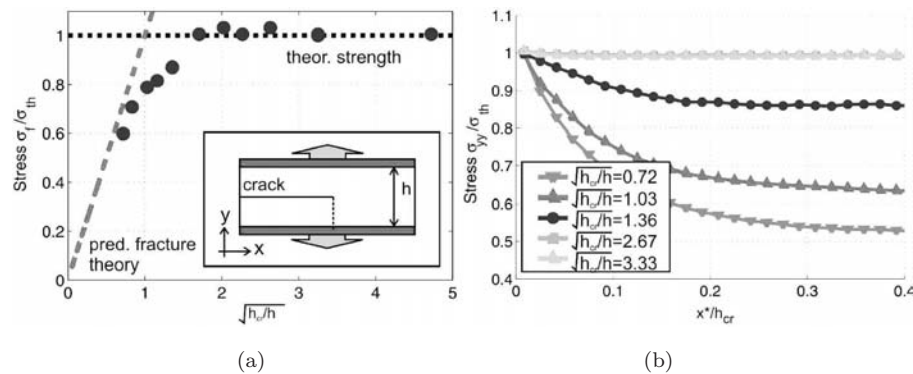


Figure 3. (a) Fracture strength as a function of layer width h , and (b) stress distribution ahead of the crack for different layer widths h .

3. Flaw Tolerant Surface Nanostructure of Gecko for Adhesion

The concept of nanoscale flaw tolerance can be discussed in a more general context to include the surface nanostructure of gecko. Among the hairy biological attachment systems, the density of surface hairs (setae) increases with the body weight of animal, and gecko has the highest density among all animal species that have been studied [10].

The most terminal (smallest) structure of gecko’s attachment mechanism is called spatula (Fig. 1b) which is about 200–500 nanometers in diameter. Why is the spatula size in the nanometer range? To understand this, we have modeled the spatula as an elastic flat-ended cylindrical hair in adhesive contact with a rigid substrate [11]. The radius of the cylinder is R . To test the ability of the flat cylinder to adhere in the presence of adhesive flaws, imperfect contact between the spatula and substrate is assumed such that the radius of the actual contact area is $a = \alpha R$, and $0 < \alpha < 1$, as shown in Fig. 4(a); the outer rim $\alpha R < r < R$ represents flaws or regions of poor adhesion. The adhesive strength of such an adhesive joint can be calculated by treating the contact problem as a circumferentially cracked cylinder, in which case the stress field near the edge of the contact area has a square-root singularity with stress intensity factor [12]. Somewhat similar to the case of nanoscale mineral platelets in bone, a critical length scale for the spatula radius exists when adhesion becomes insensitive to crack-like flaws. The critical radius is

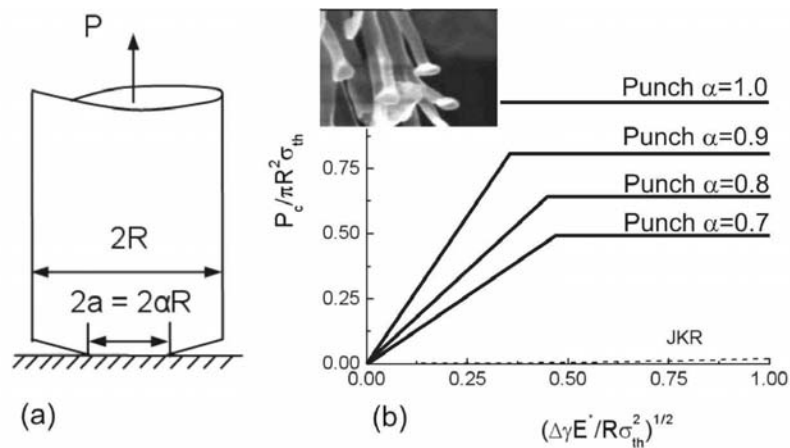


Figure 4. (a) Geometry of the model for the spatula. (b) Adhesive strength as a function of the radius. At the critical radius, the adhesive strength is independent of flaws and is at its theoretical limit.

given by

$$R_{cr} = \beta^2 \frac{\Delta\gamma E^*}{\sigma_{th}^2} \quad (2)$$

where $\beta = \sqrt{2/(\pi\alpha F_1^2(\alpha))}$, F is a function that varies slowly between 0.4 and 0.5 for $0 \leq \alpha \leq 0.8$ (for details see [11]), and $\Delta\gamma$ is the surface energy. The theoretical strength of van der Waals interaction across the interface is denoted by σ_{th} . Figure 4(b) plots the apparent adhesive strength for $\alpha=0.7$, 0.8 and 0.9, together with the case of flawless contact ($\alpha = 1$). The corresponding result of a hemispherical tip based on the JKR model is plotted as a dashed line for comparison (in plotting the JKR curve, we have taken E^*/σ_{th} to be 75) [12]. The flat-ended spatula achieves the maximum adhesion strength much more quickly than the hemispherical configuration. Further numerical studies based on the Tvergaard–Hutchinson model [13] of adhesion, as shown in Fig. 5, confirmed that the adhesion stress indeed becomes uniform as the size of the contact area is reduced to below the critical length.

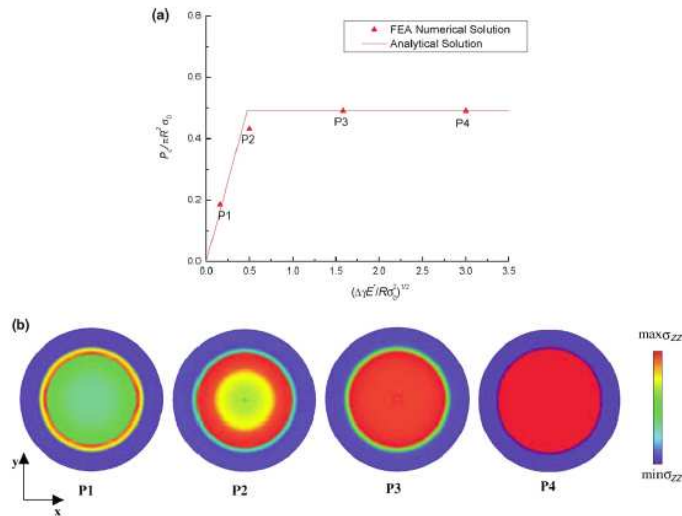


Figure 5. Numerical results of the Tvergaard–Hutchinson model for the adhesion of a flat-ended cylinder partially adhering to a rigid substrate. The real contact area is assumed to be 50% of the total area of the punch ($a=0.7$). (a) The normalized pull-off force shows saturation at a critical size, in good agreement with the simple analysis from Griffith criterion. (b) The traction distribution within the contact area becomes more uniform as the size is reduced. Below the critical size, the traction becomes uniform and equal to the theoretical strength of van der Waals interaction. An arbitrary scale has been used here to plot the traction distribution. (Figure adopted from Ref. [11].)

The parameters for the van der Waals interaction and the Young's modulus of spatula (keratin) are $\sigma_{th} = 20$ MPa, $\Delta\gamma = 0.01$ J, $\Delta\gamma/\sigma_{th} \cong 0.5$ nm and $E^* = 2$ GPa. This gives the critical size for adhesive strength saturation as $R_{cr} \cong 225$ nm which matches the radius of gecko's spatula that is typically around 100–250 nm. The analysis suggests that the nanometer size of the spatula structure of gecko may have been evolved to achieve optimization of adhesive strength in tolerance of possible contact flaws.

Further analysis on this problem with a focus on the adhesion strength of spatula arrays is given in [6]. Recently, Gao and Yao [14] have shown that, for contact between any two elastic materials, it is possible to design an optimal shape of the local contact surface to achieve theoretical pull-off force. However, such design tends to be unreliable at the macroscopic scale because the pull-off force is sensitive to small shape variations in the contact surface. A robust design of shape-insensitive optimal adhesion becomes possible when the diameter of the contact area is reduced to length scales on the order of 100 nm. In general, optimal adhesion could be achieved by a combination of size reduction and shape optimization. The smaller the size, the less important the shape. At large contact sizes, optimal adhesion could still be achieved if the shape can be manufactured to a sufficiently high precision. The robust design of optimal adhesion at nanoscale provides further support for the flaw tolerant theory of nanoscale contact in biological adhesion structures.

4. Summary

This paper aimed to provide a unified treatment of flaw tolerant nanostructures of biological materials. At a nanometer critical length determined by fracture energy, Young's modulus and theoretical strength, the mineral crystals in biological materials such as bone become insensitive to pre-existing crack-like flaws and the strength of mineral can be maintained near the theoretical strength of the material despite of defects. Following the same principle, the nanometer size of spatula, the most terminal adhesive structure of gecko, achieves maximum adhesion strength and become tolerant of potential contact flaws. This concept has been studied via continuum and atomistic modeling.

Interestingly, the protein-mineral structure of bone appears to conform to the ancient Chinese philosophy that combination of “Yin” and “Yang”, things of complementary nature or properties, results in perfection and harmony in nature. In biological materials, the mineral platelets act as the “yang” phase (stiff, hard, brittle, non-dissipative,

non-yielding), and in contrast, the protein acts as the “yin” phase (soft, gentle, ductile). The nanometer scale plays the key role in the property optimization of mineral-protein structure.

References

- [1] W.J. Landis, The strength of a calcified tissue depends in part on the molecular structure and organization of its constituent mineral crystals in their organic matrix, *Bone*, Vol. 16, No.5, pp.533–544, 1995.
- [2] P. Roschger, B.M. Grabner, S. Rinnerthaler, W. Tesch, M. Kneissel, A. Berzlanovich, K. Klaushofer, and P. Fratzl, Structural development of the mineralized tissue in the human L4 vertebral body, *J. Struct. Biol.*, Vol. 136, pp.126–136, 2001.
- [3] S. Kamat, X. Su, R. Ballarini, and A.H. Heuer, Structural basis for the fracture toughness of the shell of the conch strombus gigas, *Nature*, Vol. 405, pp.1036–1040, 2000.
- [4] H. Gao, B. Ji, I.L. Jaeger, E. Arzt, and P. Fratzl, Materials become insensitive to flaws at nanoscale: lessons from nature, *Proc. Natl. Acad. Sci. USA*, Vol. 100, pp.5597–5600, 2003.
- [5] A.A. Griffith, The phenomena of rupture and flow in solids, *Phil. Trans. R. Soc. London A*, Vol. 221, pp.163–198, 1921.
- [6] H. Gao, B. Ji, M.J. Buehler, and H. Yao, Flaw tolerant bulk and surface nanostructures of biological systems. *Mechanics and Chemistry of Biosystems*, Vol. 1, pp.37–52, 2004.
- [7] H. Gao and B. Ji, Modeling Fracture in Nano-Materials via a Virtual Internal Bond Method, *Engineering Fracture Mechanics*, Vol. 70, pp.1777–1791, 2003.
- [8] B. Ji and H. Gao, A study of fracture mechanisms in biological nano-composites via the virtual internal bond model, *Materials Science & Engineering A*, Vol. 366, pp.96–103, 2004.
- [9] B. Ji and H. Gao, Mechanical properties of nanostructure of biological materials, *Journal of the Mechanics and Physics of Solids*, Vol. 52 (9), pp.1963–1990, 2004.
- [10] M. Scherge and S.N. Gorb, Biological Micro and Nano-Tribology, *Springer-Verlag*, New York, 2001.
- [11] H. Gao, X. Wang, H. Yao, S. Gorb, and E. Arzt, Mechanics of Hierarchical adhesion structure of gecko, *Mechanics of Materials*, Vol. 37, pp.275–285, 2005.
- [12] H. Tada, P.C. Paris, and G.R. Irwin, The stress analysis of cracks handbook. *ASME Press*, New York, 2000.
- [13] V. Tvergaard and J.W. Hutchinson, Effect of strain dependent cohesive zone model on predictions of crack growth resistance, *Int. J. Solids Struct.* Vol. 33, pp.3297–3308, 1996.
- [14] H. Gao and H. Yao, Shape insensitive optimal adhesion of nanoscale fibrillar structures, *Proceedings of the National Academy of Sciences of USA*, Vol. 101, pp.7851–7856, 2004.
- [15] K.L. Johnson, K. Kendall, and A.D. Roberts, Surface energy and the contact of elastic solids, *Proc. R. Soc. London A*, Vol. 324, pp.301–313, 1971.

TRANSPORT AND MIXING IN THE ATMOSPHERE

Peter H. Haynes

*Department of Applied Mathematics and Theoretical Physics,
Wilberforce Road, Cambridge, CB3 0WA,
United Kingdom*

p.h.haynes@damtp.cam.ac.uk

Abstract Transport and mixing processes in the atmosphere operate on scales from millimeters to thousands of kilometers. In certain parts of the atmosphere the large-scale quasi-horizontal flow appears to play the dominant role in transport and in the stirring process that leads ultimately to true (molecular) mixing at very small scales. Previous work in other fluid dynamical contexts such as ‘chaotic advection’ or ‘Batchelor-regime turbulence’ is therefore potentially relevant. This article reviews how, with appropriate modification, fluid dynamical insights and methods can be used, in conjunction with observational data on large-scale velocity fields or on chemical species, to quantify different aspects of transport and mixing in the atmosphere.

1. Introduction

The transport and mixing properties of the atmospheric flow are of great significance, since they play a major role in determining the distribution of atmospheric chemical species, with implications for air quality, for absorption of ultra-violet radiation (in the case of ozone) and for climate (in the case of the many chemical species that play a role in the radiation balance of the atmosphere). Indeed it is becoming common to regard the distribution of chemical species as an integral part of the climate system. Whilst air quality considerations have typically taken account of flows on the local or regional scale, it is now realised that pollutants emitted in industrialised regions can be transported thousands of kilometers and therefore that efforts to meet local quality standards often need to take account of transport by the flow on much larger scales (e.g. Akimoto 2003).

The atmosphere is conventionally divided into layers according to the vertical temperature gradient. In the *troposphere* (the lowest 10 km or so of the atmosphere) the temperature decreases with height and whilst the associated density stratification is stable, the stability is relatively weak. In the *stratosphere* (roughly 10–50 km) the temperature is constant in height or increases with height and the stability is much stronger than in the troposphere. The transition from troposphere to stratosphere is called the *tropopause*. In both troposphere and stratosphere the stable density stratification, together with rotation, inhibits three-dimensionality of the flow. Thus three-dimensional turbulence tends to be confined to relatively localised regions, in the troposphere to the atmospheric boundary layer (the lowest kilometre or so of the atmosphere that is in direct contact with the Earth's surface) and to convective clouds and elsewhere in the troposphere and stratosphere to localised regions of turbulence that result from dynamical instabilities, perhaps associated with the breaking of inertia-gravity waves. There has been a tendency to regard the troposphere as relatively well-mixed in the vertical by convection, but observations of long-lived thin layers of anomalous chemical species (e.g. Newell et al. 1999) now show that, particularly in the extratropics, the time scales on which air masses experience convective events may be long – perhaps a few weeks.

Outside of regions of strong three-dimensional turbulence and on sufficiently large scales, e.g. larger than a few tens of kilometers, the atmospheric flow is quasi-horizontal, with air parcel trajectories along weakly sloping surfaces, so that horizontal displacements are generally much larger than vertical displacements. This flow has a dual character, with some aspects of its behaviour appearing organised and wave-like and other aspects exhibiting considerable nonlinearity and randomness. In the latter respect such flow might therefore be regarded as a kind of turbulence, analogous to the two-dimensional turbulence studied in idealised numerical simulations and laboratory experiments.

In considering the transport and mixing properties of flows it is useful to distinguish between three distinct processes. The first is *transport* – the bulk movement of chemical species away from locations of sources and towards regions of sinks. The second is *stirring* – deformation of geometric structure of chemical concentration fields so as to bring fluid parcels with different chemical characteristics into closer and closer proximity. The third is *mixing* – the homogenising action of molecular diffusion on spatially varying chemical concentration fields. The importance of stirring is, of course, that by reducing length scales of chemical concentration fields it also reduces the time scale that molecular diffusion takes to act. One might therefore say that stirring governs the

mixing ability of a flow and in some contexts the term ‘mixing’ is used to mean ‘stirring’.

Three-dimensional turbulence on the one hand and the large-scale quasi-horizontal flow on the other have very different stirring and mixing properties. In three-dimensional turbulence the strong vortex stretching, and accompanying cascade of energy to small scales imply that the velocity gradient increases as horizontal length scale shrinks. It follows that deformation at a given scale is dominated by the flow at that scale. This has two important implications. The first is that the time taken to stir a chemical field from some finite scale to the the scale at which molecular diffusion is important is independent of diffusivity (when the latter is small). The second is that the spatial structure of the concentration field is highly complex, since it mirrors the complex spatial structure of the underlying three-dimensional flow. There is a broader family of flows with these properties – we might call them ‘*Type I flows*’ – which includes, for example, flows that are ‘non-smooth’ in the terminology of recent theoretical work on the effect of random flows on chemical concentration fields (e.g. Falkovich et al. 2001)

In the large-scale quasi-horizontal flow, on the other hand, the velocity field has a finite spatial scale and there is no strong increase of velocity gradients as horizontal length scale shrinks. It follows that the deformation at given scale is dominated by the flow at the large scale. This implies that the time taken to stir a chemical field from some finite scale to the the scale at which molecular diffusion is important increases logarithmically with the inverse of diffusivity (when the latter is small). It also implies that at small scales the structure of the concentration field is locally one-dimensional, consisting of filaments (in two dimensions) or sheets (in three dimensions). Again there is a broader family of flows with these properties – we might call them ‘*Type II flows*’ – which includes, for example, ‘smooth’ flows or ‘Batchelor turbulence’ (e.g. Falkovich et al. 2001), or what are often known as ‘chaotic advection’ flows (e.g. Wiggins and Ottino 2004 and references therein).

The emphasis in the remainder of this article will be on transport and mixing by the large-scale quasi-horizontal atmospheric flow. It should be noted that the assertion that this is a ‘Type II’ flow is, to some extent, a working assumption, but is supported by basic fluid-dynamical arguments applied to strongly stratified, rapidly rotating flows (e.g. Bartello 2000, Shepherd et al. 2000).

2. Use of Atmospheric Data in Transport and Mixing Studies

Studies of transport and mixing in the atmosphere can potentially call on two types of data. The first is data on the distribution of chemical species (i.e. the concentration fields that arise as the effect of transport and mixing). Some of this data has been collected in-situ using instruments on aircraft or balloons. This has the advantage of high spatial resolution (perhaps a few tens of metres for balloon ascents, a few kilometres for horizontal aircraft sections), but, of course, is taken only along a one-dimensional section. Other such data is collected by satellite remote sensing which has lower spatial resolution (a few kilometers in the vertical, a few hundreds of kilometres in the horizontal), but provides a three-dimensional field. The second type of data are the global meteorological datasets of atmospheric dynamical quantities, including velocity fields, now routinely produced as part of the weather forecasting process. These datasets are typically at a horizontal resolution of 100 km or so. The datasets include a subtle blend of information direct from observations and information from the numerical models used to

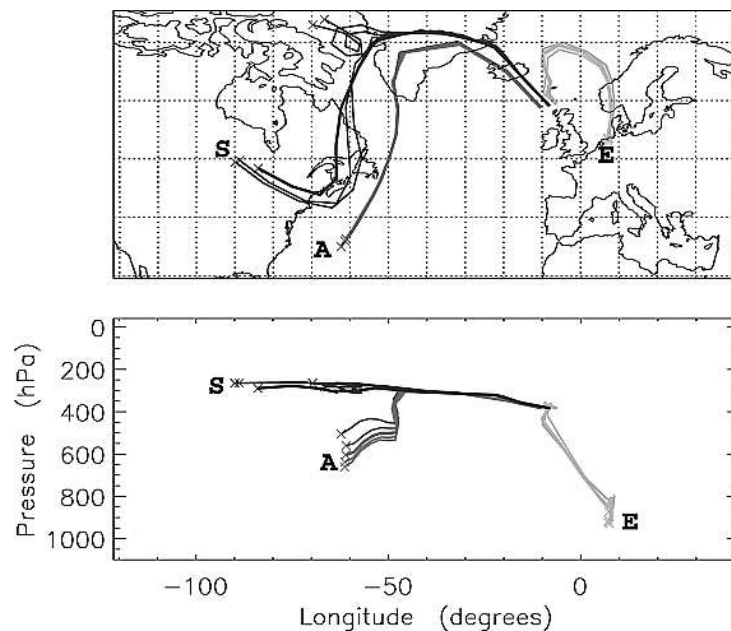


Figure 1. (From Methven et al. 2003) Three day-back trajectories from region of observation, shown in longitude-latitude in upper panel and longitude-pressure in lower panel. Copyright 2003 American Geophysical Union. Reproduced by permission of American Geophysical Union.

generate weather forecasts. The velocity datasets are now widely used as input to chemical transport models. These might be Lagrangian models, which advect large numbers of particles (or sometimes finite parcels containing reacting chemical species), or Eulerian models, which represent global fields of different chemical species. Such models have been used with great success for many different scientific purposes, e.g to interpret high-resolution one-dimensional sections of chemical species measured in observational campaigns or to predict chemical ozone destruction in the stratosphere (e.g. Waugh et al. 1994, Methven et al. 2003). Of course, this whole approach depends on the flow being Type II rather than Type I, otherwise the fact that information from spatial scales below the resolution of the datasets is not included would be a serious limitation.

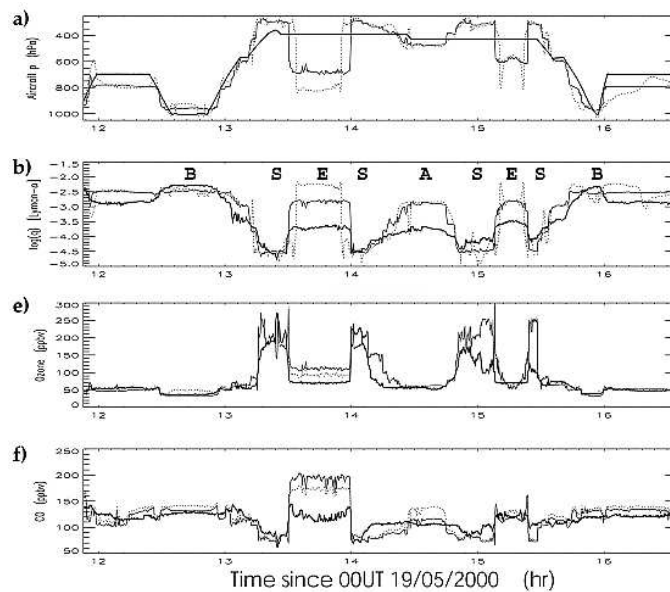


Figure 2. (From Methven et al. 2003) Time series of observations (bold lines) along the ACTO flight on 19 May 2000 compared to results from trajectory simulations. (a) Pressure and (b) $\log(q)$, where q is concentration of water in g kg^{-1} . Dotted lines show values interpolated from global meteorological data to the trajectory origins at 12UT, 17 May 2000. Solid lines show an ‘air-mass average’ of these modeled values. (c) and (d) not shown. (e) Ozone and (f) carbon monoxide concentrations. Dotted line is air-mass average at origin of trajectories. Solid is prediction of chemical model integrated along the trajectory. Copyright 2003 American Geophysical Union. Reproduced by permission of American Geophysical Union.

The Methven et al. (2003) paper gives a nice example of the sort of work that it is now possible using a combination of chemical data (in this case from aircraft) and Lagrangian calculations using the global velocity fields. The focus of the paper is a campaign (ACTO) in which a research aircraft made chemical and meteorological measurements to the northwest of Scotland. Figure 1 shows back-trajectory calculations that suggest that air sampled in the upper troposphere in this region on one particular day of the campaign converged from three distinct locations. Some of the back trajectories originate in region A, the mid-troposphere in Eastern Atlantic, some in region S, the stratosphere over central Canada, and some in region E, the lower troposphere over central Europe. Air from each of these regions has a different chemical signature. That from region A is moist and relatively low in ozone (O_3) and carbon monoxide (CO). That from region S is dry, high in O_3 and low in CO. That from region E is similar to that from A in that it is moist (both regions are in the troposphere) but different in that it is relatively polluted and therefore high in CO and in O_3 (some of which is likely to have formed through photochemical production as air moves from region E to the region of measurement). Comparison with the detailed chemical fields measured by the aircraft, as shown in Fig. 2, shows that the positions and chemical characteristics of the different air masses are generally well predicted by the back trajectory calculation, even, in many cases, down to small-scale features. See Methven et al. (2003) for further details and discussion.

3. Transport and Stirring

Given that the large-scale atmospheric flow is quasi-horizontal, models of chaotic advection in two-dimensional incompressible flow are potentially relevant. Such models and analogous dynamical systems show that transport and stirring is often highly inhomogeneous, with regions of strong stirring (i.e. strong stretching) separated by barrier regions in which stirring is weak and across which there is no, or relatively little, transport (e.g. Meiss 1992, Wiggins 1992). Many detailed investigations over the last 20 years or so have shown how the transport and stirring properties of simple flows change with the parameters defining that flow. The typical picture is as follows. For a steady incompressible two-dimensional flow the dynamical system describing particle advection is integrable. Particles move along streamlines, i.e. contours of the streamfunction, and these streamlines, which are invariant curves of the dynamical system, act as perfect barriers to transport. If a small time-periodic perturbation is added to the flow then, consistent with the

KAM theorem, many (in fact ‘almost all’ in the limit of a vanishingly small perturbation) invariant curves survive. The same is probably true for relatively large classes of quasi-periodic perturbations. Between the surviving invariant curves there are thin regions in which particle trajectories are chaotic (and stirring is therefore strong). These chaotic regions increase in thickness as the amplitude of the perturbation increases, with the thickest regions usually centred on the location of streamlines of the unperturbed flow that pass through hyperbolic stagnation points. For small perturbations the geometry of surviving invariant curves is similar to that of the streamlines of the steady flow and many features of the pattern of transport in the steady flow therefore persist to the perturbed flow. For example, two disjoint regions may be separated by many streamlines of the steady flow and by many invariant curves of the weakly perturbed flow, so that transport between those two regions is forbidden. However as the size of the perturbation increases more and more invariant curves break, so that ultimately the last invariant curve separating the two disjoint regions breaks and transport between those regions is allowed.

This sort of behaviour is illustrated in Fig. 3, which shows Poincaré sections for simple time-periodic flows, with the amplitude of the time-dependent perturbation measured by a parameter ϵ_2 . For more details see Shuckburgh and Haynes (2003). For $\epsilon_2 = 0.0125$ and $\epsilon_2 = 0.025$ there is a perfect central barrier to transport roughly indicated by the grey curve. For $\epsilon_2 = 0.05$ and $\epsilon_2 = 0.075$ this central barrier has disappeared. Nonetheless, for $\epsilon_2 = 0.05$ some memory of the barrier persists and transport between the two halves of the flow domain is relatively slow, as can be seen by (at finite time) the modest intersection of the two Poincaré sections. Again this persistence of a partial barrier after the last invariant curve has disappeared is a generic feature of such systems.

In the real atmosphere observations and models show similarly inhomogeneous transport and stirring. In the winter stratosphere, for example, the edge of the winter polar vortex seems to form a transport barrier which is not perfect, but across which transport is very weak. Outside the vortex, in mid-latitudes, and to a lesser extent inside the vortex, there are regions of strong stirring (e.g. Joseph and Legras 2002 and references therein). Lower in the atmosphere the subtropical jet seems to form a similar, if less effective, barrier to quasi-horizontal transport which separates the upper troposphere and the lowest part of the stratosphere. Once again, poleward and equatorward of the subtropical jet there are regions of strong stirring (e.g. Haynes and Shuckburgh 2000b). This sort of spatial structure, with transport barriers and stirring regions, is found in a wide class of geophysical flows.

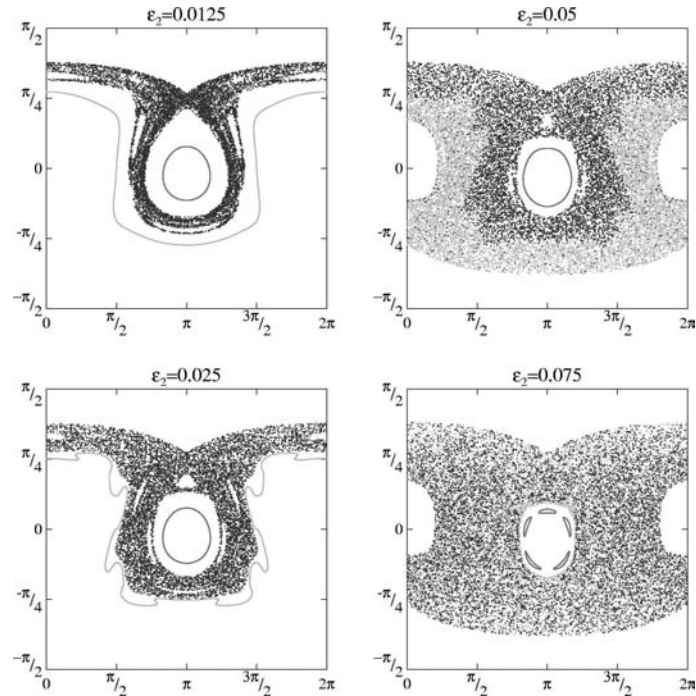


Figure 3. (From Shuckburgh and Haynes 2003) Poincaré sections (10000 periods) for a simple time periodic flow, with ϵ_2 measuring the amplitude of the time-dependent part of the flow. Three different Poincaré sections are plotted in each case. The limited intersection between two such sections for $\epsilon_2 = 0.05$ shows that whilst a ‘last’ invariant curve has broken, significant inhibition of transport remains. Copyright 2003 American Institute of Physics. Reproduced by permission of American Institute of Physics.

On a purely diagnostic level, quantifying the transport and stirring properties of an atmospheric flow, as defined by global meteorological datasets or by numerical models, poses the same challenges as quantifying transport and stirring (or ‘mixing’) in any chaotic dynamical system. Such quantification is of practical important, e.g to compare effectively the transport and stirring structure of velocity fields in different observational datasets or generated by different numerical models. Various mathematical tools originating in dynamical systems theory have been studied in this context. One example is the method of ‘lobe dynamics’ which calculates fluxes across control surfaces built up of parts of stable and unstable manifolds of particular hyperbolic trajectories (which in the particular case of time-periodic flow are usually hyperbolic fixed points of the corresponding Poincaré map) (Wiggins 1992, Malhotra and Wiggins 1998). Koh and Plumb (2000) have applied this method to

quantify transport across the polar vortex edge in a simple model and find that it gives a misleading estimate of such transport. The reason seems to be that the type of control surface that is usually constructed in lobe dynamics does not usefully correspond to the vortex edge (see Joseph and Legras 2002 for further discussion). The same difficulty is likely to arise in any attempt to use lobe dynamics to quantify transport across a disturbed jet (and many atmospheric transport problems are of this nature). It may be that these difficulties may be circumvented by a more ingenious choice of control surface. It should also be noted that lobe dynamics is more successful and, potentially, practically useful for other geophysical flows, e.g. the two-gyre oceanic flow studied by Coulliette and Wiggins (2001).

A completely different method to quantifying transport that has been applied to realistic atmospheric flows is to calculate ‘effective diffusivity’ – a measure of the geometry of a test tracer that is advected by the flow (Haynes and Shuckburgh 2000a,b). This method is apparently successful in identifying transport barriers associated with jets or edges of vortices and in calculating their strength. Shuckburgh and Haynes (2003) examine the relation of effective diffusivity to other measures of transport and stirring.

A more fundamental question concerns the apparent close similarity between the transport and stirring structure (barriers and stirring regions) seen in time-periodic flows and those observed in geophysical flows, including realistic atmospheric flows. The fact is that in the former the flow is imposed in advance (the model is ‘kinematic’), whereas in the latter the flow is the solution of a set of dynamical equations. In large-scale atmospheric and oceanic flows, those dynamical equations can be expressed to good approximation as the conservation of potential vorticity (PV) following the fluid motion (with non-conservation associated with frictional or diabatic effects), together with an invertibility relation that determines all other flow quantities instantaneously from the potential vorticity. Thus the transport and stirring properties of a flow are, because of transport and stirring of potential vorticity, inextricably linked to the dynamics. Study of the transport and stirring structure of given flows therefore poses a ‘dynamical consistency’ problem – it is not self-consistent to ignore the effect of the transport and stirring on the dynamics. Brown and Samelson (1994) argue in the case of two-dimensional PV conserving flow that one implication of dynamical consistency is that chaotic particle trajectories are forbidden, though it may be possible to escape this constraint if PV is not perfectly conserved.

One argument for the relevance of the kinematic models is that the potential vorticity field arising from the transport and stirring is in many cases dominated by small spatial scales and the smoothing nature of the inversion operator is such that the dynamical effect is weak. However it is difficult to see that the dynamical effect will always be weak and it seems likely that in some aspects of transport and mixing behaviour, e.g. the persistence versus destruction of transport barriers as perturbation amplitude is increased, the dynamical effect will be significant.

It seems extremely difficult to formulate any analytic or semi-analytic model that allows an interesting combination of dynamical consistency and chaotic transport. All attempted formulations have, to the author's knowledge, ended up considering cases where the transport (of potential vorticity) is for one reason or another uncoupled from the dynamics. An alternative approach is to consider suitable numerical experiments. Poet (2004) reports a comparison between a kinematic model of a meandering jet in a channel previously considered by Pierrehumbert (1991) and others and a corresponding dynamically consistent model based on the two-dimensional vorticity equation on a β -plane. The 'correspondence' is that if the dynamical equations are linearised about a background unidirectional flow along the channel the flow in the dynamically consistent model would be precisely that in the kinematic model.

The kinematic model is different to that for which results are shown in Fig. 3, but has the same generic behaviour, where for small time-dependence many invariant curves persist and transport from one half of the channel to the other is forbidden. Then at a critical value of the parameter ϵ governing the amplitude of the time-dependent component of the flow, the 'last' invariant curve breaks and transport from one half of the channel to the other is permitted. This is indicated in Fig. 4 (curve A) by the average transit time (from one chosen region to another) which is essentially infinite for $\epsilon < 0.34$. The slow decrease of the transit time as ϵ increases beyond 0.34 indicates that significant inhibition of transport remains (analogous to the behaviour seen for $\epsilon_2 = 0.05$ in Fig. 3). The results for the dynamically consistent model are shown as curve B. Here it is difficult to set up conditions where any transport barrier is perfect. The large average transit time for $\epsilon < 0.44$ may therefore be taken to indicate a strong barrier. In this sense the strong barrier persists to a larger value of ϵ in the dynamically consistent model than in the kinematic model – dynamical consistency apparent strengthens the barrier effect in that sense. A further important difference is that for $\epsilon < 0.44$, once the barrier has broken, the transit time is immediately significantly reduced. There is therefore no persistence of a partial barrier as seen in the kinematic case. The reason is that, in the dynam-

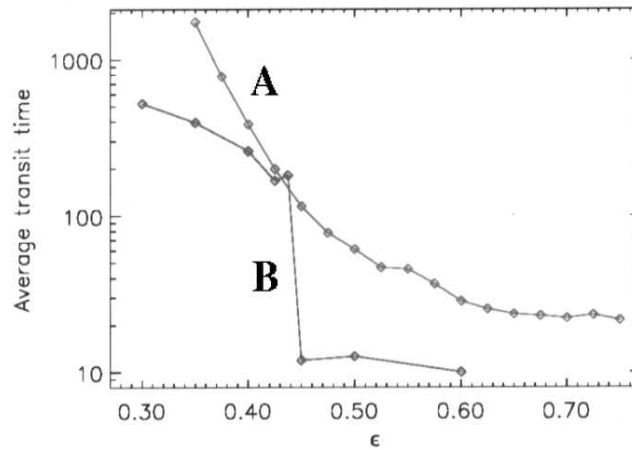


Figure 4. Transit time across central barrier as function of ϵ , amplitude of time-dependent component of flow. The upper curve A is for the kinematic model and the lower curve B is for the dynamically consistent model. See text for further details. Reproduced from Poet(2004). Copyright D.A. Poet 2004.

ically consistent case, once the central barrier is broken the potential vorticity is stirred throughout the flow domain and the character of the flow changes drastically as a result.

4. Stirring and Mixing

Mixing in the atmosphere could be achieved in laminar flow, but in practice is likely to be enhanced through intermittent encounters of air parcels with three-dimensional turbulence. This enhancement might be substantial in the troposphere, where convection is relatively common, is likely to be much weaker in the lower stratosphere and then to increase again in the upper stratosphere and mesosphere, where three-dimensional turbulence associated with the breaking of gravity waves is more widespread. One outstanding question is how to estimate the overall mixing effects of these encounters. One approach is by direct observation of the turbulent events themselves (e.g. Alisse et al. 2000), but the spatial intermittency and strong geographical and seasonal variation make it difficult to integrate such observations to give a quantitative estimate of overall mixing effect.

A different approach is to argue that the chemical concentration fields in the atmosphere arise from a combination of advection and mixing effects. If the former is dominated by the large-scale flow, then it can to some extent be estimated using the velocity fields from global meteorological datasets. This gives the possibility of an ‘inverse’ calculation,

taking the observed distributions of chemical species and trying to deduce what quantitative representation of mixing is consistent with those observations and with the (known) large-scale flow.

Predictions of the three-dimensional structure of chemical fields in necessary detail, given the large-scale flow, are beyond current computational resources (whatever mixing processes are assumed). However, there are theories for stirring and mixing of chemical species in large-scale 'Type-II' flows that offer an alternative approach to full three-dimensional computation.

A long-standing theoretical approach has been to consider the interaction between stretching and diffusion in a flow that is a random function of time and a linear function of space. This theory has undergone significant developments recently (e.g. Antonsen et al. 1996, Falkovich et al. 2001). Whilst the theory has serious limitations in the initial-value problem (i.e. free decay from a specified initial field for the chemical concentration) (Sukhatme and Pierrehumbert 2002, Fereday and Haynes 2004) these limitations do not seem to extend to the forced problem (where the chemical concentration is maintained by some source/sink distribution) and potentially it offers a quantitative theory for the chemical concentration field that arises from a specified combination of large-scale flow and small-scale mixing processes. The standard theories need some extension to be applied to the atmosphere, but this extension is relatively straightforward. On this basis Haynes and Vanneste (2004) have examined the effect of diffusivity (as a representation of small-scale turbulent mixing processes) on the spatial structure, specifically the wavenumber spectrum, of long-lived chemical species in the lower stratosphere. The simplest theoretical prediction is that the spectrum has a k^{-1} range, where k is wavenumber at small k (but larger than the forcing wavenumber) and a steeper spectrum at larger k where mixing effects become important. The results suggest that, for plausible stratospheric forcing scales, a clear k^{-1} regime would be seen only if the diffusivity D were similar in value to molecular diffusivity at about $10^{-4} \text{ m}^2 \text{ s}^{-1}$, implying little turbulent enhancement of mixing. If D were $10^{-2} \text{ m}^2 \text{ s}^{-1}$, on the other hand, which corresponds to the value estimated by the Alisse et al. (2000) study, then on scales of a few kilometers the form of the spectrum is rather close to k^{-2} , which happens to coincide with observational estimates by Sparling and Bacmeister (2001). This is certainly not the last word, however. More attention needs to be paid to the effects of spatial and temporal organisation of the stratospheric flow (the persistent stratospheric polar vortex, for example), which is not properly incorporated by the theories. Furthermore, calculations by Legras et al. (2003) using a different approach suggest that a larger value

of D gives a better match to observations. Finally, similar studies are needed of the tropopause region where mixing processes are ill-quantified and may have significant effects on chemical distributions.

References

- H. Akimoto, Global air quality and pollution, *Science*, 302, pp.1716-1719, 2003.
- J.-R. Alisse, P.H. Haynes, J. Vanneste, C. Sidi, Quantification of stratospheric mixing from turbulence microstructure measurements, *Geophys. Res. Lett.*, 27, pp.2621-2624, 2000.
- T.M. Antonsen, Z. Fan, E. Ott, E. Garcia-Lopez, The role of chaotic orbits in the determination of power spectra of passive scalars, *Phys. Fluids*, 8, pp.3094-3104, 1996.
- P. Bartello, Using low-resolution winds to deduce fine structure in tracers, *Atmos.-Ocean*, 38, pp.303-320, 2000.
- M.G. Brown, R.M. Samelson, Particle motion in incompressible, inviscid vorticity-conserving fluids, *Phys. Fluids*, 6, pp.2875-2876, 1994.
- C. Coulliette, S. Wiggins, Intergyre transport in a wind-driven, quasigeostrophic double gyre: An application of lobe dynamics, *Nonlinear Proc. Geophys.*, 7, pp.59-85, 2001.
- G. Falkovich, K. Gawedzki, M. Vergassola, Particles and fields in fluid turbulence, *Revs. Mod. Phys.* 73, pp.913-975, 2001.
- D.R. Fereday, P.H. Haynes, Scalar decay in two-dimensional chaotic advection and Batchelor-regime turbulence, *Phys. Fluids*, 16, pp.4359-4370, 2004.
- P.H. Haynes, E.F. Shuckburgh, Effective diffusivity as a diagnostic of atmospheric transport. Part I: stratosphere, *J. Geophys. Res.* 105, pp.22777-22794, 2000a.
- P.H. Haynes, E.F. Shuckburgh, Effective diffusivity as a diagnostic of atmospheric transport. Part II: troposphere and lower stratosphere, *J. Geophys. Res.*, 105, pp.22795-22810, 2000.
- P.H. Haynes, J. Vanneste, Stratospheric tracer spectra, *J. Atmos. Sci.*, 61, pp.161-178, 2004.
- B. Joseph, B. Legras, Relation between kinematic boundaries, stirring and barriers for the Antarctic polar vortex, *J. Atmos. Sci.* 59, pp.1198-1212, 2002.
- T.-Y. Koh, R.A. Plumb, Lobe dynamics applied to barotropic Rossby-wave breaking, *Phys. Fluids* 12, pp.1518-1528, 2000.
- B. Legras, B. Joseph, F. Lefèvre, Vertical diffusivity in the lower stratosphere from Lagrangian back-trajectory reconstructions of ozone profiles, *J. Geophys. Res.*, 108:D4562 – doi:10.1029/2002JD003045, 2003.
- N. Malhotra, S. Wiggins, Geometric structures, lobe dynamics, and Lagrangian transport in flows with aperiodic time-dependence, with applications to Rossby wave flow, *J. Nonlinear Sci.*, 8:401-456, 1998.
- J.D. Meiss, Symplectic maps, variational principles and transport, *Rev. Mod. Phys.*, 64, 795-848, 1992.
- J. Methven, S.R. Arnold, F.M. O'Connor, H. Barjat, K. Dewey, J. Kent, N. Brough, Estimating photochemically produced ozone throughout a domain using flight data and a Lagrangian model, *J. Geophys. Res.*, 108:D4271–doi:10.1029/2002JD002955, 2003.
- R.E. Newell, V. Thouret, J.Y.N. Cho, P. Stoller, A. Marengo, H.G. Smit, Ubiquity of quasi-horizontal layers in the troposphere, *Nature*, 398, pp.316-319, 1999.

- R.T. Pierrehumbert, Chaotic mixing of tracer and vorticity by modulated traveling Rossby waves, *Geophys. Astrophys. Fluid Dynamics*, 58, pp.285–319, 1991.
- D.A. Poet, *Dynamical consistency, barriers to transport and mixing, in chaotic advection flows*, Ph.D. thesis, University of Cambridge, pp.207, 2004.
- T.G. Shepherd, J.N. Koshyk, K. Ngan, On the nature of large-scale mixing in the stratosphere and mesosphere, *J. Geophys. Res.*, 105:, pp.12433–12446, 2004.
- E.F. Shuckburgh, P.H. Haynes, Diagnosing transport and mixing using a tracer-based coordinate system, *Phys. Fluids*, 15, pp.3342-3357, 2003.
- L.C. Sparling, J.T. Bacmeister, Scale dependence of tracer microstructure: PDFs, intermittency and the dissipation scale, *Geophys. Res. Lett.*, 28: pp.2823–2826, 2001.
- J. Sukhatme, R.T. Pierrehumbert, Decay of passive scalars under the action of single scale smooth velocity fields in bounded two-dimensional domains: From non-self-similar probability distribution functions to self-similar eigenmodes, *Phys. Rev. E.*, 66:056302-1–056302-11, 2002.
- D.W. Waugh, et al. Transport of material out of the stratospheric Arctic vortex by Rossby wave breaking, *J. Geophys. Res.*, 99, pp.1071–1088, 1994.
- S. Wiggins, *Chaotic transport in dynamical systems*, New York, Springer-Verlag, pp.301, 1992.
- S. Wiggins, J.M. Ottino, Foundations of chaotic mixing, *Phil. Trans. Roy. Soc. Lond. A*, 362, pp.937–970, 2004.

VARIATIONAL AND MULTISCALE METHODS IN TURBULENCE

Thomas J. R. Hughes*, Victor M. Calo, and Guglielmo Scovazzi
*Institute for Computational Engineering and Sciences,
University of Texas at Austin
201 E. 24th Street, ACES 5.430A
1 University Station C0200,
Austin, Texas 78712-0027, U.S.A*

Abstract An overview is presented of variational and multiscale methods used in Large-Eddy Simulations of turbulence. Results for the problem of bypass transition of a boundary layer are presented illustrating the performance of a recently developed method.

Keywords: Consistent variational multiscale method, turbulence modeling, bypass transition, finite difference method, finite volume method.

1. Introduction

Variational multiscale concepts for Large Eddy Simulation (LES) were introduced in Hughes et al., 2000. The basic idea was to use variational projections in place of the traditional filtered equations and to focus modeling on fine-scale equations rather than coarse-scale equations. Avoidance of filters eliminates many difficulties associated with the traditional approach, namely, inhomogeneous non-commutative filters necessary for wall-bounded flows, use of complex filtered quantities in compressible flows, the closure problem, etc. In addition, modeling confined to the fine-scale equations retains numerical consistency in the coarse-scale equations and thus permits full rate-of-convergence of the underlying numerical method in contrast with the usual approach which limits convergence rate due to artificial viscosity effects in the fully resolved scales ($O(h^{4/3})$ in the case of Smagorinsky-type models). Initial versions of the variational multiscale method focused on dividing resolved scales into coarse and fine designations, and eddy viscosities, inspired

*hughes@ices.utexas.edu

by traditional models, were *only* included in the fine scale equations, and acted *only* on the fine scales. This version was studied in Hughes et al., 2001a; Hughes et al., 2001b; Oberai and Hughes, 2002 and found to work very well on homogeneous isotropic flows and fully-developed equilibrium and non-equilibrium turbulent channel flows. Static eddy viscosity models were employed in these studies but superior results were subsequently obtained through the use of dynamic models, as reported in Holmen et al., 2004 and Hughes et al., 2004b. Good numerical results were obtained with the static approach by other of investigators, namely, Collis, 2002; Jeanmart and Winckelmans, 2002 and Ramakrishnan and Collis, 2002; Ramakrishnan and Collis, 2004c; Ramakrishnan and Collis, 2004b; Ramakrishnan and Collis, 2004a. Particular mention should be made of the work of Farhat and Koobus, 2002, and Koobus and Farhat, 2004, who have implemented this procedure in an unstructured mesh, finite volume, compressible flow code, and applied it very successfully to a number of complex test cases and industrial flows. We believe that this initial version of the variational multiscale concept has already demonstrated its viability and practical utility and is, at the very least, competitive with traditional LES turbulence modeling approaches.

Nevertheless, there is still significant room for improvement. The use of traditional eddy viscosities to represent fine-scale dissipation is an inefficient mechanism. Employing an eddy viscosity in the resolved fine scales to represent turbulent dissipation introduces a consistency error which results in the resolved fine scales being “sacrificed” to retain full consistency in the coarse scales. (In our opinion, this is still better than the traditional approach in which consistency in *all* resolved scales is sacrificed to represent turbulent dissipation.) This procedure is felt to be “inefficient” because approximately 7/8 of the resolved scales are typically ascribed to the fine scales. Another shortcoming noted for the initial version of the variational multiscale method is too small an energy transfer to unresolved modes when the discretization is very coarse (see, e.g., Hughes et al., 2004b). This phenomenon is also noted for some traditional models, such as the dynamic Smagorinsky model Hughes et al., 2004b, but, by design is more pronounced for the multiscale version of the dynamic model. The objectives of recent multiscale work have been to capture all scales consistently and to avoid use of eddy viscosities altogether. This holds the promise of much more accurate and efficient LES procedures. In this work, we describe a new variational multiscale formulation which makes considerable progress toward these goals. In what follows, all resolved scales are viewed as coarse scales, which obviates the issue of inefficiency *ab initio*.

We begin by taking the view that the decomposition into coarse and fine scales is exact. For example, in the spectral case, the coarse-scale space consists of all Fourier modes beneath some cut-off wave number and the fine-scale space consists of all remaining Fourier modes. Consequently, the coarse-scale space has finite dimension whereas the fine-scale space is infinite dimensional. The derivation of the coarse- and fine-scale equations proceeds, first, by substituting the split of the exact solution into coarse and fine scales into the Navier-Stokes equations, then, second, by projecting this equation into the coarse- and fine-scale subspaces. The projection into coarse scales is a finite dimensional system for the coarse-scale component of the solution, which depends parametrically on the fine-scale component. In the spectral case, in addition to the usual terms involving the coarse-scale component, only the cross-stress and Reynolds-stress terms involve the fine-scale component. In the case of non-orthogonal bases, even the linear terms give rise to coupling between coarse and fine scales. The coarse-scale component plays an analogous role to the filtered field in the classical approach, but has the advantage of avoiding all problems associated with homogeneity, commutativity, walls, compressibility, etc. The projection into fine scales is an infinite-dimensional system for the fine-scale component of the solution which depends parametrically on the coarse-scale component. We also assume the cut-off wave number is sufficiently large that the philosophy of LES is appropriate. For example, if there is a well-defined inertial sub-range, then we assume the cut-off wave number resides somewhere within it. This assumption enables us to further assume that the energy content in the fine scales is small compared with the coarse scales. This turns out to be *crucial* in our efforts to analytically represent the solution of the fine-scale equations. The strategy is to obtain approximate analytical expressions for the fine scales then substitute them into the coarse-scale equations which are, in turn, solved numerically. If the scale decomposition is performed in space and time, the *only* approximation in the procedure is the representation of the fine-scale solution. To provide a framework for the fine-scale approximation, we assume an infinite perturbation series expansion to treat the fine-scale nonlinear term in the fine-scale equation. By virtue of the smallness of the fine scales, this expansion is expected to converge rapidly under the circumstances described in many cases of practical interest. The remaining part of the fine-scale Navier-Stokes system is the *linearized* operator which is formally inverted through the use of a matrix Green's function. The combination of a perturbation series and Green's function provides an exact formal solution of the fine-scale Navier-Stokes equations. The driving force in these equations is the Navier-Stokes system residual computed

from the coarse scales. This expresses the intuitively obvious fact that if the coarse scales constitute a good approximation to the solution of the problem, the coarse-scale residual will be small and the resulting fine-scale solution will be small as well. This is the case we have in mind and it provides a rational basis for assuming the perturbation series converges rapidly. Note that one cannot use such an argument on the original problem because in this case the perturbation series would almost definitely fail to converge. (If we could have used this argument, we would have solved the Navier-Stokes equations analytically! Unfortunately, it does not work.) The formal solution of the fine-scale equations suggests various approximations may be employed in practical problem solving. We are tempted to use the word “modeling” because approximate analytical representations of the fine scales constitute the only approximation and hence may be thought of as the “modeling” component of the present approach but we want to emphasize that it is very different from classical modeling ideas which are dominated by the *addition* of *ad hoc* eddy viscosities. We will present numerical results that demonstrate these eddy-viscosity terms are unnecessary in the present circumstances. There are two aspects to the approximation of the fine scales: 1) Approximation of the matrix Green’s function for the linearized Navier-Stokes system; and 2) approximation of the nonlinearities represented by the perturbation series. The first and obvious thought for the latter aspect, nonlinearity, is to simply truncate the perturbation series. This idea is investigated, as well as another promising idea, in conjunction with some simple approximations of the Green’s function. It turns out there is considerable experience in local scaling approximations of the Green’s function based on the theory of *stabilized methods* Hughes, 1995; Hughes et al., 1998; Hughes et al., 2004a. The Green’s function is typically approximated by locally defined algebraic operators (i.e., the “ τ ’s” of stabilized methods) multiplied by local values of the coarse-scale residual. With this approximation of the solution of the linearized operator, nonlinearities can be easily accounted for in perturbation series fashion. Another approach that accounts for nonlinearities in the fine-scale equations is to introduce a nonlinear algebraic scaling of the Navier-Stokes equations. The resulting local nonlinear algebraic system can be analytically solved. It possesses the reasonable analytical property that if the coarse-scale residual is small, it converges to the linearized solution.

These newer variational multiscale ideas, and the older variants, were implemented in a finite volume code that has enjoyed widespread use in turbulence simulations (see Pierce and Moin, 2001). Following along the lines of Jacobs and Durbin, 2000; Jacobs and Durbin, 2001, who

performed DNS investigations of bypass transition of a boundary layer, we examine this difficult problem from the point of view of the variational multiscale and classical LES. Our aim was to solve this problem as an LES and demonstrate the efficacy of the new ideas in the process.

In our work we endeavor to show the effectiveness, or deficiencies, of LES approaches by studying them over a range of resolutions, from coarse to fine. In our studies of bypass transition we went as far as DNS in the fine-scale end of the spectrum, and approximately 1/8 DNS resolution in each spatial direction. The coarsest LES mesh then involves about 1/256 the number of equations as the DNS mesh and approximately 1/4,096 of the computational effort. We found, independent of the LES method, that in order to accurately simulate bypass transition, the decay of input homogeneous, isotropic, free-stream turbulence must be the same for all meshes. A procedure was developed in which we were able to simulate consistent energy decay with distance of the free-stream turbulence across the range of meshes considered. We then compared the methods to represent bypass transition. We found that the “1/8 DNS mesh” was incapable of representing either the laminar region of the boundary layer or the free-stream turbulence evolution due to too few points in the wall normal direction. We found that all methods gave essentially the same solution at the DNS level, whereas the new variational multiscale formulation was able to attain relatively mesh independent solutions without parameter adjustment for the 1/4, 1/2 and full DNS mesh cases. The 1/4 DNS involves 1/64 the number of mesh points as the DNS case and 1/256 the computational effort. We believe that the new method offers a promising new path for turbulence research in LES. However, it obviously needs testing on a wider variety of flows and implementation in a variety of numerical frameworks, such as, spectral, finite difference and finite element, before definitive conclusions can be drawn. In our experience, the particular numerical discretization method has an enormous impact on the results, and its influence is often underestimated by practitioners evaluating models.

2. Bypass Transition

The problem description is presented in Fig. 1. Parameters used in the calculations are defined in Table 1. δ_0 is the boundary layer thickness at the inlet, L_x , L_y , and L_z are the lengths of the domain in the streamwise, wall-normal, and spanwise directions, respectively, θ_0 is the momentum thickness at the inlet, and $\text{Re}_{\delta_0} (= U_0\delta_0/\nu)$ is the Reynolds number based on the free-stream velocity and length-scale δ_0 . The methods tested were incorporated in the program developed by Pierce and

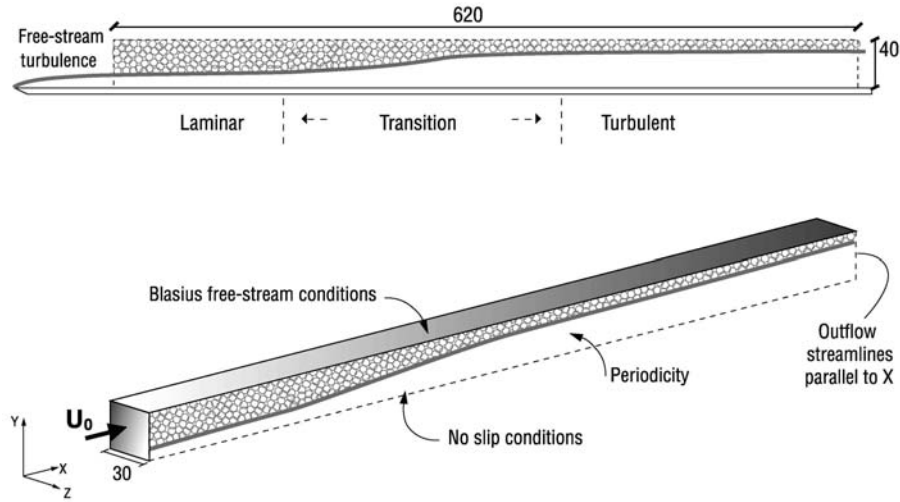


Figure 1. Bypass transition. Problem description.

Moin, 2001, which employs a second-order central difference scheme on a staggered mesh, an explicit-implicit second-order time-stepping algorithm (Akselvoll and Moin, 1995), and an approximate factorization technique which decouples the velocity and pressure equations (Le and Moin, 1994). The meshes employed in the calculations are described in Table 2. The fine mesh corresponds to the DNS mesh case 1 of Jacobs and Durbin, 2000; Jacobs and Durbin, 2001. Synthetic homogeneous isotropic turbulent fluctuations are generated at the inlet in a manner similar to that described in Jacobs and Durbin, 2000; Jacobs and Durbin, 2001. The decay of the free-stream turbulence is illustrated in Fig. 2.

It is essential that the free-stream turbulence, quantified by the turbulent kinetic energy, Tu , decays in a consistent fashion across all meshes and methods. Otherwise, there is no chance of accurately capturing the transition process which is characterized by the formation of “turbulent

L_x	$620 \delta_0$
L_y	$40 \delta_0$
L_z	$30 \delta_0$
θ_0	$0.1336 \delta_0$
Re_{δ_0}	795

Table 1. Bypass-transition parameters

Designation	N_x	N_y	N_z
Fine	2048	180	192
Medium	1024	90	96
Coarse	512	48	48

Table 2. Resolution of bypass-transition meshes.

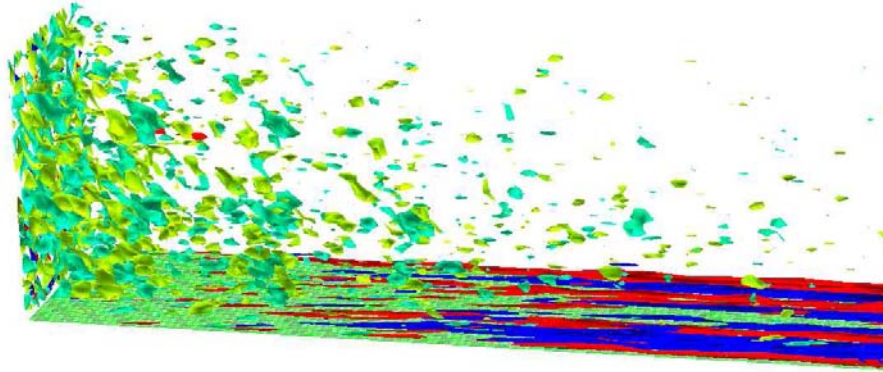


Figure 2. Bypass transition. Decay of free-stream turbulence.

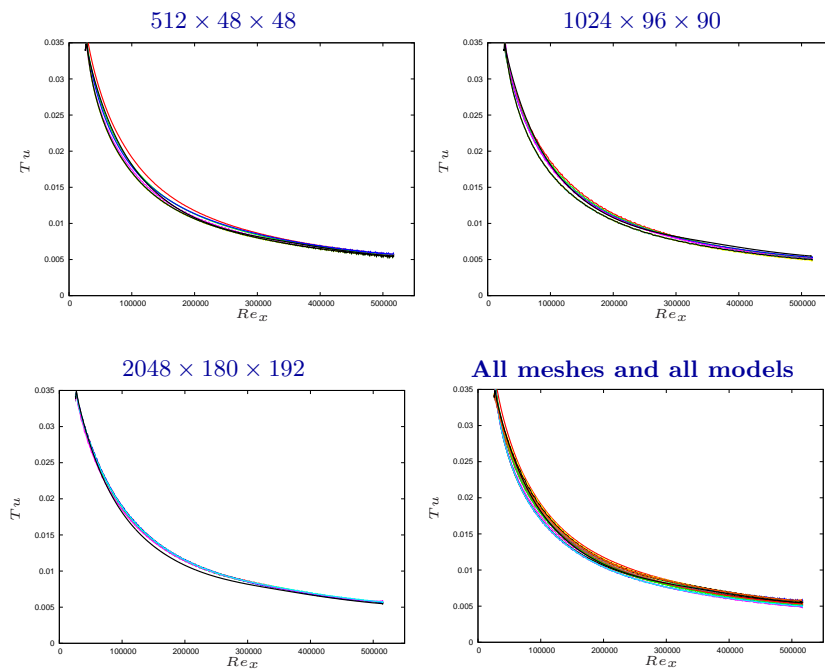


Figure 3. Bypass transition. Decay of free-stream turbulence. Turbulent kinetic energy versus streamwise position.

spots". The procedure employed to achieve this end requires a somewhat lengthy description (omitted here) but results are shown in Fig. 3 in which Tu is plotted versus Re_x , the Reynolds number based on streamwise position from the inlet. It is important to accurately represent the interaction between the free-stream turbulence and the longitudinal streaks in the laminar boundary layer. The streaks are shown in Fig. 4 in the form of isosurfaces of streamwise velocity fluctuations. Also shown are the free-stream turbulence (to the left, in the form of isosurfaces of spanwise fluctuations), the fully-developed turbulent boundary layer (to the right), and, in the detail, spot initiation.

Time- and span-averaged results are shown in Fig. 5 for the fine mesh ($2048 \times 180 \times 192$). Results are presented for the DNS case (no model), dynamic Smagorinsky, original (dynamic) multiscale, and the new residual-based multiscale models. Skin-friction coefficient is presented in Fig. 5(a), and shape factor, the ratio of the displacement thickness to the momentum thickness, is presented in Fig. 5(b). At this level of resolution, all the models are very close to each other and there is good agreement with the experimental results of Roach and Brierley, 1992. In Fig. 6, skin-friction coefficient results are presented for the no-model case and the new multiscale method for coarse, medium, and fine meshes. In the no-model case, Fig. 6(a), the coarse and medium meshes produce

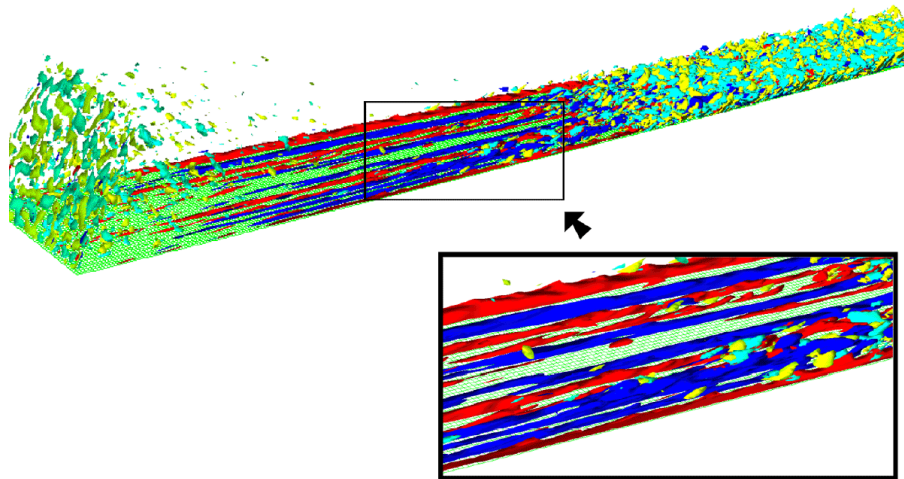


Figure 4. Bypass transition. Velocity fluctuation isosurfaces. The red and blue streaks are streamwise velocity fluctuations. The decay of free-stream turbulence is shown on the left and the fully-developed turbulent boundary layer is seen on the right.

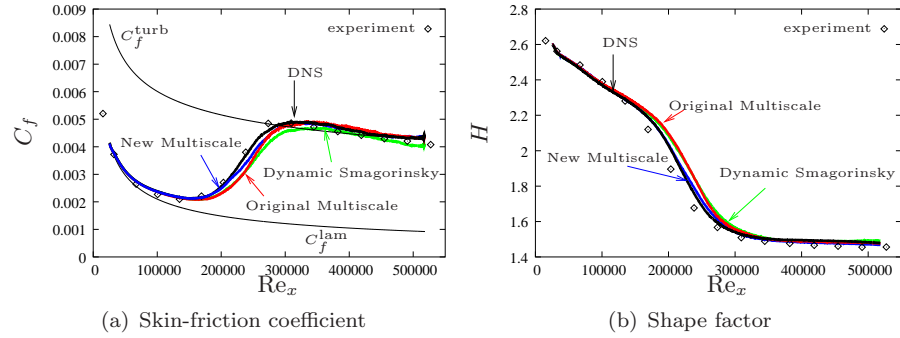


Figure 5. Bypass transition. Numerical results for the $2048 \times 180 \times 192$ mesh.

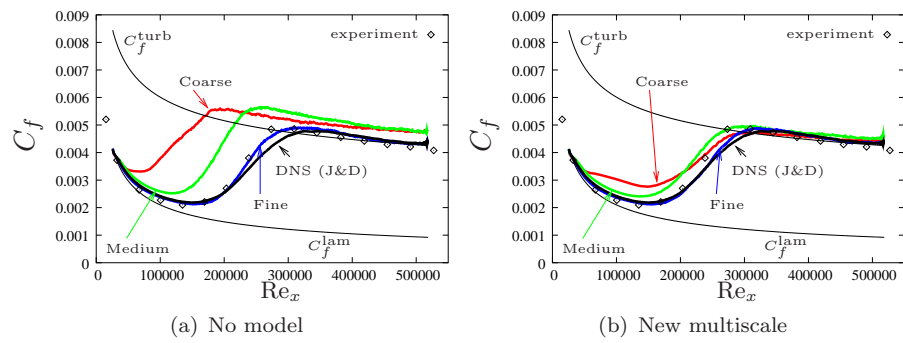


Figure 6. Bypass transition. Skin-friction coefficient for coarse, medium, and fine meshes.

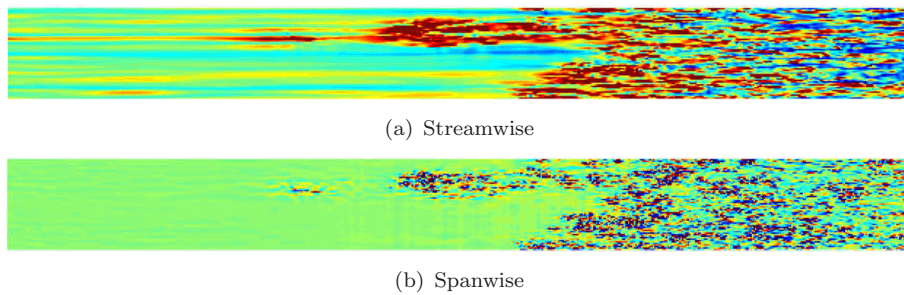


Figure 7. Bypass transition. Velocity fluctuations.

premature transitions and do not achieve correct turbulent correlations in the fully-developed region to the right. On the other hand, the new multiscale method, Fig. 6(b), attains accurate turbulent correlations in the fully-developed region for all meshes, and the transition region is also fairly accurately captured across meshes. There is discrepancy in the laminar region for the coarsest mesh because, to achieve the correct evolution of Tu , high levels of Tu needed to be specified at the inlet which, in combination with the coarse resolution, perturbed the laminar boundary layer, resulting in departure from the laminar correlation. In Fig. 7, streamwise and spanwise velocity fluctuation isosurfaces are shown for the DNS case (fine mesh, no model). The plan view corresponds to $y^+ \approx 2$, where plus units are calculated based on the maximum wall shear stress from the DNS. The formation of turbulent spots is clearly apparent.

Acknowledgement

The authors wish to gratefully acknowledge financial support provided by the Office of Naval Research under Contract No. 00014-03-1-0263, and Sandia National Laboratories under Contract No. A0340.0.

References

- K. Akselvoll and P. Moin, Large eddy simulation of turbulent confined coannular jets and turbulent flow over a backward facing step, Technical Report TF-63, Thermosciences Division, Department of Mechanical Engineering, Stanford University, 1995.
- S.S. Collis, Multiscale methods for turbulence simulation and control, Technical Report Version 1.1, Mechanical Engineering and Materials Science, Rice University. (http://www.mems.rice.edu/~collis/papers/vki2002_notes.pdf), 2002.
- C. Farhat and B. Koobus, Finite volume discretization on unstructured meshes of the multiscale formulation of large eddy simulations, In Mang H. A., Rammerstorfer F.G. and J., Eberhardsteiner, editors, *Proceedings of the Fifth World Congress on Computational Mechanics (WCCM V)*, Vienna University of Technology, Austria. Fifth World Congress on Computational Mechanics, 2002.
- J. Holmen, T.J.R. Hughes, A.A. Oberai, and G.N. Wells, Sensitivity of the scale partition for variational multiscale LES of channel flow, *Physics of Fluids*, 16(3):824–827, 2004.
- T.J.R. Hughes, Multiscale phenomena: Green’s functions, the Dirichlet-to-Neumann formulation, subgrid scale models, bubbles, and the origins of stabilized methods, *Computer Methods in Applied Mechanics and Engineering*, 127:387–401, 1995.
- T.J.R. Hughes, G. Feijóo, L. Mazzei, and J.B. Quincy, The variational multiscale method—A paradigm for computational mechanics, *Computer Methods in Applied Mechanics and Engineering*, 166:3–24, 1998.
- T.J.R. Hughes, L. Mazzei, and K.E. Jansen, Large eddy simulation and the variational multiscale method, *Computing and Visualization in Science*, 3:47–59, 2000.

- T.J.R. Hughes, L. Mazzei, A.A. Oberai, and A.A. Wray, The multiscale formulation of large eddy simulation: Decay of homogeneous isotropic turbulence, *Physics of Fluids*, 13(2):505–512, 2001a.
- T.J.R. Hughes, A.A. Oberai, L. Mazzei, Large eddy simulation of turbulent channel flows by the variational multiscale method, *Phys. Fluids*, 13(6):1784–1799, 2001b.
- T.J.R. Hughes, G. Scovazzi, and L.P. Franca, Multiscale and stabilized methods, [in:] E. Stein, R. de Borst, and T.J.R. Hughes, [eds.], *Encyclopedia of Computational Mechanics*, John Wiley & Sons, Ltd, 2004a.
- T.J.R. Hughes, G.N. Wells, and A.A. Wray, Energy transfers and spectral eddy viscosity of homogeneous isotropic turbulence: Comparison of dynamic Smagorinsky and multiscale models over a range of discretizations, *Physics of Fluids*, 16(11):4044–4052, 2004b.
- R.G. Jacobs and P.A. Durbin, Bypass transition phenomena studied by computer simulation, Technical Report TF-77, Flow Physics and Computation Division, Department of Mechanical Engineering, Stanford University, 2000.
- R.G. Jacobs and P.A. Durbin, Simulations of bypass transition, *Journal of Fluid Mechanics*, 428:185–212, 2001.
- H. Jeanmart and G.S. Winckelmans, Comparison of recent dynamic subgrid-scale models in the case of the turbulent channel flow, In *Proceedings Summer Program 2002*, pages 105–116, Stanford, CA. Center for Turbulence Research, Stanford University & NASA Ames, 2002.
- B. Koobus and C. Farhat, A variational multiscale method for the large eddy simulation of compressible turbulent flows on unstructured meshes—application to vortex shedding, *Computer Methods in Applied Mechanics and Engineering*, 193(15–16):1367–1383, 2004.
- H. Le and P. Moin, Direct numerical simulation of turbulent flow over a backward-facing step, Technical Report TF-58, Thermosciences Division, Department of Mechanical Engineering, Stanford University, 1994.
- A.A. Oberai and T.J.R. Hughes, The variational multiscale formulation of LES: Channel flow at $Re = 590$, In *40th AIAA Ann. Mtg.*, AIAA 2002-1056, Reno, NV, 2002.
- C.D. Pierce and P. Moin, Progress-variable approach for large eddy simulation of turbulent combustion, Technical Report TF-80, Flow Physics and Computation Division, Department of Mechanical Engineering, Stanford University. Available at <http://ctr.stanford.edu/Pierce/thesis.pdf>, 2001.
- S. Ramakrishnan and S.S. Collis, Variational multiscale modeling for turbulence control, In *AIAA 1st Flow Control Conference*, AIAA 2002-3280, St. Louis, MO, 2002.
- S. Ramakrishnan and S.S. Collis, Multiscale modeling for turbulence simulation in complex geometries, In *40th AIAA Aerospace Sciences Meeting and Exhibit*, AIAA 2004-0241, Reno, NV, 2004a.
- S. Ramakrishnan and S.S. Collis, Partition selection in multiscale turbulence modeling, *Preprint*, 2004b.
- S. Ramakrishnan and S.S. Collis, Turbulence control simulation using the variational multiscale method, *AIAA Journal*, 42(4):745–753, 2004c.
- P.E. Roach and D.H. Brierley, The influence of a turbulent free-stream on a zero pressure gradient transitional boundary layer development. Part 1: Test cases T3A and T3B, [In:] O. Pironneau, W. Rodi, I.L. Ryming, A.M. Savill, and T.V. Truong [eds.], *Numerical Simulation of Unsteady Flows and Transition to Turbulence*, *ERC-OFTAC*, pp.319–347, Cambridge University Press, Cambridge 1992.

MECHANICS OF THIN FILM STRUCTURES

Henrik Myhre Jensen

*Department of Building Technology and Structural Engineering,
Aalborg University, Sohngaardsholmsvej 57, DK-9000 Aalborg, Denmark*

hmj@bt.aau.dk

Abstract Cracking of thin films on substrates due to indentation is discussed. Previous results have been reviewed leading to a relationship between crack pattern and material parameters of the film. Interface fracture under steady-state conditions between thin films and substrates at corners is discussed. Crack front shapes are shown and it is shown that this mode of delamination is more critical than the plane strain edge crack. Possible explanations for the so-called telephone cord mode of buckling driven delamination are given.

Keywords: Interface fracture, delamination, thin films, telephone cord delamination

1. Cracking of Films During Indentation

Figure 1 shows crack patterns during indentation of a hard TiAlN coating with a thickness of $2.3\ \mu\text{m}$ applied to tool steel in order to increase the wear resistance. Radial cracks with certain spacing propagate to a given length. In Jensen [1] an analysis was carried out in order to reveal the information which can be extracted from these experimental observations.

Below the analysis of [1] will briefly be reviewed and especially the steady-state propagation of cracks through the film under homogeneous stress states will be focussed on. The analysis allows for a calculation of the energy release rate along the front which only requires solutions for states far behind the front. Far behind the propagating crack front a one-dimensional analysis is sufficient to characterize the state. The steady state propagation of buckling driven delamination discussed in Section 4 may be analyzed by a similar approach.

The propagation of a system of equally spaced cracks at homogeneous stress states was analyzed in Thouless [2]. The steady-state energy re-

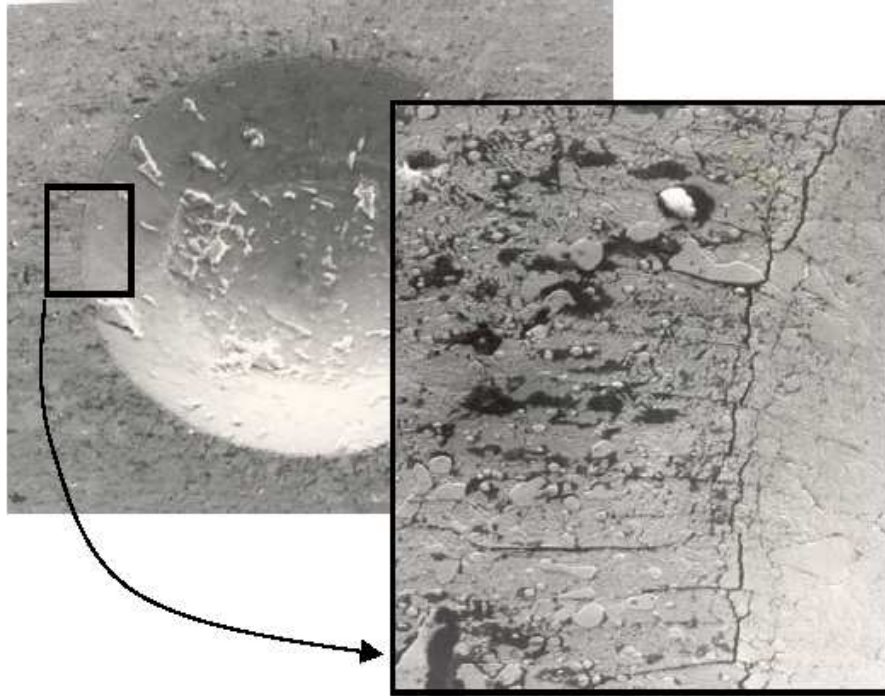


Figure 1. Crack pattern during indentation of TiAlN on steel.

lease rate, G_{ss} , at the fronts are calculated by

$$G_{ss} = \frac{1}{h} \int_0^h G(a) da \quad (1)$$

where h is the film thickness and G is the energy release rate for plane strain edge cracks propagating from the surface to the interface. A plot of G_{ss} as a function of the crack spacing is shown in Fig. 2. Next, a cross-plot of stresses in the film obtained in Drory and Hutchinson [3] with the results in Fig. 2 gives a relationship between crack length a , radius of the indent R , the plane strain Young's modulus of the film \bar{E} and the fracture toughness of the film G_c . This relationship is plotted in Fig. 3.

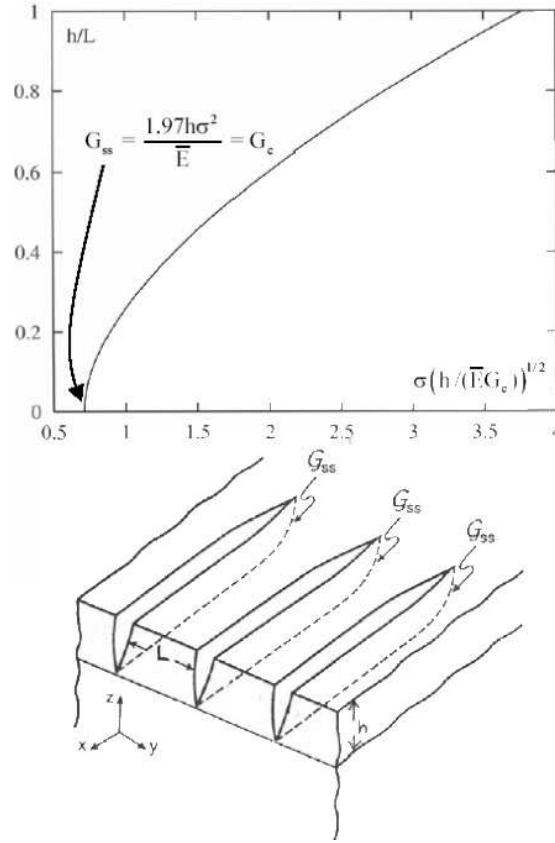


Figure 2. Steady-state energy release rate for a system of equally spaced cracks.

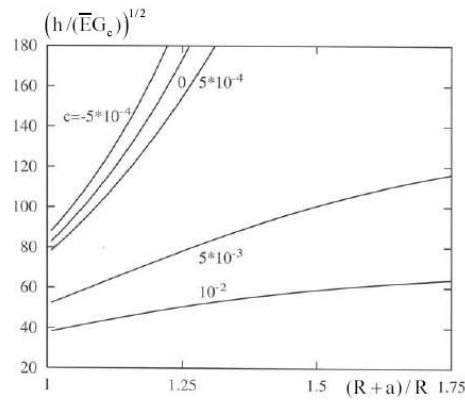


Figure 3. Crack length for a given film thickness h and residual stress σ_0 . Here $c = \sigma_0(1 - \nu^2)/E$.

2. Interface Fracture

The relations between the mode I/II and the mode III energy release rates and the normal membrane force, N , the effective moment, M , and shear membrane force, T , in the thin film along the interface crack front are given by (Jensen et al. [4])

$$G = G_{I/II} + G_{III}, \quad G_{I/II} = \frac{1 - \nu^2}{2Eh^3} (12M^2 + h^2N^2), \quad (2)$$

$$G_{III} = \frac{1 + \nu}{Eh} T^2.$$

The relationship between the energy release rate and the stress intensity factors K_I , K_{II} and K_{III} is given by

$$G = \frac{1}{\cosh^2(\pi\varepsilon)} \frac{1}{2} \left(\frac{1}{\bar{E}} + \frac{1}{\bar{E}_s} \right) (K_I^2 + K_{II}^2) + \frac{1}{2} \left(\frac{1 + \nu}{E} + \frac{1 + \nu_s}{E_s} \right) K_{III}^2. \quad (3)$$

An interface fracture criterion formulated in [4] for non-oscillating singular crack tip fields is applied here in the form

$$G_I + \lambda_2 G_{II} + \lambda_3 G_{III} = G_{1c}. \quad (4)$$

where λ_2 and λ_3 are parameters between 0 and 1 adjusting the relative contributions of mode II and III to the fracture criterion, and G_{1c} is the mode I interface fracture toughness.

3. Delamination at Corners

Delamination in thin film systems at corners as sketched in Fig. 4 was analyzed in Jensen [5] and Pane and Jensen [6]. The motivation for the study is observations in e.g. flip-chips subject to thermal cycling where spontaneous delamination usually is initiated at corners. It is for this reason of interest that we study the critical stress required to propagate a crack at a corner compared to the stress required to propagate a plane strain edge crack.

The residual stresses are assumed tensile so that Eq. (4) reduces to

$$\sigma_{nn}^2 + \frac{2\lambda}{1 - \nu} \sigma_{nt}^2 = \sigma_c^2 = \frac{2EG_c^*}{(1 - \nu^2)h} \quad (5)$$

where σ_{nn} and σ_{nt} is the effective normal and shear stress in the film at the crack front, and where

$$\lambda = \frac{\lambda_3}{1 + (\lambda_2 - 1) \sin^2 \psi}, \quad G_c^* = \frac{G_{1c}}{1 + (\lambda_2 - 1) \sin^2 \psi}. \quad (6)$$

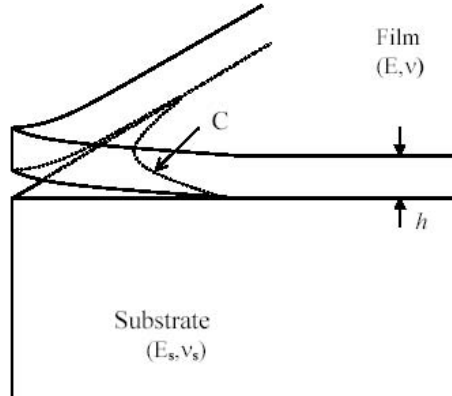


Figure 4. Delamination at a corner.

The properties of the substrate affect the fracture criterion through the phase angle of loading, ψ .

The finite element method is used for calculating σ_{nm} and σ_{nt} . The shape of the crack front is determined by an iterative procedure so that Eq. (5) is satisfied locally along the crack front.

Delamination at corners is possible at lower stress levels than σ_c and examples of delamination shapes are shown in Fig. 5.

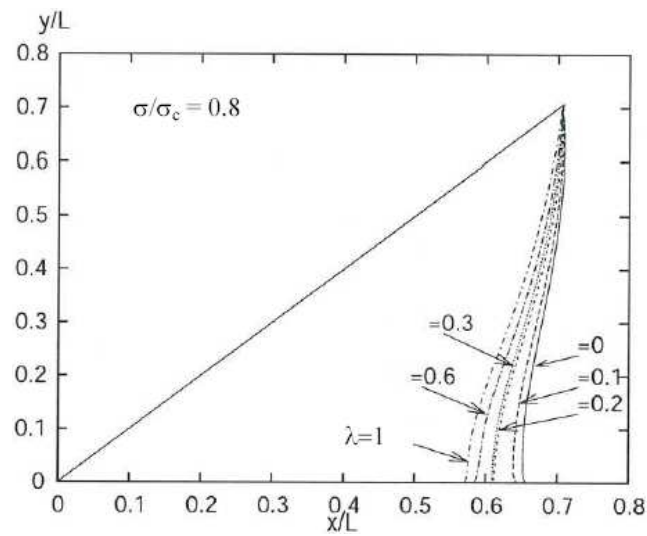


Figure 5. Predicted crack front shapes.

4. Morphology of Buckling Driven Delamination

Examples of buckling driven delaminations are shown in Fig. 6 (taken from Moon et al. [7]). Especially the telephone cord mode of delamination in Fig. 6(c) has received much attention since it is the most commonly observed mode of delamination.

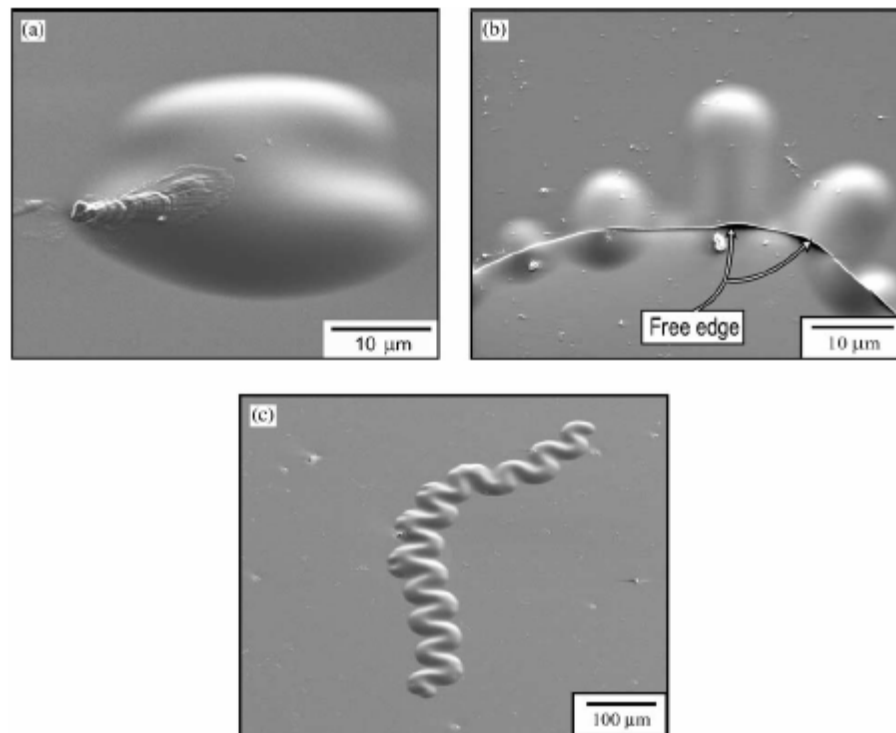


Figure 6. Shapes of buckling driven delamination, (a) circular, (b) straight sided, (c) telephone cord delamination.

The straight-sided mode of buckling driven delamination was analyzed in Hutchinson and Suo [8] along similar lines as the steady-state propagation of film cracks in Section 1. The accuracy of that approach was discussed in Jensen and Sheinman [9].

The mechanism for the telephone cord delamination suggested in Jensen and Sheinman [10] and supported by the experimental results in [7] is that steady state buckling driven delaminations which propagate along a curved path rather than a straight path release most energy at high stress levels. The cross over point for the two mechanisms of delamination growth lies roughly at $\sigma/\sigma_c = 4$. It was also found in [7]

that the straight sided and telephone cord delaminations only exist in a narrow range of mechanical parameters for the thin film system, which separates two regions where either no delamination or complete delamination of the film occurs. The two main parameters for determining whether complete or no delamination occurs is the ratio between the mode I and mode II interface fracture toughness and the total energy per unit area in the film normalised by the mode II fracture toughness.

References

- [1] H.M. Jensen, Indentation Cracking of Brittle Coatings. *Advances in Fracture Research* **5** (Eds. B.L. Karihaloo, Y.W. Mai, M.I. Ripley and R.O. Ritchie), pp.2423–2431, 1997.
- [2] M.D. Thouless, Crack Spacing in Brittle Films on Elastic Substrates. *Journal of the American Ceramic Society*, **73**, pp.2144–2146, 1990.
- [3] M.D. Drory and J.W. Hutchinson, Measurement of the Adhesion of a Brittle Film on a Ductile Substrate by Indentation, *Proceedings of the Royal Society of London*, **452**, pp.2319–2342, 1996.
- [4] H.M. Jensen, J.W. Hutchinson and K.S. Kim, Decohesion of a Cut Pre-stressed Film on a Substrate. *International Journal of Solids and Structures*, **26**, pp.1099–1114, 1990.
- [5] H.M. Jensen, Thin Film Delamination at Edges and Corners. *International Symposium on Recent Developments in the Modelling of Rupture in Solids*, (Eds. A. Benallal and S.P.B. Proença), ISBN 2-1-094072-7, 2003.
- [6] I. Pane and H.M. Jensen, Steady-State Delamination of Thin Films at Corners (in preparation), 2004.
- [7] M.W. Moon, H.M. Jensen, J.W. Hutchinson, K.H. Oh and A.G. Evans. The Characterization of Telephone Cord Buckling of Compressed Thin Films on Substrates. *Journal of the Mechanics and Physics of Solids*, **50**, pp.2355–2377, 2002.
- [8] J.W. Hutchinson and Z. Suo, Mixed Mode Cracking in Layered Materials. *Advances in Applied Mechanics*, **29**, pp.63–191, 1992.
- [9] H.M. Jensen and I. Sheinman, Straight-Sided, Buckling-Driven Delamination of Thin Films at High Stress Levels. *International Journal of Fracture*, **110**, pp.371–385, 2001.
- [10] H.M. Jensen and I. Sheinman, Numerical Analysis of Buckling-Driven Delamination. *International Journal of Solids and Structures*, **39**, pp.3373–3386, 2002.

NONLINEAR DYNAMICS IN OCEAN ENGINEERING

Edwin J. Kreuzer, Wolfgang M. Sichermann

Technical University Hamburg-Harburg

Mechanics and Ocean Engineering

[kreuzer, sichermann]@tu-harburg.de

Abstract The ability to predict and characterize the dynamic behavior of ocean engineering systems prior to financial commitments of their realization is an essential element of contemporary engineering. Linear models often do not provide sufficient accuracy and reliability to analyze and predict the dynamics of the real system in a satisfying manner. For example, ships in rough seas, moored offshore platforms and crane vessels under wave excitation show essentially nonlinear behavior. This paper illustrates how the methods of nonlinear dynamics can be employed for the prediction of operating limits and extreme responses of floating structures.

Keywords: Ship stability, mooring systems, floating cranes

1. Introduction

The international trade rests to a major extent on maritime traffic. The economic growth has led to the doubling of the global fleet size during the past three decades and, recently, to a rapid increase of the ship capacity. The marine exploitation of hydrocarbons and the power generation by offshore wind turbines assign further challenging tasks to ocean engineers. On the one hand, the design of mooring systems has to guarantee the safe positioning of drilling and production platforms in increasing water depths. And on the other hand, the development of offshore power plants in harsh environments, e.g. the North Sea, requires new approaches to the installation and maintenance procedures.

From statistical data we learn that at least one quarter of the total ship losses are caused by severe weather conditions. The current regulations and criteria for assuring the stability of a ship and preventing it from capsizing (the so-called prescriptive rules by the International Maritime Organization, IMO, 2002) are empirical and based on the properties of

the righting lever of the ship in still water. Model tests show, however, that the current stability criteria do not always correlate with the danger of capsizing. Hence, researchers agree that the actual criteria have to be modified. The IMO is working, therefore, on performance-based rules which apply to each specific ship.

Several computer programs have been developed for the numerical simulation of nonlinear ship motions in six degrees of freedom under the consideration of ship-wave interaction. Because of the complexity of the capsizing problem, these codes were used to evaluate statistical properties. The probability of capsizing was estimated, and heuristic arguments were used to interpret this probability and to derive stability criteria. Mathematically more advanced analysis techniques were recently applied to simple single-degree-of-freedom and regular wave excitation models and, with few exceptions, to more complicated models. By applying these techniques based on nonlinear dynamics theory it is possible to locate stability boundaries of the systems. The state of the art of (deterministic as well as stochastic) ship models has been very well documented in Spyrou and Thompson (2000).

For the accurate motion analysis of moored floating structures it is inevitable to account properly for the dynamic behavior of the attached mooring lines. Common practice is to use rather simple models based on a quasi-static approximation for the mooring systems to describe the interaction between the motion of structures and the restoring forces. These simplified models disregard the dynamics of the mooring line including the interaction between the fluid, the sea floor and the lines. For lines in deep water, these effects may cause a tremendous increase in the tensile force which cannot be predicted by simplified models.

We begin with the general formulation of the equations of motion for a floating body. Then, a basic model is derived for investigation of the large amplitude ship roll motions and capsizing in head and following seas. Next, we address crucial points for the dynamical modeling of mooring systems. The dynamical investigation of a floating crane serves as an example how analytical and numerical analysis techniques can be employed together successfully.

2. Large Amplitude Ship Motions and Capsizing

The linear response of floating rigid bodies to waves can be described by a coupled system of equations for the six degrees of freedom

$$(\mathbf{M} + \mathbf{A}) \ddot{\boldsymbol{\xi}} + \mathbf{B} \dot{\boldsymbol{\xi}} + \mathbf{C} \boldsymbol{\xi} = \text{Re} (\mathbf{f}_e e^{i\omega t}), \quad (1)$$

where $\boldsymbol{\xi} = (\xi, \eta, \zeta, \varphi, \theta, \psi)^T$ represents the vector of generalized coordinates, as defined in Fig. 1. Matrix \mathbf{M} denotes the inertia matrix. The

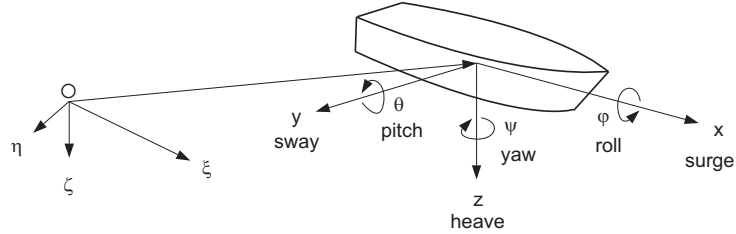


Figure 1. Definition of generalized coordinates

added mass matrix \mathbf{A} , the damping matrix \mathbf{B} , and the excitation vector \mathbf{f}_e are computed for a given wave frequency, forward velocity, and wave direction applying potential flow theory. The hydrostatic restoring characteristics are described by the matrix \mathbf{C} . Assuming harmonic response with the frequency of encounter ω , the vector of the complex Response Amplitude Operator (RAO) yields

$$\mathbf{y}(\omega) = [-\omega^2 (\mathbf{M} + \mathbf{A}) + i\omega\mathbf{B} + \mathbf{C}]^{-1} \mathbf{f}_e. \quad (2)$$

For symmetry with respect to the centerline the surge, heave and pitch motions in (1) are decoupled from the sway, roll and yaw motions, so that the linear response for each set of degrees of freedom can be determined independently from each other. This means that the out-of-plane modes sway, roll and yaw motions cannot be excited by linear mechanisms in head or following seas. The roll motion in head and following seas is induced by the nonlinear kinematic coupling of the pitch and heave motion, and primarily by the temporal variation of the righting lever curve in waves.

In order to set up an appropriate model to describe the nonlinear ship roll motion, we follow the linear order of magnitude analysis by Newman (1977) to identify the leading order forces. In waves of wavelengths comparable to the ship length, the hydrostatic forces and the Froude-Krylov forces are of leading order for heave, roll, and pitch modes. Thus, in the first place, it is important to account for the hydrostatic and Froude-Krylov force contributions in the nonlinear model. Further, the forces associated with heave and pitch are at least of one order greater than those associated with the roll motion. We deduce that the nonlinear coupling of heave, roll and pitch motion will affect the roll motion to a higher degree than vice versa, and consider linear heave and pitch behavior as an appropriate assumption.

The nonlinear roll equation of motion will account for nonlinear damping effects and employ the instantaneous righting moment

$$[I_{xx} + A_{xx}(\omega_n)] \ddot{\varphi} + b_1 \dot{\varphi} + b_3 \varphi^3 = M_r(\zeta, \varphi, \theta, t), \quad (3)$$

where I_{xx} denotes the roll inertia moment of the ship, and $A_{xx}(\omega_n)$ is the hydrodynamic inertia at the roll natural frequency ω_n with

$$\omega_n^2 = g\Delta GM / [I_{xx} + A_{xx}(\omega_n)], \quad (4)$$

where g denotes the acceleration of gravity, Δ the ship mass, and GM the initial metacentric height. The damping coefficients b_1 and b_3 are obtained by a nonlinear polynomial regression of experimental data for effective damping coefficients (Blume, 1979) for the corresponding block coefficient, beam to draft ratio, and Froude number. The righting moment M_r is determined from the pressure distribution in the incident waves at the actual position of the ship.

Parametric Rolling in Head Seas. We investigate a fast 173 m passenger ferry advancing in head seas at Froude number $F_n = 0.3$ which corresponds to 85% of the service speed. Under these conditions, the encounter frequency in waves of wavelengths comparable to ship length is about twice the natural roll frequency. This two-to-one frequency ratio is assumed to be critical for parametric excitation. The ship responds directly to the wave excitation in the heave and pitch modes and produces an oscillation of the righting lever curve with the frequency of encounter. The RAOs for heave and pitch motions are shown in Fig. 2 and Fig. 3, respectively.

Linear methods generally tend to overstate the response amplitudes at resonance, here at a wave frequency of about 0.5 rad/s for heave and pitch motions. We consider a wave frequency of 0.55 rad/s which corresponds to a wave-to-ship length ratio of 1.2. This frequency is sufficiently far from the resonant wave frequency, so that the results of the linear heave and pitch motion analysis can be employed with confidence.

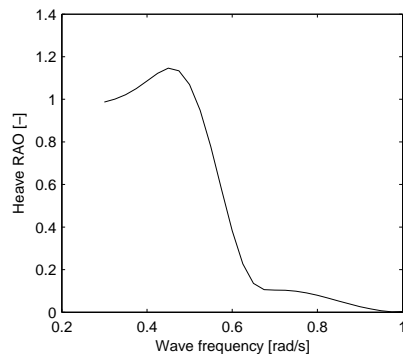


Figure 2. Heave RAO in head seas

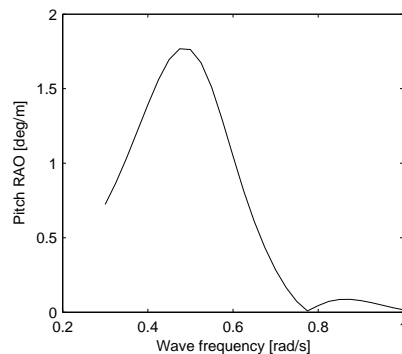


Figure 3. Pitch RAO in head seas

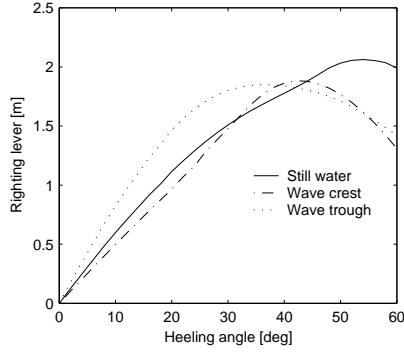


Figure 4. Righting lever curves in head seas, wave height 6 m

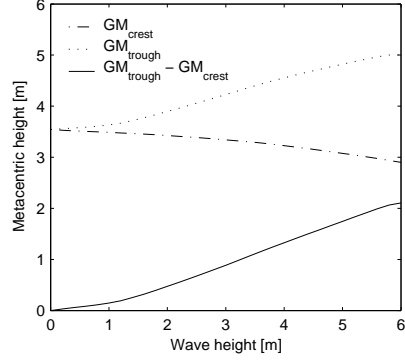


Figure 5. Variation of the initial stability with respect to the wave height

In order to study the variation of the dynamic righting moment, the righting lever curves are computed for still water, wave crest and wave trough condition. Figure 4 compares the dynamic righting lever curves at a wave height of 6 m. In both, crest and trough condition, the maximum righting lever is reduced in comparison to the still water condition.

Further investigations show that the wave crest and trough curves correspond to the limiting curves of the righting lever oscillation. Only for moderate wave heights of up to 1.5 m it can be assumed that the metacentric height GM oscillates about the metacentric height in still water. The dependence of the GM -variation on the wave height is shown in Fig. 5.

For the analytical investigation we approximate the restoring moment curve by a cubic polynomial. The temporal variation of the initial stability in waves is modeled by a harmonically oscillating component. The restoring moment has the form

$$M_r(\zeta, \varphi, \theta, t) = -c(t)\varphi + c_3\varphi^3, \quad \text{with} \quad (5)$$

$$c(t) = g\Delta \left[GM + \frac{\delta_{GM}}{2} \cos(\omega t) \right] = c_1 + c_\delta \cos(\omega t), \quad (6)$$

where δ_{GM} corresponds to the difference between the initial metacentric height in trough and crest condition.

The dynamics of (3) with the restoring moment defined by (5) and (6) can be assessed by the method of multiple scales (Oh et al., 2000). The first approximation yields

$$\varphi(t) = a \cos \left[\frac{1}{2}(\omega t - \gamma) \right], \quad (7)$$

with slowly varying amplitude a and phase γ governed by

$$a' = -\frac{b_1\omega_n^2}{2c_1}a + \frac{3b_3\omega_n^4}{8c_1}a^3 - \frac{c_\delta\omega_n}{2c_1}a \cos \gamma, \quad (8)$$

$$\gamma' = \sigma + \frac{3c_3\omega_n}{4c_1}a^2 - \frac{c_\delta\omega_n}{c_1} \sin \gamma, \quad (9)$$

where the detuning parameter σ is defined by $\omega = 2\omega_n + \sigma$. For the numerical values of all the parameters employed, we refer to Kreuzer and Sichermann (2004). The fixed points of (8) and (9) correspond to stationary solutions of (3). Setting $a' = 0$ and $\gamma' = 0$ yields a nonlinear relation for the excitation and the response amplitude. In combination with the variation of the metacentric height with respect to the wave height, as shown in Fig. 5, the expected roll amplitude can be plotted over the wave height, Fig. 6. It is observed that up to a wave height of 4.8 m, no roll motion is excited. In the interval from 4.8 m to 5.1 m both, zero amplitude and large amplitude motions are possible. Beyond the wave height of 5.1 m there exist only stable motions with large amplitudes.

The investigation of parametrically excited roll motions in harmonic waves represents only a special case of the more general situation in ocean waves. However, essential information on the roll behavior in irregular seas can be obtained from the analysis in regular waves. Numerical simulations of the roll equation (3) show that for an average wave frequency of 0.55 rad/s, large amplitude motions do not occur for significant wave heights smaller than 4.5 m. For greater wave heights, large amplitude motions are observed, and the maximum roll angles correspond to the limiting values found in the analysis of the deterministic case.

While in the deterministic case the choice of initial conditions determines whether the system exhibits large amplitude motions or settles down to the trivial solution, large amplitude motions in irregular waves occur in stochastic patterns. Figure 7 shows the time history of a numerical realization, where the occurrence of large amplitude motions was observed three times within a period of 20 minutes.

Capsizing in Following Seas. We now consider the reference ship at $F_n = 0.3$ in following seas. The frequency of encounter is significantly reduced and the righting lever curve oscillates with a longer period, so that the ship is endangered to capsize on the wave crest before sufficient stability is regained in the wave trough. The reference ship shows very high initial stability ($GM = 3.54$ m) so that the righting lever variation is unlikely to induce capsizing for realistic wave heights. In order to

illustrate the mechanism of capsizing, we reduce the initial metacentric height to 2.0 m corresponding to an increase of the ship’s center of gravity by 1.5 m.

In contrast to the scenario of parametrically excited roll motions, where the system behavior is studied in the vicinity of the upright position, the capsizing mechanism has to be investigated at large deviations from the equilibrium position. Therefore, different techniques of analysis have to be introduced. Capsizing is considered to have a mechanical equivalent in the escape problem from a potential well, where the potential is characterized by the righting lever curve. Such problems can be investigated by Melnikov’s method, which has already been applied successfully to capsizing analyses of ships in beam seas (Jiang et al., 2000; Spyrou et al., 2002). The roll equation (3) is transformed into the first order system for $\mathbf{x} = (\varphi, \dot{\varphi})^T$

$$\dot{\mathbf{x}} = \mathbf{f}(\mathbf{x}) + \epsilon \mathbf{g}(\mathbf{x}, t), \quad \text{where} \quad (10)$$

$$\mathbf{f}(\mathbf{x}) = (\dot{\varphi}, -\alpha_1 \phi + \alpha_3 \varphi^3)^T \quad \text{and} \quad (11)$$

$$\epsilon \mathbf{g}(\mathbf{x}, t) = (0, -\beta_1 \dot{\varphi} - \beta_3 \dot{\varphi}^3 + \varphi \alpha_\delta \cos(\omega t))^T. \quad (12)$$

Here, new coefficients have been introduced for the sake of clarity. The parameters α_1 , α_3 , α_δ , and the parameters β_1 and β_3 correspond to the normalized restoring and damping coefficients. The right-hand side of (10) has been split into conservative and non-conservative components. The term (11) accounts for the effect of the average righting lever curve, whereas (12) respects damping and the temporal variation of the righting lever curve. The parameter ϵ emphasizes that (12) is one order of magnitude smaller than (11). Thus, the system will behave approximately like

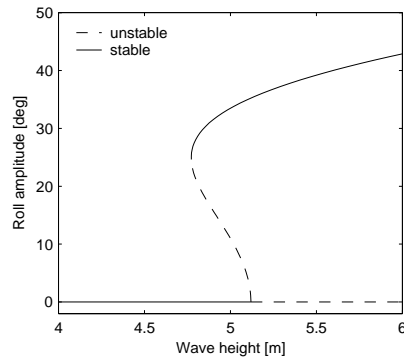


Figure 6. Roll response amplitude in regular head seas

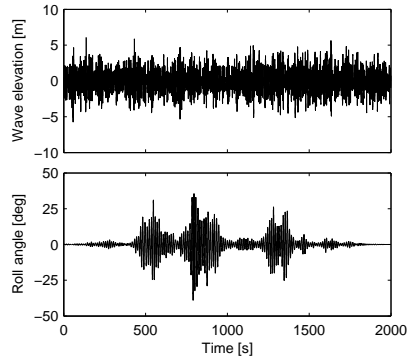


Figure 7. Roll response in irregular seas, significant wave height 5 m

$\dot{\mathbf{x}} = \mathbf{f}(\mathbf{x})$, which shows three fixed points corresponding to the upright position $\varphi = 0$ and to the angles of vanishing stability $\varphi = \pm\varphi_v$ to starboard and port side, respectively. The outer fixed points are connected by heteroclinic trajectories

$$\mathbf{x}_h(\tau) = \pm \sqrt{\frac{\alpha_1}{\alpha_3}} \left[\tanh \left(\sqrt{\frac{\alpha_1}{2}} \tau \right), \sqrt{\frac{\alpha_1}{2}} \cosh^{-2} \left(\sqrt{\frac{\alpha_1}{2}} \tau \right) \right]^T, \quad (13)$$

which separate the phase space regions of bounded and unbounded motion. The region of bounded motion, enclosed by the heteroclinic trajectories, is referred to as the safe basin. In a conservative system each trajectory corresponds to a constant energy state of the system. Hence, every trajectory starting inside the safe basin cannot cross the basin boundary since this implies increasing the system's energy. The basin boundaries for still water and wave crest condition at a wave height of 8 m are shown in Fig. 8.

Introducing the non-conservative term (12) will alter the system's energy and enable trajectories close to the heteroclinic trajectory to cross the potential barrier. The Melnikov function is here derived from a simple energy viewpoint (Simiu, 2002). The change of energy during motion along the heteroclinic trajectory corresponds to the dissipated energy and to the work performed by the parametric excitation

$$E = - \int_{-\infty}^{\infty} (\beta_1 \dot{\varphi}_h^2 + \beta_3 \dot{\varphi}_h^4) d\tau + \int_{-\infty}^{\infty} \varphi_h \dot{\varphi}_h \alpha_\delta \cos[\omega(\tau + t_0)] d\tau. \quad (14)$$

It can be shown that E is equivalent to the Melnikov function $M(t_0)$ of the system (10). For $M(t_0) > 0$, the system's energy is increased, and trajectories close to the basin boundary are likely to escape from the safe domain. The condition $M(t_0) > 0$ is therefore considered as a necessary condition for capsizing. Carrying out the integrations in (14) yields

$$M(t_0) = -k + \alpha_\delta |H(\omega)| \cos[\omega t_0 + \nu(\omega)] \quad \text{with} \quad (15)$$

$$k = \frac{2\sqrt{2}\alpha_1^{3/2}}{3\alpha_3} \beta_1 + \frac{8\sqrt{2}\alpha_1^{7/2}}{35\alpha_3^2} \beta_3, \quad (16)$$

$$H(\omega) = i \frac{\pi\omega^2}{\alpha_3} \sinh^{-2} \left(\frac{\pi\omega}{\sqrt{2\alpha_1}} \right), \quad \text{and} \quad (17)$$

$$\nu(\omega) = \arctan [\text{Im}H(\omega)/\text{Re}H(\omega)]. \quad (18)$$

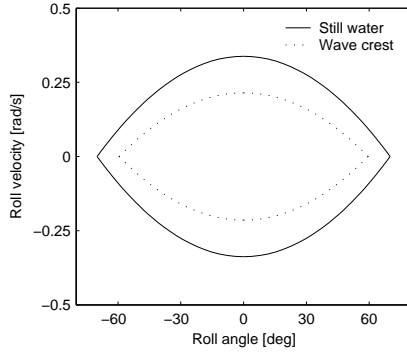


Figure 8. Safe basin boundaries

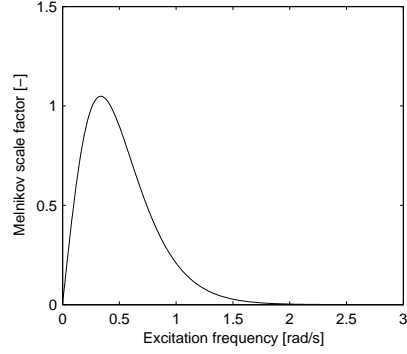


Figure 9. Melnikov scale factor

The Melnikov scale factor $|H(\omega)|$ is shown in Fig.9. When the excitation is a Gaussian process with the spectral density function $S(\omega)$, the Melnikov function is also Gaussian with mean value $-k$ and spectral density

$$S_M(\omega) = \alpha_\delta^2 |H(\omega)|^2 S(\omega). \quad (19)$$

For a Gaussian Melnikov process the mean time between consecutive zero up-crossings is

$$\tau_{up} = 2\pi \sqrt{\frac{m_0}{m_2}} \exp\left(\frac{k^2}{2m_0}\right), \quad (20)$$

where m_0 and m_2 denote the spectral moments of order zero and two, respectively. Provided that capsizing is a rare event, the probability that there are no zero up-crossings of the Melnikov process during a time interval $T \ll \tau_{up}$ can be approximated by the Poisson distribution with an average waiting time τ_{up} . The probability that there will be at least one zero up-crossing of the Melnikov process in the interval T yields

$$P_{M,T} = 1 - \exp(-T/\tau_{up}). \quad (21)$$

Since $M(t_0) > 0$ is a necessary condition for the escape from the safe basin only, $P_{M,T}$ yields an upper bound for the probability that capsizing occurs within the time interval T . For the specific case of our reference ship and the observation time $T = 1$ h, we observe that the upper bound for the capsizing probability starts to increase strongly at a significant wave height of 7.5 m. However, arbitrary choice of the time interval T and of a tolerable capsizing probability will produce distinct limiting wave heights. Nevertheless, the quantitative comparison of different designs is possible, when the considered time interval and the threshold probability are held constant.

3. Mooring Line Dynamics

The mooring lines of ocean engineering systems can spread out over many kilometers. Typically, the lines consist of anchors, heavy chains and nylon ropes or steel cables which are attached to the floating object. A displacement of the attachment point with respect to the equilibrium position causes lowering or lifting of the heavy chain links from the ground and thus results in a restoring force. The force characteristics of this system shows a significantly nonlinear behavior: as the displacement of the vessel increases, the catenary system shows stiffening of the restoring forces. The fluid forces on the transparent mooring lines are obtained from the modified Morison's equation, which gives the incremental normal force dF_n on a mooring line segment of length ds

$$dF_n = \left(\rho \frac{\pi D^2}{4} \frac{\partial v_n}{\partial t} + C_a \rho \frac{\pi D^2}{4} \frac{\partial u_{rn}}{\partial t} + C_d \frac{\rho D}{2} |u_{rn}| u_{rn} \right) ds \quad (22)$$

with the density of the fluid ρ , the line diameter D , the normalized acceleration of the fluid $\partial v_n / \partial t$, the added mass coefficient C_a , the relative normalized acceleration between the fluid and the structure $\partial u_{rn} / \partial t$, the damping coefficient C_d , and the normalized relative velocity between fluid and structure u_{rn} . Considering the dynamics of mooring lines as a multibody system leads to a large set of differential equations with hundreds of degrees of freedom. Dividing the catenary and the cable into several subsystems as shown in Fig. 10 and including the appropriate boundary conditions for each subsystem can be advantageous for the integration of the equations of motion.

While in general practice only the static forces on the mooring line are considered, the present approach reveals that the dynamical influence must not be neglected, especially in great water depths (Kreuzer and Wilke, 2003). Simulations show that instead of just following the motion of the moored vessel, some parts of the mooring system might rest or even move in the opposite direction as shown in Fig. 11.

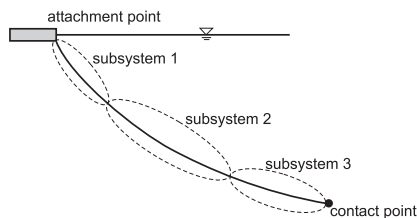


Figure 10. Possible division of subsystems in a catenary mooring system

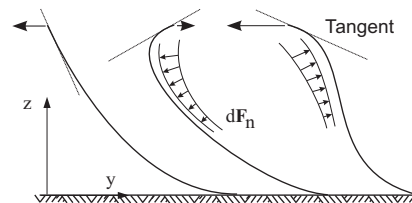


Figure 11. Line motion behavior in great water depths

4. Floating Cranes

One example of a moored multibody system is a floating crane. In addition to the mooring line forces and the fluid-structure interaction, the dynamics is influenced by coupling between the vessel and the swinging load. In our analysis, the forces of the mooring system are simplified by using a polynomial approximation of the static mooring line curve. For the case of in-plane-excitation, the system behavior can be described entirely by the surge, heave, pitch motion and the angle α of the swinging load. This gives a system with four degrees of freedom: $\mathbf{u} = (x, \theta, z, \alpha)^T$. Experiments with floating cranes in a wave tank have shown that such a system may exhibit large amplitude subharmonic motion (Clauss et al., 2000). The subharmonic response was observed to become particularly obvious from the surge motion.

In order to investigate this phenomenon mathematically, two different techniques are applied (Ellermann et al., 2002). The first technique is the multiple scales method, generally applicable to systems with weak nonlinearity. After the order of magnitude analysis and scaling of the different parameters in the equations of motion and the relation between the forcing and the resonance frequencies of the system, we obtain an analytical approximation for the solution. The advantage of this procedure is that it can easily be evaluated for any set of parameters. Figure 12 gives an example of solutions obtained by the multiple scales method. The solid curves indicate the first and the second primary resonance. The shaded areas give the range of the subharmonic P2 (period 2) motion and the dotted curve shows the amplitude of the subharmonic P3 solution.

The second technique, the numerical bifurcation analysis based on a path-following method is applied to give a more precise solution for

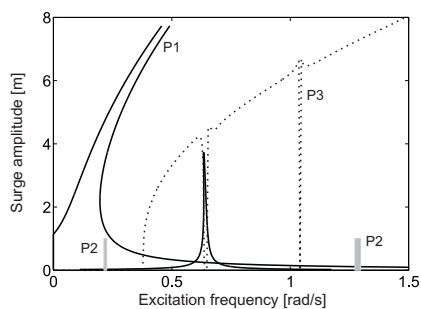


Figure 12. Surge amplitudes by multiple scales analysis

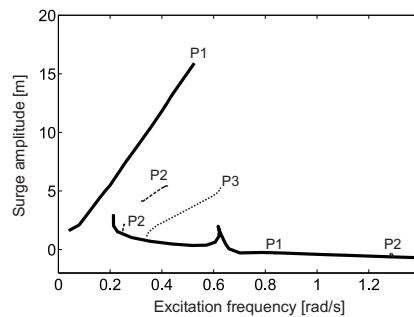


Figure 13. Surges amplitudes by path following

the individual motions and the position of the bifurcation points. Figure 13 shows an example for a numerically determined bifurcation diagram. The parameters correspond to those used in Fig.12. The bifurcation diagram clearly shows the same two peaks for the first two primary resonances; it gives the P2 motion at the frequencies predicted by the multiple scales method and it also reveals the strong bending of the curve for the P3 motion. The difficulty when applying the path-following technique is that isolated solutions such as the P2 motion at 0.35 rad/s cannot be found directly. Only those solutions which result from a bifurcation can be traced systematically. By using different free parameters in the bifurcation analysis and possibly following periodic solutions beyond the range of validity of the model, some of these different solutions can be found.

5. Conclusions

We have explored the nonlinear dynamics of ships, mooring lines, and floating cranes. The mathematical models of these and other ocean engineering systems are often of high dimensions, especially when the flow problem has to be solved explicitly. In order to promote the understanding of the rather complex dynamic nature, we have focused on the study of model equations with only few degrees of freedom. The analytical investigation of extreme ship motions has been helpful to identify the critical parameters detrimental to the seakeeping behavior of ships in regular and irregular seas.

The accuracy of the approximate models, however, has to be verified with respect to the solutions of full-order models. An example of a sophisticated high-dimensional model was presented by the modeling of mooring line dynamics. The analysis of subharmonic floating crane response has demonstrated how the combination of analytical and numerical techniques can be employed successfully. Further demand of research is identified for the investigation of the nonlinear dynamic behavior of complex systems with random excitation.

References

- Blume, P. (1979). Experimentelle Bestimmung von Koeffizienten der wirksamen Roll-daempfung and ihre Anwendung zur Abschaetzung extremer Rollwinkel. *Schiffstechnik*, 26:3–23.
- Clauss, G., Vannahme, M., Ellermann, K., and Kreuzer, E. (2000). Subharmonic oscillations of moored floating cranes. In *Proc. of the Offshore Technology Conference*, Houston, TX, 429–436.
- Ellermann, K., Kreuzer, E., and Markiewicz, M. (2002). Nonlinear dynamics of floating cranes. *Nonlinear Dyanmics*, 27:107–183.

- IMO (2002). *Code on Intact Stability for all Types of Ships Covered by IMO Instruments*. International Maritime Organization, London.
- Jiang, C., Troesch, A. W., and Shaw, S. W. (2000). Capsize criteria for ship models with memory-dependent hydrodynamics and random excitation. *Phil. Trans. R. Soc. Lond. A*, 358:1761–1791.
- Kreuzer, E. and Sichermann, W. (2004). Investigation of large amplitude roll motions and capsizing. In *Proc. of the 9th International Symposium on Practical Design of Ships and other Floating Structures*, Luebeck-Travemuende, Germany.
- Kreuzer, E. and Wilke, U. (2003). Dynamics of mooring systems in ocean engineering. *Archive of Applied Mechanics*, 73:270–281.
- Newman, J. N. (1977). *Marine Hydrodynamics*. The MIT Press, Cambridge, MA.
- Oh, I. G., Nayfeh, A. H., and Mook, D. T. (2000). A theoretical and experimental investigation of indirectly excited roll motion in ships. *Phil. Trans. R. Soc. Lond. A*, 358:1853–1881.
- Simiu, E. (2002). *Chaotic Transitions in Deterministic and Stochastic Dynamical Systems*. Princeton University Press, Princeton, NJ.
- Spyrou, K. J., Cotton, B., and Gurd, B. (2002). Analytical expressions of capsizing boundary for a ship with roll bias in beam waves. *Journal of Ship Research*, 46:167–174.
- Spyrou, K. J. and Thompson, J. M. T. (eds.) (2000). The nonlinear dynamics of ship motions. *Phil. Trans. R. Soc. Lond. A (Theme Issue)*, 358:1731–1981.

A BRIDGE BETWEEN THE MICRO- AND MESOMECHANICS OF LAMINATES: FANTASY OR REALITY?

Pierre Ladevèze

*LMT-Cachan, ENS Cachan/CNRS/Paris 6 University,
61 avenue du Président-Wilson,
Cachan 94235, France*

Abstract The main topics discussed here are how one can bridge the micro- and mesomechanics of laminates and how this affects the understanding and prediction of localization and final fracture.

Keywords: Damage, laminate, micromechanics, computation

1. Motivations: the Scientific and Industrial Challenges

The last quarter-century has witnessed considerable research efforts in the mechanics of composites in order to understand their behavior and to model or calculate them – the ultimate goal being the design of the materials/structures/manufacturing processes. Even in the case of stratified composites (which are the most studied and, therefore, the best understood), the prediction of the evolution of damage up to and including final fracture remains a major challenge in the modern mechanics of composite materials and structures. Today, the use of stratified composites in the aerospace industry always involves characterization procedures consisting of huge numbers of tests, which shows the low level of confidence in models. A significant improvement in this situation, i.e. a drastic reduction in the number of industrial tests, could be achieved if one could create a real synergy among the approaches on different scales which, today in the case of stratified composites, are followed quite independently of one another. One could jokingly say that there is, on the one hand, the micromechanics of laminates in which one counts cracks and, on the other, the meso- or macromechanics of laminates in which one measures stiffnesses – with only few links between the two. How one

can bridge the micro- and mesomechanics aspects and how this affects the understanding and prediction of localization and final fracture are the two main questions discussed here.

2. The Damage Micromechanics of Laminates What Working Scale?

Up to now, there have been numerous theoretical and experimental works on the micromechanics of laminates (see the two review papers – Nairn and Hu, 1994; Berthelot, 2003, the references at the end of the present paper and, in particular, the book by Herakovich, 1998). In micromechanics, the working scale lies between the dimension of the structure and the diameter of a fiber. In fact, the structure is described as an assembly of cracked interfaces and cracked layers made of a “fiber-matrix” material considered homogeneous or quasi-homogeneous.

Phenomenology on the Microscale

In most practical cases, the sequence of scenarios is as follows.

Scenarios 3 and 4 occur first, leading to rather diffuse damage within the plies and interfaces. Through a percolation phenomenon, transverse

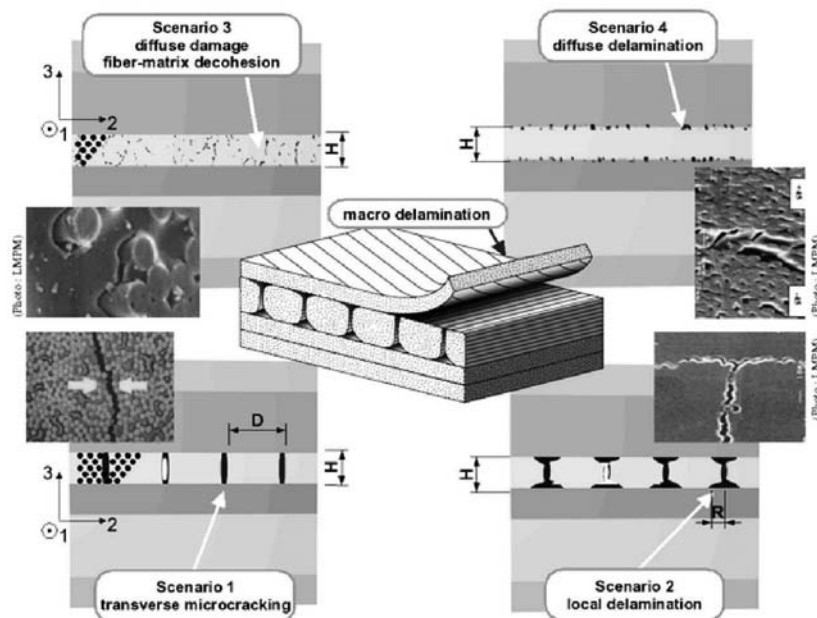


Figure 1. The mechanisms of degradation on the microscale.

microcracking appears; then, Scenario 1 takes over. The competition between transverse microcracking and local delamination ends with the saturation of Scenario 1 and is followed by the catastrophic development of Scenario 2. Ultimately, final fracture occurs with fiber breakage and delamination.

Several Key Points in Micromechanics

Key point 1: the need for Scenarios 3 and 4. Scenarios 3 and 4 are not commonly encountered in micromechanics. Nevertheless, they can be observed by performing the $[45^\circ - 45^\circ]_{2n}$ tension test; a clear and definitive experimental proof was recently given in (Lagattu and Lafarie-Frénol, 2000).

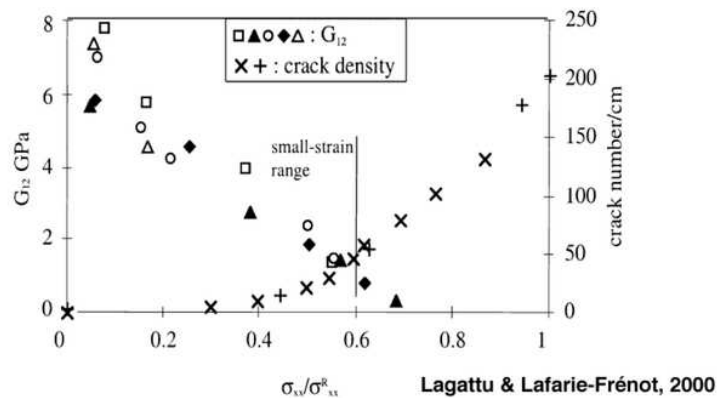


Figure 2. Shear modulus and microcracking density vs. the longitudinal stress for the $[45^\circ - 45^\circ]_{2s}$ tension test.

A major consequence is that there are at least two main damage mechanisms. Therefore, mesomodels with one mesodamage variable per layer are valid only for particular loading types; this is the case of most approaches other than our mesomodel.

Remarks:

- These scenarios are also responsible for the viscoplastic behavior which can be observed on the mesoscale.
- An open question is how to improve one's understanding of the surprising non-percolation phenomenon which occurs under shear on the fiber's scale.

Key point 2: modeling of initiation/propagation – the thickness effect. Most of the basic papers – Garrett and Bailey, 1977; Parvizi et al., 1978; Wang and Crossman, 1980; Boniface et al., 1996; Yang et al., 2003 – are not recent. For tension tests of stacking sequences built with 0° and 90° plies, two main observations have been made: first, the behavior of thick 90° plies is different from that of thin 90° plies; in thick plies, the transverse microcracks always run throughout the width of the specimen, whereas in thin plies they could stop near the edges. The second observation is related to thickness effects (see Fig. 3); the transition thickness \bar{h} is about twice the thickness of the elementary ply.

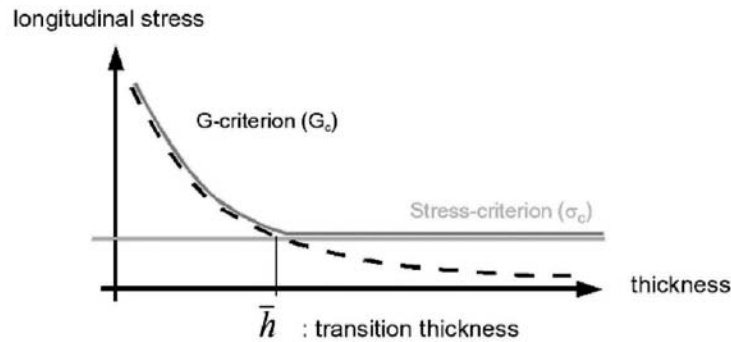


Figure 3. Failure stress vs. the number of 90° plies.

The theoretical explanation is quite old and well-known. Let us consider a flaw in the form of a penny-shaped crack which could propagate either in the longitudinal or in the transverse direction. It has been proven that the transverse energy release rate is much higher than the longitudinal energy release rate and, therefore, that the flaw propagates in the transverse direction, which is the thickness of the layer.

Keypoint 3: microcracking as a stochastic phenomenon. Several probabilistic models (Wang et al., 1984; Fukunaga et al., 1984; Laws and Dvorak, 1988; Manders et al., 1983; Berthelot and Le Corre, 2000) have already been proposed. For high cracking densities, heuristic coefficients have been introduced in order to characterize the non-perfect periodicity (Dvorak and Laws, 1988; Nairn et al., 1993; Ladevèze and Lubineau, 2002). This is necessary in order to have reasonable agreement with experiments (Yalvac et al., 1991).

Here, we support the idea that the process is stochastic, but quasi-independent of the probabilistic law. Let G_c be the critical value associated with the fiber-matrix material. One prescribes a uniform proba-

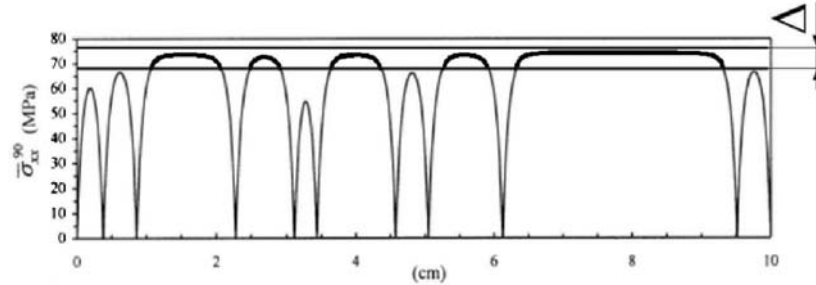


Figure 4. The G -curve as a function of the longitudinal abscissa – domain associated with Δ .

bility density over the domain:

$$\left\{ \underline{M} \mid \max_{\underline{M}'} G(\underline{M}') - G(\underline{M}) \leq \Delta \right\} \quad (1)$$

where G denotes the tunneling energy release rate and Δ a small parameter (see Fig. 4).

Figure 5 shows several samples for different values of Δ ; the “mean” curve appears to be insensitive to Δ and to the samples and is a quasi-deterministic curve which is quite different from the curve related to a perfect periodic pattern.

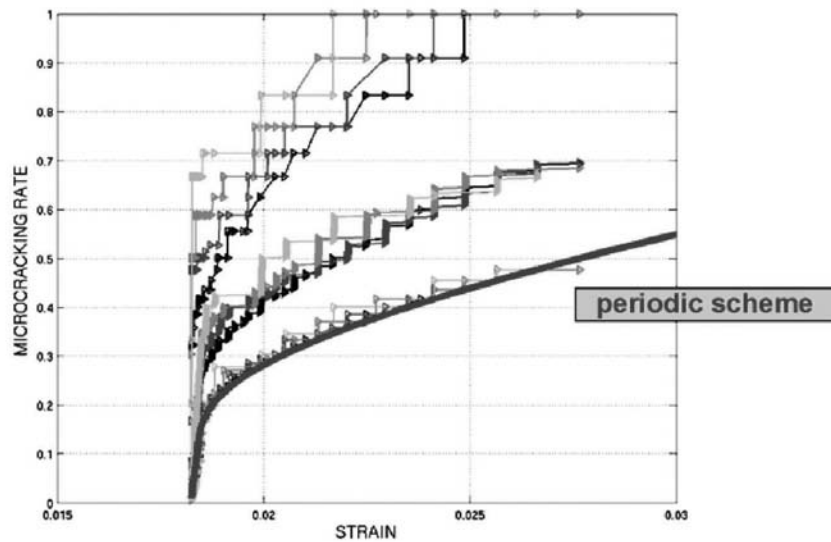


Figure 5. Max., mean and min. values of the microcracking rate vs. the longitudinal strain.

Such a model is in reasonable agreement with experiments (see Fig. 6); the test results for AS4/Hercules 3501-6 are given in Nairn and Hu, 1994.

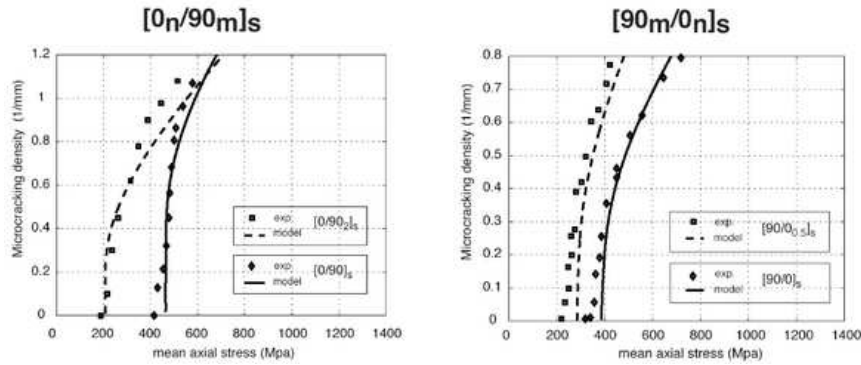


Figure 6. Comparison of tests vs. model.

3. A Bridge Between the Micro- and Mesomechanics

A rather complete bridge was developed in Ladevèze and Lubineau, 2001, 2002; Ladevèze et al., 2004.

The Method for Bridging the Two Mechanics

The real structure described on the microscale is subjected to a given loading. Its analysis constitutes a two-scale problem which we solve using a classical two-step scheme. The first step consists in calculating the large-wavelength part of the solution – the mesosolution – by solving what one calls the homogenized structure. In the second step, the micropart (i.e. the small-wavelength part) of the solution is determined in terms of the mesoquantities. This approach is applied to two basic problems which are representative of all engineering situations: the basic ply problem and the basic interface problem. These problems are described in Figs. 7 and 8. Periodic conditions are applied and elastic behavior is assumed. Classically, the solution of the homogenized problem is built first. For the real structure, this solution needs to be corrected because the residuals associated with discontinuities, which are assumed to be locally uniform, must be equilibrated.

The equivalence should hold true for any set of residuals which can be written in terms of mesoquantities.

The fundamental micro-meso link which defines what one calls the homogenized structure is exactly true for the two basic problems; it can

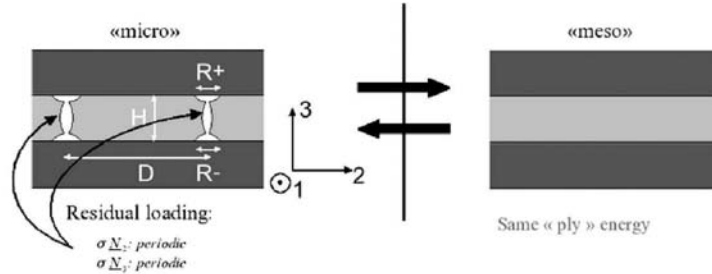


Figure 7. The basic ply problem.

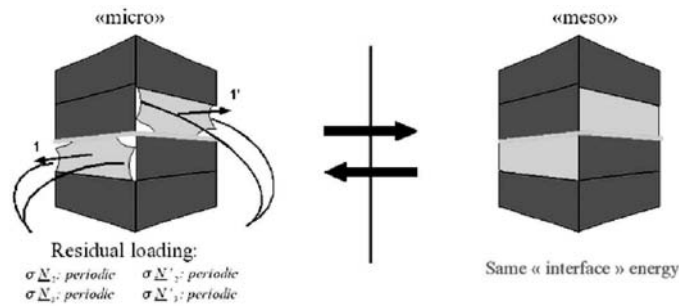


Figure 8. The basic interface problem.

be written as:

$$\begin{aligned}
 \forall \Gamma \quad \mathbb{III} \varepsilon_{\text{meso}} \mathbb{III} &= \langle \mathbb{III} \varepsilon_{\text{micro}} \mathbb{III} \rangle, \\
 \varpi_{\text{meso}} \underline{N}_3 &= \langle \varpi_{\text{micro}} \underline{N}_3 \rangle, \\
 \left(\langle \bullet \rangle &= \frac{1}{\text{mes}\Gamma} \int_{\Gamma} \bullet \, dS. \right)
 \end{aligned}
 \tag{2}$$

Γ is any cross section orthogonal to \underline{N}_3 and compatible with the periodicity associated with the layer or the interface containing Γ . In practice, for high crack densities, Γ could be replaced by any cross section which is wide with respect to the ply's thickness. \mathbb{III} is the projector onto the plane orthogonal to \underline{N}_3 .

The resolution of the microproblem has been a major issue in micromechanics; quasi-analytical approximations have been derived (Hashin, 1985; Nairn, 1989; Aboudi et al., 1988; Nuismer and Tan, 1998; Zhang et al., 1992; McCartney, 1992, 2000; Schoeppner and Pagano, 1998; Varna et al., 1992; Berthelot et al., 1996; Selvarathimam and Weitsman, 1999 ...) Here, we follow another calculation method which, in fact, is a functional analysis: first, the solution is determined in terms of

material operators which depend on the microdamage variables and the different additional parameters. Then, these operators are calculated for all values of the parameters and microdamage variables (in practice, in the range $\rho \in [0, 0.7]$ $\tau \in [0, 4]$). Consequently, a very large number of calculations are being performed.

Virtual Testing of the Ply

- The basic ply problem

The mesoenergy of the cracked ply can be written:

$$e_{\text{meso}}(\mathbf{III} \boldsymbol{\varepsilon}_{\text{meso}} \mathbf{III}, \boldsymbol{\omega}_{\text{meso}} \underline{N}_3) = \frac{1}{2} \text{Tr} [\mathbf{H} \mathbf{III} \boldsymbol{\varepsilon}_{\text{meso}} \mathbf{III} \mathbf{III} \boldsymbol{\varepsilon}_{\text{meso}} \mathbf{III}] + \frac{1}{2} \boldsymbol{\omega}_{\text{meso}} \underline{N}_3 \cdot \mathbf{A} \boldsymbol{\omega}_{\text{meso}} \underline{N}_3 + \boldsymbol{\omega}_{\text{meso}} \underline{N}_3 \cdot \mathbf{B} \mathbf{III} \boldsymbol{\varepsilon}_{\text{meso}} \mathbf{III} \quad (3)$$

where \mathbf{H} , \mathbf{A} and \mathbf{B} depend on the microdamage variables and on the parameters of the upper and lower parts. Numerically, it has been proved that:

Fundamental property:

Operators \mathbf{H} , \mathbf{A} and \mathbf{B} are quasi-intrinsic homogenized operators. In practice, they do not depend on the parameters of the upper and lower parts.

Additional results:

Mesoenergy has the following remarkable expression:

$$e_{\text{meso}}(\mathbf{III} \boldsymbol{\varepsilon}_{\text{meso}} \mathbf{III}, \boldsymbol{\omega}_{\text{meso}} \underline{N}_3) - e_{\text{meso}}^0 = -\frac{1}{2} \left[\frac{d_{22}}{1 - d_{22}} \frac{\sigma_{22}^2}{E_2^0} + \frac{d_{12}}{1 - d_{12}} \frac{\sigma_{12}^2}{G_{12}^0} \right] - \frac{1}{2} \left[\frac{d_{33}}{1 - d_{33}} \frac{\sigma_{33}^2}{E_3^0} + \mathbf{III} \boldsymbol{\omega}_{\text{meso}} \underline{N}_3 \cdot \mathbf{C} \mathbf{III} \boldsymbol{\omega}_{\text{meso}} \underline{N}_3 \right] \quad (4)$$

All the stresses involved are mesoquantities; moreover, the meso-damage variables d_{22} , d_{12} , d_{33} and \mathbf{C} (which is diagonal) can be calculated very easily in terms of the microdamage variables:

$$d_{ij}(\rho, \tau^+, \tau^-) = f_{ij}(\rho, \tau^+) + f_{ij}(\rho, \tau^-). \quad (5)$$

- The extended basic ply problem

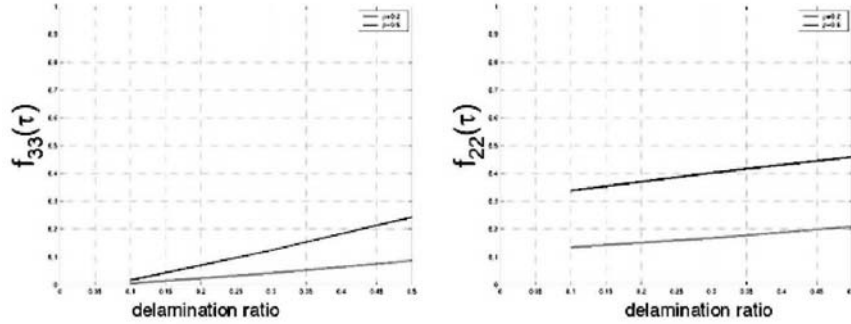


Figure 9. The functions f_{33} and f_{22} related to the basic ply problem.

Now, the cracked ply being studied is located between two adjacent cracked plies. The fundamental property is still valid; in practice, the ply's mesomodel depends only on the ply and its adjacent interfaces. A similar property holds for the damage variables. Consequently, the ply's mesomodel can be derived easily through a sequence of calculations.

Virtual Testing of the Interface

The basic interface problem is a 3D problem which can be approximated with good accuracy by two 2D problems. The mesoenergy can be written:

$$E_{\text{meso}}(\varpi_{\text{meso}} \underline{N}_3) = \frac{1}{2} \varpi_{\text{meso}} \underline{N}_3 \cdot \mathbf{D} \varpi_{\text{meso}} \underline{N}_3 \quad (6)$$

where \mathbf{D} depends on the microdamage variables and on the parameters of the upper and lower parts. Numerically, it has been proved that:

Fundamental property:

In practice, operator \mathbf{D} does not depend on the parameters of the lower and upper parts. The interface's mesomodel depends on the interface and its adjacent plies.

Additional results:

The mesodamage quantity D_{33} related to the opening delamination mode (Mode I) depends only on the total delamination ratio. Figure 10 shows the other mesodamage quantities D_{13} and D_{23} associated with Modes II and III, which quantifies the interaction between intra- and interlaminar mesodamage.

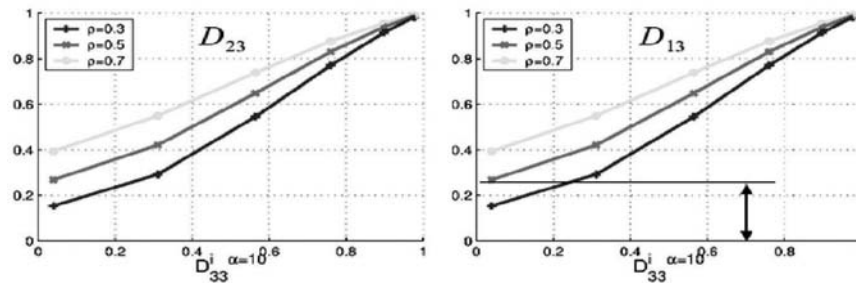


Figure 10. Interface mesodamage quantities D_{13} and D_{23} related to Modes II and III.

4. Perspectives for Damage Analysis

An Enhanced Mesomodel

The standard mesomodel has been extensively used for the resolution of impact and quasi-static engineering problems. We are now developing an enhanced version in order to improve the prediction of delamination. This development is an application of the bridge which has just been presented. The interface's damage mesomodel is made nonlocal by coupling it with the microcracking of the adjacent plies. Another improvement consists in using the micro-meso relations to describe damage in terms of micromechanics.

This mesomodel needs to go through the identification procedure again. A further improvement would be to work with the true, complete mesomodel, which is nonlocal both for the interface and for the ply.

A Computational Damage Micromodel of Laminates

The starting point is an initial state including thermal stresses, which can be calculated by simulation of the curing process or, classically, by applying a negative temperature variation ΔT .

The model is discrete; in fact, it is hybrid. The fiber-matrix material follows the continuum mechanics framework; more precisely, its behavior is given by the mesomodel restricted to (visco)plasticity and diffuse damage (Scenarios 3 and 4). The cracked surfaces related to microcracking and delamination follow what is called "finite fracture mechanics" (Hashin, 1996), for which we introduced minimum cracked surfaces (Fig.11). Initiation and propagation criteria are considered

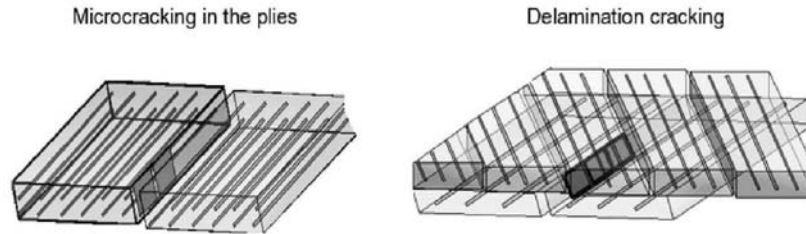


Figure 11. The minimum cracked surfaces.

only for microcracking. For fiber breakage, a minimum cracked volume, whose height is the thickness of the ply, is prescribed.

Remarks:

- When a surface is cracked, unilateral contact conditions with friction are applied.
- Mode I is distinct from Modes II and III.
- Stochastic modeling is used for the critical parameters of the material.

This rather simple computational micromodel could be used as a reference. It is *a priori* in good agreement with experimental micro- and macroinformation. However, computational difficulties pose a serious problem with this model. If we consider a low-velocity impact problem (T300/914 24 plies), the calculation procedure leads to the following numbers of degrees of freedom for the largest problem to be solved:

- classical finite element method: $2 \cdot 10^{10}$ DOFs
- multiscale computational strategy: $4 \cdot 10^8$ DOFs (one macroscale) and 10^6 DOFs (two macroscales).

Consequently, a research challenge consists in deriving alternative computational strategies capable of solving such engineering problems. This is currently a hot issue, known as “multiscale computational strategies including uncertainties”, for which several proposals have already been made (in particular Devries et al., 1989; Feyel, 2003; Fish et al., 1997; Kouznetsova et al., 2002; Ladevèze et al., 2001; Ladevèze and Nouy, 2003; Zohdi et al., 1996).

Conclusion

Let us come back to the central question discussed in this paper: is there a bridge between the micro- and mesomechanics of laminates? The answer is yes, but the mesomechanics of laminates is not a simple field, because it is nonlocal.

Among the applications of this bridge are multiscale computational approaches for the prediction of final fracture, which require further research, especially in computational mechanics, prior to becoming engineering tools.

References

- L. Aboudi, S.W. Lee, and C.T. Herakowich, Three dimensional analysis of laminates with cross cracks, *ASME J. Appl. Mech.*, Vol. 55, pp.389–397, 1988.
- D.H. Allen, S.E. Groves, and C.E. Harris, A cumulative damage model for continuous fiber composite laminates with matrix cracking and interply delaminations, [in:] *Composite Materials: Testing and Design*, J. D. Withcomb, [ed.], ASTM STP 972, Washington DC, USA, pp.57–80, 1988.
- O. Allix, Interface damage mechanics: application to delamination, [in:] *Continuum Damage Mechanics of Materials and Structures*, O. Allix and F. Hild, [Eds.], Elsevier, pp.295–324, 2002.
- O. Allix, N. Bahlouli, N. Cluzel, and C. Perret, Modelling and identification of temperature-dependent mechanical behavior of the elementary ply in carbon/epoxy laminates, *Comp. Sci. Techn.*, Vol. 56, pp.883–888, 1996.
- O. Allix and P. Ladevèze, Interlaminar interface modelling for the prediction of laminate delamination, *Composite Structures*, Vol. 22, pp.235–242, 1992.
- O. Allix, D. Lévèque, and L. Perret, Interlaminar interface model identification and forecast of delamination in composite laminates, *Comp. Sci. Techn.*, Vol. 56, pp.671–678, 1998.
- J.M. Berthelot, Transverse cracking and delamination in cross-ply glass-fiber and carbon-fiber reinforced plastic laminates: static and fatigue loading, *Appl. Mech. Rev.*, Vol. 56(1), pp.1–37, 2003.
- J.M. Berthelot, and J.F. Le Corre, Statistical analysis of the progression of transverse cracking and delamination in cross-ply laminates, *Comp. Sci. Techn.*, Vol. 60, pp.2659–2669, 2000.
- J.M. Berthelot, P. Leblond, A. El Mahi, and J.F. Le Corre, Transverse cracking of cross-ply laminates, Part 1: Analysis, *Composites*, Vol. 27A, pp.989–1001, 1996.
- L. Boniface, P. Smith, M. Bader, and A. Rezaifard, Transverse ply cracking in cross-ply CFRP laminates – Initiation or propagation controlled?, *J. Comp. Materials*, Vol. 31, pp.1080–1112, 1997.
- F.W. Crossman and A.S.D. Wang, The dependence of transverse cracking and delamination on ply thickness in graphite/epoxy laminates, [in:] *Damage in Composite Materials*, ASTM STP 775, K.L. Reissner, [ed.], pp.118–139, 1982.
- L. Daudeville and P. Ladevèze, A damage mechanics tool for laminate delamination, *Composite Structures*, Vol. 25, pp.547–555, 1993.

- F. Devries, H. Dumontet, G. Duvaut, and F. L  n  , Homogenization and damage for composite structures, *Int. J. for Numerical Methods in Engineering*, Vol. 27, pp.285–298, 1989.
- G.J. Dvorak and N. Laws, Analysis of progressive matrix cracking in composite laminates, II. First ply failure, *J. Comp. Materials*, Vol. 21, pp.309–329, 1987.
- F. Feyel, A multilevel finite element method (FE^2) to describe the response of highly non-linear structures using generalized continua, *Computer Methods in Applied Mechanics and Engineering*, Vol. 192, pp.3233–3244, 2003.
- J. Fish, K. Sheck, M. Pandheeradi, and M.S. Shepard, Computational plasticity for composite structures based on mathematical homogenization: theory and practice, *Computer Methods in Applied Mechanics and Engineering*, Vol. 148, pp.53–73, 1997.
- H. Fukunaga, T.W. Chou, P.W.M. Peters, and K. Schulte, Probabilistic failure strength analyses of graphite/epoxy cross-ply laminates, *J. Comp. Materials*, Vol. 18, pp.339–356, 1984.
- K.W. Garrett and J.E. Bailey, Multiple transverse fracture in 90° cross-ply laminates of a glass fiber reinforced polyester, *J. Mater. Sci.*, Vol. 12, pp.157–168, 1977.
- S. Ghosh, K. Lee, and S. Moorthy, Multiple scale analysis of heterogeneous elastic structures using homogenization theory and Vorono   cell finite element method, *J. Solids Structures*, Vol. 32(1), pp.27–62, 1995.
- P. Gudmunson and W. Zang, An analytical model for thermoelastic properties of composite laminates containing transverse matrix cracks, *Int. J. Solids Structures*, Vol. 30, pp.3211–3231, 1993.
- F.J. Guild, S.L. Ogin, and P.A. Smith, Modelling of 90° ply cracking in cross ply laminates, including three-dimensional effects, *J. Comp. Materials*, Vol. 27, pp.646–667, 1993.
- S. Hashemi, A. Kinloch, and J. Williams, Mechanics and mechanisms of delamination in a poly(ether sulphone)-fiber composite, *Comp. Sci. Techn.*, Vol. 37, pp.429–462, 1990.
- Z. Hashin, Analysis of cracked laminates: a variational approach, *Mech. Mater.*, Vol. 4, pp.121–136, 1985.
- Z. Hashin, Analysis of orthogonally cracked laminates under tension, *ASME J. Appl. Mech.*, Vol. 4, pp.121–136, 1985.
- Z. Hashin, Finite thermoelastic fracture criterion with application to laminate cracking analysis, *J. Mech. Phys. Solids*, Vol. 44(7), pp.1129–1145, 1996.
- C. Herakovich, *Mechanics of Fibrous Composites*, J. Wiley, 1998.
- A.L. Highsmith and K.L. Reifsnider, Stiffness reduction mechanisms in composite laminates, [in:] *Damage in Composite Materials*, ASTM STP 775, K.L. Reifsnider, [ed.], pp.103–117, 1982.
- V. Kouznetsova, M.G.D. Geers, and W.A.M. Brekelmans, Multiscale constitutive modelling of heterogeneous materials with a gradient-enhanced computational homogenization scheme, *Int. J. for Numerical Methods in Engineering*, Vol. 54, pp.1235–1260.
- P. Ladev  ze, O. Allix, J.F. De  , and D. L  v  que, A mesomodel for localisation and damage computation in laminates, *Computer Methods in Applied Mechanics and Engineering*, Vol. 1832, pp.105–122, 2000.
- P. Ladev  ze, About the damage mechanics of composites, [in:] *Comptes-Rendus des JNC5*, pp.667–683, C. Bathias and D. Menk  s, [eds.], Pluralis Publication, Paris 1986.

- P. Ladevèze, About a damage mechanics approach, [in:] *Mechanics and Mechanisms of Damage in Composite and Multimaterials*, MEP, pp.119–142, 1989.
- P. Ladevèze and E. Le Dantec, Damage modeling of the elementary ply for laminated composites, *Comp. Sci. Techn.*, Vol. 43, pp.257–267, 1992.
- P. Ladevèze, O. Loiseau and D. Dureisseix, A micro-macro and parallel computational strategy for highly heterogeneous structures, *Int. J. for Numerical Methods in Engineering*, Vol. 52, pp.121–138, 2001.
- P. Ladevèze and G. Lubineau, On a damage mesomodel for laminates: micro-meso relationships, possibilities and limits, *Comp. Sci. Techn.*, Vol. 61(15), pp.2149–2158, 2001.
- P. Ladevèze and G. Lubineau, On a damage mesomodel for laminates: micromechanics basis and improvement, *Mech. Materials*, Vol. 35, pp.763–775, 2001.
- P. Ladevèze and G. Lubineau, An enhanced mesomodel for laminates based on micromechanics, *Comp. Sci. Techn.*, Vol. 62, pp.533–541, 2002.
- P. Ladevèze, G. Lubineau, and D. Marsal, Towards a bridge between the micro- and the mesomechanics of delamination for laminated composites, *Comp. Sci. Techn.*, to appear 2004.
- P. Ladevèze, and A. Nouy, On a multiscale computational strategy with time and space homogenization for structural mechanics, *Computer Methods in Applied Mechanics and Engineering*, Vol. 192, pp.3061–3087, 2003.
- F. Lagattu and M. Lafarie-Frénot, Variation of PEEK matrix crystallinity in APC-2 composite subjected to large shearing deformation, *Comp. Sci. Techn.*, Vol. 60, pp.605–612, 2000.
- N. Laws and G.J. Dvorak, Progressive transverse cracking in composite laminates, *J. Comp. Materials*, Vol. 22, pp.900–916, 1988.
- D.S. Li and M. Wisnom, Evaluating Weibull parameters for transverse cracking in cross-ply laminates, *J. Comp. Materials*, Vol. 31(9): pp.935–951, 1997.
- J.E. Masters and K.L. Reifsnider, An investigation of cumulative damage development in quasi-isotropic graphite/epoxy laminates, [in:] *Damage in Composite Materials*, ASTM STP 77, pp.40–62, 1982.
- L.N. McCartney, Theory of stress transfer in a $0^\circ - 90^\circ - 0^\circ$ cross-ply laminate containing a parallel array of transverse cracks, *J. Mech. Phys. Solids*, Vol. 40, pp.27–68, 1992.
- L.N. McCartney, Model to predict effects of triaxial loading on ply cracking in general symmetric laminates, *Comp. Sci. Techn.*, Vol. 60, pp.2255–2279, 2000.
- L.N. McCartney, G.A. Schoeppner, and W. Becker, Comparison of models for transverse ply cracks in composite laminates, *Comp. Sci. Techn.*, Vol.60, pp.2347–2359, 2000.
- J.A. Nairn, The strain energy release rate of composite microcracking: a variational approach, *J. Comp. Materials*, vol. 23, pp.1106–1129, 1989.
- J.A. Nairn and S. Hu, The initiation and growth of delaminations induced by matrix microcracks in laminated composites, *Int. J. Fract.*, Vol. 57, pp.1–24, 1992.
- J.A. Nairn and S. Hu, Micromechanics of damage: a case study of matrix cracking, pp.187–243, [in:] *Damage Mechanics of Composite Materials*, R. Talreja, [ed.], Elsevier, Amsterdam 1994.
- J. Nairn, S. Hu, and J. Bark, A critical evaluation of theories for predicting microcracking in composite laminates, *J. Materials Science*, Vol. 28, pp.5099–5111, 1993.
- R.J. Nuismer and S.C. Tan, Constitutive relations of a cracked composite lamina, *J. Comp. Materials*, Vol. 22, pp.306–321, 1988.

- S.L. Ogin, P.A. Smith, and P.W.R. Beaumont, Matrix cracking and stiffness reduction during the fatigue of a $(0/90)_s$ GFRP laminate, *Comp. Sci. Techn.*, Vol. 22, pp.23–31, 1985.
- N. Pagano, G. Schoeppner, R. Kim, and F. Abrams, Steady-state cracking and edge effect in thermo-mechanical transverse cracking of cross-ply laminates, *Comp. Sci. Techn.*, Vol. 58, pp.1811–1825, 1998.
- A. Parvizi, K.W. Garrett, and J.E. Bailey, Constrained cracking in glass fiber-reinforced epoxy cross-ply laminates, *J. Mater. Sci.*, Vol. 13, pp.195–201, 1978.
- J. Renard and T. Jeggy, Modélisation de la fissuration transverse dans les matériaux composites carbone/résine, [in:] *Groupe de Réflexion sur l'Endommagement*, Cetim, Senlis 1989.
- G. Schoeppner and N. Pagano, Stress fields and energy release rates in cross-ply laminates, *Int. J. Solids and Structures*, Vol. 35(11), pp.1025–1055, 1998.
- A. Selvarathimam and J. Weitsman, A shear-lag analysis of transverse cracking and delamination in cross-ply carbon-fiber/epoxy composites under dry, saturated and immersed fatigue conditions, *Comp. Sci. Techn.*, Vol. 59, pp.2115–2123, 1999.
- N. Takeda and S. Ogihara, Initiation and growth of delamination from the tips of transverse cracks in CFRP cross-ply laminates, *Comp. Sci. Techn.*, Vol. 52 pp.309–318, 1994.
- R. Talreja, Stiffness based fatigue damage characterization of fibrous composites, [in:] *Advances in Composite Materials*, A. R. Bunsell et al., [eds.], Vol. 2, pp. 1732–1739, Pergamon Press, Oxford 1980.
- R. Talreja, Transverse cracking and stiffness reduction in composite laminates, *J. Comp. Materials*, Vol. 19, pp.355–375, 1985.
- J. Tong, F.J. Guild, S.L. Ogin, and P.A. Smith, On matrix crack growth in quasi-isotropic laminates, I. Experimental investigations, *Comp. Sci. Techn.*, Vol. 57, pp.1527–1535, 1997.
- J. Varna and L.A. Berglund, A model for prediction of the transverse cracking strain in cross-ply laminates, *J. Reinf. Plast. Comp.*, Vol. 11, pp.708–728, 1992.
- A.S.D. Wang, P.C. Chou, and S. Lei, A stochastic model for the growth of matrix cracks in composite laminates, *J. Comp. Materials*, Vol. 18, pp.239–254, 1984.
- A.S.D. Wang and F.W. Crossman, Initiation and growth of transverse cracks and edge delamination in composite laminates, Part 1: An energy method, *J. Comp. Materials*, Vol. 14, pp.71–87, 1980.
- S. Yahvac, L. Yats, and D. Wetters, Transverse ply cracking in toughened and un-toughened graphite/epoxy and graphite/polycyanate cross-ply laminates, *J. Comp. Materials*, Vol. 25, pp.1653–1667, 1991.
- J. Zhang, J. Fan, and C. Soutis, Analysis of multiple matrix cracking in $[\pm 0_m/90_n]$ composite laminates, *Composites*, Vol. 23, pp.291–298, 1992.
- T.I. Zohdi, J.T. Oden, and G.J. Rodin, Hierarchical modeling of heterogeneous bodies, *Computer Methods in Applied Mechanics and Engineering*, Vol. 155, pp.181–192, 1996.

TURBULENCE AND LARGE-EDDY SIMULATIONS

Marcel R. Lesieur

Geophysical and Industrial Flows Lab. (LEGI)

BP 53, 38041 Grenoble-Cedex 9. France

marcel.lesieur@inpg.fr

Abstract After having discussed the limits of turbulence direct-numerical simulations, one presents large-eddy simulations methods, where small scales are filtered out and modelled by appropriate eddy coefficients in the evolution of large scales. We concentrate on models developed originally in Fourier space, then adapted to physical space. One presents coherent-vortex dynamics and statistical data obtained thanks to these models for incompressible isotropic turbulence, channel flow and controlled round jet. Then large-eddy simulations are considered in the compressible case, where we study first the free jet at Mach 0.7 and 1.4, then the controlled supersonic jet. Finally LES of compressible flows above riblets in subsonic and supersonic cases are considered.

Keywords: Turbulence, large-eddy simulations, coherent vortices, jets, compressible flows, control, riblets.

Introduction

Direct-numerical simulations (DNS) of turbulence are based on deterministic solutions of Navier-Stokes equation, obtained through a proper discretization on a spatio-temporal grid of partial-differential operators involved, and where one advances in time starting from a given initial state. This implies that the typical grid mesh Δx in space should be inferior to the Kolmogorov scale $l_D = k_D^{-1}$, under which velocity fluctuations are damped out by molecular viscosity. Another important point is that numerical schemes should be sufficiently precise, and hence of high order, if possible. In fact the number of spatial grid points necessary for a well-resolved DNS in developed three-dimensional turbulence is $\approx (L/l_D)^3$, where L is the typical size of large structures. One can show that this is of the order of $\sim R_\lambda^{9/2}$, where $R_\lambda = u'\lambda/\nu$ is defined thanks to the rms longitudinal velocity and the Taylor microscale. R_λ may

be determined experimentally, for instance on a commercial-plane wing where it is equal to 3000 (Jimenez, 2000). This yields $\approx 10^{15}$ grid points to handle on the computer, which permits to envisage a DNS of such a flow within 30 to 50 years. For the atmospheric boundary layer it is worse, since we have $R_\lambda = 10000$, and hence 10^{18} grid points. To be able to perform a simulation in such cases, one is thus obliged to reduce drastically the number of degrees of freedom of the system. Large-eddy simulations (LES) are a powerful tool for this purpose. More details concerning the rest of this talk may be found in Lesieur (1997), Lesieur & Métais (1996), and Lesieur et al. (2004).

1. Incompressible LES

Physical Space

Density $\rho = \rho_0$ is uniform. Let Δx be a given spatial grid mesh comprised between L and l_D , and $G_{\Delta x}$ a low-pass spatial filter of width Δx , chosen in order to eliminate properly subgrid-scale motions of wavelength $< \Delta x$. One associates to any quantity $f(\vec{x}, t)$ its locally-filtered counterpart

$$\bar{f}(\vec{x}, t) = f * G_{\Delta x} = \int f(\vec{y}, t) G_{\Delta x}(\vec{x} - \vec{y}) d\vec{y}. \quad (1)$$

The filter commutes with spatial and temporal derivatives (if Δx is uniform). Let us write Navier-Stokes equation as

$$\frac{\partial u_i}{\partial t} + \frac{\partial}{\partial x_j} (u_i u_j) = -\frac{1}{\rho_0} \frac{\partial p}{\partial x_i} + \frac{\partial}{\partial x_j} (2\nu S_{ij}), \quad (2)$$

where

$$S_{ij} = \frac{1}{2} \left(\frac{\partial u_i}{\partial x_j} + \frac{\partial u_j}{\partial x_i} \right) \quad (3)$$

is the deformation tensor, symmetric part of the velocity gradient, and ν is assumed constant. When applying the filter, it is obtained

$$\frac{\partial \bar{u}_i}{\partial t} + \frac{\partial}{\partial x_j} (\bar{u}_i \bar{u}_j) = -\frac{1}{\rho_0} \frac{\partial \bar{p}}{\partial x_i} + \frac{\partial}{\partial x_j} (2\nu \bar{S}_{ij} + \bar{u}_i \bar{u}_j - \overline{u_i u_j}). \quad (4)$$

I call $T_{ij} = \bar{u}_i \bar{u}_j - \overline{u_i u_j}$ the subgrid-stresses tensor. This is in fact Navier-Stokes equation for \bar{u}_i , provided T_{ij} is added to the filtered viscous stress $2\nu \bar{S}_{ij}$. Continuity $\partial \bar{u}_j / \partial x_j = 0$ holds for the filtered Navier-Stokes equation if Δx is uniform. The simplest way chosen to close the problem is to make an eddy-viscosity assumption

$$T_{ij} = 2\nu_t(\vec{x}, t) \bar{S}_{ij} + \frac{1}{3} T_{ll} \delta_{ij}, \quad (5)$$

where ν_t has to be determined (see later). With such an hypothesis, the filtered Navier-Stokes equation writes

$$\frac{\partial \bar{u}_i}{\partial t} + \frac{\partial}{\partial x_j} (\bar{u}_i \bar{u}_j) = -\frac{1}{\rho_0} \frac{\partial \bar{P}}{\partial x_i} + \frac{\partial}{\partial x_j} [2(\nu + \nu_t) \bar{S}_{ij}], \quad (6)$$

where one has introduced a modified pressure (macro-pressure)

$$\bar{P} = \bar{p} - \frac{1}{3} \rho_0 T_u. \quad (7)$$

Let us now consider the mixing of a scalar $T(\vec{x}, t)$ transported by the flow (with a molecular diffusivity κ), which obeys heat Fourier equation following the fluid motion:

$$\frac{\partial T}{\partial t} + \frac{\partial}{\partial x_j} (T u_j) = \frac{\partial}{\partial x_j} \left\{ \kappa \frac{\partial T}{\partial x_j} \right\}. \quad (8)$$

Filtering this equation and making the assumption of an eddy diffusivity $\kappa_t(\vec{x}, t)$ yields for the filtered scalar:

$$\frac{\partial \bar{T}}{\partial t} + \frac{\partial}{\partial x_j} (\bar{T} \bar{u}_j) = \frac{\partial}{\partial x_j} \left\{ (\kappa + \kappa_t) \frac{\partial \bar{T}}{\partial x_j} \right\}. \quad (9)$$

$\kappa_t(\vec{x}, t)$ is determined from ν_t thanks to a “turbulent Prandtl number” $P_r^{(t)} = \nu_t / \kappa_t$. These eddy coefficients need to be determined. In Smagorinsky’s model (1963), the eddy viscosity is based on velocity gradients and taken proportional to $(\Delta x)^2 \sqrt{\bar{S}_{ij} \bar{S}_{ij}}$. There are interesting improvements of this model made by Germano et al. (1991) where the constant is calculated dynamically by a double filtering. In fact, the major drawback of an eddy-viscosity assumption in physical space is that it assumes a scale-separation between filtered and subgridscales, as the molecular-viscosity concept in a continuous medium is based upon the existence of a scale separation between macroscopic and molecular scales. This explains the poor correlation between T_{ij} and \bar{S}_{ij} found in a-priori tests based on DNS. This is a serious motivation to work in Fourier space if the geometry of the problem permits it.

Grenoble Models in Fourier Space

Turbulence is first assumed statistically homogeneous. Let $\hat{f}(\vec{k}, t)$ be the spatial Fourier transform of any quantity $f(\vec{x}, t)$:

$$\hat{f}(\vec{k}, t) = \left(\frac{1}{2\pi} \right)^3 \int e^{-i\vec{k} \cdot \vec{x}} f(\vec{x}, t) d\vec{x}. \quad (10)$$

The optimal filter to eliminate small scales considered as waves with a given spatial wavelength is a sharp filter, such that

$$\bar{f} = \hat{f} \text{ for } k = |\vec{k}| < k_C = \frac{\pi}{\Delta x}; \quad \bar{f} = 0 \text{ for } k > k_C, \quad (11)$$

the factor $\pi/\Delta x$ coming when one works using pseudo-spectral methods in a spatially-periodic flow. If turbulence is statistically isotropic, one can define the kinetic-energy spectrum $E(k, t)$, such that $E(k, t)\delta k$ is the mean (in the sense of a statistical average upon an ensemble of realizations) kinetic energy per unit mass in a spatial-frequency band $[k, k + \delta k]$.

In Fourier space, nonlinear interactions go through “resonant” triads of wavevectors such that $\vec{k} = \vec{p} + \vec{q}$. Indeed, due to incompressibility, the nonlinear term of Navier-Stokes turns out to be the projection in a plane perpendicular to \vec{k} of the Fourier transform of $(\partial/\partial x_j)u_i u_j$, equal to k_j times the Fourier transform of $u_i u_j$, which is a convolution product in Fourier space (Remark that the so-called “projection methods” in the numerical analysis of Navier-Stokes equation are based on that). The subgrid modelling consists here in evaluating the momentum transfers due to triads where $k < k_C$ and one at least of wavenumbers p and q is larger than k_C . In analogy with the fact that the Fourier transform of Navier-Stokes dissipative term is $-\nu k^2 \hat{u}_i(\vec{k}, t)$, the subgrid momentum transfer will be modelled as $-\nu_t(k|k_C)k^2 \hat{u}_i(\vec{k}, t)$, the eddy viscosity in spectral space being calculated at the level of subgrid kinetic-energy transfers through an advanced theory of turbulence, the EDQNM. One gets

$$\nu_t(k|k_C) = 0.441 C_K^{-3/2} \left[\frac{E(k_C)}{k_C} \right]^{1/2} X\left(\frac{k}{k_C}\right), \quad (12)$$

assuming that k_C lies in a Kolmogorov spectrum $E(k) = C_K \epsilon^{2/3} k^{-5/3}$. Here, $X(k/k_C)$ is a “plateau-peak function” equal to 1 for $k/k_C < \approx 1/3$, and rising above. In fact, ν_t^+ on Fig.1 is the spectral eddy viscosity renormalized by $\sqrt{E(k_C)/k_C}$. Notice that the same kind of eddy-viscosity had been found by Kraichnan (1976) with another turbulence stochastic model, the Test-Field model, but he did not consider the scaling in $\sqrt{E(k_C)/k_C}$, nor used this spectral eddy-viscosity for LES purposes. Figure 1 shows also the renormalized eddy-diffusivity, which has the same scaling and plateau-peak behaviour, and the turbulent Prandtl number, approximately constant and equal to 0.6. This plateau-peak model has been used by Chollet & Lesieur (1981) to perform the first LES of three-dimensional isotropic turbulence. In fact, it was shown numerically by Domaradzki et al. (1987) on the basis of direct-numerical

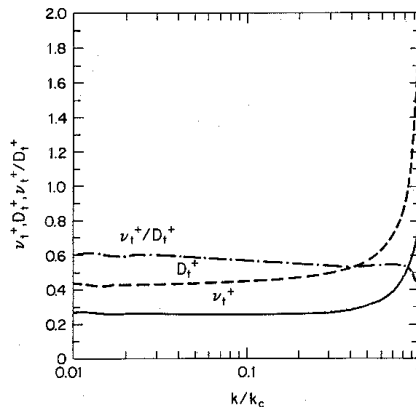


Figure 1. Spectral eddy viscosity, diffusivity and turbulent Prandtl number calculated using the EDQNM theory (from Chollet & Lesieur, 1981)

simulations that the plateau part of the eddy viscosity goes to 0 at low Reynolds number. In the spectral-dynamic model (Lamballais, Métais and Lesieur, 1998), one accounts (still thanks to the EDQNM theory) in the plateau elevation for a spectral slope at k_C different from $5/3$.

We give two applications of this model: the first one concerns the decay of isotropic turbulence at zero molecular viscosity in a periodic box, starting from a Gaussian velocity profile. Pseudo-spectral numerical methods are used. The initial peak is $k_i = 4$. One presents an animation taken from Lesieur et al. (2003, 2004) showing the formation and evolution of the spaghetti-type vortices. They are identified thanks to isosurfaces at a positive fixed threshold of $Q = (1/2)(\Omega_{ij}\Omega_{ij} - S_{ij}S_{ij})$, the second invariant of the velocity gradient. This criterion, due to Hunt et al. (1988), characterizes regions where local rotation dominates deformation, and where pressure has a local minimum. This criterion is very efficient to visualize coherent vortices, and simpler to implement than its very close cousin the λ_2 criterion of Jeong & Hussain (1995).

The spectral-dynamic model has also been applied to a plane channel of width $2h$ at $h^+ = 204$ and 395 . The symbol $+$ means that length is normalized by the viscous length ν/v_* , which is equivalent for a boundary layer to Kolmogorov dissipative scale. Numerical methods are here pseudo-spectral in directions parallel to the walls, and finite differences of sixth order in the normal direction. A calculation with the first grid point at a distance of one viscous length from the wall (and a stretched grid away) yields very good statistical results compared with Kim's DNS published in Antonia et al. (1992). At $h^+ = 395$, the LES is 70 times faster than the DNS.

It is clear that the use of stretched grids invalidates the assumption of regular grid done above. However, LES carried out in this improper manner give valuable results concerning statistics and coherent-vortex dynamics, as far as comparisons with experiments and DNS are done.

Grenoble Models in Physical Space: Structure-function Models

For complicated geometries, numerical methods impose to work in physical space. The spectral eddy viscosity is thus set to a constant calculated assuming the subgrid kinetic-energy dissipation equals ϵ in a Kolmogorov cascade. Then we lose the advantage of not assuming a spectral gap. But results of the model are however good, as it will be seen. We have $\nu_t(\vec{x}, \Delta x) = (2/3)C_K^{-3/2} [E_{\vec{x}}(k_C)/k_C]^{1/2}$, where $E_{\vec{x}}(k_C)$ is a local kinetic-energy spectrum, determined with the aid of the local second-order velocity structure function. This model, due to Métais & Lesieur (1992), improves classical Smagorinsky model for non-sheared turbulence. For sheared turbulence (without or with walls), two excellent versions of the model exist to eliminate the damping effects of large-scale shears: the selective structure-function model (David, 1993), and the filtered structure-function model (Ducros et al., 1996). They work very well for free-shear flows and boundary layers and can be utilized on unstructured grids.

An example is provided with the control by upstream perturbations (superposed to a close to top hat profile) of a round jet, presented in Silva & Métais (2003). The calculation involves the combination of “harmonic varicose” and “sub-harmonic flapping” modes (harmonic is defined with respect to the preferred frequency of vortices shed in the free jet and passing at the level of the potential core). In such a flow, the jet collapses in the so-called bisecting plane, and widens in the bifurcating plane. It is possible to see on an animation (enclosed on the CD-ROM) of positive Q isosurfaces in a LES at molecular Reynolds number 5000. The numerical code is the same as for the channel presented above, with a Cartesian orthogonal system of coordinates. Resolution is $201 \times 128 \times 128$. In the animation, the jet is artificially rotating from the bisecting to the bifurcating planes. One can see in particular alternate-pairing interaction between vortex rings, which is a sub-harmonic reconnection of vortices, analogous to helical pairing of Kelvin-Helmholtz vortices found in DNS and LES of temporal mixing layers (see eg Comte et al., 1992). With other types of forcings, one can generate Reynolds blooming jet.

2. Compressible LES

Formalism

We work with an ideal gas. The LES formalism is much more complicated in the compressible case. Equations expressing conservation of mass, total momentum $\rho\vec{u}$ and total energy ρe are still filtered by the “bar-filter”. Gravity is neglected. One can make important simplifications by using Favre filtering \tilde{f} and introducing a “macro-temperature”

$$\vartheta = \tilde{T} - \frac{\mathcal{T}_{ll}}{2C_v\bar{\rho}} \quad , \quad (13)$$

where \mathcal{T}_{ll} is the trace of the subgrid-scale tensor $\mathcal{T}_{ij} = \bar{\rho}\tilde{u}_i\tilde{u}_j - \overline{\rho u_i u_j}$. The latter is related to the macro-pressure ϖ by the relation

$$\varpi = \bar{\rho}R\vartheta + \frac{3\gamma - 5}{6}\mathcal{T}_{ll} \quad . \quad (14)$$

In this relation, the last term is small even at high Mach, so that we neglect it and use the law of ideal gases between $\varpi, \bar{\rho}$ and ϑ . After some other approximations, one obtains a system equivalent to compressible Navier-Stokes equation for $\tilde{u}_i, \bar{\rho}, \varpi, \vartheta, \tilde{e}$, most of the molecular-diffusion coefficients being complemented by an eddy counterpart which is the same as in the incompressible case. We work with the filtered structure-function model.

Round Jet

Then one studies a compressible round jet at Mach (defined at the upstream jet centreline) 0.7 and 1.4 forced upstream by a close to top-hat velocity to which a weak isotropic random perturbation is superposed. The associated temperature profile is given by Crocco-Busemann relation for a boundary-layer without pressure-gradient.

Numerical methods are now for nonlinear terms fourth-order MacCormack’s predictor-corrector scheme modified by Gottlieb & Turkel (1976). Boundary conditions are based upon Poinso & Lele (1992) characteristics-based method, with a sponge zone downstream, following the procedure developed by Sandhu and Sandham (1994). The Reynolds number is 36000. We show on Fig. 2 a picture of the jet (top, Mach 0.7; bottom Mach 1.4) in the case of a white-noise forcing: the supersonic jet is much more focussed in space than the subsonic one, with an increase of the potential core. This is related to the delay of Kelvin-Helmholtz instability due to convective Mach number effects, as shown by Papamoschou & and Roshko (1988) in an experimental spatially-growing mixing layer, and by Sandham & Reynolds (1991) for temporal mixing layers. Further

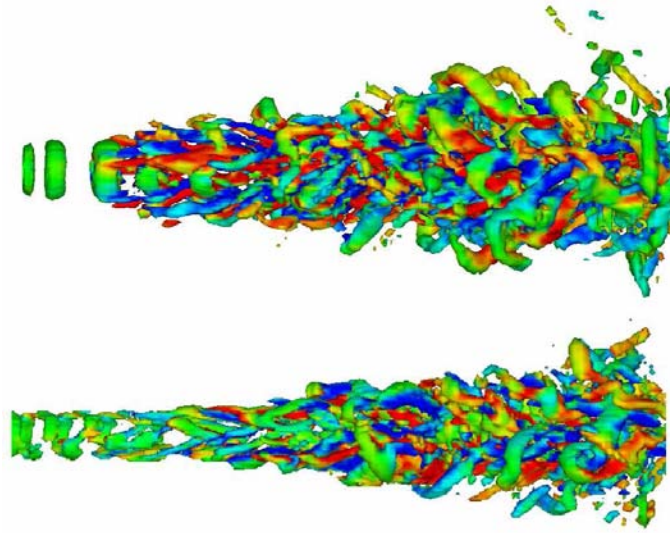


Figure 2. LES of a compressible round jet forced by a weak isotropic random perturbation. Positive Q isosurfaces coloured by longitudinal vorticity. Top, Mach 0.7; bottom, Mach 1.4 (courtesy M. Maldi).

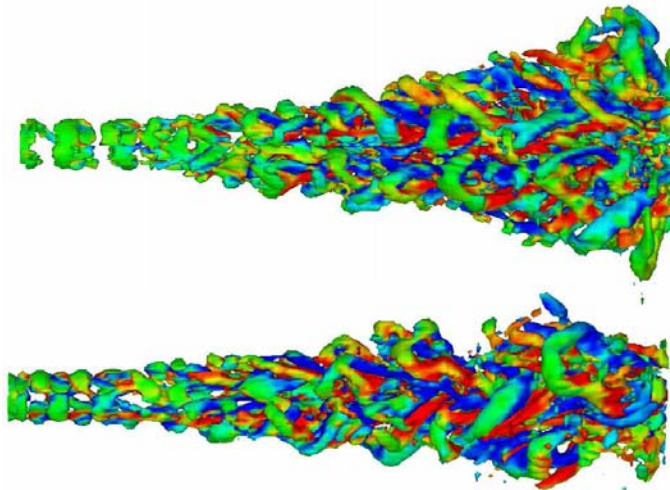


Figure 3. LES of a the forced jet at Mach 1.4. Positive Q isosurfaces coloured by longitudinal vorticity. Top, bifurcating plane; bottom, bisecting plane (courtesy M. Maldi).

downstream, the supersonic jet has reduced its convective Mach number, and starts spreading out as the subsonic one. Notice that the supersonic jet we have simulated does not exit from a real nozzle, and no shocks or Mach waves can be produced. We have estimated the noise radiated away from the jets on the basis of an approximate Lighthill equation due to Witkowska and Juve (1994), and found that the supersonic jet is much more noisy than the subsonic one. This agrees with laws predicting that the acoustic energy is proportional to the jet exit velocity raised to a high power.

Let us now consider the LES of a jet at Mach 1.4 and Reynolds 36000 controlled by the same mixed harmonic varicose/sub-harmonic flapping upstream perturbation as in the incompressible case. Figure 3 presents Q coloured by longitudinal vorticity in the bifurcating and bisecting planes.

Drag Reduction by Riblets

We briefly recall the numerous studies associated to passive turbulence control by longitudinal riblets put on some parts of planes, boats, and more recently on competition swimming costumes made of so-called shark skin. The optimal spanwise wavelength of triangular riblets was empirically found to be $\lambda_z^+ = 10 \approx 20$. In fact, the DNS of Choi et al. (1993) using equilateral triangles have shed a new light on the role of quasi-longitudinal vortices in drag reduction by riblets. Indeed, the diameter of quasi-longitudinal vortices travelling in a turbulent boundary layer on a flat plate is $d^+ \approx 25$. Choi et al's DNS show that for λ_z^+ larger than 25 (they took 40), the quasi-longitudinal vortices are trapped in the valleys of the riblets, which increases the drag. On the other hand, in the simulation with $\lambda_z^+ = 20$, the longitudinal vortices sit above the riblets peak, and the drag is decreased.

A very important question for aeronautic applications concerns the influence of compressibility in a perfect gas for riblets efficiency. For this purpose, we consider a compressible channel of ideal gas, one wall being flat and the other equipped of longitudinal triangular riblets. Our LES are the continuation of compressible-channel DNS (with two flat walls) of Coleman et al. (1995) and Lechner et al. (2001). One defines the bulk density ρ_b and velocity U_b as

$$2h\rho_b = \int_{-h}^{+h} \langle \rho \rangle dy, \quad 2h\rho_b U_b = \int_{-h}^{+h} \langle \rho u \rangle dy. \quad (15)$$

Simulations are carried out at fixed bulk density and wall temperature T_w , whatever the Mach number. The latter is defined as U_b/c_w , c_w being the sound speed at the wall. The Reynolds number is $\rho_b U_b h / \mu_w$, in which

μ_w is the dynamic viscosity at the wall. For each U_b , the simulation is thus done at constant mass flux, which generates a turbulent state rapidly. The velocity gradients within the channel produce a heating by molecular-viscous effects, and the channel interior becomes warmer than the walls. Coleman et al. (1995) and Lechner et al. (2001) show that, when turbulence has developed, the average temperature (resp. density) remain approximately uniform in the major part of the channel, while decreasing (resp. rising) close to the walls. The inner plateau-part of the density is very slightly inferior to ρ_b .

LES of the same problem using the selective-structure function model and well-validated immersed-boundary methods have been carried out in Grenoble by Hauët (2003). Hauët has also developed LES at Reynolds 6000 of the compressible channel, one side of which is equipped of longitudinal triangular riblets. Two riblets were studied: the “high” one, of height and width (at Mach 0.33) 11 and 22 wall units; the “great” one, of height and width (at Mach 0.33) 22 and 44 wall units. Hauët has first validated satisfactorily at low Mach the numerical code used against Choi et al.’s DNS. The physical size of each system of riblets was unchanged when going from Mach 0.33 to Mach 1.5. In these simulations, the “high” riblet turns out to reduce the drag ($\approx 5\%$ for the mean friction coefficient at Mach 1.5, against $\approx 3\%$ at Mach 0.33). The

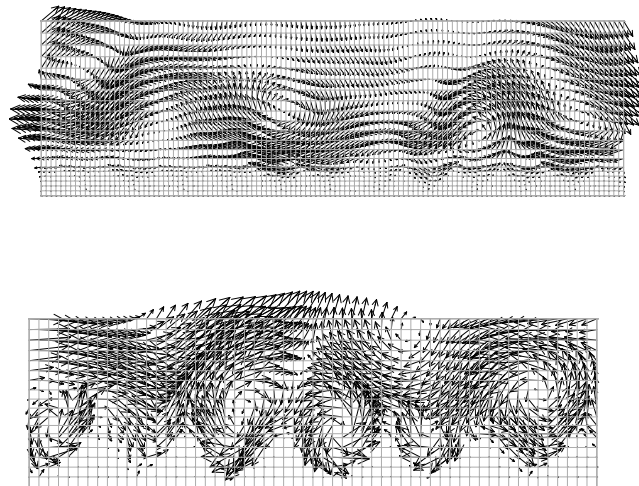


Figure 4. Cross section of the velocity in a channel above riblets at Mach 0.33; top, “high” riblet; bottom, “great” riblet (courtesy G. Hauët).

“great” one increases it. Hauët recovers the same vortex phenomenology as Choi et al. (1993), with longitudinal vortices above the riblet tips in the “high”-riblet case, and inside the valleys in the “great”-riblet case. This is confirmed by two animations which present longitudinal vorticity in Hauët’s high- and great-riblet study at Mach 0.33. Figure 4 shows an instantaneous projection of the velocity vector in a cross section for the two riblets. It is clear from these animations and plots that alternate vortices lie within the valleys for the great riblet, while thinner longitudinal vortices stay above the peaks for the high riblet.

If, in a free compressible boundary layer, the optimal physical size of riblets does not vary from subsonic to supersonic regimes, then a plane will be able with the same riblets system to reduce drag at all speeds. Similar conclusions have been drawn from experiments carried out by Coustols and Cousteix (1994). This is quite satisfactory from the point of view of plane designers.

3. Some Concluding Remarks

It is now obvious from comparisons with experiments and DNS that LES are a unique tool to study both coherent-vortex dynamics and statistics in a wide class of turbulent flows. LES are faster than DNS by a factor going from approximately 10 at low Reynolds number to 100 at high Reynolds.

LES models we have used are universal in the sense that they are fixed once for all, and need no further adjustment when various external forcings or actions such as rotation, separation, thermal stratification or compressibility are considered. This makes a great difference with respect to Reynolds Averaged Navier-Stokes (RANS) models. Another interesting point is that our models are “intelligent” and adapt automatically to the flow conditions: they are inactive for laminar or transitional flows, which permits thus to study the whole transition to fully-developed turbulence. Contrary to RANS, LES give deterministic informations on high-amplitude kinematic or thermal fluctuations, which are crucial for systems safety. LES are very well adapted to simulate control systems in combustion or aeroacoustics, and see in details the effect of vortex manipulation. For more complex industrial applications, I think the next few years will see a great advance with the merging of LES and unstationary RANS which, to me, are just loosely-resolved large-eddy simulations.

References

- R.A. Antonia, M. Teitel, J. Kim, and L.W.B. Browne, Low-Reynolds-number effects in a fully developed turbulent channel flow, *J. Fluid Mech.*, 236:579–605, 1992.
- H. Choi, P. Moin, and J. Kim, Direct-numerical simulation of turbulent flow over riblets, *J. Fluid Mech.*, 225:503–539, 1993.
- J.P. Chollet and M. Lesieur, Parameterization of small scales of three-dimensional isotropic turbulence utilizing spectral closures, *J. Atmos. Sci.*, 38:2747–2757, 1981.
- G.N. Coleman, J. Kim, and R.D. Moser, A numerical study of turbulent supersonic isothermal-wall channel flow, *J. Fluid Mech.*, 305:159–183, 1995.
- P. Comte, M. Lesieur, and E. Lamballais, Large and small-scale stirring of vorticity and a passive scalar in a 3D temporal mixing layer, *Phys. Fluids A*, 4:2761–2778, 1992.
- E. Coustols and J. Cousteix, Performances of riblets in the supersonic regime, *AIAA Journal*, 32:431–433, 1994.
- E. David, *Modélisation des Écoulements Compressibles et Hypersoniques: une Approche Instationnaire*, PhD thesis, Grenoble University, 1993.
- J.A. Domaradzki, R.W. Metcalfe, R.S. Rogallo, and J.J. Riley, Analysis of subgrid-scale eddy viscosity with the use of results from direct numerical simulations, *Phys. Rev. Lett.*, 58:547–550, 1987.
- F. Ducros, P. Comte, and M. Lesieur, Large-eddy simulation of transition to turbulence in a boundary layer developing spatially over a flat plate, *J. Fluid Mech.*, 326:1–36, 1996.
- M. Germano, U. Piomelli, P. Moin and W. Cabot, A dynamic subgrid-scale eddy-viscosity model, *Phys. Fluids A.*, 3:1765–1760, 1991.
- D. Gottlieb and E. Turkel, Dissipative two-four methods for time-dependant problems, *Math. Comp.*, 30:703–723, 1976.
- G. Hauët. *Contrôle de la Turbulence par Simulation des Grandes Echelles en Transport Supersonique*, PhD thesis, Grenoble University, 2003.
- J. Hunt, A. Wray, and P. Moin, Eddies, stream, and convergence zones in turbulent flows, *Center for Turbulence Research Rep.*, CTR-S88:193, 1988.
- J. Jeong and F. Hussain, On the identification of a vortex, *J. Fluid Mech.*, 285:69–94, 1995.
- J. Jimenez, Turbulence, [in:] *Perspectives in Fluid Mechanics*, G.K. Batchelor, H.K. Moffatt, and M.G. Woster [Eds.] Cambridge University Press, 283–231, 2000.
- R.H. Kraichnan, Eddy viscosity in two and three dimensions, *J. Atmos. Sci.*, 33:1521–1536, 1976.
- E. Lamballais, O. Métais, and M. Lesieur, Spectral-dynamic model for large-eddy simulations of turbulent rotating channel flow, *Theor. Comp. Fluid Dyn.*, 12:149–177, 1998.
- R. Lechner, J. Sesterhenn, and R. Friedrich, Turbulent supersonic channel flow, *J. Turbulence*, 2:001, 2001.
- M. Lesieur and O. Métais, New trends in large-eddy simulations of turbulence, *Ann. Rev. Fluid Mech.*, 28:82–45, 1996.
- M. Lesieur, *Turbulence in Fluids*, 3rd edition, Kluwer, 1997.
- M. Lesieur, P. Begou, E. Briand, A. Danet, F. Delcayre, and J.L. Aider, Coherent-vortex dynamics in large-eddy simulations of turbulence, *Journal of Turbulence*, 4:016, 2003.
- M. Lesieur, O. Métais, and P. Comte, *Large-Eddy Simulations of Turbulence*, Cambridge University Press, in press, 2004.

- O. Métais and M. Lesieur, Spectral large-eddy simulations of isotropic and stably-stratified turbulence, *J. Fluid Mech.*, 239:157–194, 1992.
- D. Papamoschou and A. Roshko, The compressible turbulent shear layer: an experimental study, *J. Fluid Mech.*, 197:453–477, 1988.
- T. J. Poinso and S. K. Lele, Boundary conditions for direct simulations of compressible viscous flows. *J. Comp. Phys.*, 101:104-129, 1992.
- N.D. Sandham and W.C. Reynolds, Three-dimensional simulations of large eddies in the compressible mixing layer. *J. Fluid Mech.*, 224:133-158, 1991.
- H. S. Sandhu and N. D. Sandham, Boundary conditions for spatially growing compressible shear layers, *Tech. rep.*, Department of Aeronautical Engineering, Queen Mary & Westfield College, 1994.
- C. Silva and O. Métais, Vortex control of bifurcating jets: A numerical study, *Phys. Fluids*, 14:3798–3819, 2003.
- J. Smagorinsky, General circulation experiments with the primitive equations, *Mon. Weath. Rev.*, 91-3:99–164, 1963.
- A. Witkowska and D. Juvé, Estimation numérique du bruit rayonné par une turbulence homogène et isotrope, *C. R. Acad. Sci. Paris, Ser II*, 318:597–602, 1994.

NANO MECHANICAL ANALYSIS OF IFM FORCE PROFILES ON SELF-ASSEMBLED MONOLAYERS

Mingji Wang, Kenneth M. Liechti
*Center for Mechanics of Solids, Structures and Materials,
Department of Aerospace Engineering and Engineering Mechanics,
The University of Texas, Austin, TX 78712*

Vibha Srinivasan
*Institute for Theoretical Chemistry,
The University of Texas, Austin, TX 78712*

John M. White
*Center for Nanomolecular Science and Technology,
The University of Texas, Austin, TX 78712*

Peter J. Rossky
*Institute for Theoretical Chemistry,
The University of Texas, Austin, TX 78712*

Abstract In this study, a defect-free, self-assembled monolayer of octadecyltrichlorosilane (OTS) was deposited on a silicon substrate. Nanoindentation experiments were performed with an interfacial force microscope (IFM) on these 2.5 nm monolayers. As a first step in continuum finite element analyses, the OTS was assumed to be linearly elastic and isotropic. Adhesive interactions were also accounted for via a cohesive zone model. However, the assumption of linearity gave rise to force profiles that did not match the measurements. Molecular dynamics simulations were therefore employed in order to provide further insight into the behavior of OTS. These simulations indicated that the OTS had a highly non-linear and nearly incompressible response. Based on these results, a hypo-elastic material model was developed as a convenient continuum representation of the mechanical behavior of OTS. This was then used in finite element analyses, which were able to fully reproduce the IFM force profiles. As a result, molecular and microscopic scales were linked in a relatively simple but very effective manner. This suggests that there is a class of problems where the continuum representation of the material behavior may be directly obtained from molecular analyses.

Keywords: Interfacial force microscope, self-assembled monolayer, nanoindentation.

1. Introduction

Self-assembled monolayers are used in MEMS devices for the reduction of stiction, friction and wear [1–4]. The frictional behavior between scanning probe microscope tips (functionalized [5] and bare [5] and surfaces coated with self-assembled monolayers has been examined. Self-assembled monolayers have also been used to control interfacial toughness [7–9]. In the latter experiments, the locus of fracture was close the self-assembled monolayer. In both the friction and fracture studies, the mechanical behavior of the self-assembled monolayers is needed for the determination of fracture and frictional properties.

The objective of the present study was to provide a nanomechanical analysis of interfacial force microscope (IFM) force profiles produced by a tungsten tip probing a self-assembled monolayer. An octadecyltrichlorosilane (OTS) self-assembled monolayer was deposited on a silicon (100) surface covered with an oxide layer. This configuration was first numerically analyzed based on the assumption that the OTS was isotropic and linearly elastic. Surface interactions were also included in the model. An isotropic, non-linear elastic constitutive model for the OTS was then developed that was based on molecular dynamics simulations. This was used in a continuum analysis of the IFM experiment.

2. Experimental

Self-assembled monolayers of OTS were deposited on Si (100) surfaces whose native oxide layer had been removed by a HF etch and replaced with a well hydroxylated oxide layer using a piranha solution. The OTS deposition was conducted in a dry box using an anhydrous solution of OTS in dicyclohexyl. Clusters were removed from the monolayer using sonication in various solvents. This process [10] resulted in stable monolayers with an rms roughness less than 0.07 nm. Ellipsometry was used to determine the thickness of the OTS monolayers was 2.5 ± 0.1 nm, which means that they were tilted at 16° from the normal.

The coated specimens were probed with an IFM [11], which has a self balancing force sensor (Fig. 1) that allows nanoindentation experiments to be conducted in displacement control and avoids the instabilities associated with AFM experiments. Electrochemically etched tungsten wires with tip radii ranging from 100 to 200 nm were used as the probes. The tips were examined in a scanning electron microscope after each experiment in order to ensure that no blunting had occurred.

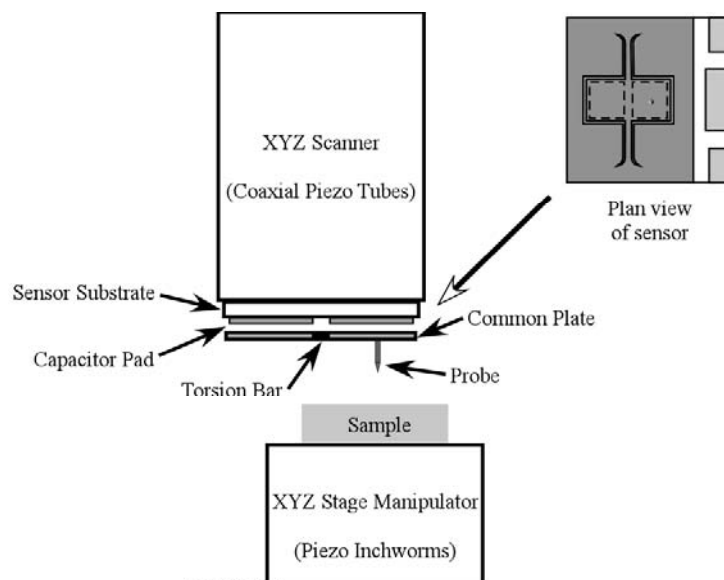


Figure 1. A schematic of the IFM. The orientation of the common plate is maintained parallel via a feedback loop with the force being proportional to the feedback signal. This provides a force sensor which is capable of being used in displacement controlled experiments.

3. Analysis

The specimens consisted of an OTS monolayer covering the SiO_2 layer ($2.0 \pm 0.1 \text{ nm}$) that had been grown in the piranha solution. These two thin layers on top of the Si meant that substrate effects would be present, thereby disallowing [12] the use of classical contact mechanics theories for extracting the mechanical behavior of the OTS layer. Accordingly, a finite element analysis of the IFM experiment was conducted that incorporated normal surface interactions via a traction-separation law of the form shown in Fig. 2. The area underneath the curve gives the thermodynamic work of adhesion $\omega = 0.5\sigma_0\delta_t$ between the tungsten tip and the OTS. In all analyses, the tungsten tip, silicon and silica were assumed to be linearly elastic and isotropic following the properties given in Table 1. The OTS was first assumed to be linearly elastic and isotropic and its modulus was extracted by matching finite element solutions for the force profiles with measured ones. The OTS was also taken to be an isotropic hypo-elastic material based on the results of a molecular dynamics analysis of uniaxial compression straining of the OTS.

The molecular analysis was conducted using the code DL_POLY 2.0. A simulation cell of 30 OTS molecules was compressed between rigid

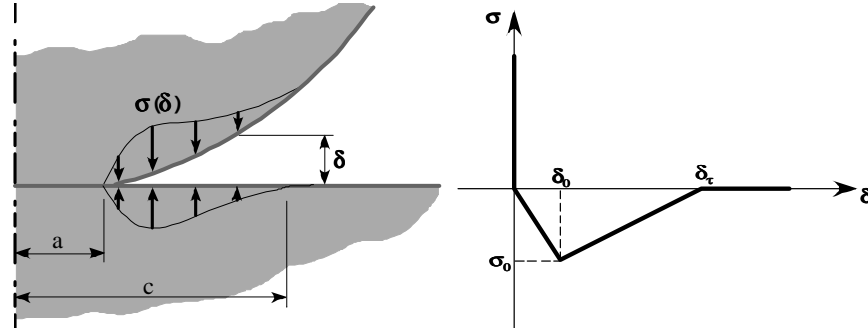


Figure 2. Contact geometry and normal traction-separation law.

tungsten and tridymite planes. Periodic boundary conditions were used to simulate the infinite in-plane extent of the OTS layer relative to its thickness. The CH_3 , CH_2 and OH groups in the OTS molecules were treated as united atoms in a room temperature calculation of the stresses that resulted from moving the rigid planes together at a strain rate of $10^7/\text{s}$. The harmonic, valence angle, cosine dihedral angle and van der Waals potentials that were used in the analysis are given in [13].

Table 1. Properties of tungsten, silica and silicon that were used in all analyses.

Material	Young's Modulus E [GPa]	Poisson's Ratio ν
Tungsten	392	0.28
Silica	73.6	0.17
Silicon	168	0.22

4. Results

Detailed IFM force profiles resulting from the probing of hydroxylated silicon and OTS-coated silicon are shown in Fig. 3. The IFM clearly distinguished the presence of the OTS monolayer in the compressive regime. There were some interesting differences in the tensile regime shown in the magnified insert. For the hydrolyzed silicon, there was an adhesive step in the response of about 0.2 mN as a water bridge presumably formed in the ambient humidity in which the experiment was conducted. There was a slightly smaller initial step when the OTS-coated specimen was probed. We think that this was due to a reduction in the 16° tilt as the tungsten tip approached. The water explanation is also possible, but less likely, due to the hydrophobic nature of OTS.

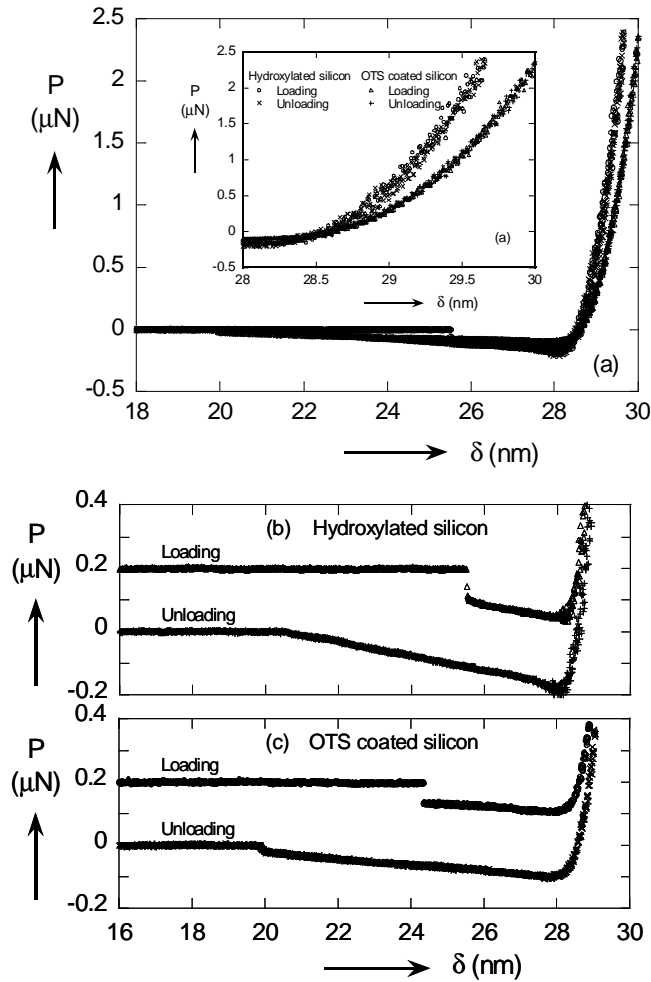


Figure 3. IFM force profiles from bare and OTS-coated silicon. (a) overall response, (b) detail of the adhesive response for bare silicon and (c) detail of the adhesive response for OTS-coated silicon.

The results from the analyses that assumed that the OTS was linearly elastic are shown in Fig. 4. The first result (Fig. 4a) was for bare silicon. In this case, all the properties were known and the finite element solution agreed well with the measured force profile. Solutions for OTS coated specimens are shown in Figs. 4b,c for Poisson's ratios of 0 and 0.44, respectively. As will be seen shortly, the latter was obtained from the molecular analysis. The match between solutions and measurements was not as good as was just noted for bare silicon, particularly

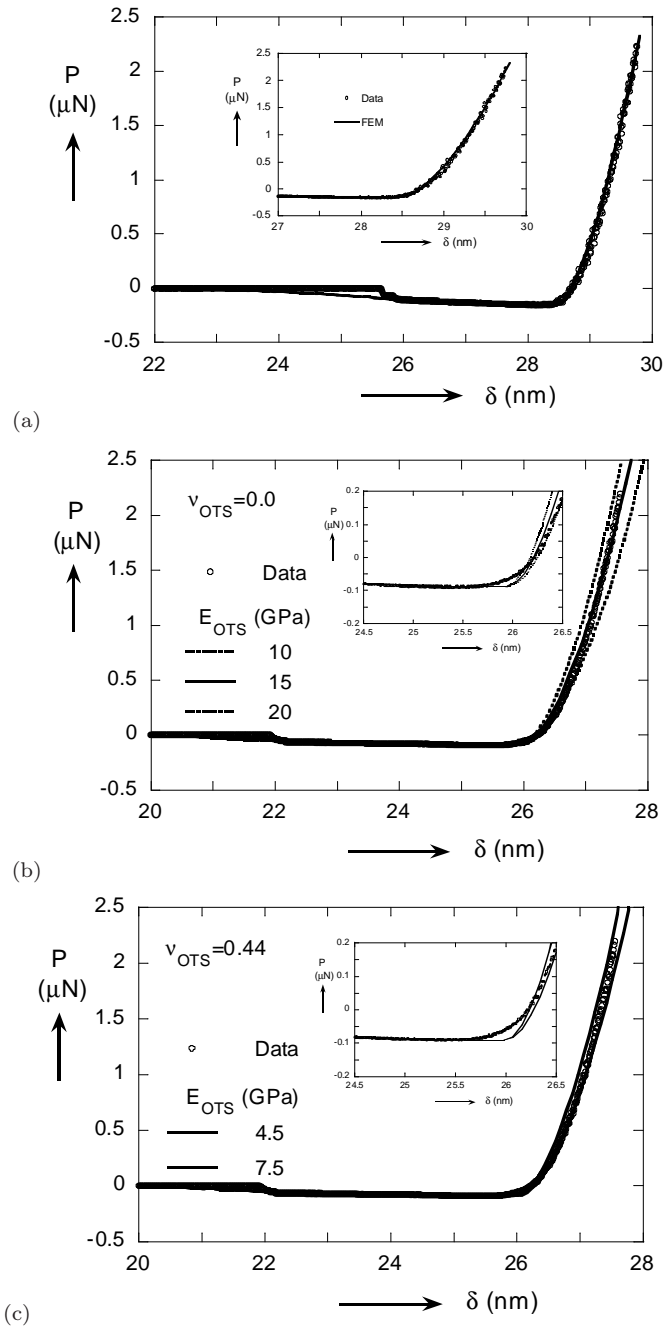


Figure 4. Comparison of linear elastic solutions and measured force profiles for (a) bare and OTS coated silicon with (b) $\nu = 0$ and (c) $\nu = 0.44$ for the OTS.

at low and high force levels. The reduced moduli extracted from the best fit between solutions and measurements are shown in Table 2. The extracted values are higher than those commonly associated with amorphous polymers and are consistent with the higher degree of order in self-assembled monolayers. The parameters for the traction-separation laws for bare and coated silicon are also listed in Table 2. The work of adhesion between the tungsten tip and the bare silicon was higher than the value obtained for tungsten probing an OTS monolayer. Such values are consistent with the formation of water bridges and the ordering reflects the hydrophobic nature of OTS.

Table 2. Extracted modulus and adhesion parameters for bare and coated silicon.

	Poisson's Ratio ν	Reduced Modulus E^* [GPa]	σ_0 [MPa]	δ_0 [nm]	δ_t [nm]	ω [mJ/m ²]
Bare silicon	0.22	168	60	3	7	210
OTS on silicon	0.0	15±5	35	5	7	122.5
OTS on silicon	0.44	6±1.5	35	5	7	122.5

The stress-strain behavior of the OTS under uniaxial compressive strain as obtained from the molecular analysis is shown in Fig. 5. The response was quite nonlinear and reminiscent of rubbery materials. There were several discontinuities in the response, which are probably due to configurational changes. At higher stress levels, the three normal stresses were nearly the same, indicating an approach to incompressibility. The tangent modulus and Poisson's ratio of the hypo-elastic model were extracted from the molecular analysis results. The values are shown in Fig. 6 and reflect the nonlinear behavior with an initial modulus of 1 GPa, rising to 30 GPa at high compressive strains. The early, relatively soft response suggests some partial contact and localized rearrangements of the end groups as the rigid tungsten plate first approaches. The increasing stiffness reflects the interaction between the lateral expansion of each chain that is associated with the zig-zag assembly of the individual molecules and the confinement provided by the infinite extent of the monolayer in the analysis. The Poisson's ratio remained constant at 0.44. These values of tangent modulus and Poisson's ratio were used in a hypo-elastic model of uniaxial compressive strain and compared (Fig. 5) with the results of the molecular analysis. There was very reasonable agreement up to about 40% nominal strain, which was sufficient for modeling the IFM experiment.

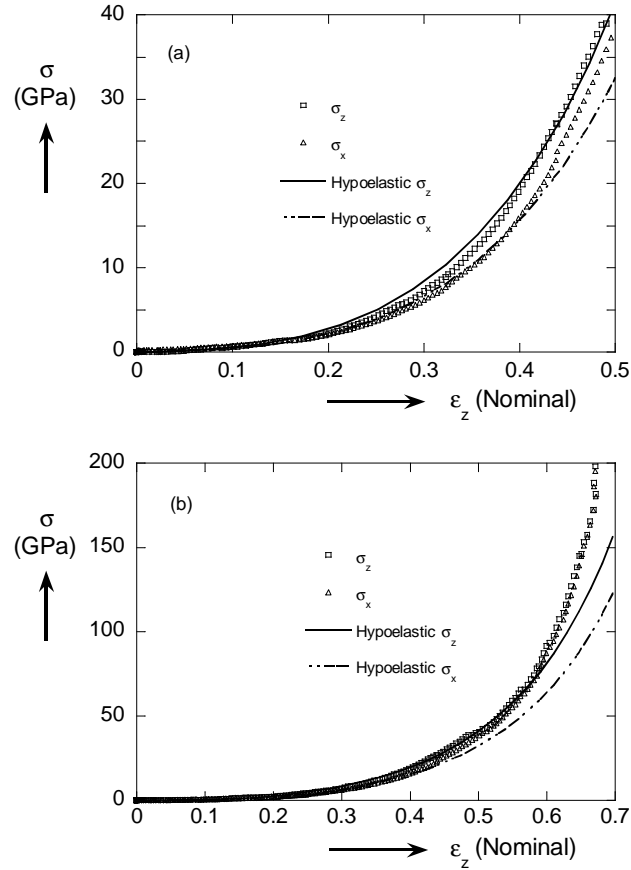


Figure 5. Stress-strain behavior of OTS under uniaxial strain. Data obtained from molecular analysis is compared with a hypo-elastic fit.

This continuum representation of the mechanical behavior of an OTS monolayer was then used in a finite element analysis of the IFM experiment. The same traction-separation law that had been derived from the linear analysis was used because it mainly affects the tensile response while the mechanical behavior is reflected in the compressive response with very little interaction between the two regimes. The finite element solution compared well with the measurements (Fig. 7) even in the low compressive force regime without any further adjustments to the hypo-elastic model.

The agreement between analysis and experiment in Fig. 7 is remarkable, given that the constitutive law that was used in the continuum model was based directly on molecular dynamics simulations without

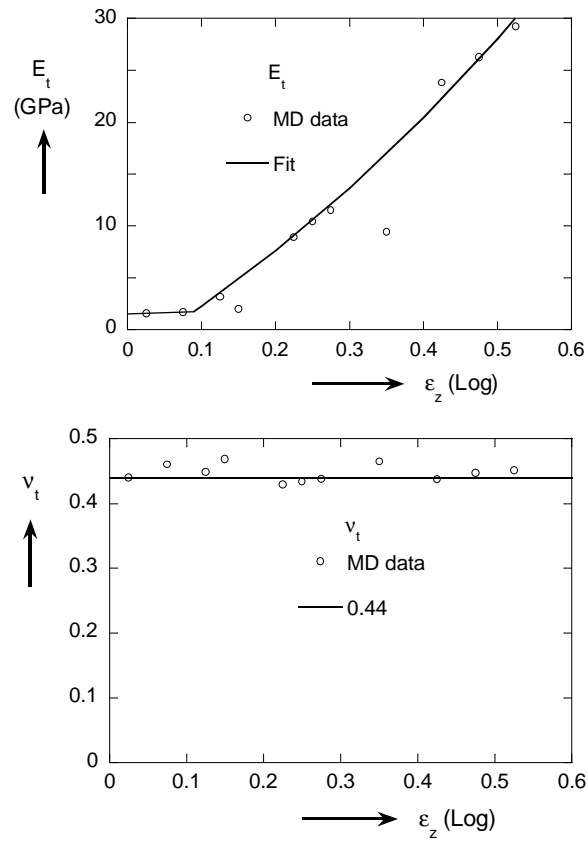


Figure 6. Tangent modulus and Poisson's ratio for a hypo-elastic model of OTS behavior.

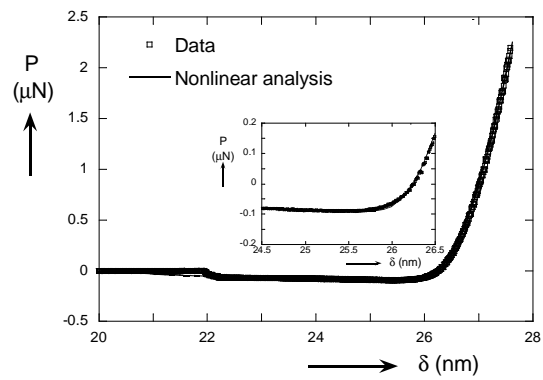


Figure 7. Comparison of the hypo-elastic solution for the IFM experiment with measurements.

any adjustment. This result suggests that the behavior of the OTS is indeed simple enough that differences in the time scales of the molecular dynamics analyses and the actual experiments are not important. It appears that a class of problems has been opened up where spatial and temporal scales can be crossed in a relatively simple manner, and molecular dynamics analyses may be used to motivate continuum representations of self-assembled monolayers in a simple but direct manner.

This result has a direct bearing on analyses of the frictional behavior of self-assembled monolayers where the contact area is required for the determination of the frictional strength. The usual approach is to use the classical JKR contact mechanics analysis developed for contact of monolithic bodies or layered media with sufficiently thick layers that substrate effects are not important. The load versus contact radius response of the OTS monolayer was obtained from Hertz, DMT and JKR analyses of the contact using a reduced modulus of 6 GPa and a Poisson's ratio of 0.44 for the OTS and 122.5 J/m^2 for the work of adhesion between tungsten and OTS. These were the same parameters were used in the linear elastic finite element analysis of the IFM experiment. The results of the classical contact mechanics analyses are compared (Fig. 8) with the con-

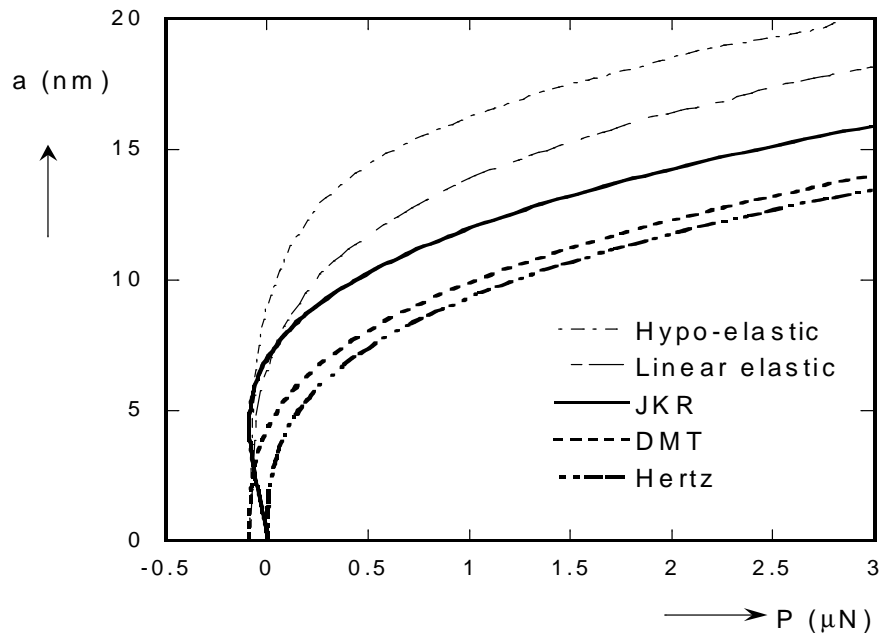


Figure 8. Contact radii from classical contact mechanics and finite element analyses of IFM probing of an OTS monolayer.

tact radii that were extracted from the analyses that produced the force profiles in Fig. 7. The JKR contact mechanics analyses underestimated the contact radius by as much as 50%. The DMT and Hertz solutions differed even more from the finite element analyses. This means that frictional strengths derived from JKR analyses are about 50% higher than the actual values.

5. Conclusions

The experiments conducted in this study demonstrated that the IFM has sufficiently high resolution in both force and displacement for conducting nanoindentation experiments on ultra thin films whose thickness is on the order of nanometers. The interpretation of the force profiles from such experiments is complicated by substrate effects and interface mismatch, requiring a numerical approach rather than classical contact mechanics analyses.

The IFM experiments showed that the OTS monolayers were elastic, even when the indentation depth was relatively large. Linear elastic analyses of the IFM experiments suggested that the Young's modulus of OTS monolayers is relatively high. These high values are not surprising given the highly ordered structure of the OTS monolayers. However, the linear elastic analyses were unable to fully match the measured force profiles. Molecular dynamics simulations were used to develop a non-linear constitutive model for OTS, which could be represented as a hypo-elastic material. The measured response was fully reproduced when the hypo-elastic behavior was incorporated in the finite element analyses of the IFM experiments. This result suggests that representations of the behavior of self-assembled monolayers that are obtained from molecular simulations can be readily incorporated in continuum analyses.

The analysis also showed how important it is to account for the non-linear behavior of the OTS monolayer in determining the true contact radius. This has a large impact on estimates of frictional strength.

Acknowledgements

This work was supported by National Science Foundation (Grant number CMS9978678). PJR acknowledges the support of the R.A. Welch Foundation. The authors would like to thank Dr. Jack Houston at Sandia National Laboratory for his generous assistance in setting up and operating the IFM facility at UT Austin.

References

- [1] R. Maboudian, W.R. Ashurst, and C. Carraro, Tribological challenges in micro-mechanical systems, *Tribology letters*, 12, pp.95–100, 2002.
- [2] B. Bhushan, *Principles and Applications of Tribology*, p.739, John Wiley and Sons Inc., New York, 1999.
- [3] T.M. Mayer, J.W. Elam, S.M. George, P.G. Kotula, and R.S. Goetze, Atomic-layer deposition of wear-resistant coatings for microelectromechanical devices, *Applied Physics Letters*, 82, pp.2883–2885, 2003.
- [4] A.D. Jr. Romrig, M.T. Dugger, P.J. McWhorter, Materials issues in micro-electromechanical devices: science, engineering, manufacturability and reliability, *Acta Materialia*, 51, pp.5837–5866, 2003.
- [5] J.E. Houston and T. Kim, Separating mechanical and chemical contributions to molecular-level friction, *J. Am. Chem. Soc.*, 122, pp.12045–12046 2000.
- [6] R.W. Carpick, N. Agrait, D.F. Ogletree, and M. Salmeron, Variation of the interfacial shear strength and adhesion of a nanometer-sized contact, *Langmuir*, 12, pp.3334–3340, 1996.
- [7] A.V. Zhuk, A.G. Evans, J.W. Hutchinson, and G.M. Whitesides, The adhesion energy between polymer thin films and self-assembled monolayers, *Journal of Materials Research* 13, pp.3555–3564, 1998.
- [8] M.S. Kent, E.D. Reedy, H. Yim, A. Matheson, J. Sorenson, J. Hall, K. Schubert, D. Tallant, M. Garcia, T. Ohlhausen, and R. Assink, Using self-assembling monolayers to study crack initiation in epoxy/silicon joints, *Journal of Materials Research*, 19, pp.1682–1695, 2004.
- [9] A.W. Mello, and K.M. Liechti, Controlling mixed-mode interfacial fracture toughness with self-assembled monolayers, to appear *J. Appl. Mech.*, 2004.
- [10] M. Wang, K.M. Liechti, Q. Wang, and J.M. White, Self-assembled silane monolayers: fabrication with nanoscale uniformity, to appear *Langmuir*, 2004.
- [11] J.E. Houston and T.A. Michalske, The interfacial-force microscope, *Nature* 356, pp.266–267, 1992.
- [12] M. Wang, K.M. Liechti, J.M. White, and R.M. Winter, Nanoindentation of polymeric thin films with an interfacial force microscope, *J. Mech. Phys. Solids*, 52(10), pp.2329–2354, 2004.
- [13] M. Wang, K.M. Liechti, V. Srinivasan, J.M. White, P.J. Rossky, T.M. Stone, A hybrid molecular-continuum analysis of IFM experiments of a self-assembled monolayer, to appear *J. Appl. Mech.*, 2004.

COLLISIONAL GRANULAR FLOWS WITH AND WITHOUT GAS INTERACTIONS IN MICROGRAVITY

Michel Y. Louge and Haitao Xu
Sibley School of Mechanical and Aerospace Engineering
Cornell University
Ithaca, NY 14850 USA
MYL3@cornell.edu

Abstract We illustrate the convenience of a long-lasting microgravity environment to study flows of granular materials with and without gas interaction. We consider collisional granular flows of nearly elastic identical spheres in an axisymmetric Couette channel featuring two cylindrical moving bumpy boundaries and two flat walls. We review governing equations for these flows, illustrate their solutions and compare them with numerical simulations.

Keywords: Gas-solid interaction, microgravity, granular flows

Introduction

Flows of gases loaded with granular materials occur in nature and in industrial processes. On Earth, applications are found in the chemical, mining and pharmaceutical industries. The long-term human or robotic exploration of the Moon and Mars requires the development of “In-Situ Resource Utilization” for propellant production, habitat, infrastructure, and extraction of water and breathable gas. These new technologies all require a deeper understanding of interactions among grains and between grains and gases. On the particle scale, viscous hydrodynamic interactions and grain collisions are a crucial attribute of the physics.

In such processes, collisions induce agitation among grains that is quantified by the “granular temperature” $T \equiv (1/3)\overline{u'_i u'_i}$, in which u'_i is the fluctuation velocity along the direction i . Defined by analogy with the translational temperature of a hard-sphere gas, the granular temperature is responsible for the transport of momentum among grains

interacting through brief collisions [1]. It plays a central role in suspensions of gases and agitated solids.

In the absence of gravity, sheared suspensions of spherical grains in a gas are characterized by three dimensionless numbers. The Stokes number $St \equiv \tau_v \Gamma$ measures the relative importance of grain inertia and viscous forces acting on a sphere of viscous relaxation time $\tau_v = \rho_s d^2 / 18 \mu_g$, where ρ_s is the material density of the sphere, d is its diameter, μ_g is the gas viscosity, and Γ is the applied shear rate. For its part, the Reynolds number compares fluid inertia and viscous forces. It may be based on shear rate, $Re \equiv \rho_g \Gamma d^2 / \mu_g$, where ρ_g is the gas density; or on granular temperature, $Re_T \equiv \rho_g \sqrt{T} d / \mu_g$; or on the difference between the mean gas velocity u_g and its counterpart u_s for the solids in the flow direction x , $Re_{slip} \equiv \rho_g |u_g - u_s| d / \mu_g$. If the suspensions involve such relative velocity, the corresponding mean gas pressure gradient dP_g/dx is made dimensionless with $R_\tau \equiv (-dP_g/dx) / \rho_s \Gamma^2 d$.

In this work, we plan to exploit long-lasting microgravity to isolate the effects of hydrodynamic forces from those of gravitational accelerations in generic flows of granular materials with and without significant gas interaction. This paper briefly outlines this effort.

We begin with an overview of the objectives of the project. We then sketch the theories that we used to design the experiments. Finally, we illustrate the nascent promise of Lattice-Boltzmann (LB) simulations by comparing their results with theory for particles colliding in a gas within a bounded flow geometry.

1. Objectives

NASA is designing an axisymmetric Couette shear cell to accommodate three experiments in granular segregation and gas-solid interactions (Fig. 1). In the first, we will observe the segregation of a binary mixture of granular materials that collide with each other and with the moving boundaries of the cell at a Stokes number large enough that the gas plays no role. In the absence of gravity, the only segregation mechanism is driven by gradients of the granular temperature [2]. We discussed the corresponding theories, simulations and experiments at ICTAM 2000 [3, 4], and will not repeat these here for conciseness.

The second series of tests involves “Viscous/Dissipation Experiments”. Here, the motion of the boundaries is progressively slowed, and thus the Stokes number is reduced, until the dissipation of granular temperature by viscous forces in the gas dominates its counterpart due to inelastic collisions [5]. In these experiments, the mean relative velocity between

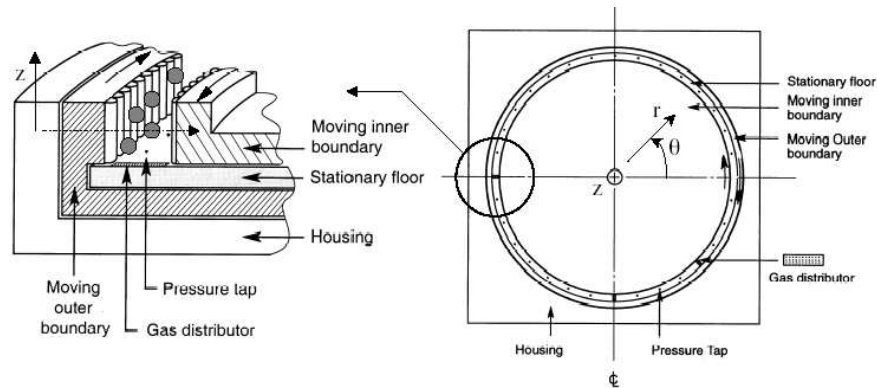


Figure 1. Sketch of the axisymmetric Couette cell. It is described by cylindrical coordinates centered on the rotation axis of the moving cylindrical rough boundaries half-way between the planes of the flat side walls. When $R_r \neq 0$, gas is introduced at $\theta = 0$ and withdrawn at $\theta = \pi$. Left: detail near $\theta = \pi$ shown without the top flat cover.

solids and gases is negligible, $R_r = 0$, and we typically keep Re_T low as well.

In the third kind of tests, called “Viscous Drag Experiments”, we introduce and withdraw gas through distributors at opposite ends along the rectangular channel of the cell, thus creating a mean relative velocity and, consequently, a mean drag between solids and gas. Pressure taps are located at regular intervals on the rear flat wall to monitor the corresponding evolution of the static gas pressure along the channel. Further gas is injected through a distributor located at $\theta = 7\pi/4$ to create an “isokinetic” region with $P_g(\theta = 7\pi/4) = P_g(\theta = 0)$. Because $u_s \approx u_g$ in that region, it is possible to infer the gas volume flow rate there from a measurement of the mean granular velocity and volume fraction [6, 7].

The microgravity shear cell will thus create suspensions in a range of laminar, steady, fully developed conditions where viscous forces dominate the gas flow and inertial forces proportional to the gas density are nearly eliminated. Unlike terrestrial flows, where the gas velocity must be set to a value large enough to support the weight of particles, microgravity of sufficient duration and quality [7] will permit us to control the agitation of the particles and the gas flow independently by adjusting the pressure gradient along the flow and the relative motion of the boundaries.

An important outcome of these experiments will be to validate numerical simulations of the flow. In the Viscous Dissipation and Viscous Drag experiments we will compare profiles of granular velocity, tem-

perature and species volume fraction that are observed using computer vision techniques [8] against those predicted by LB simulations like those of Ladd [9]. We anticipate that these simulations will soon be capable of handling our entire microgravity shear cell, and thus allow direct comparisons with profiles of granular velocity and temperature.

Once such simulations are validated in these experiments, they can inform the development of constitutive relations, and extrapolate to situations where the grains are neither spherical nor monodisperse.

2. Theory

We sketch here the outlines of a theory that we have used to design the experiments. We consider steady collisional flows of nearly elastic, nearly frictionless grains featuring a single constituent of identical spheres in a gas. Because the “Viscous Dissipation” experiments are conducted in an axisymmetric channel, their flows are everywhere fully-developed along the polar angle θ shown in Fig. 1. We also extend the analysis to regions of the “Viscous Drag” experiments where the flow has reached a nearly fully-developed state with $dP_g/d\theta = \text{constant}$. By integrating the flow in the channel cross-section, Xu [7] and Xu et al. [10] calculated the flow development and predicted where such fully-developed regions can be observed.

We begin by discussing the role of centripetal accelerations in the simpler case of a monodisperse flow of spheres without interstitial gas or gravity. When the mean velocity has no components in the radial and axial direction, then the granular momentum balance in the outward radial direction r reduces to

$$\frac{dP_s}{dr} = \rho_s \nu \frac{u_s^2}{r}, \quad (1)$$

where ν is the solid volume fraction and $u_s = u_s(r, z)$ is the mean velocity in azimuthal direction.

The importance of centripetal accelerations can be estimated by comparing variations of the granular pressure along the radial direction with its magnitude

$$P_s = \rho_s \nu (1 + 4G)T. \quad (2)$$

Combining Eqs. (1) and (2) we find that the relative change in granular pressure ΔP_s from the inner to the outer wall scales as

$$\frac{\Delta P_s}{P_s} \sim \left(\frac{\Delta R}{R} \right) \left(\frac{\overline{u_s^2}}{(1 + 4G)\overline{T}} \right), \quad (3)$$

where the overbar denotes the typical magnitude of a quantity in the channel, ΔR is the distance between the two cylindrical moving boundaries, and \bar{R} is the average radius of the channel. Because in the absence of gravity or gas \bar{u}_s^{-2} and \bar{T} both scale as the square of the boundary velocity, the second parenthesis of Eq. (3) is independent of the rotation rate of the cell boundaries. Thus, the effects of centripetal acceleration are only minimized by operating a cell with a distance $\Delta R \ll \bar{R}$. Our calculations indicate that, for typical flows, $\Delta P_s/P_s < 10\%$ for $\Delta R/\bar{R} < 1/15$.

A convenient way to circumvent the complexity presented by variations of flow variables in two dimensions r and z is to integrate the balance equations in the direction perpendicular to the flat side walls. Because the latter are nearly elastic and frictionless, the flow variables hardly vary in the depth z from one side wall to the other. Then, we can integrate the momentum and energy balance equations in that direction by assuming that u_g , u_s , T and ν are functions of r only [4]. For simplicity, we assume here that both flat walls are identical. (Xu relaxed that assumption for a rectilinear flow [7]). To facilitate integration of the balance of fluctuation energy, we follow Jenkins and Arnarson [11] in assuming that shear stresses on surfaces perpendicular to z vary linearly between the side walls separated by a distance W , $\tau_{\theta z} = \tau_{\theta z_0} 2z/W$.

We now consider the case where the viscous gas plays a significant role in the balances of momentum and fluctuation energy. Upon integration along z , the solid momentum balance in the azimuthal flow direction becomes

$$\frac{1}{r^2} \frac{d}{dr} \left[\eta_s r^3 \frac{d}{dr} \left(\frac{u_s}{r} \right) + \nu R_\mu \mu_g r^3 \frac{d}{dr} \left(\frac{u_g}{r} \right) \right] + \frac{2}{W} \left(\tau_{\theta z_0}^s + \tau_{\theta z_0}^{gs} \right) + \beta(u_g - u_s) - \nu \frac{1}{r} \frac{dP_g}{d\theta} = 0, \quad (4)$$

where $\eta_s = (8J/5\sqrt{\pi})\rho_s\nu GT^{1/2}d$ is the granular viscosity [1] with

$$J \equiv 1 + (\pi/12)(1 + 5/8G)^2, \quad G = \nu(2 - \nu)/[2(1 - \nu)^3]$$

and $\tau_{\theta z_0}^s$ is the granular shear stress function of r at $z = W/2$. The second term in straight brackets represent the stress exerted by grains on each other through the viscous gas [12]. At the flat side walls, it is $\tau_{\theta z_0}^{gs}(r)$. Inspired by the expression of Happel and Brenner [13] for the effective viscosity $\mu_g R_\mu$ of a mixture of spheres suspended in a viscous fluid, we assume that the shear stress exerted among solids through the gas is proportional to the solid volume fraction and the mixture shear

stress with $R_\mu \approx \exp(4.58\nu)$. Thus, for example, it is

$$\tau_{\theta z_0}^{gs}(r) = \nu R_\mu \mu_g (\partial u_g / \partial z)_{z=W/2} \quad (5)$$

at the front side wall.

The remainder of the mixture shear stress belongs to the gas phase. In this view, neglecting the inertia of the gas, the steady, fully-developed gas momentum balance in the radial direction is $(dP_g/dr) = 0$, where P_g is a function of θ only. Along the flow, it is

$$\begin{aligned} \frac{1}{r^2} \frac{d}{dr} \left[(1-\nu) R_\mu \mu_g r^3 \frac{d}{dr} \left(\frac{u_g}{r} \right) \right] + \frac{2}{W} \tau_{\theta z_0}^g \\ - \beta (u_g - u_s) - (1-\nu) \frac{1}{r} \frac{dP_g}{d\theta} = 0, \end{aligned} \quad (6)$$

where

$$\tau_{\theta z_0}^g(r) = (1-\nu) R_\mu \mu_g (\partial u_g / \partial z)_{z=W/2} \quad (7)$$

at the front side wall. The drag between gas and solids is captured by the coefficient $\beta = 18\mu_g\nu(1-\nu)^2 R_{drag}(\nu)/d^2$. Koch and Sangani [22] determined R_{drag} from numerical simulations in the range $0 < \nu \leq 0.4$, and adopted Carman's expression for $\nu > 0.4$ [14]. Van der Hoef et al. fitted the results of their LB simulations with $R_{drag} = [10\nu/(1-\nu)^3] + (1-\nu)(1+1.5\sqrt{\nu})$ and obtained similar numerical results [15].

In the axisymmetric geometry, the balance of granular fluctuation energy has the form

$$\begin{aligned} \frac{1}{r} \frac{d}{dr} \left(r \kappa \frac{dT}{dr} \right) + \frac{2q_{z_0}}{W} + \eta_s \left[r \frac{d}{dr} \left(\frac{u_s}{r} \right) \right]^2 + \frac{\tau_{\theta z_0}^s{}^2}{3\eta_s} \\ + \nu \mu_g R_\mu \left[r \frac{d}{dr} \left(\frac{u_g}{r} \right) \right] \left[r \frac{d}{dr} \left(\frac{u_s}{r} \right) \right] + \frac{\tau_{\theta z_0}^s \tau_{\theta z_0}^{gs}}{3\eta_s} - \gamma_s - \gamma_g + \gamma_{gs} = 0, \end{aligned} \quad (8)$$

where $\kappa = (4M/\sqrt{\pi})\rho_s\nu Gd\sqrt{T}$ is the granular conductivity of fluctuation energy with $M \equiv 1 + (9\pi/32)(1 + 5/12G)^2$, and $q_{z_0}(r)$ is the flux of fluctuation energy into the flow through either the front or the rear flat side wall.

In Eq. (8), the last three terms represent volumetric rates of dissipation and production of fluctuation energy. The collisional dissipation rate for nearly elastic, frictionless spheres is

$$\gamma_s = (12/\sqrt{\pi})(1-e^2)\rho_s\nu T^{3/2}G/d, \quad (9)$$

where e is Newton's kinematic coefficient of normal restitution. For slightly frictional spheres, Jenkins and Zhang calculated an effective

restitution coefficient that takes into account the energy lost by tangential impulses in an impact [16]. Goldhirsch discusses the challenges involved in establishing a rigorous theoretical framework for handling spheres with arbitrary elasticity and friction [17].

Using theoretical calculations for dilute simple shear flows, and numerical simulations at greater solid volume fractions, Sangani, Koch and others calculated the dissipation due to the viscous gas at low Re_T [18, 5],

$$\gamma_g = 54\mu_g T \nu R_{diss}(\nu, \epsilon_m) / d^2, \quad (10)$$

where

$$R_{diss} \simeq 1 + \frac{3\nu^{1/2}}{\sqrt{2}} + \frac{135\nu \ln \nu}{64} + 7.422\nu + G \ln(1/\epsilon_m). \quad (11)$$

Sundararajakumar and Koch calculated $\epsilon_m \simeq 9.76\lambda_g/d$, where λ_g is the molecular mean free path of the gas [19]. Recently, Wylie et al. [20] and Verberg and Koch [21] extended these results to higher Re_T .

Finally, mean velocity differences between gas and solids produce fluctuation energy. Koch and Sangani [22] calculated

$$\gamma_{gs} = \frac{162\mu_g^2 \nu (1-\nu)^2}{\rho_s d^3 \sqrt{T}} |u_g - u_s|^2 S^*(\nu), \quad (12)$$

where

$$S^* = \frac{\nu R_{drag}^2}{2\sqrt{\pi}G(1 + 3.5\nu^{1/2} + 5.9\nu)}. \quad (13)$$

Our experience is that γ_{gs} has a relatively small effect on most flows of interest.

To close Eqs. (4) and (8), we evaluate $\tau_{\theta z_0}^s(r)$ and q_{z_0} using boundary conditions for flat, frictional planes [23] that provide $\tau_{\theta z_0}^s/P_s$ and $q_{z_0}/P_s\sqrt{T}$ in terms of impact parameters, such as restitution and friction, and in terms of the dimensionless relative velocity at the contact point, which we assume equal to u_s/\sqrt{T} [4].

A separate calculation is needed to find the stresses $\tau_{\theta z_0}^{gs}(r)$ and $\tau_{\theta z_0}^g(r)$ appearing in Eqs. (4) and (6). To that end, as Eqs. (5)–(7) suggest, we must estimate the gas velocity gradient at the flat walls. We do so by considering the idealized case of a two-dimensional simple shear flow of gas and particles confined between two infinite flat plates parallel to the flow and perpendicular to the vorticity axis. We ignore the effect of the plates on particles and assume that the particle phase is homogeneous with a mean velocity profile $u_s = \Gamma y$. Applying the “no-slip” gas boundary condition at the flat plates to the two-dimensional gas momentum

balance

$$\frac{\partial}{\partial y} \left((1-\nu) R_\mu \mu_g \frac{\partial u_g}{\partial y} \right) + \frac{\partial}{\partial z} \left((1-\nu) R_\mu \mu_g \frac{\partial u_g}{\partial z} \right) - \beta(u_g - u_s) - (1-\nu) \frac{dP_g}{dx} = 0, \quad (14)$$

we find the analytical solution

$$u_g = \left(\Gamma y - \frac{(1-\nu)}{\beta} \frac{dP_g}{dx} \right) \left[1 - \frac{\cosh(kz/W)}{\cosh(k/2)} \right], \quad (15)$$

where

$$k \equiv \frac{W}{d} \sqrt{18\nu(1-\nu) \frac{R_{drag}}{R_\mu}}. \quad (16)$$

Because $W/d \gg 1$ and $k \gg 1$ in typical cases of interest, the average gas velocity in the y -direction is almost equal to its maximum value in Eq. (15), and the velocity gradient at the wall is, to a good approximation,

$$\frac{\partial u_g}{\partial z} \Big|_{z=W/2} \approx -\frac{k}{W} u_g, \quad (17)$$

where u_g now indicates the gas velocity averaged from one side wall to the other. In turn, this yields $\tau_{\theta z_0}^{gs}(r)$ and $\tau_{\theta z_0}^g(r)$ from Eqs. (5) and (7).

Once closed in this way, the integral Eqs. (1), (4) and (8) are solved subject to boundary conditions at the moving bumpy boundaries. In our experiments, these walls are made of cylinders with axis parallel to the rotation axis. Xu [7] and Xu et al. [4] report the corresponding stress ratio $\tau_{r\theta}^s/P_s$ and dimensionless flux in the r -direction $q_r/P_s\sqrt{T}$ at the walls. Boundary conditions for the derivatives du_s/dr and dT/dr are then calculated by matching the prescriptions of $\tau_{r\theta}^s$ and q_r to their respective constitutive relations in the interior at the radial location of the center of a sphere in contact with the crest of a wall bump.

A difficulty arising from the simultaneous use of continuum equations for gas and solids is that the locations where their respective boundary conditions are applied do not coincide. In the gas, the usual “no-slip” condition arises at the wall, while boundary conditions of the kinetic theory concern particles with center located a sphere radius away from the crest of wall bumps. Fortunately, because our flows have relatively large volume fraction and Stokes number, the mean and fluctuation velocity of the solids and the solid stresses are not sensitive to the precise position where u_g matches the boundary velocity. Under these conditions, the mean gas velocity quickly rises to a value that is consistent with the imposed gas pressure gradient and the drag force

within a short distance from the wall. Thus, for simplicity, we ignore this difficulty and solve the gas and solid phases in the same domain $r \in [R_i + (d_i + d)/2, R_o - (d_o + d)/2]$, where R_i and R_o are the radial positions of the center of boundary bumps on the inner and outer moving boundaries, respectively, and d_i and d_o are the bump diameters on these respective boundaries. However, because the spheres can contribute mass to a volume bounded by the bump crests and the flat walls, we define the overall solid volume fraction \bar{v} in the apparatus as the total volume of all spheres divided by the volume of a domain within $r \in [R_i + d_i/2, R_o - d_o/2]$, $\theta \in [0, 2\pi]$ and $z \in [-W/2, +W/2]$.

3. Results

It is common for granular theories to consider unbounded simple shear flows. However, the latter only exist in numerical simulations that are periodic in the flow and vorticity directions and that apply the ‘‘Lees-Edwards’’ wrapping artifact across the sheared boundaries of the simulation domain [24]. In particular, the Lees-Edwards condition ensures that there is no velocity jump and no flux of fluctuation energy across those boundaries. Unfortunately, because it is impossible to engineer physical walls that have no dissipation and no slip, real experiments cannot exhibit profiles of flow variables that are consistent with simple shear. The principal contribution of the theory outlined in the previous section is to predict profiles that a practical experiment design can generate.

Comparisons with experiments must wait for the availability of a long-term microgravity platform. In the meantime, we illustrate how the theory can be used by comparing its predictions with the recent periodic LB simulations of Verberg and Koch [21], who considered rectilinear sheared flows of elastic frictionless spheres in a viscous gas between two infinite parallel boundaries with spherical bumps arranged on a nearly hexagonal planar lattice. Xu et al. calculated the corresponding boundary conditions and solved the more straightforward governing equations for this one-dimensional rectilinear geometry. Figure 2 is a snapshot of the simulations. Figure 3 shows lateral profiles of granular temperature at decreasing values of the Stokes number $St \equiv [\rho_s d^2 U] / [18 \mu_g H]$, where U is the relative velocity of the two moving boundaries and H is the distance between bump crests. Here, \bar{v} is the volume of all particles divided by H and by the other two periodic dimensions of the simulations. As Fig. 3 indicates, the theory has merit down to $St \sim 15$. Below this value, the velocity distribution function of the spheres is affected by the gas in a manner that the theory has yet to predict well.

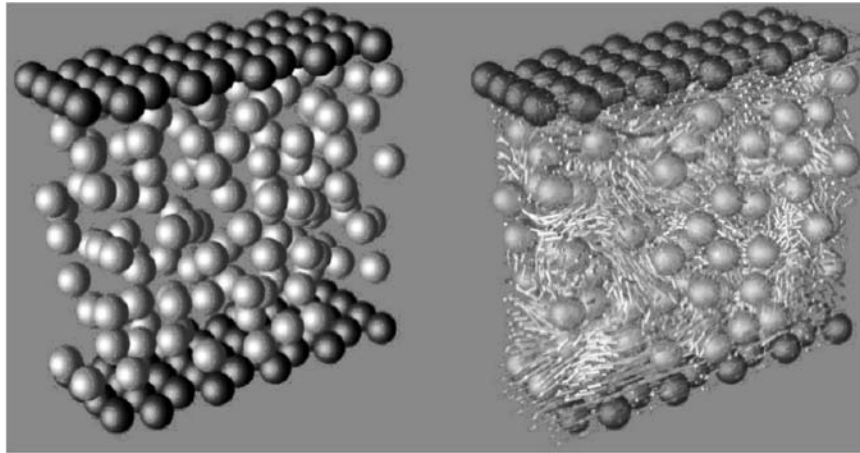


Figure 2. Snapshot of the simulations of Verberg and Koch [21, 12] for the conditions $\bar{\nu} = 0.19$, $St = 30$, $Re = 0.8$, $H/d = 8.22$, $\rho_s/\rho_g = 675$, and $R_\tau = 0$. Left: only particles are shown; right: same realization with gas velocity vectors and particles.

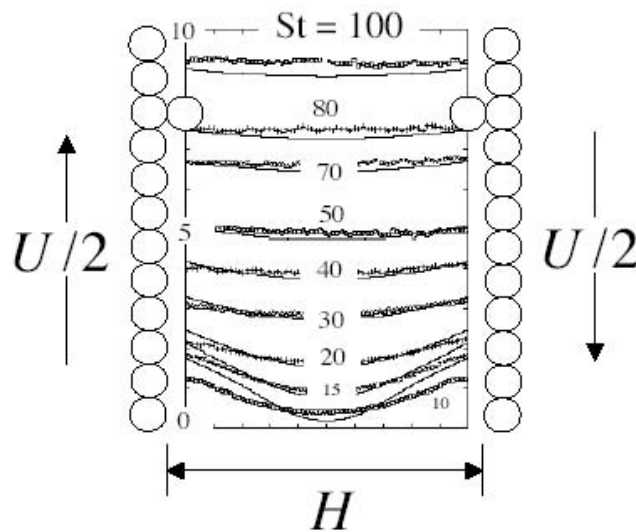


Figure 3. Lateral profiles of dimensionless granular fluctuation velocity $[2\sqrt{T}/U][H/d]$ at values of the Stokes number shown and the conditions $H/d = 12$, $Re = 0.4$, $R_\tau = 0$ and $\bar{\nu} = 0.3$. Symbols are simulation data and lines are predictions of the theory.

Acknowledgments

This work was supported by NASA grants NCC3-468 and NAG3-2112. It is the result of a long-standing collaboration with James T. Jenkins and Anthony Reeves. The authors are grateful to Rolf Verberg and Donald Koch for access to their Lattice-Boltzmann simulations and for fruitful discussions on the subject, and to Martin van der Hoef for providing his new expression for the drag coefficient. The authors also acknowledge Stephen Keast and the NASA engineering and science team led by Enrique Rame and John Caruso in helping design the microgravity experiments mentioned in the paper. Chris Pelkie rendered the simulation pictures in Fig. 2.

References

- [1] J.T. Jenkins and M.W. Richman, Grad's 13-moment system for a dense gas of inelastic spheres, *Arch. Rat. Mech. Anal.*, Vol.87, pp.355-377, 1985.
- [2] J.T. Jenkins and F. Mancini, Kinetic theory for binary mixtures of smooth, nearly elastic spheres, *Phys. Fluids A*, Vol.1, pp.2050-2057, 1989.
- [3] M.Y. Louge, J.T. Jenkins, H. Xu, B. Arnarson, Granular segregation in collisional shearing flows, in: A. Aref, J.W. Phillips (Eds.), *Mechanics for a New Millennium*, Kluwer Academic Publishers, pp.239-252, 2001.
- [4] H. Xu, M.Y. Louge, A. Reeves, Solutions of the Kinetic Theory for Bounded Collisional Granular Flows, *Continuum Mech. Thermodyn.*, Vol.15, pp.321-349, 2003.
- [5] A.S. Sangani, G. Mo, H.-K. Tsao, D.L. Koch, Simple shear flows of dense gas-solid suspensions at finite Stokes number, *J. Fluid Mech.*, Vol.313, pp.309-341, 1996.
- [6] H. Xu, M.Y. Louge, J.T. Jenkins, Flow development of a gas-solid suspension in a microgravity Couette apparatus, *Conference and Exhibit on International Space Station Utilization, Cape Canaveral, FL, Oct. 15-18, 2001*, AIAA-2001-4992, NY, 2001.
- [7] H. Xu, Collisional Granular Flows with and without Gas Interaction in Microgravity, Cornell University, 2003.
- [8] H. Xu, A. Reeves, M.Y. Louge, Measurement Errors in the Mean and Fluctuation Velocities of Spherical Grains from a Computer Analysis of Digital Images, *Rev. Sci. Instrum.*, Vol.75, pp.811-819, 2004.
- [9] A.J.C. Ladd, Numerical simulations of particulate suspension via a discretized Boltzmann equation, *J. Fluid Mech.*, Vol.271, pp.285-339, 1994.
- [10] H. Xu, M.Y. Louge, J.T. Jenkins, Flow development of a sheared collisional granular flow, in: Y. Kishino (Eds.), *Powders and Grains*, pp.259-262, Swets & Zeitlinger, Lisse, 2001.
- [11] J.T. Jenkins, B. Arnarson, Private Communication, 2000.
- [12] H. Xu, R. Verberg, D.L. Koch, M.Y. Louge, Dense bounded shear flows of agitated solid spheres in a gas at intermediate Stokes and finite Reynolds numbers, *J. Fluid Mech.*, under review, 2004.

- [13] J. Happel, H. Brenner, Low Reynolds number hydrodynamics, Prentice-Hall, NY, 1965.
- [14] P.C. Carman, The determination of the specific surface area of powder, *I. J. Soc. Chem. Ind.*, Vol.57, pp.225-236, 1937.
- [15] M.A. van der Hoef, R. Beetstra, J.A.M. Kuipers, Lattice Boltzmann simulations of low Reynolds number flow past mono- and bidisperse arrays of spheres: results for the permeability and drag force, *J. Fluid Mech.*, under review, 2004.
- [16] J.T. Jenkins, C. Zhang, Kinetic theory for identical, frictional, nearly inelastic spheres, *Phys. Fluids*, Vol.14, pp.1228-1235, 2002.
- [17] I. Goldhirsch, Rapid Granular Flows, *Ann. Rev. Fluid Mech.*, Vol.35, pp.267-293, 2003.
- [18] D.L. Koch, Kinetic theory for a monodisperse gas-solid suspension, *Phys. Fluids A*, Vol.2, pp.1711-1723, 1990.
- [19] R.R. Sundararakumar, D.L. Koch, Non-continuum lubrication flows between particles colliding in a gas, *J. Fluid Mech.*, Vol.313, pp.283-308, 1996.
- [20] J.J. Wylie, D.L. Koch, A.J.C. Ladd, Rheology of suspensions with high particle inertia and moderate fluid inertia, *J. Fluid Mech.*, Vol.480, pp.95-118, 2003.
- [21] R. Verberg, D.L. Koch, Rheology of suspensions with low to moderate fluid inertia at finite Stokes number, *J. Fluid Mech.*, in preparation, 2004.
- [22] D.L. Koch, A.S. Sangani, Particle pressure and marginal stability limits for a homogeneous monodisperse gas fluidized bed: kinetic theory and numerical simulations, *J. Fluid Mech.*, Vol.400, pp.229-263, 1999.
- [23] J.T. Jenkins, M.Y. Louge, On the flux of fluctuation energy in a collisional grain flow at a flat, frictional wall, *Phys. Fluids*, Vol.9, pp.2835-2840, 1997.
- [24] M.A. Hopkins, M.Y. Louge, Inelastic Microstructure in Rapid Granular Flows of Smooth Disks, *Phys. Fluids A*, Vol.3, pp.47-57, 1991.

PROBABILITY PHENOMENA IN PERTURBED DYNAMICAL SYSTEMS

Anatoly Neishtadt

Space Research Institute, Profsoyuznaya 84/32, Moscow 117810, Russia

Abstract We discuss probability phenomena associated with passages through separatrices and passages through resonances in perturbed dynamical systems. The theory which describes these phenomena has applications in different problems including problems of capture of satellites into resonances, acceleration of charged particles, chaotic advection of impurities.

1. Introduction

If in a deterministic dynamical system a small variation of initial data produces a big variation of dynamics, then the behavior of such a system can be treated as a random one. This non-rigorous assertion known as a principle “small causes and big effects” is in the basis of the theory of deterministic chaos. Remarkably, such quasi-random behavior exists also in the systems which differ by an arbitrarily small perturbations from systems with very simple (periodic, quasi-periodic) dynamics. Different types of perturbed dynamics have certain probabilities. Analysis of long-term dynamics leads to random walk problems.

We discuss probability phenomena associated with passages through separatrices and passages through resonances in perturbed dynamical systems.

2. Origin of Probability Phenomena in Perturbed Systems

We consider probability phenomena in systems which can be described by ordinary differential equations (ODE). These are deterministic systems: for ODE under consideration on a given time interval the solution is uniquely defined by initial data and depends smoothly on these data. The origin of probability phenomena in such systems is associated with sensitive dependence of dynamics on initial data. To note this sensitive

dependence and probability phenomena one should observe behavior of the system on a long enough time interval. Let initial data be known with an accuracy δ and behavior of a system be observed on time interval of length T . For given T one can choose δ small enough such that any δ -variation of initial data almost does not change the solution of the ODE on the time interval of the length T . But for given δ it can happen that for T big enough a δ -variation of initial data changes the solution over time T considerably (by a value which does not depend on δ). In this case knowledge of initial data with accuracy δ is not enough to predict behavior of the system over the time T . From more formal viewpoint this is the situation when limits as $\delta \rightarrow 0$ and as $T \rightarrow \infty$ do not commute. Probabilistic approach is useful in this situation.

We will consider systems which can be described by ODE of the form

$$\dot{y} = v(y) + \varepsilon w(y, \varepsilon), \quad y \in R^l, \quad 0 < \varepsilon \ll 1. \quad (1)$$

Here y is a vector of phase variables, ε is a small parameter. (In Eq. (1) instead of $y \in R^l$ often one should consider $y \in M^l$, where M^l is an l -dimensional smooth manifold, say cylinder, sphere or torus.) For $\varepsilon = 0$, we get *the unperturbed system*. Term εw in Eq. (1) is called *the perturbation*. System (1) is called *perturbed system*.

To note a considerable (of order 1) effect of the perturbation one should observe behavior of solutions of the system (1) on time interval whose length tends to ∞ as ε tends to 0. We will consider cases when such time interval should be at least of the length of order of $1/\varepsilon$. If limits as δ (accuracy of knowledge of initial data) tends to 0 and as ε tends to 0 do not commute, probabilistic approach is useful.

The *averaging method* is one of the methods of approximate description of dynamics of perturbed systems on long time intervals.

Assume that for system (1) the unperturbed ($\varepsilon = 0$) system is integrable. There are different definitions of integrability (see, e.g. [5]). But we here will call a system *integrable* in some domain of the phase space if the following holds. This domain up to a residue set of a measure zero is smoothly foliated by invariant tori (in particular case, by invariant closed curves), and in a neighborhood of every such torus one can introduce new variables (x, φ) , $x = (x_1, \dots, x_n) \in R^n$, $\varphi = (\varphi_1, \dots, \varphi_m) \in T^m \text{ modd } 2\pi$, $n + m = l$, such that the equations of the motion in the new variables have the form

$$\dot{x} = 0, \quad \dot{\varphi} = \omega(x). \quad (2)$$

Therefore, components of the vector x are first integrals of the unperturbed system. Variable x enumerate invariant tori of the unperturbed

system. Components of vector φ are angular variables (phases) on these tori; ω is a vector of frequencies of motion on tori.

Transformation of variables $y \mapsto (x, \varphi)$ transforms perturbed system (1) into the form

$$\dot{x} = \varepsilon f(x, \varphi, \varepsilon), \quad \dot{\varphi} = \omega(x) + \varepsilon g(x, \varphi, \varepsilon). \quad (3)$$

System (3) is called *system with rotating phases*. Variables x and φ in it are called *slow variables* and *fast variables (fast phases)* respectively.

For approximate description of the evolution of the slow variables x the averaging method (see, e.g. [5, 9]) prescribes to average rate of changing of x over fast phases φ . In other words, one should replace Eq. (3)₁ with the *averaged equation* (or the *averaged system*)

$$\dot{x} = \varepsilon F(x), \quad F(x) = \frac{1}{(2\pi)^m} \int_0^{2\pi} \dots \int_0^{2\pi} f(x, \varphi, 0) d\varphi_1 \dots d\varphi_m. \quad (4)$$

The recipe of the averaging method is not always applicable for approximate description of dynamics of a perturbed system. In particular, obstacles for applicability of the averaging method are separatrices and resonances.

A) Separatrices. Assume that some domain in the phase space of the unperturbed system up to a residue set of a measure zero is smoothly foliated by invariant closed curves. On the residue set this foliation is singular. The residue set consists of points of equilibrium and *separatrices* passing through them. Examples of separatrices are shown in Figs. 2, 6. Separatrices divide the phase space into several regions. In every one of these regions equations of the unperturbed motion can be written in the form of Eq. (2), and equations of the perturbed motion can be written in the form of Eq. (3). On separatrices these equations have singularities. In the neighborhood of separatrices the equations of the unperturbed (respectively, perturbed) motion can not be written in the form of Eq. (2) (respectively, Eq. (3)). Under the action of perturbation phase points that initially were at the distance of order 1 from the separatrix of unperturbed system can arrive to the separatrix during the time of order $1/\varepsilon$.

B) Resonances. Assume that perturbed system can be written in the form of the system with rotating phases (3). Consider for simplicity two-frequency case: $m = 2$, $\varphi = (\varphi_1, \varphi_2)$, $\omega = (\omega_1, \omega_2)$. Invariant torus of unperturbed system is said to be *resonant* (respectively, *nonresonant*), if the ratio of unperturbed frequencies of the motion on this torus $\omega_1(x)/\omega_2(x)$ is a rational (respectively, an irrational) number.

On a resonant torus all unperturbed trajectories are closed curves. On a nonresonant torus every unperturbed trajectory fills the torus densely. Averaging in Eq. (4) is performed over invariant torus of unperturbed system. On a resonant torus an unperturbed trajectory is a closed curve. So, averaging over torus may be not adequate for description of dynamics near a resonance.

Assume that $\partial(\omega_1/\omega_2)/\partial x \neq 0$. For given integer nonzero numbers k_1, k_2 the relation $k_1\omega_1(x) + k_2\omega_2(x) = 0$ defines in the space of the slow variables x a surface which is called the *resonant surface* for (k_1, k_2) -resonance. Under the action of a perturbation phase points that initially were at the distance of order 1 from this resonant surface can arrive to it during the time of order $1/\varepsilon$.

The obstacles to the averaging method play an important role in the origin of probabilistic behavior in perturbed systems. In absence of these obstacles the sensitive dependence on initial data and probabilistic behavior appear first (in time) in dynamics of fast variables (phases). However, from the viewpoint of applications more important is dynamics of slow variables. Averaging method ignores dynamics of fast phases by averaging it out. At separatrices and at resonances the indeterminacy in fast phases is transformed into indeterminacy in slow variables.

There are probability phenomena associated with passages through separatrices and with passages through resonances in different classes of systems: in general systems (i.e. in systems without any specific structure), in Hamiltonian systems with slowly varying parameters and in Hamiltonian systems with slow and fast variables, in volume-preserving systems. For each of these classes of systems there is corresponding theory of probability phenomena.

3. Passages through Separatrices

We start with a basic example of probabilistic scattering on separatrix.

EXAMPLE 1 (SEE [3]) *Consider motion of a material point in one-dimension in a double-well potential $V(q)$ (Fig. 1) in presence of a small friction $\varepsilon f(\dot{q}, q)$.*

Equations of motion have the form

$$\dot{p} = -\frac{\partial V(q)}{\partial q} + \varepsilon f(p, q), \quad \dot{q} = p. \quad (5)$$

Consider motion of points whose initial energy is higher than the energy of potential hump separating the wells. Under the action of friction almost every such point after some time (typically, after the time of order $1/\varepsilon$) will be trapped into one of the potential wells, A or B. But into exactly which one?

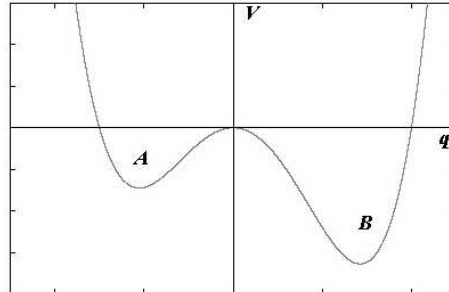


Figure 1. Double-well potential.

The phase portrait of the unperturbed ($\varepsilon = 0$) system is shown in Fig. 2. The separatrices l_1 and l_2 divide it into domains G_1, G_2, G_3 . On the phase portrait of the perturbed ($\varepsilon > 0$) system (Fig. 3) the initial data that lead to trapping into different wells alternate.

If initial data are known with accuracy δ , then for $\varepsilon \ll \delta$ we cannot predict the final result of the evolution. So, in the limit as $\varepsilon \rightarrow 0$ the deterministic approach to the problem fails. However, it is possible to treat trapping into one well or the other as random events and calculate probabilities of these events.

The probabilities $P_1(M_0)$ and $P_2(M_0)$ of the trapping of the initial point $M_0 = (p_0, q_0)$ into potential well A (or, which is the same, into domain G_1) and, respectively, into potential well B (or, which is the same, into domain G_2) can be defined as follows. Let $U^\delta(M_0)$ be δ -neighborhood of M_0 in the phase plane. Let $U_i^{\delta, \varepsilon}(M_0)$ be set of points from $U^\delta(M_0)$ that will be trapped into domain $G_i, i = 1, 2$. Then, by definition

$$P_i(M_0) = \lim_{\delta \rightarrow 0} \lim_{\varepsilon \rightarrow 0} \frac{\text{mes } U_i^{\delta, \varepsilon}(M_0)}{\text{mes } U^\delta(M_0)}. \tag{6}$$

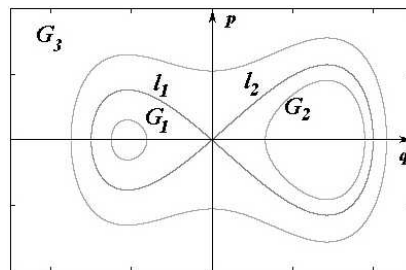


Figure 2. Phase portrait of the motion in the double-well potential.

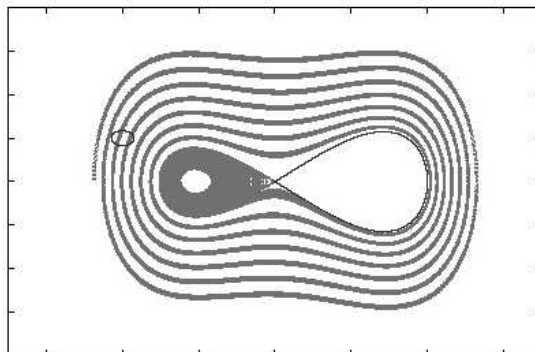


Figure 3. Phase portrait of the motion in the double-well potential in presence of a small friction.

Here $\text{mes}(\cdot)$ is an area in the phase plane. It turns out that the probabilities of trapping into different wells exist and are computed by the formulas

$$P_i(M_0) = \frac{\Theta_i}{\Theta_1 + \Theta_2}, \quad i = 1, 2, \quad \Theta_\nu = - \oint_{l_\nu} p f(p, q) dt, \quad \nu = 1, 2. \quad (7)$$

The integrals in Eq. (7) are taken over separatrices l_ν of the unperturbed system in the unperturbed motion. The probabilities do not depend on the initial point M_0 and are defined by the values of $f(p, q)$ on the critical energy level corresponding to separatrices.

In the problem under consideration it is usually of interest to consider evolution of the energy $h = p^2/2 + V(q)$ with time. Far from separatrices of the unperturbed system this evolution is approximately described using averaging: one can rewrite the equations of the perturbed motion in the standard form of Eq. (3) and then average the equation for slow variable over the fast phase. As a slow variable we can use the unperturbed energy h . How does one describe the passage through the separatrices? Fig. 4 shows three solutions of the averaged system. Value $h = 0$ corresponds to the unperturbed separatrix. Variable τ is the slow time: $\tau = \varepsilon t$. The solution $h_3(\tau)$ in the domain $G_3 = \{h > 0\}$ starts for $\tau = 0$ with a value equal to the energy of the initial point M_0 , and arrives to the separatrix ($h = 0$) at some $\tau = \tau_*$. We glue to this solution the solutions $h_1(\tau)$ and $h_2(\tau)$ in domains G_1 and G_2 respectively starting at $\tau = \tau_*$ on the separatrix: $h_{1,2}(\tau_*) = 0$. It turns out that the motion of majority of the phase points trapped into the well A (respectively, B) at time intervals of the length $\sim 1/\varepsilon$ is approximately described by gluing of the solutions h_3 and h_1 (respectively, h_3 and h_2). The exception is formed by the points that pass very close to the saddle point C and because of this are

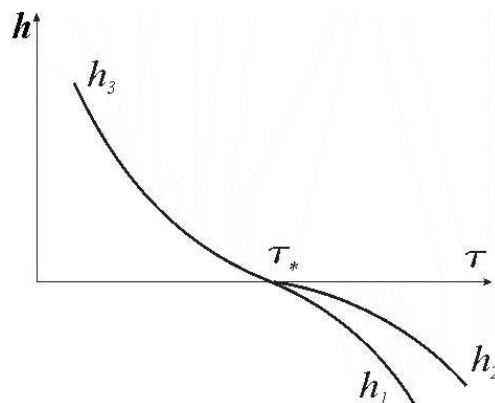


Figure 4. Evolution of the energy for the averaged equation in a case of separatrix crossings.

moving near it for a long time; the measure of the set of these points tends to zero as $\varepsilon \rightarrow 0$. We can say that with probability P_1 the motion is described by gluing of h_3 and h_1 , and with probability P_2 by gluing of h_3 and h_2 .

An analogous loss of determinacy occurs if the friction is replaced by a slow variation of the potential in time leading to a fall into one well or the other (for example, if a point is moving along a curve with two minima in a slowly increasing gravity field).

A general situation in which such phenomena arise can be described as follows. We have the system of equations

$$\dot{p} = -\frac{\partial H}{\partial q} + \varepsilon f_1, \quad \dot{q} = \frac{\partial H}{\partial p} + \varepsilon f_2, \quad \dot{\lambda} = \varepsilon f_3, \quad (8)$$

where $0 < \varepsilon \ll 1$, $(p, q) \in \mathbb{R}^2$, $\lambda \in \mathbb{R}^k$, $H = H(p, q, \lambda)$, $f_i = f_i(p, q, \lambda, \varepsilon)$. The functions f_i are assumed to be smooth enough. The unperturbed ($\varepsilon = 0$) system for p, q is a Hamiltonian one; its Hamiltonian function H depends on parameter λ . For definiteness we shall assume that the phase portrait of the unperturbed system for all λ has the same form in Fig. 2 (but other portraits can also be considered, in which there are nondegenerate saddles joined by the separatrices). The separatrices l_1 and l_2 divide the unperturbed phase plane into three domains: G_1, G_2, G_3 (see Fig. 2). Under the influence of the perturbation the points from the domain G_i cross the separatrix and are trapped in one of the domains G_j , $j \neq i$. Capture by one domain or the other thus should be treated as a random event. The probabilities of these events for an initial point $M_0 = (p_0, q_0, \lambda_0)$ are defined by the relation (6).

We shall assume the Hamiltonian H to be normalized so that $H = 0$ at the saddle point (and hence, on the separatrices). Then $H > 0$ in G_3 and $H < 0$ in $G_{1,2}$.

The averaged system in each of the domains G_i has the form

$$\dot{h} = \frac{\varepsilon}{T} \oint \left(\frac{\partial H}{\partial p} f_1^0 + \frac{\partial H}{\partial q} f_2^0 + \frac{\partial H}{\partial \lambda} f_3^0 \right) dt, \quad \dot{\lambda} = \frac{\varepsilon}{T} \oint f_3^0 dt, \quad (9)$$

where $T = \oint dt$ is the period of the unperturbed motion, $f_i^0 = f_i(p, q, \lambda, 0)$, $i = 1, 2, 3$, and the integrals are taken along the solution of the unperturbed system on which $H(p, q, \lambda) = h$. The averaged system for any of domains G_i can be extended to the separatrix by continuity by putting $\dot{h}|_{h=0} = 0$, $\dot{\lambda}|_{h=0} = f_{3C}^0$, where f_{3C}^0 is the value of function f_3^0 at the saddle point C . Now we can define the phase space of the averaged system. This is the object obtained by gluing along the surface $\{h = 0\}$ the phase spaces of the averaged systems for the domains G_i , $i = 1, 2, 3$ (Fig. 5).

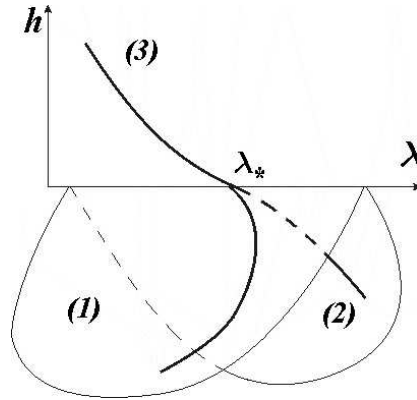


Figure 5. Phase space and trajectories of the averaged system in a case of separatrix crossings.

We define

$$\Theta_\nu(\lambda) = - \oint_{l_\nu} \left(\frac{\partial H}{\partial p} f_1^0 + \frac{\partial H}{\partial q} f_2^0 + \frac{\partial H}{\partial \lambda} f_3^0 \right) dt, \quad \nu = 1, 2, \quad (10)$$

$$\Theta_3(\lambda) = \Theta_1(\lambda) + \Theta_2(\lambda),$$

where the integrals are taken along a separatrix in the unperturbed motion. These integrals are improper (since motion along a separatrix takes an infinite amount of time), but, it is not hard to verify that they converge for the normalization of the Hamiltonian that we have

chosen. The quantities Θ_ν are assumed to be positive below. The value $-\varepsilon\Theta_\nu$ is close to the variation of the energy on the segment of perturbed trajectory close to an unperturbed separatrix l_ν . Therefore the positivity of Θ_ν ensures a sufficiently fast approach to a separatrix in the domain G_3 and a sufficiently fast moving away from a separatrix in the domains G_1 and G_2 for the majority of initial data.

The following assertions hold for the motion for $0 \leq t \leq 1/\varepsilon$ of a point with initial condition (p_0, q_0, λ_0) , where $(p_0, q_0) \in G_3$ for $\lambda = \lambda_0$.

- 1 Denote by $(h_3(\varepsilon t), \lambda_3(\varepsilon t))$ the solution of the averaged system in the domain G_3 with initial condition $(H(p_0, q_0, \lambda_0), \lambda_0)$ (Fig. 5). Suppose that for some $\varepsilon t = \tau_* < 1$ this solution arrives to a separatrix: $h_3(\tau_*) = 0$. Then for $0 \leq \varepsilon t \leq \tau_*$ the behavior of H, λ along the true motion is described by the solution (h_3, λ_3) with accuracy $O(\varepsilon)$.
- 2 Let λ_* be the value of the parameter λ at the moment when the averaged solution arrives to the separatrix: $\lambda_* = \lambda_3(\tau_*)$. Then the probabilities of capture of the point $M_0 = (p_0, q_0, \lambda_0)$ in the domains G_1 and G_2 are calculated by the formulas:

$$P_i(M_0) = \frac{\Theta_i(\lambda_*)}{\Theta_1(\lambda_*) + \Theta_2(\lambda_*)}, \quad i = 1, 2. \quad (11)$$

- 3 Let $(h_1(\varepsilon t), \lambda_1(\varepsilon t))$ and $(h_2(\varepsilon t), \lambda_2(\varepsilon t))$ be solutions of the averaged system in the domains G_1 and G_2 with initial condition “on the separatrix”, glued to (h_3, λ_3) : $h_{1,2}(\tau_*) = 0, \lambda_{1,2}(\tau_*) = \lambda_*$ (see Fig. 5). Then for the majority of the initial points M_0 trapped in the domain G_ν the behavior of H, λ along the motion for $\tau_* \leq \varepsilon t \leq 1$ is described by the solution (h_ν, λ_ν) with accuracy $O(\varepsilon + \varepsilon |\ln \varepsilon| / (1 + |\ln |h_\nu(\varepsilon t)||))$.
- 4 The measure of the exceptional set of initial points whose motion cannot be described in this way, does not exceed $O(\varepsilon^r)$ for any prescribed $r \geq 1$.

Thus, to describe the motion we need to use the averaged system up to the separatrix, to compute the probability of being trapped in one domain or the other on a separatrix, and to use again the averaged system, starting at the separatrix in the domain in which the trapping has occurred. This scheme of analyzing the problem was first used in [32] for analysis of motion of charged quasiparticles. Detailed proofs of assertions 1–4 are contained in [39, 44].

Remark. The exposed approach for introducing concept of probability in the deterministic system under consideration can be interpreted as follows. Initial data are considered as random values with the smooth not depending on ε distribution in a δ -neighborhood of a point M_0 . In this case capture into a prescribed domain is the random event, and we can calculate its probability. The limit value of this probability when we proceed to the limit first as $\varepsilon \rightarrow 0$ and after that as $\delta \rightarrow 0$ is called the probability of capture of a point M_0 into the prescribed domain for the original deterministic system. There is another approach for introducing concept of probability [19, 67]. Let us add white noise with the variance $\varepsilon\delta$ to the right hand sides of equations (8) (one can consider also other random perturbations with strong enough mixing properties [19]). In this new system the capture into prescribed domain is truly a random event. The limit of the probability of this event as $\varepsilon \rightarrow 0$ and then as $\delta \rightarrow 0$ is by definition the probability of capture for the original deterministic system. For the classes of systems considered in [19, 67] this approach also leads to formulas (11) for probabilities.

Here is the list of some problems with separatrix crossings in the systems of the form (8):

- scattering of charged quasi-particles [32],
- tidal evolution of planetary rotation [21],
- motion of charged particles in the field of slowly evolving electrostatic wave [7],
- evolution of the orbital motions of satellites [62, 22, 38, 26],
- propagation of radio-waves in ionospheric wave-guides [23],
- tumbling of a rigid body under the action of small perturbations [51, 40],
- resonant heating of plasma in magnetic traps [63, 55],
- origin of a Kirkwood gap in the asteroid belt [66, 43],
- motion of charged particles in the Earth magneto-tail [13],
- rotation of dual-spin spacecraft [25, 24, 50].

For problems with separatrix crossings the small deviation of behavior of slow variables from the solutions of the averaged system also has property of sensitive dependence on initial data. Thus, this deviation should be treated as a random value. Properties of this deviation were

studied mainly for the cases of Hamiltonian systems which depend slowly on time (Hamiltonian is $H = H(p, q, \varepsilon t)$) and of Hamiltonian systems with fast and slow motions (Hamiltonian is $H = H(p, q, y, x)$, pairs of canonically conjugated variables are (p, q) and $(y, \varepsilon^{-1}x)$). Equations of perturbed motion in these cases have the form (8) with slow variable $\lambda = \varepsilon t$ in the first case and $\lambda = (y, x)$ in the second case. Let a phase portrait of the unperturbed ($\lambda = \text{const}$) system be such as in Fig. 2. In every one of domains G_i we can introduce “action” variable $I(h, \lambda)$ of the unperturbed system as area surrounded by the line $H = h$ divided by 2π . “Action” is the first integral of the averaged system in every one of domains G_i (see, e.g., [1, 5]). In the approximation of the averaging method (which for problems under consideration is called an adiabatic approximation), “action” has a jump at separatrix crossing due to discontinuity of “action” at separatrices. For example, if phase point from G_3 is captured into G_1 this jump of the “action” is equal to the area of G_2 divided by 2π . In exact system the “action” is an adiabatic invariant (approximate integral): for motion far from separatrices in every one of domains G_i value of the “action” is conserved with accuracy $O(\varepsilon)$ over time interval $O(1/\varepsilon)$. Adiabatic perturbation theory allows to construct improved adiabatic invariant J of the form $J = I + \varepsilon u(p, q, \lambda)$ such that for motion far from separatrices in every of domains G_i value of J is conserved with accuracy $O(\varepsilon^2)$ over time interval $O(1/\varepsilon)$ (see, e.g., [5]). It turned out that the improved adiabatic invariant J undergoes small deviation from prediction of the adiabatic approximation as a result of crossing by phase trajectory a narrow neighborhood of separatrices. The asymptotic formula for this jump of (improved) adiabatic invariant was obtained in pioneer work [65] for pendulum in the slowly varying gravity field, in [14, 41] for general case of Hamiltonian system depending on slowly varying parameters and in [42] for Hamiltonian system with slow and fast variables. Typical value of this jump is of order $\varepsilon \log \varepsilon$ for systems without special symmetry and of order ε for systems with some special symmetry (say, for passing from G_3 to G_1 or G_2 if $\Theta_1 = \Theta_2$, where Θ_ν is defined in Eq. (10) or for passing from rotation to oscillation and back for pendulum in the slowly varying gravity field). The formulas for jump of adiabatic invariant at separatrix express this jump through so called pseudo-phase which is a certain value characterizing a point where phase trajectory crosses separatrix. Pseudo-phase is sensitive to change of initial data and should be treated as a random value. Statistical distribution of pseudo-phase is uniform on $(0, 1)$ interval (for appropriate definition of probability similar to Eq. (7)). Thus, jump of adiabatic invariant at separatrix also should be treated as a random value; formulas expressing the jump through pseudo-phase provide sta-

tistical distribution of jumps. There are formulas expressing value of pseudo-phase through initial data for Hamiltonian system depending on slowly varying parameters [15] and for Hamiltonian system with slow and fast variables [59]. For different cases of separatrix crossings near degeneration of a saddle asymptotic formulas for jump of adiabatic invariant at a separatrix are obtained in [17, 20]. An analog of asymptotic formulae for jumps of adiabatic invariant at separatrix crossings and variation of pseudo-phases in a class of dissipative systems is given in [10, 11].

Quasi-random deviations of exact motion from predictions of the averaging method and, in particular, jumps of adiabatic invariant at separatrix play an important role in problems with multiple separatrix crossings on a time interval of the length $\gg 1/\varepsilon$. Consider as an example motion of a pendulum in a slowly periodically varying gravity field. Phase portrait of the pendulum for fixed gravity field is shown in Fig. 6.

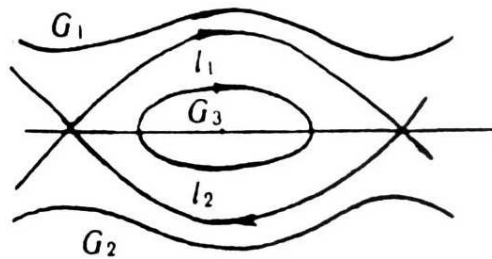


Figure 6. Phase portrait of a mathematical pendulum.

Separatrices divide it into the domain of oscillations and domains of rotations. For the domain of oscillations “action” on an unperturbed trajectory is the area surrounded by this trajectory divided by 2π . For domain of rotations “action” on an unperturbed trajectory is the area between this trajectory and axis of abscissa on any segment of this axis of the length 2π divided by 2π . There is a domain of initial data for which adiabatic approximations predicts that pendulum will periodically pass from regime of rotation to regime of oscillation and back. In this approximation, when pendulum passes from regime of rotation to regime of oscillation the value of the adiabatic invariant (i.e. value of “action”) is doubled, and when pendulum passes back to regime of rotation the value of adiabatic invariant becomes two times smaller again. So, in this approximation the value of adiabatic invariant in the regime of rotation is the same for all times. However, every change of the regime leads to a small quasi-random jump of adiabatic invariant. Accumulation of these jumps for many separatrices crossings leads to quasi-random walk

process. In many numerical experiments it was shown that this process leads to diffusion of adiabatic invariant for set of initial data of measure of order 1 (see, e.g. [12]). But there is no accurate theoretical prove of this. In Fig. 7a Poincaré section of the problem is presented.

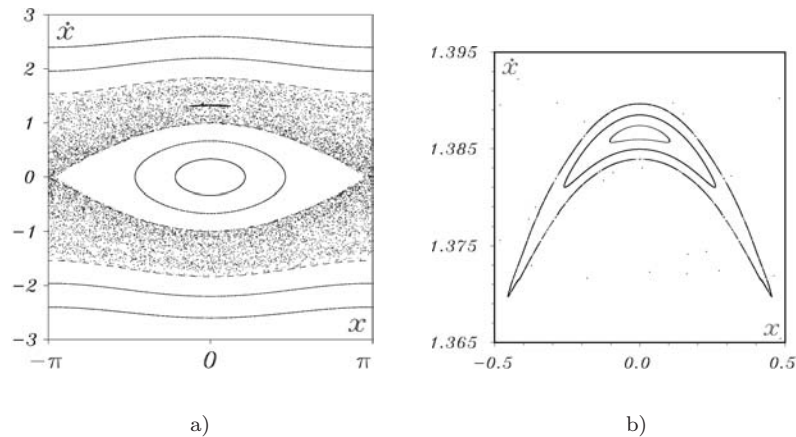


Figure 7. a) Poincaré section for a pendulum in a slowly periodically varying gravity field. b) Stability island.

The positions of several (eight) phase points at the time moments multiple to period of change of the gravity field are shown (calculations are performed by V.V. Sidorenko). By dotted lines we show boundary of the domain of separatrix crossings calculated in the adiabatic approximation. Smooth curves out of the domain of separatrix crossings are invariant curves of Poincaré return map. (Arnold theorem about perpetual adiabatic invariance [3] imply that the phase plane out of the domain of separatrix crossings up to a residue of a small measure is foliated by such curves.) Chaotically scattered points in the domain of separatrix crossings represent trajectory of one initial phase point. It turned out, that in this chaotic see there are islands of regular motion of total area of order 1 (this is the case for all problems where due to a special symmetry asymptotic formula for jump of the adiabatic invariant does not contain term of order $\varepsilon \log \varepsilon$). The islands surround stable fixed points of Poincaré return map. These fixed points correspond to stable periodic motions such that the pendulum passes from regime of rotation to regime of oscillation and back. There are $\sim 1/\varepsilon$ such periodic motions; stability island for each of them has an area at least $\sim \varepsilon$ [52, 53]. Total area of islands is therefore bounded from below by a value that does not depend on ε . (It is shown in [18] that area of individual stability island can not be bigger than a value $\sim \varepsilon$.) In Fig. 7a in the domain of

separatrix crossings one can see the object which looks like a segment of a smooth curve. After enlargement of vertical scale one can see that this object is a smooth closed curve which is (approximately) a boundary of a stability island surrounding a fixed point of Poincaré map (Fig. 7b).

In problems without special symmetry, where jump of adiabatic invariant is of order $\varepsilon \log \varepsilon$, there are no stable periodic motions of period $\sim 1/\varepsilon$ deep inside the domain of separatrix crossings [52].

Probability phenomena associated with passages through separatrices exist also in volume-preserving systems close to integrable ones. In [6] the following volume-preserving system of equations is considered:

$$\dot{x} = -8xy + \varepsilon z, \quad \dot{y} = 11x^2 + 3y^2 + z^2 - 3, \quad \dot{z} = 2zy - \varepsilon x. \quad (12)$$

This system describes a steady Stokes flow inside the unit sphere. For the unperturbed ($\varepsilon = 0$) flow all streamlines are closed curves except streamlines in the (invariant) meridional plane $x = 0$. This plane is a separatrix; it is filled up by streamlines passing from the point $x = 0, y = 1, z = 0$ to the point $x = 0, y = -1, z = 0$. It was shown numerically in [6] that the perturbed ($\varepsilon > 0$) flow possesses the following remarkable property: for arbitrarily small $\varepsilon > 0$ the entire unit sphere is the domain of streamline chaos, typical streamline under unbounded continuation tends to fill densely the entire unit sphere. Detailed study of probabilistic properties of this flow can be found in [54].

Another flow with similar property was considered in [64]. Under arbitrary small perturbation a large domain of streamline chaos arises inside the unit sphere.

These phenomena are associated with jumps of adiabatic invariant at separatrices. To study the effect of a perturbation we can use averaging method. For system (12) all trajectories of the averaged system are periodic. In the approximation of the averaging method all perturbed streamlines cross the separatrix of the unperturbed system. The flux of the vector field of the perturbation through a surface spanning an unperturbed streamline is an integral of the averaged system and adiabatic invariant of the exact perturbed system for motion far from the separatrix. When a perturbed streamline crosses a narrow neighborhood of the separatrix of the unperturbed system this adiabatic invariant undergoes a small jump which should be treated as random because of its sensitive dependence on initial data. Accumulations of these jumps in series of separatrix crossings lead to destruction of adiabatic invariance and streamline chaos. For the system in [64] the situation is similar, but the unit sphere can be divided into two parts: in one of these parts perturbed streamlines cross separatrix, and in the other part these trajectories do not cross separatrix. Streamline chaos arises in the part

where perturbed streamlines cross separatrix. Asymptotic formulas for jump of adiabatic invariant in the above mentioned volume-preserving systems are obtained in [56, 57]. General formula of such kind is obtained in [58].

4. Passages through Resonances

Consider system with rotating phases (3) and corresponding averaged system (4). In the course of the evolution the frequencies of motion in Eq. (3) are changing slowly and at some time moments they become resonant, i.e. linearly rationally dependent. Due to the influence of resonances the actual motion can be considerably different from the one predicted by the averaging method. The two basic phenomena that are associated with the effect of a single resonance are capture into the resonance and scattering on the resonance.

Capture into a resonance can be described as follows. First the system evolves as it is predicted by the averaging method. At a certain time moment the system approaches a resonance. After that the system evolves in such a way that the resonant relation between frequencies is being kept approximately. As a result, after a time $\sim 1/\varepsilon$ the state of the system is completely different from the one predicted by the averaging method. Initial conditions for trajectories with a capture and trajectories without captures are mixed, if ε is small. Thus, it is reasonable to consider the capture as a random event and to calculate a probability of this event. Capture into a resonance was first discussed in [21, 34] in connection with problems of celestial mechanics.

Scattering on resonances is observed for trajectories that pass through resonances without being captured. Scattering is a deviation of such a trajectory from that predicted by the averaging method. During a passage through a narrow neighborhood of the resonance state slow variables undergo a small jump. The amplitude of this jump is very sensitive to the variation of initial conditions if ε is small. Thus, it is reasonable to consider this jump as random scattering on the resonance. Scattering on a resonance was first discussed in [16, 4].

Henceforth we will consider two-frequency systems: $m = 2$, $\varphi = (\varphi_1, \varphi_2)$, $\omega = (\omega_1, \omega_2)$. In two-frequency case in the frequency plane resonances are represented by straight lines with rational slopes passing through the origin of the coordinates. Such a simple structure of the resonant set simplifies the problem essentially. Under some additional assumptions it is possible to study an effect of each resonance separately of the others and combine the results together afterwards.

Study of the effect of a single resonance is based on reduction of the problem near the resonant surface to a standard “perturbed pendulum-like system” form. This transformation has been used in a number of works (see [5, 16, 30, 31, 33–37]). For the resonance $k_1\omega_1 + k_2\omega_2 = 0$ introduce resonant phase $\gamma = k_1\varphi_1 + k_2\varphi_2$, and normalized distance of point x from the resonant surface $\rho = (k_1\omega_1 + k_2\omega_2)/\sqrt{\varepsilon}$. Denote projection of the point x onto the resonant surface as σ . We introduce also “semi-slow” time $\theta = \sqrt{\varepsilon}t$ and use a prime to denote differentiation with respect to θ . One can show (see, e.g., [2, 5, 49]) that dynamics of variables γ, ρ, σ in a neighborhood of the resonant surface where $\rho = O(1)$ (called a resonant zone) is approximately described by the system of equations

$$\begin{aligned}\gamma' &= \rho + \sqrt{\varepsilon}\alpha_1(\gamma, \sigma), \\ \rho' &= L(\sigma) - \partial V(\gamma, \sigma)/\partial\gamma + \sqrt{\varepsilon}\rho\alpha_2(\gamma, \sigma), \\ \sigma' &= \sqrt{\varepsilon}\alpha_3(\gamma, \sigma).\end{aligned}\tag{13}$$

Here V, α_i are certain functions 2π -periodic in γ .

System (13) still contains a small parameter and can be treated by the perturbation theory. Putting in Eq. (13) $\varepsilon = 0$ we get for ρ, γ a Hamiltonian system with one degree of freedom; this system contains σ as a parameter. Hamiltonian of this system is

$$E(\rho, \gamma, \sigma) = \frac{1}{2}\rho^2 + V(\gamma, \sigma) - L(\sigma)\gamma, \quad \sigma = \text{const.}\tag{14}$$

Equation of motion can be written in the form

$$\gamma'' = -\partial V(\gamma, \sigma)/\partial\gamma + L(\sigma).\tag{15}$$

This system is called a *pendulum-like system* as it resembles a pendulum under the action of a constant torque (for a pendulum $V \sim -\cos\gamma$).

There are two basic types of the phase portraits of the Eq. (15): with an oscillation region, Fig. 8b, and without such a region, Fig. 8a.

In Fig. 8 the resonant surface is represented by the coordinate line $\gamma' = 0$. A resonant zone is a strip $|\gamma'| < \text{const.}$ Motion in oscillation region in Fig. 8b corresponds to motion of phase points that are captured into the resonance. Motion in supplementary region in Fig. 8b (the rotation region) corresponds to motion of phase points that cross the resonant zone without capture.

Now take into account terms $O(\sqrt{\varepsilon})$ in Eqs. (13). Under the action of these terms phase point may cross a separatrix in Fig. 8b and change the regime of the motion from a rotation to an oscillation or from an oscillation to a rotation. This means a capture into the resonance or an escape from the resonance respectively.

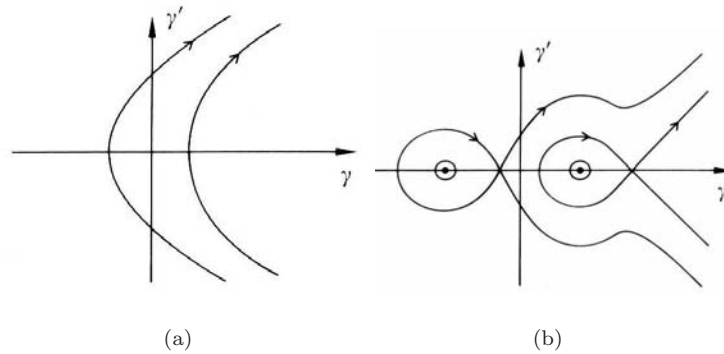


Figure 8. Phase portraits of a pendulum-like system: a) without an oscillation region, b) with an oscillation region.

Initial conditions for trajectories with a capture into a resonance and without a capture are mixed, if ε is small. Variation $\sim \varepsilon$ in initial value of x can change the motion considerably. It is reasonable to consider a capture as a random event and to calculate the probability of this event.

Consider motion of a phase point $(x(t), \varphi(t))$ that passes through the resonance without capture. Far from the resonant surface $x(t)$ oscillates with an amplitude $\ll \varepsilon^{1/2}$ near some solution of the averaged system. Before passage through the resonance this is a solution $X_-(t)$. After passage through the resonance this is a solution $X_+(t)$. Therefore, result of the passage through a narrow neighborhood of the resonant surface (actually, through a resonant zone) can be interpreted as a jump ΔX from one solution of the averaged system to another one. This jump creates scattering on resonance. Value of this jump depends on the value of the resonant phase γ at the moment of crossing of the resonant surface and is very sensitive to changes of initial data. Therefore, it is reasonable to consider the value of γ at the crossing of resonance as a random value. Then ΔX should be considered as a random value as well.

There are formulas for probability of capture into resonance, asymptotic description of motion of captured phase points, formulas for probabilistic distribution of amplitude of scattering on resonance (see, e.g. [49] and references therein). Versions of these formulas for Hamiltonian systems depending on slowly varying parameters and for Hamiltonian systems with slow and fast variables can be found in [47] and [48] respectively. Under rather general assumptions typical values of probabilities of captures and amplitudes of scattering are of order $O(\varepsilon^{1/2})$.

Examples of problems with passages through resonances and captures into resonances see, e.g., in [8, 21, 27–31, 34–36, 45, 61, 68, 69].

Acknowledgment

This work was supported in part by Grants from Russian Fundamental Research Foundation (03-01-00158, 04-01-10634, NSH 136.2003.1) and “Integration Program” (B0053). The author thanks Organizing Committee of ICTAM2004 for the hospitality during the Congress.

References

- [1] V.I. Arnold, *Mathematical methods of classical mechanics*, p.462, Springer Verlag, New York 1978.
- [2] V.I. Arnold, *Geometrical methods in the theory of ordinary differential equations*, p.334, Springer Verlag, New York 1983.
- [3] V.I. Arnold, Small denominators and problems of stability of motion in classical and celestial mechanics, *Russ. Math. Surv.*, Vol. 18, pp.85–192, 1963.
- [4] V.I. Arnold, Conditions of the applicability and estimates of the error of averaging method for systems which pass through states of resonance in the course of their evolution, *Soviet Math. Dokl.*, Vol. 6, pp.331–334, 1965.
- [5] V.I. Arnold, V.V. Kozlov, and A.I. Neishtadt, *Mathematical aspects of classical and celestial mechanics*. Encyclopaedia of mathematical sciences, vol. 3, p.291, Springer Verlag, Berlin 1988.
- [6] K. Bajer and H.K. Moffatt, On a class of steady confined Stokes flow with chaotic streamlines, *J. Fluid.Mech.*, Vol. 212, pp.337–363, 1990.
- [7] A.S. Bakai, On coefficient of capture of particles into accelerator, *Atomnaya energiya*, Vol. 21, pp.503–504, 1966. (Russian)
- [8] C. Beauge and S. Ferraz-Mello, Capture in exterior mean-motion resonances due to Poynting-Robertson drag, *Icarus*, Vol. 110, pp.239–260, 1994.
- [9] N.N. Bogolyubov and Yu. A. Mitropol’skii, *Asymptotic methods in the theory of nonlinear oscillations*, p.537, Gordon and Breach, New York 1961.
- [10] F.J. Bourland and R. Haberman, Separatrix crossing: time invariant potentials with dissipation, *SIAM J. Appl. Math.*, Vol. 50, pp.1716–1744, 1990.
- [11] F.J. Bourland and R. Haberman, Connection across a separatrix with dissipation, *Stud. Appl. Math.*, Vol. 91, pp.95–124, 1994.
- [12] D.L. Bruhwiler and J.R. Cary, Diffusion of particles in a slowly modulated wave, *Physica D*, Vol. 40, pp.265–282, 1989.
- [13] J. Bücher and L.M. Zelenyi, Regular and chaotic charged particle motion in magnetotaillike field reversals, 1. Basic theory of trapped motion, *J. Geophys. Res.*, Vol. 94, pp.11821–11842, 1989.
- [14] J.R. Cary, D.F. Escande, and J.L. Tennyson, Adiabatic invariant change due to separatrix crossing, *Phys. Rev. A*, Vol. 34, pp.4256–4275, 1986.
- [15] J.R. Cary and R.T. Scodje, Phase change between separatrix crossings, *Physica D*, Vol. 36, pp.287–316, 1989.

- [16] B.V. Chirikov, Passage of nonlinear oscillatory system through resonance, *Soviet Phys. Dokl.*, Vol. 4, pp.390–394, 1959.
- [17] D.C. Diminnie and R. Haberman, Slow passage through homoclinic orbits for the unfolding of a saddle-center bifurcation and the change in the adiabatic invariant, *Physica D*, Vol. 162, pp.34–52, 2002.
- [18] Y. Elskens and D.F. Escande, Slowly pulsating separatrices swept homoclinic tangles where islands must be small: an extension of classical adiabatic theory, *Nonlinearity*, Vol. 4, pp.615–667, 1991.
- [19] M.I. Freidlin, Random and deterministic perturbations of nonlinear oscillators, *Doc. Math. J. DMV., Extra volume Proc. ICM 1998, III*, pp.223–235, 1998.
- [20] A.I. Glebov and O.A. Kiselev, An asymptotic solution slowly crossing the separatrix near a saddle-centre bifurcation point, *Nonlinearity*, Vol. 16, pp.327–362, 2003.
- [21] P. Goldreich and S. Peale, Spin-orbit coupling in the Solar System, *Astron. J.*, Vol. 71, pp.425–438, 1966.
- [22] R. Greenberg, Evolution of satellite resonances by tidal dissipation, *Astron. J.*, Vol. 78, pp.338–346, 1978.
- [23] A.V. Gurevich and E.E. Tsidilina, Long-distance propagation of HF radio-waves, p.268, Springer Verlag, Berlin 1975.
- [24] R. Haberman, R. Rand, and T. Yuster, Resonance capture and separatrix crossing in dual-spin spacecraft. *Nonlinear Dynamics*, Vol. 18, pp.159–184, 1999.
- [25] C.D. Hall, Resonance capture in axial gyrostats, *J. Astronaut. Sci.*, Vol. 43, pp.127–138, 1995.
- [26] J. Henrard, Capture into resonance: an extension of the use of the adiabatic invariant, *Celest. Mech.*, Vol. 27, pp.3–22, 1992.
- [27] A.P. Itin, Resonant phenomena in classical dynamics of three-body Coulomb systems, *Phys. Rev. E*, Vol. 67, pp.026601–026010, 2003.
- [28] A.P. Itin, A.I. Neishtadt, and A.A. Vasiliev, Captures into resonance and scattering on resonance in dynamics of a charged relativistic particle in magnetic field and electrostatic wave, *Physica D*, Vol. 141, pp.281–296, 2000.
- [29] A.P. Itin and A.I. Neishtadt, Resonant phenomena in slowly perturbed elliptic billiards, *Regul. Chaotic Dyn.*, Vol. 8, pp.59–66, 2003.
- [30] J. Kevorkian, On a model for reentry roll resonance, *SIAM J. Appl. Math.*, Vol. 26, pp.638–669, 1974.
- [31] J. Kevorkian and J.D. Cole, Multiple scale and singular perturbations methods, p.632, Springer Verlag, New York 1996.
- [32] I.M. Lifshits, A.A. Slutskin and V.M. Nabutovskii, On phenomenon of scattering of charged quasi-particles at singular points in p -space, *Sov. Phys. JETP*, Vol. 14, pp.669–675, 1962. (Russian)
- [33] V.K. Melnikov, On the stability of the center for time-periodic perturbations, *Trans. Mosc. Math. Soc.*, 1963, pp.1–56, 1965.
- [34] A.M. Moltchanov, The resonant structure of the Solar System. *Icarus*, Vol. 8, pp.203–215, 1968.
- [35] A.D. Morozov, A complete qualitative investigation of Duffing's equation, *Differ. Equations*, Vol. 12, pp.164–174, 1976.

- [36] J. Murdock, Qualitative theory of nonlinear resonance by averaging and dynamical systems methods, *Dynamics reported*, Vol. 1, pp.91–172, 1988.
- [37] A.I. Neishtadt, Passage through resonances in the two-frequency problem, *Soviet Phys. Dokl.*, Vol. 20, pp.189–191, 1975.
- [38] A.I. Neishtadt, Passage through a separatrix in a resonance problem with slowly varying parameter, *J.Appl.Math.Mech.*, Vol. 39, pp.594–605, 1975.
- [39] A.I. Neishtadt, Some resonant problems in nonlinear systems, Ph.D.Thesis, Moscow State Univ., Moscow 1975. (Russian)
- [40] A.I. Neishtadt, On the evolution of the rotation of a rigid body under the action of the sum of constant and dissipative perturbing moments, *Izv. Akad. Nauk SSSR. Mekh. Tverd. Tela.*, Vol. 6, pp.30–36, 1980. (Russian)
- [41] A.I. Neishtadt, Change of an adiabatic invariant at a separatrix, *Sov. J. Plasma Phys.*, Vol. 12, pp.568–573, 1986.
- [42] A.I. Neishtadt, On the change in the adiabatic invariant on crossing a separatrix in systems with two degrees of freedom, *PMM USSR*, Vol. 51, pp.586–592, 1987.
- [43] A.I. Neishtadt, Jumps of the adiabatic invariant on crossing the separatrix and the origin of the Kirkwood gap $3 : 1$, *Sov. Phys. Dokl.*, Vol. 32, pp.571–573, 1987.
- [44] A.I. Neishtadt, Problems of perturbation theory of nonlinear resonant systems, Dr.Sci.Thesis, Moscow State Univ., Moscow 1989. (Russian)
- [45] A.I. Neishtadt, Averaging, capture into resonances and chaos in nonlinear systems, [in:] Campbell D. (ed.) *Chaos/Xaoc*, pp. 261–275, AIP, New York 1990.
- [46] A.I. Neishtadt, Probability phenomena in perturbed systems, *Selecta Mathematica Sovietica*, Vol.12, pp.195–209, 1993.
- [47] A.I. Neishtadt, On destruction of adiabatic invariants in multi-frequency systems, [in:] C. Perelló, C. Simó, and J. Solà-Morales [eds.] *Equadiff 91, International Conference on Differential Equations*, Vol. 1, pp.195–207, 1993.
- [48] A.I. Neishtadt, On adiabatic invariance in two-frequency systems. [in:] C. Simó [ed.], *Hamiltonian systems with three or more degrees of freedom. Proceedings of NATO ASI, Series C, Vol. 533*, pp. 193–212, Kluwer, Dordrecht 1999.
- [49] A.I. Neishtadt, Scattering by resonances, *Celestial Mechanics and Dynamical Astronomy*, Vol. 65, pp.1–20, 1997.
- [50] A.I. Neishtadt and M.L. Pivovarov, Separatrix crossings in dynamics of dual-spin satellite, *PMM*, Vol. 64, pp.741–746, 2000.
- [51] A.I. Neishtadt and M.L. Pivovarov, On evolution of the rotation of artificial satellite under the action of constant perturbing moment, *Preprint 434 IKI AN SSSR*, 1978. (Russian)
- [52] A.I. Neishtadt, V.V. Sidorenko, and D.V. Treschev, Stable periodic motions in the problem on passage through a separatrix, *Chaos*, Vol. 7, pp.2–11, 1997.
- [53] A.I. Neishtadt, V.V. Sidorenko, and D.V. Treschev, On stability islands in domain of separatrix crossings, [in:] V.M. Matrosoy, V.V. Romyantsev, and A.V. Karapetyan [eds.], *Nonlinear Mechanics*, Moscow, Fizmatlit, pp.192–201, 2001.
- [54] A.I. Neishtadt, C. Simó, and A.A. Vasiliev, Geometric and statistical properties induced by separatrix in volume-preserving systems, *Nonlinearity*, Vol. 16, pp.521–557, 2003.

- [55] A.I. Neishtadt and A.V. Timofeev, Autoresonance in electron cyclotron heating of a plasma, *Sov. Phys. JETP*, Vol. 66, pp.973–979, 1987.
- [56] A.I. Neishtadt, D.L. Vainshtein, and A.A. Vasiliev, Changes in the adiabatic invariant and streamline chaos in confined incompressible Stokes flow, *Chaos*, Vol. 6, pp.67–77, 1996.
- [57] A.I. Neishtadt, D.L. Vainshtein, and A.A. Vasiliev, Chaotic advection in a cubic Stokes flow, *Physica D*, Vol. 111, pp.227–242, 1998.
- [58] A.I. Neishtadt and A.A. Vasiliev, Change of adiabatic invariant at a separatrix in a volume-preserving 3-D system, *Nonlinearity*, Vol. 12, pp.303–320, 1999.
- [59] A.I. Neishtadt and A.A. Vasiliev, Phase change between separatrix crossings in slow-fast Hamiltonian systems, *Nonlinearity*, submitted 2004.
- [60] O. Piro, and M. Feingold, Diffusion in three-dimensional Liouvillian maps, *Phys. Rev. Lett.*, Vol. 61, pp.1799–1802, 1988.
- [61] V.V. Sidorenko, Capture and escape from the resonance in the dynamics of the rigid body in viscous medium, *Journal of Nonlinear Science*, Vol. 4, pp.35–57, 1994.
- [62] A.T. Sinclair, On the origin of commensurabilities among the satellites of Saturn, I, II, *Monthly Notices Roy. Astron. Soc.*, Vol. 160, pp.169–187, 1972 and Vol. 166, pp.165–179, 1974.
- [63] V.V. Soloviev and D.R. Shklyar, Heating of particles by low-amplitude wave in non-homogeneous magnetoactive plasma, *Zh. Eksp. Teor. Fiz.*, Vol. 90, pp.471–480, 1986. (Russian)
- [64] H.A. Stone, A. Nadim, S.H. Strogatz, Chaotic streamlines inside drops immersed in steady Stokes flows, *J. Fluid. Mech.*, Vol. 232, pp.629–646, 1991.
- [65] A.V. Timofeev, On the constancy of an adiabatic invariant when the nature of the motion changes, *Sov. Phys. JETP*, Vol. 48, pp.656–659, 1978.
- [66] J. Wisdom, A perturbative treatment of motion near 3/1 commensurability, *Icarus*, Vol. 63, pp.272–289, 1985.
- [67] G. Wolansky, Limit theorem for a dynamical system in the presence of resonances and homoclinic orbits, *J. Diff. Equat.*, Vol. 83, pp.300–335, 1990.
- [68] Yu. M. Zabolotnov, V.V. Lyubimov, Nonlinear resonance evolution effects in the motion of a rigid body about a fixed point, *J. Appl. Math. Mech.*, Vol. 66, pp.401–408, 2002.
- [69] V.A. Yaroshevskii, Investigation of conditions for plane autorotation of a spacecraft entering the atmosphere, *Cosmic Research*, Vol. 39, pp.38–46, 2001.

MECHANICS OF RUBBERLIKE SOLIDS

Ray W. Ogden

*Department of Mathematics, University of Glasgow
Glasgow G12 8QW, UK*

rwo@maths.gla.ac.uk

Abstract In this paper we discuss: (i) the large deformation stress-strain response of rubberlike solids based on experimental observations, including both elastic and inelastic behaviour of particle-filled and unfilled rubber, (ii) the mathematical modelling of this behaviour through its phenomenological treatment using elasticity theory and extensions of the theory to account for inelastic responses such as the Mullins effect, stress softening and hysteretic stress-strain cycling, (iii) an introduction to the analysis of the coupling of mechanical and magnetic effects in so-called magneto-sensitive elastomers, which are being used as 'active' components in various applications where the mechanical properties of the material are changed rapidly when a suitable magnetic field is applied.

Keywords: Rubber elasticity, rubber inelasticity, Mullins effect, stress softening, large deformations, magneto-sensitive elastomers, magnetoelasticity

1. Introduction

In this paper we provide an account of the mechanics of rubberlike solids, including both elastic and inelastic behaviours. Additionally, we discuss the influence of magnetic fields on magneto-sensitive elastomers. Because of limited space the account is largely descriptive but includes detailed references to the literature to enable the reader to follow up both the experimental and theoretical aspects of the subject. We begin, in Sec. 2, with an overview of the large deformation stress-strain response of rubberlike solids based on experimental observations. First, experimental results that characterize the *elastic* behaviour of rubber are described. This is followed by illustrations of how the behaviour departs from the purely elastic. When subjected to cyclic loading many elastomers exhibit a *stress softening* phenomenon widely known as the *Mullins effect* (Mullins [32]). The Mullins effect is closely related to the fatigue of elastomeric parts used in engineering applications. A detailed

qualitative and quantitative understanding of the Mullins effect is thus a necessary step towards the scientific evaluation of the *life* of a rubber product.

Next, in Sec. 3, we discuss briefly some theoretical approaches to the modelling of the inelastic behaviour of rubberlike solids.

The final section of the paper, Sec. 4, is motivated by recent renewed interest in the subject of electromagnetic continua generated by the development of so-called ‘smart’ materials. These are used, for example, in devices for controlling the damping characteristics of vibration absorbers. In particular, we are concerned here with elastomers containing a distribution of ferrous particles embedded within their bulk so that they respond to the application of magnetic fields by changing significantly their stress-strain behaviour. We outline recent theoretical work concerning the coupling of mechanical and magnetic effects in these so-called *magneto-sensitive (MS) elastomers*.

2. Description of Experimental Results

Figure 1(a) shows the characteristic sigmoid-shaped curve associated with the stress-stretch behaviour of rubber. Specifically, this is for loading of unfilled vulcanized natural rubber in simple tension based on data of Treloar [47], which correspond to the solid circles. Similar behaviour is found for other standard experimental tests such as pure shear and equibiaxial tension (see, for example, Treloar [48] and Ogden [36–38] and the recent collection of papers [49]). In pure shear and equibiaxial tension, however, the largest stretch achievable is generally less than for simple tension. The general characteristics of the results shown in Fig. 1(a) are also evident in many synthetic rubbers, but in some cases the largest stretch obtained can be much larger than for natural rubber (as much as 10–15 in simple tension for example).

Figure 1(a) shows only the loading curves. In general, the loading curve is not re-traced exactly on unloading but for natural rubber (and for many synthetic rubbers) there is only a small stress softening or hysteresis effect if the strains are not too large, and the materials are therefore modelled as perfectly elastic. Generally, the tests are conducted at a relatively low strain rate so that the curves can be regarded as corresponding essentially to quasi-static behaviour.

A different picture is evident, however, when unloading is accounted for. Figure 1(b) shows the typical simple tension behaviour of a specimen of natural rubber filled by 1% by volume of carbon black particles. From its virgin state the material is loaded to a stretch $\lambda = 3$, unloaded, then loaded again to the same stretch in several loading-unloading cycles until

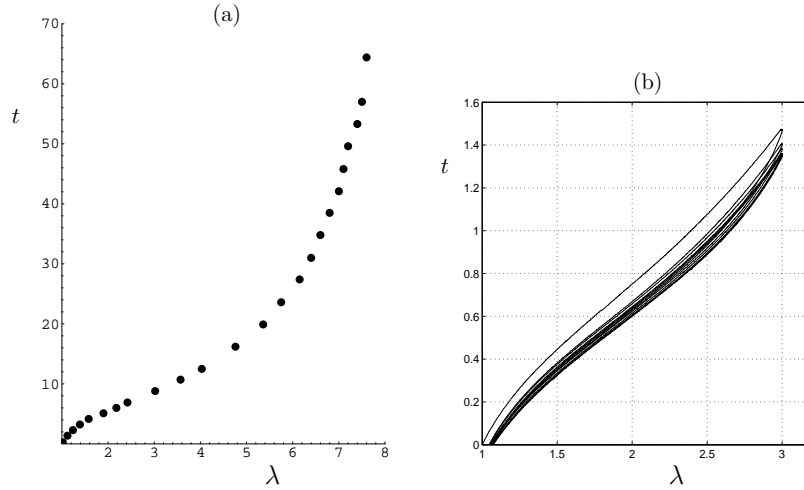


Figure 1. Simple tension data, with nominal stress t vs stretch λ : (a) data of Treloar [47] – units of t , kg cm^{-2} ; (b) from Dorfmann and Ogden [11] – units of t , N mm^{-2} .

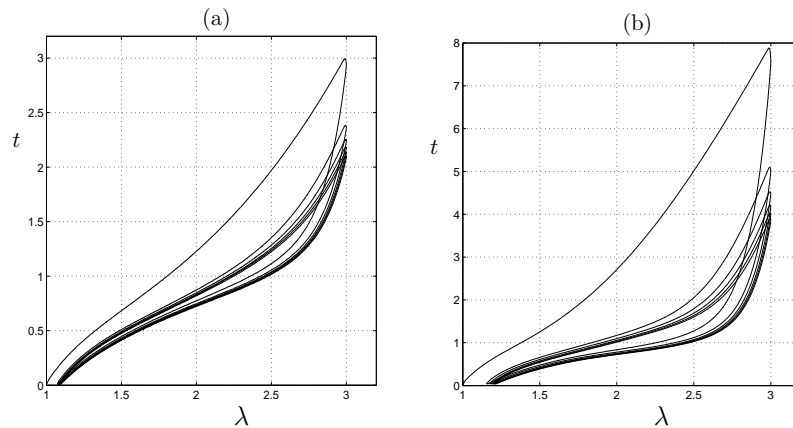


Figure 2. Cycles of nominal stress t (units N mm^{-2}) vs stretch λ : rubber compound with (a) 20% and (b) 60% by volume of carbon black filler.

a repeatable pattern is established (typically after 5 or 6 cycles). Since the filler content is small the behaviour approximates that of an unfilled rubber. In this case there is little difference between the loading and unloading curves, particularly after the initial loading.

Figure 2 shows the corresponding picture for filled natural rubber with (a) 20% and (b) 60% by volume of carbon black filler. Here, the residual strain, which is also evident in Fig. 1(b), is much more noticeable. Moreover, there is a very marked stress softening, particularly on the first loading-unloading cycle, i.e. the stress on unloading is less than that on loading at the same level of stretch. This effect, associated with

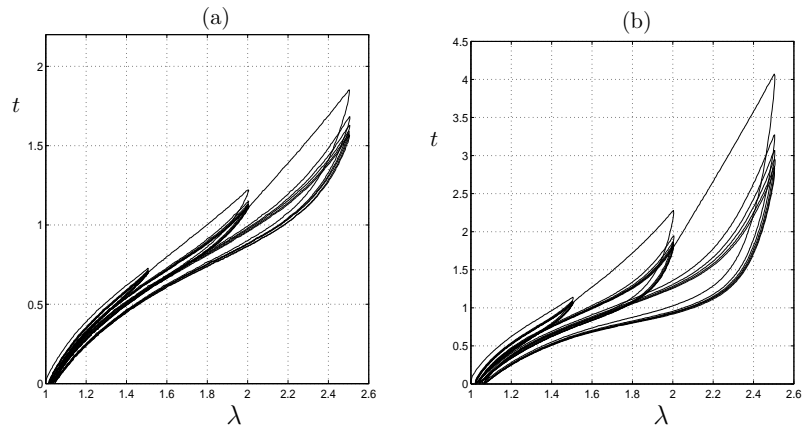


Figure 3. Cycles of nominal stress t (units N mm^{-2}) vs stretch λ up to $\lambda = 1.5, 2, 2.5$: rubber compound with (a) 20% and (b) 60% by volume of carbon black filler.

deformation from the virgin state and known as the *Mullins effect*, increases as the percentage of filler increases. The first cycle essentially provides a pre-conditioning of the material and was examined in detail by Mullins [32, 33] and Mullins and Tobin [34] and in several other papers. However, the effect had apparently been recorded in the literature much earlier by Bouasse and Carrière [3]. Figure 3 shows data for the same two materials as in Fig. 2 but with the stretch cycled first up $\lambda = 1.5$, then to $\lambda = 2$ and finally to $\lambda = 2.5$. These curves show clearly how the pre-conditioning, stress softening and residual strain effects depend on the maximum stretch achieved and on the proportion of filler.

The degree of stress softening and magnitude of the residual strain depend very much on the maximum stretch achieved and on the particular material under consideration. For example, for a liquid silicone rubber filled with silica particles, there is a very significant stress softening, but the residual strain is very small [35]. Moreover, the reloading curves are very close to the unloading curves. This pattern is very close to what may be described as the *idealized Mullins effect*, for which residual strain is absent and the reloading curves re-trace the unloading curves exactly. It is this idealized description that has formed the basis of most of the modelling in the literature.

As indicated above, the Mullins effect is associated with deformation from the virgin state of the material. Once the material has been deformed there is then (at least in the idealized situation) no further stress softening generated provided the material is not strained beyond the maximum value of the stretch already achieved. This observation is the basis for pre-conditioning the material: in pre-conditioning the

material is strained to a level beyond that expected to be achieved in service conditions so that the Mullins effect is no longer operative. This pre-conditioning is evident in Figs. 1(b) and 2.

For further discussion of many of the aspects of material behaviour considered briefly here we refer to the three volumes of proceedings from the series of conferences on constitutive models for rubber [8, 2, 6] and the volume [49]. These include the effects of time dependence (creep, relaxation and recovery, for example), frequency dependence, hysteresis and viscoelasticity.

3. Theoretical Approaches

As far as the *elasticity* of rubber is concerned there are some fundamental assumptions that are adopted in the phenomenological theory: the material is (a) hyperelastic, (b) isotropic, and (c) incompressible. *Hyperelasticity* means that the properties of the material are described in terms of a strain-energy function. *Isotropy* (relative to a stress-free configuration) is a very good approximation in most circumstances and is almost invariably used by practitioners. *Incompressibility* is an idealization, justified by the fact that the shear modulus of the material is very much smaller than the bulk modulus (typically the ratio is of order 10^{-4}) and volume changes can be neglected except in extreme situations where the hydrostatic stress is very large. For the most part isotropy and incompressibility are assumed in practical applications.

The strain energy is a function of the deformation gradient \mathbf{F} (relative to some fixed reference configuration), and is written $W(\mathbf{F})$ per unit volume. This theory is well established and we omit details here. Suitable references are the review articles [37, 38, 4] and the volume [49]. Here we focus on models for the Mullins effect.

Many phenomenological theories aimed at modelling the Mullins effect have been proposed in the literature. Some of these are based on the two-phase micro-structural model introduced by Mullins and Tobin [34] and developed more recently by, for example, Johnson and Beatty [25, 26]. Another class of models is based on the introduction of a damage (or stress-softening) variable to describe the internal damage in the bulk material associated with the Mullins effect (see, for example, Gurtin and Francis [18], De Souza Neto et al. [7], Beatty and Krishnaswamy [1] and Zúñiga and Beatty [50] and references cited therein). Ogden and Roxburgh [42, 43] have developed a model based on a theory of *pseudo-elasticity* in which a pseudo-energy function is introduced as in standard nonlinear elasticity theory except that an additional scalar variable (the damage variable) is incorporated. All of these models share the common

feature that the virgin material response is determined by a standard strain-energy function or a stress constitutive function for a perfectly elastic isotropic material. A connection between this theory and that of materials with multiple natural configurations due to Rajagopal and Wineman [44] has also been noted [20].

A model of the Mullins effect based on micro-mechanical continuum damage theory was proposed by Govindjee and Simo [17]. The constitutive equation for this model involves the integration of the inverse Langevin function over a history-dependent domain in the phase space of the rubber network. Recently Marckmann et al. [30] have proposed another model using the inverse Langevin function in the description of network alteration associated with the Mullins effect. The non-Gaussian statistics allow one to take into account the limiting stretch of the chains composing the polymeric network. In the Marckmann et al. [30] model the Mullins effect is explained by reference to an alteration of the average chain length driven by the previous maximum stretch in a given deformation. The network alteration idea has been investigated recently by Horgan et al [20] on the basis of the phenomenological model proposed by Gent [16] for rubberlike elasticity. This is a very simple strain-energy that accounts for the limiting chain extensibility of rubberlike polymers (for further discussion we refer to Horgan and Saccomandi [21–23]). The use of the Gent model allows one to bypass the computational problems associated with the inverse Langevin function and to provide a simpler and deeper interpretation of the network alteration phenomenon. Further references are contained in the paper by Horgan et al. [20].

An important feature of the effect of stress softening and any associated residual strains is the change in material symmetry generated. This has received very little attention in the literature thus far, although there is a recent discussion by Horgan et al. [20]. An extensive review of different aspects of rubber mechanics and thermomechanics, from the molecular to the phenomenological level, is provided in the volume edited by Saccomandi and Ogden [49], which contains many pointers to the literature.

In order to capture the essence of the Mullins effect with a relatively simple theory that requires only a slight modification of the theory of elasticity discussed so far, we use the theory of *pseudo-elasticity* based on the papers by Ogden and Roxburgh [42, 43] and Ogden [41]. We refer to these papers for full details of the theoretical development since only a brief summary is provided below. We consider the deformation of a continuous body which in its initial (virgin) stress-free configuration occupies the region \mathcal{B}_r and in the deformed configuration \mathcal{B} . The deformation gradient relating \mathcal{B} to \mathcal{B}_r is again denoted by \mathbf{F} .

In *pseudo-elasticity* the strain-energy function $W(\mathbf{F})$ of elasticity theory is modified by incorporating an additional variable, here denoted η , into the function and we write $W = W(\mathbf{F}, \eta)$. The variable η is referred to as a *damage variable* or *softening variable*. In the simplest case it is taken to be a scalar quantity, but more generally it may be a tensor variable, for example. It provides a means of changing the form of the energy function during the deformation process and hence changing the description of the material properties. In a deformation process in which η changes, the overall response of the material is not elastic and we refer to $W(\mathbf{F}, \eta)$ as a *pseudo-energy function*. The variable η may be active or inactive and may be switched from active to inactive (or conversely) according to some suitable criterion, thereby inducing a change in the material properties. This change may be either continuous or discontinuous.

A suitable means of determining the dependence of η on \mathbf{F} is the equation

$$\frac{\partial W}{\partial \eta}(\mathbf{F}, \eta) = 0. \quad (1)$$

For an incompressible material the nominal stress tensor then has the form

$$\mathbf{S} = \frac{\partial W}{\partial \mathbf{F}}(\mathbf{F}, \eta) - p\mathbf{F}^{-1}, \quad \det \mathbf{F} = 1, \quad (2)$$

where the right-hand side is evaluated for η given implicitly by 1. The nominal stress is given by 2 whether η is active or inactive. In the latter case $\eta \equiv 1$.

We may regard equation 1 as a field equation, which, in the absence of body forces, is coupled with the equilibrium equation in the form

$$\text{Div } \mathbf{S} = \mathbf{0} \quad \text{in } \mathcal{B}_r, \quad (3)$$

where Div denotes the divergence operator in \mathcal{B}_r .

There is considerable flexibility in the choice of specific models, in particular the dependence of W on η , subject to appropriate objectivity restrictions. A criterion for switching η on or off is also needed. Such considerations depend on the application in question. For the stress softening associated with the Mullins effect, for example, η is taken to be inactive during loading and to switch on during unloading (with loading and unloading being defined relative to the energy expended on a loading path). Moreover, the material is assumed to be isotropic. The theory gives a good fit to data, as demonstrated in the original paper by Ogden and Roxburgh [42], and has been extended to allow for partial unloading-reloading and residual strains [9, 11]. We refer to the above cited papers for further details and additional references.

4. Magneto–Sensitive Elastomers

The equations for a continuum deforming in the presence of an electromagnetic field are well established, as exemplified by the work of Hutter and van de Ven [24] and Maugin [31]. Here we are concerned with the static situation for materials that respond to a magnetic field. Specifically, such materials are elastomers with a distribution of ferrous particles embedded within their bulk. Background details of the theory of magnetoelasticity can be found in the work of Brown [5], while the book by Kovetz [29] contains a readable account of some aspects of the theory. In Kovetz the magnetic induction vector \mathbf{B} was taken as the basic variable, which was also the case with the work of the present authors (Dorfmann and Ogden [10, 12]). Alternative formulations based on the use of the magnetic field vector \mathbf{H} or the magnetization vector \mathbf{M} have been discussed by Steigmann [46], while Kankanala and Triantafyllidis [28] base their recent analysis on use of \mathbf{M} as an independent variable. A treatment of universal relations for magnetoelastic solids is contained in a paper by Dorfmann et al. [15].

A refined version of the theory that enables boundary-value problems to be formulated in a very simple form has been provided recently by Dorfmann and Ogden [13] (see also [14]). References to the (limited) literature are given in these papers. The theory is applied to some simple prototype boundary-value problems of practical interest, notably the axial shear and combined extension and torsion of MS material contained within a circular cylindrical tube in the presence of either an axial magnetic field (uniform) or an azimuthal field. The influence of the magnetic field strength on the various shear stiffnesses of the material has been evaluated. Data for the considered material is rather limited, but the paper by Jolly et al. [27], for example, shows how the shear modulus of the material stiffens with the application of a magnetic field and how this depends on the volume fraction of magnetic filler particles.

We consider a magnetoelastic body that is initially in an unstressed configuration, not subject to mechanical loads or magnetic fields. Let the region in three-dimensional Euclidean space occupied by the body in this configuration be denoted \mathcal{B}_r . Suppose next that the material is subject to a magnetic field, denoted \mathbf{H} , and an associated magnetic induction vector \mathbf{B} and magnetization vector \mathbf{M} , together with mechanical boundary tractions, so that the deformation gradient is \mathbf{F} .

These (Eulerian) vector fields satisfy the standard relation and the Maxwell field equations given by

$$\mathbf{B} = \mu_0(\mathbf{H} + \mathbf{M}), \quad \operatorname{div}\mathbf{B} = 0, \quad \operatorname{curl}\mathbf{H} = \mathbf{0}, \quad (4)$$

where μ_0 is the vacuum permeability.

In respect of the reference configuration \mathcal{B}_r , the Lagrangian counterparts of \mathbf{B} and \mathbf{H} are denoted \mathbf{B}_l and \mathbf{H}_l , respectively, and (for an incompressible material) they are related to \mathbf{B} and \mathbf{H} by

$$\mathbf{B} = \mathbf{F}\mathbf{B}_l, \quad \mathbf{H} = \mathbf{F}^{-T}\mathbf{H}_l, \quad (5)$$

respectively (see, for example, [31, 12, 46]). Standard identities ensure that the pair of Eq. (4)_{2,3} is entirely equivalent to the pair

$$\text{Div}\mathbf{B}_l = 0, \quad \text{Curl}\mathbf{H}_l = \mathbf{0}, \quad (6)$$

provided the deformation is suitably regular. Similarly to \mathbf{H}_l , a Lagrangian form of \mathbf{M} , denoted \mathbf{M}_l , is defined by $\mathbf{M}_l = \mathbf{F}^T\mathbf{M}$.

The equilibrium equation may be written in the equivalent forms

$$\text{div}\boldsymbol{\tau} = \mathbf{0}, \quad \text{Div}\mathbf{T} = \mathbf{0}, \quad (7)$$

in the absence of mechanical body forces, where $\boldsymbol{\tau}$ is the total stress tensor and \mathbf{T} is the total nominal stress tensor related to $\boldsymbol{\tau}$ by $\mathbf{T} = J\mathbf{F}^{-1}\boldsymbol{\tau}$. Balance of angular momentum requires that $\boldsymbol{\tau}$ is symmetric.

The constitutive law for a magnetoelastic solid may be expressed in various different but equivalent forms. For an incompressible magnetoelastic solid, for example, a simple description of the constitutive properties of the material is provided through an amended energy function, denoted Ω and defined per unit volume, given by

$$\Omega = \rho\Phi + \frac{1}{2}\mu_0^{-1}\mathbf{B}_l \cdot (\mathbf{c}\mathbf{B}_l), \quad (8)$$

where ρ is the mass density, $\mathbf{c} = \mathbf{F}^T\mathbf{F}$ is the right Cauchy-Green tensor and Φ is the free energy of the material (per unit mass). With objectivity invoked, we take Ω to depend on \mathbf{B}_l and \mathbf{c} as independent variables. The total stress \mathbf{T} and the magnetic field \mathbf{H}_l are then given by

$$\mathbf{T} = \frac{\partial\Omega}{\partial\mathbf{F}} - p\mathbf{F}^{-1}, \quad \mathbf{H}_l = \frac{\partial\Omega}{\partial\mathbf{B}_l}, \quad (9)$$

where p is a Lagrange multiplier associated with the incompressibility constraint. Corresponding equations may also be given in which the independent magnetic variable \mathbf{B}_l is replaced by \mathbf{H}_l [13].

Material symmetry has been discussed in detail in the papers cited above, and, in particular, constitutive laws specified in various forms for *isotropic* magnetoelastic solids. The material symmetry considerations are similar to those that arise for a transversely isotropic elastic material for which there is a preferred direction in the reference configuration analogous to \mathbf{B}_l . For relevant discussion of material symmetry

for anisotropic elastic solids we refer to Spencer [45], Holzapfel [19] and Ogden [40], for example. For discussion of material symmetry in the magnetoelastic context we refer to Steigmann [46].

Important differences between the formulations based on use of \mathbf{B}_I and \mathbf{H}_I in respect of their application to particular boundary-value problems have been discussed in Dorfmann and Ogden [13, 14].

References

- [1] M.F. Beatty and S. Krishnaswamy, A theory of stress-softening in incompressible isotropic materials, *J. Mech. Phys. Solids*, 48, pp.1931–1965, 2000.
- [2] D. Besdo, R.H. Schuster and J. Ihlemann, *Constitutive Models for Rubber II*, Balkema, 2001.
- [3] H. Bouasse and Z. Carrière, Courbes de traction du caoutchouc vulcanisé, *Ann. Fac. Sciences de Toulouse*, 5, pp.257–283, 1903.
- [4] M.C. Boyce and E.M. Arruda, Constitutive models of rubber elasticity: a review, *Rubber Chem. Technol.*, 73, pp.504–523, 2000.
- [5] W.F. Brown, *Magnetoelastic Interactions*, Springer, 1966.
- [6] J.J.C. Busfield and A.H. Muhr, *Constitutive Models for Rubber III*, Balkema, 2003.
- [7] E.A. De Souza Neto, D. Perić and D.R. Owen, A phenomenological three-dimensional rate independent continuum model for highly filled polymers: formulation and computational aspects, *J. Mech. Phys. Solids*, 42, pp.1553–1550, 1994.
- [8] A. Dorfmann and A. Muhr, *Constitutive Models for Rubber*, Balkema, 1999.
- [9] A. Dorfmann and R.W. Ogden, A pseudo-elastic model for loading, partial unloading and reloading of particle-reinforced rubber, *Int. J. Solids Structures*, 40, pp.2699–2714, 2003.
- [10] A. Dorfmann and R.W. Ogden, Magnetoelastic modelling of elastomers, *European J. Mech. A/Solids*, 22, pp.497–507, 2003.
- [11] A. Dorfmann and R.W. Ogden, A constitutive model for the Mullins effect with permanent set in particle-filled rubber, *Int. J. Solids Structures*, 41, pp.1855–1878, 2004.
- [12] A. Dorfmann and R.W. Ogden, Nonlinear magnetoelastic deformations of elastomers, *Acta Mechanica*, 167, pp.13–28, 2003.
- [13] A. Dorfmann and R.W. Ogden, Nonlinear magnetoelastic deformations. Q. J. Mech. Appl. Math., in press, 2004.
- [14] A. Dorfmann and R.W. Ogden, Some problems in nonlinear magnetoelasticity, *ZAMP*, in press, 2004.
- [15] A. Dorfmann, R.W. Ogden and G. Saccomandi, Universal relations for magnetoelastic solids, *Int. J. Nonlinear Mech.*, 39, pp.1699–1708, 2004.
- [16] A.N. Gent, A new constitutive relation for rubber, *Rubber Chem. Technol.*, 69, pp.59–61, 1996.

- [17] S. Govindjee and J.C. Simo, A micro-mechanically based continuum damage model for carbon black-filled rubbers incorporating the Mullins' effect, *J. Mech. Phys. Solids*, 39, pp.87–112, 1991.
- [18] M.E. Gurtin and E.C. Francis, Simple rate-independent model for damage, *J. Spacecraft Rockets*, 18, pp.285–286, 1981.
- [19] G.A. Holzapfel, *Nonlinear Solid Mechanics: a Continuum Approach for Engineering*, 2nd ed. John Wiley & Sons Ltd, 2001.
- [20] C.O. Horgan, R.W. Ogden and G. Saccomandi, A theory of stress softening of elastomers based on finite chain extensibility, *Proc. R. Soc. Lond. A*, 460, pp.1737–1754, 2004.
- [21] C.O. Horgan and G. Saccomandi, Constitutive modelling of rubber-like and biological materials with limiting chain extensibility, *Math. Mech. Solids*, 7, pp.353–371, 2002.
- [22] C.O. Horgan and G. Saccomandi, Finite thermoelasticity with limiting chain extensibility, *J. Mech. Phys. Solids*, 51, pp.1127–1146, 2003.
- [23] C.O. Horgan and G. Saccomandi, A molecular-statistical basis for the Gent constitutive model of rubber elasticity, *J. Elasticity*, 68, pp.167–176, 2002.
- [24] K. Hutter and A.A.F. van de Ven, *Field Matter Interactions in Thermoelastic Solids*, Lecture Notes in Physics, vol. 88. Springer, 1978.
- [25] M.A. Johnson and M.F. Beatty, The Mullins effect in uniaxial extension and its influence on the transverse vibration of a rubber string, *Continuum Mech. Thermodyn.*, 5, pp.83–115, 1993.
- [26] M.A. Johnson and M.F. Beatty, A constitutive equation for the Mullins effect in stress controlled uniaxial extension experiments, *Continuum Mech. Thermodyn.*, 5, pp.301–318, 1993.
- [27] M.R. Jolly, J.D. Carlson and B.C. Muñoz, A model of the behaviour of magnetorheological materials, *Smart Mater. Struct.*, 5, pp.607–614, 1996.
- [28] S.V. Kankanala and N. Triantafyllidis, On finitely strained magnetorheological elastomers, *J. Mech. Phys. Solids*, in press, 2004.
- [29] A. Kovetz, *Electromagnetic Theory*, Oxford University Press, 2000.
- [30] G. Marckmann, E. Verron, L. Gornet, G. Chagnon, P. Charrier and P. Fort, A theory of network alteration for the Mullins effect, *J. Mech. Phys. Solids*, 50, pp.2011–2028, 2002.
- [31] G.A. Maugin, *Continuum Mechanics of Electromagnetic Solids*, North Holland, 1988.
- [32] L. Mullins, Effect of stretching on the properties of rubber, *J. Rubber Res.*, 16, pp.275–289, 1947.
- [33] L. Mullins, Softening of rubber by deformation, *Rubber Chem. Technol.*, 42, pp.339–362, 1969.
- [34] L. Mullins and N.R. Tobin, Theoretical model for the elastic behavior of filler-reinforced vulcanized rubbers, *Rubber Chem. Technol.*, 30, pp.555–571, 1957.
- [35] A.H. Muhr, J. Gough and I.H. Gregory, Experimental determination of model for liquid silicone rubber: Hyperelasticity and Mullins' effect. In *Proceedings of the First European Conference on Constitutive Models for Rubber*, pages 181–187, Vienna, 1999. Balkema, 1999.

- [36] R.W. Ogden, Large deformation isotropic elasticity: on the correlation of theory and experiment for incompressible rubberlike solids, *Proc. R. Soc. Lond. A*, 326, pp.565–584, 1972.
- [37] R.W. Ogden, Elastic deformation of rubberlike solids. In *Mechanics of Solids*, pages 499–537. The Rodney Hill 60th Anniversary Volume. Pergamon Press, 1982.
- [38] R.W. Ogden, Recent advances in the phenomenological theory of rubber elasticity, *Rubber Chem. Technol.*, 59, pp.361–383, 1986.
- [39] R.W. Ogden, *Non-linear Elastic Deformations*, Dover Publications, 1997.
- [40] R.W. Ogden, Elements of the theory of finite elasticity. In *Nonlinear Elasticity: Theory and Applications*, London Mathematical Society Lecture Notes 283, pages 1–57. Cambridge University Press, 2001.
- [41] R.W. Ogden, Pseudo-elasticity and stress softening. In *Nonlinear Elasticity: Theory and Applications*, London Mathematical Society Lecture Notes 283, pages 491–522. Cambridge University Press, 2001.
- [42] R.W. Ogden and D.G. Roxburgh, A pseudo-elastic model for the Mullins effect in filled rubber, *Proc. R. Soc. Lond. A*, 455, pp.2861–2877, 1999.
- [43] R.W. Ogden and D.G. Roxburgh, An energy-based model of the Mullins effect. In *Proceedings of the First European Conference on Constitutive Models for Rubber*, pages 23–28, Vienna, 1999. Balkema, 1999.
- [44] K.R. Rajagopal and A.S. Wineman, A constitutive equation for nonlinear solids which undergo deformation induced microstructural changes, *Int. J. Plasticity*, 8, pp.385–395, 1992.
- [45] A.J.M. Spencer, Theory of Invariants. In *Continuum Physics Vol. 1*, pages 239–353. Academic Press, 1971.
- [46] D.J. Steigmann Equilibrium theory for magnetic elastomers and magnetoelastic membranes, *Int. J. Nonlinear Mech.*, 39, pp. 1193–1216, 2004.
- [47] L.R.G. Treloar, Stress-strain data for vulcanized rubber under various types of deformation, *Trans. Faraday Soc.*, 40, pp.59–70, 1944.
- [48] L.R.G. Treloar, *The Physics of Rubber Elasticity*, 3rd edition, Oxford University Press, 1975.
- [49] G. Saccomandi and R.W. Ogden, *Mechanics and Thermomechanics of Rubberlike Solids*, CISM Courses and Lectures Series 452. Springer, 2004.
- [50] A.E. Zúñiga and M.F. Beatty, A new phenomenological model for stress-softening in elastomers, *ZAMP*, 53, pp.794–814, 2002.

ELASTIC WAVE PROPAGATION DEVELOPMENT FOR STRUCTURAL HEALTH MONITORING

Wiesław Ostachowicz

Institute of Fluid Flow Machinery,

14 Fiszera St., 80-952 Gdańsk, Poland;

Gdynia Maritime University, Faculty of Navigation,

Al. Zjednoczenia 3, 81-345 Gdynia, Poland

Abstract This paper is a personal perspective of structural health monitoring technology and its applications as seen from a current literature and projects. The proposed approach deals with the spectral finite element analysis method as a means of solving the wave propagation problems in structures. The change of the wave propagation process due to a damage appearance is examined by comparing the differences between the responses from damaged and undamaged structures. The influence of the damage growth for the wave propagation is also analysed. The differences in the propagating waves allow indicating the damage location and size in a very precise way.

Keywords: Damage detection, structural health monitoring

1. Introduction

Undetected damage in buildings, bridges, aerospace structures, containers and other large structures will develop if undetected and in some cases result in the collapse of the whole structure. This may have costly disastrous consequences for people and the environment including deaths, injuries, fires, contamination, economic losses, legal costs, etc. It has been found that in a lot of cases a small-undetected damage (crack, plastification, delamination) has been the cause for the collapse.

Damage in structures should be detected at an early stage, before it can cause any problems and so that proper decisions for repair and/or part replacement can be taken.

The most popular methods used for non-destructive evaluation are: visual inspection, eddy current, X-ray, ultrasound, strain gauge, and thermal contours. Unfortunately, most of those methods have significant

disadvantages. Usually, they are quite impractical for monitoring large, complex structures.

Several of NDT methods being currently developed. The most promising approaches are based on detecting: acoustic emissions (AE), strain variations in optical fiber sensors (OFS), vibration-based methods (VBM), and structural health monitoring (SHM).

This paper is focused on structural health monitoring technology and its applications in aerospace and civil engineering. The investigated damage detection system is based on the known fact that material discontinuities affect the propagation of elastic waves in solids. The change in material characteristics, such as a local change in stiffness or inertia caused by a crack or material damage, will affect the propagation of elastic waves and will modify the received signals.

Better understanding of phenomena associated with propagation of elastic waves in structural elements is very important from both the theoretical and the practical point of view.

In recent years significant progress has been evident in this particular field of applications.

2. Structural Health Monitoring Technology

SHM (Structural Health Monitoring) technology is the technological platform for a new maintenance philosophy. SHM technology works with a built-in sensor network on a structure. These sensors provide information regarding the condition and damage state of the structures as they age.

A new philosophy based on SHM technology creates feedback loops within the design, manufacturing, and maintenance procedures by providing additional knowledge about a specific design performance, material quality, and structure condition respectively.

Changes in propagation of elastic waves when observed in structural elements can be used for the purpose of damage detection or identification of material parameters within those elements.

Elastic waves are generated and sensed by an array of transducers either embedded in, or bonded to, the surface of the structure. Wave frequencies associated with the highest detection sensitivity depend, among others, on the type of the structure, the type of material, and the type of the damage. Figure 1 presents a general concept of this technology.

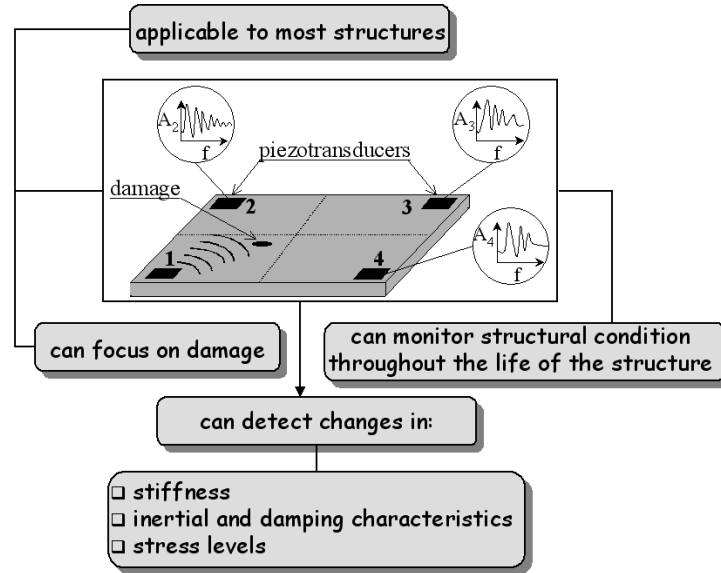


Figure 1. Build in sensor network on a plate.

3. Spectral Finite Element Technique

Among many frequency domain methods, the spectral method is found to be suitable due to its adaptation of displacement based FE technique and therefore enabling one to handle arbitrary skeletal structures.

The SFEM approach is based on exact solution to governing Partial Differential Equations (PDE) in the frequency domain. This exact solution is used as interpolating function for spectral element formulation. As a consequence, relatively small number of elements can be used for modelling without losing the accuracy. The solution is obtained in terms of generalised displacements, subsequent calculations for velocity, acceleration, strain and stress for any applied load can then be found with relatively inexpensive postprocessing calculations. The spectral element method directly computes a structure's frequency response function and in this manner gives additional information that bridges the gap between modal methods based on free vibrations and time reconstruction based on direct integration. This is particularly useful for wave propagation modelling.

Figure 2 shows a flow diagram for the basic algorithm to propagate a wave. The governing wave equations are first transformed from the time domain to the frequency domain using a discrete Fourier transform

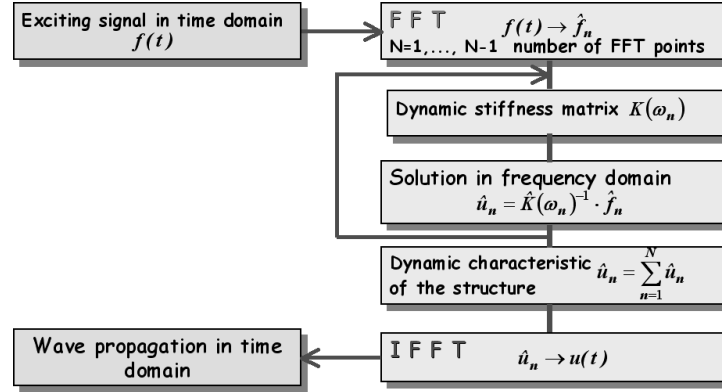


Figure 2. Flow diagram for the wave reconstruction program.

(DFT). For computational implementation we use the FFT algorithm built into the FE code.

In a simple form, the solution to a wave propagation problem can be represented as by Doyle [1]:

$$\hat{u} = \sum_n \hat{P}_n \left\{ \hat{G}_1(k_{1n}x) + \hat{G}_2(k_{2n}x) + \dots \right\} \exp(i\omega_n t)$$

$$= \sum_n \hat{P}_n \hat{G}_1(k_{mn}x) \exp(i\omega_n t) \quad (1)$$

where: \hat{G} is the analytically derived transfer function of position x , \hat{G} has different numerical values at each frequency. \hat{P}_n is the amplitude spectrum and is known from input conditions or from measurements. $\hat{P}_n \hat{G}$ is recognised as the Fourier transform of the solution.

The spatial variation is semi-explicitly obtained by solving the characteristic equation in k -space. This results in a complex shape function matrix representing the linear superposition of all the wave modes. Also, the complex dynamic strain-displacement matrix and the dynamically consistent force vector can both be derived. Following the conventional FE method, the complex dynamic stiffness matrix is then formed, and this is exact. This makes the proposed SEM an efficient model suitable for use within the framework of an automated FE method rather than a trade-off for broadband wave propagation analysis. But the fundamental difference from the conventional FE method is that all the spectral amplitudes that correspond to elemental nodal variables are evaluated at each frequency step (FFT sampling points) instead of pseudo-static variables evaluated at each time step or at each eigenfrequency. The global system is solved for unit spectral amplitude of the applied load

history at each FFT sampling frequency. Therefore, computation in this way of the frequency response function (FRF) of the global system is straightforward. The time domain response is obtained using the inverse FFT.

This paper presents a method of wave propagation, which can be used to detect small failures in rod, beam-like and plate structures.

Cracked Rod Spectral Element

A spectral rod finite element with a transverse open and non-propagating crack is presented in Fig. 3. The crack is substituted by a dimensionless spring, which flexibility θ is calculated by using Castigliano's theorem and laws of the fracture mechanics [2, 3].

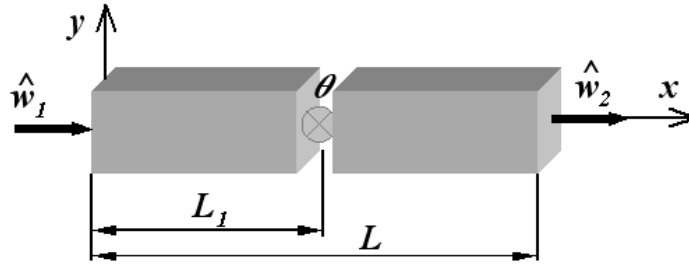


Figure 3. The model of the rod with a transverse open and not propagating crack simulated by elastic hinge.

Nodal spectral displacements are assumed in the following form for the left (Eq. 2) and right (Eq. 3) part of the rod:

$$\hat{w}_1(x) = A_1 e^{-ik_n x} + B_1 e^{-ik_n(L_1-x)} \quad \text{for } x \in (0, L_1), \quad (2)$$

$$\hat{w}_2(x) = A_2 e^{-ik_n(x+L_1)} + B_2 e^{-ik_n[L-(L_1+x)]} \quad \text{for } x \in (0, L - L_1) \quad (3)$$

where: L_1 denotes the location of the crack, L is the total length of the rod and k_n is the wave number calculated as follows:

$$k_n = \omega_n \sqrt{\frac{\rho}{E}} \quad (4)$$

where: ρ is the density of the rod material, E denotes Young's modulus and ω_n is a natural frequency.

The coefficients A_1 , A_2 , B_1 and B_2 can be calculated as a function of the nodal spectral displacements using the element boundary conditions [3]. Using boundary conditions can relate the coefficients A_1 , A_2 , B_1 and B_2 to the nodal spectral displacements. The nodal spectral forces

can be determined by differentiating the spectral displacements with respect to x . Finally, using the relation between nodal forces and nodal displacements the dynamic stiffness matrix of a cracked rod spectral finite element can be evaluated. Propagation of elastic waves in rods is presented in [3].

Cracked Timoshenko Beam Spectral Element

A spectral Timoshenko beam finite element with a transverse open and non-propagating crack is presented in Fig. 4. The length of the element is L , and its area of cross-section is A . The crack is substituted by a dimensionless spring, which flexibility θ is calculated by using Castigliano's theorem and laws of the fracture mechanics [2, 4].

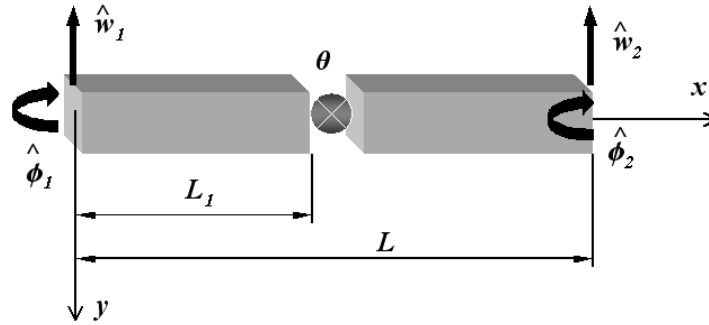


Figure 4. The model of the Timoshenko beam with a transverse open and not propagating crack simulated by elastic hinge.

Nodal spectral displacements \hat{w} and rotations $\hat{\phi}$ are assumed in the following forms, for the left (Eq. 5) and right (Eq. 6) part of the beam:

$$\hat{w}_1(x) = [\Phi_1] \cdot [\Psi] \cdot \{\alpha_1\} \text{ and } \hat{\phi}_1(x) = [\Phi_1] \cdot \{\alpha_1\} \text{ for } x \in (0, L_1), \quad (5)$$

$$\hat{w}_2(x) = [\Phi_2] \cdot [\Psi] \cdot \{\alpha_2\} \text{ and } \hat{\phi}_2(x) = [\Phi_2] \cdot \{\alpha_2\} \text{ for } x \in (0, L-L_1) \quad (6)$$

where:

$$[\Phi_1] = \begin{bmatrix} e^{-ik_1 x} & e^{-ik_2 x} & e^{-ik_1(L_1-x)} & e^{-ik_2(L_1-x)} \end{bmatrix},$$

$$[\Phi_2] = \begin{bmatrix} e^{-ik_1(x+L_1)} & e^{-ik_2(x+L_2)} & e^{-ik_1[L-(L_1+x)]} & e^{-ik_2[L-(L_1+x)]} \end{bmatrix},$$

$$\{\alpha_1\} = \text{col}[A_1 \quad B_1 \quad C_1 \quad D_1] \text{ and } \{\alpha_2\} = \text{col}[A_2 \quad B_2 \quad C_2 \quad D_2],$$

$$[\Psi] = \text{diag}[R_1 \quad R_2 \quad -R_1 \quad -R_2]$$

where L_1 denotes the location of the crack, L is the total length of the beam, R_n is the amplitude ratio given by:

$$R_n = \frac{ik_n GAK_1}{GAK_1 k_n^2 - \rho A \omega^2}, \quad K_1 = \left(\frac{0.87 + 1.12\nu}{1 + \nu} \right)^2 \quad \text{for } (n = 1, 2) \quad (7)$$

where ν is Poisson ratio, G is shear modulus, ρ denotes density of the material and ω is a natural frequency.

The wave numbers k_1 and k_2 are roots of characteristic equation in the general form:

$$(GAK_1 E J) k^4 - (GAK_1 \rho J K_2 \omega^2 + E J \rho A \omega^2) k^2 + (\rho J K_2 \omega^2 - GAK_1) \rho A \omega^2 = 0 \quad (8)$$

where: $K_2 = 12K_1/\pi^2$, E denotes Young's modulus and J is the geometrical moment of inertia of the beam cross-section.

The coefficients $A_1, B_1, C_1, D_1, A_2, B_2, C_2$, and D_2 can be calculated as a function of the nodal spectral displacements using the boundary conditions, as in [5, 6]. The nodal spectral forces can be determined by differentiating the spectral displacements with respect to x . Finally, using relation between the nodal forces and nodal displacements the dynamic stiffness matrix of a cracked rod spectral finite element can be evaluated. Propagation of elastic waves in beams including damping effects is presented in [7].

Delaminated Multilayer Composite Beam Spectral Element

A schematic of a conceptual damage model of a multilayer composite beam is presented in Fig. 5. The beam under consideration is divided into four parts with lengths $L_1, L_2 = L_3$ and L_4 . The length of the beam is L , width b , and height h . The delamination is situated between parts 2 and 3. Its length is $L_2 = L_3$.

Displacements and rotations are assumed with Timoshenko beam theory and have the following form:

$$\begin{aligned} \hat{w}_1(x) &= [\Phi_1] \cdot [\Psi_1] \cdot \{\alpha_1\} \quad \text{and} \quad \hat{\phi}_1(x) = [\Phi_1] \cdot \{\alpha_1\}, \\ \hat{w}_2(x) &= [\Phi_2] \cdot [\Psi_2] \cdot \{\alpha_2\} \quad \text{and} \quad \hat{\phi}_2(x) = [\Phi_2] \cdot \{\alpha_2\}, \\ \hat{w}_3(x) &= [\Phi_3] \cdot [\Psi_3] \cdot \{\alpha_3\} \quad \text{and} \quad \hat{\phi}_3(x) = [\Phi_3] \cdot \{\alpha_3\}, \\ \hat{w}_4(x) &= [\Phi_4] \cdot [\Psi_4] \cdot \{\alpha_4\} \quad \text{and} \quad \hat{\phi}_4(x) = [\Phi_4] \cdot \{\alpha_4\} \end{aligned} \quad (9)$$

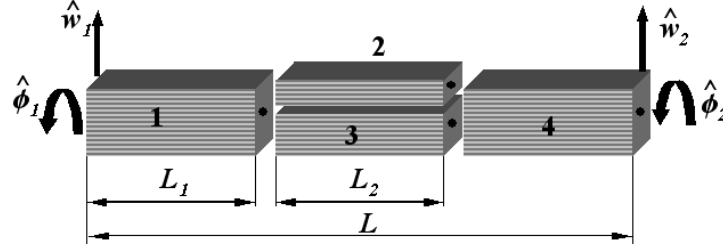


Figure 5. Model of a composite beam with delamination.

where:

$$\begin{aligned}
 [\Phi_1] &= \begin{bmatrix} e^{-ik_1x} & e^{-ik_2x} & e^{-ik_1(L_1-x)} & e^{-ik_2(L_1-x)} \end{bmatrix}, \\
 [\Phi_2] &= \begin{bmatrix} e^{-ik_1x} & e^{-ik_2x} & e^{-ik_1(L_2-x)} & e^{-ik_2(L_2-x)} \end{bmatrix}, \\
 [\Phi_3] &= \begin{bmatrix} e^{-ik_1x} & e^{-ik_2x} & e^{-ik_1(L_3-x)} & e^{-ik_2(L_3-x)} \end{bmatrix}, \\
 [\Phi_4] &= \begin{bmatrix} e^{-ik_1x} & e^{-ik_2x} & e^{-ik_1(L-x)} & e^{-ik_2(L-x)} \end{bmatrix},
 \end{aligned} \tag{10}$$

$$\begin{aligned}
 [\Psi_1] &= \text{diag} \begin{bmatrix} R_{1,1} & R_{2,1} & -R_{1,1} & -R_{2,1} \end{bmatrix}, \\
 [\Psi_1] &= \text{diag} \begin{bmatrix} R_{1,2} & R_{2,2} & -R_{1,2} & -R_{2,2} \end{bmatrix}, \\
 [\Psi_1] &= \text{diag} \begin{bmatrix} R_{1,3} & R_{2,3} & -R_{1,3} & -R_{2,3} \end{bmatrix}, \\
 [\Psi_1] &= \text{diag} \begin{bmatrix} R_{1,4} & R_{2,4} & -R_{1,4} & -R_{2,4} \end{bmatrix},
 \end{aligned} \tag{11}$$

$$\begin{aligned}
 \{\alpha_1\} &= \text{col} \begin{bmatrix} A_1 & A_2 & A_3 & A_4 \end{bmatrix} \quad \text{for } x \in (0, L_1), \\
 \{\alpha_2\} &= \text{col} \begin{bmatrix} A_5 & A_6 & A_7 & A_8 \end{bmatrix} \quad \text{for } x \in (L_1, L_1 + L_2), \\
 \{\alpha_3\} &= \text{col} \begin{bmatrix} A_9 & A_{10} & A_{11} & A_{12} \end{bmatrix} \quad \text{for } x \in (L_1, L_1 + L_3), \\
 \{\alpha_4\} &= \text{col} \begin{bmatrix} A_{13} & A_{14} & A_{15} & A_{16} \end{bmatrix} \quad \text{for } x \in (L_1 + L_3, L)
 \end{aligned} \tag{12}$$

where $L_{1,2}$ denote the beginning and the end of the delamination area, R_n are the amplitude ratios given by Doyle [1]:

$$R_{n,j} = \frac{ik_n b A_{66,j} I_{o,j}}{b A_{66,j} I_{o,j} k_n^2 - I_{2,j} \omega^2} \quad \text{for } n = 1, 2, \quad j = 1 \dots 4. \tag{13}$$

Stiffness coefficient A_{66} describes functions of individual ply properties and orientation, and are integrated over the beam cross-section, I_o and

I_2 are inertia properties of the cross-section. Note that ω is a natural frequency and $i = \sqrt{-1}$. Subscript j denotes the number of the part of the beam element.

The coefficients A_j ($j = 1$ to 16) in Eq. 12 can be calculated as a function of the nodal spectral displacements, taking into account the boundary conditions at the tips of the delamination [8, 9], and the frequency dependent dynamic stiffness matrix, which correlate the nodal spectral forces with the nodal spectral displacements as presented in [10, 11]. The nodal spectral forces can be determined by differentiating the spectral displacements with respect to x .

Spectral Plate Element With a Crack

A model of a spectral plate finite element with a transverse open and non-propagating crack is presented in Fig. 6.

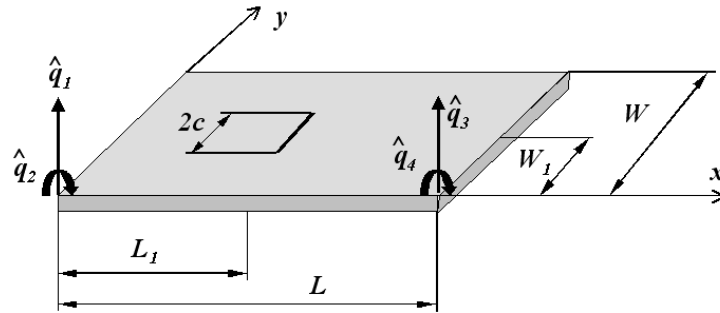


Figure 6. Model of the plate with a transverse open and non-propagating cracks.

The length of the element in the x direction is L , in the y direction is W , and the thickness of the plate is H . The crack is located at a distance of L_1 from the left edge of the plate and has length $2c$.

Nodal spectral displacements (dependent on the wave numbers, consequently on frequencies) are assumed in the following form, for the left (Eq. 14) and right (Eq. 15) part of the plate:

$$\hat{w}_1(x, y) = \sum_{m=1}^M \left(A_{mn}e^{-ik_1x} + B_{mn}e^{-ik_2x} + C_{mn}e^{-ik_1(L_1-x)} + D_{mn}e^{-ik_2(L_1-x)} \right) e^{-i\zeta_my} \quad \text{for } x \in (0, L_1), y \in (0, W), \quad (14)$$

$$\begin{aligned} \hat{w}_2(x, y) = & \sum_{m=1}^M \left(E_{mn} e^{-ik_1(L_1-x)} + F_{mn} e^{-ik_2(L_1-x)} + G_{mn} e^{-ik_1(L-(L_1+x))} \right. \\ & \left. + H_{mn} e^{-ik_2(L-(L_1+x))} \right) e^{-i\zeta_m y} \quad \text{for } x \in (0, L - L_1), y \in (0, W) \end{aligned} \quad (15)$$

where: $k_{1,2}$ are the waves numbers calculated as follows:

$$k_1 = \sqrt{\beta^2 - \xi^2} \quad \text{and} \quad k_2 = -i\sqrt{\beta^2 + \xi^2} \quad (16)$$

with

$$\xi_m = \frac{2\pi m}{W}; \quad \beta^4 = \frac{\rho h \omega_n^2 - i\eta H \omega_n}{D}; \quad D = \frac{EH^3}{12(1-\nu^2)} \quad (17)$$

where: ρ is the density of the plate material, η is the damping factor, D is the plate stiffness, ν is the Poisson ratio, E denotes Young's modulus and ω_n is a natural frequency. The coefficients A_{mn} , B_{mn} , C_{mn} , D_{mn} , E_{mn} , F_{mn} , G_{mn} and H_{mn} can be calculated as a function of the nodal spectral displacements using the element boundary conditions [12–14].

The nodal spectral forces can be determined by differentiating the spectral displacements with respect to x and y . From the commonly known fact that the dynamic stiffness matrix can relate forces with displacements, the nodal forces can be written as [12–14]:

$$\{\hat{F}\} = [K] \cdot \{\hat{q}\} \quad (18)$$

where

$$\{\hat{F}\} = \text{col} \left[\hat{T}(0, y) \quad \hat{M}(0, y) \quad \hat{T}(L, y) \quad \hat{M}(L, y) \right]$$

$$\{\hat{q}\} = \text{col} [\hat{q}_1 \quad \hat{q}_2 \quad 0 \quad \dots \quad 0 \quad \hat{q}_3 \quad \hat{q}_4]$$

where the square matrix $[K]$ denotes the frequency dependent dynamic stiffness matrix for the spectral plate element with a transverse open and non-propagating crack.

The dimensionless form of the bending flexibility at both sides of the crack can be expressed using formulas investigated by Khadem and Rezee [15], as follows:

$$\theta \left(\frac{\bar{y}}{W} \right) = \frac{6H}{W} \alpha_{bb} \left(\frac{\bar{y}}{W} \right) \cdot F \left(\frac{\bar{y}}{W} \right) \quad (19)$$

where: h is the thickness of the plate, W is the width of the plate, α_{bb} is a function representing the dimensionless bending compliance coefficient and F is a correction function. The function α_{bb} is given in [14]. Propagation of elastic waves in the plate with a transverse open and non-propagating crack is presented in [13, 14].

4. Conclusions

In this study the author has discussed the dynamics of a cracked rod, a cracked Timoshenko beam, a delaminated multilayer composite beam, and cracked plate spectral finite elements. The way of modelling the stiffness loss due to the crack appearance and the excitation force has also been presented. Damage detection is formulated as an optimisation problem which is then solved by using a genetic algorithm.

The results obtained indicate that the current approach is capable of detecting cracks and delaminations of very small size, even in the presence of considerable measurement errors. Only from the differences between the signals measured from undamaged and damaged structures can there be information about the location of the damage. The influence of the growth of the damage for wave propagation in the damaged structure has been shown.

The approach presented is very promising as a fatigue damage detection method. As concluded spectral analysis is very sensitive and allows one to detect damage in its very early state of growth. This fact is extremely important from the practical and economical point of view.

The proposed model can easily be used for detection of damage in more complicated situations, i.e. multiple delaminations located in different places.

The paper is not intended to be a comprehensive survey but merely to present a flavour of recent activity in this important subject.

References

- [1] J. Doyle, *Wave Propagation in Structures*, Springer-Verlag, New York 1997.
- [2] W. Ostachowicz, M. Krawczuk, On modelling of structural stiffness loss due to damage, *Key Engineering Materials*, Vols. 204–205, pp.185–200, 2001.
- [3] M. Krawczuk, W. Ostachowicz, Spectral finite element and genetic algorithm for crack detection in cantilever rod, *Key Engineering Materials*, Vols.204–205, pp.241–250, 2001.
- [4] M. Krawczuk, W. Ostachowicz, Spectral beam finite element and genetic algorithm for crack detection in beams, *Proceedings of the 3rd International Workshop on Structural Health Monitoring*, Stanford, CA, USA, pp.889–898, 2001.
- [5] M. Krawczuk, Application of spectral beam finite element with a crack and iterative search technique for damage detection, *Finite Elements in Analysis and Design*, 38, pp.537–548, 2002.
- [6] M. Krawczuk, M. Palacz, W. Ostachowicz, The dynamic analysis of cracked Timoshenko beam by the spectral element method, *Journal of Sound and Vibration*, 264, pp.1139–1153, 2003.
- [7] M. Krawczuk, A. Żak, W. Ostachowicz, M. Cartmell, Propagation of elastic waves in beams – including damping effects, *Materials Science Forum*, Vols. 440–441, pp.179–186, 2003.

- [8] M. Krawczuk, W. Ostachowicz, Identification of delamination in composite beams by genetic algorithm, *Science and Engineering of Composite Materials*, Vol.10, No.2, pp.147–155, 2002.
- [9] W. Ostachowicz, M. Krawczuk, M. Cartmell, M. Gilchrist, Detection of delaminations using spectral finite element, *Proceedings of the First European Workshop on Structural Health Monitoring*, Paris, France, 10–12 July, pp.344–351, 2002.
- [10] W. Ostachowicz, M. Krawczuk, M. Palacz, Detection of delamination in multi-layer composite beams, *Key Engineering Materials*, Vols.245–246, pp.483–490, 2003.
- [11] W. Ostachowicz, M. Krawczuk, M. Cartmell, M. Gilchrist, Wave propagation in delaminated beam, *Computers and Structures*, 82, pp.475–483, 2004.
- [12] M. Krawczuk, W. Ostachowicz, Wave propagation in damaged structures, *Proceedings of the 15th International Conference on Computer Methods in Mechanics CMM 2003*, Wisła, June 3–6, pp.197–199, 2003.
- [13] M. Krawczuk, M. Palacz, W. Ostachowicz, Spectral plate element for crack detection with the use of propagating waves, *Materials Science Forum*, Vols.440–441, pp.187–194, 2003.
- [14] M. Krawczuk, M. Palacz, W. Ostachowicz, Wave propagation in plate structures for crack detection, *Finite Elements in Analysis and Design*, Vol.40, pp.991–1004, 2004.
- [15] S.E. Khadem, M. Rezaee, Introduction of modified comparison functions for vibration analysis of a rectangular cracked plate, *Journal of Sound and Vibration*, 236(2), pp.245–258, 2000.

ON THE DAMPING OF A PIEZOELECTRIC TRUSS

Andre Preumont

Active Structures Laboratory, Université Libre de Bruxelles
CP. 165-42, 50 Av. F.D. Roosevelt, B-1050 Brussels, Belgium
andre.preumont@ulb.ac.be

Abstract This paper re-examines the classical problem of active and passive damping of a piezoelectric truss. The active damping strategy is the so-called IFF (Integral Force Feedback) which has guaranteed stability; both voltage control and charge (current) control implementations are examined; they are compared to resistive shunting. It is shown that in all three cases, the closed-loop eigenvalues follow a root-locus; closed form analytical formulas are given for the poles and zeros and the maximum modal damping. It is shown that the performances are controlled by two parameters: the modal fraction of strain energy ν_i in the active strut and the electromechanical coupling coefficient k . The paper also briefly addresses the inductive shunting, for which a new parameter comes in: the tuning ratio ω_e/ω_i between the electrical circuit and the mechanical vibration. Due to space limitations, this paper includes only a small part of the sectional lecture at the 21st ICTAM.

1. Introduction

The active damping of a truss with piezoelectric struts has been largely motivated by producing large, lightweight spacecrafts with improved dynamic stability; this classical problem has received a lot of attention over the past 15 years and very effective solutions have been proposed (e.g.[1]). One of them known as Integral Force Feedback (IFF) is based on a collocated force sensor and has guaranteed stability [2].

Traditionally, the piezoelectric actuators have been controlled with a voltage amplifier; this is known to lead to substantial hysteresis caused by the ferroelectric behavior of the material, which requires an external sensor and closed-loop control for precision engineering applications. On the contrary, charge control allows to achieve a nearly linear relationship between the driving electrical value and the free actuator extension (e.g.

[3]). One of the purposes of this paper is to re-examine the theory of the IFF when it is implemented with a current amplifier (charge control).

For space applications, because of the inherent constraints of the launch loads, the space environment, and the impossibility of in-orbit maintenance, there is a strong motivation to reduce or eliminate the power electronics associated to the piezoelectric actuators as well as the complex electronics associated to sensing (particularly in the sub-micron range where the sensor sensitivity becomes an issue). This has motivated the use of passive electrical networks as damping mechanisms [4], [5], [6]. The efficiency of such a damping mechanism depends very much on the ability to transform mechanical (strain) energy into electrical energy, measured by the electromechanical coupling factor, and recent improvements have led to piezoelectric materials with coupling factors of $k_{33} = 0.7$ and more ($0.9 \sim 0.95$ is advertised for PMN-PT single crystal), making them a very attractive option for damping trusses. The second purpose of this paper is to compare the passive and the active options. They are presented in a very similar formalism and closed-loop results are presented, which allow a direct evaluation of the performances in terms of two physical parameters: the *modal fraction of strain energy* ν_i in the piezoelectric strut and the *electromechanical coupling coefficient* k . Due to space limitations, the discussion is restricted to SISO systems, but most of the extensions for decentralized MIMO control apply here (some of them are discussed in [2]).

Consider the constitutive equations of a one-dimensional piezoelectric material:

$$\begin{Bmatrix} D \\ S \end{Bmatrix} = \begin{bmatrix} \varepsilon^T & d_{33} \\ d_{33} & s^E \end{bmatrix} \begin{Bmatrix} E \\ T \end{Bmatrix}, \quad (1)$$

where the standard IEEE notations have been used. If one assumes constant strain, stress and electric fields over the actuator, the constitutive equation can be integrated over the volume of the actuator. With the notations of Fig. 1, one gets

$$\begin{Bmatrix} Q \\ \Delta \end{Bmatrix} = \begin{bmatrix} C & nd_{33} \\ nd_{33} & 1/K_a \end{bmatrix} \begin{Bmatrix} V \\ f \end{Bmatrix}, \quad (2)$$

where $Q = DAn$ is the total electric charge, $\Delta = Sl$ is the total extension, $f = AT$ is the total force and V is the total voltage applied to the piezo ($E = nV/l$). In Eq. (2), $C = \varepsilon^T An^2/l$ is the capacitance of the piezo, $K_a = A/(s^E l)$ is the stiffness of the piezoelectric strut under short-circuited conditions ($V = 0$). Alternatively, using the current

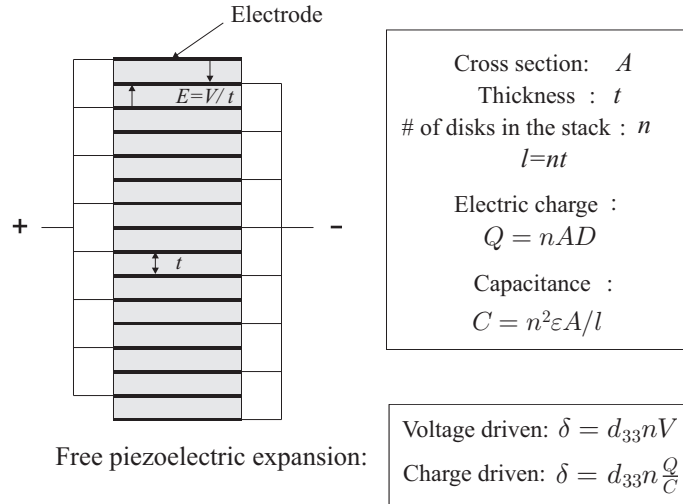


Figure 1. Piezoelectric linear actuator.

I instead of Q , Eq. (2) can be written

$$\begin{Bmatrix} I \\ \Delta \end{Bmatrix} = \begin{bmatrix} sC & snd_{33} \\ nd_{33} & 1/K_a \end{bmatrix} \begin{Bmatrix} V \\ f \end{Bmatrix}, \quad (3)$$

where s is the Laplace variable.

Consider the truss structure of Fig. 2, provided with an active strut consisting of a piezoelectric linear actuator co-linear with a force sensor; the total force in the strut is f . Assuming that the system is undamped, the dynamics of the truss is governed by

$$M\ddot{x} + K^*x = bf, \quad (4)$$

where K^* is the stiffness matrix with the active strut removed (Fig. 2) and b is the influence vector of the active strut in the global coordinate system (the non-zero components of b are the direction cosines of the active strut in the structure). To make things simpler, but without loss of generality, we will assume that the active strut is massless, so that the mass matrix M is the same, with and without the active strut. Note that the total extension of the active strut can be expressed in terms of the global structural displacements as

$$\Delta = b^T x, \quad (5)$$

where b^T is the transposed of the influence vector appearing in the previous equation.

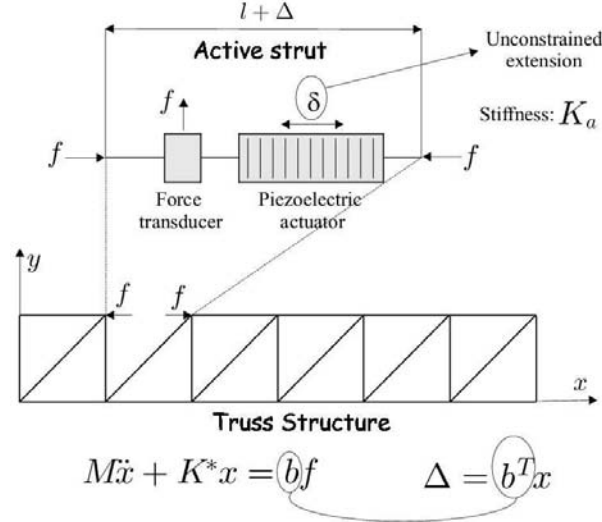


Figure 2. Truss equipped with an active strut (piezoelectric linear actuator co-linear with a force sensor).

2. Voltage Control

Combining Eqs. (3)-(5), one easily gets

$$M\ddot{x} + (K^* + K_a bb^T)x = bK_a d_{33} nV, \quad (6)$$

where $\delta = d_{33}nV$ is the unconstrained expansion under voltage V . In Laplace form, the equation can be written alternatively

$$Ms^2x + (K^* + K_a bb^T)x = bK_a \delta. \quad (7)$$

From Eq. (3), the output equation is

$$y = f = K_a(b^T x - \delta). \quad (8)$$

According to the IFF, the collocated force output is integrated and fed back to the voltage actuator:

$$\delta = \frac{g}{K_a s} y. \quad (9)$$

Combining Eqs. (7)-(9), one gets the closed-loop characteristic equation

$$[Ms^2 + (K^* + K_a bb^T) - \frac{g}{s+g}(K_a bb^T)]x = 0. \quad (10)$$

The asymptotic roots for $g \rightarrow 0$ are solutions of

$$[Ms^2 + (K^* + K_a bb^T)]x = 0, \quad (11)$$

which corresponds to the global truss when the electrodes of the active strut are short-circuited, while for $g \rightarrow \infty$ (open-loop zeros), the eigenvalue problem is reduced to

$$[Ms^2 + K^*]x = 0, \quad (12)$$

which corresponds to the situation where the axial contribution of the active strut has been removed.

3. Charge Control

Upon inverting Eq. (3) and using the fact that

$$k^2 = d_{33}^2 / (s^E \varepsilon^T) = n^2 d_{33}^2 K_a / C,$$

one gets

$$\begin{Bmatrix} V \\ f \end{Bmatrix} = \frac{K_a}{sC(1-k^2)} \begin{bmatrix} 1/K_a & -snd_{33} \\ -nd_{33} & sC \end{bmatrix} \begin{Bmatrix} I \\ \Delta \end{Bmatrix}. \quad (13)$$

Combining the second of these equations with Eq. (4), one gets

$$M\ddot{x} + \left[K^* + bb^T \frac{K_a}{1-k^2} \right] x = b \left[\frac{K_a}{1-k^2} \right] \cdot d_{33} n \frac{I}{sC}. \quad (14)$$

From the second Eq. (13), we note that $d_{33}nI/(sC)$ is the unconstrained expansion ($f = 0$) under the electric charge $Q = I/s$, that we will denote again by δ . As compared to Eq. (7) of the previous section, Eq. (14) shows that the piezoelectric strut behaves with an increased stiffness $K_a/(1-k^2)$, which is the strut stiffness under open electrodes conditions ($I = 0$). Also from Eq. (13), the output equation reads:

$$y = f = \frac{K_a}{1-k^2} (b^T x - \delta). \quad (15)$$

As in the previous section, we introduce the IFF feedback law

$$\delta = \frac{(1-k^2)g}{K_a s} y, \quad (16)$$

(same as Eq. (9), except for the stiffness of the piezoelectric strut). Combining Eqs. (14)-(16), one gets the closed-loop characteristic equation:

$$\left[Ms^2 + \left(K^* + \frac{K_a}{1-k^2} bb^T \right) - \frac{g}{s+g} \frac{K_a}{1-k^2} bb^T \right] x = 0, \quad (17)$$

identical to Eq. (10) except that the open electrode stiffness $K_a/(1-k^2)$ has been substituted to the short-circuited stiffness K_a . The asymptotic roots for $g \rightarrow 0$ (open-loop poles) are solutions of

$$\left[Ms^2 + \left(K^* + \frac{K_a}{1-k^2} bb^T \right) \right] x = 0, \quad (18)$$

which corresponds to the global truss when the electrodes of the active strut are open, while for $g \rightarrow \infty$, the eigenvalue problem is reduced to

$$[Ms^2 + K^*]x = 0, \quad (19)$$

which corresponds to the situation where the active strut has been removed. Thus, the open-loop zeros are identical to those for the voltage control case.

4. Passive Shunting

Figure 3(a) shows the electrical analog of the piezo. If a passive shunt of admittance Y_{SH} is connected in parallel with the piezo (Fig. 3(b)), the constitutive equations of the active strut become

$$\begin{Bmatrix} I \\ \Delta \end{Bmatrix} = \begin{bmatrix} sC + Y_{SH} & snd_{33} \\ nd_{33} & 1/K_a \end{bmatrix} \begin{Bmatrix} V \\ f \end{Bmatrix}. \quad (20)$$

This equation applies to active as well as passive control. In the former case, the control input is I or V ; in the latter case, $I = 0$ and V can be eliminated from Eq. (20). Combining with Eq. (4) and (5), one finds:

$$\left[Ms^2 + (K^* + K_a bb^T) + \frac{k^2 K_a bb^T}{(1-k^2) + Y_{SH}/sC} \right] x = 0. \quad (21)$$

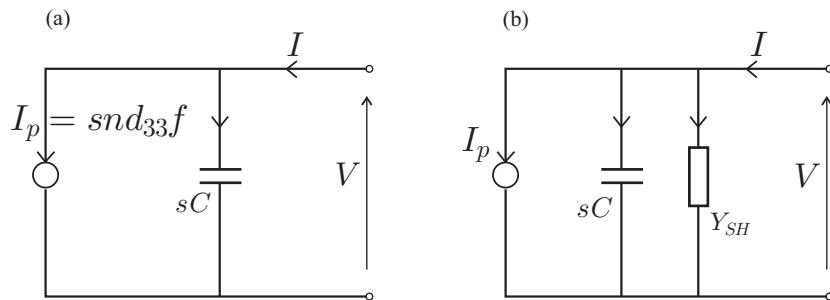


Figure 3. (a) Electrical analog of the piezo. (b) with a passive shunt.

Note that we recover the expected asymptotic forms for $Y_{SH} = 0$ (open electrodes)

$$\left[Ms^2 + \left(K^* + \frac{K_a}{1 - k^2} bb^T \right) \right] x = 0 \quad (22)$$

and, for $Y_{SH} = \infty$ (short-circuited electrodes):

$$[Ms^2 + (K^* + K_a bb^T)] x = 0. \quad (23)$$

In the special case of a resistive shunting,

$$\frac{Y_{SH}}{sC} = \frac{1}{sRC}. \quad (24)$$

5. Modal Damping

We now consider the closed-loop characteristic equation in modal coordinates and derive analytical results for the modal damping, for all three cases considered in the previous sections, namely IFF with voltage control, IFF with charge (current) control and resistive shunting. In all cases, the results take the form of a root locus with striking similarities.

IFF, Voltage Control

The development follows closely that of [2]; transforming in modal coordinates according to $x = \Phi z$, assuming normal modes normalized according to $\Phi^T M \Phi = I$; the mode shapes are solution of the eigenvalue problem Eq. (11). Denoting

$$\Phi^T (K^* + K_a bb^T) \Phi = \omega^2 = \text{diag}(\omega_i^2), \quad (25)$$

where ω_i are the natural frequencies of the truss with short-circuited electrodes, Eq. (10) is rewritten

$$\left[Is^2 + \omega^2 - \frac{g}{s + g} \Phi^T (K_a bb^T) \Phi \right] z = 0. \quad (26)$$

The matrix $\Phi^T (K_a bb^T) \Phi$ is in general fully populated; assuming that it is diagonally dominant, and neglecting the off-diagonal terms, it can be rewritten

$$\Phi^T (K_a bb^T) \Phi \simeq \text{diag}(\nu_i \omega_i^2) \quad (27)$$

where

$$\nu_i = \frac{\phi_i^T (K_a bb^T) \phi_i}{\phi_i^T (K^* + K_a bb^T) \phi_i}, \quad (28)$$

is the fraction of modal strain energy in the active strut when the truss vibrates according to mode i . According to the assumption Eq. (27), the

open-loop frequency response function (FRF) between the unconstrained expansion δ and the output force y of the collocated sensor can be written ([2], p.61)

$$G(\omega) = \frac{y}{\delta} = K_a \left[\sum_{i=1}^n \frac{\nu_i}{1 - \omega^2/\omega_i^2} - 1 \right], \quad (29)$$

where the sum extends to all the modes. Thus, the fractions of modal strain energy ν_i constitute the residues of the modal expansion of the open-loop FRF (Fig. 4). The fact that they are all positive guarantees alternating poles and zeros, as one would expect from a collocated (and dual) actuator/sensor configuration.

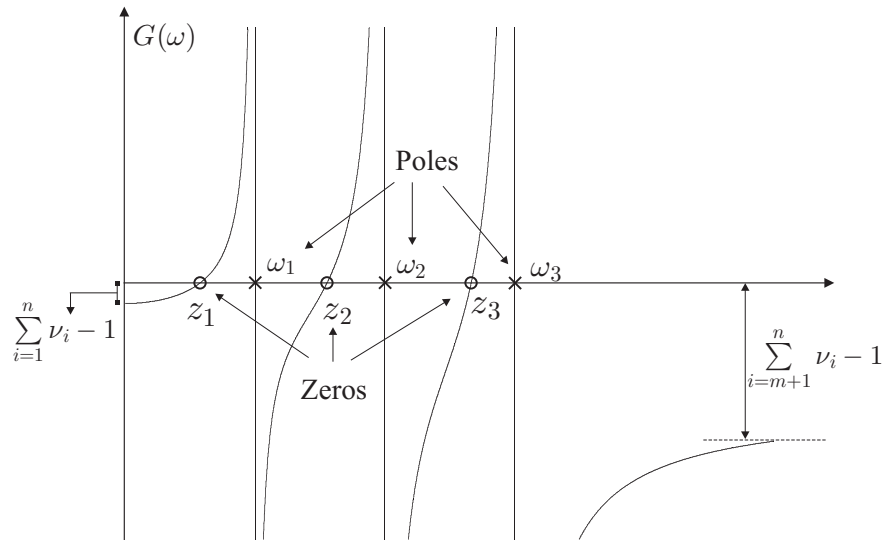


Figure 4. Open loop FRF $G(\omega)$ of the active truss.

It follows also from the assumption Eq. (27) that the eigenvalue problem Eq. (26) reduces to a set of uncoupled equations

$$s^2 + \omega_i^2 - \frac{g}{s+g} \nu_i \omega_i^2 = 0. \quad (30)$$

Denoting

$$z_i^2 = \omega_i^2 (1 - \nu_i), \quad (31)$$

Eq. (30) can be transformed into

$$1 + g \frac{s^2 + z_i^2}{s(s^2 + \omega_i^2)} = 0, \quad (32)$$

which shows that every mode follows a root locus with poles at $\pm j\omega_i$ and at $s = 0$, and zeros at $\pm jz_i$ (Fig. 5). Comparing with Eq. (12), the latter are readily identified as the natural frequencies of the structure when the axial contribution of the active strut has been removed. The maximum modal damping is given by

$$\xi_i^{max} = \frac{\omega_i - z_i}{2z_i} \quad (33)$$

and it is achieved for $g = \omega_i \sqrt{\omega_i/z_i}$ [2].

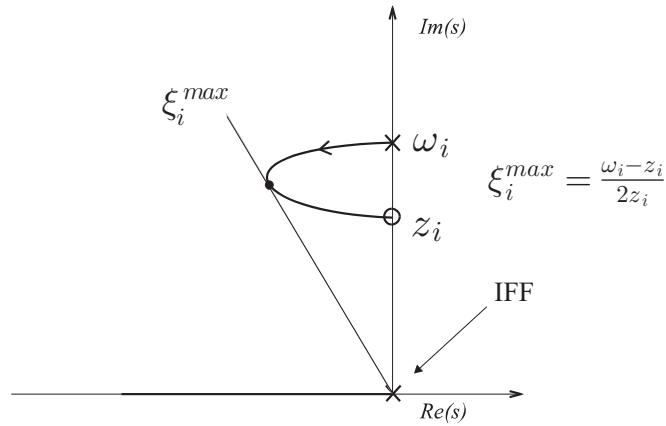


Figure 5. Root locus of the IFF, voltage control (only half of the locus is shown).

IFF, Charge Control

If we consider the charge implementation of the IFF (with a current amplifier), the closed-loop characteristic equation is given by Eq. (17). Transforming in modal coordinates as in the previous section, but using the normal modes of the truss with open electrodes, solutions of the eigenvalue problem (Eq. (18)), the natural frequencies and the fraction of modal strain energy are defined respectively by

$$\Phi^T (K^* + \frac{K_a}{1-k^2} bb^T) \Phi = \Omega^2 = \text{diag}(\Omega_i^2), \quad (34)$$

$$\nu_i = \frac{\phi_i^T (\frac{K_a}{1-k^2} bb^T) \phi_i}{\phi_i^T (K^* + \frac{K_a}{1-k^2} bb^T) \phi_i}. \quad (35)$$

Following the same development as in the previous section, one finds that the closed-loop poles follow the root locus

$$1 + g \frac{s^2 + z_i^2}{s(s^2 + \Omega_i^2)} = 0, \quad (36)$$

which is similar to that of Fig. 5, except that the poles at $\pm j\Omega_i$ correspond in this case to the natural frequencies of the truss with open electrodes; the zeros are identical to those of the previous case.

Resistive Shunting

For resistive shunting, the characteristic equation is given by Eq. (21) with $Y_{SH} = 1/R$; denoting $RC = \rho$ and transforming in modal coordinates as in the previous sections, one finds that every mode follow the characteristic equation

$$s^2 + \omega_i^2 + \frac{k^2 \nu_i \omega_i^2}{1 - k^2 + 1/\rho s} = 0 \quad (37)$$

which can be rewritten in a root locus form

$$1 + \frac{s^2 + \omega_i^2}{\rho(1 - k^2)s[s^2 + \omega_i^2 + \frac{k^2}{1 - k^2} \nu_i \omega_i^2]} = 0 \quad (38)$$

where $1/\rho(1 - k^2)$ plays the role of the gain in a classical root locus. At the denominator, one recognizes that the poles are located at the natural frequencies of the truss with open electrodes

$$\Omega_i^2 \simeq \omega_i^2 \left(1 + \frac{k^2}{1 - k^2} \nu_i \right), \quad (39)$$

while the zeros are at $\pm j\omega_i$, the natural frequencies of the truss with short-circuited electrodes. Figure 6 and Table 1 summarize the results of the three control configurations. Column 4 of Table 1 gives an analytical expression for the maximum achievable modal damping based on the poles and zeros; the approximation given in column 5 is based on

$$\xi_i^{max} = \frac{\omega_i - z_i}{2z_i} \simeq \frac{\omega_i^2 - z_i^2}{4z_i^2}. \quad (40)$$

The influence of the fraction of modal strain energy ν_i and the electromechanical coupling factor k appear much more clearly in the approximate results. Figure 7 shows a chart of the maximum achievable modal damping for the three control strategies, as a function of ν_i and k (based on the exact solution); the contour lines correspond to constant modal damping. Note that:

- (i) For the IFF with voltage control, the maximum damping is independent of the electromechanical coupling factor.

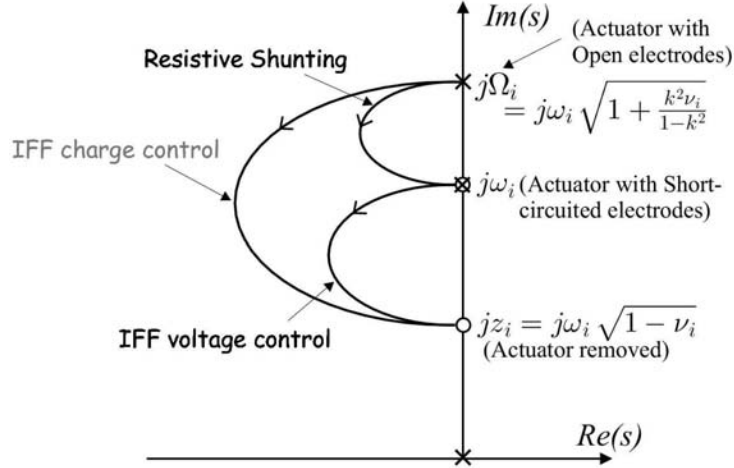


Figure 6. Root locus plots corresponding to various control configurations.

- (ii) The IFF with charge control gives always better performances than with voltage control; the advantage increases with k .
- (iii) Significant modal damping with resistive shunting can only be achieved when the electromechanical coupling factor is large (say $k \geq 0.7$); the availability of materials with such properties was actually part of the motivations for this study.

6. Inductive Shunting

Inductive shunting was first proposed in [4]; if the piezoelectric transducer is shunted on a RL circuit such that the natural frequency of the electrical circuit is tuned on the natural frequency of one mode, the system behaves like a tuned mass damper [6]. The extension to multiple modes has been addressed in [7], where the use of a set of parallel shunts is suggested; other methods are reviewed in [8]. This section is by no means comprehensive but, once again, the closed-loop poles for inductive shunting are presented in the form of a root locus where the major structural (ν_i), material (k), and electrical (ω_e/ω_i) parameters appear explicitly.

The characteristic equation for an arbitrary passive shunting is given by Eq. (21). Upon transforming in modal coordinates, with the same assumptions as in the previous section, one finds that the characteristic equation for mode i reads:

Table 1. Open-loop poles and zeros and maximum achievable modal damping

Type of Control	Open-loop poles	Open-loop zeros	ξ_i (exact solution)	ξ_i (approximate)
IFF (voltage control)	$\pm j\omega_i$	$\pm jz_i$ $\simeq \pm j\omega_i\sqrt{1-\nu_i}$	$\frac{\sqrt{1-\nu_i}-(1-\nu_i)}{2(1-\nu_i)}$	$\frac{\nu_i}{4(1-\nu_i)}$
IFF (charge control)	$\pm j\Omega_i$ $\pm j\omega_i\sqrt{1+\frac{k^2\nu_i}{1-k^2}}$	$\pm jz_i$	$\frac{\sqrt{1+\frac{k^2\nu_i}{1-k^2}}-\sqrt{1-\nu_i}}{2\sqrt{1-\nu_i}}$	$\frac{\nu_i}{4(1-\nu_i)(1-k^2)}$
Resistive shunting	$\pm j\Omega_i$	$\pm j\omega_i$	$\frac{\sqrt{1+\frac{k^2\nu_i}{1-k^2}}-1}{2}$	$\frac{k^2\nu_i}{4(1-k^2)}$

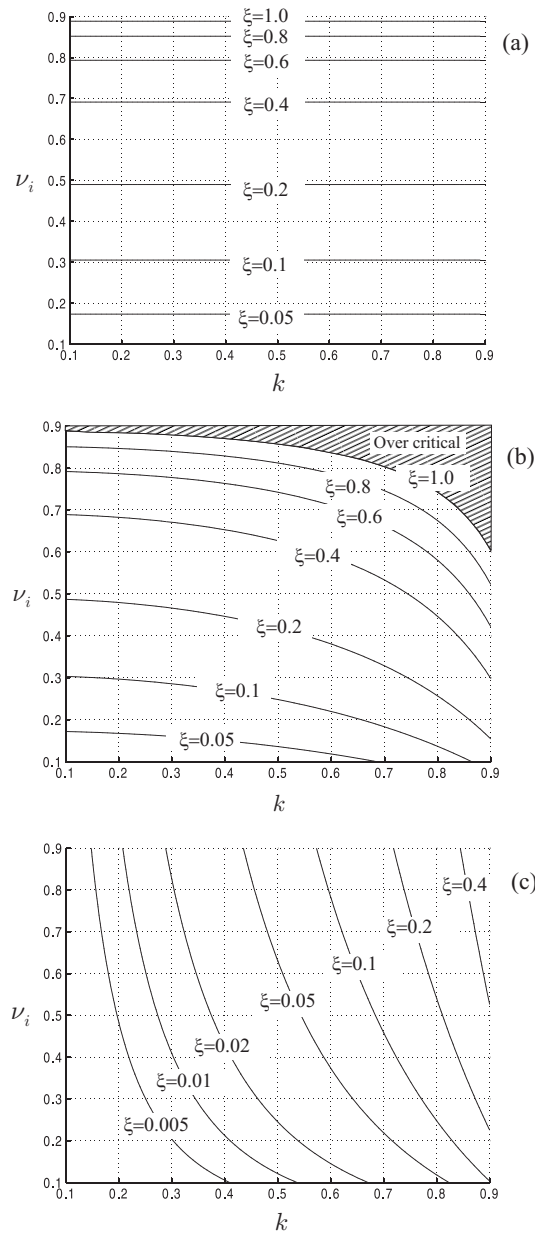


Figure 7. Maximum achievable modal damping as a function of ν_i and k . (a) IFF voltage control, (b) IFF charge control, (c) Resistive shunting.

$$s^2 + \omega_i^2 + \frac{k^2 \nu_i \omega_i^2}{1 - k^2 + Y_{SH}/sC} = 0. \quad (41)$$

If the passive shunt consists of a RL circuit, $Y_{SH} = (Ls + R)^{-1}$ and

$$\frac{Y_{SH}}{sC} = \frac{1}{LCs^2 + RCs}. \quad (42)$$

Upon introducing the electrical natural frequency $\omega_e^2 = (LC)^{-1}$ and the fraction of critical damping ξ_e such that $2\xi_e\omega_e = R/L$, one gets

$$\frac{Y_{SH}}{sC} = \frac{1}{s^2/\omega_e^2 + 2\xi_e s/\omega_e} \quad (43)$$

and the characteristic Eq. (41) becomes

$$s^2 + \omega_i^2 + \frac{k^2 \nu_i \omega_i^2 (s^2 + 2\xi_e \omega_e s)}{(1 - k^2)(s^2 + 2\xi_e \omega_e s) + \omega_e^2} = 0. \quad (44)$$

This equation can, once again, be rearranged in the form of a root locus

$$1 + 2\xi_e \omega_e \cdot \frac{s(s^2 + \Omega_i^2)}{(s^2 + p_1^2)(s^2 + p_2^2)} = 0, \quad (45)$$

in which $2\xi_e \omega_e$ plays the role of the gain. Ω_i is the natural frequency with open electrodes ($\pm j\Omega_i$ are indeed the asymptotic poles when the resistor R becomes very large), and p_1^2 and p_2^2 are solutions of the characteristic equation

$$\frac{s^4}{\omega_i^4} + \frac{s^2}{\omega_i^2} \left[1 + \frac{k^2 \nu_i}{1 - k^2} + \frac{\omega_e^2}{\omega_i^2} \frac{1}{1 - k^2} \right] + \frac{\omega_e^2}{\omega_i^2} \frac{1}{1 - k^2} = 0 \quad (46)$$

which, in addition to ν_i and k , also depends on the tuning ratio ω_e/ω_i between the electrical circuit and the mechanical vibration. The upper half of the root locus consists of two loops whose size depends on the values of the parameters; the depth of the smaller loop in the left half plane tends to be bigger when the tuning ratio is close to 1.

7. Conclusions

Various active and passive ways of damping a piezoelectric truss have been examined; the results have been presented in the common form of a root locus, and analytical formulae have been established for the maximum achievable modal damping. The influence of the modal fraction of strain energy ν_i in the active strut (structural parameter) and the electromechanical coupling coefficient k (material parameter) on the performance has been pointed out.

Acknowledgments

This study was partly supported by ESA (*SSPA* project).

References

- [1] A. Preumont, J.P. Dufour, C. Malekian, Active damping by a local force feedback with piezoelectric actuators, *AIAA J. of Guidance*, Vol.15, No 2, 390-395, March-April, 1992.
- [2] A. Preumont, *Vibration Control of Active Structures, An Introduction*, (2nd Edition), Kluwer, 2002.
- [3] C. Dörlemann, P. Muss, M. Schugt, R. Uhlenbrock, New high speed current controlled amplifier for PZT multilayer stack actuators, *ACTUATOR-2002*, Bremen, June, 2002.
- [4] R.L. Forward, Electronic damping of vibrations in optical structures, *Journal of Applied Optics*, Vol.18, 690-697, March, 1979.
- [5] N.W. Hagood, A. von Flotow, Damping of structural vibrations with piezoelectric materials and passive electrical networks, *Journal of Sound and Vibration*, Vol.146, No 2, 243-268, 1991.
- [6] N.W. Hagood, E.F. Crawley, Experimental investigation of passive enhancement of damping for space structures, *AIAA J. of Guidance*, Vol.14, No 6, 1100-1109, Nov.Dec. 1991.
- [7] J.J. Hollkamp, Multimodal passive vibration suppression with piezoelectric materials and resonant shunts, *J. Intell. Material Syst. Structures*, Vol.5, Jan.1994.
- [8] S.O.R. Moheimani, A survey of recent innovations in vibration damping and control using shunted piezoelectric transducers, *IEEE Transactions on Control Systems Technology*, Vol.11, No 4, 482-494, July 2003.

STRENGTH OF NANOSTRUCTURES

*Do materials become insensitive to flaws at nanoscale?
An answer based on Quantized Fracture Mechanics
and Nanoscale Weibull Statistics*

Rodney S. Ruoff

*Department of Mechanical Engineering
Northwestern University, Evanston, IL 60208-3111, USA*
r-ruoff@northwestern.edu

Nicola M. Pugno

*Department of Structural Engineering
Politecnico di Torino, Corso Duca degli Abruzzi 24, 10129, Italy*
nicola.pugno@polito.it

Abstract Quantized Fracture Mechanics is applied for predicting the strength of nanostructures. An application to defective carbon nanotubes, compared with atomistic simulations and experiments, clearly shows that atomistic flaws in nanotubes can strongly reduce their strength, e.g., by a factor of $\sim 20\%$ if just one atom vacancy is considered. The analysis suggests that very few defects, relatively small in size, were responsible for breaking of the tested nanotubes. This result is confirmed by an application of “Nanoscale Weibull Statistics”. Thus, it seems to us that the answer to the question posed in the title is – at least in general – “no”.

Keywords: Nanomechanics, nanostructures, nanotubes, quantized fracture mechanics, nanoscale Weibull statistics, quantized strength

1. Introduction

In Linear Elastic Fracture Mechanics [1], the energy release rate is defined as $G = K_I^2/E' + K_{II}^2/E' + K_{III}^2(1 + \nu)/E$, where $K_{I,II,III}$ are the stress-intensity factors for modes I, II, III of crack propagation, with $E' = E$ (for plane stress) or $E' = E/(1 - \nu^2)$ (for plane strain), where E is the Young's modulus and ν is the Poisson's ratio of the material.

According to classical Fracture Mechanics, the crack propagation will arise for [1]:

$$G \equiv -dW/dA = G_C \quad \text{or} \quad K_{I,II,III} = K_{I,II,III C} \quad (1)$$

where W is the total potential energy and the subscript C denotes a critical condition for the crack propagation (G_C and $K_{I,II,III C}$ are the fracture energy and toughness of the material). On the other hand, according to Quantized Fracture Mechanics [2] (QFM) the crack propagation will arise for:

$$G^* \equiv -\Delta W/\Delta A = G_C \quad \text{or} \quad K_{I,II,III}^* \equiv \sqrt{\langle K_{I,II,III}^2 \rangle_A^{A+\Delta A}} = K_{I,II,III C} \quad (2)$$

where

$$\langle \cdot \rangle_A^{A+\Delta A} \equiv \frac{1}{\Delta A} \int_A^{A+\Delta A} \cdot \, dA.$$

QFM assumes “dissipation energy” in quanta $G_C \Delta A$ where ΔA is the fracture quantum. Values for the stress intensity factors $K_{I,II,III}$ are available for the most interesting cases [3]: thus QFM can be applied by integration (Eq. (2)) in a very simple way. In contrast to classical fracture mechanics, that can treat only “large” (with respect to the fracture quantum) and sharp (vanishing tip radius) cracks, QFM has no restriction in treating defects with any size and shape [2]. Thus, QFM can be applied also at nanoscale, where classical fracture mechanics does not work [4].

2. Do Materials Become Insensitive to Flaws at Nanoscale?

Consider a linear elastic infinite plate in tension, of uniform thickness t , with a blunt crack with tip radius ρ and length $2l$, orthogonal to the applied far field σ (crack opening mode I). The material is described by the fracture toughness K_{IC} and by the fracture quantum at the considered size-scale $\Delta A = at$. Applying QFM, the failure strength is predicted as [2]:

$$\sigma_f(l, \rho) = K_{IC} \sqrt{\frac{1 + \rho/2a}{\pi(l + a/2)}} = \sigma_C \sqrt{\frac{1 + \rho/2a}{1 + 2l/a}} \quad (3)$$

where σ_C is the strength of the plain structure (coincident with the ideal material strength only at a very small scale); accordingly, the fracture quantum is estimated as $a \approx 2K_{IC}^2/(\pi\sigma_C^2)$. Equation (3) shows that

for $2l \ll a$ (“short” cracks) the structure becomes insensitive to flaws, whereas for $2l \gg a$ (and $\rho = 0$) QFM recovers classical fracture mechanics, that is not able to predict such “short crack behaviour”. Roughly speaking, it is clear that structures having characteristic size of the order of the fracture quantum are predicted to be insensitive to flaws. Thus materials with a large value of $a \approx 2K_{IC}^2/(\pi\sigma_C^2)$ present a significant zone in which they become insensitive to flaws, in agreement to what has been recently observed in bio-nanocomposites [4]. On the other hand, at nanoscale such a parameter can be *of the order of* the interatomic spacing, as observed for nanotubes (see next section). Thus, the statement reported in the title of Ref. [4] (“materials become insensitive to flaws at nanoscale”) cannot be considered to be true in general, as demonstrated in the next section.

The Counterexample of Carbon Nanotubes

The tensile strengths of individual multiwalled carbon nanotubes (MWCNTs) were measured [5] with a *nanostressing stage* composed of two opposing atomic force microscope (AFM) tips, Fig. 1a,b, located in a scanning electron microscope (SEM).

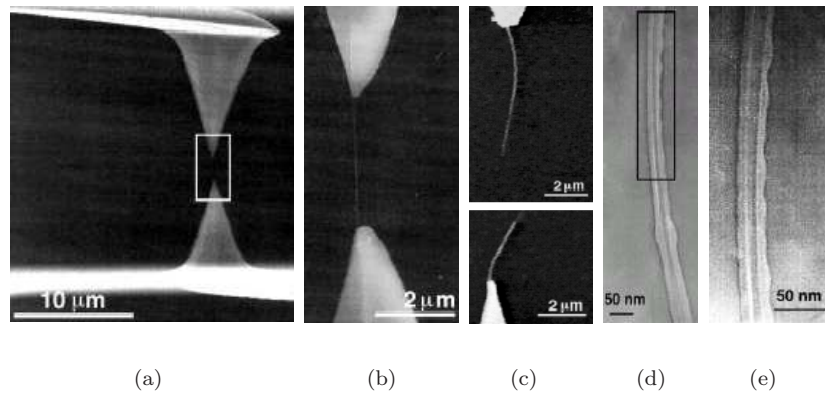


Figure 1. Experiments on fracture strength of nanotubes, [5].

The tensile experiment was prepared and observed entirely within the microscope and was recorded on video until fracture, [5]. The sum of the fragment lengths, Fig. 1c, far exceeded the original nanotube length. This apparent discrepancy was explained by a *sword-in-sheath* type fracture mechanism, similar to that observed in carbon fibers, i.e., the MWCNTs broke in the outermost layer. The tensile and fracture strength of this layer ranged from 11 to 63 GPa for the set of 19 MWCNTs that were loaded (Table 1). Analysis of the stress-strain curves for indivi-

dual MWCNTs indicated that the Young's modulus E of the outermost layer varied from 270 to 950 GPa. Transmission electron microscopic (TEM) examination of the broken nanotube fragments revealed a variety of structures, such as a nanotube ribbon, a wave pattern, and partial radial collapse, Figs. 1d,e.

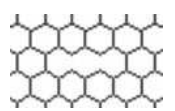
The experimental results on nanotubes [5] show distinct clusters about a series of decreasing values of strength, with the maximum 63 GPa, and the other values "quantized" at 43, 36–37, 25–26, 19–20 and 11–12 GPa, see the complete data set collection reported in Table 1. The measured higher strength of 63 GPa is not in agreement with the ideal tensile strength of nanotubes (~ 100 GPa). Moreover, the observed strength quantization could be related to the quantization in the size of the defects.

Table 1. Experiments on fracture strength of nanotubes [5].

Test number	Diameter [nm]	Length [μm]	Strength [GPa]
1	28.0	4.10	11
2	28.0	6.40	12
3	19.0	3.03	18
4	31.0	1.10	18
5	28.0	5.70	19
6	19.0	6.50	20
7	18.5	4.61	20
8	33.0	10.99	21
9	28.0	3.60	24
10	36.0	1.80	24
11	29.0	5.70	26
12	13.0	2.92	28
13	40.0	3.50	34
14	22.0	6.67	35
15	24.0	1.04	37
16	24.0	2.33	37
17	22.0	6.04	39
18	20.0	8.20	43
19	20.0	6.87	63

We apply QFM assuming the fracture quantum to be identical to the distance between two adjacent broken chemical bonds, i.e., $a \approx \sqrt{3}r_0$, with $r_0 \approx 1.42 \text{ \AA}$ interatomic length. For example, considering defects like n adjacent vacancies $2l = na$ in Eq. (3). This case was also treated by molecular mechanics (MM) atomistic simulations [6]. The comparison between these MM simulations and the predictions of Eq. (3) (we thus neglect here boundary effects) is summarized in Table 2;

Table 2. MM [6] and QFM [2] comparison of fracture strength of nanotubes with n adjacent vacancies (the graph reports the example of $n=2$, the applied load is vertical). The observed strengths are in parentheses [5].

Strength [GPa]	$n=2$ (63)	$n=4$ (...)	$n=6$ (43)	$n=8$ (39)	
MM - (80,0)	64.1	50.3	42.1	36.9	
QFM	64.1	49.6	42.0	37.0	

the MM-calculated strengths clearly follow the $(1+n)^{-1/2}$ dependence predicted by QFM with a fit of $\sigma_C \sqrt{1 + \rho/2a} = 111$ GPa. Starting from the value of the ideal strength [6] $\sigma_C = 93.5$ GPa, it gives a reasonable tip radius of the atomistic flaws as $\rho \approx 0.8a \approx 2.0$ Å. In Table 2 between brackets are reported the measured strengths. The first three values are well fitted assuming atomistic flaws having lengths of $n = 2, 4, 8$ (in units of fracture quanta). Thus, it is clear that atomistic flaws affect the strength of nanotubes. For a more detailed comparison, including also atomistic pinhole defects, see the QFM paper [2].

3. Nanoscale Weibull Statistics

Weibull statistics [7] for strength (or time to failure) of solids and deterministic Linear Elastic Fracture Mechanics do not apply properly at the nanoscale. Weibull statistics assumes that the number of critical flaws is proportional to the volume or to the surface area of the structure, whereas single crystal nanostructures are anticipated to be either defect-free or to have a small number of (critical) defects. As classical Fracture Mechanics has been modified (also) for nanoscale applications (by QFM [2]), similarly Weibull statistics has been modified by Nanoscale Weibull Statistics [8] (NWS) for describing the distribution of the strength of solids (also) at the nanoscale.

The simplest form of the volume-flaw based Weibull distribution [7] is

$$F(\sigma) = 1 - \exp \left[-V \left(\frac{\sigma}{\sigma_0} \right)^m \right],$$

where $F(\sigma)$ is the probability that a fiber will fail under tensile stress σ , σ_0 and m are Weibull's scale (with anomalous physical dimension) and shape (dimensionless) parameters respectively, and V is the fiber volume. The surface-flaw based Weibull distribution simply replaces V with the surface area S of the fiber (note that σ_0 , m are then different compared to the σ_0 , m obtained from the volume-flaw based Weibull distribution).

The cumulative probability $F(\sigma_i)$ can be obtained experimentally as

$$F(\sigma_i) = \frac{i - 1/2}{N},$$

where N is the total number of tests and the observed strengths $\sigma_1, \dots, \sigma_N$ are ranked in ascending order [9]. The volume- and surface-based approaches become identical for the case of fracture of the external wall of nanotubes under tension, such as for the 19 nanotubes experimentally investigated [5]. This is true because $V = St = \pi DLt$, where t is the constant spacing between nanotube walls (~ 0.34 nm) and thus assigned as the shell thickness, and D and L are the nanotube diameter and length, respectively.

In terms of the number n of critical defects, Weibull statistics becomes:

$$F(\sigma) = 1 - \exp \left[-n \left(\frac{\sigma}{\sigma_0} \right)^m \right]. \quad (4)$$

Weibull statistics applied to fibers assumes $n = kD^\alpha L^\beta$, with $\alpha = 2$ and $\beta = 1$ if volume-flaws are considered, or $\alpha = 1$ and $\beta = 1$ if surface-flaws are considered (and k is a constant). On the other hand, we note that for nearly defect-free structures, one may assume “point-flaws” defects, i.e., that failure occurs at $n = 1$ (or equivalently at a value of n which is independent of the specimen size) for which $\alpha = 0$, $\beta = 0$, so that in general, it may be more appropriate to expect $0 \leq \alpha \leq 2$ and $0 \leq \beta \leq 1$. For example, if “length-flaws” defects are considered $\alpha = 0$ and $\beta = 1$. We note that the proposed NWS, that is, Eq. (4) with $n = kD^\alpha L^\beta$ and $0 \leq \alpha \leq 2$, $0 \leq \beta \leq 1$ (or $n = kH^\alpha L^\beta W^\gamma$ for rectangular cross-section areas $W \times H$, with $0 \leq \alpha, \beta, \gamma \leq 1$), corresponds for the limiting case of $\beta = 1$ to the modified Weibull distribution proposed for the study of the strength of sapphire whiskers [9].

Defining the nominal strength σ_n of the material for a specified value of F , e.g., $F(\sigma = \sigma_n) = (1 - e^{-1}) = 0.63$ (σ_n is thus defined as the strength corresponding to the 63% probability of failure), the corresponding size/shape-effect is predicted according to Eq. (4) as:

$$\sigma_n = \sigma_0 k^{-1/m} D^{-\alpha/m} L^{-\beta/m}. \quad (5)$$

The corresponding size-effect (that considers self-similar structures, i.e., $D \propto L$) is a power-law, in agreement with the Carpinteri's fractal law [10]. Strictly speaking Eq.(4) is defined for $\sigma < \sigma_C$, where σ_C is the (finite) ideal strength of solids, whereas obviously $F(\sigma \geq \sigma_C) \equiv 1$. Accordingly, in Eq. (5) σ_n is limited by σ_C . Note that the ratio between the exponents of D and L in Eq. (5) is equal to α/β . In the classical Weibull

statistics this ratio is set equal to 2 (volume-flaws) or 1 (surface-flaws). In contrast, as recently emphasized in [9], the ratio α/β can also be significantly different (for example for sapphire ($\alpha\text{-Al}_2\text{O}_3$) whiskers it was observed to be equal to 7 or 15). Thus, it is clear that such size/shape effects cannot be explained by Weibull statistics, whereas Eq. (5) is compatible with the observations.

The standard Weibull statistics [7] applied to nanotubes [5] (Table 1) is shown in Fig. 2. The Weibull modulus is found to be ~ 3 . This represents the first estimation of the Weibull modulus for nanotubes. However, the correlation is very poor, showing a coefficient of correlation $R^2 = 0.67$.

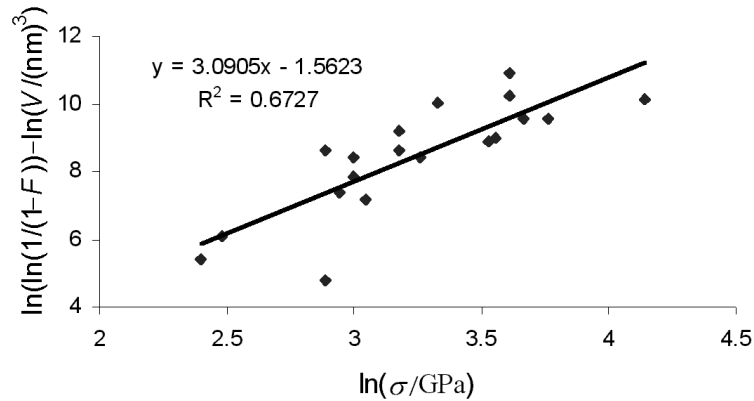


Figure 2. Weibull Statistics [7] applied to the observations on nanotubes [5].

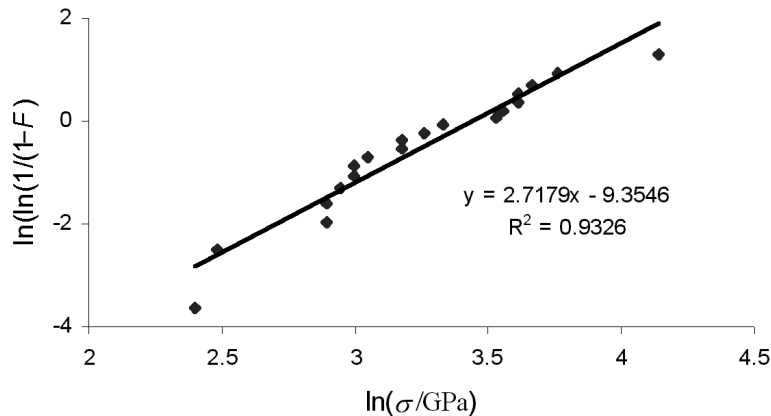


Figure 3. Nanoscale Weibull Statistics [8] applied to the observations on nanotubes [5].

In contrast, applying the NWS [8] with $n = 1$, we find $m \sim 2.7$ (and $\sigma_0 \approx 31$ GPa) with a significantly better correlation of $R^2 = 0.93$ (Fig. 3; please compare also Figs. 2 and 3).

In particular, the statistical data analysis suggests that a small number of defects (perhaps simply one critical nanoscale defect in each of the 19 different carbon nanotubes that were fractured) were responsible for these nanotubes breaking. The QFM deterministic argument is assessed by the NWS approach. Small numbers of atomistic defects can be crucial for the strength of nanostructures.

4. Concluding Remarks

The analysis, based on Quantized Fracture Mechanics and Nanoscale Weibull Statistics, corroborated by atomistic simulations and direct measurements, suggests that the answer to the question posed in the title must be considered – at least in general – to be “no”.

Acknowledgements

RSR gratefully acknowledges the support from the NSF grant “Mechanics of Nanoropes” (NSF #0200797, Ken Chong program manager), and the NSF grants NIRT: Electrical and Mechanical Properties of Boron and Metal and Nanoscale Devices Built from them (NSF #0210120) and NIRT: Synthesis, Characterization and Modeling of Aligned Nanotube Arrays for Nanoscale Devices and Composites (NSF #030450); from the Office of Naval Research “Mechanics of Nanostructures” grant under award No. N000140210870 and the NASA University Research, Engineering and Technology Institute on Bio Inspired Materials (BI-Mat) under award No. NCC-1-02037 (Jeff Jordan, program manager).

References

- [1] A.A. Griffith, The phenomenon of rupture and flow in solids, *Phil. Trans. Roy. Soc.*, Vol. A221, pp.163–198, 1921.
- [2] N. Pugno and R. Ruoff, Quantized fracture mechanics, *Philosophical Magazine*, Vol. 84/27, pp.2829–2845, 2004.
- [3] H. Murakami, *Stress Intensity Factors Handbook*, Oxford (UK), Publ. Pergamon, 1986.
- [4] H. Gao, B. Ji, I.L. Jaeger, E. Arzt, and P. Fratzl, Materials become insensitive to flaws at nanoscale: lesson from Nature, *Proc. National Academy of Sciences USA*, Vol. 100, pp.5597–5600, 2003.
- [5] M.-F. Yu, O. Lourie, M.J. Dyer, K. Moloni, T.F. Kelly, and R.S. Ruoff, Strength and breaking mechanism of multiwalled carbon nanotubes under tensile load, *Science*, Vol. 287, pp.637–640, 2000.

- [6] T. Belytschko, S.P. Xiao, and R.S. Ruoff, Effects of defects on strength of nanotubes: experimental-computational comparison, Los Alamos National Laboratory, Preprint Archive, *Physics*, 1–6, 2002.
- [7] W. Weibull, *A statistical theory of the strength of materials*. *Ingénjörsvetenskapsakademiens Handlingar*, n.151, 1939.
- [8] N. Pugno and R. Ruoff, *Nanoscale Weibull Statistics*, submitted to Journal of Aerospace Engineering; Special Issue on Nanomechanics, 2004.
- [9] Y.T. Zhu, W.R. Blumenthal, S.T. Taylor, and T.C. Lowe, Analysis of size dependence of ceramic fiber and whisker strength, *J. Am. Ceram. Soc.*, Vol. 80, pp.1447–1452, 1997.
- [10] A. Carpinteri, Fractal nature of material microstructure and size effects on apparent mechanical properties, *Mechanics of Materials*, Vol. 18, pp.89–101, 1994.

MICROMECHANICS OF CELLS

Viscoelastic Microscopy of Cells

Erich Sackmann, Andreas Reuther, and Doris Heinrich
*E22, Physics Department, Technische Universität München,
D-85747 Garching, Germany*

Abstract Magnetic tweezer microrheometry combined with shear field mapping allows local measurements of mechanical properties of cell envelopes and cytoplasm. The viscoelastic impedance of cell envelopes reflects the rheological signature of the actin networks enabling real time studies of structural reorganization of actin cortices by cell stimulating agents. The cytoplasm behaves as viscoplastic bodies. Velocity distributions of endosomes/magnetosomes exhibit log-normal distributions driven by intracellular transport forces of 5 to 30 pN.

Keywords: Micro-viscoelasticity of cells, actin network, plasticity of cells, intracellular transport

1. Introduction

Mechanical forces control life processes from nanoscopic to macroscopic scales. Forces generated by molecular motors drive the DNA replication or mediate the intracellular material transport between the nuclear region and the cell periphery. Cell adhesion is controlled by complex interplay of universal interfacial forces, specific lock-and-key forces and the chemo-elastic forces generated within the cell envelope (Sackmann and Bruinsma, 2002). On a higher level of organisation mechanical forces determine the structure and mechanical strength of biomaterials such as wood and bones (Lichtenegger, 1999 and Ashby, 1999). By self assembly of the constituents, cells act both as mechanical sensors and as material producing machines which can adapt the production of constituents such as cellulose, collagen or bone in such a way that the material properties are optimized.

Since the mechano-chemical control of biological processes are determined by the continuum mechanical properties of the biomaterials systematic studies of viscoelastic moduli of the materials making up cells

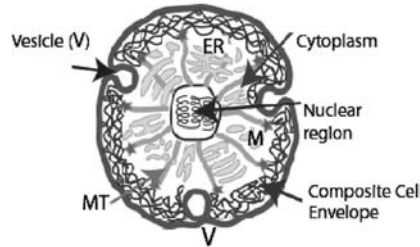


Figure 1. Mechanical model of cells assumed to be composed of three viscoelastic sub-bodies: (i) the composite cell envelope, (ii) the cytoplasm and (iii) the nuclear shell with the associated centrosome acting as focal center of star like arrangement of microtubule (MT). Note that microtubules are coupled to the actin cortex and that plasma membranes can exchange material with cytoplasm through exchange of vesicles.

(e.g. membranes and the cytoskeleton) or tissue (collagen or bone) are essential for our understanding of the mechanical control of cell signal processes. On the other hand we know from long standing material research (in fact since the time of Maxwells introduction of the concept of viscoelasticity at about 1850) that measurements of viscoelastic impedances can yield valuable insights into the dynamics of structural reorganisations of complex materials. The systematic study of the unique continuum mechanical properties of biomaterials may also stim-

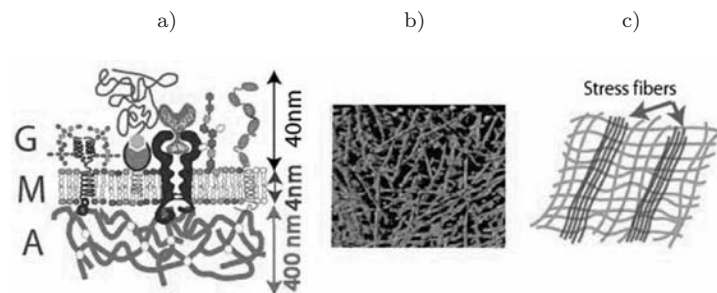


Figure 2. a) Composite shell of cell envelope consisting (i) of glycocalix (G) mediating the communication with the environment; (ii) of lipid/protein bilayer (M) site of numerous biochemical processes; and (iii) of actin cortex (dots mark crosslinkers). The lipid/protein bilayer and glycocalix are called plasma membrane in the following. b) Electron tomography image of randomly crosslinked actin which is characteristic for the structure of cortex of quiescent cells (case of Dictyostelium Discoideum after Medalia et al 2003). c) In stimulated cells (such as endothelial cells after stimulation with histamine) actin bundles are formed owing to activation of bundles favoring crosslinkers such as filamin and myosin.

ulate the development of new technical materials with novel mechanical properties.

For the introduction of the concept of micro-viscoelasticity it is helpful to consider cells to be designed of three distinct, but mutually coupled sub-bodies: (i) the (composite) cell envelope, (ii) the cytoplasm and (iii) the nucleus with the associated centrosome. The cell envelope (Fig. 2) is a composite shell made up of the lipid/protein bilayer (the plasma membrane) and the associated actin cortex. The $\sim 0.3 \mu\text{m}$ thick actin cortex is locally coupled to intracellular domains of cell surface receptors (Fig. 2a) by coupling proteins such as talin and vinculin (Alberts et al., 2002). In quiescent cells it forms a random network while after activation bundles and muscle-like structures can form.

2. Concept of Microrheometry

Figure 3 shows the concept of microrheometry. A magnetic bead (of radius $a \sim 1 \mu\text{m}$) is embedded in an entangled actin network. This force probe is pulled by a step-like force, σ generated by an inhomogeneous magnetic field switched on at time t . In the linear regime of deformation the deflection $u(t)$ is proportional to the force amplitude f_o : $u(t) = J(t)f_o/6\pi a$. The proportionality factor is $J(t)$ (the so-called shear compliance $J(t)$), which is a measure for the softness of the material studied. Note that the geometric factor $6\pi a$ is introduced to yield the familiar equation for the friction coefficient $\zeta = 6\pi\eta a$ in a fluid of viscosity η (Ziemann et al 1994).

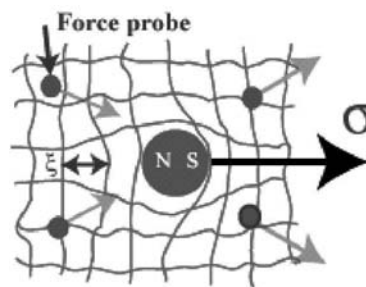


Figure 3. Concept of microrheometry with magnetic tweezers. Illustration of the (inhomogeneous) deformation of the actin network by a magnetic bead subjected to a step-like force \tilde{f}_o , $u(t)$ denotes the deflection of the bead at a time t and the thin arrows indicate the deformation field. ξ is the mesh size of the network. The deformation field can be visualized by analysing the induced deflection of nonmagnetic colloids (small beads) also embedded into the network.

It is often helpful to discuss the viscoelastic responses in terms of mechanical equivalent models composed of a linear array of springs and dashpots in parallel (so-called Voigt bodies; Fig. 4c):

$$J(t) = \sum_{i=1}^N \left(\frac{f_o}{k_i} \right) \left(1 - \exp \left(-\frac{t}{\tau_i} \right) \right). \quad (1)$$

The viscoelastic behaviour is determined by two sets of viscoelastic parameters: the spring constants, k_i , and the frictional coefficients $\zeta_i = k_i \tau_i$, where τ_i is the time it takes to switch on the element $\#i$ (hence the name retardation function for $J(t)$).

An alternative experiment would be to measure the time dependence of the internal force $\sigma(t)$ exerted on the magnetic bead after a sudden deformation $u(t)$ of the whole network. The shear stress observed by our reporter bead would then again follow a linear law

$$\sigma(t) = G(t)u(t) \quad (2)$$

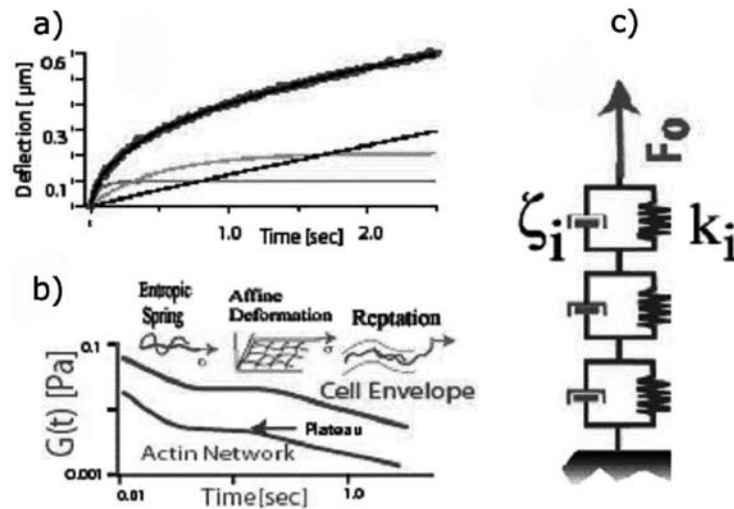


Figure 4. a) Thick curve: typical viscoelastic retardation function of the cell envelope evoked by the force pulse of 5 pN. The thin drawn curves show responses of three Voigt bodies which represent the measured response curves optimally. b) Representation of viscoelastic responses in terms of relaxation functions $G(t)$. The curves for entangled actin networks and the cell envelope are shown together to demonstrate their similar shape (cf. Fig. 7 below). Insets at top illustrate the molecular processes associated with the three relaxation regimes. c) Mechanical equivalent model (three Voigt bodies) representing the response curve.

$\sigma(t)$ is a measure for the relaxation of the force an internal observer would feel after the initial deformation and therefore $G(t)$ is called the relaxation modulus.

The two moduli $J(t)$ and $G(t)$ are interrelated by the convolution

$$\int_0^t J(t-t')G(t')dt' = t \quad (3)$$

$G(t)$ can be calculated from the creep compliance $J(t)$ and vice-versa by numerical integration (Feneberg et al. 2001 and 2004).

The convolution of the retardation function $J(t)$ in Fig. 4a is shown in Fig. 4c. It is seen that the relaxation moduli of the entangled network and the cell envelope agree astonishingly well. One can clearly distinguish three regimes of $G(t)$: (I) a rapid relaxation at short times ($t = \tau_e < 0.04$ s); (II) a plateau regime where $G(t)$ is stationary over nearly an order of magnitude in time and (III) a terminal regime at $t = \tau_t \sim 0.2$ sec where the bead starts to flow feeling only a frictional tension $\sigma(t) = 6\pi\eta a du(t)/dt$.

3. From Filament Dynamics to Viscoelasticity of Networks

F-Actin is a prototype of a semiflexible macromolecule since it exhibits pronounced thermally excited bending fluctuations (cf Fig. 6a). The flexibility of the filaments is characterized by a bending modulus B or persistence length $L_p (= B/k_B T)$. L_p is a measure for the contour length along the filament over which the local tangents to the filaments are correlated. The elastic behaviour of a single actin filament depends on the length L . For $L \ll L_p$ the filament behaves as a rigid rod and its elasticity is determined by the bending flexibility B . For $L \gg L_p$ it behaves more as an entropic spring similar to normal polymers but the spring constant $\gamma = B^2/k_B T L^4$ depends on the bending modulus; in striking contrast to the universal law $\gamma = 2/3 \cdot k_B T$ characteristic for flexible molecules. The actin filaments are very sensitive with respect to forces parallel to the long axis and show mechanical instabilities (buckling) at a force of a few pN. Eulers theory of rigid rods is more appropriate to describe the mechanical properties of short filaments (Wilhelm and Frey 1996).

The unique elastic properties of single filaments are carried over to the viscoelasticity of the actin networks enabling us to attribute the three different regimes of $G(t)$ to distinct mechanical relaxation processes (Kroy and Frey 1996, Morse 1998, MacKintosh et al 1995). This led

to useful scaling laws relating viscoelastic parameters to the physical properties of the network, such as the mesh size, the bending stiffness or to the degree of crosslinking. Most importantly, this will allow us to gain also quantitative insight into structural features of actin cortices in cells.

The high frequency regime of $G(t)$ is determined by the relaxation of the entropic mechanical tension of single filaments generated by thermally excited bending fluctuations. The relaxation modulus decays with a power law (Morse 1998)

$$G(t) = \rho k_B T \left(\frac{k_B T}{\zeta L_p^{5/3}} t \right)^{3/4} \quad (4)$$

Where ρ is the total length of filaments per unit area (Morse 1998). This law can be applied to measure the effective viscosities of the networks. In the plateau regime the filament tensions have relaxed and the network behaves as an elastic solid such as rubber. The plateau value G_0 of $G(t)$ is a measure for the pure shear elasticity of the network which allows us to determine the Young modulus of the network as a function of the mesh size ξ by making use of the law

$$G_0 = k_B T L_p^{-1/5} \xi^{-14/5}$$

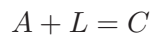
This scaling law has been well verified experimentally (Hinner et al 1998) and will allow us to estimate the actin density in the actin cortex of cells. The flow like regime is determined by the self diffusion of the filaments (which can be described as reptation like motion in a tube). The transition time, τ_t , to the flow regime (= terminal relaxation time) yields the self diffusion coefficient of filaments according to $D_{\text{self}} = L^2/2\tau_t$ (Dichtl and Sackmann, 2002).

4. Structural Manifold of Cross-Linked Actin Networks and the Design of Smart Gels

Nature has invented numerous smart actin helper proteins to manipulate the structure of actin networks. These include (i) severing proteins (severin, gelsolin) which can cleave long filaments or bind to the fast growing end thus controlling their length L ; (ii) sequestering molecules (β -Thymosin, Profilin) which bind actin monomers strongly thus enabling the control of the mesh size; (iii) a manifold of crosslinkers for the generation of various types of gels; and (iv) actin membrane couplers. Important members of the crosslinker family are α -actinin which tends to form gels with orthogonal orientation of filaments, filamin favouring the

formation of bundles and Arp2 which induces to the growth of branched (Bethe type) networks. A distinct type of crosslinker is the motor myosin II which tends to form bundles or primitive forms of micromuscles.

The role of actin gels in cells is determined by the following features. The bonds between actin (A) and linkers (L) are in general reversible. The binding is governed by a chemical equilibrium ($K = k_{on}/k_{off}$)



with off-rates of the order $k_{off} \sim 0.4 \text{ sec}^{-1}$, showing that the gels can undergo slow plastic changes (Tempel et al. 1996). Since K is temperature dependent, the degree of crosslinking may be controlled at fixed crosslinker density in a reversible way by changing the temperature. In case of myosin II transitions between active and passive states can be triggered by changing the ATP-to-ADP ratio.

The change from the entangled (sol-like) state to the gel exhibits typical features of gelation transitions as shown for the actin/ α -actinin-system. At an increasing degree of crosslinking ζ (which is equal to the ratio of the mesh size to the average distance, d_{cc} , between crosslinkers, Fig. 5) the shear modulus increases only slightly but diverges at the tran-

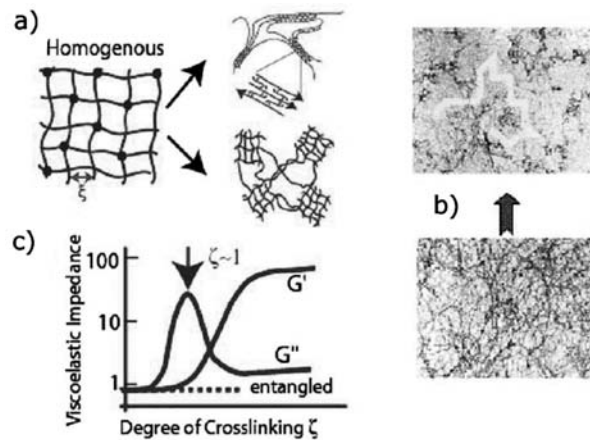


Figure 5. a) Transition from entangled network to microgel-states composed of clusters interconnected by single filaments or thin bundles. The percolated clusters can consist of tightly linked filaments with orthogonal orientation (as for α -actinin) or short bundles (as formed by myosin or filamin). b) Electron micrograph of actin network prior to and after the percolation transition. Note that in heterogel-states large voids are generated enabling the transport of small compartments (as in cell; cf Fig. 9 below). The percolation transition (at $\zeta \sim 1$) leads to a sharp rise of the shear elastic modulus by about two orders of magnitude and a broad band of the viscosity (after Tempel et al. 1996).

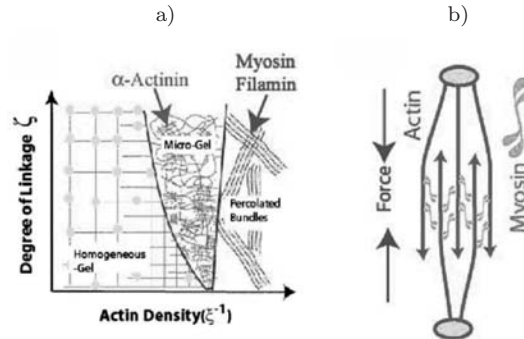


Figure 6. a) Generalized phase diagram of crosslinked actin networks showing the transition from a homogeneous network to the microgel-states. $\zeta = \xi/d_{cc}$ is equal to the ratio of the mesh size to the average distance (d_{cc}) of the crosslinkers. b) Micromuscle as a possible state of heterogels.

sition resulting in an increase by two orders of magnitude as predicted by the theory of percolation (Templ et al. 1996). At further increase of ζ , highly heterogeneous gels form. For α -actinin these consist of dense clusters of a crosslinked gel interconnected by single filaments or slender bundles. In the case of myosin (both in the absence and presence of ATP) a percolated system of interconnected bundles is formed. As indicated in Fig. 6b, the bundles can form primitive micro-muscles. If these are connected to the membrane (as in smooth muscles) their activation causes contraction of the cell envelope (Fig. 6b).

5. Microrheometry of the Composite Cell Envelope

With few exceptions (such as erythrocytes or quiescent, freely suspended cells of *Dictyostelium discoideum*) cell envelopes form highly heterogeneous shells exhibiting pronounced variations of the mechanical properties of the cell surface. The apical shell of adhering endothelial cells is much softer than the adhering basal surface. The surface shear elastic modulus (characterizing the mechanical resistance of the cellular shell against tangential deformations) is much smaller in areas over the nucleus than close to the rim of the cell and can vary by a factor of ten (Bausch et al. 1998). Micromechanical experiments with magnetic tweezers provide a convenient tool to characterize the mechanical heterogeneity of the cell envelopes in a quantitative way. The beads can be coupled to distinct cell surface receptors (e.g. integrins) through antibodies or specific ligands grafted to the bead surface. The repro-

ducibility and the linearity of the viscoelastic response can be tested by the application of sequences of force pulses of different amplitude and length, or detailed insight into the effect of pre-stress can be gained by analysing responses evoked by more complex force scenarios, such as staircase-like or triangular force ramps.

Fig. 7c shows a typical time dependence of the relaxation modulus. It clearly exhibits the same viscoelastic signature as the purely entangled or weakly crosslinked actin network, thus demonstrating that the elasticity of the cell envelope is determined by the associated actin cortex. This conclusion is further supported by the change of $G(t)$ induced by a small dose of latrunculin (a fungal toxin which binds monomeric actin strongly thus impeding the natural turnover of actin). It causes a fast decrease of the elastic modulus by an order of magnitude.

Another powerful microrheometric technique to study cell surfaces is atomic force microscopy (Rotsch and Rademacher, 2000). It is complementary to the magnetic tweezers technique in several ways: a different mode of deformation (namely the bending modulus), much stronger forces can be applied to study the elasticity of the very stiff thin cell lobes

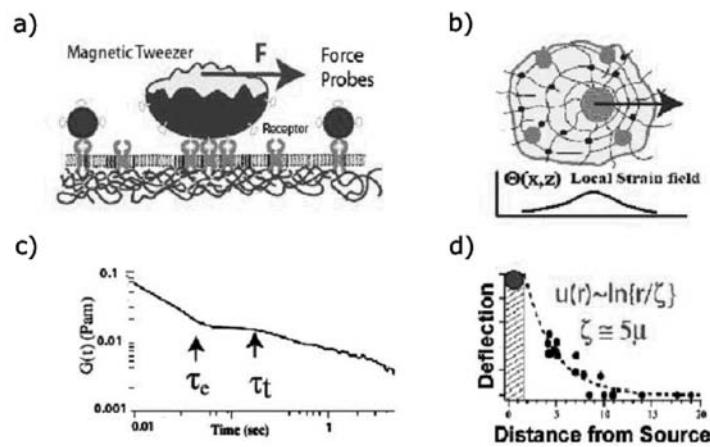


Figure 7. a) Illustration of microrheometry of cell envelope. Magnetic tweezers are coupled to cell surface receptors of the integrin family via invasins: the pathogenic coat protein of bacteria (Yersinia) causing gastrointestinal infections. Non-magnetic colloidal probes are coupled to integrins via invasins to measure the deformation fields induced by point-like forces. b) Illustration of in-plane shearing of actin networks. c) Relaxation modulus $G(t)$ of the cell envelope showing the typical mechanical signature of entangled or slightly crosslinked actin networks. The plateau value of $G(t)$ corresponds to the surface shear modulus of the cell envelope. d) Decay of the strain field. The drawn line shows the logarithmic law $u(r) \sim \ln r$.

(pseudopods) of adhering cells and measurements can be performed with nanometer resolution.

All micromechanical experiments yield in general relative measures of the viscoelastic moduli which agree only within an order of magnitude. To determine true elastic (e.g. Young) moduli one has to consider well defined modes of deformations allowing the application of distinct models of elasticity which account for the boundary conditions. In the case of AFM technique the indentation is analyzed in terms of the Hertz model. It yields a Young modulus which is, however, only defined for infinite elastic bodies. In the magnetic tweezers experiment the plateau value of $G(t)$ (measured in units N/m) corresponds to the shear modulus μ^* of a two-dimensional plate. It can be transformed into a shear modulus, μ , of a shell of finite thickness d according to: $\mu = \mu^*/d$. However, μ is proportional to but not yet equal to the Young modulus E of the cell envelope. This value may only be obtained by analysing the deformation field $u(r)$ generated by the point-like tangential force using colloidal force probes (Fig. 7a). $u(r)$ has been found to decay logarithmically according to $u(r) = (F/4\pi\mu^*) \ln(r/R)$ with a persistence length of $R \sim 6 \mu\text{m}$.

Analysing the Young modulus in terms of the scaling law $E \sim \xi^{-14/5}$ we can conclude that the actin cortex exhibits a mesh size of $\zeta \sim 0.1 \mu\text{m}$ in agreement with experimental findings (cf Fig. 2a) and is only slightly crosslinked below the percolation limit (Feneberg et al. 2004).

6. Real Time Analysis of the Structural Reorganization of the Actin Cortex During Cell Stimulation

Viscoelastic microscopy can be applied to evaluate structural reorganizations of the actin cortex evoked by biochemical agents and mutations (e.g. knock-out of distinct actin binding proteins). Since viscoelastic response curves can be measured repeatedly, the temporal evolution of structural changes can be measured in real time (Feneberg and Sackmann 2004). We studied the stimulation of endothelial cells (which line the inner wall of blood vessels) by histamine. This hormone exerts an allergic reaction which leads to the contraction of blood vessels and makes them more permeable for white blood cells. As shown in Fig. 8, histamine increases the surface shear modulus of the cell by a factor of ~ 100 within seconds. Simultaneously actin stress fibres are formed close to the adhering membrane and the cells contract in a centripetal way, resulting in rounding. If cells are embedded in closed monolayers, only a few respond, leading to local gaps within the endothelium. With increasing

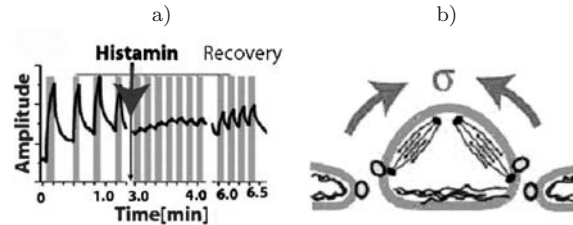


Figure 8. Effect of histamine on the viscoelastic response of the endothelial cell envelope. Plot of deflection of a magnetic bead by pulses (indicated by grey bars) of $T = 2.5$ sec duration and amplitude $F = 1.8$ nN. $10 \mu\text{M}$ of histamine was added at the time indicated by the arrow. It induces a rapid decrease of deflection amplitude by two orders of magnitude which recovers again after about 3 minutes.

concentration of the stimulating agent the fraction of cells responding increases. The stiffening of the apical membrane relaxes within ~ 5 min while the stress fibers remain suggesting that the two effects are evicted by different mechanisms. The gap formation can be understood in terms of the following generic mechanism (Feneberg et al. 2004): Histamine is known to weaken the interaction between the actin cortex and the cytoplasmic domains of the cadherin receptors mediating cell-cell adhesion. The concomitant reduction of the membrane bending decreases the adhesion strength between the cells (Sackmann and Bruinsma 2002). The gaps form due to the rounding of the cell which may be simply caused in a passive way by the stiffening of the actin cortex or more likely by its active contraction mediated by mini-muscles (Fig. 8).

7. Cytoplasm: Viscoplastic Body or Viscoelastic Fluid

The micro-viscoelastic behavior of the cytoplasm differs fundamentally from that of the cell envelope. Due to the high degree of heterogeneity and the unavoidable (quasi-random) active transport of internalized force probes, viscoelastic parameters are difficult (and often impossible) to measure and they depend on the size of the force probes. The simple force-free microrheometry fails unless the fluctuating spectrum of active forces on the beads are known (Caspi et al. 2000). Despite of these difficulties, relatively well defined viscoelastic response curves can be observed and shear moduli can be measured in densely packed mammalian cells such as macrophages (Bausch et al., 1998), most likely due to the network of intermediate filaments. The situation is much more complex in amoeba such as *Dictyostelium Discoideum* (Feneberg and Sackmann 2001). The high degree of dynamics and heterogeneity

inside these cells becomes evident by following the motion of colloidal beads (e.g. magnetosomes) engulfed by cells (Feneberg et al 2001) or internal particles such as mitochondria. After entering, the endosomes are transported back and forth between the rim and the nucleus. Figure 9 shows the situation for magnetosomes of $1.45 \mu\text{m}$ diameter. The motion consists of rapid movements (with $v \sim 1.5 \mu\text{m}/\text{sec}$) along rather straight tracks (some of which are indicated by arrows) and localized walks with $v < 1 \mu\text{m}/\text{sec}$ exhibiting complex Levy like random walks.

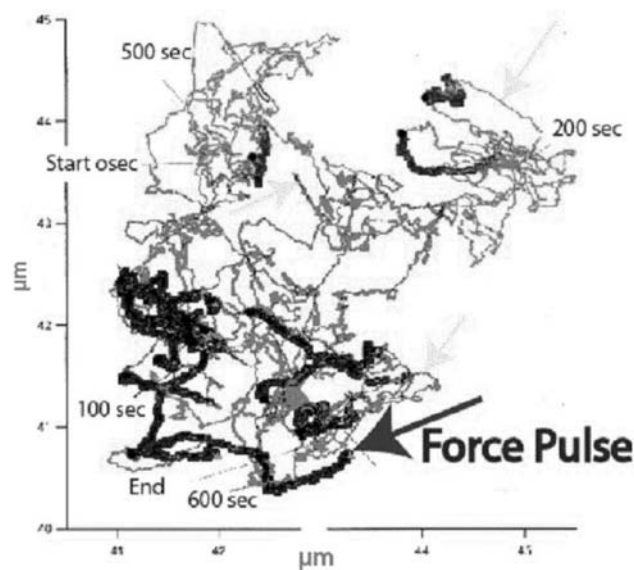


Figure 9. Particle Transport: visualization of the random walk of the $1.45 \mu\text{m}$ diameter bead in a Dictyostelia cell embedded in agarose to slow down motion. Trajectories consist of nearly straight lines (velocities $\sim 1.5 \mu\text{m}/\text{sec}$) some of which are indicated by thin arrows and quasi-random walks ($v \sim 0.5 \mu\text{m}/\text{sec}$). Note that beads can revisit sites repeatedly. The thick tracks show motions under the action of external force pulses of $\sim 20 \text{pN}$. The force is directed to the left.

An informative and convenient way to analyze the active transport is the measurement of the distributions $P(v)$ of the local velocity which is more directly related to the forces than the mean square displacements. Figure 10a shows distributions $P(v)$ for two small latex beads and a magnetosome obtained by analysis of about 10000 data points. Most of the time the beads perform quasi-random walks in constrained areas and $P(v)$ has a broad maximum at $v \sim 0.5 \mu\text{m}/\text{sec}$ which corresponds well with the velocity of the flagella-like motions of the microtubule (Fig. 10a). This motion is driven by coupling of the microtubules to the actin cortex which appears to undergo translational motions. It

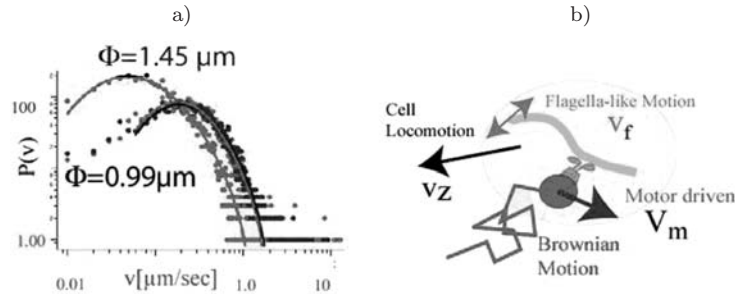


Figure 10. a) Log-log plot of the velocity distribution $P(v)$ of particles of diameter $\Phi = 1.45 \mu\text{m}$ (magnetosome) and of $\Phi = 0.99 \mu\text{m}$ (polystyrene) transported in wild type Dictyostelia cells. The drawn curve superimposed on the measured distribution for $0.99 \mu\text{m}$ bead is an optimal fit of log-normal distribution. b) Model of the superposition of velocities.

plays an important role for the separation of the two nuclei during cell division (Rosenblatt et al. 2004)

A more detailed recent analysis of the motion in free cells (not embedded in agarose) showed that the velocity exhibits indeed a log-normal distribution (Fig. 10a, Doris Heinrich, unpublished data). The log-normal distribution is attributed to the fact that at each moment the momentaneous velocity of the bead is determined by the superposition of several distinct, statistically independent motions comprising the flagella like motion of the microtubules, the active motion of the bead along microtubules driven by kinesin and dynein motor molecules and the locomotion of the cell.

Measurement of transport forces: Fig. 11 shows how magnetic tweezer microrheometry may be applied to measure active forces. The trajectory marked by the thick arrow (bottom left) in Fig. 9 was induced by a force pulse of about 50 pN directed towards the left. The track at the bottom is shown at higher resolution in Fig. 11 together with the tangential local velocity immediately before (v_0) and after application (v_1) of the force pulse. From the velocity change the local viscosity η_{loc} and thus the active force can be determined according to: $\mathbf{v}_1 = \mathbf{v}_0 + \mathbf{f}_{ex}/\eta_{loc}$ (\mathbf{v}_0 and \mathbf{v}_1 are velocity vectors). The active forces measured in Dictyostelia cells (embedded in agarose) vary between 9 and 30 pN while larger forces (up to 100 pN) were found in macrophages or free Dictyostelia. The large forces can not be generated by microtubule-based motors kinesin and dynein and are most likely due to local instabilities within the action myosin network (D. Heinrich and E. Sackmann, unpublished). The cytoplasm is a viscoplastic medium: An outstanding feature of the cytoplasm of Dictyostelia cells is that the viscoelastic response curves are

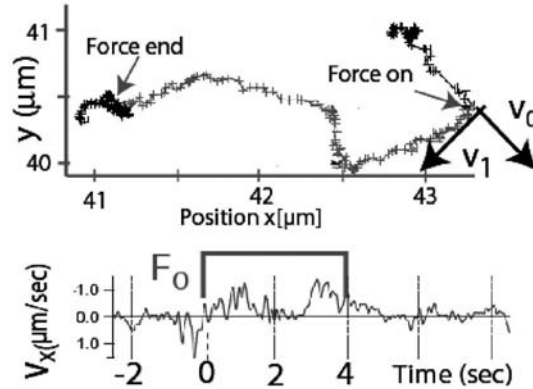


Figure 11. Top: Track of bead subjected to a force of 50 pN directed towards the left. The velocity changes from v_0 to v_1 after the application of the force. Under the force, the bead moves first fast in the force direction. It is then deflected nearly into the perpendicular direction with low velocity and moves again parallel to the force with higher speed until it is slowed down towards the end of the pulse by penetration into the region of the actin cortex. Bottom: Plot of tangential velocity showing change of velocity after application of the force pulse at $t = 0$.

strongly force dependent (Fig. 12a). At $f = 200$ pN the response is immediate but irreversible whereas at $f = 50$ pN the bead is deflected with a delay of several seconds. It moves then in the direction of the force and relaxes partially. The trajectory for 200 pN is straight showing that the force is larger than the yield stress of the cytoplasm while at 50 pN a more random deflection is found. The viscosities obtained from the initial velocities of the deflections are much smaller ($\eta_{loc} \sim 10$ Pa sec) for the weak forces (< 50 pN) than for strong forces ($\eta_{loc} \sim 300$ Pa sec for 400 pN).

In summary, the cytoplasm is a crowded colloidal system and behaves only elastic at very short times and small deflection. The nonlinear mechanical response is most conveniently described by the concept of mobility (similar to the transport of electrons in periodic potentials). The response to external forces can be described as a diffusive walk of a particle in a quasi-periodic potential. For step-like forces the beads move with a finite, spatially varying velocity which is in general not parallel to the external force. The local velocity can be expressed as $\langle v \rangle = \mu(r, F)F$, where $F = F_{ex} + F_{act}$ is the sum of the external and the active forces. The direction is determined by the constraints imposed by the microtubules and the intracellular compartment and μ has to be considered as a tensor. The average velocity is then determined by the probability (per unit time) of passages over the potential walls separa-

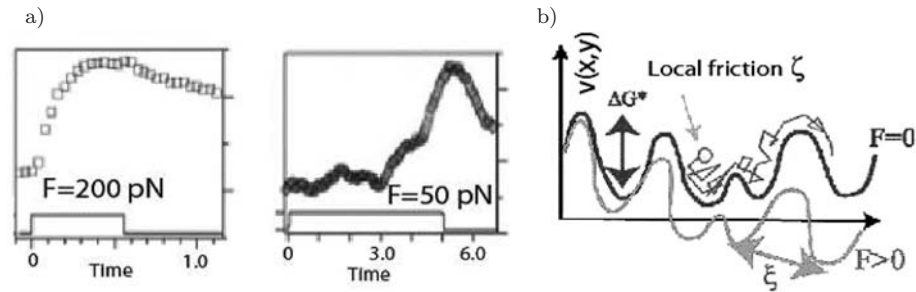


Figure 12. Two examples of the viscoelastic responses in Dictyostelia cells obtained for high and low forces. At 200 pN we are above the yield force and the trajectory of the bead is straight and irreversible. At low force the bead is deflected after 3 sec along a quasi-random partially reversible path.

ting adjacent equilibrium positions. This behaviour can be expressed in terms of the modified Arrhenius law $\langle v \rangle = \mu_0 \exp\{(\Delta G^\# - F\xi^3)/RT\}$ where $F\xi^3$ is the work associated with each transitional step. This motional law is well known from the physics of fracture. A very important practical consequence (or message) of the above concept is that particles may be transported through strongly crowded regions of the cytoplasm exhibiting yield stress large compared to the active forces (e.g. forces of 5 pN generated by single molecular motors) by statistical breakage of local bonds.

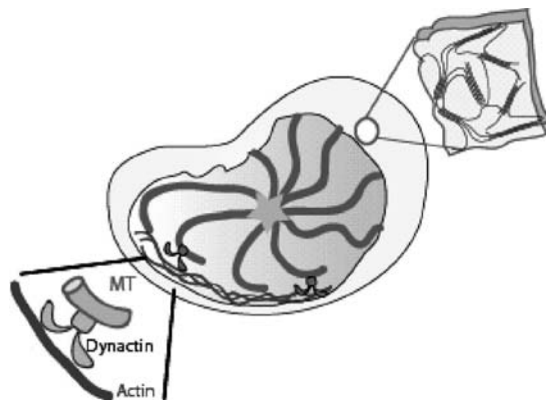


Figure 13. Tensegrity-like model of a cell with spider-like microtubuli network coupled to the actin cortex (left inset) which can be composed of a random network in quiescent cells or of percolated bundles after simulation (inset on right).

More recent studies show, however, that short time mechanical coupling between different parts of the cytoskeleton can be mediated by the microtubules (D. Heinrich and E. Sackmann, unpublished). The finding that they exhibit flagella like motion provides evidence that they are coupled to the actin cortex, which can be composed of percolated bundles as indicated in Fig. 13. This then suggests that the concept of tensegrity strongly propagated by D. Ingber may indeed mediate the signal transmissions in cells at short times on the order of seconds. On the other hand, according to Fig. 8 and work by Alon and Feigelson, such short time reorganizations of the cytoskeleton are well possible.

References

- B. Alberts et al., *Molecular Biology of the Cell*, Garland Sciences, New York 2002.
- R. Alon and S. Feigelson, *Immunology*, Vol. 14, pp.93–104, 2002.
- M.F. Ashby, *Materials selection in mechanical design*, Butterworth, Oxford 1999.
- A. Bausch et al., *Biophys. J.*, Vol. 75, pp.2038–2049, 1998.
- A. Caspi, R. Granek, and M. Elbaum, *Phys. Rev. Letters*, Vol. 85, pp.5655–5658, 2000.
- M. Dichtl and E. Sackmann, *Proc. Natl. Acad. Sci.*, Vol. 99, pp.6533–6538, 2002.
- W. Feneberg, M. Aepfelbacher, and E. Sackmann, *Biophys. J.*, Vol. 87, pp.1338–1350, 2004.
- W. Feneberg, M. Westphal, and E. Sackmann, *Eur. Biophys. J.*, Vol. 30, pp.284–294, 2001.
- B. Hinner, M. Tempel, E. Sackmann, K. Kroy, and E. Frey, *Phys. Rev. Lett.*, Vol. 81, pp.2614–2617, 1998.
- D. Humphrey et al., *Nature*, Vol. 416, 413, 2002.
- D.E. Ingber, S.R. Heideman, Ph. Lamoureux, and R.E. Buxbaum, *J. Appl. Physiol.*, Vol. 89, pp.1663–1678, 2000.
- K. Kroy and E. Frey, *Phys. Rev. Letters*, Vol. 77, 306, 1996.
- H. Lichtenegger et al., *J. Structure Biology*, Vol. 128, pp.257–265, 1999.
- F. MacKintosh, J. Kaes and P.A. Janmey, *Phys. Rev. Letters*, Vol. 75, pp.4425–4428, 1995.
- O. Medalia et al., *Sciences*, Vol. 298, pp.1209–1213, 2002.
- D. Morse, *Macromolecules*, Vol. 31, pp.7030–7043, 1998.
- J. Rosenblatt, L. Cramer, P. Baum, and K. McGee, *Cell*, Vol. 117, pp.361–371, 2004.
- C. Rotsch and M. Rademacher, *Biophys. J.*, Vol. 78, pp.520–535, 2000.
- E. Sackmann, *Structure and Dynamics of Membranes*, [in:] *Handbook of Biological Physics*, Vol. IA, Elsevier 1996.
- E. Sackmann, *Physics of composite cell membrane and actin based cytoskeleton*, Nato Advanced Study Institute *Physics of bio-molecules and cells*, Session LXXV, Les Houches, H. Flyvberg et al. [eds.], Springer Verlag, Berlin Heidelberg 2002.
- E. Sackmann and R. Bruinsma, *Chem. Phys. Chem.*, Vol. 3, pp.262–269, 2002.
- M. Sheetz, *Nature Reviews*, Vol. 2, p.392, 2001.
- M. Tempel, G. Isenberg, and E. Sackmann, *Phys. Rev. E*, Vol. 54, pp.1802–1810, 1996.
- J. William and E. Frey, *Phys. Rev. Letters*, Vol. 77, pp.2581–2584, 1996.
- F. Ziemann, J. Raedler, and E. Sackmann, *Biophys. J.*, Vol. 66, pp.2210–2216, 1994.

ELASTIC INTERACTIONS OF BIOLOGICAL CELLS

Samuel A. Safran

*Dept. Materials and Interfaces, Weizmann Institute of Science,
Rehovot, Israel 76100*

sam.safran@weizmann.ac.il

A. Nicolas

CRPP, Bordeaux, France 33600

nicolas@crpp-bordeaux.cnrs.fr

U. S. Schwarz

MPI of Colloids and Interfaces, Potsdam, Germany 14424

ulrich.schwarz@mpikg-golm.mpg.de

Abstract We review recent theoretical work that analyzes experimental measurements of elastic interactions of biological cells with their environment. Recent experiments have shown that adhering cells exert polarized forces on substrates. The interactions of such “force dipoles” in either bulk gels or on surfaces can be used to predict the nature of self-assembly of cell aggregates and may be important in the formation of artificial tissues. Cell adhesion strongly depends on the forces exerted on the adhesion sites by the tension of the cytoskeleton. The size and shape of the adhesion regions is strongly modified as the tension is varied and we present an elastic model that relates this tension to deformations that induce the recruitment of new molecules to the adhesion region.

Keywords: Cell elasticity, cytoskeleton, adhesion

1. Introduction

In this review, we summarize recent progress in our understanding of the physics of the interaction of biological cells on elastic substrates and in bulk gels. Cell adhesion is quite different from adhesion of fluid-filled vesicles because the interior of the cell is an elastic medium (that

is continuously and actively reorganized) due to the presence of the cytoskeleton. In most cells, the cytoskeleton [1] is composed of several components, including actin, microtubules and intermediate filaments, each of which have different elastic properties [2] that can be used by the cell in a variety of circumstances. Force generation that leads to tension in the actin network arises from the action of myosin bundles that are activated by ATP to change conformation and exert forces on the actin filaments.

Recent experiments [3, 4] show that, in contrast to artificial vesicles that exert only normal forces when they adhere to a substrate, adhering cells show both normal and lateral forces. The normal forces arise from the action of either specific adhesion molecules or non-specific interactions (*e.g.* van der Waals interactions) while the lateral forces arise from elastic deformations of the adhesion region by cytoskeletal forces. These lateral forces regulate the size and shape of the adhesion regions (often called focal adhesions (FA)) [4] and allow a cell to probe and to adjust the strength of its adhesion to its physical environment. The physical origin of the mechanosensor in the cell and the conversion of elastic information to a biochemical response that recruits additional proteins to the adhesion region is an important problem in cell biology today.

These forces that arise from the tension in the actin cytoskeleton tend to polarize the actin filaments (also called stress fibers). Thus, one can sum over all the local focal adhesions and in a coarse-grained picture, model such an adhering cell as a pair of nearly equal and oppositely directed contraction forces (termed an elastic force dipole) with typical forces of 100 nN over a scale of tens of microns. An interesting physics problem [5, 6] concerns the interactions and self-assembly of many such force dipoles; this corresponds to the interactions of many cells, each of which adheres to an elastic medium such as a substrate or in a three-dimensional gel. These dipoles interact via the elastic deformations of the medium, and can form chains or other self-assembled structures. Because these interactions are long-range, the details depend on the boundary conditions and sample shape. In addition, the interaction strength depends on the elasticity of the substrate as well as on its deformations and cells have been observed to migrate towards stiffer substrates and to rotate on elastically strained media [7]. The physics of cell adhesion and the interactions of cells in elastic media are important for the understanding of tissue formation and engineering [8] as well as wound-healing and metastasis.

2. Elastic Effects in Cell Adhesion

Adhesion of live cells to external surfaces [9] plays an important role in many cellular processes, such as cell growth, differentiation, motility and apoptosis (programmed cell death) [10]. Cell adhesion is not a passive process, restricted to the formation of bonds between membrane receptors and extracellular ligands. Adhering cells actively probe the physical properties of the extracellular matrix; their cellular contractile machinery participates in the formation of the adhesive junctions. It has been shown that rigid surfaces give rise to large and stable adhesions, termed focal adhesions (FA), that are associated with the termini of actin stress fibers and trigger signaling activity that affects gene expression, cell proliferation, and cell survival. On the other hand, soft surfaces mainly support the development of relatively small, transient dot-like or fibrillar adhesions that are involved respectively in cell motility and matrix reorganization. In addition, observation of the early phase in the assembly of FA shows small, primordial adhesions, termed focal complexes (FX) as precursors of FA. FX are formed close to the edge of the advancing membrane protrusions of cells and can grow in some cases into FA when subjected to mechanical stress due to either cell contractility or external perturbations [11]. Indeed, the adhesion process has been shown to be mechanosensitive; cells can probe the physical properties of their environment and respond by modulating their adhesions or migratory activity [6, 12, 13].

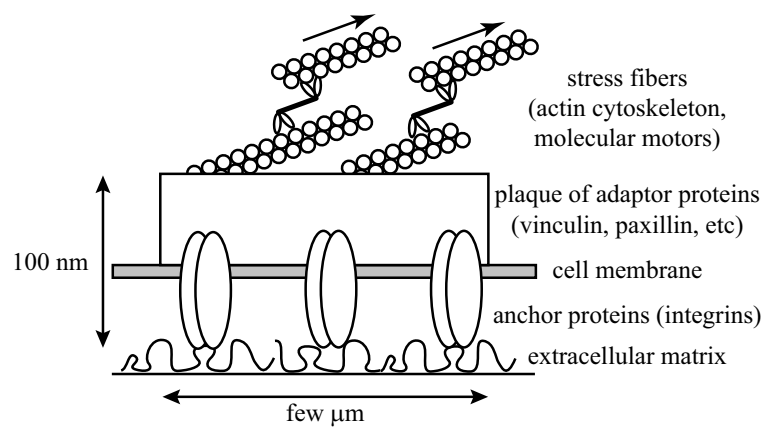


Figure 1. Schematic representation of a focal adhesion. The bottom of the contact is anchored to the extracellular matrix and the top surface is acted upon by the cytoskeletal tension. (Reprinted with permission from [27], Copyright (2004), American Physical Society).

Live cells exert directional, lateral forces on adhesive junctions; these forces originate from the organization of actin filaments and their associated molecular motors into stress fibers (Fig. 1). Adhesions respond dynamically to the local stresses: increased contractility leads locally to larger adhesions, whereas FA are disrupted when myosin II is inhibited [14]. The physics challenge in the understanding of these effects lies in (i) quantifying on a coarse-grained scale, the forces that cells exert on surfaces or in the bulk (ii) understanding the implication of these forces for adhesion of a single cell, the interactions among many cells in an elastic medium and the consequent self-assembled structures that may form (iii) predicting the microscopic origin of these forces and why adhesion growth is sensitive to the magnitude and direction of the internal or external cytoskeletal stresses.

Lateral Forces at Adhesion Sites

Biological cells can exert strong physical forces on their surroundings. One example are fibroblasts, that are mechanically active cells found in connective tissue. The main technique to measure cellular forces is the elastic substrate method [15] which was introduced by Harris and coworkers in the early 1980s [16]. Quantitative analysis of elastic substrate data was pioneered by Dembo and co-workers [17].

Recently, a novel elastic substrate technique to measure cellular forces at the level of single FA [4] was developed using a micropatterned, thick polymer film. From the deformations of the grid on the film surface, the forces exerted by FA were estimated. Correlation of these forces with the lateral size of the FA showed that there exists a linear relationship between force, F , and area, A , of a single FA. This finding translates into a force of several pN per receptor, which is consistent with recent experiments on strength of single molecular bonds at slow loading [18].

Since the adhering cells are rather flat, forces exerted on the substrate can be considered to be tangential to the plane of the substrate surface. Also, because surface displacements are much smaller than the film thickness, one can use linear elasticity theory for an elastic isotropic halfspace. For incompressible elastic substrates, the resulting displacement of the substrate surface remains within the plane of the substrate surface [19]. Therefore, the whole elastic problem becomes two-dimensional. Since lateral deformations of the substrate are not observed in the absence of FA, we assume that forces are exerted mainly at the sites of FA. For a single, discrete force density (force per unit volume) \vec{f} at position \vec{r} , the displacement field \vec{u} at position \vec{r} is:

$$u_i(\vec{r}) = \int d\vec{r}' G_{ij}(\vec{r} - \vec{r}') f_j(\vec{r}'), \quad (1)$$

where the subscripts refer to the vector components and where G_{ij} is the Green function of the elastic isotropic halfspace, that is, a tensor of rank two:

$$G_{ij}(\vec{r}) = \frac{3}{4\pi E r} \left(\delta_{ij} + \frac{r_i r_j}{r^2} \right). \quad (2)$$

We use the convention of summation over repeated indices, δ_{ij} denotes Kronecker Delta and E is the Young modulus. The Poisson ratio has been set to 0.5 and the indices i, j take the values 1,2. Note that in finite systems, the Green function $G_{ij}(\vec{r} - \vec{r}')$ will be an explicit function of both \vec{r} and \vec{r}' . This is because the elastic forces can be long range and thus depend on the boundary conditions. In the case of the half-space, the displacements are mostly in the plane; there are negligible normal displacements and the translational symmetry is approximately restored.

Since linear elasticity theory allows for superposition, one can generalize the above to treat a set of discrete forces that act at the sites of the observed focal adhesions. One must solve the inverse problem of predicting the forces, given the observed displacement. The resulting force pattern turns out to be very sensitive to small changes in the displacement data. To regularize the problem [20], a reasonable constraint is that the forces should not be exceedingly large.

The combination of the experimental and computational method described above allowed, for the first time, a measurement of the cellular force at the level of FA and its correlation with aggregation characteristics [4]. One finds a linear relationship between magnitude of force and the area of the FA. The direction of force usually coincided with the major axis of the elliptically shaped FA. The observed force is proportional to the area of the FA, with a stress constant of $5.5 \text{ nN}/\mu\text{m}^2$. Since several thousand integrin adhesion molecules and myosin II molecular motors correspond to one FA, the pN scale of single molecules is amplified to the nN-range at FA.

Elastic Interactions of Cells: Force Dipoles

Anchorage-dependent cells constantly assemble and disassemble focal adhesions, thereby probing the mechanical properties of their environment. The protein aggregates in FA are connected to the actin cytoskeleton. This generates a contractile force pattern, that is actively produced by myosin II molecular motors interacting with the actin cytoskeleton. The minimal configuration of this machinery is a set of two focal adhesions connected by one bundle of actin filaments (*stress fiber*), that

leads to a pinch-like force pattern. In condensed matter physics, such an object is known as an *anisotropic force contraction dipole* [21, 22].

By analogy with electric dipoles, a force dipole, P_{ij} is a second rank tensor defined as the second moment of a spatially distributed force density (force per unit volume), $\vec{f}(\vec{r})$

$$P_{ij} = \int d\vec{s} s_i f_j(\vec{s}), \quad (3)$$

where the subscripts refer to the vector components. The elastic deformation field, $\vec{u}(\vec{r})$, is related to the force distribution and to the Green function as given in Eqs. (1,2) above. If the force distributions are described in terms of force dipoles, the displacement field at point \vec{r} due to a dipole at point \vec{r}' can be written [6]

$$u_i(\vec{r}) = G_{il,k'}(\vec{r}, \vec{r}') P'_{kl}, \quad (4)$$

where the extra index after the comma, denotes a derivative of the Green function with respect to the variable \vec{r} ; a prime on this index indicates that the derivative is with respect to the variable \vec{r}' . As before, there is an implied summation over repeated indices. The prime on P indicates that the dipole is located at position \vec{r}' . The interaction of two dipoles proceeds via the deformation of the medium; each dipole feels the deformations induced by the other and this creates an effective interaction between them. For dipoles located at \vec{r} and \vec{r}' one can derive the effective interaction due to the elastic deformation energy of the medium. This energy is proportional to the elastic constant tensor and the product of the gradients of the displacements, $\vec{u}(\vec{r})$ that are related to the forces by Eqs. (1,2). One finds [6] that the elastic deformation of the medium results in a contribution to the elastic energy, W :

$$W = P_{li} u_{i,l} = P_{li} G_{ij,lk'}(\vec{r}, \vec{r}') P'_{kj}, \quad (5)$$

where P_{li} and P'_{kj} are the force dipoles located at \vec{r} and \vec{r}' respectively, $u_{i,l}$ is the derivative of the displacement component u_i with respect to component l of the position vector \vec{r} ; the last two subscripts in the Green function represent derivatives with respect to \vec{r} and \vec{r}' respectively. For translationally invariant systems, such as an elastic half space with planar displacements,

$$G_{ij,lk'}(\vec{r}, \vec{r}') = G_{ij,lk'}(\vec{r} - \vec{r}') = -G_{ij,lk}(\vec{r} - \vec{r}'). \quad (6)$$

This interaction energy scales as $1/|\vec{R}|^3$ where \vec{R} is the distance between dipoles and is proportional to P^2/E where P is the dipole strength and E is the Young's modulus of the medium. Equation (5) is not the only

relevant energy to be considered since in the case of inert matter one must add to the deformation energy of the medium, an energy proportional to the product of the local force and the local displacement; this accounts for the direct interaction of the dipole with the environment. The elastic theory can also describe [6] the interaction of a single dipole with an external strain imposed on the elastic medium or with the boundary of a finite-sized sample.

Recently, we have extended the concept of force dipoles to model the mechanical activity of cells [5]. Cells in an isotropic environment often show isotropic (that is round or stellate) morphologies. However, since the focal adhesion dynamics is local, even in this case there is an anisotropic probing process, that can be modeled by anisotropic force *contraction* dipoles. The anisotropy of focal adhesion dynamics becomes apparent when stress fibers begin to orient in one preferential direction, either spontaneously during a period of large mechanical activity, or in response to some external anisotropy, or during cell locomotion. In this case, cellular dipoles have been measured to be of the order of $P \approx -10^{-11} J$ (this corresponds to two forces of 200 nN each, separated by a distance of $60 \mu\text{m}$) [4, 23]. In Fig. 2 we show schematic representations of the physical and cellular cases discussed here.

For inert, physical dipoles, the equilibrium configuration follows by minimizing the sum of the elastic energy of the strained medium and the direct interaction energy between the force dipole and elastic environment. The first term represents a restoring force and raises the energy (*i.e.*, its sign is always positive), while the second term is a driving force that reduces the total energy (*i.e.*, its contribution will always be negative). The total interaction between two dipoles has the form of Eq. (5) but with a negative sign due to the effect of the local force-displacement interaction.

The equilibrium configuration corresponds to the minimum of the total energy as a function of position and orientation of the force dipoles, which results in an effective, so-called *elastic interaction* between the force dipole and other dipoles, sample boundaries or external strain fields. We have predicted that the competition between direct and image interactions should lead to hierarchical structure formation, with the direct interaction leading to structure formation on a length scale set by the elastic constants and similar to that of electric quadrupoles [5]. We suggested that such a behaviour should be expected for artificial or inert cells, that is for physical particles with a static force contraction dipole, but without any internal dynamic or regulatory response.

In contrast to this physical case, the effective behavior of active cells usually follows from dynamic and tightly regulated non-equilibrium pro-

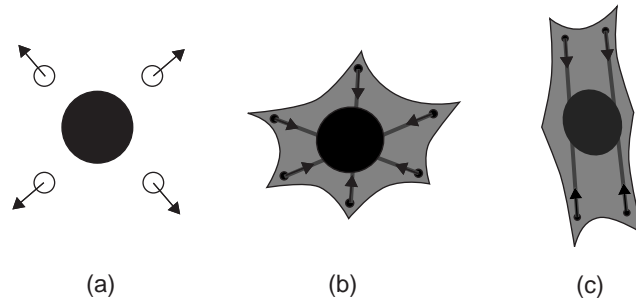


Figure 2. Schematic representation of physical and cellular force dipoles. (a) Physical case: an intercalated defect deforms the simple cubic host lattice, thus acting as an isotropic force expansion dipole. (b) Cellular case: anchorage-dependent cells probe the mechanical properties of the soft environment through their contractile machinery. Actin stress fibers (lines) are contracted by myosin II molecular motors and are connected to the environment through focal adhesions (dots). Even if cell morphology is round or stellate, different stress fibers probe different directions of space and compete with each other for stabilization of the corresponding focal adhesions. Therefore the probing process can be modeled as an anisotropic force contraction dipole. (c) Cell morphology becomes elongated in response to anisotropic external stimuli, during locomotion or spontaneously during times of strong mechanical activity. Then most stress fibers run in parallel and the whole cell appears as an anisotropic force contraction dipole. (Reprinted with permission from [6], Copyright (2004), American Physical Society).

cesses inside the cell. More recently, we have shown that despite this severe complication, it is still possible to describe the active response of mechanosensing cells in an elastic material in the same framework as the physical case [6]. Motivated mainly by recent experiments with elastic substrates [24], we have suggested that effective cellular behavior can be described as simple preference for large effective stiffness in the environment (including both rigidity and tensile prestrain). Moreover, we have shown that this principle is equivalent to minimization of the energy cost of straining the environment. (But this does not include the energy due to the direct force-displacement interaction.) This results in an interaction energy between two force dipoles with a positive sign as given in Eq. (5). The direct elastic interaction between cells has been predicted to be similar to that of electric dipoles, leading to strings of cells [6]. This is not the case for inert dipoles (due to the difference in the sign of their interaction), where more compact structures are predicted [6].

The different energies and opposite sign of the interactions for the case of inert force dipoles and active cell force dipoles leads to interesting differences in their behavior. For example, active cells are attracted and repelled by clamped [25] and free sample boundaries, respectively. In the

case of inert dipoles, this behaviour is inverted. The predictions for the elastic response cells explain several experimental findings reported in the literature [6] and can be used for rational design of tissue equivalents.

3. Theoretical Model for Mechanosensitivity of Adhesion

Cell Adhesion Mechanosensitivity

The coupling of the FA to the internal stresses that are regulated by the cell (*e.g.*, via actin-myosin activity or actin polymerization) means that the cell can respond to the elasticity of its adhesive environment. Recent experiments have shown that external forces can also cause the anisotropic growth of focal adhesions. Independent of the origin of the stress (*e.g.* internal contractility [4], shear flow [26], micropipette-induced shear stress [14]), small adhesions grow into focal adhesions (FA), that elongate in the direction of the force. The FA grows via a biochemical process that is very sensitive to the force applied to the adhesion region by the cytoskeleton and the origin of this mechanosensitivity is an important problem in cell biology.

Our model (see Fig. 1) assumes that the biochemical response of adhesions to cytoskeletal stresses originates from the stress-induced elastic deformation of the adhesion site. These force-induced deformations modify the local density of the proteins found in and around the adhesive junction, and thus their interactions. This, in turn, can trigger a conformational change or a molecular reorganization that initiates the biochemical cascade responsible for the aggregation of new proteins and the directional, anisotropic growth of the adhesion. For example, one could identify the mechanosensor with the layer of transmembrane, integrin proteins [11], since they are connected to the extracellular matrix and are elastically deformed by cytoskeletal forces; this deformation can activate conformational or organizational changes that enhance their binding with plaque proteins [10].

In addition to the fact that adhesion to an anchoring surface makes a junction sensitive to shear [27] (even if the latter is composed of fluid-like assemblies of molecules), several observations support the view we propose. First is the observation that independent of the origin of the stress, small adhesions grow into focal adhesions (FA), that elongate in the direction of the force. This anisotropy is predicted by our theory since stress-induced deformations are correlated with the applied force and exert different effects on the proximal (front) and the distal (back) aspects of the adhesive junctions. In our model, where we relate the biochemical response to deformations, this anisotropy also leads to an

anisotropic addition (or loss) of proteins. Moreover, the size and the strength of the adhesive junctions depend on the elastic properties of the extracellular matrix [28, 29]. Our model predicts that a local force applied to an adhesive junction induces a pure translation of the junction (and thus no deformation) if the extracellular matrix is very soft, whereas strongly grafted adhesions on a rigid matrix are elastically deformed by lateral, local stresses.

Description of the Model

The total force transmitted by FA has been shown to be proportional to their surface [4], suggesting that the region over which stress fibers act grows with the junction. As a model, we consider the adhesion and the membrane-associated integrins as an elastic, thin film grafted at its bottom surface and stressed by a local lateral force on its top surface; “local” means here that the force only acts on a finite region of the adhesive junction, which, as explained below, needs only to be somewhat smaller than the total area of the adhesion by a few thicknesses of the FA (typically, a few tens of nanometers).

The localization of the force is a crucial aspect of our model, since a homogeneously applied stress would give rise to a uniform shear of the adhesive junction and a translational motion of the surrounding lipid membrane. A *local*, tangential stress induces a compression at the front edge and an expansion at the back of the stressed region because the unstressed part is also grafted and cannot slide. In this case, a lateral force induces anisotropic density changes in proteins located inside or close to the stressed region. The resulting stress-induced deformation profile can be calculated using continuum elasticity theory [27]. Our model assumes that this change in density triggers the biochemical response responsible for the growth or dissolution of FA. Anisotropic variations of density thus give rise to different molecular dynamics in the front and back regions near the edge and can result in either overall growth or shrinking of the FA as shown below.

We first consider a quasi-two-dimensional model of FA in which the elastic thin film is represented by particles that interact via springs of stiffness k_0 (see Fig. 3). The particles are bound to the anchoring surface by springs of stiffness k_b , that measure the resistance to normal shear. Each particle in our model is a protein complex consisting of one integrin molecule and the associated intracellular proteins that connect it to the actin cytoskeleton. The elastic properties of the extracellular matrix and its connection to the anchoring surface are included by fixing the anchors to the surface via a sinusoidal potential which, in the limit of

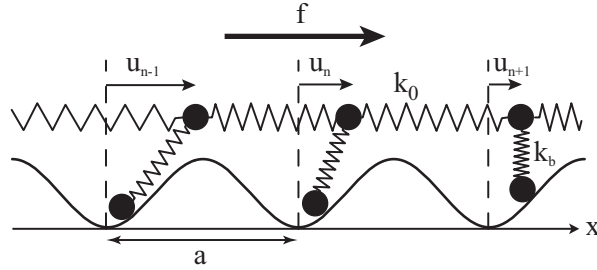


Figure 3. One dimensional chain of interacting particles bound to anchors, as a model for focal adhesions grafted to an extracellular matrix. The potential $V(x)$ accounts for the grafting properties of the extracellular matrix. The distance a between the anchors is the integrin-integrin spacing and u_n is the displacement of the n^{th} particle from its position in absence of force. (From Ref. [30], Copyright (2004), National Academy of Sciences, USA)

small displacements, reduces to a spring-like interaction where k_m is the stiffness of the anchorage close to the equilibrium position. The case of a grafted layer is found by taking the limit $k_m \rightarrow \infty$.

Predictions of the Model

In a one dimensional version of this approach (Fig. 3, which can easily be generalized to a two-dimensional layer), the mechanical equilibrium for a such a system of particles pulled by a force $F(x)$ is, in the continuum limit:

$$k_0 a^2 \frac{d^2 u}{dx^2} - k_b u + F(x) = 0, \quad (7)$$

where k_0 is the spring constant connecting the particles and k_b accounts for the restoring force due to the connections to the fixed and rigid extracellular matrix; the integrin-integrin spacing is denoted by a . We solve Eq. (7) for a gate-shaped field of force of amplitude, f , per unit length and width L ; that is, the force is only non-zero for $-L/2 < x < L/2$. This force profile corresponds to the local pulling force due to stress fibers, and induces the following spatial variation of the local, average density, $\delta\Phi(x)$, relative to the undeformed density Φ :

$$\begin{aligned} \frac{\delta\Phi}{\Phi}(x) &= -\frac{du}{dx} \\ &= \frac{f}{\sqrt{k_b k_0}} \begin{cases} \sinh \frac{x}{\ell} e^{-L/2\ell} & \text{if } |x| < L/2 \\ \sinh \frac{L}{2\ell} e^{-|x|/\ell} \text{sign}(x) & \text{if } |x| \geq L/2. \end{cases} \quad (8) \end{aligned}$$

Equation (8) is derived in the case of a stiff matrix ($k_m \rightarrow \infty$) and shows that the deformation decreases exponentially with a range $\ell = a\sqrt{\frac{k_0}{k_b}}$. Remembering that an actual adhesion has a finite thickness fixes the order of magnitude of ℓ : force-induced deformations must vanish at the bottom surface due to the grafting boundary condition appropriate to the case of a immobilized extracellular matrix. The range ℓ is thus of order of the thickness of the junction (~ 100 nm). The representation of the adhesion as an infinite elastic medium pulled by a force acting on a region of size L is therefore valid once the actual size of the adhesion is larger than $L + 2\ell$, where $\ell \sim 100$ nm $\ll L$.

The three dimensional case is treated more rigorously in [27], using a full elastic treatment of a thin film subject to a surface force, F , on its top surface with zero displacement boundary conditions at the bottom surface where the film is grafted to the substrate. The density, $\delta\Phi$ at the top surface is anisotropic and varies like,

$$\delta\Phi \sim \frac{F h e^{-r/\ell}}{E \ell \sqrt{r/\ell}} \cos \phi, \quad (9)$$

where ϕ is the azimuthal angle, E is the Young's modulus of the film, h is the film thickness, r is the distance from the applied force, and as above, ℓ is proportional to the thickness and is a function of the elastic constants of the film [27]. This predicts a highly anisotropic response to the force in two dimensions and is consistent with the observation that the FA only grow in the direction of the applied force. The variation of density due to a local stress is only significant close (within a distance ℓ) to the edges of the stressed area. The predicted anisotropy means that changes in density are therefore much smaller on the sides of the stressed area perpendicular to the force, in accord with observations [14].

Growth of Focal Adhesions

The main hypothesis of our model is that force-induced deformations trigger the biochemical response of FA, via conformational (e.g. activation of integrins) and/or organizational changes (e.g. binding of plaque proteins) of molecules embedded in a narrow region of size ℓ where the density varies. This local activation increases the rate of association of free proteins within this area. The competition of the elastic and biochemical energies determine whether additional proteins will join the FA. Within our model, the addition of a protein complex of cross-sectional area a^2 to the FA results in a deformation with an elastic energy cost, ΔE_{el} proportional to $\frac{f^2 a^2}{2k}$ where k (which replaces k_b defined above) is an effective elastic constant that includes the finite stiffness of the extra-

cellular matrix. We now suppose that the association of a free protein complex to the front edge of the adhesion releases an energy, ΔE_a , that depends on the change in density at the front edge of the stressed region. In the absence of density variations, the probability of attaching a new particle is unchanged, and $\Delta E_a = 0$. For small variations of the density, ΔE_a can be taken to vary linearly with the change in density at the edge. This energy also scales with the free energy of reaction of one protein complex, e . Adding a protein complex to an adhesive junction thus involves an overall variation of free energy:

$$\Delta E = \frac{f^2 a^2}{2k} - e \frac{f}{\sqrt{k k_0}}. \quad (10)$$

When $e < 0$, aggregation of new particles to an existing adhesion is thermodynamically unfavorable ($\Delta E > 0$), and an additional input of energy is required to stabilize the protein cluster. For this thermodynamically unfavorable growth process, increasing the force per unit length, f , leads to smaller adhesions. FA can only grow when the overall free energy of Eq. (10) is negative, corresponding to $e > 0$ – *i.e.* favorable aggregation energy and an exothermic, local chemical interaction. However immobilization of the extracellular matrix ($k \rightarrow 0$) or very large forces can lead to positive value for ΔE , and, if large enough, may arrest the growth process, even if $e > 0$. This analysis can be generalized to predict the kinetics of growth of FA [30].

Acknowledgments

The authors acknowledge very fruitful experimental collaborations with L. Addadi, N. Balaban, A. Bershadsky, B. Geiger, D. Riveline, and theoretical discussions with I. Bischofs and M. Kozlov. This work has been supported by the Israel Science Foundation, the U.S. – Israel Binational Science Foundation, the Minerva Foundation, the German – Israel Foundation and an EU Network Grant. USS is grateful for the support of the Emmy Noether Program of the German Science Foundation.

References

- [1] B. Alberts, D. Bray, J. Lewis, M. Raff, K. Roberts, J. Watson, *Molecular Biology of the Cell*, Garland Publishing, New York, 1994.
- [2] D. Boal, *Mechanics of the Cell*, Cambridge University Press, Cambridge, 2002.
- [3] B. Geiger, A.D. Bershadsky, *Cell*, Vol. 110, pp.139–142, 2002.
- [4] N.Q. Balaban, U.S. Schwarz, D. Riveline, P. Goichberg, G. Tzur, I. Sabanay, D. Mahalu, S.A. Safran, A.D. Bershadsky, L. Addadi, B. Geiger, *Nature Cell Biol.*, Vol. 3, pp.466–472, 2001.

- [5] U.S. Schwarz, S.A. Safran, *Phys. Rev. Lett.*, Vol. 88, 048102, 2002.
- [6] I.B. Bischofs, U.S. Schwarz, *Proc. Natl. Acad. Sci. USA*, Vol. 100, pp.9274–9279, 2003; I.B. Bischofs, S.A. Safran, U.S. Schwarz, *Phys. Rev. E*, Vol. 69, 021911, 2004.
- [7] P.C. Dartsch, H. Hämmerle, E. Betz, *Acta Anat.*, Vol. 125, pp.108, 1986.
J.H.-C. Wang and E.S. Grood, *Connect. Tissue Res.*, Vol. 41, 29, 2000.
- [8] K. Jakab, A. Neagu, V. Mironov, R.R. Markwald, G. Forgacs, *PNAS*, Vol. 101, pp.2804, 2004.
- [9] B. Geiger, *Science* Vol. 294, pp.1661–1663, 2001.
- [10] F.G. Giancotti, E. Ruoslahti, *Science*, Vol. 285, pp.1028–1032, 1999.
- [11] R. Zaidel-Bar, C. Ballestrem, Z. Kam, B. Geiger, *J. Cell Sci.*, Vol. 116, pp.4605–4613, 2003.
- [12] R.J. Jr Pelham, Y.-L. Wang, *Proc. Natl. Acad. Sci. USA*, Vol. 94, pp.13661–13665, 1997.
- [13] C.-M. Lo, H.-B. Wang, M. Dembo, Y.-L. Wang, *Biophys. J.*, Vol. 79, pp.144–152, 2000.
- [14] D. Riveline, E. Zamir, N. Q. Balaban, U. S. Schwarz, T. Ishizaki, S. Narumiya, Z. Kam, B. Geiger, A.D. Bershadsky, *J. Cell Biol.*, Vol. 153, pp.1175–1185, 2001.
- [15] K.A. Beningo, Y.-L. Wang, *Trends Cell Biol.*, Vol. 12, 79, 2002.
- [16] A.K. Harris, P. Wild, D. Stopak, *Science*, Vol. 208, pp.177–179, 1980; A.K. Harris, D. Stopak, P. Wild, *Nature*, Vol. 290, pp.249–251, 1981.
- [17] M. Dembo, T. Oliver, A. Ishihara, K. Jacobson, *Biophys. J.*, Vol. 70, pp.2008–2022, 1996; M. Dembo, Y.-L. Wang, *Biophys. J.*, Vol. 76, pp.2307–2316, 1999.
- [18] R. Merkel, P. Nassoy, A. Leung, K. Ritchie, E. Evans, *Nature*, Vol. 397, 50, 1999.
- [19] L. D. Landau, E. M. Lifshitz, *Theory of Elasticity*, Pergamon, Oxford, 1970.
- [20] U.S. Schwarz, N.Q. Balaban, D. Riveline, B. Geiger, S.A. Safran, *Biophysical Journal*, Vol. 83, pp.1380, 2002.
- [21] R. Siems, *Phys. Stat. Sol.*, Vol. 30, pp.645, 1968.
- [22] H. Wagner, H. Horner, *Adv. Phys.*, Vol. 23, pp.587, 1974.
- [23] J. P. Butler, I. M. Tolic-Norrelykke, B. Fabry, J. J. Fredberg, *Am. J. Physiol. Cell Physiol.*, Vol. 282, pp.C595, 2002.
- [24] J. Y. Wong, A. Velasco, P. Rajagopalan, Q. Pham, *Langmuir*, Vol. 19, pp.1908, 2003.
- [25] F. Grinnell, *Trends in Cell Biol.*, Vol. 10, pp.362, 2000.
- [26] P.F. Davies, A. Robotewskyj, M.L. Griem, *J. Clin. Invest.*, Vol. 93, pp.2031–2038, 1994.
- [27] A. Nicolas, S.A. Safran, *Phys. Rev. E*, Vol. 69 pp.051902-1–051902-7, 2004.
- [28] B.Z. Katz, E. Zamir, A.D. Bershadsky, Z. Kam, K.M. Yamada, B. Geiger, *Mol. Cell Biol.*, Vol. 11, pp.1047–1060, 2000.
- [29] D. Choquet, D.P. Felsenfeld, M.P. Sheetz, *Cell*, Vol. 88, pp.39–48, 1997.
- [30] A. Nicolas, B. Geiger, S. A. Safran, *PNAS*, Vol. 101, pp.12520–12525, 2004.

ELECTROKINETIC FLOW INSTABILITIES IN MICROFLUIDIC SYSTEMS

Hao Lin, Michael H. Oddy and Juan G. Santiago

*Mechanical Engineering Department, Stanford University
Stanford, CA 94305, USA*

juan.santiago@stanford.edu

Abstract The stability of electrokinetic flow in a rectangular cross-section microfluidic channel with transverse conductivity gradients and driven by streamwise electric fields was explored. Such a system exhibits a critical electric field above which the flow is highly unstable, resulting in fluctuating velocities and rapid stirring. The problem was studied using theoretical and numerical analyses, as well as experimental observations. It was found that the internally generated electric body force was responsible for the instability, whereas the diffusion of ion species provided a stabilizing mechanism. Various models including two-dimensional and depth-averaged formulations were studied; modeling results compare well with experimental observations. These results have application to the design and control of on-chip assays that require high conductivity gradients, and provide a rapid mixing mechanism for low Reynolds number flow in microchannels.

Keywords: Electrokinetics, electrokinetic instability, critical electric field, electric conductivity gradient, microfluidics, microchannel, micromixing

1. Introduction

Over the past decade there has been an extensive research into the design of devices that perform chemical analysis in micro-fabricated fluidic channel structures. Often referred to as Micro Total Analysis Systems (μ TAS), these systems exhibit a mass transport regime that is often different from that of macro-scale flow devices. Many of these devices apply electrokinetic liquid-phase, bioanalytical techniques including capillary electrophoresis and isoelectric focusing, and often manipulate the samples having poorly characterized or unknown electrical conductivi-

ties. As a result, conductivity mismatches often occur between the sample/reagent species and the background electrolyte. In the presence of applied electric fields, conductivity gradients can induce electrohydrodynamic coupling, which can in turn generate complex, unstable flow-fields. Flows exhibiting these physics have been reported in the classical electrohydrodynamics literature (see for example, the seminal paper by Høburg and Melcher, 1976, and a later work by Baygents and Baldessari, 1998). In this paper, we review flow instabilities due to electric field and conductivity gradients coupling in electrokinetic systems. Electrokinetic flows are a subset of electrohydrodynamics characterized by the presence of an electrical double layer and regimes, where transport due to molecular diffusion is important.

Although desirable for rapid-mixing applications, the electrokinetic instabilities are unwanted in microfluidics applications such as sample injection, separation, and controlled diffusion-limited reaction processes where minimal sample dispersion is required. This motivates research toward a better understanding of the conditions necessary for the onset of electrokinetic flow instability. In 2001 Oddy et al. first reported observation of electrokinetic instability (EKI) in a microchannel system. These experiments were performed in 4-mm-long glass capillaries with rectangular cross-sections, and the instabilities were in general of temporal nature (Oddy et al., 2001). In a slightly different geometry (microfluidic T-junction), Chen and Santiago also reported spatial amplification of disturbances which was later identified as convective instability (Chen and Santiago, 2002, Chen et al., 2004). In all of these experiments, conductivity gradients were in the spanwise direction (perpendicular to the electric field), and there existed critical values of the applied streamwise electric field above which instabilities and significant stirring occurred.

Following these initial experimental observations, there has been a development of models for electrokinetic flow instabilities. Models are useful in predicting threshold conditions for instability onset as well as other flow features including coherent wave structures and mixing rate. Lin et al. (2004) and Chen et al. (2004) showed that a generalized EHD modeling framework (derived from the so-called “leaky dielectric” model first developed by Melcher and Taylor, 1969) can be used to describe both the low-conductivity, non-diffuse charge dynamics of classical EHD, and the more recently reported flow instabilities of high-conductivity electrolyte in electrokinetic microsystems. Lin et al. (2004) analyzed the temporal stability properties based on a two-ion model, comprising the conductivity transport equation along with the conservation of momentum and electromigration current. They showed that the model provided good qualitative and fair quantitative agreement with regard to

the threshold electric fields and critical wavenumbers. Lin et al. (2004) also presented non-linear simulations of their set of governing equations that capture the high Peclet (or the so-called electric Rayleigh) number stirring events observed in experiments. Using a convective framework, Chen et al. (2004) showed that EKI could manifest itself convectively in the presence of a strong electroosmotic flow. In the latter analysis, EKI is modeled using a linearized, thin-layer limit of the Navier-Stokes equations coupled with conservation equations for electrical conductivity and current. The model reveals both convectively and absolutely unstable eigenmodes. More recently, Storey et al. (2004) presented a depth-averaged version of the governing equations used by the Lin et al. (2004) model. Their depth-averaged model compared favorably with a complete three-dimensional model for thin channel geometries.

In this paper we present our experimental, analytical, and computational results and some progress in the pursuit of modeling and understanding of EKI in electrokinetic microchannels. We shall briefly introduce the experimental results, followed by a general theoretical formulation developed in Lin et al. (2004). Using these equations we show the results from various linear analyses as well as nonlinear simulations, and assess their qualitative and quantitative agreements with experimental data. We conclude the paper by introducing our latest development in a depth-averaged framework suitable for the study of generalized electrokinetic flows in microchannels with thin channel geometry.

2. Experimental Observations

Here we show a few exemplary results from our experiments. The microchannel consisted of a borosilicate glass capillary (Wilmad-Labglass, NJ) with a rectangular cross-section. The channel was 4 mm long (in the x or streamwise direction), 1 mm wide (in the y or spanwise direction), and 0.1 mm deep (in the z or depth direction). Two buffer streams initially occupied the upper and lower halves of the microchannel, resulting in a diffuse conductivity gradient along the spanwise, y -direction; an electric field was subsequently applied along the streamwise, x -direction. The conductivity of the buffer streams were 50 and $5 \mu\text{S}/\text{cm}$, respectively, resulting in a conductivity ratio of $\gamma = 10$. For flow visualization, an electrically neutral, heavy-molecular-weight dye (70 kDalton) composed of a dextran-rhodamine B conjugate (Molecular Probes, OR) was added to the high-conductivity buffer stream. The imposed electric potential initiated an electroosmotic flow in the channel and, for electric fields above a threshold value, electrokinetic instabilities.

A representative set of images from experiments conducted at 1, 2, and 3 kV applied potentials are shown in Fig. 1. The potentials were applied over a distance of 40 mm, such that they were equivalent to applied fields of 25,000, 50,000 and 75,000 V/m, respectively. In each case, the top figure of each series shows the initial, undisturbed interface between the dyed and undyed buffer streams in the channel ($t = 0$). The successive images in each column show the temporal evolution of the imaged dye under a constant, DC potential. In this color scheme, blue corresponds to the undyed, low-conductivity stream, and red to the dyed high-conductivity stream. For an applied field of 25,000 V/m, the interface was only slightly perturbed and only slight fluctuations are apparent in the images captured at 4.0 s and 5.0 s. At the two higher applied voltages, the interface exhibited a rapidly-growing wave pattern within the first 1 s. The unstable fluid motion in the channel buckled the interface and proceeded to stretch and fold the material lines. The transverse

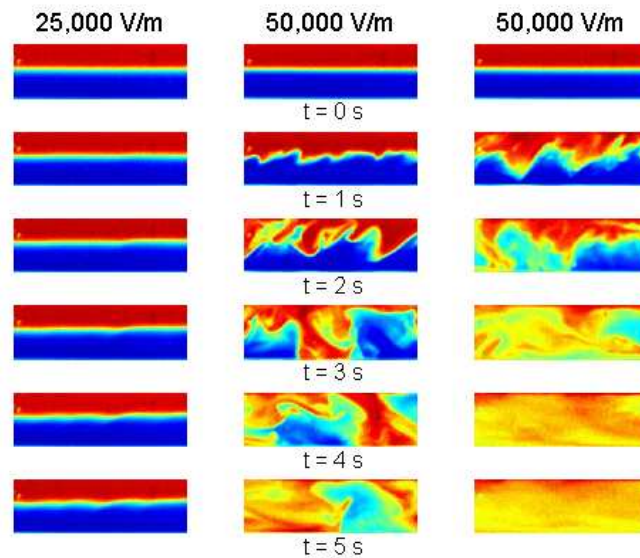


Figure 1. Sample images from the experiment, shown for applied fields of 25,000, 50,000, and 75,000 V/m, corresponding to the first, second, and third column. Images obtained at various times are shown for each column. The electric field and bulk flow directions were from left to right. High voltage was applied as a Heaviside function at $t = 0$ s. Each image corresponds to a physical area 1 mm wide (y) and 3.6 mm long (x). The depth of the channel is $100\ \mu\text{m}$ along the z -direction (into the page). Small amplitude waves at $t = 1$ s grew and led to rapid stirring of the initially distinct buffer streams. The instability stretched and folded material lines and, after about 4 s for the 75,000 V/m applied field, resulted in a well-stirred, relatively homogeneous dye concentration field. The time of the images in each row are shown in the figure.

and fluctuating velocities associated with this unstable motion resulted in rapid mixing of the two streams. At the 75,000 V/m applied field, the channel reached a well-stirred state and with nearly-homogeneous concentration fields observable within 5 s.

3. Formulation

The description of experiments given above serves as an introduction to the problem and describes the observed features of electrokinetic flow instability. We now turn to a theoretical formulation of the flow. In this section, we summarize the governing equations and discuss the parameters of interest in our experiment. The equations of our model are derived from the conservation laws for a dilute, two-species electrolyte solution (Probstein, 1994), and we have adopted (with justification) a relaxation assumption to simplify the equations. The scaling analysis and derivations are discussed in detail in Lin et al. (2004) and should not be repeated here. The (*dimensionless*) equations read

$$\frac{\partial \sigma}{\partial t} + v \cdot \nabla \sigma = \frac{1}{\text{Ra}_e} \nabla^2 \sigma, \quad (1)$$

$$\nabla \cdot (\sigma \nabla \Phi) = 0, \quad (2)$$

$$\nabla^2 \Phi = -\rho_E, \quad (3)$$

$$\nabla v = 0, \quad (4)$$

$$\text{Re} \left(\frac{\partial v}{\partial t} + v \cdot \nabla v \right) = -\nabla p + \nabla^2 v - \rho_E \nabla \Phi, \quad (5)$$

where σ is the conductivity, v is the bulk fluid velocity, Φ is the electric field (which includes both the applied and generated components), and p is pressure. The electric Rayleigh number (similar to the Peclet number) and the Reynolds number that arise from the nondimensionalization are defined as

$$\text{Ra}_e \equiv \frac{U_{ev} H}{D}, \quad \text{Re} \equiv \frac{U_{ev} H}{\nu}.$$

Here H is half-channel width, D is an effective diffusivity of the conductivity, and ν is the kinematic viscosity of the electrolyte solution (usually aqueous). The velocity U_{ev} , the so-called electroviscous velocity, is velocity scale derived by setting equal the electric body force and the viscous force in the momentum equation. (See Hoburg and Melcher, 1976, Lin et al., 2004 and Chen et al., 2004; more discussions on these parameters can also be found in these references.)

4. Two-dimensional Model

We first present a model where we assume that the flow exists only in the $x - y$ plane, and that there is no dynamics in the z -direction. This analysis will capture the basic physics of the instability mechanisms due to the conductivity gradient.

We first use a linear stability analysis to predict the regimes where we would expect rapid mixing to occur. The base states are a diffused, spanwise conductivity profile $\sigma_0 = \sigma_0(y)$ with a (high-to-low) conductivity ratio of 10, and a shear electroosmotic flow $u_0 = u_0(y)$. Note that the spanwise dependence of the latter was induced by that of the former *via* the dependence of zeta potential on conductivity.

We assume that disturbance is periodic in the x direction, and the growth of amplitude is exponential in time. We have obtained, for each streamwise wave number k and applied field E_0 , a set of eigenvalues (the exponential growth rates), together with their respective eigenfunctions. In Fig. 2 we show a contour plot of the growth rates of the most unstable eigenfunction in the wave number-Rayleigh number (electric field) parameter space. Symbol s denotes the real and dimensional growth rate. The neutral stability curve is obtained by setting $s = 0$. A threshold electric field is successfully captured from the minimal value of E_0 on the neutral stability curve. As originally reported by Baygents and Baldessari (1998), we found that the inclusion of the diffusive term $\nabla^2 \sigma / \text{Ra}_e$ in Eq. (1) is crucial for the existence of the neutral stability curve.

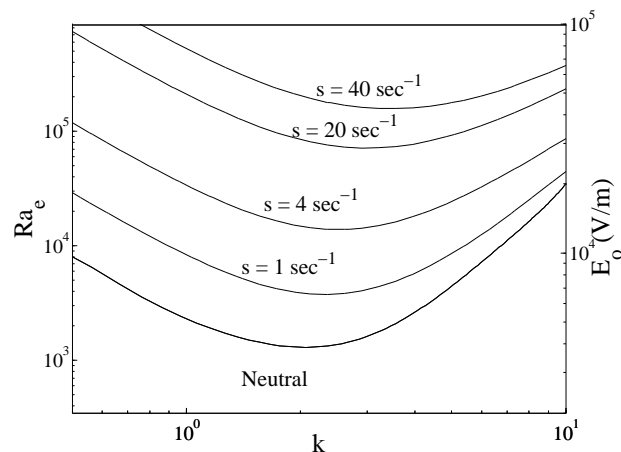


Figure 2. Contour plot of growth rates (s) versus wave number and Rayleigh number. Dimensional applied electric field is provided on the right-hand axis. For the case plotted here, the ratio of the conductivity between the two streams is 10.

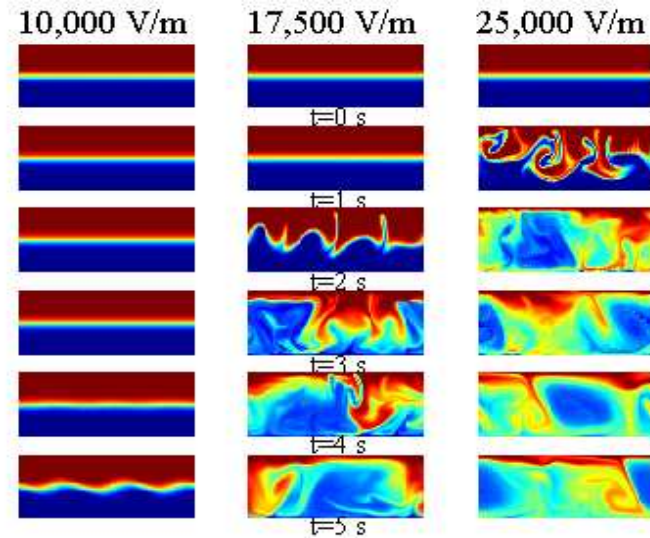


Figure 3. Snapshots of the simulated dye field at various instances in time for different driving electric fields. In this color scheme red corresponds to the high conductivity buffer, and blue to the low one. Each column indicates a different applied field and the rows within each column present the selected snapshots in time. The image corresponds to a physical domain of $3.6\text{ mm} \times 1\text{ mm}$. The time for noticeable waves to develop is decreased as the field is increased.

In addition to the two-dimensional linear stability analysis presented above, we have also solved the full nonlinear governing Eqs. (1-5) numerically to capture the nonlinear evolution of the instability observed in the experiments. The initial conditions are the base states plus a small white noise perturbation. The solution details are documented in Lin et al. (2004). Figure 3 shows the nonlinear evolution of the simulated dye at various instances in time and for three different electric fields. The model reproduces many of the essential features observed in the experiments, including the shape and initial break-up dynamics of the interface, the transverse growth of a wave pattern in the interface, and the roll-up of scalar structures observed at later times. Note the similarity in the most unstable (and most apparent) wave number at later times between the simulation and experiments.

Despite the similarities between the wave number and dynamics of the interface breakup, the threshold imposed fields from both the linear and nonlinear predictions are lower than those shown for the experiment in Fig. 1. For example, compare the evolution of the dye at $25,000\text{ V/m}$ from the experiments (Fig. 1, column 1) and the simulation (Fig. 3, column 3). We see that the simulation at $25,000\text{ V/m}$ predicts

a well-stirred flow field in less than three seconds, while experiments show that the flow is stable on the time-scale of the experiments. The simulation of 25,000 V/m is qualitatively similar to the experimental flow at 75,000 V/m (Fig. 1, column 3). Despite the discrepancy in the magnitude of the applied field, our simulation captures a threshold field and scalar features qualitatively similar to the experiment. In the following section we address possible causes for the under-prediction of the threshold electric field by including three-dimensional effects.

In comparison with the temporal instability analysis presented here (which is consistent with the experimentally observed instability in the previous section), Chen et al. (2004) analyzed the instability in a convective framework which is consistent with the spatial growth that was observed in T-junction microfluidic channels. Among other contributions, the authors found that an important dimensionless group R_ν , defined as the ratio of the electroviscous to electroosmotic velocity, is critical in demarcating the absolute/convective instability boundary. Interested readers are referred to Chen et al. (2004).

5. Depth-averaged Model

In the previous sections we have provided a two-dimensional framework which appears to capture the primary physics of our flow. However, the primary flaw in that model is the two-dimensional assumption, for a channel with an aspect ratio of $\delta \equiv d/H = 0.1$, where d denotes the channel half-width. Such a thin channel geometry was also used in the experimental work of Chen et al. (Chen et al., 2002; Chen et al., 2004). In three dimensions, an EDL forms not only on the top and bottom walls of $y = \pm 1$, but also along the side walls ($z = \pm 1$), and strongly drives the flow due to the small depth of the channel. The three-dimensional nature of a thin channel has the added dynamics that the fluid motion in the interior of the channel is directly coupled to the top and bottom wall boundary condition (determined in part by the local value of ion density).

In Lin et al. (2004) we presented a 3D linear analysis and found that the predicted threshold field was one order-of-magnitude higher than that from the 2D linear analysis, in much closer agreement with the experimental observations. However, a depth-averaging approach is preferred since in general, the 3D analysis (simulations) are computationally more expensive, and considering that the microchannels of our interest are “shallow” in the depth (z) direction. In Chen et al. (2004) a depth-averaged analysis was performed on a set of linearized governing equations and the resulted linear equation system was used for convective

instability analysis. In Storey et al. (2004) a more complete Hele-Shaw type of integrated momentum equation was used. Both models yielded favorable quantitative results when compared with experimental data.

Here we extend and complete the ideas that were first developed by Chen et al. (2004) and Storey et al. (2004). We develop a generalized, nonlinear depth-averaged model suitable for the study of electrokinetic microchannel flows with thin channel geometries. We accomplish this through a complete asymptotic analysis of the full three-dimensional equations based on a smallness parameter which is the channel cross-sectional aspect ratio δ . Our general methodology follows a combined lubrication (for the momentum equations) and Taylor-Aris (for the convective-diffusion of the conductivity field) approach. Without presenting the details of the derivation, we list the final equations as

$$\frac{\partial \bar{\sigma}}{\partial t} + \bar{u} \cdot \nabla_H \bar{\sigma} = \frac{1}{\text{Ra}_e} \left\{ \nabla_H^2 \bar{\sigma} + \frac{2}{105} \text{Ra}_e^2 \delta^2 \nabla_H \cdot [\bar{U}(\bar{U} \cdot \nabla_H \bar{\sigma})] \right\}, \quad (6)$$

$$\nabla_H \cdot (\bar{\sigma} \nabla_H \bar{\Phi}) = 0, \quad (7)$$

$$\nabla_H \cdot \bar{u} = 0, \quad (8)$$

$$\text{Re} \delta^2 \left(\frac{\partial \bar{u}}{\partial t} + \bar{u} \cdot \nabla_H \bar{u} \right) = -\nabla_H \bar{p} + \nabla_H^2 \bar{\Phi} \nabla_H \bar{\Phi} - 3\bar{U} + \delta^2 \nabla_H^2 \bar{u}. \quad (9)$$

Here the overbar denotes depth-averaged quantity, the operator ∇_H denotes the in-plane gradient (to distinguish from the full three-dimensional gradient), and $\bar{U} \equiv \bar{u} - u_\infty$ is the difference between the total depth-averaged velocity and the electroosmotic velocity.

The main contributions of this new equation set are the Taylor-dispersion-type term in the conductivity equation, and the Darcy-Brinkman-Forchheimer (DBF) type of momentum equation which is of second-order consistency in δ (Chen et al., 2004; Liu and Masliyah, 1996). We present preliminary results in the assessment of the validity and accuracy of the model.

Figure 4 compares the linear stability results for growth rate of disturbances versus wave number at a single Rayleigh number of $\text{Ra}_e = 5.000$. We perform linear analyses using the following three models:

1. The linear integrated momentum equations used by Storey et al. (2004).
2. The linearized three-dimensional equations (Lin et al., 2004).
3. The depth-averaged DBF formulation presented here.

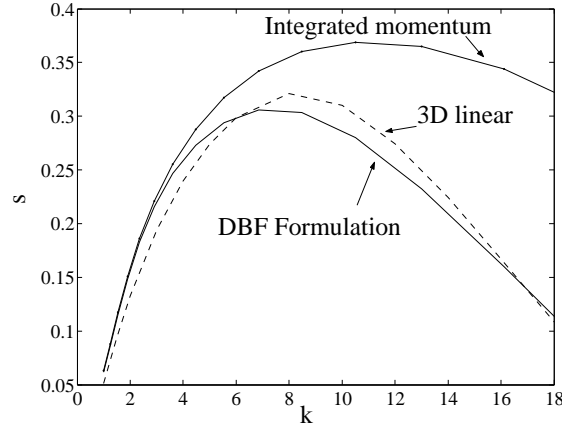


Figure 4. Comparison of growth rates of disturbances as predicted by three models. Shown here are the real part of the growth rates versus the wave number for $Ra_e = 5.000$ as computed with the DBF momentum equation presented here, the integrated momentum equation (δ^0 approximation, Storey et al., 2004), and the three-dimensional equation set. The DBF formulation represents in-plane viscous stresses that quench the unphysically high wave number growth and is in agreement with the three-dimensional result.

Note that at the linear regime, the Taylor dispersion in Eq. (6) drops as a higher-order term, and the only difference between the models are within the momentum equations. We find that all three models are in good agreement for wave numbers below about 4. However, when compared with the more accurate three-dimensional analysis, the DBF momentum equation provides significantly better results at higher wave numbers than the lower-order, integrated momentum approximation.

The characteristics of the DBF momentum equations also make it more advantageous to use in nonlinear simulations when compared with the integrated momentum equation. In particular, the inclusion of in-plane diffusion $\delta^2 \nabla_H^2 \bar{u}$ preserves a mathematical structure similar to the original Navier-Stokes equations, and enables reproduction of the boundary effects (*e.g.*, at $y = \pm 1$ walls) that are not captured by lower-order approximations. This will be discussed further in a future work, and here we simply show some sample results of the full nonlinear, depth-averaged simulations with Eqs. (6–9). That is, a model with the combined effects of Taylor dispersion and the DBF momentum equation. We try to reproduce the experimental image presented in Fig. 1 at the two lower voltages (25,000 and 50,000 V/m); the result is shown in Fig. 5. Again the model reproduces essential features observed in the experiments such

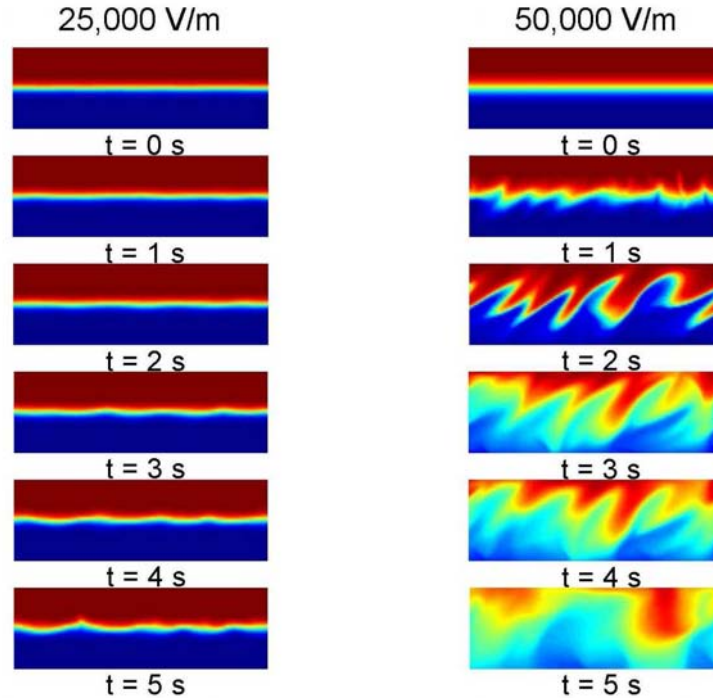


Figure 5. Nonlinear simulation of the depth-averaged equation system. This model includes the combined effects of the Taylor dispersion and the DBF momentum equation. In the strongly nonlinear regime the Taylor dispersion acts as an extra smoothing mechanism. The results compare favorably with the experimental data presented in Fig. 1.

as the fastest growing wave numbers and the growth rates of the interface disturbance amplitude. However, note that the computations are now at exactly the same field strength as those applied in the experiments (as opposed to the unnaturally low fields used for comparison with the simple 2D model results of Fig. 3). Future work will also include the application of the model to different flow configurations such as those used in field amplified sample stacking (FASS).

6. Summary

In this work we have presented experimental, numerical, and analytical results that explain the basic mechanisms behind an electrokinetic mixing phenomenon observed in microfluidic channels. We have presented analysis and computations based on various sets of assumptions for electrokinetic flows in a long, thin channel with a transverse conduc-

tivity gradient. Our models are able to predict general trends in the data, as well as many of the qualitative and quantitative aspects of the observed flow field. Ongoing work includes the development of a generalized, depth-averaged model for a wide class of electrokinetic flows (such as FASS) in thin microfluidic channels.

The models presented in this work are useful in optimization studies, as parameter space can be spanned in simulations more quickly than in the laboratory. The results described by Oddy et al. (2001) has demonstrated that oscillatory electric field can potentially drive even more vigorous mixing. The models presented here can be used to optimize the form of the forcing function, to design the shape of a micro-mixer, and to develop optimal control strategies for both the micro-mixing and the suppression of instabilities.

Acknowledgments

This work was sponsored by DARPA (Contract Number F30602-00-2-0609) with Dr. Anantha Krishnan as contract monitor and by an NSF CAREER Award (J.G.S.) with Dr. Michael W. Plesniak as contract monitor.

References

- [1] J. Baygents, F. Baldessari, Electrohydrodynamic instability in a thin fluid layer with an electrical conductivity gradient, *Phys. Fluids*, Vol.10, 1, 301–311, 1998.
- [2] C.-H. Chen, J.G. Santiago, Electrokinetic instability in high concentration gradient microflows, *Proceedings of IMECE-2002*, CD Vol.1, #33563, 2002.
- [3] C.-H. Chen, H. Lin, S.K. Lele, J.G. Santiago, Convective and absolute electrokinetic instability with conductivity gradients, *J. Fluid Mech.*, in press, 2004.
- [4] J.F. Hoburg, J.R. Melcher, Internal electrohydrodynamic instability and mixing of fluids with orthogonal field and conductivity gradients, *J. Fluid Mech.*, Vol.73, 333, 1976.
- [5] H. Lin, B.D. Storey, M.H. Oddy, C.-H. Chen, J.G. Santiago, Instability of electrokinetic microchannel flows with conductivity gradients, *Phys. Fluids*, Vol.16(6), 1922–1935, 2004.
- [6] S. Liu, S. Masliyah, Single fluid flow in porous media, *Chem. Eng. Comm.* Vol.148–150, 653–732, 1996.
- [7] J.R. Melcher, G.I. Taylor, Electrohydrodynamics: a review of the role of interfacial stresses, *Annu. Rev. Fluid. Mech.*, Vol.1, 111–146, 1969.
- [8] M.H. Oddy, J.G. Santiago, J.C. Mikkelsen, Electrokinetic instability micromixing, *Anal. Chem.*, Vol.73, 5822–5832, 2001.
- [9] R.F. Probstein, *Physicochemical Hydrodynamics*, John Willey & Sons, New York, 1994.
- [10] B.D. Storey, B.S. Tilley, H. Lin, J.G. Santiago, Electrokinetic instabilities in thin microchannels, *Phys. Fluids*, in review, 2004.

MOLECULAR MECHANICS OF CYTOSKELETAL COMPONENTS

M. Atakhorrami

*Vrije Universiteit Amsterdam, Dept. Phys.
Amsterdam, The Netherlands*

K.M. Addas

*Rowland Institute at Harvard
Cambridge, MA, USA*

M. Buchanan, G.H. Koenderink, F.C. MacKintosh

*Vrije Universiteit Amsterdam, Dept. Phys.
Amsterdam, The Netherlands*

J.X. Tang

*Brown University, Dept. Phys.
Providence, RI, USA*

Christoph F. Schmidt

*Vrije Universiteit Amsterdam, Dept. Phys.,
Amsterdam, The Netherlands*

cfs@nat.vu.nl

Abstract Semiflexible polymers are of great biological importance in determining the mechanical properties of cells. We have used optical tweezers to trap pairs of micron-sized silica spheres in solutions of semiflexible polymers, and laser interferometry to detect their thermal motions with high bandwidth. Frequency-dependent complex shear moduli were extracted from the auto- and cross-correlated bead motions, with the response functions being derived from position-fluctuation data using dispersion relations from linear response theory.

Keywords: Cytoskeleton; semiflexible polymers; microrheology; optical tweezers; laser interferometry

1. Introduction

One of the characteristic lengths that describes a polymer in a solution is the persistence length L_p , which is the length traversed along the filament contour before the tangent vector thermally randomizes its orientation. L_p is proportional to the bending stiffness of the polymer. Flexible polymers are characterized by $L_p \ll L$, rigid rod polymers by $L_p \gg L$. Semiflexible polymers are in the intermediate regime, characterized by $L_p \approx L \gg d$, with filament diameter d . The dynamics of polymer solutions and networks greatly depends on the degree of flexibility of the individual polymers. Recent theoretical treatments have addressed semiflexible polymer networks [1-4]. Such polymers are found particularly in biology where they form networks that determine the mechanical properties of cells.

We report here on rheology experiments on such polymer systems, and in particular on a new microrheology method. There are clear advantages to the miniaturization of a rheology experiment: only small amounts of material are necessary, spatial inhomogeneities can be studied, and the bandwidth of the measurement can be high. We have developed a microrheology technique using laser interferometric tracking of the Brownian motion of micron-sized beads embedded in viscoelastic materials [5]. The simplest implementation of the technique consists of tracking one probe particle at a time (1-bead microrheology) [5]. A further development, avoiding local artefacts due to the insertion of the probe particles into the system, consists of measuring the correlated fluctuations of pairs of probe particles (2-bead microrheology). We have studied the dynamics of several systems and have compared 1-bead and 2-bead results for wormlike micelle, semiflexible fd virus and actin solutions. Particularly in the actin systems, which is a first approximation to the cytoskeleton of cells, we explore the rich multitude of length and time scales in the dynamic behavior of these networks, which are not accessible to conventional macrorheology.

2. Principle of the Technique

The microrheology (MR) technique used here is a passive one in which the thermal fluctuations of pairs of micron-sized beads are observed. Complex auto- and cross-correlation response functions of the beads are calculated using the fluctuation-dissipation theorem [5,6]. The complex response function $\alpha_{ij}^{(n,m)}(f)$ relates the Fourier transform $r_i^{(n)}(f)$ of the displacement of the n^{th} bead $r_i^{(n)}(t)$ to the Fourier transform $F_j^{(m)}(f)$ of the force $F_j^{(m)}(t)$ acting on the m^{th} bead (i and j are either 1 or 2 for

the parallel and perpendicular directions with respect to the line joining the bead centers, respectively),

$$r_i^{(n)}(f) = \alpha_{ij}^{(n,m)}(\vec{r}, f) F_j^{(m)}(f). \quad (1)$$

The measured response function must first be corrected for the trapping effect of the optical tweezers [7]. The fluctuation-dissipation theorem [5] provides the link between the single-sided power spectral density (PSD) [8]

$$S_{ij}^{(n,m)}(f) = \lim_{t' \rightarrow \infty} (2/t') r_{t'i}^{(n)}(f) r_{t'j}^{(m)*}(f) \quad (2)$$

and the imaginary part of the response function, where $r_{t'i}^{(n)}(f)$ is the Fourier transform of the position $r_i^{(n)}(t)$, defined over a finite time t' . A Kramers-Kronig integral can then be used to calculate the real part of the response function, provided that the imaginary part is known over a large enough frequency range. The connection between the auto-correlation response $\alpha_{ii}^{(n,m)}(f)$ of a bead and the corresponding complex shear modulus

$$G_{ii}^{(n,m)}(f) = G_{ii}'^{(n,m)}(f) + iG_{ii}''^{(n,m)}(f) \quad (3)$$

of the viscoelastic medium surrounding the bead is assumed to be provided by the generalized Stokes-Einstein relation (GSER) [5],

$$G_{ii}^{(n,m)}(f) = \frac{1}{[6\pi a \alpha_{ii}^{(n,m)}(f)]}, \quad (4)$$

where G' and G'' are the elastic and loss modulus respectively, and a is the radius of the bead. The cross-correlation shear modulus of the solution is derived from the parallel $a_{\parallel} \equiv \alpha_{11}^{(1,2)}$ response by [9]

$$G_{\text{cross}}(f) = \frac{1}{[4\pi r \alpha_{\parallel}(f)]}, \quad (5)$$

where r is the distance between the centers of the beads.

3. Experimental Setup

Two focused laser beams were used to form optical tweezers and trap pairs of probe particles imbedded in solutions of semiflexible polymers. Position fluctuation data was recorded with a 200 kHz sampling rate, using laser interferometry and quadrant photodiode detection as described in detail elsewhere [5,6,10]. A near-infrared (1064 nm) laser was used for one trap and a 830 nm laser for the second trap. The beams

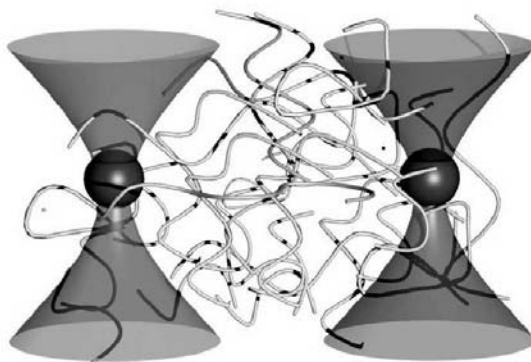


Figure 1. Schematic illustration of the 2-bead microrheology experiment. Two spheres of radius a , are held in two optical tweezers, created by focusing lasers of different wave lengths $\lambda = 830$ nm and $\lambda = 1064$ nm at a separation distance r . The displacements of both particles are detected separately in x and y direction with interferometry.

are brought to a focus in the sample chamber by a high numerical aperture objective. The laser light emerging from the condenser lens, after passing through the sample, is projected onto two quadrant photodiodes in such a way that the back-focal plane of the condenser is imaged [10]. The signals from the four quadrants of each photodiode are combined to obtain the X - and Y -voltages corresponding to the displacements of each bead in these directions in the plane normal to the propagation direction of the laser. The output voltages are, after analog amplification and pre-processing, recorded using an A/D interface and digital data acquisition.

4. Results

Worm-like Micelle Solutions

Figure 2 presents the loss and the viscous shear modulus of a worm-like micelle solutions for 1wt % concentration. The worm-like micelle solutions were made of binary mixtures of cetylpyridium chloride (CPyCL) and sodium salicylate (NaSal) dissolved in brine (0.5 M NaCl). A characteristic feature of worm-like micelle solutions is that they relax low-frequency applied stress with a single dominant relaxation time, reflecting breakage and reptation of the filaments [11]. The system we used

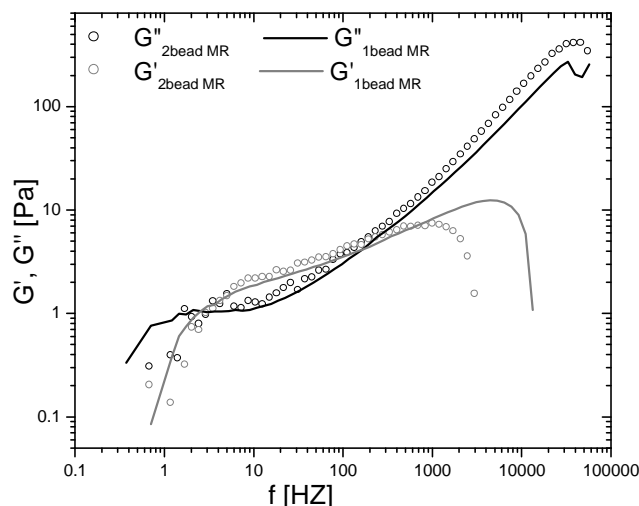


Figure 2. Elastic modulus and loss modulus for a 1wt% worm-like micelle solution. Figure shows the comparison of 1-bead and 2-bead microrheology. The diameter of the beads was $D = 2.1 \mu\text{m}$.

produces micelles with typical diameters of 2-3 nm, a persistence length L_p 10 nm, and an average length between 100 nm and $1 \mu\text{m}$. We have performed 1-bead MR and 2-bead MR for different concentrations of micelles. Bead diameters were $1.16 \mu\text{m}$ and $2.1 \mu\text{m}$.

For this system 1-bead and 2-bead MR results show excellent agreement (Fig. 2). More experimental noise is usually found in 2-bead results since the cross-correlation signal between the displacement of two beads is always weaker than the auto-correlation signal of one bead. The abrupt decrease in both G' and G'' at high frequencies is artefactual and due to anti-alias filtering at the Nyquist frequency and to the finite frequency cut-off effects on the result of the Kramers-Kronig integral. The effect on G' is stronger than on G'' , reflected in about a decade less usable data for G' [5].

It is expected that 1-bead measurements could be sensitive to the local medium properties in the direct vicinity of the probe bead, which could be different from bulk properties due to surface chemistry or steric (entropic) effects. The unmodified bulk viscoelastic properties of the solutions should, on the other hand, be reported by the 2-bead results [9]. Even in the absence of specific chemical or electrostatic interactions, steric depletion of polymer in the vicinity of the probe particles is expected to cause differences in the 1- and 2-bead results, provided that probe size and network length scales are comparable. In the case of

the worm-like micelle solutions we studied here, network length scales are at least a decade smaller than bead radius and we therefore did not expect differences due to surface artefacts. The data nicely confirms this expectation and confirms the validity of both methods. It should be noted that independently measured parameters enter the data evaluation for the two cases, bead diameter for 1-bead results and bead distance (only) for 2-bead results. These results further establish microrheology, both 1-bead and 2-bead methods, as a highly sensitive and high-bandwidth technique to measure shear elastic moduli of viscoelastic materials. Good agreement between more conventional macrorheology and microrheology on similar samples is reported elsewhere [12].

Fd Virus Solutions

Fd virus is a filamentous DNA bacteriophage [6], which is here used as a monodisperse model system for semiflexible polymers. Filaments have a diameter of 7 nm, persistence length $L_p = 2.2 \mu\text{m}$ and contour length $L = 0.9 \mu\text{m}$. Fd solutions were probed with a bead diameter of $D = 1.16 \mu\text{m}$. Fig. 3(a) shows the concentration dependence of the 1-bead (circles) and 2-bead (triangles) elastic moduli. The loss modulus is shown in Fig. 3(b). Data are displayed for 2, 5, 10, and 14 mg/ml fd concentrations. The high-frequency slope of the loss modulus is consistent with single filament dynamics predictions [1,4]. At such high frequencies, the entanglement of the polymer in its network does not contribute to the modulus. The modulus is proportional to concentration and expected to scale with a power law exponent of 3/4. The elastic modulus is expected to exhibit the same behavior but due to the cut-off in the Kramers-Kronig integral, the reliably measured elastic modulus extends to about 10 kHz, a frequency apparently still in the transition regime between collective dynamics and high-frequency single filament dynamics because a true scaling regime would require both moduli to scale with the same power law. The high-frequency behavior is attributed to tension in the filaments due to the shear-induced extension. At lower frequencies, the tension contributes less, and the dominating contribution to the stress is that of bending and orientational dynamics [1,2]. The data demonstrate that for this system 1-bead MR and 2-bead MR are in good agreement. This is remarkable since the length scales of the system, contour length and persistence length, are comparable with the probe bead diameter. If there was a steric depletion effect, it has evidently led to a negligible effect on the 1-bead results.

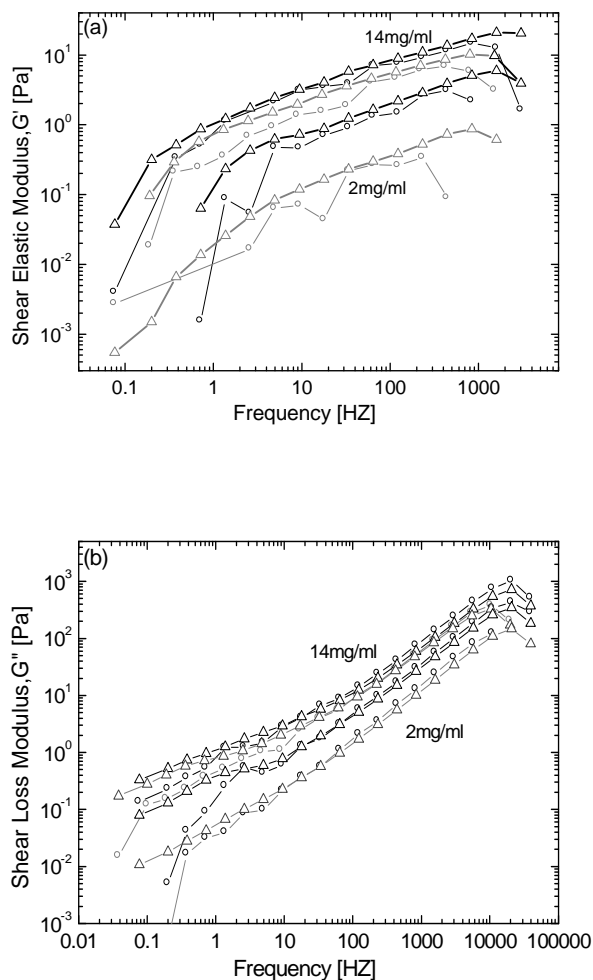


Figure 3. (a) The concentration dependence of 1-bead and 2-bead elastic modulus data of $1.16 \mu\text{m}$ diameter beads in 2, 5, 10 and 14 mg/ml fd solutions. (b) The same for the loss modulus. Pairs of 1-bead (circles) and 2-bead (triangles) moduli are higher for higher concentrations.

Entangled Actin Solutions

Actin is a protein of 42 kD molecular weight and a major component of the cytoskeleton of most eukaryotic cells. It forms double-helical filaments of about 7 nm diameter, with a persistence length $L_p = 17 \mu\text{m}$, and with a polydisperse length distribution with an average length of approximately $L = 17 \mu\text{m}$ in our *in vitro* reconstituted model systems.

Actin stress relaxation is essential for cytoskeleton dynamics and is *in vivo* strictly regulated by a large number of associated regulatory proteins. We study here simplified model systems of just pure actin without additional proteins to explore the fundamental properties and dynamic characteristics of the networks it forms. In contrast to the two systems presented above, characteristic length scales in actin networks are large compared to bead size and we expect interesting differences between 1-bead and 2-bead results, which would report on local network structure near the probes.

Figures 4(a-b) show the results of 1-bead and 2-bead MR for entangled actin networks at 1 mg/ml actin concentration as a function of bead size. Figure 4(a) shows the elastic shear modulus for 1-bead MR, recorded with various probe bead sizes in comparison with the 2-bead results. Both the 1- and 2-bead curves show the $3/4$ power-law scaling at high frequencies, which is expected for semiflexible polymer networks [1,2,4,5]. This regime connects to more complex dynamics with no clear power law characteristics at lower frequencies. There are also clear differences among the results on identical samples, with 1-bead MR systematically underreporting the bulk moduli of the sample in the high frequency regime. These differences between 1-bead and 2-bead MR as well as the systematic trend with probe bead size in the 1-bead results are consistent with the formation of an entropic depletion layer around the beads. The extent of the depletion layer is, roughly speaking, dominated by the shortest of the three characteristic lengths: bead radius, entanglement length and persistence length [1,2,5]. As long as bead size is the shortest length, this depletion layer will dominate the bead response and thereby the 1-bead results. This appears to be the case in the actin networks, and the trend towards less of an influence of local environment with increasing bead size reflects the fact that the other length scales, particularly entanglement length which is estimated to be on the order of 5-10 μm , begin to compete with bead radius. The depletion effect nevertheless does not entirely disappear even at the largest probe size, $D = 5 \mu\text{m}$. This behavior is visible in both the elastic and the loss modulus (Figs. 4(a-b)). A different type of discrepancy is observed at low frequencies within the 1-bead results for the elastic modulus with varying bead size, as well as between 1-bead results with smaller beads and 2-bead results. 2-bead results were independent of bead size and bead distance (after conversion to shear moduli) and the curve shown is the result of averaging data taken at the different bead distances (data for $D = 1.16 \mu\text{m}$ bead diameter is shown). We hypothesize that this phenomenon is due to local non-affine deformations of the actin filaments forming the network and will publish further research on these dyna-

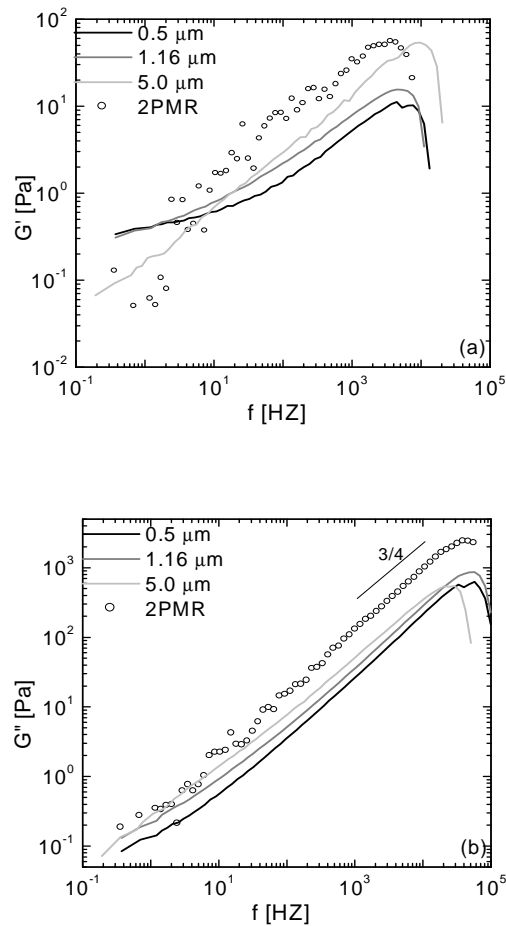


Figure 4. (a) Elastic modulus and (b) loss modulus for 1 mg/ml entangled actin solutions. Comparison of the moduli from 1-bead MR for bead diameters $D = 0.5 \mu\text{m}$, $D = 1.16 \mu\text{m}$ and $D = 5 \mu\text{m}$. 2-bead MR data taken at different distances all collapse after scaling by bead distance. Data for bead diameter $D = 1.16 \mu\text{m}$ is shown.

mics elsewhere. It is important to note that video-based microrheology methods that have also been applied to actin networks will mainly test this regime and may therefore be difficult to interpret.

5. Conclusions

We have applied a passive microrheology technique, evaluating both single-probe particle fluctuations and correlated two-particle fluctuations to measure the complex shear moduli of solutions of various semiflexible

polymers. Results with fd solutions and worm-like micelle solutions show good agreement between 1-bead and 2-bead MR. This strongly confirms that one can measure bulk viscoelastic properties of these polymer systems with 1-bead MR, which is the simpler and less noisy technique compared to 2-bead MR. Such a confirmation has been lacking up to now. More complex behavior was observed for actin solutions, providing strong evidence for local depletion effects near the bead surface as well as indications of non-affine filament dynamics visible at low frequencies. The results together advocate 1-bead MR as a reliable high resolution and high bandwidth technique to study simple systems far surpassing conventional rheology both in sensitivity and bandwidth. A combination of 1-bead and 2-bead MR, on the other hand, provides a way to explore more complex scale-dependent and local dynamic properties in various polymers, biological and colloidal systems.

Acknowledgments

We thank David Morse, Alex Levine and Matteo Pasquali for extensive discussions. Erwin Peterman helped with technical advice. Joost van Mameren, Fredrick Gittes, Mark Buchanan and Joanna Kwiecinska helped at various stages with software for data processing. Karen Vermeulen purified actin. This project was supported by NSF DMR 9988389 (J.X.T.) and the Dutch Foundation for Fundamental Research on Matter (FOM).

References

- [1] D.C. Morse, *Macromolecules*, Vol.31, pp.7030, 1998.
- [2] D.C. Morse, *Macromolecules*, Vol.31, pp.7044, 1998.
- [3] A.C. Maggs, *Phys. Rev. E*, Vol.55, pp.7396, 1996.
- [4] F. Gittes, F.C. MacKintosh, *Phys. Rev. E*, Vol.58, pp.1241, 1998.
- [5] B. Schnurr, F. Gittes, F.C. MacKintosh, et al., *Macromolecules*, Vol.30, pp.7781, 1997.
- [6] K. Addas, J.X. Tang, C.F. Schmidt, *Phys. Rev. E*, Vol.70, 021503, 2004.
- [7] A. J. Levine and F. Mackintosh, pp.manuscript in preparation.
- [8] F. Gittes, C.F. Schmidt, *Method. Cell. Biol.*, Vol.55, pp.129, 1998.
- [9] A. J. Levine, T.C. Lubensky, *Phys. Rev. E*, Vol.63(4), 041510, 2001.
- [10] M. W. Allersma, F. Gittes, M. J. deCastro, et al., *Biophys. J.*, Vol.74, pp.1074, 1998.
- [11] J. F. Berret, J. Appell, G. Porte, *Langmuir*, Vol.9, pp.2851, 1993.
- [12] M. Buchanan, M. Atakhorrami, J.F. Paliarne, F.C. Mackintosh, C. F. Schmidt, (manuscript in preparation).

TOPICS IN ASTROPHYSICAL FLUID DYNAMICS

Edward A. Spiegel
Astronomy Department
Columbia University, New York, NY, USA
eas@astro.columbia.edu

Abstract This brief description of some fluid dynamical problems of astrophysical interest focuses on two effects that are characteristic of the subject: self-gravity and radiative forces. Self-gravity is important in determining the basic structures of cosmic bodies as well as producing some intriguing instabilities. Radiation, by which we observe these bodies, produces forces that may be disruptive to their basic structures and be a source of vigorous fluid dynamical activity in the form of photon bubbles and radiatively driven vortices.

Keywords: Gravitational instability, solitary waves, astrophysical vortices, photon bubbles

This sampler of problems in AFD begins with the classical problem of gravitational instability and continues with some current problems that I find very intriguing. Given the imposed space limitations, I can only touch on these and I need to be very stingy with references (not of my own, of course) and will assume that I need not provide many fluid references for the expected readership of this volume. (But feel free to use the email address above.)

1. Gravitational Instability

Massaged Models

The observable part of our universe looks homogeneous in the large, but it is clearly rather lumpy on smaller scales. There are stars, clusters of stars, galaxies and clusters of galaxies. Possibly there are even larger structures but here we come to a less clearly defined topic where people may yet argue about how (or whether) to study such issues as the dimension of the point set that approximates the distribution of galaxies. But it is undoubtedly interesting to inquire into the origin of the inho-

mogeneities of the universe. Our current understanding of cosmology is that the early universe was dense and hot and very dissipative. Hence it is thought to have been rather homogeneous in the earliest times that we can reasonably think about and the lumpiness is considered to have been caused by gravity.

The breakup of a homogenous fluid into reasonably discrete structures is believed to be caused by an instability whose qualitative nature was already imagined by Newton. Jeans [13] was apparently the first to formulate this problem. He assumed a perfect barotropic fluid with self-gravity and used these simple equations of motion:

$$\partial_t(\rho\mathbf{u}) + \nabla \cdot (\rho\mathbf{u}\mathbf{u}) = -\nabla p - \rho\nabla V, \quad (1)$$

$$\partial_t\rho + \nabla \cdot (\rho\mathbf{u}) = 0, \quad (2)$$

$$\nabla^2 V = 4\pi G\rho, \quad (3)$$

$$p = K\rho^\Gamma. \quad (4)$$

Jeans posited a static homogenous solution to these equations (though one presumes that he knew better) and studied perturbations on this “solution”. But there is no infinite, homogenous, static, self-gravitating medium in cosmology, not even in Einstein’s original theory of gravity [11]. Einstein added a term to his equation for the curvature of spacetime that allowed him to find a static solution, unstable though it is. Similarly, we may add a term to the right side of the Euler equation to provide our Newtonian universe with a static solution. This term, $\rho\lambda\mathbf{r}$, represents a repulsive force, as Eddington [10] pointed out. Now we may introduce $\tilde{V} = V - \frac{1}{2}\lambda r^2$ and replace (1) and (3) by

$$\partial_t(\rho\mathbf{u}) + \nabla \cdot (\rho\mathbf{u}\mathbf{u}) = -\nabla p - \rho\nabla\tilde{V}, \quad (5)$$

$$\nabla^2\tilde{V} = 4\pi G(\rho - \rho_\lambda) \quad (6)$$

where $\rho_\lambda = \lambda/G$. This recalls the device used in plasma physics to maintain charge neutrality and we may now find a homogenous static solution and study its stability to clumping.

Einstein’s extra term, “the cosmological term”, intrigued people from its beginning, but its status was uncertain until recently. The recent discovery that the expansion of the universe is accelerating has brought this extra term into vogue, though its physical meaning remains unclear. Does the cosmological term mean what the simple statement given here suggests — the existence of matter with negative gravitational mass [21]? If so, we should perhaps add a fluid equation for this odd material

as in the two-fluid plasma model. Many cosmologists look on the added term as a negative pressure that can drive the expansion velocity ever upward. Here it merely serves Einstein's original purpose for it: to produce a static solution.

The Dispersion Relation

To study the stability of the homogenous medium, we let $\rho = \rho_0 + \delta\rho$, $\tilde{V} = \tilde{V}_0 + \delta\tilde{V}$ and so on. With the extra term in place, we may assume that the basic fields are constant. If we then linearize the equations about the static state, we are led by standard manipulations to a Klein-Gordon equation for $\delta\rho$:

$$(\partial_t^2 - \nabla^2) \delta\rho = (4\pi G\rho_0)\delta\rho. \quad (7)$$

For plane waves with $\delta\rho \propto \exp(i\omega t - i\mathbf{k} \cdot \mathbf{x})$, we obtain the dispersion relation

$$\omega^2 = c^2(k^2 - k_J^2) \quad \text{with} \quad k_J^2 = (4\pi G\rho_0)/c^2, \quad (8)$$

and $c^2 = \Gamma p_0/\rho_0$.

The quantity k_J is called the Jeans wavenumber and, when the wavenumber of the perturbation is much larger than this, we recover ordinary sound waves. But for $k < k_J$, ω^2 becomes negative and we have instability. Because of the difference in sign from the electrostatic case, we get instability rather than oscillation. The Jeans length $1/k_J$ tells us the scale on which the gravity just balances the pressure gradient much as the balance of surface tension and pressure dictates the size of a liquid drop. When the length scale of a perturbation is larger than this critical size, collapse occurs. For a perfect gas with temperature T , we find from these formulae that $k_J^{-1} \approx 100\sqrt{(T/n)}$ light years where n is the number density and the collapse time for very small k is $\approx 5 \times 10^7/\sqrt{n}$ yr.

Cosmology's Fictitious Forces

To study the formation of inhomogeneities in the universe properly, we need to take account of its expansion. This was first done for the linear stability problem by Lifshitz in 1946 in the context of relativistic cosmology, but the Newtonian case conveys the idea [5]. Even that story is on the long side so, to indicate how the expansion reduces the degree of instability, a brief look at the kinematics in an expanding medium may suffice.

For a universe that is infinite and homogeneous in the large, it does not matter where we put the origin of coordinates, so let us presume that one has been chosen. The position with respect to the arbitrary origin

of a fluid element is \mathbf{r} . We then transform to isotropically expanding coordinates such that

$$\mathbf{r} = R(t)\mathbf{x} \quad (9)$$

where $R(t)$ is a nondimensional function that tells us how the global scale of the universe changes in time. For some suitable origin of time we let t_0 be the present and take $R(t_0) = 1$. We find

$$\dot{\mathbf{r}} = \dot{R}\mathbf{x} + R\dot{\mathbf{x}} = H\mathbf{r} + R\dot{\mathbf{x}} \quad (10)$$

where $\mathbf{v} = H\mathbf{r}$ is the *Hubble flow* or global expansion and $H_0 = H(t_0)$ is called the Hubble constant. The acceleration of the fluid element is then

$$\ddot{\mathbf{r}} = R\left(\ddot{\mathbf{x}} + 2H\dot{\mathbf{x}} + \dot{H}\mathbf{x} + H^2\mathbf{x}\right). \quad (11)$$

In the expanding coordinates, we acquire three additional terms or fictitious forces reminding us of those gained in going into a rotating frame. The scalar H plays the role of the rotation rate in that comparison, hence the analogue of the Coriolis force is a drag term. Material particles moving through an expanding medium are slowed down with respect to the background. This is an effect analogous to the cosmological redshift of photons. (You may think of this as a stretching of the de Broglie wavelengths.) Since H is not a constant, we get a force $\dot{H}\mathbf{x}$ corresponding to the Euler force. Finally there is the analogue of the centrifugal force, $H^2\mathbf{x}$. These extra terms appear in the Euler equation when we go to expanding coordinates.

The main point is that the cosmological drag term inhibits the development of gravitational instability but it does not kill it completely in standard cosmological models. Rather, it converts the exponential growth to an algebraic growth. It appears that this feeble instability may suffice to produce the structures we see in the universe around us according to many simulations. Still, if you want to get your hands analytically on the way gravitational instability develops, as one may do for weak instabilities, it is best to consider another static configuration of the mass.

Polytropic Slabs

If, in equation (4), you treat Γ as a parameter and not necessarily the ratio of specific heats, you have what is called the polytropic gas law. The spherically symmetric, static, self-gravitating solutions of Eqs. (1)–(4), served as models of stars in the nineteenth century and they remain qualitatively useful even now. The disks in spiral galaxies may also be modeled as polytropes to good effect and these are useful for studying their gravitational instability.

As a prelude to studying fluid dynamics in disks, one may study simpler flattened objects such as polytropic layers or slabs. The simplest case is a static configuration with the layer extending infinitely in two directions that we may call horizontal. The third, or vertical, direction is given the designation z . Just as for a stratified atmosphere, we may write the hydrostatic condition, the only difference being that the gravity is not specified but is governed by the Poisson equation.

Static solutions have $\rho = \rho_0(z)$ with

$$\rho_0(z) = \rho_0(0)\mathcal{C}_\Gamma(z) \quad (12)$$

where $\mathcal{C}_\Gamma(z)$ is given by a simple integral that, for general Γ , is a beta function. Several special cases may be identified, notably

$$C_1 = \operatorname{sech}^2(k_J z), \quad C_2 = \cos(k_J z). \quad (13)$$

Here

$$k_J^2 = \left[\frac{4\pi G \rho_0}{c^2} \right]_{z=0} = \frac{4\pi G}{\Gamma K} [\rho_0(0)]^{2-\Gamma}. \quad (14)$$

The characteristic thickness of the slab is $\sim 1/k_J$ as before but now we have a static solution with no artifice. The model is admittedly simplified but it has scope for interesting dynamics. For instance, the distribution of density on the midplane controls the layer thickness and this may vary in the rotating case so that we may find Rossby waves propagating through disks.

Ledoux [14] derived the marginal stability condition for linearized perturbations on the isothermal slab ($\Gamma = 1$). He found two horizontal wavelengths that are marginal, with $k_{\text{hor}} = 2k_J$ and 0. Here is a situation in which we can make use of asymptotic approaches for the modes of long wavelength where the instability first arises weakly. This is unlike the homogeneous case, for which the maximum growth rate occurs at $k = 0$. The real case is even more favorable to this approach since disks of galaxies are embedded in very massive halos that make the disk thicknesses even less than the Jeans lengths of the disks. The halos themselves, though not visible, are generally believed to exist on the basis of their gravitational effects. Their influence strengthens the validity of the thin-layer approximation.

Linear theory reveals that there are acoustic modes and gravity modes, just as in models of standard atmospheres. The surprise is that the instability occurs in the gravity modes and not in the acoustic modes as in the original Jeans problem. The gravity waves combine both thickness variations and true density variations, so have all that is needed. Since the largest scales are nearly marginal, one can assume slow times

and long lengths to develop shallow layer theories [18]. With the additional restriction to small amplitudes, as in weakly nonlinear theories, one may derive nonlinear wave equations in the manners of Boussinesq and Korteweg and de Vries [19].

The familiar form of the theory is modified by a term representing the effect of self-gravity that comes in through the Poisson equation. For instance, in the case of nonlinear waves of small amplitude in a thin layer with $\Gamma = 2$ (the easiest case) one finds for the surface deformation that:

$$\eta_T - 3\eta\eta_X + \frac{1}{2}\eta_{XXX} = \mu\mathcal{H}[\eta] \quad (15)$$

where the Hilbert transform is

$$\mathcal{H}[\eta] = \frac{1}{\pi}\mathcal{P} \int_{-\infty}^{\infty} \frac{\eta(Y)}{Y-X} dY \quad (16)$$

and X and T are suitably stretched variables. This equation has pole solutions, but we cannot say whether it is completely integrable. However, there are certainly solutions resembling solitons. The interest in such a result is that it has sometimes been thought that the highly dispersive nature of the waves in this kind of problem would not allow the formation of coherent structures. In fact, the nonlinearity in this problem leads to the formation of long-lived nonlinear waves.

What happens in the more realistic case of a rotating disk? This is an issue that is unresolved as yet in the nonlinear case. The finiteness of the disk brings discrete modes into play and they behave chaotically [4]. Still, some global order may emerge, perhaps with the help of other effects.

2. Astrophysical Vortices

The masses of stars range from 60-80 times the mass of the sun (4×10^{33} gm) down to a few tenths of a percent of the solar mass, that is, down to the masses of the giant planets. The massive stars have very hot atmospheres, (tens of thousands of Kelvins), while the low mass ones have much cooler atmospheres as a rule (6000 K for the sun). At both ends of this spectrum, atmospheric turbulence is observed. At the cool end, this is caused by thermal convection resulting from the lowering of the thermal conductivity through the raising of opacity by partially ionized hydrogen. The ionization of hydrogen also favors convection by raising the specific heat. In the atmospheres of the hottest stars, turbulence is detected through broadening of the spectral lines and it is often supersonic. The origin of this turbulence is not agreed upon, though

there is no shortage of possible sources. Hot atmospheres are fully ionized and are not subject to thermal convection in the usual way, but they are rapid rotators and they pulsate. When the pulsation is vigorous, thermal convection may be driven parametrically. Moreover, hot stars have high radiation pressure that provokes instability and complicates the dynamics. Already at the qualitative level there are some interesting fluid dynamical issues.

We see spots on the sun and these are caused by magnetic flux tubes that protrude from the solar surface. The fields are locally strong enough to inhibit the convective transport of heat outward and so relatively cool (but still quite warm) spots are produced. By contrast, in Jupiter's atmosphere, a much cooler place, we find evidence for vortex tubes at the surface. Since there is a full range of masses between the two limits (sun and Jupiter) we may someday be able to observe the transition between the two kinds of coherent structures, but there is no reason why this transition could not be studied theoretically at present, perhaps numerically. This is a potentially revealing instance of the transition between the purely fluid and the magnetofluid regimes.

Related questions arise in the study of the accretion disks that form around condensed objects on many scales. These are rather different from the disks in spiral galaxies. Accretion disks represent inflows of mass from various sources such as companion stars in the case of binary stars, to the ambient stars around massive black holes in the centers of galaxies. The primitive nebula that might have preceded the formation of our solar system, as Kant and Laplace first suggested, are cooler examples of this kind of structure. As the matter flows toward the central object, its net angular momentum makes itself felt and a disk is formed. Before it can settle into the central object, the inflowing matter must get rid of its angular momentum. Various mechanisms have been proposed for expelling the angular momentum, mostly calling on some form of turbulence though waves and magnetic fields have been considered. Vortices could also play a part in the process. There are some similarities here to the flow around the polar vortex on earth that is central to the ozone problem, though accretion disks frequently are magnetized.

The large scale flow in accretion disks is governed mainly by Kepler's laws so that the circular velocity around the central object in an axially symmetric disk varies like $1/\sqrt{r}$. This represents a linearly stable shear and it is not yet decided whether nonlinear instability can occur in such a flow. (I first heard people arguing about that some thirty-five years ago.) However, as Chandrasekhar and others showed, magnetic fields can catalyze the conversion of the energy in the rotational flow of disks

into turbulence, but it was some time till the importance of this result for disks was appreciated [3]. Can the resulting disorder lead to the formation of vortices?

Twenty-five years ago I put a drawing of a disk with whorls in it in an article on turbulence for an encyclopaedia aimed at twelve-year olds. The hope was that in ten years one of them would appear in my office with a fully completed simulation that revealed what the disk really looked like. This did not happen, so the next message in a bottle was sent as a remark at the end of a paper on vortices in stars and planets [9]. This got a response from P.A. Yecko whose thesis revealed that large-scale spiral vortices formed. (At the suggestion of A. Ingersoll, Yecko adapted a code written by E. Chassignet for simulating the oceanic thermocline.) Several astronomers objected that the Keplerian shear in disks would shred a vortex. The shredding is avoided by anticyclonic vortices which shield themselves with protective cocoons of reduced shear. Several subsequent simulations with higher resolution have shown their robustness [6, 12, 15]. A recent, 2-D, compressible simulation at high resolution by G. Murante and colleagues in Torino strikingly shows how a single anticyclonic vortex survives in the Keplerian shear, at least for the ten disk rotations they followed. That vortex also generated large-scale spiral extensions in line with Yecko's results. The issue of what magnetic fields do to these processes needs clarification as do theoretical questions about how vortices form. But their existence would play a role in forming observable inhomogeneities on disks [1]. An example of a disk simulation in a two-dimensional Keplerian flow with slowly decaying turbulence is shown after [7] in Fig. 1.

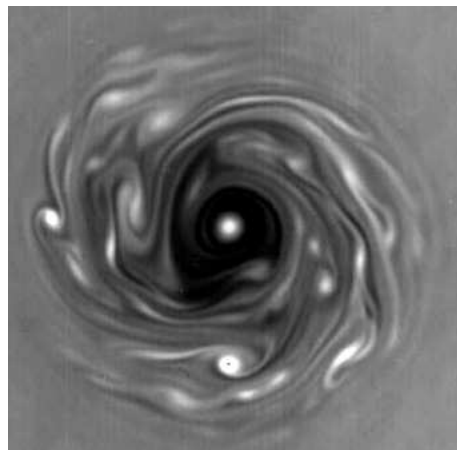


Figure 1. Vortices on a Keplerian Disk

3. Photofluidynamics

The radiation that permits us to observe cosmic bodies also plays a role in their formation, structure and evolution. The thermal aspects of the radiation are familiar to fluid dynamicists, at least qualitatively. What may be of more interest in an introduction to AFD is the way that the force of radiation on matter may influence the dynamics of the ambient material medium. The phenomena arising in this subject seem sufficiently different from ordinary fluid dynamics that I have followed the advice of M. E. McIntyre and sought a suitably distinctive terminology. The name used here for the subject is inspired by Lighthill's "Biofluidynamics." What follows is a very brief introduction to some aspects of this subject. For some background on the equations see [16].

The Radiative Fluid

The most direct derivation of the basic equations of fluid dynamics subject to stresses from a coexisting radiation field is by way of the transport equations for radiation and matter. These are kinetic equations that contain terms representing the interaction of the matter with the radiation. This somewhat technical problem is best formulated by treating the radiation fluid as a gas of photons. Nevertheless, there are some real complications depend on the frequencies of the photons and the state of the matter. Such details are out of place here, so we simply assume that the matter is grey, that is, indifferent to the frequencies of the photons passing through it. We shall also omit the details of the state of the matter such as the degree of ionization, which we shall take to be complete for very hot objects. So we may go straight to the first two moments of the transfer equation which, for a gas of photons, are equations for the moments of the distribution function or specific intensity.

Let \mathcal{E} , \mathcal{F} and \mathbb{P} be the energy density, energy flux and pressure tensor of the radiation fluid. These satisfy the two moment equations

$$\partial_t \mathcal{E} + \nabla \cdot \mathcal{F} = \text{interactions with matter} \quad (17)$$

and

$$\partial_t \mathcal{F} + c^2 \nabla \cdot \mathbb{P} = -\rho \kappa c \mathcal{F} \quad (18)$$

where $(\rho \kappa)^{-1}$ is the mean free path of a photon. We see that the latter equation may be written as

$$\nabla \cdot \mathbb{P} = -\frac{\rho \kappa}{c} \mathcal{F} + \mathcal{O}(c^{-2}). \quad (19)$$

Naturally, we face the usual problem of closing off the moment hierarchy and here we take the simplest closure, $\mathbb{P} = \frac{1}{3} \mathcal{E} \mathbb{I}$. Thus we ignore

the (sometimes important) radiative contribution to the viscous stress. In some limits, we may argue from (17) that the divergence of the flux is quite small. (In effect, we are leaving out retardation terms with this approximation.) This is about as simple as we can make this problem, yet much of interest remains as we see when we write the equation for the material fluid as

$$\rho(\partial\mathbf{u} + \mathbf{u} \cdot \nabla\mathbf{u}) = -\nabla p - \frac{1}{3}\nabla\mathcal{E} - \rho\nabla V. \quad (20)$$

To this we add the mass conservation equation and the radiative equations which have been reduced to the diagnostic conditions

$$\nabla \cdot \mathcal{F} = \mathbf{0} \quad \text{and} \quad \nabla\mathcal{E} = \frac{1}{3}\rho\kappa c\mathcal{F}. \quad (21)$$

Radiatively Induced Instabilities

To see in what kind of conditions radiative effects may become important dynamically, consider the simple case of a plane-parallel medium stratified under gravity. The foregoing equations show that the hydrostatic condition is

$$\frac{1}{\rho} \frac{dp}{dz} = -\frac{1}{3}\nabla\mathcal{E} - \rho\nabla V = \frac{1}{3}\kappa c\mathcal{F} - \rho\nabla V \quad (22)$$

where z is the upward vertical coordinate. In the typical case where the flow of radiation is outward, hence upward, the radiative force is one of levitation and it balances the gravitational attraction downward when the right side of this equation vanishes. That condition is called the Eddington limit. Near this condition, we find instabilities of both sound waves and gravity waves [22]. These are induced by both the thermal and dynamical effects of radiation and there is still room for a better physical understanding of these processes.

Those familiar with fluidized beds will recognize a commonality between the Eddington limit and the onset of fluidization, although the medium being traversed by the radiation is a fluid even below the critical condition. As in fluidization, the material layers are rendered unstable by the traversing fluid, though the details of the instability mechanisms do differ. As in those cases where voids form in fluidized beds, the radiative fluid is much less dense than the particles of the medium. This and other arguments suggest that photon bubbles will form in hot stars near to the Eddington limit [17]. Approximate solutions for photon bubbles can be constructed in the way that this is done in the theory of fluidization [20]. Related discussions have been given in the context

of convection in the chimerical supermassive hot objects [23] and polar caps of pulsars where the magnetic fields are strong (10^{12} gauss) [2].

An interesting aspect of this process bears on the question of the lifetimes of objects that exceed the Eddington limit. In the case of fluidized beds, flow through the bed in excess of the value needed for fluidization is observed to escape in voids, or bubbles. We may similarly expect cosmic bodies to survive above the Eddington limit. A modified limit needs to be calculated but another feature of this problem needs to be addressed first.

Photovorticity

The hottest objects are relatively rare and there are very few nearby. We see them because they are intrinsically luminous but it is hard to know whether they are like other rotating, turbulent cosmic bodies in forming vortices or concentrated magnetic flux tubes. However, it is clear that the hot objects do rotate rapidly and are turbulent in their outer layers. Moreover, there are observational grounds for supposing that there are spots on hot stars [8] and disks [1]. What can cause spots in such conditions?

Hot stratified media are unstable and, as for fluidized beds, we may expect the formation of (photon) bubbles in objects near the Eddington limit. If we make a vortex in such conditions, we anticipate that, as in many laboratory experiments on rotating turbulence, bubbles are attracted into vortices. Indeed, it is the practice to use small bubbles as markers of vortices in such experiments. On the other hand, bubbles flowing into a vortex will bring with them angular momentum and, when this is of the right sign, the vortex will be intensified. We have in such a situation the makings of an instability for vortex production analogous to what has been seen in laboratory experiments [24].

Vortex formation in hot media is of interest since it would lead to strong inhomogeneities in the emerging radiation field that would have diagnostic implications. It would also be important in the fluid dynamics of hot objects since a vortex of the right kind is a conduit through which radiation may escape from a hot object or disk without disrupting it. A simple calculation reveals the nature of this process.

Let us omit the complications of global rotation and consider an isolated vortex in a stratified polytropic fluid with radiation coming from below [9]. A standard vortex with gravity balancing the pressure gradient in the vertical direction and the centrifugal force in the (horizontal) radial direction is readily constructed. Then, in radiative equilibrium, we have $\mathcal{E} = aT^4$, where T is the temperature. For radiative prob-

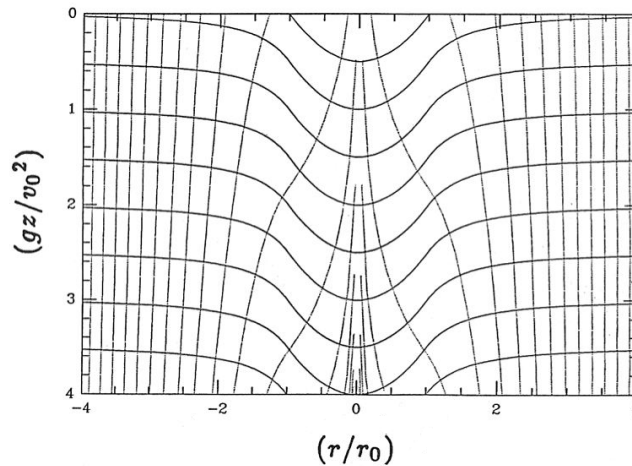


Figure 2. Flow through a phortex

lems the parameter value $\Gamma = 4/3$ is frequently adopted. This value has the advantage of making ρ^3/T a constant and that greatly simplifies the second of (21). That pair of equations is then readily solved and the streamlines of the radiative energy flux \mathcal{F} are as shown in Fig. 2; the contours of T are also indicated. This vortex provides not only a safety valve by which the radiation may escape but such a beam should make itself apparent in observations of hot stars and disks.

References

- [1] M.A. Abramowicz, A. Lanza, E.A. Spiegel, and E. Szuszkiewicz, Vortices on accretion disks, *Nature*, Vol. 356, 41, 1991.
- [2] J. Arons, Photon bubbles – Overstability in a magnetized atmosphere, *Astrophys. J.*, Vol. 399, pp.561–578, 1987.
- [3] S.A. Balbus and J.S. Hawley, Instability, turbulence and enhanced transport in accretion disks, *Rev. Mod. Phys.*, Vol. 70, pp.1–53, 1998.
- [4] N.J. Balmforth and E.A. Spiegel, Nonlinear ringing of polytropic disks, *Physica D*, Vol. 97, pp.1–28, 1996.
- [5] W.B. Bonnor, Jeans’ formula for gravitational instability, *Mon. Not. Roy. Ast. Soc.*, Vol. 117, 104, 1957.
- [6] A. Bracco, A. Provenzale, E.A. Spiegel, and P.A. Yecko, Spotted Disks, [in:] *Theory of Black Hole Accretion Disks*, M. Abramowicz, G. Bjornsen & J. Pringle, [eds.], Cambridge Univ. Press, 1998.
- [7] A. Bracco, P.-H. Chavanis, A. Provenzale, and E.A. Spiegel, Particle Aggregation in Keplerian Flows, *Phys. Fluids* Vol. 11, 2280, 1999.
- [8] J.P. Cassinelli, [in:] *The origin of Nonradiative Heating/Momentum in Hot Stars*, A.B. Underhill and A.G. Michalitsianos, [eds.], (NASA 2358), pp.2–23, 1985.

- [9] T.E. Dowling and E.A. Spiegel, Stellar and jovian vortices, *Ann. N.Y. Acad. Sci.*, Vol. 617, pp.190–216, 1990.
- [10] A.S. Eddington, *The Mathematical Theory of Relativity*, Cambridge Univ. Press., 1924.
- [11] A. Einstein, Kosmologische Betrachtung zur allgemeinen Relativitätstheorie, Berlin: *Sitzungsberichte*, p.149, 1917.
- [12] P. Godon and M. Livio, On the nonlinear hydrodynamic stability of thin keplerian disks, *Astrophys. J.*, Vol. 521, 318, 1999.
- [13] J.H. Jeans, *Astronomy and Cosmogony*, Cambridge Univ. Press., 1928.
- [14] P. Ledoux, Sur la Stabilité Gravitationnelle d'Une Nebuleuse Isotherme, *Ann. d'Astrophys.*, Vol. 14, pp.438–447, 1951.
- [15] H. Li, S.A. Colgate, B. Wendroff, and R. Liska, Rossby wave instability of thin accretion disks. III. Nonlinear simulations, *Astrophys. J.*, Vol. 551, pp.874–896, 2002.
- [16] D. Mihalas and B.W. Mihalas, *Foundations of Radiation Hydrodynamics*, Oxford Univ. Press, 1984.
- [17] K.H. Prendergast and E.A. Spiegel, Photon Bubbles, *Comments on Astrophys. and Space Phys.*, Vol. 5, 43, 1973.
- [18] Z.-S. Qian, E.A. Spiegel, and M.R.E. Proctor, The gravitational instability of a gaseous slab, *Stability and Applied Analysis of Continuous Media*, Vol. 1, 33, 1990.
- [19] Z.-S. Qian and E.A. Spiegel, Autogravity waves in a polytropic layer, *Geophys. & Astrophys. Fluid Dyn.*, Vol. 74, pp.225–244, 1994.
- [20] E.A. Spiegel, Photoconvection, [in:] *Problems in Stellar Convection*, E.A. Spiegel and J.-P. Zahn, [eds.], Springer-Verlag, 1977.
- [21] E.A. Spiegel, Gravitational screening, *On Einstein's Path: Essays in Honor of Engelbert Schucking*, A. Harvey, [ed.] (Springer-Verlag, N.Y.), Chapt. 32, pp.465–474, 1998.
- [22] E.A. Spiegel and L. Tao, Photofluid instabilities of hot stellar envelopes, *Phys. Rep.*, Vol. 311, pp.163–176, 1999.
- [23] V.S. Thorne, Thesis, Univ. of Manchester, 1968.
- [24] J.S. Turner and D.K. Lilly, The carbonated-water tornado vortex, *J. Atmos. Sciences*, Vol. 20, pp.468–471, 1963.

MINIATURIZATION OF EXPLOSIVE TECHNOLOGY AND MICRODETONICS

D. Scott Stewart

University of Illinois

Department of Theoretical and Applied Mechanics

dss@uiuc.edu

Abstract Condensed phase explosives used in conventional explosive systems have a charge size on the order of a meter or a sizable fraction of a meter. We discuss a range of issues, theoretical, computational and experimental, required to scale the size of explosive systems downwards by a factor of one hundred to one thousand, applications and prospects for a ubiquitous new technology.

Keywords: Detonation, shock physics, compressible flow, miniaturization, explosives, new technology

1. Introduction

A detonation is a chemical reaction driven shock wave in molecularly premixed material called an explosive. The chemical energy released in the reaction zone behind the lead shock is converted into kinetic energy and pressure/volume work done by the reactants. Explosives can be gases, liquids and solids. Detonation pressures in organically based condensed phase explosives (typically made from nitrated hydrocarbons) are in the range of 300–400 Kbar (30–40 GPa), and can potentially induce hundreds of Kbars of pressure in inert materials for fractions of microseconds. Detonation shock speeds are on the order of 3–10 kilometers/sec. The thermodynamic cycle and high pressure, high compression states that can be induced in materials are unlike those that can be obtained with other thermo-mechanical systems, including lasers. Hence detonative processes offer unique methods of altering the state of material surfaces and can serve as a high energy density source for micro-devices. Properly engineered, stable explosive detonation fronts work in combination by a principle of synchronicity (i.e. the detonation is a phase-controlled explosion front) and detonations can generate precise

motion-controlled flows that can be used for materials processing and other applications.

2. Applications

While condensed phase explosives are used in military, mining and demolition applications, other less commonly known applications of explosives include their use for materials processing, precision cutting and pulsed power application. Specifically, detonation of explosive films can be used in surface treatment and hardening of materials. Other material processing applications include cladding and explosive welding, sintering, shock consolidation of powders and shock-induced chemical synthesis. Pulsed power applications include magnetic flux compression, pulsed detonation engines, explosive lasing and the generation of extremely high intensity light pulses. There are biomedical applications for detonation of micro-sized explosive charges that include lithotripsy and localized destruction of pathological tissue [1]. Explosive and pyrotechnic elements pervade satellite and aerospace systems and hence there is interest in the miniaturization of explosive systems for micro-aerospace and satellite platforms. Suitably controlled detonation fronts represent a basic technology with unique aspects. By establishing the basic parameters of micro-scale explosive systems it should be possible to design micro-scale devices for welding, cladding, pulsed power, surface treatment and so on (as mentioned above) in novel, ubiquitous and unforeseen ways. Micro-explosive systems hold the promise of being a basic enabling technology with wide-spread application.

Figure 1 shows a sketch of a experimental configuration being designed at the University of Illinois, in collaboration with Prof. W. Kriven (Material Science and Engineering, UIUC) and Prof. R. Adrian (TAM, UIUC), to study high pressure, temperature synthesis of ceramic materials. The initiator consists of a capacitance discharge unit (CDU) that fires a 10-micron thick wire (typically gold) or metallic film embedded in the detonable film. The electrical current dump causes the metal to expand from a nominally cylindrical or flat source as plasma and drive a shock wave into the film to start the chemical reaction in the film. The detonation supported shock wave sweeps across the sample and the detonation shock drives an inert shock into the donor material to do the localized processing of near surface material. Other initiation configurations include laser driven micro-flyers that induce shocks to start reaction.

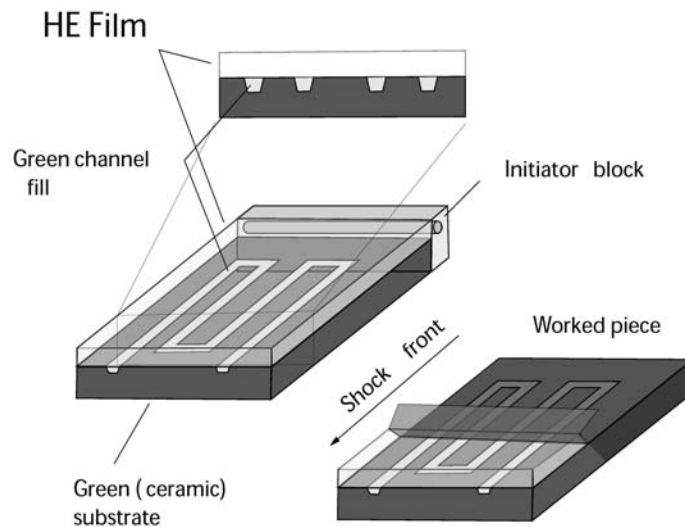


Figure 1. Micro-explosive system for materials processing of ceramics

3. Explosive System Scaling Arguments and Requirements

An explosive system includes the main charge (the secondary explosive), the initiation system (which includes the initiation train and booster made of primary explosives or electrical or optical laser initiators) and the inerts, upon which the explosive products act. Conventional macro-scale explosive system design paradigms exist for explosive systems that have dimensions on the order of a meter or sizable fraction of a meter. The question, what are the scaling principles for small-scale design that are consistent with existing large-scale design, can be addressed by dimensional analysis, based on the Euler equations and consideration of matching shock initiation and propagation experiments of small-scale systems to their large-scale counterparts. Scaling arguments, [2] show that extreme miniaturization by a scale reduction of current large-scale explosive systems by a factor of 100 to 1000 is possible. To employ existing large-scale design rules, the detonation reaction zone length scale must scale with the device dimension size. Short reaction-zone explosive materials (with small critical diameters) must be used for main charges. This means that one must select the main charge explosives from the list of primary explosives (used in large-scale initiator trains or detonators). Also one might consider using very short

reaction zone explosives that have never been considered for use in the past, because of safety considerations.

The other route to miniaturization uses explosive materials for propagation in sub critical charge dimensions. One expects to experience significant transients that do not fall in the existing quasi-steady design paradigms. This route requires a detailed understanding of transient detonation propagation.

4. A definition of Microdetonics and the Initiation of Small Systems

This brings us to a definition of the term “microdetonics” that we attribute to James E. Kennedy of Los Alamos National Laboratory. Kennedy’s definition of microdetonics is the detonation physics behaviors that are dominated by transient effects such as detonation acceleration, detonation spread and curvature effects that are commonly associated with initiation of explosives by small sources. This definition includes both small charges and small initiation sources, where transient phenomena is dominant.

Reliable and safe initiation systems for miniaturized systems can be built using existing exploding wire and exploding foil initiation systems with existing, well-understood electrical designs. Initiation energy is stored in a standard capacitance discharge unit. It is also possible to build optical initiation systems whereby energy is transmitted through an optical fiber to the explosive charge. Initiation system can be placed on chips, [3] and designed with standard photo-lithographic techniques, [4].

5. New Science Needed to Enable the Technology

In order to define the properties of the new explosive materials there is a need for a comprehensive linear and nonlinear stability theory for non-ideal detonation that can incorporate non-ideal equation of state and realistic reaction rate laws for condensed explosives. Recent efforts are underway to develop novel nano-engineering composite energetic materials and explosives that can be candidates for the miniaturized secondary charge. An entirely new linear stability theory for steady detonation has been developed by us at Illinois, [5] to guide design of miniaturized explosive systems in a rational way that incorporates descriptions of nonideal equation of state and reaction rate kinetics.

In order to define detonation propagation in small dimensions, one must understand the critical conditions required for ignition and propagation of detonation for both ideal and nonideal explosives [6]. This

includes the development of asymptotic theory for fast and sensitive chemical kinetics. It is important to understand aspects of detonation and shock diffraction and how that phenomena affects successful detonation propagation.

High Resolution Multi-Material Simulation Technology is Required

Design of integrated systems requires modern high resolution, multi-dimensional and multi-material, time-dependent simulation. High fidelity simulation is an essential tool that is required to specify the geometry and select materials for miniaturized explosive system. Figure 2 shows a recent simulation of a “corner turning” experiment carried out by E. Ferm of Los Alamos National Laboratory. The corner turning experiment measures the transient effect of the change in confinement of detonation. The initial configuration of Ferm’s experiment has a 6 mm radius, 125 mm long cylindrical stick (donor charge) of explosive PBX-9502 joined to a wider/shorter 25 mm radius, 50 mm long (acceptor charge) cylinder of PBX-9502. The detonation is started and travels as a curved steady detonation in the donor. Once the detonation

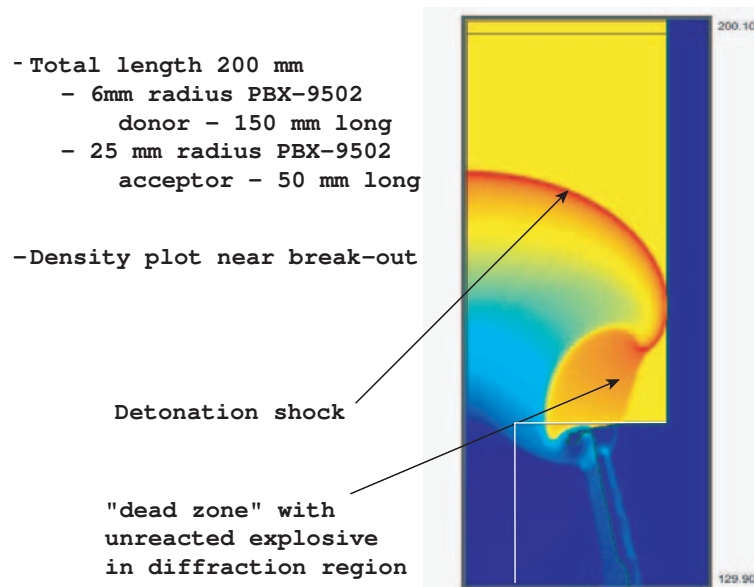


Figure 2. MULTIMAT Simulation: The density record of a corner turning experiment that shows the effects of detonation diffraction and the appearance of dead zones

in the donor charge enters the acceptor, the detonation must expand into the large acceptor region. Because the lateral boundary of the acceptor charge is perpendicular to the axial propagation direction of the detonation in the donor and that the lateral boundary is unconfined, a large depressurization (rarefaction) of the detonation occurs. When the reaction rate of the explosive is pressure sensitive, the depressurization effectively slows or stops the reaction in the region affected by the corner turning diffraction event. Hence a large region appears where the explosive does not burn. That region is dubbed a “dead zone”. Instead of reacting, the explosive in the dead zone is simply shocked. For microcharges or for initiation by small sources, the corner turning experiment is a generic configuration that must be studied in detail.

Figure 2 is a snapshot of a density record from a simulation carried out by members of our group (D. S. Stewart, B. Wescott and S. Yoo) with our UIUC-code MULTIMAT. Our simulation shows the detonation after the detonation in the donor has entered the acceptor. The explosive charges are initially adjacent to a very low density inert material (shown to the right). As the simulation progresses the material interface between the explosive products and the inert material expands. Our simulation show the appearance of large dead zone preceded by a low pressure shock in the diffraction region nearest the corner, connected to a fully emergent detonation in center and conforms closely to Ferm’s experiment. The code MULTIMAT uses high-resolution (4th order in space and 3rd order in time) compressible reactive flow solvers combined with a modern level-set treatment that represent interfaces to enable multi-material simulation required for microdetonic devices.

High Speed Measurement and Other New Areas of Mechanics Research

The events of explosive technology take place at the limits of conventional experimental methods that measure mechanical quantities. Microdetonics is an area whose investigation will stimulate the creation of new measurement technologies. Recently our colleague, R. Adrian and his co-workers are working to develop PIV systems, [7] that can make capture motion events generated by shocks in optically accessible solids. These test solids can be used as a measuring instrument and a “full-field” witness plate to capture the energy and momentum transfer from adjacent shock materials that are under investigation. Unlike lower speed PIV systems that take full-field velocity measurements in water or air, full field measurements in the interior of solids have not been available experimentally. This emerging measurement technology should allow

for unprecedented improvements in understanding load transfer at the interface between materials.

The physics of exploding wire and foils involves the coupling of the mechanics of phase transformations and the magneto hydrodynamics. Target ceramic materials require new thermo-mechanical theories for ceramic formation under rapid high pressure/temperature loading. The theory of critical energy and pulse duration for initiation of detonation is at the heart of fundamental questions in reactive flow science. It is very likely microdetonic devices can be made for use for other basic material property investigations of a fundamental nature. In short, the area of microdetonics and the creation of precisely controlled miniaturized explosive systems will surely be coupled to fundamental advances in thermomechanics and have an impact on areas of technology that can use precision, high energy density output sources applied to materials with precision.

Acknowledgments

This work is supported by the US Department of Energy, DOE/LANL and the US Air Force Research Laboratory, AFOSR-Mathematics and Munitions Directorate, Eglin AFB, Florida.

References

- [1] K. Takayama, T. Saito, Shock Wave/Geophysical and Medical Applications, Annual Review of Fluid Mechanics, Vol.36, pp.347-379, 2004.
- [2] D.S. Stewart, Toward Miniaturization of Explosive Technology, Shock Waves, Shock Waves, Vol.11, pp.467-473, 2002.
- [3] T.A. Baginski, S.L. Taliaferro, D.W. Fahey, Novel Electroexplosive Device Incorporating a Reactive Laminated Metallic Bridge, *Propulsion and Power*, Vol.17, No.1, 2001.
- [4] A.S. Tappan, A.M. Renlund, G.T. Long, S.H. Kravitz, K.L. Erickson, W.M. Trott, M.R. Baer, Microenergetic processing and testing to determine energetic material properties at the mesoscale, Proceedings of the 12th International Symposium on Detonation, San Diego, USA, 2002. Available online at <http://www.sainc.com/onr/detsymp/detsymp2002/technicalProgram.htm>.
- [5] A.R. Kasimov, D.S. Stewart, B.L. Wescott, Sunhee Yoo, Linear Instability Analysis of Non-Ideal, Condensed Phase Detonation, University of Illinois, submitted for publication, 2004.
- [6] A. Kasimov, D.S. Stewart, Asymptotic theory of the evolution and failure of self-sustained detonations, TAM Report No. 1042 UILU-ENG-2004-6003, ISSN 0073-5264, to appear in the *Journal of Fluid Mechanics*, 2004.
- [7] M.J. Murphy, R.J. Adrian, D.S. Stewart, G.S. Elliott, K.A. Thomas, J.E. Kennedy, Visualization of blast waves created by exploding wires, submitted to the *Journal of Visualization*.

FOAMS IN MICROGRAVITY

Denis Weaire and Simon Cox

Department of Physics, Trinity College, Dublin 2, Ireland

dweaire@tcd.ie

1. Introduction

Ordinary aqueous foam, which is our main subject in this paper, needs no introduction. Who has not taken a few minutes to study its beautiful structure (Fig. 1) and to watch it change? If you do so, you may study it from at least three different perspectives:

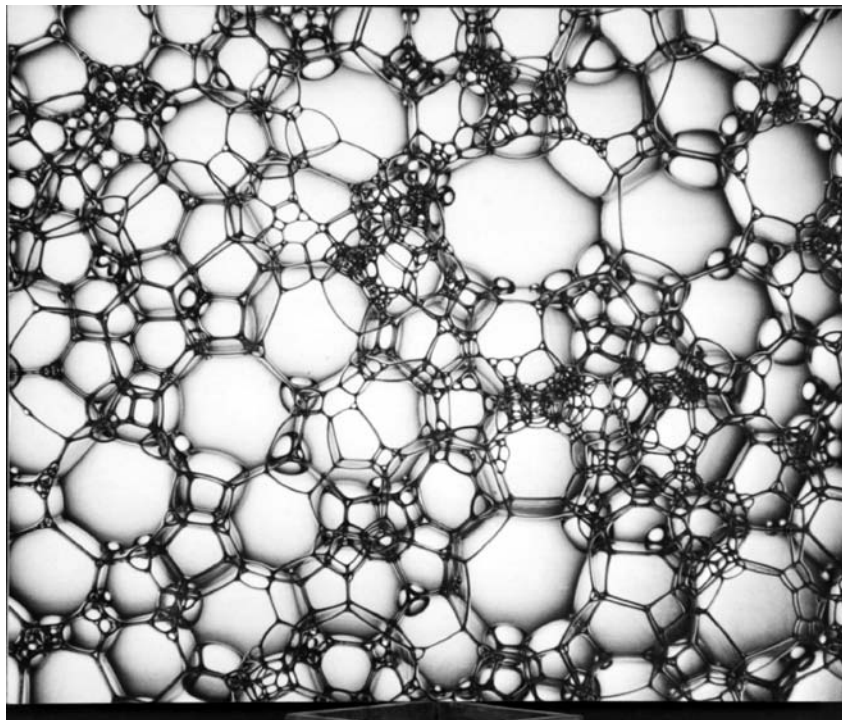


Figure 1. An aqueous foam as seen by the photographer-artist Michael Boran.

- as a compacted heap of individual *bubbles* of widely varying shape and size.
- as a division of space by conjoined soap *films*, all slightly curved.
- as a network of *lines*, the so-called *Plateau borders* where the films meet.

The first description relates to the manner of formation of the foam, which can even be designed to produce highly monodisperse foams. The second is the key to its stability: how long will the films survive without rupture? The third description often comes to the fore in theories of physical properties, such as conductivity, drainage or the mechanics of solidified foam.

Plateau(1873) gave us the first coherent account of the basic rules to which the structure must conform, particularly for relatively *dry* foams, of low liquid content. Underlying these rules is the essential principle of the minimization of surface energy (usually under the constraint of fixed bubble volumes). Indeed, most of the static and quasi-static properties of a foam may be explained by arguments which derive from that principle. It entails the Laplace-Young law (which we should celebrate in 2004/5 as this is its bicentenary year), and Plateau's rules for the junctions of films and borders (Weaire and Hutzler(1999)).

As the liquid content is increased, some of Plateau's strictures are relaxed. Whereas only fourfold confluences of borders are possible for the ideal dry foam, higher numbers may come together in stable junctions of the wet foam. We have not yet grasped the complexities of wet foam structures, except perhaps in two dimensions. Even in the carefully chosen special case of the symmetric eight-fold junction, shown in Fig. 2, progress has been slow since Weaire and Phelan(1996) raised questions

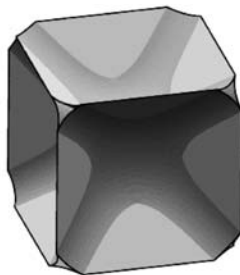


Figure 2. This wet eight-fold junction of Plateau borders is stable until the liquid fraction is reduced to an exceedingly small value, as shown by Brakke. Image courtesy of K. Brakke.

about it, on the basis of experiment (see in het Panhuis et al.(1998)), neatly following the tradition of Plateau. Very recently, Ken Brakke has completed a masterful analysis which leads to the conclusion that a *finite but exceedingly small* liquid fraction Φ is required to stabilize this junction.

2. The Surface Evolver

Brakke is the originator and chief exponent of the Surface Evolver (Brakke(1992)), a suite of software which has been applied to such static problems. Its impact on this field is only part of a wider influence, whenever surface energy is dominant in physics and engineering (e.g. Collicott and Weislogel(2004)). As the crystallographer Alan Mackay has said

The Evolver is a spectacular example of the effects of a gift to science which advances a whole field.

Figure 3 gives some further examples of the applications of the Evolver undertaken by our group. The most celebrated of these is the 1994 discovery (Weaire and Phelan(1994)) of a structure of monodisperse dry

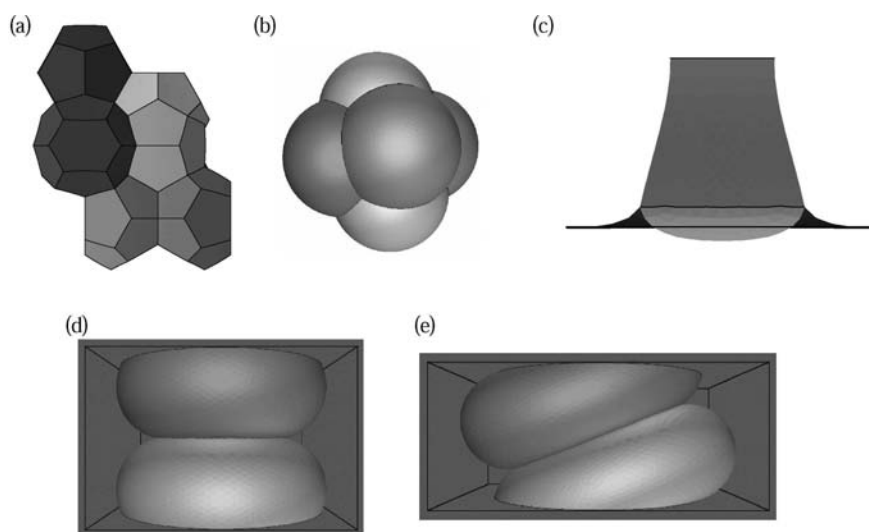


Figure 3. Examples of the use of the Surface Evolver. (a) The Weaire-Phelan structure which is conjectured to fill space with the lowest surface area. (b) A finite cluster of bubbles, used to investigate their local structure (Cox and Graner(2004)). (c) The meniscus surrounding a single bubble trapped between a glass plate and a liquid pool (Vaz et al.(2004)). (d) When two drops of oil are squeezed between parallel plates, there is a symmetry-breaking instability (e) at a certain critical separation (Bradley and Weaire(2001)).

foam that has a lower surface energy than that conjectured by Lord Kelvin (Thomson(1887); Weaire(1994)).

This structure has two different bubble shapes that fit together to form a structure of overall (body-centred-) cubic symmetry. It is about to be manifested in a spectacular building for the Beijing Olympics – the Water Cube – illustrated in Fig. 4. Its construction is based on a network of steel beams, corresponding to the Plateau borders of the Weaire-Phelan structure. In analyzing its stability, the engineers must have repeated the kind of exercise undertaken by materials scientists for open-celled solid foams such as polyurethane (Warren and Kraynik(1991)). It should prove to be an inspiring instance of the harmony of scientific and aesthetic principles.

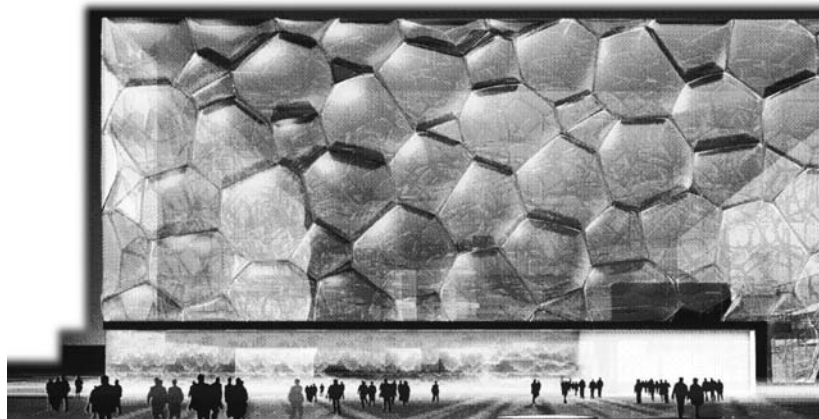


Figure 4. The designer's vision for the Beijing National Swimming Centre for the 2008 Olympics. The interior of its transparent walls consist of the Weaire-Phelan structure of Fig. 3(a). Image courtesy of Arup, PTW and CSCEC.

3. Debates Over Drainage

As anticipated in the closing chapter of the book of Weaire and Hutzler(1999), the focus of foam physics has moved from static to dynamic properties, related to drainage and rheology.

Drainage is the passage of liquid through the foam (mainly through the Plateau borders), driven by gravity or by pressure gradients. Its main properties are captured by a simple continuum theory expressed in a nonlinear partial differential equation.

Suppose we pour liquid steadily into the top of a foam: how fast does it travel downwards under gravity? Assuming Poiseuille flow in the

borders, a relation may be derived for which the velocity is

$$v \sim Q^{1/2}, \quad (1)$$

where Q is the flow-rate of added liquid. Although supported by several experiments (Weaire et al.(1997)), this was challenged (Koehler et al.(1999)), in favour of an index of *one-third*. It transpired that the discrepancy between the old and the new results lay in the use of different surfactants to stabilize the foam. Some of these produce relatively rigid surfaces (hence Poiseuille flow) while others leave the surfaces mobile (Durand et al.(1999)). In future, we will be more cautious in asserting generic properties!

4. Getting Rid of Gravity

Beyond a certain flow-rate, the steady drainage described above becomes unstable, giving rise to a slow convective motion (Hutzler et al. (1998), Vera et al. (2000), Weaire et al. (2003)). It therefore cannot be used as a proxy for the equilibrium structure of a very wet foam, which was part of the original motivation for its study. How then are we to prepare such uniform wet foams?

A static foam under gravity has only a very limited height of wet foam (if any) at the bottom. It may be estimated to extend to the height

$$h = \frac{l_0^2}{d}, \quad (2)$$

where d is the bubble diameter and the capillary length is

$$l_0^2 = \frac{\sigma}{g\Delta\rho}. \quad (3)$$

Here σ is the surface tension, $\Delta\rho$ the density difference between gas and liquid and g the acceleration due to gravity.

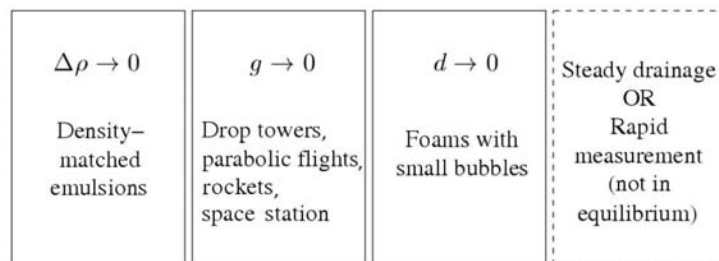


Figure 5. Strategies for preparing and studying wet foams.

The rest of the foam is essentially dry. Hence the ease of preparing dry foams and our frustration in wishing to study wet samples. Several strategies present themselves, and are summarized in Fig. 5. Of these, *density-matched emulsions* have been used by Mason et al.(1995) and others to probe static properties which are common to foams and emulsions, in theory. Another strategy is to use small enough bubbles that the wet foam thickness in Eq. (2) above becomes considerable.

Thirdly, we may use steady drainage or attempt measurements in a short time-scale, before drainage has developed (Saint-Jalmes and Durian(1999)).

All of these suffer from limited applicability: hence the appeal of getting rid of gravity altogether, in drop towers, parabolic flights, rockets or space-stations.

5. Foams under Microgravity

An honoured mention should be made of early space microgravity experiments on foams, particularly by David Noever (1994) and Noever and Cronise (1994), but these isolated efforts did not result in any coherent progress. Following the creation and operation of a Topical Team for this subject by the European Space Agency, there is some hope of a more systematic approach.

Currently the subject is being tackled in two ESA-sponsored projects. The first aims to utilize microgravity conditions to create homogeneous *metallic* foams (Wübben et al.(2002)). An example of a metallic foam is shown in Fig.6. These materials are proving their potential in, for example, the automobile industry. The foamed metal should not suffer from drainage while in its liquid state, since this would lead to variations of density within the solid product (Banhart and Weaire(2002); Cox et al.(2001)). Obviously, microgravity sidesteps that limitation.

The second project is a study of *wet* aqueous foams in equilibrium, so that the processes of drainage, rheology and coarsening due to gas diffusion can be examined independently (Saint-Jalmes and Langevin(2004)).

6. Conclusions

For its satisfactory completion, the basic theory of the physics of foams needs to be extended to wet foams, initially in a state of static equilibrium. Describing dynamic wet foams will still be a considerable challenge. But it will reward success: churning, flowing wet foams lie at the heart of the chemical industry. As Weaire and Hutzler(1999) said, *throwing down the challenge, a walk by the seaside on a stormy day is*

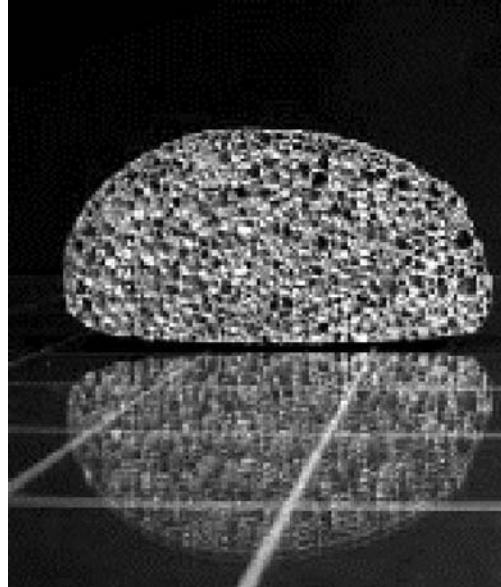


Figure 6. An example of foamed zinc. The bubbly melt must be solidified quickly to retain the homogeneous structure, a stricture not required in the microgravity environment. Image courtesy of J. Banhart.

enough to excite curiosity. But it may be that the calmer environment of space is needed for the first progress in understanding wet foams.

Acknowledgments

Tristram Carfrae (Arup) kindly provided details of the Water Cube (Fig. 4). We wish to thank the European Space Agency for support under ESA Contract 14308/00/NL/SH (AO-99-031) CCN 002 MAP Project AO-99-075.

References

- [1] J. Banhart and D. Weaire, On the road again: metal foams find favor, *Physics Today*, July:37–42, 2002.
- [2] G. Bradley and D. Weaire, Instabilities of Two Liquid Drops in Contact, *Comp. Sci. Eng.*, Sept/Oct:16–21, 2001.
- [3] K. Brakke, The Surface Evolver, *Exp. Math.*, **1**:141–165, 1992.
- [4] S.H. Collicott and M.M. Weislogel, Computing existence and stability of capillary surfaces using surface evolver, *AIAA J.*, **42**:289–295, 2004.
- [5] S.J. Cox, G. Bradley, and D. Weaire, Metallic foam processing from the liquid state: the competition between solidification and drainage, *Euro. J. Phys: Appl. Physics*, **14**:87–97, 2001.

- [6] S.J. Cox and F. Graner, Three-dimensional bubble clusters: shape, packing and growth-rate, *Phys. Rev. E*, **69**:031409, 2004.
- [7] M. Durand, G. Martinoty, and D. Langevin, Liquid flow through aqueous foams: From the Plateau border-dominated regime to the node-dominated regime, *Phys. Rev. E*, **60**:R6307–R6308, 1999.
- [8] S. Hutzler, D. Weaire, and R. Crawford, Convective instability in foam drainage, *Europhysics Lett.*, **41**:461–465, 1998.
- [10] S.A. Koehler, S. Hilgenfeldt, and H.A. Stone, Liquid flow through aqueous foams: The node-dominated foam drainage equation, *Phys. Rev. Lett.*, **82**:4232–4235, 1999.
- [11] T.G. Mason, J. Bibette, and D.A. Weitz, Elasticity of Compressed Emulsions, *Phys. Rev. Lett.*, **75**:2051–2054, 1995.
- [12] D.A. Noever, Foam Fractionation of Particles in Low Gravity, *J. Spacecraft Rockets*, **31**:319–322, 1994.
- [13] D.A. Noever and R.J. Cronise, Weightless bubble lattices: A case of froth wicking, *Phys. Fluids*, **6**:2493–2500, 1994.
- [9] M. in het Panhuis, S. Hutzler, D. Weaire, and R. Phelan, New variations on the soap film experiments of Plateau. I. Experiments under forced drainage, *Phil. Mag. B*, **78**(1):1–12, 1998.
- [14] J.A.F. Plateau, *Statique Expérimentale et Théorique des Liquides Soumis aux Seules Forces Moléculaires*, Gauthier-Villars, Paris, 1873.
- [15] A. Saint-Jalmes and D.J. Durian, Vanishing elasticity for wet foams: Equivalence with emulsions and role of polydispersity, *J. Rheol.*, **43**:1411–1422, 1999.
- [16] A. Saint-Jalmes and D. Langevin, The foam experimental module for the ISS, *Microg. Sci. Tech.*, in press, 2004.
- [17] W. Thomson, On the Division of Space with Minimum Partitional Area, *Phil. Mag.*, **24**:503–514, 1887.
- [18] M.F. Vaz, S.J. Cox, and M.D. Alonso, Minimum energy configurations of small bidisperse bubble clusters, *J. Phys.: Condens. Matter*, **16**:4165–4175, 2004.
- [19] M.U. Vera, A. Saint-Jalmes, and D.J. Durian, Instabilities in a liquid-fluidized bed of gas bubbles, *Phys. Rev. Lett.*, **84**:3001–3004, 2000.
- [20] W.E. Warren and A.M. Kraynik, The Nonlinear Elastic Behavior of Open-Cell Foams, *J. Appl. Mech.*, **58**:376–381, 1991.
- [21] D. Weaire, editor, *The Kelvin Problem*, Taylor & Francis, London, 1994.
- [22] D. Weaire and S. Hutzler, *The Physics of Foams*, Clarendon Press, Oxford, 1999.
- [23] D. Weaire, S. Hutzler, S. Cox, N. Kern, M.D. Alonso, and W. Drenckhan, The Fluid Dynamics of Foams, *J. Phys.: Condens. Matter*, **15**:S65–S73, 2003.
- [24] D. Weaire, S. Hutzler, G. Verbist, and E. Peters, A review of foam drainage, *Advances in Chemical Physics*, **102**:315–374, 1997.
- [25] D. Weaire and R. Phelan, A counter-example to Kelvin’s conjecture on minimal surfaces, *Phil. Mag. Lett.*, **69**:107, 1994.
- [26] D. Weaire and R. Phelan, Vertex instabilities in foams and emulsions, *J. Phys.: Condensed Matter*, **8**:L 37–L 43, 1996.
- [27] T. Wübber, J. Banhart, and S. Odenbach, Production of metallic foam under low gravity conditions during parabolic flights, *Microgravity Sci. Tech.*, **13**:36–42, 2002.

Author Index

On the following pages authors and co-authors of all presentations are listed. The extended summaries of the presentations can be found on the enclosed CD-ROM. Each name is followed by sequence of entries consisting of session and presentation IDs. For the lectures contained in the present book, the appropriate page number is also given, and the presenting author entry is additionally highlighted by boldface letters. IDs of contributions of presenting authors are printed in upright typeface.

Only *eligible* presentations are listed, i.e. presented during the Congress, excluding multiple presentations and those given by a proxy.

- Abbott J.R. — *FM16.11725*
 Abdalla H.M. — *FSM6.11806*
 Abdou L. — *SM2.12082*
 Abdul-Latif A. — *SM4.10456*
 Abdunabi T.A. — *SM25.11082*
 Abed F.H. — *SM18.10393*
 Abedi R. — *SM1.12441*
 Abkarian M. — *FM1.12423*
 Aboudi J. — *MS1.12011*
 Acartuerk A. — *SM15.11194*
 Acharya A. — *SM18.11820*
 Acrivós A. — *FM16.10361*
 FM4.10753
 Adachi S. — *FM25.12041*
 Adachi T. — *FM5.11864*
 Adams N.A. — *FM24.10455*
 FM24.11256 *FM24.11802*
 FM24.12564 *FSM6.10399*
 Adda-Bedia M. — *SM9.10338*
 Addas K. — *MS2.10709* (p. 355)
 D'Addetta G.A. — *SM4.11414*
 Aderogba K. — *SM13.10745*
 Adrian R.J. — *FM25.12161*
 FM25.12196 *MS4.11607*
 Agapov D. — *SM17.11688*
 Agarwal R.K. — *FM11.10872*
 Aghalovyan L.A. — *SM6.11526*
 Ahcene B. — *FSM4.13050*
 Ahlwat A.S. — *SM3.10098*
 Ahmetolan S. — *SM11.10891*
 Aider A.A. — *FM13.10185*
 Aidun C.K. — *FM1.12124*
 Aifantis K. — *SM13.11782*
 Aitta A. — *FM21.11328*
 Aksel N. — *FM14.10642*
 FM14.10928
 Akylas T.R. — *FM26.10762*
 Al-Abduljabbar A. — *SM9.12798*
 Albers B. — *SM11.10072*
 Alderliesten R. — *SM8.12217*
 Alexander J.I.D. — *MS5.12447*
 Alexeev A. — *FM14.12293*
 FSM1.12516
 Ali R. — *FM2.11887*
 Alibiglu A. — *SM13.13009*
 Alleborn N. — *FM14.11413*
 Allix O. — *SM1.12237*
 Almeida S.F.M. de — *SM13.12148*
 Altenbach H. — *SM27.11368*
 Altobelli S.A. — *FM18.10983*
 Alvarez J.O. — *FSM1.12477*
 Amalia P. — *SM17.11352*
 Amberg G. — *FM21.12312*
 Ambrósio J. — **SL1.11040** (p. 61)
 Ammann M. — *SM15.10792*
 Amyot O. — *FM12.11343*
 Anderson D.M. — *FM21.12768*
 Andersson L.-E. — *SM2.10686*
 Andreev O. — *FM19.11120*
 Andreeva T.A. — *FSM1.12149*
 Andrejczuk M. — *FM9.12592*
 Andrews M.G. — *SM13.11162*
 Andrianov I.V. — *SM13.12588*
 Antkowiak A. — *FM13.12483*
 Antretter T. — *SM14.10088*
 Anweiler S. — *FM20.11745*
 Arakelian V. — *SM16.10553*
 Arbez P. — *FM6.12510*
 Aref H. — *FM25.11676*
 FSM7.10003
 Argyriadi K. — *FM14.10557*
 Arias I. — *SM9.12171*
 Ario I. — *SM22.12688*
 Ariza M.P. — *FSM6.11471*
 Arora M. — *FM8.11999*
 Arroyo M. — *SM1.12455*
 Asai M. — *FM13.10489*
 Aschenbrenner C. — *FM13.10188*
 Ashawesh G.M. — *SM25.11082*
 Ashida F. — *MS1.12018*
 Ashmore J. — *FM21.12276*
 Askes H. — *SM12.11277*
 SM1.12924
 Asmolov E.S. — *FM16.11480*
 Astley J. — *FSM1.11249*
 Atakhorrami M. —
 MS2.10709 (p. 355)
 Aubouy M. — *FSM5.11095*
 Auregan Y. — *FM24.12740*
 Aurnou J.M. — *FM7.11440*
 Auslender F. — *SM13.11507*
 Aussillous P. — *FM21.11320*
 Avalos-Zuniga R.A. — *FM19.12120*
 Avramov K.V. — *SM25.12989*
 Awrejcewicz J. — *SM25.12989*
 SM2.11481
 Baaijens F.P.T. — *SM18.11344*
 Baars A. — *FM10.13048*
 Babinsky H. — *FM5.10984*
 Babushkin I.A. — *FM7.12267*
 Bachorz P. — *SM25.12770*
 Badel P.-B. — *SM4.12913*
 Bai X. — *SM9.12174*
 Bai Y. — *FSM7.11765*
 SM7.11764
 Baillis C. — *SM22.11174*
 Bajaj K. — *FM25.12275*
 SL2.10042 (p. 89)
 Balamurugan V. — *MS1.12147*
 Balandin D.V. — *SM3.11219*
 Baldessari F. — *FM8.11289*
 Balint A.M. — *FM21.11362*
 Balint D.S. — *MS3.12386*

- Balint S. — *FM21.11362*
 Baltov A.I. — *SM18.11953*
 Balueva A.V. — *SM9.11856*
 Bambrey R.R. — *MS6.11336*
 Banach Z. — *FSM6.11237*
 Banaszak J. — *SM15.13006*
 Banaszek J. — *FM21.11364*
 Banerjee A. — *SM17.11375*
 Banta R.M. — *MS6.10513*
 Bar-Lev O. — *FM17.12308*
 Bar-Yoseph P.Z. — *FM13.11461*
 Baracho Neto O.G.P. — *SM25.11494*
 Baradat C. — *SM16.10553*
 Barba L.A. — *FM6.11937*
 Barbe F. — *SM14.12421*
 SM14.12747
 Barber T.J. — *FM14.11477*
 Bargmann S. — *SM1.12924*
 Barkley D. — *FM13.12431*
 Barmin A.A. — *FM9.11703*
 Barnea D. — *FM20.11655*
 Baroud C.N. — *FM1.11013*
 MS4.12047 *SL18.10495*
 Barral S. — *FM19.12363*
 Barrau J.-J. — *SM13.11180*
 Bartel T. — *SM14.12077*
 Barthés-Biesel D. — *MS2.11961*
 Batra R.C. — *SM10.12594*
 Baty H. — *FM19.11429*
 Bauer D. — *SM15.12614*
 Bauruelle J.C. — *SM22.11174*
 Baweja M. — *SM3.12756*
 Bayer I.S. — *FM4.11603*
 Bazant M.Z. — *MS4.11777*
 Bazin B. — *FM12.10234*
 Bałdyga J. — *FM22.12415*
 Becache E. — *SM2.12382*
 Becker M. — *FSM6.12118*
 Becker W. — *SM15.11463*
 SM9.11484
 Beda P.B. — *SM12.10314*
 Bednarz T. — *FM7.13022*
 Behringer R.P. — *FM17.12399*
 Behringer R. — *FM12.12617*
 Belcher S.E. — *FM26.10746*
 Belzons M. — *FM17.11751*
 Ben Dhia H. — *SM11.12763*
 Ben Hamida A. — *SM1.12727*
 Benallal A. — *SM12.10265*
 Benilov E.S. — *FM26.11468*
 Benilov E. — *FM25.11467*
 Bennacer R. — *FM15.11386*
 Bennett D.J. — *FM4.10753*
 Benzerga A.A. — *SM1.12737*
 Berbenni S. — *SM18.11498*
 Beresneva E.N. — *FM7.10538*
 Berezovski A. — *SM10.11592*
 SM14.11393
 Berfield T. — *MS1.11685*
 Berg A. van den — *FM1.12400*
 Bergdorff M. — *FM6.12583*
 Bergeon A. — *FM22.12731*
 Bergerot A. — *SM13.11180*
 Bergman L.A. — *SM25.10408*
 Bergmann R. — *FM10.11909*
 FM17.10253
 Bergougnot L. — *FM16.11588*
 FM16.12345
 Bernardo M. di — *FSM2.11363*
 Beron-Vera F.J. — *MS6.12776*
 Berton G. — *FM17.12883*
 Bertram A. — *SM18.12549*
 Beskos D.E. — *SM1.12845*
 Bessonnet G. — *SM17.12539*
 Betelu S.I. — *FM8.12548*
 Beysens D.A. — **SL3.10880** (p. 117)
 Bezpalcova K. — *FM9.10467*
 Bhattacharya K. — *MS1.11731*
 SM14.10721
 Bi W. — *FM17.12883*
 Bialecki R.A. — *SM24.11137*
 Bidulya A. — *SM17.11688*
 Bielski J. — *SM4.11796*
 Bielski P. — *FM8.12311*
 Bielski W.R. — *FM12.11248*
 Bigoni D. — *SM12.10265*
 Billant P. — *FM25.11391*
 FM25.12108 *MS6.12294*
 Billardon R. — *SM4.10974*
 Bin G. — *SM1.10559*
 Binding D.M. — *FM4.12254*
 Bing-Zheng G. — *SM10.11572*
 Bioul F. — *FM15.12591*
 Biros G. — *FSM1.12691*
 Bisgaard A. — *FM23.10247*
 Blab R. — *SM27.11981*
 Blachut J. — *SM22.10378*
 Blackmore D. — *FM25.11683*
 Blajer W. — *SM17.10026*
 Blanc X. — *FSM6.12336*
 Blasinska A. — *FM4.11184*
 Blekhman I.I. — *SM25.11055*
 SM25.11719
 Blekhman I. — *SM25.11055*
 Błachowski B.D. — *SM3.10457*
 Błoński S. — *FM17.11169*
 FM4.11184 *FM8.12873*
 Blume H. — *SM2.12086*
 Blyth M.G. — *FM18.10766*
 Bo W. — *SM24.13013*
 Bobaru F. — *SM24.12789*
 Bobylov A.A. — *SM2.11933*
 Bociarelli M. — *SM18.10797*

- Bochenek B. — SM24_12075
 Bodnar A. — SM4_11665
 Boeck T. — FM19_12090
 FM8_11723
 Boehlke T. — SM18_12549
 Boehm H.J. — SM13_12321
 Boehm R. — SM13_12576
 Boer P. de — FM11_12258
 Boer R. de — SM15_10198
 Boerner E.F.I. — SM1_12584
 Bogacz R. — SM22_12931
 Bogaert N. van den — FM15_12591
 Boguslawski A. — FM3_11914
 FM6_12076
 Bohatier C. — SM17_11361
 Bokhove O. — MS6_10716 (p. 103)
 Bolotnik N.N. — SM3_11219
 Bolotnova R.Kh. — FM8_12190
 Bolzon G. — SM18_10797
 Bonamy D. — SM9_12378
 Bonn D. — FM8_13025
 Bonnecaze R.T. — FM16_11991
 FM16_12574
 Bonnevie Harbitz C. — FM9_12270
 Bonsel J.H. — SM25_11783
 Bontoux P. — FM6_13051
 FM15_11893 FM25_12080
 Bontozoglou V. — FM14_10557
 Borg U. — SM13_12214
 Borges L.S.A. — SM10_13018
 Borisov A.V. — SM1_12351
 Bornert M. — SM13_11507
 SM13_11805
 Borodich F.M. — SM2_11135
 SM2_11215
 Borodulin V.I. — FM24_12675
 FM2_10275
 Boronska K. — FM7_10914
 Boroński P. — FM6_10921
 Borrell M. — FM8_11289
 Borve S. — FM19_11809
 Bos F. van der — FM6_13030
 Bostrom A. — FSM7_12603
 Bottaro A. — FM11_12602
 Bottausci F. — FM22_12761
 Bouchet G. — FM24_12740
 Bouch V. — FM7_11972
 Boudaoud A. — FM8_13025
 Boudifa M. — SM4_11885
 Bouizi O. — FM15_12636
 Boukpeti N. — SM20_11667
 Boulanger P.S. — FSM3_11818
 SM11_11812
 Bouruet-Aubertot P. — MS6_12601
 Boussa H. — SM1_12727
 Bouvet C. — SM13_11180
 SM14_12225
 Bouville M. — FSM6_11476
 Boyland P. — FM22_12442
 Bozhko A.A. — FM7_10538
 Brady J.F. — FM16_12452
 SL4_12160
 Braescu L. — FM21_11362
 Bragov A.M. — SM20_10374
 Brancher J.P. — FM13_10185
 Brancher P. — FM13_12483
 Branicki M. — FM18_12164
 FSM6_11862
 Braud P. — FM5_13016
 Brauer H. — FM19_12605
 Braun S. — FM2_11084
 Braunbrueck A. — SM11_11620
 Bravo-Castillero J. — SM13_11176
 Brechet Y. — SM1_12737
 Brekelmans W.A.M. — FSM6_11830
 SM18_11344 SM18_11963
 SM1_12723
 Bremond N. — FM8_11317
 Brenner H. — FM16_11725
 Brenner M.P. — FM8_11330
 Breuer K.S. — MS4_11604
 Breyse D. — SM18_12634
 Brinckmann S. — SM8_11927
 Brinson C.L. — MS1_12027
 Brizuela E. — FM3_11888
 Broeckhoven T. — FM3_11888
 Brons M. — FM23_10247
 Brovchenko I.A. — FM26_12268
 Brown E.N. — MS1_13010
 MS1_13011
 Browne D.J. — FM21_11364
 Bruls O. — SM17_12208
 Brun C. — FM24_12740
 Brunet E. — MS4_12130
 Brunig M. — SM4_11406
 Bruyn J.R. de — FM17_12338
 Buehler O. — MS6_10977
 Buhl T. — SM24_12079
 Bulgakova G.T. — FM12_10548
 Bulgarelli U.P. — FM8_12547
 Burachik R. — SM24_10594
 Burczyński T.S. — SM24_11137
 Burde G.I. — FM26_12813
 Burde G. — FM2_11984
 Burnett D.S. — FSM1_11373
 Burton D. — MS1_12027
 Buryachenko V. — SM6_12685
 Buschmann M.M. — FM2_10948
 Busilas A. — SM16_12546
 Busse F. — FM19_10931
 Byrne H.M. — FM23_11060
 Byrtus M. — SM25_11759
 Byskov E. — SM22_12297
 Byun Y.-H. — FM6_11569

- Blawdziewicz J. — *FM8_11411*
 Bühler O. — *MS6_12157*
- C**
 Caffrey J.P. — *MS1_13007*
 Cailletaud G. — *SM14_10088*
 Calhoun R. — *FM9_12738*
 Callegari G. — *FM4_10140*
 Calloch S. — *SM14_12225*
 SM18_12469
 Camotim D. — *SM22_12558*
 Campana E.F. — *FM8_12547*
 Campregher R. — *FM6_11456*
 Cannata G. — *FM24_11151*
 Cantat I. — *FSM5_12052*
 Carabineanu A.S. — *FM1_11943*
 Carbonneau X. — *FM6_12510*
 Cardin P. — *FM19_12330*
 Cardon A. — *SM13_12818*
 Cardonne C. — *FM22_12761*
 Carey M. — *FM12_12617*
 Carlotti P. — *MS6_10513*
 Carnasciali M.-I. — *MS5_12651*
 Carneiro C.A.V. — *SM10_13018*
 Carpen I.C. — *FM16_12452*
 Carpenter P.W. — *FM2_11887*
 Carpinteri A. — *FSM6_11224*
 Carriere P. — *FM13_11186*
 Cartraud P. — *SM1_12359*
 Casalis G. — *FM13_12508*
 Casandjian C. — *SM4_10011*
 Case S. — *SM23_10242*
 Casey J. — *FSM3_11096*
 Cassar C. — *FM16_11749*
 Cassardo C. — *MS6_13017*
 Castellanos A. — *FM4_12437*
 Castro F. — *FM8_11670*
 Cataldi-Spinola E. — *FSM1_12586*
 Caughey T.K. — *MS1_13007*
 Caulliez G. — *FM13_12233*
 FM26_11230
 Cazacu O. — *SM18_11930*
 SM20_12779
 Cazalbou J.B. — *FM6_12510*
 Cebers A. — *MS2_11102*
 Cenedese A. — *FM7_11673*
 Cercignani C. — *MS4_10723*
 Chabert E. — *SM13_11805*
 Chaboche J.L. — *SM4_11885*
 Chadli M. — *SM4_10456*
 Chakraborty P. — *FM25_12161*
 Challamel N. — *SM4_10011*
 Chang C.-C. — *FM25_11741*
 Chang F.-R. — *SM16_12712*
 Chang H.-H. — *SM10_10364*
 Chang J.-T. — *SM1_11193*
 Chang K.T. — *FM11_11043*
 Chang S.-Y. — *SM24_11826*
- Chao G. — *SM11_11271*
 Chaplin J.R. — *FSM4_12557*
 Charrier Mojtabi M.C. — *MS5_10980*
 Chassaing P. — *FM6_12510*
 Chassiakos A.G. — *MS1_13007*
 Chatterjee A. — *SM25_12814*
 Chatzidai N. — *FM18_12859*
 Chatzigeorgiou G. — *SM4_12749*
 Chauve M.-P. — *FM24_10506*
 Chazallon C. — *SM18_12634*
 Chen B. — *SM24_11532*
 Chen C.F. — *FM21_11058*
 Chen F. — *FM9_11294*
 Chen H.-C. — *FM25_11741*
 Chen J. — *SM25_10166*
 Chen L.-Q. — *FSM2_12674*
 Chen P. — *FM13_11995*
 Chen S. — *SM14_11395*
 Chen T. — *SM6_11960*
 Chenchiah I. — *SM14_10721*
 Cheng G.D. — *SM24_13013*
 Cheong K.B. — *FM8_12596*
 Chern M.-J. — *FSM4_11668*
 Cherniy D.I. — *FM23_12868*
 Chernoray V.G. — *FM10_11455*
 FM2_11339
 Chernousko F.L. — *SM3_11243*
 Chew H.K. — *FM8_12596*
 Chiba N. — *SM18_10652*
 Chickichev I. — *SM20_12364*
 Chien W.Z. — *FM21_11208*
 Chini G.P. — *FM14_12155*
 Chiskis A. — *MS3_12432*
 Chizhik S.A. — *SM2_10999*
 Chmielniak T.J. — *FM6_11578*
 FM10_11916
 Cho J.-H. — *SM27_11827*
 Cho Y.-S. — *SM1_11817*
 Choi C.K. — *FM21_13008*
 Choi H. — *FM11_11636*
 FM19_11637
 Choi J. — *FM11_11636*
 Choi S.T. — *MS3_12778*
 Cholet C. — *SM17_11361*
 Chomaz J.-M. — *FM13_12425*
 FM13_12711 *FM25_11391*
 FM25_12108 *MS6_12294*
 Chow C.L. — *SM4_10961*
 Christophorou C. — *FM24_12965*
 Chrościelewski J. — *SM19_11890*
 Chrzanowski M. — *SM4_11665*
 Chu C.-C. — *FM25_11741*
 Chucholowski C. — *SM26_11672*
 Chung C.A. — *FM21_11208*
 Chung S.-H. — *SM1_12441*
 Churochkin D.V. — *FSM1_11508*
 Chwał M. — *MS3_12251*

- Cichocki B. — *FM16_10993*
 FM18.11300
- Ciechanowski J. — *FM9_12266*
- Cieslik J. — *SM25_12498*
- Cieszko M. — *FM12_12611*
- Cilliers J.J. — *FSM5_12851*
- Claire D. — *SM4_12021*
- Clamond D. — *FM26_11417*
- Clanet C. — *FM8_11317*
- Clavel M. — *SM8_12228*
- Clayton J.D. — *SM18_10955*
- Clercx H.J.H. — *FM25_11964*
- Clercx H. — *FM22_12633*
- Cleri F. — *FSM6_12334*
- Clifford M.J. — *SM13_11387*
- Cloirec M. — *SM1_12359*
- Cloitre M. — *FM16_12574*
- Cocks A.C.F. — *SM15_12903*
- Cocou M. — *SM2_12382*
- Coelho I. — *SM12_12682*
- Coelho P.J. — *FM3_12348*
- Cohen J. — *FM13_11461*
- Cohen-Addad S. — *FSM5_12578*
- Coiffet F. — *FM5_13016*
- Coker D. — *SM2_11987*
- Cola B.A. — *FM22_12158*
- Colette A. — *FM25_11391*
- Collicott S.H. — *MS5_12447*
- Colombo L. — *FSM6_12334*
- Colonius T. — *FM11_12387*
- Coman C.D. — *SM22_12967*
- Combescure A. — *SM1_11797*
 SM22.11174
- Comte P. — *FM19_11429*
 FM24.12740
- Constantin P. — *FM23_10938*
- Constantinescu D.M. — *SM9_10864*
- Cooker M.J. — *FM26_11345*
- Coons J. — *FSM5_12435*
- Cordeiro Fernandes P. — *FM20_12139*
- Cornwell P. — *FSM7_12642*
- Costa M. — *FM3_12348*
- Costanzo F. — *FSM7_12642*
- Cottet G.-H. — *FM6_12583*
- Cottron M. — *SM9_10429*
- Courrech du Pont S. — *FM17_13029*
- Cox B.N. — *SM13_11162*
- Cox S.M. — *FM22_10497*
 FM23.11060
- Cox S. — *MS5_10598* (p. 387)
- Craig W. — *FM26_11548*
- Cramer A. — *FM15_12349*
- Crandall S.H. — *SM25_10863*
- Cristescu N.D. — *SM18_11930*
 SM20.12779
- Crochet M.W. — *SM15_12771*
- Croll J.G.A. — *FM9_12072*
- Cudzilo S. — *FM3_12745*
- Cugy P. — *SM18_12469*
- Cummins S.J. — *FM8_12163*
- Cunningham J.C. — *SM15_12917*
- Currie P.K. — *FSM5_12986*
- Cuyppers Y. — *FM24_11303*
- Czarnecki S. — *SM24_11760*
- Czechowski L. — *FM21_12743*
- Czerwińska J. — *FM24_11802*
 FSM6.10399
- Dahan M. — *SM6_11901*
- Dahl S.R. — *FM17_12073*
- Dail B. — *FM15_10363*
- Dal Pont S. — *SM15_12114*
- Dalziel S.B. — *FM25_12051*
- Dam D.B. van — *FM14_11509*
- Dam R. — *SM22_12297*
- Daneshmand F. — *FM9_10733*
- Daneshmehr A. — *SM13_13009*
- Danishevs'kyy V.V. — *SM13_12588*
- Dankowicz H. — *SM17_11020*
- Danner T. — *FM8_11669*
- Daru V. — *FM8_11979*
- Darve E. — *FM16_12005*
- Daube O. — *FM13_10640*
- Davaille A. — *FM7_12126*
- Daive B. — *SM12_11254*
- Davidson P.A. — *FM19_11124*
- Davis R.H. — *FM16_11473*
 FM8.12329 FM8.12741
- Deblaise D. — *SM16_10553*
- Debatin K. — *FM5_11864*
- Debin S. — *SM1_10559*
- Decamp S. — *FM9_12410*
- Degre G. — *MS4_12130*
- Dekajlo K. — *FM9_10576*
- Delannay R. — *FM17_12883*
 FSM5.12052
- Delgado A. — *MS2_12031*
- Dell'Aversana P. — *MS5_12651*
- Delsaute B. — *FM15_12591*
- Delville J. — *FM5_13016*
- Dems K. — *SM24_11349*
- Denda M. — *MS1_12786*
- Denier J.P. — *FM2_10103*
- Denis A. — *SM18_12634*
- Denkov N.D. — *FM8_11669*
- Deprince X. — *SM18_11110*
- Derby J.J. — *FM15_10363*
- Derksen J. — *FM20_12397*
- Deshpande V.S. — *SM5_11022*
- Destrade M. — *FSM3_11950*
- Detournay E. — *SM15_12713*
 SM25.12535
- Dettmar J. — *FSM6_12112*
- Di G. Sigalotti L. — *FM6_10857*
- Dias F. — *FM26_12089*

- Dick E. — FM6_11602
 Didelle H. — MS6_12494
 Dijkman J.F. — FM4_12894
 Dimakopoulos Y. — FM14_12858
 Ding E.-J. — FM1_12124
 Dinkler D. — SM25_12785
 Dmitrochenko O. — SM17_10893
 Dobler W. — FM7_10306
 Dobovsek I. — SM12_12419
 Dobrolyubov A.I. — FM26_11144
 Doche O. — FM11_11394
 Dodge A. — MS4_12536
 Doerffer P.P. — FM5_12997
 Doghri I. — SM4_11886
 SM18_13038
 Dohnal F. — SM25_12026
 Dolezel I. — SM2_10211
 Dollet B. — FSM5_11095
 Domaas U. — FM9_12270
 Domański W. — FSM3_11840
 Domaradzki A.J. — FM24_10149
 Domenico C. — SM12_11254
 Dominguez J. — SM8_10698
 Dominguez J. — SM17_12071
 SM9_11321
 Dommelen J.A.W. van — SM18_11344
 Dongen M.E.H. van — SM11_11271
 Dorfman K.D. — FM4_11209
 Dorfmann L.A. — FSM3_11227
 Dormieux L. — SM15_11941
 Doudard C. — SM18_12469
 Doval-Montes L. — SM13_11176
 Dovgal A.V. — FM2_11339
 Dovgiy S.A. — FM23_12868
 Dowling A.P. — FSM1_12527
 Dragon A. — SM18_11110
 Drazer G. — FM16_10361
 Dreiden G.V. — SM11_10114
 Drescher A. — SM20_11667
 Dritschel D.G. — MS6_11336
 Drobiński P. — MS6_10513
 Drobnik S. — FM3_11914
 Drugan W.J. — SM12_12025
 Du J. — SM24_10433
 Dual J. — FSM1_12586
 MS3_12384
 Dubois F. — SM17_11361
 Duchemin L. — FM8_12388
 Duck P.W. — FM13_10916
 FM2_10103
 Dudeck M. — FM19_12363
 Dufour G. — FM6_12510
 Duineveld P.C. — FM4_12894
 Duluc M.C. — FM8_11979
 Dumais J. — MS2_11581
 Dumontet H. — SM1_12727
 Dupere I.D.J. — FSM1_12527
 Duplat J. — FM22_12326
 Dupont R. — FM13_12233
 Dupret F. — FM15_12591
 Durgin W.W. — FSM1_12149
 Duschlbauer D. — SM13_12321
 Dusek J. — FM13_12766
 Duszyński P. — FM6_12565
 Duysinx P. — SM17_12208
 Dvorak V. — FM5_12219
 Długosz A. — SM24_11137
 Eberhard P. — SM17_12133
 Eberhardsteiner J. — SM27_11981
 Eck C. — FSM6_11340
 Eckert K. — FM21_12365
 Eckert S. — FM21_12365
 Eckhardt B. — FM13_10313
 Edwards N.R. — FM26_12424
 Eggers J. — FM14_11089
 Ehlers W. — SM15_10792
 SM15_11194
 Ehrenstein U. — FM13_12372
 Ehrlacher A. — SM15_12114
 SM15_12614
 Eidelman A. — FM10_12070
 Ekiel-Jeżewska M.L. — FM16_11409
 FM18_11300
 El Abd A. — SM18_12634
 El G. — FM26_11134
 El Ganaoui M. — FM15_11386
 FM15_11893
 El Maihy A. — FM22_10130
 Elaguine D. — SM2_11365
 Eldredge J.D. — FSM1_12180
 Elias F. — FSM5_11095
 Elmabrok A.M. — SM25_11082
 Elperin T. — FM10_12070
 FM7_11053
 Emelin V.K. — SM7_11556
 Emmerich H. — FSM6_11340
 Engel R.S. — SM27_10906
 Engelbrecht J. — SM10_11592
 SM11_11813
 Engelen R.A.B. — SM4_11415
 England A.H. — SM10_12273
 Epstein M. — SM6_12122
 Eremeyev V.A. — SM19_10287
 Erenburg V. — FM3_12199
 Erickson J. — SM1_12441
 Ermakov M.K. — FSM7_11869
 MS5_11843
 Ern P. — FM20_12139
 Erofejev V.I. — SM11_12203
 Escalona J.L. — SM17_12071
 Esveld C. — SM24_11015
 Etling D. — MS6_12035
 Etnyre J.B. — FM23_11677

- Evans D.L. — FSM7_12642
 Evans G.M. — FM15_11903
 Evers L.P. — SM18_11963
- F**
 Faciu C. — SM14_11852
 Faisst H. — FM13_10313
 Faivre M. — FM1_12423
 Falcovitz J. — FM5_11049
 Falk M. — FSM6_11476
 Falkovich G. — FM22_12048
 Fan J. — SM27_11506
 Fan Y. — SM1_12441
 Fang D. — MS1_12016
 Fayzrakhmanova I.S. — FM21_12278
 Fedenkova A.A. — FM2_10275
 Feissel P. — SM1_12237
 Felderhof B.U. — FM16_11236
 Feng L. — SM24_12287
 Feng X.-Q. — MS3_12314
 Feng X. — MS1_12016
 Fenghuan S. — MS3_12181
 Fenili A. — SM3_13004
 Feraille T. — FM13_12508
 Fernandes A. — SM10_12093
 Fernandez-Feria R. — FM9_11346
 Fernando H.J.S. — FM9_10576
 FM9_12738
 Ferrarese S. — MS6_13017
 Ferreira M.J.F. — FM20_10690
 Ferri F. — FM10_10445
 Feuillebois F. — FM16_10248
 Fey R.H.B. — SM25_11783
 Fidlin A. — SM25_11679
 SM25_12694
 Finn M.D. — FM22_10497
 FM23_11060
 Firsova A.D. — SM25_11712
 Fischer F.D. — SM14_10088
 Flanagan J.D. — FM26_11468
 Fleck N.A. — SM13_12680
 SM5_11022
 Fleck N. — MS2_10988
 Floryan J.M. — FM13_10489
 Flukiger F. — FM12_11343
 Flór J.-B. — MS6_11829
 Fochesato C. — FM26_12089
 Fomin N.A. — FM10_12213
 Fontelos M.A. — FM8_12548
 Fornalik E. — FM7_12173
 Forterre Y. — FM17_11775
 MS2_11581
 Foure T.M. — FM13_10188
 Fourment C. — FM5_13016
 Fowler P.W. — SM1_11482
 Foyssi H. — FM24_11116
 Fraigneau Y. — FM13_10188
 Frana K. — FM19_12587
 Franciosi P. — SM18_11498
- Francius M. — FM26_11417
 Francois M.M. — FM8_12163
 Frankel I. — FM7_12850
 Franklin J. — FM16_11884
 Franz S. — FM24_11256
 Fredriksson P. — SM18_11410
 Freidin A. — SM14_11837
 Freund J.B. — FSM1_10907
 Friedrich R. — FM24_11116
 Frischmuth K. — SM11_11853
 Fröhlich J. — FM6_11348
 Frolova N.Yu. — SM7_12272
 Frost T. — SM22_12297
 Fructus D. — FM26_11417
 Freund E.-T. — FM1_11851
 Fu S. — FM24_12652
 Fu Y. — SM14_11837
 Fuchs P. — SM22_12084
 Fuenmayor J. — SM8_10698
 Fuetterer C. — FM4_11209
 Fujinuma S. — SM18_11295
 Fujita K. — SM17_12582
 Fukumoto Y. — FM25_11615
 SM25_12593
 Fukunishi Y. — FM11_12491
 Funakoshi M. — FM23_12484
 Furutani Y. — SM12_11432
- G**
 Gabrielli P.G. — FSM6_12334
 Gad-el-Hak M. — FM11_10128
 FM2_10948
 Gadaj S.P. — SM14_10046
 SM14_11308
 Galaktionov O.S. — FM1_12063
 Galambos P.C. — FM4_10753
 Galanov B.A. — SM2_11135
 Gallaire F. — FM13_12372
 FM13_12425
 Gallerano F. — FM24_11151
 Galperin B. — MS6_11152
 MS6_11942
 Galtier A. — SM18_12469
 Galvanetto U. — FSM2_11241
 Galvin J.E. — FM17_12073
 Gamallo P. — FSM1_11249
 Gambarotta L. — MS2_13049
 SM4_12298
 Gambaryan-Roisman T. —
 FM14_12293
 Gambin B. — SM13_11895
 SM13_12667
 Gambin W.L. — SM18_11975
 Ganczarski A. — SM4_12335
 Gandzha I.S. — FM26_11591
 MS2_12059
 Ganguly P. — SM1_12458
 Ganqing F. — SM24_12287

- Gao C.-F. — MS1.11857
 Gao H. — **SL5.10772** (p. 131)
 Gao X. — MS1.12027
 Garcia-Sanchez F. — SM9.11321
 Garcia-Villalba M. — FM6.11348
 Gardeniers H. — FM1.12400
 Garikipati K. — FSM6.11476
 Garstecki A. — SM24.12628
 Garstecki P. — MS4.12966
 Gaspar Z. — SM22.10915
 Gautier P.-E. — SM17.11361
 Gavrillov S.N. — SM6.12324
 Gavrillova E. — FSM4.10520
 Galka A.A. — SM13.12732
 Galka A. — SM13.11895
 SM13.12667
 Geers M.G.D. — FSM6.11830
 SM14.11395 SM18.11963
 SM1.12131 SM1.12723
 SM4.11415 SM4.12341
 Geffroy P. — FM11.12244
 Gelder B. van — FSM5.12373
 Gendelman O.V. — SM25.11079
 Geoffroy S. — FM12.11343
 Georgelin M. — FM21.12543
 Gerbeth G. — FM11.12068
 FM13.12542 FM15.12349
 FM19.12613
 Gerkema T. — FM26.12087
 Gerland P. — SM16.12417
 Germay C. — SM25.12535
 Gerstmayr J. — SM17.12029
 Getling A.V. — FM7.10306
 Geubelle P.H. — SM10.11177
 Geurts B.J. — FM6.13030
 Gharib M. — FM1.12784
 Ghicini S. — FM16.11588
 FM16.12345
 Ghrist R.W. — FM23.11677
 Gibson A.N. — FM10.11455
 Giessen E. van der — MS2.10627
 SM1.12737 SM8.11927
 Gilat R. — MS1.12011
 Gilewicz J. — FSM3.11642
 Gill S.P.A. — MS3.12627
 Gilles L. — SM4.12277
 Ginalski M.K. — FM1.12409
 Girgis I.G. — FM13.10487
 Girish J. — SM13.12531
 Giusti A. — FM20.13012
 Gladden L.F. — FM21.11320
 Glema A. — SM5.12949
 Glicksman M.E. — FSM5.11240
 Gloaguen J.M. — SM18.12339
 Glocker C. — FSM2.11183
 Gloria A. — FSM6.12078
 Godard V. — SM4.12913
 Goddard J.D. — FM17.10371
 Godoy-Diana R. — FM25.12108
 Goektepe S. — SM4.12116
 Goetsch M. — FSM1.12586
 Goldhirsch I. — FM17.12308
 Goldobin D.S. — FM13.12280
 Golfer F. — FM12.10234
 Golinval J.-C. — SM17.12208
 Gollub J.P. — FM17.12445
 Goncalves P.B. — SM22.12420
 Goncharova O.N. — MS5.11757
 Gondret P. — FM17.13029
 Gong L. — FSM5.11605
 Gonik M.A. — FM21.11331
 Gontarowskiy P. — SM2.10211
 Gonthier K.A. — SM15.12771
 Gonthier Y. — SM2.12773
 Gonzalez A. — FM4.12437
 Goo B. — SM8.11737
 Gorbatikh L. — SM2.12412
 Goryacheva I. — SM2.11196
 Goto T. — FM1.11441
 Goujon-Durand S. — FM11.12736
 Goulitski K. — FM26.10245
 Gourjii A.A. — FM22.12110
 FM25.12196
 Govindarajan R. — FM2.12631
 Govorukhin V.N. — FM12.10199
 Graf T. — SM15.10792
 Graham A.L. — FM16.11725
 Gramstad O. — FSM4.12956
 Graner F. — FSM5.11095
 Grants I. — FM13.12542
 Gravouil A. — SM1.11797
 Gray G.L. — FSM7.12642
 Grebe R. — SM15.12614
 Green M.L. — SM20.12779
 Green N.G. — FM4.12437
 Grekova E.F. — SM6.12434
 Griffiths R. — MS6.11499
 Griggs A.J. — FM8.12741
 Grimshaw R.H.J. — SM11.11242
 Gristchak V.Z. — SM25.10656
 Grondin F. — SM1.12727
 Grossman-Clarke S. — FM9.12738
 Grue J. — FM26.11417
 FSM4.12956
 Grunefeld G. — FM10.12070
 Gryscha M. — MS6.12035
 Gu Y. — SM24.11532
 Guazzelli E. — FM16.11588
 FM16.11850 FM16.12345
 Guba P. — FM21.11270
 Guddati M.N. — FSM1.11973
 Gudmundson P. — SM18.11410
 Guedes de Carvalho J.R.F. —
 FM20.10690

- Guegan A. — FM11.12305
 Guerses E. — SM1.12115
 Guest S.D. — SM1.11482
 SM22.12669
 Gueydan F. — SM12.12751
 Guinovart-Diaz R. — SM13.11176
 Guitong Y. — MS3.12181
 Gundrum T. — FM19.12613
 Guo J.-G. — SM16.10510
 Guo L. — SM10.11551
 Guo Z. — FSM4.12521
 Gupta N.K. — SM5.12982
 Guse N. — SM17.11223
 Gutfinger C. — FSM1.12516
 Gutkowski W. — SM3.10457
 SM3.10458
 Guz I.A. — SM9.10824
 Guzina B. — SM20.12364
- H**aber R.B. — SM1.12441
 Haberkorn M. — FM24.12740
 Hachemi A. — SM18.12058
 Hackl K. — SM14.12077
 SM24.12074
 Haddad J. — FM4.11648
 Hadjiconstantinou N.G. — MS4.11437
 Hagedorn P. — SM25.11261
 Hahn S. — FM11.11636
 Hajzman M. — SM25.11759
 Halbedel B. — FM19.11906
 Halkjaer S. — SM24.11744
 Halley P. — FSM5.12435
 Hallworth M.A. — FM17.10524
 Hammerton P.W. — FM2.12241
 FSM1.12497
 Hanada S. — SM11.12418
 Hanagud S. — SM10.12968
 Hansen J.S. — SM13.12148
 Hansen L.V. — FSM1.12533
 Hao S. — SM9.10676
 Haque A. — MS3.12705
 Hara T. — FM26.10746
 Harambat F. — FM22.11190
 Harrison P. — SM13.11387
 Hartmann C. — MS2.12031
 FM10.13048
 Hasegawa S. — FM5.11560
 Hata T. — SM11.10344
 Hattori Y. — FM19.11458
 FM25.11615
 Haughton D.M. — SM6.11220
 Hayashi S. — MS1.10821
 Hayes M.A. — FSM3.11818
 SM11.11812
 Haynes P. — MS6.10987 (p. 139)
 Hazel A.L. — FM1.12295
 He J. — FM24.12652
- He Y. — SM27.11506
 Healey J.J. — FM13.12150
 Heijst G.J.F. van — FM22.12110
 FM22.12633 FM25.11964
 FM25.12051
 Heil M. — FM1.11013
 FM1.12295
 Heintz A. — FM6.11763
 Hellmich C. — SM11.12313
 Herakovich C.T. — FSM7.10226
 Herczyński A. — FM2.11984
 FSM4.11986
 Herrada M.A. — FM25.10683
 Herrmann K.P. — SM9.10824
 SM9.12249
 Herskovits J. — SM24.10594
 Herve I. — FM11.12244
 Hickel S. — FM24.11256
 FM24.12564
 Hierck B.P. — FM1.11900
 Higashi A. — SM25.11066
 Hikiyara T. — FSM2.12014
 Hild F. — SM18.12469
 SM4.12021
 Hilgenfeldt S. — FM1.12400
 FSM5.10597 FSM5.12373
 Hinch J. — FM16.11588
 FM16.12345
 Hino R. — SM24.12870
 Ho K.H. — FM21.11208
 Ho Y.G. — SM24.12185
 Hochlenert D. — SM25.11261
 Hodson H.P. — FSM5.12395
 Hogan J.S. — FSM2.10499
 Hohe J. — SM15.11463
 SM9.11484
 Hohler R. — FSM5.12578
 Hojjati H.M. — SM1.11291
 Holeman J.E. — FM9.12738
 Holm D.D. — FM6.13030
 Holnicki-Szulc J. — MS1.13015
 Hołobut P. — SM3.10458
 Holopainen S. — SM24.12200
 Homayoun Heidari A. — FSM1.11973
 Homsy G.M. — MS5.11133
 Hong Y. — SM8.12391
 Hopkins M.M. — FM18.10983
 Horanyi S. — FM19.10931
 Horimoto H. — FSM1.10294
 Hornowski T. — SM15.12567
 Hornych P. — SM18.12634
 Horst E. — SM25.12026
 Hosseini-Godarzi A. — SM9.10646
 Hosseini-Tehrani P. — SM9.10646
 Howle L. — FM12.12617
 Howlin C.P. — FM26.11468
 Hoyer K.W. — FM25.12821

- Hrenya C.M. — FM17_12073
 Hribersek M. — FSM4_10826
 Hu X.X. — SM19_12224
 Hu X. — FM24_11802
 Huang H. — FM26_11126
 FM4_12894
 Huang I.-D. — SM1_11193
 Huang P. — MS4_11604
 Huang R.F. — FM11_11043
 Huang R. — MS3_10699
 Huang X. — FM4_11165
 Huang Y. — MS3_12314
 Huerre P. — FM11_12305
 FM13_12425
 Hufenbach W. — SM13_12576
 Hughes G. — MS6_11499
 Hughes T.J.R. — **SL6_13003** (p. 153)
 Hulbert G.M. — SM11_12772
 Hulin J.-P. — FM20_12092
 Hulsbaek L. — SM22_12297
 Hulsenberg D. — FM19_11906
 Hunt G.W. — SM22_12688
 Hunter J.K. — FM5_11730
 Huppert H.E. — FM17_10524
 FM21_11320 FM21_11328
 FM9_10366
 Hussein M.I. — SM11_12772
 Hutchinson J.W. — MS3_12386
 Hutter K. — FSM6_12040
 Huu Nam T. — SM1_12844
 Hwang I.G. — FM21_13008
 Hwang K.-C. — MS1_12016
 MS3_12314
 Hwang P.A. — FM26_11230
 Hwang W.-S. — SM24_11858
- I**
 Iafrati A. — FM8_12547
 Ignaczak J. — SM13_10347
 Ilison O. — SM11_12568
 Im S.H. — MS3_10699
 Im S. — SM1_11817
 Imai K. — SM15_10790
 SM18_11295
 Imanishi E. — SM17_12537
 Imielowski S. — SM22_12931
 Indinger T. — FM24_12564
 Inoue T. — SM14_10434
 Insperger T. — FSM2_10252
 Ionita A. — SM13_11014
 Iooss G. — FM26_11290
 Ippolito M. — FSM6_12334
 Irannejad R.H. — SM2_10718
 Irgens F. — FM9_12270
 Irschik H. — MS1_10784
 SM17_12029
 Isermann R. — SM16_12758
 Ishihara M. — MS1_11857
- Ishii K. — FM25_12041
 Isoda H. — FM1_12522
 Itihara M. — SM17_12582
 Ivanov A.V. — FM2_10275
 Ivanov I.B. — FM8_11669
 Ivanov M. — FM5_10531
 Ivanov T.P. — SM6_10972
 Iwai K. — FM15_10860
 Iwankiewicz R. — FSM2_12972
 Iwnicki S.D. — SM26_10909
 Izawa S. — FM11_12491
- J**
 Jacqmin D. — FM4_10753
 Jacques N. — SM18_11309
 Jacquin L. — FM11_12244
 Jaeger A. — SM27_11981
 Jakobsen B. — FM23_10247
 Jakubiak B. — FM9_12592
 James C.D. — FM4_10753
 James R.D. — MS1_10722
 Jang G.-W. — SM24_10048
 Jankowski R. — SM25_12659
 Janour Z. — FM9_10467
 Jansen E.L. — SM19_12346
 Jarza A. — FM9_12266
 Jarzębowski A. — SM20_12848
 Jasińska M. — FM22_12415
 Jasiński M. — SM1_11389
 Jasiuk I.M. — SM6_12189
 Jaszczur M. — FM22_12610
 Javaitis I. — MS2_11102
 Jemiolo S. — MS2_12100
 Jenkins A.D. — MS6_12463
 Jensen H.M. — **MS3_11070** (p. 165)
 Jensen J.S. — SM24_12222
 Jensen O.E. — FM14_12155
 Jeon W.-P. — FM11_11636
 Jiang H. — SM24_12789
 Jiang J.-B. — FM24_11488
 Jiang L.J. — FM22_12209
 Jie M. — SM4_10961
 Jinnouchi Y. — SM7_10691
 Joensson P.-A. — SM26_11795
 John A. — SM1_12562
 Johnson M.E. — FSM1_12497
 Jolivet L. — SM12_12751
 Joly P. — SM2_12382
 Jones A.S. — MS1_13011
 MS1_13010
 Jones N. — SM5_11107
 Jones R.B. — FM18_10565
 Jones W.P. — FM3_11914
 Jop P. — FM17_11775
 Jordan P. — FM5_13016
 Joseph D.D. — FM20_10843
 Joseph P. — MS4_12673
 Jossierand C. — FM8_11614

- Joubert P. — *FM7_12220*
 Jullien C. — *MS4_12536*
 Jun S. — *SM1_11817*
 Jung J.-Y. — *MS1_10985*
 Jung S. — *SL18_10495*
 Juric D. — *FM8_11979*
- K**abouya N. — *FM13_12766*
 Kachanov Y.S. — *FM24_12675*
 FM2_10275
 Kaczmarek M. — *SM15_12566*
 SM15_12567 *SM15_12577*
 Kaczyński A. — *SM9_11980*
 Kagemoto H. — *FSM4_11758*
 Kaiser I. — *SM25_12322*
 Kaliszky S. — *SM24_12573*
 Kalliadasis S. — *FM14_10220*
 Kallivokas L.F. — *FSM1_12691*
 FSM1_12717
 Kaltayev A. — *FM3_11031*
 Kam Liu W. — *SM1_12167*
 Kambe T. — *FM23_11166*
 Kameyama T. — *FM15_10860*
 Kan K. — *FM14_11739*
 Kanarska Y. — *MS6_12408*
 Kanaun S.K. — *SM11_11989*
 Kaneda M. — *FM7_13022*
 Kaneko Y. — *FM17_11876*
 Kang L.-C. — *SM1_10270*
 Kanno Y. — *SM2_12646*
 Kapania R.K. — *FSM7_12752*
 Kaplański F.B. — *FM25_12032*
 Kappl K. — *SM27_11981*
 Karagiozova D. — *SM5_11107*
 Karaiwa M. — *SM13_11426*
 SM9_11425
 Karajan N. — *SM15_11194*
 Karakasidis T.E. — *FSM2_12482*
 Karapetsas G. — *FM18_12859*
 Karas M.S. — *SM1_12340*
 Karcher C. — *FM19_12290*
 Karihaloo B.L. — *FSM6_11806*
 Karpenko E.E. — *SM25_10470*
 Karpov E.G. — *SM1_12167*
 Kashtalyan M. — *SM9_10824*
 Kasperski G. — *FM15_12636*
 Kataoka T. — *FM26_11746*
 Katsuyama T. — *FSM2_11535*
 Kawamoto A. — *SM24_12302*
 Kawazoe H. — *FM23_12484*
 Kazakevitch M.I. — *SM25_12632*
 Kazemzadeh-Parsi M.J. — *FM9_10733*
 Kaźmierczak B. — *MS2_10838*
 Ke F. — *SM7_11764*
 Keane R.J. — *FM22_12545*
 Keer L.M. — *SM2_11215*
 Kent E.F. — *FM18_11915*
- Keppens R. — *FM19_11429*
 Kere P. — *SM13_10667*
 Kerr R.M. — *FM24_12430*
 Kerschen E.J. — *FSM1_12477*
 Keunings R. — *SL7_10512*
 Khabakhpasheva T.I. — *FSM4_10911*
 Kharif C. — *FM26_11417*
 Khasanov M.M. — *FM12_10548*
 Khelidj A. — *SM4_12749*
 Kheradvar A. — *FM1_12784*
 Khoei R.A. — *SM2_10718*
 Khom'yak T.V. — *SM17_10779*
 Khoo B.C. — *FM24_11802*
 Khoshravan M.R. — *SM13_10189*
 Khotyanovsky D.V. — *FM6_11485*
 Khotyanovsky D. — *FM5_10531*
 Khusid B. — *FM16_10361*
 FM4_10753
 Khusnutdinova K.R. — *SM11_11242*
 Kiger K.T. — *FM1_11900*
 Kim B.-K. — *SM27_11827*
 Kim J.-H. — *MS1_10985*
 Kim J. — *FM11_11636*
 FM11_12013 *FM19_11637*
 Kim K.-S. — *MS3_12778*
 SM8_12034
 Kim Y.-M. — *FM1_12655*
 Kim Y.Y. — *FSM7_12752*
 SM24_10048
 Kimura Y. — *FM23_11660*
 Kinell M. — *FM5_10789*
 King G.P. — *FM22_12545*
 King J.R. — *FM14_12155*
 King M.P. — *FM7_10438*
 King R. — *FM11_12624*
 Kireenkov A.A. — *SM2_11778*
 Kishino Y. — *SM20_12462*
 Kit E. — *FM26_10245*
 Kitagawa H. — *MS3_11122*
 Kityk A. — *FM8_11462*
 Kiyono K. — *FSM2_11535*
 Klapp J. — *FM6_10857*
 Klarbring A. — *MS2_10670*
 SM2_10686
 Kleeorin N. — *FM10_12070*
 FM7_11053
 Klepaczko J.R. — *SM11_11360*
 SM14_10046 *SM18_10734*
 Klingbeil D. — *SM4_10865*
 Kloker M.J. — *FM13_12381*
 Kluwick A. — *FM2_11083*
 FM2_11084 *FM5_10789*
 Knap J. — *SM1_11154*
 SM9_12171
 Knight D. — *FM5_11560*
 Kobayashi S. — *FM5_11864*
 Kobiera A. — *FM3_12843*

- Kocańda D. — SM8.12914
 Kocourek V. — FM19.12290
 Koenderinck G.H. — MS2.10709 (p. 355)
 Koikari S. — FM23.11660
 Kolandavel M.K. — FM1.11851
 Kolcavova Sirkova B. — FSM3.11247
 Kolesnikov Y. — FM19.11120
 FM19.12090
 Kolk K. — SM9.12044
 Kolmychov V.V. — FM15.11893
 Komarova V.Y. — FM2.10275
 Kondic L. — FM17.12399
 Kondo D. — SM15.11941
 Kondrachuk A.V. — MS2.12059
 Konieczny P. — FM11.12602
 Kononov Y.N. — SM17.10779
 Kopiev V.F. — FM11.12156
 Koplík J. — FM16.10361
 Korczyk P.M. — FM10.12855
 Korepanov V.V. — SM6.12289
 Kornev K.G. — FM4.10140
 Korvink J.G. — SM24.11316
 Koseki T. — SM17.12582
 Kosiński W. — SM11.11853
 Kositsyn A. — FSM7.11724
 Kothe D.B. — FM8.12163
 Kotucha G. — SM24.12074
 Koudella C. — MS6.12601
 Koumoutsakos P. — FM24.11256
 FM6.12583
 Kouznetsova V. — FSM6.11830
 SM14.11395
 Kovacs F. — SM1.11482
 Kovaleva A. — SM3.11265
 Kovaleva L. — FM12.12528
 Kowalczyk P. — SM24.12679
 Kowalczyk P. — FSM2.11363
 Kowalczyk P.G. — FM6.11763
 Kowalczyk-Gajewska K. — MS2.11808
 SM6.10442
 Kowalewski T.A. — FM10.12855
 FM14.11477 FM21.11331
 FM4.11184 FM7.11160
 FM7.12173 FM8.12873
 FM9.10576
 Kowalewski Z.L. — SM27.11957
 Kowalski S.J. — SM15.13006
 Kozien M.S. — SM25.12511
 Kozlov A.A. — FM7.12267
 Kozlov V.V. — FM2.11339
 Krasnikovs A. — SM23.10242
 Krasnopolskaya T.S. — FM22.12257
 Krasovskyy V.L. — SM19.11815
 Krauklis A.V. — FM10.12213
 Krause E. — FM25.12690
 Kravtsova M.A. — FM2.11780
 Krawczyk J. — FM9.12592
 Kraynik A.M. — FSM5.10597
 Krein A. — FM10.12070
 Kreuzer E.J. — SL8.10544 (p. 173)
 FSM4.11912
 Krieger U. — FM19.11906
 Kristiansen O. — FM26.11417
 Krivtsov A.M. — SM11.12481
 Kroeger M. — SM2.12086
 Kruszka L. — SM20.10374
 Kruyt N.P. — SM20.10866
 Kruzelecki J. — SM24.11634
 Kubacki S. — FM6.12076
 Kubair D.V. — SM10.11177
 Kubik J. — SM15.12566
 SM15.12577
 Kucaba-Piętal A. — MS4.10971
 Kuczma M.S. — MS1.10136
 Kudela H. — FM25.12836
 Kudryavtsev A.N. — FM6.11485
 Kudryavtsev A. — FM5.10531
 Kuhl A. — FM3.12745
 Kuhl E. — SM12.11277
 SM1.11211 SM1.12924
 Kuhn G. — SM9.12044
 Kuilekov M. — FM19.12605
 Kuistiala A. — SM4.10960
 Kujawski D. — SM9.10334
 Kulesh M.A. — SM6.12289
 Kullander F. — FSM1.12533
 Kulvietis G. — SM16.10900
 Kumagai T. — FM8.11299
 Kumar A. — FM4.10753
 Kuna M. — SM9.11045
 Kuna-Ciskał H. — SM4.11796
 Kurashige M. — SM15.10790
 SM18.11295
 Kurkin A.A. — FM9.11433
 Kurnik W. — SM22.12931
 SM22.12934
 Kuroda M. — FM11.12491
 Kurowski M. — FM25.12275
 Kurowski P. — SM7.12799
 Kurpa L.V. — SM19.12350
 Kursa M. — SM24.11760
 Kurzydłowski K.J. — SM7.12666
 Kurzyna J. — FSM2.12927
 Kus W. — SM24.11137
 Kwon Y.-I. — FM15.10363
 Kyriakides S. — FSM5.11605
 SM22.11600
- Llorca J. — SM13.11080
 Labiausse V. — FSM5.12578
 Labuz J.F. — SM20.11845
 Lac E. — MS2.11961
 Lacaze L. — FM13.11396
 Lackner R. — SM27.11981

- Lacor C. — *FM3_11888*
 Ladd A.J.C. — *FM16_11418*
 Ladd T. — *FM12_11994*
 Ladevéze P.J. — **SL9_10508** (p. 187)
SM1_11769 SM25_11246
 Lagha M. — *FM13_11647*
 Lamanna G. — *FM10_10445*
 Lambros J. — *SM10_11177*
 Lampis M. — *MS4_10723*
 Landa M. — *MS1_12637*
 Lane-Serff G.F. — *FM9_11182*
 Lange C. — *SM2_12773*
 Lange U. — *FM8_12388*
 Langevin D. — *FSM5_12212*
 Langkamp A. — *SM13_12576*
 Langre E. de — *FSM4_11801*
 Lanos C. — *SM4_10011*
 Larecki W. — *FSM6_11237*
 Larsson R. — *SM15_12518*
 Larue de Tournemine A. —
FM20_12383
 Lathrop D.P. — *FM19_11681*
 Lauga E. — *FM8_11330*
 Lavinskaya E.I. — *FM10_12213*
 Lavrenteva O.M. — *FM8_11250*
 Le Bars M. — *FM7_12126*
 Le Bris C. — *FSM6_12078*
FSM6_12336
 Le Dizes S. — *FM13_11396*
FM13_12509
 Le Gal P. — *FM13_11396*
FM24_10506
 Le Grogne P. — *SM22_11962*
 Le Quere P. — *FM7_12220*
FM8_11979
 Le van A. — *SM22_11962*
 Leal G.L. — *FM8_11289*
 Lebensohn R.A. — *SM18_11005*
 Leblanc S. — *FM13_10525*
 Leblond J.-B. — *SM4_12913*
SM9_12393
 Lecomte-Beckers J. — *SM1_11298*
 Lee C. — *FM6_11569*
 Lee D.-H. — *SM24_11858*
 Lee D. — *FM11_11636*
 Lee H.T. — *FSM5_12851*
 Lee J.-W. — *FM6_11569*
 Lee J. — *FM16_11418*
 Lee S.-J. — *FM1_12655*
 Lee S.M. — *FM9_12738*
 Lee W.-S. — *SM27_11827*
 Lefik M. — *SM13_12970*
 Legarth B.N. — *SM13_11794*
 Legendre D. — *FM8_11911*
 Legoll F. — *FSM6_12336*
 Leine R.I. — *FSM2_11183*
 Leiner W. — *FM7_12173*
 Lekszycki T. — *MS2_12315*
 Lele S.K. — *FSM1_11561*
 Lemak M. — *SM17_11375*
 Lenci S. — *FSM2_12129*
 Lengyel A. — *SM1_12101*
 Lenormand R. — *FM12_10234*
 Lentzen S. — *MS1_11752*
 Leonard A. — *FM6_11937*
 Leonardi E. — *FM14_11477*
FM15_11386
 Leong S.S. — *FM14_11477*
 Leorat J. — *FM19_11621*
 Lerbet J. — *SM17_11674*
 Leroy Y.M. — *SM12_12751*
 Lesieur M. — **SL10_10731** (p. 203)
 Letser Y.A. — *SM2_11933*
 Leung R.C.K. — *FM6_10163*
 Leungvichcharoen S. — *SM11_12514*
 Levin V.M. — *SM11_11989*
 Levitas V.I. — *SM14_11325*
 Levitsky S.P. — *FM4_11648*
 Levy Y. — *FM3_12199*
FM3_12348
 Lewandowski J. — *FSM1_12555*
 Lewiński T. — *SM24_10052*
SM24_11760
 Lewis D.M. — *FM1_11908*
 Lewis S.R. — *MS6_12494*
 LExcellent C. — *SM14_12225*
 Li H. — *SM9_10676*
 Li J. — *FM2_10103*
FSM7_12752 SM25_10166
SM4_12036
 Li K. — *SM7_10492*
 Li Q. — *SM9_11934*
 Li X.M. — *FM6_10163*
 Li Y. — *MS6_12194*
 Liakopoulos A.B. — *FSM2_12482*
 Liang B. — *SM26_10909*
 Liao X. — *FM7_12168*
MS6_12169
 Libersky L.D. — *SM1_10829*
 Liechti K.M. — **MS3_12132** (p. 217)
 Lijuan L. — *SM24_12287*
 Lik Chan C. — *FM21_11058*
 Lim C.W. — *SM19_12224*
 Lim J. — *FM11_12013*
 Lim K.-M. — *SM1_12901*
 Lim K.-W. — *FSM1_11973*
 Lima R. — *FM8_11026*
 Lin C.Y. — *SM25_11867*
 Lin J. — *SM11_11099*
 Lin Y. — *SM1_10559*
 Linden P.F. — *MS6_10261*
 Lindner M. — *SM2_12086*
 Ling Z. — *SM13_12242*
 Lipniacki T. — *FM24_11161*

- Lippermann F. — FSM5.13033
 Lipson S. — FM16.11884
 Lisitsin Y.V. — SM2.10342
 Lisowski W. — SM7.12799
 Lister J. — FM8.12388
 Litewka A. — SM4.11228
 Liu J.T.C. — FM13.10487
 Liu T. — SM24.11532
 Liu X. — SM6.11998
 Liu Y.-C. — FM3.10367
 Liu Y.-L. — FM24.11488
 Liu Y. — SM18.11005
 Lo Jacono D. — FM22.12731
 FM3.10918
 Loboda V.V. — SM9.12249
 Lobov N.I. — FM7.12344
 Loefeldahl L. — FM2.11339
 Loehnert S. — SM1.12534
 SM1.12584
 Lofdahl L. — FM10.11455
 Loginov M.S. — FM24.10455
 Loglisci N. — MS6.13017
 Logo J. — SM24.11623
 SM24.12573
 Logvinova K. — FM12.12376
 Lohse D. — FM10.11909
 FM17.10253 FM1.12400
 Loimer T. — FM12.11487
 Lomunov A.K. — SM20.10374
 Long A.C. — SM13.11387
 Long S.G. — SM13.12496
 Longere P. — SM18.11110
 Longhetto A. — MS6.13017
 Longmao Z. — MS3.12181
 Lopes S.R.X. — SM22.12420
 Lopez-Lopez E. — SM13.11176
 Louge M.Y. — MS5.10714 (p. 229)
 Love B.M. — SM10.12594
 Lozia Z. — SM26.11832
 Lu J.-Z. — FSM4.11668
 Lu K. — FM4.11165
 Lu T.J. — FSM1.12527
 FSM5.12395
 Lu W. — SM12.11432
 Lu X. — SM10.12968
 Lube G. — FM17.10524
 Lubowiecka I. — SM19.11890
 Lucey A.D. — FSM4.11736
 Luczak M. — SM25.11273
 Luding S. — SM17.12133
 Lukes V. — SM10.11671
 Lukomsky V.P. — FM26.11591
 MS2.12059
 Lund E. — SM24.12098
 SM24.12916
 Lund F. — FSM1.12643
 Lundberg B. — SM7.12551
 Lusseyran F. — FM13.10188
 Lvov G.I. — SM19.10071
 Lyakh V.V. — SM6.12575
 Lyly M. — SM13.10667
 Lysenko V.V. — SM25.10656
 Lyubimov D.V. — FM13.12280
 FM7.12344 MS5.12402
 Lyubimova T.P. — FM21.12278
 FM7.12344 MS5.12402
 Łobocki L. — FM9.12592
 Lodygowski T. — SM5.12949
 Łukasiewicz S.A. — SM1.11291
 Ma J. — SM8.11686
 Ma L. — SM10.11551
 Mac Sithigh G. — SM6.12354
 MacKintosh F.C. — MS2.10709 (p. 355)
 MacMartin D.G. — FM11.12387
 Maciejewski J. — SM20.12848
 Mader M. — FM1.10741
 Maderich V.S. — FM26.12268
 Maderich V. — MS6.12408
 Maeda T. — SM11.10422
 SM25.12593
 Magara Y. — SM9.11425
 Magariyama Y. — FM1.11441
 Magatti D. — FM10.10445
 Magnaudet J. — FM20.12139
 FM8.11911
 Mahadevan L. — MS2.11581
 Maier G. — SM18.10797
 Mailybaev A.A. — SM25.11536
 Maj M. — SM18.11185
 Majewski J. — FM6.12618
 Majewski T. — SM25.12984
 Majkut M.M. — FM10.11916
 Majorkowska-Knap K. — SM8.11371
 Makhovskaya Y. — SM2.11196
 Makin V.K. — FM26.11230
 Makinde O.D. — FM3.10747
 Makipelto J. — SM1.12310
 Makowski K. — FM19.12363
 Malinowski S.P. — FM10.12855
 Malinowski S. — FM9.12592
 Maliwan K. — MS5.10980
 Malki-Epshtein L. — FM9.10366
 Maluleke G.H.-S. — SM6.12039
 Mamaev I.S. — SM1.12351
 Mandal P. — SM19.10233
 Mandelis A. — FM10.12719
 Manela A. — FM7.12850
 Mang H.A. — SM11.12313
 SM19.11021
 Manneville P. — FM13.11647
 Mansukh M. — MS1.12786
 Mansur S.S. — FM6.11456

- Manucharyan G.V. — SM25_12989
 Marah D. — *MS6_10261*
 Marchioli C. — *FM20_13012*
 Margulies S.S. — *MS2_10933*
 Marian J. — *SM1_11154*
 Marie Habraken A. — *SM1_11298*
 Marinho W. — *FM6_11456*
 Marinova D. — *SM3_11036*
 Markert B. — *SM15_11194*
 Markine V.L. — *SM24_11015*
 Marmottant P. — *FM1_12400*
 Marquillie M. — *FM13_12372*
 Marsavina L. — *SM9_10864*
 Marsik F. — *FM11_12258*
 FM2_12062 MS1_12637
 Martinand D. — *FM13_11186*
 Martins J.A.C. — *SM12_12682*
 SM2_12646
 Maruschak P.O. — *SM8_11920*
 Marvalova B. — *SM1_12844*
 Marze S. — *FSM5_12212*
 Maslov B.P. — *SM27_10018*
 Mason D.P. — *SM6_12039*
 Masri R. — *SM5_12043*
 Masri S.F. — *MS1_13007*
 Massabo R. — *SM13_11162*
 Massart T.J. — *SM4_12341*
 Masuda M. — *FSM1_10294*
 Matalon M. — *FM3_10918*
 Matas J.P. — *FM16_11850*
 Matioukevitch S.I. — *SM9_10897*
 Matsuda H. — *SM19_12224*
 Matsui R. — *MS1_10821*
 Matsumoto Y. — *MS2_12192*
 Mattioni A. — *FSM6_12334*
 Matveyenko V.P. — *SM6_12289*
 Matvienko A. — *FM10_12719*
 Matysiak S.J. — *SM9_11980*
 Matyukhin Y. — *SM2_10211*
 Maugin G.A. — *FSM3_11347*
 SM10_11592 SM14_11393
 SM6_12434
 Maurel A. — *FM24_11303*
 FSM1_12643
 Maurine P. — *SM16_10553*
 Mavletov M. — *FM12_12528*
 Maxworthy T. — *FM13_11995*
 Maździarz M. — *MS2_11808*
 SM20_11584
 Mazeika D. — *SM16_10900*
 Mazhorova O.S. — *FM15_11893*
 Mazza E. — *MS2_12064*
 Mazzilli C.E.N. — *SM25_11494*
 McElwaine J.N. — *FM9_12396*
 McFarland M.D. — *SM25_10408*
 McGlashan S. — *FSM5_12435*
- McIntyre M.E. — *MS6_10977*
 MS6_12157
 McPhee J. — *SM2_12773*
 McPhie M.G. — *FM16_11431*
 Mebarki A. — *SM2_12082*
 Medeiros M.A.F. — *FM13_12381*
 Medyanik S.N. — *SM1_12167*
 Meer D. van der — *FM10_11909*
 FM17_10253
 Meftah F. — *SM2_12082*
 Meftah S. — *SM14_12747*
 Megaridis C.M. — *FM4_11603*
 Mehandia V. — *FM16_10603*
 Mehshikov Y.L. — *SM25_11716*
 Meiburg E. — *FM13_11995*
 FM13_12425
 Meijaard J.P. — *SM25_11338*
 Meinhart C. — *FM22_12761*
 Meironke H. — *FM7_11905*
 Mejak G. — *SM1_11334*
 Meleshko V.V. — *FM22_12110*
 FM22_12257 FM22_12633
 FM23_12868 FM25_12196
 Melnik O.E. — *FM9_11703*
 Melo J. — *FM3_12348*
 Melville W.K. — *MS6_12722*
 Men S. — *FM19_12605*
 Mendez C. — *FM8_11670*
 Mendonca M.T. — *FM13_12381*
 Mendoza G. — *FM6_10857*
 Mendrok K. — *SM7_12799*
 Menetrier L. — *MS4_12047*
 Menon N. — *FM5_11072*
 Menshykov O.V. — *SM9_11195*
 Menzel A. — *FSM3_12392*
 Mercier J.F. — *FSM1_12643*
 Mercier S. — *SM18_11309*
 Mergheim J. — *SM1_11211*
 Merodio J. — *SM12_11705*
 Mestel J.A. — *FM19_12979*
 Meunier P. — *FM22_10532*
 Meysman F.J.R. — *FM1_12063*
 Mezic I. — *FM22_12439*
 FM22_12761 FSM2_12468
 Mezyk A. — *SM25_12770*
 Micciche P. — *FM10_10445*
 Michaltsos G.T. — *SM22_11172*
 Michałek T. — *FM7_11160*
 Michałowski R.L. — *FM17_12790*
 Michel U. — *FM21_12365*
 Micunovic M. — *SM18_10383*
 Middelburg J.J. — *FM1_12063*
 Mieke C. — *FSM6_12112*
 FSM6_12113 FSM6_12118
 SM1_12115 SM4_12116
 Miettinen A. — *SM2_10459*
 Mikhailchenko G. — *SM26_11589*

- Mikhayalov D.N. — *FM12.11115*
 Mikkelsen R. — *FM17.10253*
 Millet C. — *FM13.12509*
 Miloh T. — *FM20.12342*
 Min B.-Y. — *FM6.11569*
 Minc N. — *FM4.11209*
 Minier J.-P. — *FM24.10564*
 Miozzi M. — *FM7.11673*
 Miskiewicz M.A. — *SM7.12666*
 Mitsuhoji T. — *FM13.12291*
 Miura K. — *SM17.12464*
 Miyamoto H. — *FM9.11164*
 Miyazaki T. — *FM24.10937*
 MS6.12194
 Mizerski K.A. — *FM19.12107*
 Mizuguchi F. — *SM25.11066*
 Mizuno M. — *SM18.11350*
 Moctezuma M. — *FM8.11026*
 Modarres-Sadeghi Y. — *FSM4.11078*
 Moe A. — *FM9.12270*
 Moes N. — *SM1.12359*
 Moffatt H.K. — *FM18.12164*
 FM19.11458 *FSM7.10016*
 Moffatt K. — *FSM6.11862*
 Mohan J.A. — *FM5.11072*
 Moisy F. — *FM24.11814*
 Mojtabi A. — *MS5.10980*
 Mokos V.G. — *SM1.10665*
 Molenaar D. — *FM25.11964*
 Molinari A. — *SM14.11852*
 SM18.11309
 Moller H.T. — *SM24.12916*
 Mondy L.A. — *FM18.10983*
 Monetto I. — *SM4.12298*
 Moniuk W. — *FM8.12311*
 Monkewitz P.A. — *FM13.11186*
 FM24.11454 *FM3.10918*
 Monkewitz P. — *FM24.12965*
 Moo Koh H. — *SM8.12034*
 Morch K.A. — *FM8.11999*
 Moreau J.-J. — *SM17.11361*
 Moreau R. — *FM15.10860*
 Morel A. — *MS2.11961*
 Moreno M.J. — *FM20.11189*
 Morgan H. — *FM4.12437*
 Morita C. — *SM19.12224*
 Morize C. — *FM24.11814*
 Morland L.W. — *FM18.10297*
 Moroni M. — *FM7.11673*
 Morozov N.F. — *SM9.10897*
 Morris J.F. — *FM16.11850*
 Morro A. — *SM11.11596*
 Morzyński M. — *FM11.12624*
 FM11.12736 *FM24.11454*
 SM24.12413
 Mouaze D. — *FSM4.12557*
 Moulia B. — *FSM4.11801*
 Moulin F. — *MS6.11829*
 Mounajed G. — *SM1.12727*
 Mousavi S. — *SM7.12551*
 Movchan A.B. — *FSM1.11896*
 Movchan N.V. — *FSM1.11896*
 Mróz Z. — *SM18.10064*
 SM24.11349 *SM2.11074*
 Muc A. — *MS3.12251*
 SM13.11457 *SM13.12560*
 Mueller A. — *SM9.11484*
 Mueller U. — *FM19.10931*
 Mullarney J. — *MS6.11499*
 Muller-Slany H.H. — *SM1.10423*
 Murai M. — *FSM4.11758*
 Musalimov V.M. — *SM2.10342*
 Muth B. — *SM17.12133*
 Mutschke G. — *FM11.12068*
 Myagkov N.N. — *SM11.10426*
 Na S.-W. — *FSM1.12691*
 FSM1.12717
 Nägele G. — *FM16.11431*
 FM18.11300
 Nagata M. — *FM13.12291*
 Nagib H. — *FM24.12965*
 Nagy P. — *MS5.12651*
 Nait Abdelaziz M. — *SM18.12339*
 Nakamura M. — *FM1.12522*
 Nakano H. — *MS6.11152*
 Nakas A.A. — *SM25.11082*
 Nakata K. — *FM1.11441*
 Nakatani A. — *MS3.11122*
 Nalepka K. — *MS3.11444*
 Nalepka P. — *MS3.11444*
 Narayanan S. — *MS1.12147*
 Narita F. — *SM13.11426*
 SM13.11610 *SM9.11425*
 Naumavicius R. — *SM16.12546*
 Naumenko K. — *SM27.11368*
 Nava A. — *MS2.12064*
 Navarro C. — *SM8.10698*
 Nayak H.V. — *FM16.11991*
 Nazarenko L. — *SM13.10555*
 Needleman A. — *SM1.12737*
 SM2.11987 *SM9.10910*
 Neel M.-C. — *FM12.12376*
 Neethling S.J. — *FSM5.12851*
 Neimark A.V. — *FM4.10140*
 Neishtadt A. — *FM22.12439*
 SL11.10551 (p. 241)
 Neitzel G.P. — *MS5.12651*
 Nepomnyashchy A.A. — *FM14.10543*
 Nerinckx K. — *FM6.11602*
 Nesteruk I. — *FM2.11017*
 Netto T.A. — *SM22.11600*
 Newsom R.K. — *MS6.10513*
 Ngan A.H.W. — *FSM5.11663*

- Nguyen A.V. — *FM15_11903*
 Nguyen Q.P. — *FSM5_12986*
 Nicolas A. — *MS2_12811* (p. 329)
 Nicolas M. — *FM16_11749*
 FM17_11751
 Nicolleau F. — *FM22_10130*
 Nigmatulin R.I. — *FM8_12190*
 Nihei T. — *FM25_12041*
 Nijmeijer H. — *SM25_11783*
 Nikifirov S. — *FM5_10531*
 Nikiforovich E.I. — *FM25_12196*
 Nikitin N.V. — *FM15_11929*
 Nikitin S.A. — *FM15_11929*
 FSM7_11869
 Nikolaevskiy V.N. — *FM12_11109*
 Nikrityuk P.A. — *FM21_12365*
 Niordson C.F. — *SM18_11790*
 Nir A. — *FM8_11250*
 Nishimura J. — *SM3_10879*
 Nishimura M. — *FM1_11441*
 Nishimura T. — *SM10_12461*
 SM17_12464
 Niss K. — *FM23_10247*
 Niziol J. — *SM25_12511*
 Noack B.R. — *FM11_12624*
 FM11_12736 *FM24_11454*
 Noda N. — *MS1_11857*
 Nogarede B. — *FM11_12602*
 Noguchi H. — *SM1_12177*
 SM22_10692
 Nohguchi Y. — *FSM7_12488*
 Nore C. — *FM13_10640*
 Norman J.T. — *FM16_11991*
 Norris A.N. — *SM25_12404*
 Noskowicz S.H. — *FM17_12308*
 Nott P.R. — *FM16_10603*
 Nouar C. — *FM13_12766*
 Nouy A. — *SM1_11769*
 Novak V. — *MS1_12637*
 Novosiadlii V.A. — *FM7_13005*
 Nowacki W.K. — *SM14_10046*
 SM14_11308
 Nowak A.J. — *FM1_12409*
 Nowak M. — *SM24_12413*
 Nowak Z. — *SM19_12328*
 SM4_12333
 Nycander J. — *MS6_12210*
- O**berste-Brandenburg C. —
 SM14_12121
 Obrecht H. — *SM22_12084*
 Oertel H. Jr. — *FM5_11864*
 Ogasawara N. — *SM18_10652*
 Ogdan R.W. — *FSM3_11227*
 SM12_11705 **SL12_10143** (p. 263)
 Ohkitani K. — *FM23_10938*
 Ohl C.-D. — *FM8_11999*
- Ohno N. — *SM1_12177*
 SM22_10692
 Okada M. — *SM17_11700*
 Okandan M. — *FM4_10753*
 Okkels F. — *MS4_12047*
 MS4_12130 *MS4_12536*
 Okulov V.L. — *FM13_13019*
 Okumura D. — *SM1_12177*
 SM22_10692
 Olascoaga M.J. — *MS6_12776*
 Olhoff N. — *SM24_10433*
 Oliferuk W. — *SM18_11185*
 Olshevsky A.A. — *SM2_12559*
 SM2_12559
 Olsson T. — *MS2_10670*
 Omang M. — *FM19_11809*
 Onck P. — *MS2_10627*
 Ong R. — *MS1_11685*
 Ootao Y. — *SM10_12465*
 Orantek P. — *SM1_12562*
 Orlov S.V. — *SM2_10342*
 Oron A. — *FM14_10543*
 Ortiz M. — *FSM6_11471*
 SM1_11154 *SM9_12171*
 Osipov M.N. — *SM7_11556*
 Osipov V. — *FSM1_11508*
 Osiptsov A.A. — *FM9_11703*
 Ospennikov N.A. — *FM7_12344*
 Ostachowicz W.M. —
 MS1_10680 (p. 275)
 Ostoja-Starzewski M. — *SM11_11682*
 Ostrowska-Maciejewska J. —
 SM6_10442
 Ostrowski Z. — *SM24_11137*
 Otheguy P. — *MS6_12294*
 Ottino J.M. — *FM22_11293*
 Ovsyannikov S.V. — *SM7_12272*
 Ozawa H. — *MS6_11732*
 Ozoe H. — *FM7_12173*
 FM7_13022
- P**agneux V. — *FM24_12740*
 Paidoussis M.P. — *FSM4_11078*
 Pakiela Z. — *SM7_12666*
 Pakleza J. — *FM8_12873*
 Pakula M. — *SM15_12566*
 SM15_12577
 Palaniappan D. — *FM18_12981*
 Pamplona D.C. — *SM22_12420*
 Pandolfi A. — *SM9_12171*
 Pantelyat M. — *SM2_10211*
 Papageorgiou D. — *FM26_12715*
 Papas P. — *FM24_11454*
 FM3_10918
 Papoulia K. — *SM1_12458*
 Parau E. — *FM26_11345*
 Park J. — *FM19_11637*

- Park N. — *FM17_12790*
 Park S.-J. — *SM17_10893*
 Parland H. — *SM2_10459*
 Parnes R. — *MS3_12432*
 Parra M.T. — *FM8_11670*
 Parsons A.T. — *FM2_12320*
 Pasero E. — *FM24_11151*
 Pasol L. — *FM16_10248*
 Pasqualino I.P. — *SM1_12607*
 Passarel W. — *SM24_10594*
 Pastoor M. — *FM11_12624*
 Patterson M.D. — *FM25_12051*
 FM9_12396
 Paulino G.H. — *SM10_12665*
 Paulino G. — *SM10_10135*
 Pavlidis M. — *FM18_12859*
 Pavlovskaja E.E. — *FSM2_11302*
 SM11_12481
 Pavlovskaja E. — *SM25_10470*
 Pawłowski P. — *MS1_13015*
 Payne D.A. — *MS1_11685*
 Páczelt I. — *SM2_11074*
 Peacock T. — *FM26_11199*
 Pecquet E. — *SM1_11298*
 Pedersen E.M. — *FM1_11851*
 Pedersen N.L. — *SM24_10669*
 SM24_11936
 Pedersen P. — *SM24_10669*
 Pedersen S.L. — *SM17_12569*
 Peerlings R.H.J. — *SM4_11415*
 SM4_12341
 Pegushin A.G. — *SM11_12203*
 Pellegrino S. — *SM22_11097*
 Peradźyński Z. — *FM19_12363*
 FSM2_12927 *MS4_10971*
 Perelmuter M.N. — *MS3_11599*
 Perov V. — *MS6_11942*
 Perrin B. — *FM17_13029*
 FM20_12092
 Perzyna P. — *SM5_12949*
 Petermann M. — *FM22_12610*
 Petersen R. — *FM23_10247*
 Petit S. — *SM13_11180*
 Petrova V.E. — *SM9_10579*
 Petryk H. — *SM12_10996*
 Pettermann H.E. — *SM13_12321*
 Pęcherski R.B. — *MS3_11444*
 SM18_10064
 Pfeiffer F.G. — *SM16_10809*
 Phedina M.E. — *SM4_11779*
 Philippidis T. — *SM13_12818*
 Phillips O.M. — *FM9_10366*
 Phillips W.R.C. — *FM26_11179*
 Photiadis D.M. — *SM25_12404*
 Picandet V. — *SM4_12749*
 Picciotto M. — *FM20_13012*
 Pichler B. — *SM11_12313*
 Pichler U. — *MS1_10784*
 Piechór K. — *MS2_10838*
 Pieczyska E.A. — *SM14_11308*
 Piedboeuf J.-C. — *SM2_12773*
 Piekarski J. — *MS2_11808*
 Pienkowska I.T. — *FM18_11922*
 Pierard O. — *SM4_11886*
 SM18_13038
 Pierre L. — *SM4_12277*
 Pietraszkiewicz W. — *SM19_10287*
 Piironen P. — *FSM2_11363*
 Pijaudier-Cabot G. — *SM4_12749*
 Pilgun G.V. — *SM19_12350*
 Pinto da Costa A. — *SM12_12682*
 SM2_12646
 Piotrowski Z. — *FM9_12592*
 Pivovarov M. — *SM25_11699*
 Placidi L. — *FSM6_12040*
 Plamenevskii B.A. — *SM9_10897*
 Plotnikov P. — *FM26_11290*
 Plouraboué F. — *FM12_11343*
 Plourabou F. — *FM22_12731*
 Plunian F. — *FM19_12120*
 Pocheau A. — *FM21_12543*
 FM22_11190
 Pocwierz M. — *FM6_12565*
 Podgorski T. — *FM1_10741*
 Pogorelov D. — *SM17_10893*
 SM17_11640 *SM17_11688*
 SM26_11589
 Pohorecki R. — *FM8_12311*
 Polach P. — *SM17_10647*
 Polezhaev V.I. — *FM15_11929*
 FSM7_11869
 Poloukhina O.E. — *FM9_11433*
 Polyakov N.V. — *SM25_11716*
 Polyzos D. — *SM1_12845*
 Pommier S. — *SM8_12228*
 Poncet S. — *FM24_10506*
 Ponta F. — *FM25_11676*
 Ponte Castañeda P. — *SM18_11005*
 Ponter A.R.S. — *SM27_11201*
 Pop O. — *SM9_10429*
 Popov Y.P. — *FM15_11893*
 Popp K. — *SM25_12322*
 SM2_12086
 Pouget J. — *SM10_12093*
 Pouliquen O. — *FM16_11749*
 FM17_11751 *FM17_11775*
 Powers T.R. — *MS2_11866*
 Pozorski J. — *FM24_10564*
 Pozorski Z. — *SM24_12628*
 Pozrikidis C. — *FM18_10766*
 Prat M. — *FM12_11343*
 Preumont A. — **SL13_10930** (p. 287)
 Price W.G. — *FM2_12320*
 FSM4_11833 *SM25_11834*

- Princevac M. — *FM9_12738*
 Prioris S. — *FM5_10984*
 Proczek M. — *FM21_11364*
 Prokunin A.N. — *FM18_11460*
 Prosperetti A. — *FM10_11909*
 Prunet-Foch B. — *FM4_11954*
 Pukhnachov V.V. — *MS5_11757*
 Pumir A. — *FM22_12048*
 Purini R. — *MS6_13017*
 Putelat T. — *SM2_12563*
 Putin G.F. — *FM7_10538*
 FM7_12267
 Puzzi S. — *FSM6_11224*
 Py C. — *FSM4_11801*
 Pyryev Y. — *SM2_11481*
 Pyrz R. — *SM13_10244*
 SM13_12489
- Q**iu X. — *FM24_11488*
 Qiu Z. — *FM4_10753*
 Qu J. — *SM8_11686*
 Querin O.M. — *SM24_11623*
 Quey R. — *SM14_12421*
 Quilliet C. — *FSM5_11095*
 Quintard M. — *FM12_10234*
- R**abaud M. — *FM17_13029*
 FM24_11814
 Radkowski S. — *SM25_12977*
 Radler K.-H. — *FM19_12120*
 Rafai S. — *FM8_13025*
 Raftoyiannis I.G. — *SM22_11172*
 Raghu Prasad B.K. — *SM9_10419*
 Rajasekhar G.P. — *FM17_11876*
 Rajchenbach J. — *FM17_10959*
 Ramachandra L.S. — *SM13_12531*
 Ramaswamy A. — *SM3_10098*
 Rambod E. — *FM1_12784*
 Ramm E. — *SM4_11414*
 Ramos A. — *FM4_12437*
 Randles P.W. — *SM1_10829*
 Rao R.R. — *FM18_10983*
 Raszillier H. — *FM14_11413*
 Ravasoo A. — *SM11_11620*
 Ravi-Chandar K. — *SM9_12378*
 Razi Y.P. — *MS5_10980*
 Read P.L. — *FM22_12545*
 MS6_12494
 Reardon P.T. — *FM16_11725*
 Rebow M. — *FM21_11364*
 Redelsperger J.-L. — *MS6_10513*
 Rega G. — *FSM2_12129*
 Regnier V. — *FM15_12591*
 Regucki P. — *FM25_12836*
 Reinaud J.N. — *MS6_11336*
 Reinelt D.A. — *FSM5_10597*
 Reinl A. — *FM4_12254*
- Rejniak K.A. — *MS2_10689*
 Rekik A. — *SM13_11507*
 Ren M. — *FM7_11251*
 Ren W. — *SM7_10492*
 Ren Z. — *FSM4_10826*
 Renotte A. — *FM11_12602*
 Resagk C. — *FM19_12605*
 Resseguier T. de — *SM18_11110*
 Rethore J. — *SM1_11797*
 Reusch F. — *SM4_10865*
 Rhines P.B. — *SL14_12781*
 Ribeiro P. — *SM25_12759*
 Ricci S. — *SM4_11406*
 Richard P. — *FM17_12883*
 Richard T. — *SM25_12535*
 Richiardone R. — *MS6_13017*
 Richterova J. — *FSM3_11247*
 Ricken T. — *SM15_10198*
 Ricoeur A. — *SM9_11045*
 Riedel J.J. — *SM20_11845*
 Rill G. — *SM26_11672*
 Rindt C.C.M. — *FM7_11251*
 Ringgaard S. — *FM1_11851*
 Rinoshika A. — *FM24_12004*
 Riou H. — *SM25_11246*
 Ris V.V. — *FM7_12730*
 Risbet M. — *SM8_12228*
 Risso F. — *FM20_12139*
 Rochinha F.A. — *SM10_13018*
 Rodi W. — *FM6_11348*
 Rodriguez M.A. — *FM8_11670*
 Rodriguez-Ramos R. — *SM13_11176*
 Rodzewicz M. — *SM8_11371*
 Rogachevskii I. — *FM10_12070*
 FM7_11053
 Rohan E. — *SM10_11671*
 Roig V. — *FM20_12383*
 Rojiani K.B. — *FSM7_12752*
 Rosakis A.J. — *SM2_11987*
 Rosenthal B. — *SM22_12084*
 Rossky P.J. — *MS3_12132* (p. 217)
 Rothenburg L. — *SM20_10866*
 Rother M.A. — *FM8_12329*
 Roumi F. — *SM13_10483*
 Roux S. — *SM4_12021*
 Roy A. — *SM18_11820*
 Roy D. — *SM25_10750*
 Rozhkov A. — *FM4_11954*
 Rozvany G.I.N. — *SM24_11623*
 Ruan H.H. — *SM5_11051*
 Ruban A.I. — *FM2_11397*
 Rubin M.B. — *SM1_12584*
 Rubinstein A.A. — *SM9_11626*
 Rudi Y.A. — *FM25_12032*
 Rudnyi E.B. — *SM24_11316*
 Rueberg T. — *SM15_11119*
 Ruimy C. — *SM6_11901*

- Ruith M.R. — *FM13_11995*
 Ruith M. — *FM13_12425*
 Ruo A.C. — *FM9_11294*
 Ruoff R.S. — **MS3_11594** (p. 303)
 Rusinek A. — *SM14_10046*
 SM18_10734
 Rymuza Z. — *SM2_10999*
 Ryzhak E.I. — *SM12_10867*
- S**
 Saada R.A. — *SM2_12082*
 Saanouni K. — *SM4_11885*
 Sabina F.J. — *SM13_11176*
 Sackmann E. — **SL15_11327** (p. 313)
 Sadlej K. — *FM16_10993*
 Sadowski T. — *SM7_11617*
 Saez A. — *SM9_11321*
 Safarik P. — *FM5_12219*
 Safran S.A. — **MS2_12811** (p. 329)
 Sahn D. — *FM1_12784*
 Saida S. — *FM8_11299*
 Saif T. — *MS3_12705*
 Saint-Jalmes A. — *FSM5_12212*
 Saintillan D. — *FM16_12005*
 Saito T. — *FM5_11049*
 Sakalo V.I. — *SM2_12559*
 Sakiyama T. — *SM19_12224*
 Saksala T. — *SM24_10621*
 Salalha W. — *FM4_12319*
 Salem A. — *FM13_12766*
 Salin D. — *FM20_12092*
 Salmon J.-B. — *MS4_12047*
 Salupere A. — *SM11_11813*
 SM11_12568
 Sam C.-H. — *SM1_12458*
 Sam Han J. — *SM24_11316*
 Samborski S. — *SM7_11617*
 Samsonov A.M. — *SM11_10114*
 Samsonowicz J. — *SM25_12977*
 Sanches C.T. — *SM25_11494*
 Sanchez U. — *FM20_11189*
 Sanchis A. — *FSM4_12956*
 Sano O. — *FM17_11876*
 FM17_11883
 Sanomura Y. — *SM18_11350*
 Santaoja K. — *SM4_10960*
 Santiago J.G. — **MS4_12961** (p. 343)
 Sapountzakis E.J. — *SM1_10665*
 Sarkar S. — *FM24_11116*
 Sarler B. — *FM7_11160*
 Sarout J. — *SM15_12713*
 Sartorius D. — *FM24_12675*
 Sato K. — *SM15_10790*
 SM19_10770
 Sato M. — *SM7_10691*
 Saussine G. — *SM17_11361*
 Sauzay M. — *SM18_12697*
 Savic L. — *FM2_12030*
- Saville D.A. — *SL16_10529*
 Savova R. — *SM6_10972*
 Sayir M.B. — *SM11_11085*
 Sburlati R. — *SM6_12987*
 Scarella G. — *SM2_12382*
 Schaeffer N. — *FM19_12330*
 Schanz M. — *SM15_11119*
 Scheichl B. — *FM2_11083*
 Scheimberg S. — *SM24_10594*
 Schenkel T. — *FM5_11864*
 Schiehlen W. — *SM17_11223*
 SM17_12134
 Schjoedt-Thomsen J. — *SM13_12489*
 Schlogl S.M. — *SM14_11625*
 Schmid M. — *FM9_12626*
 Schmid P. — *FM11_12305*
 Schmidt C.F. — **MS2_10709** (p. 355)
 Schmidt M.J. — *SM20_12779*
 Schmidt R. — *MS1_11752*
 Schneider L.C.R. — *SM15_12903*
 Schnerr G.H. — *FM5_12066*
 Schranz C. — *SM19_11021*
 Schrefler B.A. — *SM15_12114*
 Schreurs P.J.G. — *SM1_12131*
 Schroeder W. — *FM25_12690*
 Schuette H. — *SM4_12088*
 Schulte H. — *SM16_12417*
 Schulze D. — *FM19_12290*
 Schulze T.P. — *FM21_12768*
 Schumacher J. — *FM22_10896*
 Schuster M. — *FM6_12337*
 Schwarz U. — *MS2_12811*
 Scott R.A. — *SM11_12772*
 Sederman A.J. — *FM21_11320*
 Sedlak P. — *MS1_12637*
 Segev R. — *SM6_11523*
 Seguin P. — *SM17_12539*
 Segurado J. — *SM13_11080*
 Seidel C. — *SM25_12785*
 Seiden G. — *FM16_11884*
 Seifried R. — *SM17_12134*
 Sejnoha M. — *SM23_12380*
 Selezov I. — *SM11_11401*
 Self B.P. — *FSM7_12642*
 Sellier A. — *FM19_10025*
 Semenov Y.A. — *FM8_10580*
 Semenova I.V. — *SM11_10114*
 Semler C. — *FSM4_11078*
 Semma E. — *FM15_11386*
 Seon T. — *FM20_12092*
 Serebryakov V. — *FM5_12066*
 Sergeichev I.V. — *SM20_10374*
 Sergeant A. — *FM7_12220*
 Serre E. — *FM25_12080*
 Seto T. — *SM10_12461*
 Seyranian A.P. — *SM22_11939*
 Shakeri M. — *SM13_13009*

- Shaqfeh E.S.G. — *FM16.12005*
 Shardakov I.N. — *SM6.12289*
 Sharma P. — *MS3.11474*
 Sharp R.S. — *SM26.10701*
 Shasholko D.I. — *SM2.10999*
 Shchennikov V.V. — *SM7.12272*
 Shemer L. — *FM20.11655*
 FM26.10245
 Shen C. — *SM1.11580*
 Sheng P. — *FM4.11165*
 Sherbaum V. — *FM3.12199*
 Shergold O. — *MS2.10988*
 Sheu T.W. — *FM1.11187*
 Shevchenko I.V. — *FM12.10199*
 Shevchenko K.V. — *SM2.12559*
 Shevchuk V. — *SM2.11697*
 Shevtsov I.Y. — *SM24.11015*
 Shi D.-L. — *MS3.12314*
 Shibutani Y. — *SM23.12571*
 Shillor M. — *SM2.11452*
 Shimizu M. — *FM8.11299*
 Shimokawa S. — *MS6.11732*
 Shimomura Y. — *FMS6.11862*
 Shimoyama K. — *FM9.11164*
 Shindo Y. — *SM13.11426*
 SM13.11610 *SM9.11425*
 Shiono Y. — *SM17.12582*
 Shishkina E. — *SM25.11055*
 Shklyaev S.V. — *FM7.12344*
 Shleykel A.L. — *FM7.13005*
 Shodja H.M. — *SM13.10483*
 Shrira V.I. — *FM13.12233*
 FM26.12087
 Shrivastava S.C. — *SM22.11653*
 Shtern V. — *FM19.10235*
 FM25.10683
 Shulzhenko M. — *SM2.10211*
 Shy S.S. — *FM22.12209*
 Shyshkanova G. — *SM2.11611*
 Sichermann W.M. — *FMS4.11912*
 Sideman S. — *MS2.11148*
 Sidoroff F. — *SM14.12747*
 Sielamowicz I. — *FM17.11169*
 Siemaszko A. — *SM1.12579*
 Sigmund O. — *SM24.11744*
 Silva E.C.N. — *SM10.12665*
 Silveira Neto A. — *FM6.11456*
 Silvestre N. — *SM22.12558*
 Simons G. — *MS3.12384*
 Simpson J.E. — *FM25.12051*
 Simes F.M.F. — *SM12.12682*
 Sinclair G.B. — *FMS3.11704*
 Sinka C.I. — *SM15.12903*
 SM15.12917
 Sira E. — *FM6.10857*
 Siso-Nadal F. — *FM19.11124*
 Sittner P. — *MS1.12637*
 Skali S. — *FM13.10185*
 Skews B.W. — *FM5.11072*
 Skotheim J. — *MS2.11581*
 Skrzypek J.J. — *SM4.11796*
 Sladek J. — *SM10.10836*
 SM19.11238
 Sladek V. — *SM10.10836*
 SM19.11238
 Slobozhanin L.A. — *MS5.12447*
 Sławianowski J.J. — *FMS3.12406*
 Słowicka A. — *FM4.12910*
 Smas P. — *SM24.11634*
 Smeulders D.M.J. — *SM11.11271*
 Smirnov E.M. — *FM7.12730*
 Smirnov S. — *FM3.11888*
 Smirnovskii A.A. — *FM7.12730*
 Smith F.T. — *FM2.11210*
 Smits A. — *SM13.12818*
 Smyth A.W. — *MS1.13007*
 So R.M.C. — *FM6.10163*
 Soares M.E.S. — *SM25.11494*
 Sobczyk K. — **CL.10697** (p. 19)
 Sobieczky H. — *FM5.10945*
 Sofonea M. — *SM2.11452*
 Sokołowska R. — *SM25.12984*
 Sokołowski J. — *SM24.10052*
 SM24.11486
 Soldati A. — *FM20.13012*
 Sommeria J. — *FM9.12410*
 MS6.11547 *MS6.12494*
 MS6.12601
 Soomere T. — *FM9.12099*
 Sorensen J.N. — *FM13.13019*
 Sorokin S. — *FMS1.11337*
 Sotera M.R. — *FMS2.12972*
 Sottos N.R. — *MS1.11685*
 MS1.13011 *MS1.13010*
 Sousa J.M.M. — *FM3.12348*
 Souza L.C.G. — *SM3.13004*
 Souza L.F. — *FM13.12381*
 Sparks R.S. — *FM17.10524*
 Spelt P.D.M. — *FM8.12106*
 Spencer A.J.M. — *SM10.12273*
 Spiegel E. — **SL17.10158** (p. 365)
 Spiegl M. — *SM27.11981*
 Squires T.M. — *FM16.12452*
 MS4.11777
 Sreenivasan K.R. — *FM22.10896*
 Srigiriraju S.V. — *MS2.11866*
 Staalhand J. — *MS2.10670*
 Stachurski A. — *SM4.12333*
 Staicu A.D. — *FMS5.12373*
 Staquet C. — *FM26.12424*
 Staroszczyk R. — *FM18.10297*
 Stavroulakis G. — *SM3.11036*
 Steblyanko P.A. — *SM1.11202*
 Steen M. — *FM12.12617*

- Steenhoven A.A. van — *FM7.11251*
 Stefanelli R. — *FSM1.12586*
 Stefani F. — *FM19.12613*
 Stegmann J. — *SM24.12098*
 Steigenberger J. — *SM25.11699*
 Steinberg L. — *FSM3.11140*
 Steindl A. — *SM22.11816*
 Steinmann P. — *FSM3.12392*
 SM12.11277 SM1.11211
 SM1.12924
 Steinrueck H. — *FM2.12030*
 Stepan G. — *FSM2.10252*
 Stepanova L.V. — *SM4.11779*
 Stephan P. — *FM14.12293*
 Stevanovic-Hedrih K. — *SM17.10624*
 Stewart D.S. — **MS4.12976** (p. 379)
 Stichel S. — *SM26.11795*
 Stieglitz R. — *FM19.10931*
 Stijnman M. — *FM10.11909*
 Stiller J. — *FM19.12587*
 Stokes Y.M. — *FM8.11855*
 Stolpe M. — *SM24.12302*
 Stone H.A. — *FM16.12056*
 FM1.12423 MS4.12966
 Storakers B. — *SM2.11365*
 Stoychev G.B. — *SM18.11953*
 Stremmler M.A. — *FM22.12158*
 Striz B. — *FSM3.11247*
 Strozik M.D. — *FM10.11916*
 Struzewska J. — *FM9.12592*
 Stulov A. — *SM1.10728*
 Stupkiewicz S. — *SM2.12553*
 Styczek A. — *FM6.12565*
 Su A. — *FM3.10367*
 Sudak L. — *SM6.12122*
 Sudhakar V. — *SM25.12984*
 Sugano N. — *SM17.12537*
 Sugii T. — *MS2.12192*
 Sugimoto N. — *FSM1.10294*
 Sugimoto T. — *FM1.10132*
 Sugiura T. — *SM11.12418*
 Sugiura Y. — *SM25.12593*
 Suiker A.S.J. — *SM13.12680*
 SM14.10648
 Sukoriansky S. — *MS6.11152*
 MS6.11942
 Sullivan J.M. — *FSM5.10597*
 Sun H. — *FM10.10445*
 Sun L. — *SM10.10135*
 Sun M. — *FM5.11049*
 Sun Q. — *SM14.12881*
 Sun Y. — *SM8.11686*
 Sundaresan S. — *FM20.12397*
 Sung Lee H. — *SM8.12034*
 Suponitsky V. — *FM13.11461*
 Suzuki T. — *FM11.12387*
 FSM1.11561
- Svendsen B. — *SM4.10865*
 Swaters G.E. — *MS6.10634*
 Swevers J. — *SM16.11282*
 Swift F.J. — *SM26.10909*
 Swinney H.L. — *SL18.10495*
 Symens W. — *SM16.11282*
 Sypeck D.J. — *FSM5.12395*
 Szabo R. — *FM21.11362*
 Szalai R. — *FSM2.10252*
 Sze K.Y. — *SM9.11568*
 Szekrenyes A. — *SM13.11747*
 Szmyd J.S. — *FM7.12173*
 FM7.13022
 Szmyd J. — *FM22.12610*
 Szojda L. — *SM4.11228*
 Szumbariski J. — *FM6.12565*
 Szumowski A. — *FM11.11918*
 Szwaba R. — *FM5.12997*
 Szymczak P. — *FM12.11994*
 Szymczyk J.A. — *FM21.11331*
 FM7.11905
 Szyszkowski W. — *SM3.12756*
- Świtoński E. — *SM25.12770*
- T**abaei A. — *FM26.10762*
 FM26.11199
 Tabeling P. — *MS4.12047*
 MS4.12130 MS4.12536
 MS4.12673 MS4.12960
 Taberlet N. — *FM17.12883*
 Tadmor G. — *FM11.12624*
 FM24.11454
 Tagawa T. — *FM7.13022*
 Taillard K. — *SM14.12225*
 Takada T. — *MS1.10821*
 Takagi M. — *SM14.11308*
 Takagi S. — *MS2.12192*
 Takahashi N. — *FM24.10937*
 Takayama K. — *FM5.11049*
 Takeda T. — *SM13.11610*
 Talagrand O. — *MS6.10803*
 Taleb L. — *SM14.12421*
 SM14.12747
 Tamai K. — *FM5.11049*
 Tamuzs V. — *FSM7.12259*
 Tan L.H. — *FM14.11477*
 Tan S.H.N. — *SM13.10412*
 Tan V.B.C. — *SM13.10412*
 Tang J.X. — *MS2.10709*
 Tang M. — *FM24.12652*
 Tang Y. — *SM9.11626*
 Tanigawa Y. — *SM10.12465*
 Tanizawa K. — *SM17.11700*
 SM3.10879
 Tanno H. — *FM5.11049*
 Tardu S. — *FM11.11394*

- Tarn J.-Q. — SM10.10364
 Tarnai T. — SM1.11482
 SM25.11384
 Tartar M. — FM13.10640
 Tatsumi T. — FM24.12151
 Tauchert T.R. — MS1.12018
 Tay A.A.O. — SM1.12901
 Tay T.-E. — SM13.10412
 Taya M. — SM10.12978
 Tcholakova S.S. — FM8.11669
 Tejchman J. — SM15.12358
 Telega J.J. — FM12.11248
 FSM3.11642 MS2.12100
 SM13.11895 SM13.12667
 SM13.12732 SM1.12562
 SM2.11452
 Ten Hagen T.L.M. — FM1.11900
 Teodorczyk A. — FM3.12911
 Terletska K.V. — SM11.11377
 Tesdall A.M. — FM5.11730
 Teymur M. — SM11.10891
 Thermann K. — SM12.10996
 Thess A. — FM19.11120
 FM19.11906 FM19.12090
 Thiria B. — FM11.12736
 Thite S. — SM1.12441
 Thivolle-Cazat E. — MS6.11547
 Thomas P.J. — MS6.10261
 Thomer O. — FM25.12690
 Thompson A.F. — FM21.11328
 Thomsen J.J. — SM25.12694
 SM25.11679
 Tian J. — FSM5.12395
 Tian Z. — SM9.12174
 Tigoiu V.M. — FSM3.11638
 Tihon J. — FM14.12656
 Tilgner A. — FM19.12125
 Timchenko V. — FM15.11386
 Ting E.C. — SM1.10270
 Ting L. — FM25.11683
 Tkachev P.V. — SM12.12223
 Tobushi H. — MS1.10821
 SM14.11308
 Tokarzewski S. — FSM3.11642
 SM13.11895 SM13.12667
 Toland J.F. — FM26.11290
 Toll S. — SM15.12518
 Tomita Y. — SM12.11432
 Topolnikov A.S. — FM8.12190
 Toropov V. — SM24.12870
 Touhei T. — SM1.10274
 Tran-Cong T. — FSM5.12435
 Travnicek Z. — FM11.12258
 Trębicki J. — SM11.11682
 Trevelyan P. — FM14.10220
 Troger H. — SM22.11816
 Trostinetsky E. — FM20.11655
 Trotsyuk A. — FM5.10531
 Trulsen J. — FM19.11809
 Trumel H. — SM18.11110
 Trzciński R. — FM8.12873
 Trzebicki M. — SM13.12560
 Tsai J.C. — FM17.12445
 Tsai P.-S. — SM16.12712
 Tsamopoulos J. — FM14.12858
 FM18.12859
 Tsekhmister Y.V. — FM26.11591
 Tsemakh D. — FM8.11250
 Tsepoura K.G. — SM1.12845
 Tsubota K.-I. — FM1.12522
 Tsubota K. — MS2.12453
 Tsuru T. — SM23.12571
 Tsutahara M. — FM26.11746
 Tsyppkin G.G. — FM21.11926
 Tuck E.O. — FM8.11855
 Tucker P.G. — FM24.12430
 Tuckerman L.S. — FM13.10640
 FM13.12431
 Tuckerman L. — FM6.10921
 FM7.10914
 Tuliszka-Sznitko E. — FM25.12080
 Tumin A. — FSM1.12477
 Tur M. — SM8.10698
 Turner M.R. — FM2.12241
 Turska E. — SM24.12679
 SM9.11910
 Turteltaub S. — SM14.10648
 Tutty O.R. — FM2.12320
 Tvergaard V. — SM9.10910
 Tylikowski A. — SM10.10045
 Tyliczszak A. — FM3.11914
 Tyrkiel E. — FSM2.11416
 Ualiev Z. — FM3.11031
 Ualiyev G. — SM17.10533
 Ualiyev Z.G. — SM17.10533
 Ubachs R.L.J.M. — SM1.12131
 Udwdia F.E. — SM3.11163
 Ugawa A. — FM17.11883
 Uhl T. — SM7.12799
 Uj J. — SM13.11747
 Ulbrich R. — FM20.11745
 FM20.12886
 Ulrych B. — SM2.10211
 Ungarish M. — FM16.11884
 MS6.11585
 Urban D. — SM5.12043
 Ursem N.T.C. — FM1.11900
 Ustohalova V. — SM15.10198
 Vadillo J.L. — FM11.10872
 Vainchtein D. — FM22.12439
 Vakakis A.F. — SM25.10408
 Vakhitova N.K. — FM8.12190
 Vakhrouchev A.V. — SM1.12054

- Valance A. — *FM17_12883*
 Valdek U. — *SM7_12551*
 Valle V. — *SM9_10429*
 Valtorta D. — *MS2_12064*
 Valverde J. — *SM17_12071*
 Van Brussel H. — *SM16_11282*
 Van Hemelrijck D. — *SM13_12818*
 Vanden-Broeck J.-M. — *FM26_11345*
 FM26_12715
 Vanneste J. — *MS6_12104*
 Varghese S. — *FM9_12980*
 Varhsney K. — *FM15_12349*
 Varyanychko M.A. — *SM19_11815*
 Vasiljev P. — *SM16_10900*
 Vasudeva Murthy A.S. — *FM9_12980*
 Velasco Fuentes O.U. — *FM25_12748*
 Vennemann P. — *FM1_11900*
 Verecke B. — *SM4_10974*
 Veres I.A. — *SM11_11085*
 Vereshchaka S.M. — *SM19_10071*
 Veron F. — *MS6_12722*
 Versluis M. — *FM17_10253*
 FM1_12400
 Vesenjak M. — *FSM4_10826*
 Viallat A. — *FM1_12423*
 Viatkina E.M. — *SM1_12723*
 Viba J. — *FSM7_12259*
 Vidya Sagar R. — *SM9_10419*
 Vierendeels J. — *FM6_11602*
 Vignes-Adler M. — *FM4_11954*
 Villafruela J.M. — *FM8_11670*
 Villermaux E. — *FM22_10532*
 FM22_12326 FM8_11317
 Vimmr J. — *FM6_11702*
 Vinod N. — *FM2_12631*
 Viovy J.-L. — *FM4_11209*
 Vit T. — *FM11_12258*
 FM2_12062
 Vitkova V. — *FM1_10741*
 Vlachogiannis M. — *FM14_10557*
 Voigt L.K. — *FM23_10247*
 Volkov K.N. — *FM20_10416*
 Volkova V.E. — *SM25_12632*
 Volles R. — *SM1_11298*
 Vollmann J. — *MS3_12384*
 Vorobev A.M. — *MS5_12402*
 Voyiadjis G.Z. — *SM18_10393*
 Vu-Delcarte C.D. — *FM15_12636*
- W**aarsing J.H. — *MS2_11808*
 Waclawczyk M. — *FM24_10564*
 Wada S. — *FM1_12522*
 MS2_12453
 Wadley H.N.G. — *FSM5_12395*
 Wagner C. — *FM8_11462*
 Wagner S. — *FM24_12675*
 Wahi P. — *SM25_12814*
- Wajnryb E. — *FM16_11409*
 FM18_11300 FM8_11411
 Walenta Z.A. — *FM3_12911*
 FM4_12910 MS4_10971
 Walker P.G. — *FM1_11851*
 Wall D.P. — *FM13_12291*
 Walsh A.M. — *FM17_12338*
 Wan F.S. — *FM8_12596*
 Wan Y. — *MS1_12016*
 Wang C.-Y. — *SM1_10270*
 Wang C. — *FM8_12596*
 SM1_11580
 Wang D.W. — *FM26_11230*
 Wang H.-T. — *SM9_11568*
 Wang H. — *SM1_11720*
 Wang J. — *SM11_11099*
 Wang L.-S. — *SM16_12712*
 Wang M. — *MS3_12132* (p. 217)
 Wang P. — *SM1_11720*
 SM9_12174
 Wang R.-Z. — *SM1_10270*
 Wang Z. — *SM9_12174*
 Weaire D. — **MS5_10598** (p. 387)
 Weber J.E. — *FM26_11803*
 Weber M. — *SM16_12758*
 Wei M. — *FSM1_10907*
 Wei Q. — *MS6_12194*
 Wei Y. — *MS3_11279*
 Weichen S. — *SM10_10501*
 Weichert D. — *SM13_12588*
 SM18_12058
 Weidman P. — *FM26_11199*
 FM2_11984 FSM4_11986
 Weier T. — *FM11_12068*
 Weigand B. — *FM10_10445*
 Weir G.J. — *SM2_11008*
 Weiss D.A. — *FM4_12254*
 Weitsman Y.J. — *SM13_11014*
 Weiwen L. — *SM24_12287*
 Welch K. — *SM7_12551*
 Wen W. — *FM4_11165*
 Weronko J. — *SM22_12934*
 Wesfreid J.E. — *FM11_12736*
 Westerweel J. — *FM10_11088*
 FM1_11900
 Wheeler L. — *MS3_11474*
 White J.M. — *MS3_12132* (p. 217)
 White S.R. — *MS1_13010*
 MS1_13011
 Whitesides G.M. — *MS4_12966*
 Widmann R. — *SM15_10198*
 Wiercigroch M. — *FSM2_11302*
 SM11_12481 SM25_10470
 Wierschem A. — *FM14_10642*
 FM14_10928
 Wieteska R. — *FM6_12618*
 Więckowski Z. — *SM20_10231*

- Wiggins S. — FM22.11293
 Wijeyewickrema A.C. — SM11.12514
 Wijngaarden L. van —
 OL_10498 (p. 1)
 Willers B. — FM21.12365
 Williams P.D. — MS6.12494
 Willis J.R. — SM13.11782
 SM2.12563
 Wilmański K. — SM11.10612
 Wilson H.J. — FM16.11473
 Wilson M. — FM7.10438
 Wingerde A.M. van — SM13.12318
 Winter R.M. — MS3.12132 (p. 217)
 Wiśniewski K. — SM19.12328
 SM24.12679 SM9.11910
 Witkowski A.S. — FM10.11916
 Witkowski W. — FM3.12911
 SM19.11890
 Wnuk M.P. — SM9.10250
 Wojciechowski J. — FM11.11918
 Wojnar R. — SM13.12732
 Wolański P. — FM3.12745
 FM3.12843
 Wong Y.W. — SM22.11097
 Woods A.W. — FM21.11926
 Worster M.G. — FM21.11270
 FM21.11320 FM21.11328
 FM21.12276
 Woude D. van der — FM22.12633
 Woznica K. — SM18.12339
 Wriggers P. — SM1.12534
 SM1.12584
 Wu D. — SM9.12492
 Wu J. — SM4.12036
 Wu L. — FM15.12591
 SM10.11551
 Wuest A. — FM9.12626
 Wurz W. — FM24.12675
 Wysocki M. — SM15.12518
- X**ia M. — SM7.11764
 Xiao Q.Z. — FSM6.11806
 Xing T.J. — FSM4.11833
 SM25.11834
 Xiong A.-K. — FM11.12491
 Xiong P.Y. — SM25.11834
 Xu H. — MS5.10714 (p. 229)
 Xu X. — SM7.11764
- Y**adav A. — FM3.12348
 Yamaguchi E. — MS4.11607
 Yamaguchi T. — FM1.12522
 MS2.12453
 Yamamoto K. — SM17.11700
 SM3.10879
- Yamashita K. — FSM1.10294
 Yamasue K. — FSM2.12014
 Yamazaki Y.H. — MS6.12494
 Yang J. — SM1.11580
 Yang S. — FM4.11165
 SM8.11737
 Yang X. — FM24.10149
 Yang Y. — FSM4.12521
 Yano J.-I. — MS6.12140
 Yao Z. — SM1.11720
 Yaremchuk V.P. — FSM7.11869
 Yarin A.L. — FM4.10932
 Yasinskyi A. — SM2.11697
 Yasniy P.V. — SM8.11920
 Yau J.-D. — SM3.11287
 Yazdi S.S.H. — SM25.11904
 Yazykov V. — SM26.11589
 Yevdokymov D.V. — MS5.10958
 Yin H. — SM10.10135
 Yokosawa S. — FM1.12522
 Yokota K. — FM8.11299
 Yoo W.-S. — SM17.10893
 Yoon Y. — FM8.11289
 Yoshida F. — SM24.12870
 SM27.12450
 Yoshimura T. — FM24.12151
 Yoshinaga T. — FM14.11739
 Youn S.-K. — SM24.11826
 SM27.11827
 Young K.Y. — SM24.12185
 Young T.H. — SM25.11867
 Yourdkhani A. — SM13.10189
 Yu S. — SM9.11934
 Yu T.X. — SM5.11051
 Yuan T.H. — FM22.12209
- Z**abielski L. — FM19.12979
 Zachara A. — FM8.12873
 Zaera R. — SM18.10734
 Zahn M. — FM4.11982
 Zairi F. — SM18.12339
 Zajac D. — FM20.12886
 Zakharov V.E. — FM26.10861
 Zaleski S. — FM8.11614
 FM8.11723
 Zametaev V.B. — FM2.11780
 Zammali C. — SM11.12763
 Zampolli M. — FSM1.11373
 Zangeneh M.S. — SM25.11904
 Zaoui A. — SM13.11507
 SM13.11805
 Zardecki D. — SM26.11832
 Zavala-Garay J. — MS6.12776
 Zavaliangos A. — SM15.12917
 Zboiński G. — SM1.11389
 Zeidis I. — SM25.11699
 Zeilstra C. — FM17.10253

- Zelinger Z. — *FM9_10467*
 Zeman J. — *SM23_12380*
 Zeman V. — *SM25_11759*
 Zenit R. — *FM8_11026*
 Zenkovskaya S.M. — *FM7_13005*
 Zhang C. — *SM10_10836*
 Zhang K. — *FM7_12168*
 MS6_12169
 Zhang N.-H. — *FSM2_12674*
 Zhang R. — *SM8_11686*
 Zhang R. — *SM27_10906*
 Zhang W.W. — *FM8_12429*
 Zhang X. — *FM26_11680*
 Zhao X. — *SM17_11020*
 Zhao Y.-P. — *SM16_10510*
 Zheltovodov A.A. — *FM24_10455*
 Zheng L. — *SM9_12174*
 Zheng X.J. — *MS3_12486*
 Zheng X. — *SM6_11998*
 Zhou C. — *SM8_12391*
 Zhou M. — *MS3_10105*
 Zhou W. — *SM1_12901*
 Zhou Y.C. — *MS3_12486*
 SM13_12496 *SM9_12492*
 Zhou Y. — *FM24_12004*
 FSM4_12521
 Zhu H.X. — *FSM5_11292*
 Zilitinkevich S. — *FM7_11053*
 Zimmermann K. — *SM25_11699*
 Zinchenko A.Z. — *FM8_12329*
 FM8_12741
 Ziopaja K. — *SM24_12628*
 Ziółkowski M. — *FM19_12605*
 Zitha P.L.J. — *FSM5_12986*
 Zmitrowicz A. — *SM2_11613*
 Zouhar G. — *FM21_12365*
 Zussman E. — *FM4_10932*
 FM4_12319
 Żochowski A. — *SM24_11486*
 Żukowski J.M. — *FM10_11916*
 Życzkowski M. — *SM24_12075*